THE UNIVERSITY OF CHICAGO

ENERGY-CONVERTING METAL-ORGANIC NANOMATERIALS FOR BIOMEDICAL AND PHOTOCATALYTIC APPLICATIONS

A DISSERTATION SUBMITTED TO
THE FACULTY OF THE DIVISION OF THE PHYSICAL SCIENCES
IN CANDIDACY FOR THE DEGREE OF
DOCTOR OF PHILOSOPHY

DEPARTMENT OF CHEMISTRY

BY

GUANGXU LAN

CHICAGO, ILLINOIS

AUGUST 2020

Table of contents

List of Figures

List of Tables

List of Abbreviations

$^{\bullet}OH$	hydroxyl radicals
$^1O_2$	singlet oxygen
2D	two-dimensional
AcOH	acetic acid
AFM	atomic force microscopy
APF	aminophenyl fluorescein
BET	Brunauer-Emmett-Teller
BIH	1,3-dimethyl-2-phenyl-2,3-dihydro-1H-benzo[d]imidazole
BMPO	5-tert-butoxycarbonyl-5-methyl-1-pyrroline-N-oxide
BNAH	1-benzyl-1,4-dihydronicotinamide
bpy	2,2’-bipyridine
BTB	benzene-1,3,5-tribenzoate
CLSM	confocal laser scanning microscope
CRT	calreticulin
CV	cyclic voltammogram
DBB	4,4'-di(4-benzoato)-2,2'-bipyridine
dF(CF_3)ppy	2-(2,4-difluorophenyl)-5-(trifluoromethyl)pyridine
DLS	dynamic light scattering
DMA	dimethylamine
DMF	N,N-dimethylformamide

DPV	differential pulse voltammetry
DSB	double strand break
EDS	energy-dispersive X-ray spectroscopy
ELISPOT	enzyme-linked immunoSpot
EPR	electron paramagnetic resonance
ET	electron transfer
EtBr	ethidium bromide
EXAFS	extended X-ray absorption fine structure
FFT	fast Fourier transform
FITC	fluorescein isothiocyanate
GC	gas chromatography
GSH	glutathione
GSSG	glutathione disulfide
H_2O_2	hydrogen peroxide
H_3BPY	4',6'-dibenzoato-[2,2'-bipyridine]-4-carboxylic acid
H_4TBP-Zn	5,10,15,20-tetra(*p*-benzoato)porphyrinatozinc
HAADF	high-angle annular dark-field
HER	hydrogen evolution reaction
HRMS	high resolution-mass spectrum
HRTEM	high-resolution transmission electron microscopy
IC_{50}	half maximal inhibitory concentration
ICD	immunogenic cell death

ICP-MS	inductively coupled plasma mass spectrometry
IR	infrared
K_{SV}	Stern-Völmer constant
LED	light-emitting diode
LMCT	ligand to metal charge transfer
MLCT	metal-to-ligand charge transfer
MOF	metal-organic framework
MOL	metal-organic layer
MTS	3-(4,5-dimethylthiazol-2-yl)-5-(3-carboxymethoxyphenyl)-2-(4-sulfophenyl)-2H-tetrazolium
nMOF	nanoscale metal-organic framework
nMOL	nanoscale metal-organic layer
NP	nanoparticle
O_2	oxygen
O_2^-	superoxide
PBS	phosphate buffer solution
PDT	photodynamic therapy
POM	polyoxometalate
PS	photosensitizer
PXRD	powder X-ray diffraction
REF_{10}	radiation enhancement factors at 10% cell survival
RITC	rhodamine-B isothiocyanate

RNO	4-nitroso-N,N-dimethylanaline
ROS	reactive oxygen species
RT-RDT	radiotherapy and radiodynamic therapy
SBU	secondary building unit
SET	single electron transfer
SOSG	Singlet Oxygen Sensor Green
TBAH	tetrabutylammonium hydroxide
TBP	5,10,15,20-tetra(*p*-benzoato)porphyrin
TEM	transmission electron microscopy
TEOA	triethanolamine
TFA	trifluoroacetic acid
TFE	trifluoroethanol
TGA	thermogravimetric analysis
TOF	turnover frequency
TON	turnover number
XANES	X-ray absorption near edge spectroscopy
XAS	X-ray absorption spectroscopy
X-PDT	X-ray induced photodynamic therapy
XPS	X-ray photoelectron spectroscopy

Abstract

Guangxu Lan: Energy-Converting Metal-Organic Nanomaterials

for Biomedical and Photocatalytic Applications

Under Direction of Professor Wenbin Lin

Metal-organic frameworks (MOFs), an emerging class of crystalline inorganic-organic hybrid materials constructed from metal or metal-oxo secondary building units (SBUs) and organic or metal-containing bridging ligands, have been intensively explored over the past two decades. Characterized by structural regularity and tunability, compositional diversity, and intrinsic porosity, MOFs have shown tremendous potential in gas storage and separation, catalysis and photocatalysis, and biomedical imaging and therapy, among other areas. Particularly, these structural advantages of MOFs present a unique opportunity for energy-converting photoreactions, in which MOFs can hierarchically incorporate both sensitizers to capture the photons, including X-ray photons and visible-light photons, and catalysts to convert the energy of these captured photons into high-energy molecules, such as reactive oxygen species (ROSs) and solar fuels. The proximity of these incorporated components (<2 nm) within MOFs allows for facile energy transfer, in the form of electromagnetic waves or moving particles (electrons or reactive intermediates), leading to efficient energy-converting reactions and, in certain instances, unparalleled synergy between these functional subunits.

By carefully modifying synthetic conditions, two evolved classes of MOFs are

achieved either by scaling down the size of MOFs to the nanoscale regime, affording nanoscale metal-organic frameworks (nMOFs), or by reducing the dimensionality of MOFs to a single layer (<2 nm in thickness), affording metal-organic layers (MOLs). nMOFs, while inheriting all aforementioned merits of conventional MOFs, also possess advantageous characteristics of nanomaterials, such as the enhanced permeability and retention (EPR) effect and strong biocompatibility, which engender nMOFs as promising candidates for biomedical applications. On the other hand, MOLs are two-dimensional with high specific surface areas, which not only eliminates diffusion constraints of MOFs, but also allows for post-synthetic surface functionalization through carboxylate-exchange modifications.

In my research, I designed and synthesized a series of MOFs, nMOFs, and MOLs, systematically studied their growth mechanisms, and investigated their interactions with photons, including X-ray and visible-light photons, leading to unique energy-converting applications.

Chapter 1 of this thesis generally discusses the design strategy of MOFs and MOLs. The composition diversity and structural regularity of MOFs and MOLs provide an ideal platform to incorporate multifunctional components to realize synergetic energy-converting reactions.

Chapter 2 and 3 describe the rational design of nMOFs for photodynamic therapy (PDT). In this section, I designed and synthesized two photosensitizing nMOFs, Fe-TBP and Ti-TBP, to realize hypoxia-overcoming PDT and type-I PDT, respectively. Upon light irradiation, Fe-TBP enabled a cascade reaction, in which tumor-enriched hydrogen peroxide (H_2O_2) was transformed into molecular oxygen (O_2) by Fe-based SBUs through a Fenton-like reaction and subsequently converted into singlet oxygen ($^1O_2$) by excited porphyrin-derived TBP ligands.

Ti-TBP was obtained as a new MOF, constructed from Ti-oxo chain SBUs and TBP ligands. Upon light irradiation, the proximity between TBP ligands and Ti-oxo SBUs enabled facile electron transfer from excited TBP* ligands to redox-active Ti^{4+} to simultaneously generate TBP^{+} and Ti^{3+}. The generated Ti^{3+} reduced O_2 to propagate the sequential generation of superoxide (O_2^{-}), H_2O_2, and hydroxyl radicals ($^{\bullet}OH$), realizing the first nMOF-based type I PDT.

Chapter 4 through chapter 6 describe the rational design of nMOFs/MOLs for radiotherapy and radiodynamic therapy (RT-RDT). In this section, I designed and synthesized a series of nMOFs/nMOLs, including Hf_{12}-DBB-Ir, W_{18}@Hf_{12}-DBB-Ir, Hf_{12}-DBB-Ir(F), Hf_6-BPY-Ir(F), Hf_6-BPY-Ir, and Hf_6-BPY-Ru as radioenhancers. These nMOFs/MOLs are constructed with high-Z Hf-oxo SBUs to harvest the energy of radiation and with photosensitizing ligands to convert this energy to generate ROSs, including $^{\bullet}OH$, $^1O_2$, and O_2^{-}. In the case of W_{18}@Hf_{12}-DBB-Ir, Wells-Dawson-type $[P_2W_{18}O_{62}]^{6-}$ (W_{18}) polyoxometalates (POMs) were loaded into the cavities of Hf_{12}-DBB-Ir to further enhance the harvest of radiation energy and to efficiently convert this energy to produce O_2^{-}. By generating these ROSs, the nMOFs/MOLs enabled RT-RDT to elicit superb anti-cancer efficacy with low-dose X-ray irradiation.

Chapter 7 describes the rational design of MOLs for bioimaging. In this section, I reported the design of the first nMOL biosensor for ratiometric pH and oxygen sensing in mitochondria. Cationic Hf_{12}-Ru nMOL was solvothermally synthesized by laterally connecting Hf_{12} SBUs with oxygen-sensitive $Ru(bpy)_3^{2+}$-derived DBB-Ru ligands. The Hf_{12}-Ru nMOL was then covalently functionalized with pH-sensitive fluorescein isothiocyanate (FITC) and pH/oxygen-

independent Rhodamine-B isothiocyanate (RITC) through thiourea linkages to afford Hf_{12}-Ru-F/R as a mitochondria-targeted ratiometric sensor for pH and O_2 in live cells.

Chapter 8 through chapter 10 describe the rational designs of MOFs/MOLs for artificial photosynthesis and photocatalysis. In this section, I developed three MOF/MOL systems (Ru-TBP, Hf_{12}-DBB-Ru-Re, and Hf_{12}-Ir-Ni MOL), hierarchically assembling photosensitizers and catalysts into the same MOFs/MOLs for photocatalytic hydrogen evolution, CO_2 reduction, and C-S, C-O, and C-C coupling reactions, respectively. In the case of Ru-TBP, photosensitizing porphyrin and catalytic Ru_2 paddlewheels were incorporated into the TBP ligands and SBUs, respectively. In the case of Hf_{12}-DBB-Ru-Re, photosensitizing $Ru(bpy)_3^{2+}$ and catalytic $Re(bpy)(CO)_3Cl$ were combined into the DBB-Ru ligands of Hf_{12}-DBB-Ru MOLs and the capping moieties of these MOLs, respectively. In the case of Hf_{12}-Ir-Ni MOL, the photosensitizing $Ir(bpy)[dF(CF_3)ppy]_2^+$ and catalytic $Ni(bpy)Cl_2$ were incorporated into the bridging and capping ligands, respectively. The proximity between these photosensitizers and catalysts allows for efficient electrons or activated intermediate transfer, achieving highly activated hydrogen evolution, CO_2 reduction, and C-S, C-O, and C-C coupling.

Chapter 11 describes the rational design of Metal-organic-Zyme (MOZ). In this section, I present a new form of artificial enzyme, a MOZ, with metal centers, amino acids, and cofactors integrated into a MOL for efficient and selective conversion of CO_2 to CH_4. Evolution of this MOZ system through amino acid substitution enhances catalytic activity through proton coupled electron transfer and stabilization of reactive intermediates by hydrogen bonds. Optimization of MOZs with stabilized intermediates afforded a turnover frequency for CH_4 generation under direct sunlight of 150.7 h^{-1} with >99% selectivity.

Chapter 12 describes the Ligand-directed MOF synthesis. In this section, I present an inverted pathway toward MOF synthesis where organic ligands first organize into a molecular scaffold which is subsequently intercalated by metal ions in a process of ligand-directed crystal engineering (LDCE). This LDCE approach was demonstrated through the construction of an isostructural MOF library incorporating each naturally occurring transition metal in Groups 5 through 12. The incorporation of diverse metal ions into this isostructural family affords highly tunable electronic structures allowing systematic optimization of photocatalytic activities within a conserved framework.

Acknowledgement

The past five years as a PhD student at the University of Chicago have been a great scientific journey. At the conclusion of my doctoral studies, I would like to acknowledge many people for helping, accompanying, and supporting me.

First, I would like to express my deepest thanks and respect to my PhD advisor, Professor Wenbin Lin, the most important person in my scientific career. He has offered me a singular platform to learn and tremendous support in following my scientific aspirations. In Professor Lin's multidisciplinary group, I have been exposed to many fields of research, from molecular chemistry to material science, from photocatalysis to biomedical technology, and from fundamental sciences to real-world applications. Beyond providing this breadth of knowledge, Professor Lin has shared his love, passion, and rigorous attitude towards science. Professor Lin is always steadfast in the face of unknowns, adventurous in the pursuit of the untapped knowledge, and relentless in his aims of discovery, all while pursuing impactful applications of his science. He has offered himself as a scientific ideal for me to live up to and will encourage me for the remainder of my scientific career.

Second, I would like to thank Professor Chun-Hua Yan at Peking University, another very important person in my scientific career. When I was an undergraduate student, he provided me with the opportunity to join his group and the RESIM family, which began my scientific career. I cherish the memories of our three years working closely together. Furthermore, during my PhD studies he has continued to provide me with guidance and enthusiasm through our numerous emails. He has continued to encourage and challenge me to set high scientific goals

and to never be satisfied with just my current achievements. I also want to thank Professors Ya-Wen Zhang and Ling-Dong Sun at Peking University, two additional advisors during my undergraduate studies, who have taught me much about chemistry and prepared me well for my graduate studies.

I would like to thank Professors Chuan He, John Anderson, and Bozhi Tian. Each of these individuals has been incredibly supportive throughout my graduate studies and has continued to provide me with constructive queries and suggestions. I would also like to thank Professors Chuan He and John Anderson for serving on my defense committee.

I would like to thank the staff members in University of Chicago and Argonne National Lab. I to thank Dr. Yu-Sheng Chen and Alexander Filatov for sharing their knowledge of crystallography; Dr. Yimei Chen and Dr. Fengyuan Shi for help with electron microscopy; and Dr. Qiti Guo and Dr. Justin Jurller for help with MRSEC facilities.

I would like to thank Samuel Veroneau, a great research partner and best friend. Sam was the first undergraduate I worked with during my PhD and we spent two productive and enjoyable years together in the lab. He is very smart, hardworking, optimistic, and humorous, (and is also my best English teacher). I hope he has a successful graduate career at Harvard.

I would also like to thank my research collaborators: I thank Kaiyuan Ni for collaboration on many biomedical projects; Yingjie Fan for his hard work on many interesting projects; Zhe Li and Wenjie Shi for their computational works; and Drs. Yuanyuan Zhu and Yangjian Quan for their help with organic catalysis.

I would like to thank the other members of my lab as well: I first want to thank the senior members, Dr. Kuangda Lu, Dr. Zekai Lin, Dr. Christina Chan, Dr. Pengfei Ji, and Dr. Nining

Guo for taking care of me, particularly when I first joined the lab, and for teaching me numerous laboratory techniques. I further want to thank the junior members, Eric You, Maolin Wang, Ziwan Xu, and Geoffrey Nash for their hard work during our time together. I also want to thank all the other lab members present during my time, Dr. Dan Micheroni, Dr. Xiaopin Duan, Dr. Ruoyu Xu, Dr. Youfu Wang, Wenbo Han, Yang Song, Dr. Shuyi Li, Dr. Kui Yang, Xuanyu Feng, Taokun Luo, Xiaomin Jiang, Dr. Xiang Ling, Deyan Gong, Yunhong Pi, Youyou Li for all their help and support.

I would like to thank my many friends at the University of Chicago. I thank Dr. Yu Zhong, Dr. Yin Fang, Dr. Mingzhan Wang, Dr. Yiliang Lin, Dr. Yuanwen Jiang, Dr. Yuanyuan Wang, Dr. Zhao Wang, Dr. Hailing Shi, Tong Wu, Zhi Wang, Chengpeng Wang, and Jiaxin Xie for their continual help, advice, and support in both my research and my life.

Finally, I would like to thank my family for their unconditional love and support my whole life. Particularly, I would like to thank my girlfriend and soulmate Ge Zhang for her love in the last five years. Although we are on different sides of the globe much of the time, our hearts are always with one another. She has always stood firmly beside me, encouraging me to chase my scientific dreams. Meeting you is the most beautiful thing in my life.

Chapter 1. Energy-Converting Systems Based on Metal-Organic Frameworks and Metal-Organic Layers

1.1 Metal-Organic Frameworks (MOFs)

Metal-organic frameworks (MOFs) are a class of hybrid materials composed of inorganic secondary building units (SBUs) and organic ligands (**Figure 1-1**).[1] These SBUs, generally metal ions or metal-oxo clusters, are interconnected by bridging ligands, generally organic molecules or metal-organic complexes with at least two coordinating groups (e.g., carboxylate groups) in terminal positions, to afford MOF structures. These ordered connections (e.g., metal-carboxylate coordination) afford the porous and crystalline nature of MOFs and further determine their properties and functions.

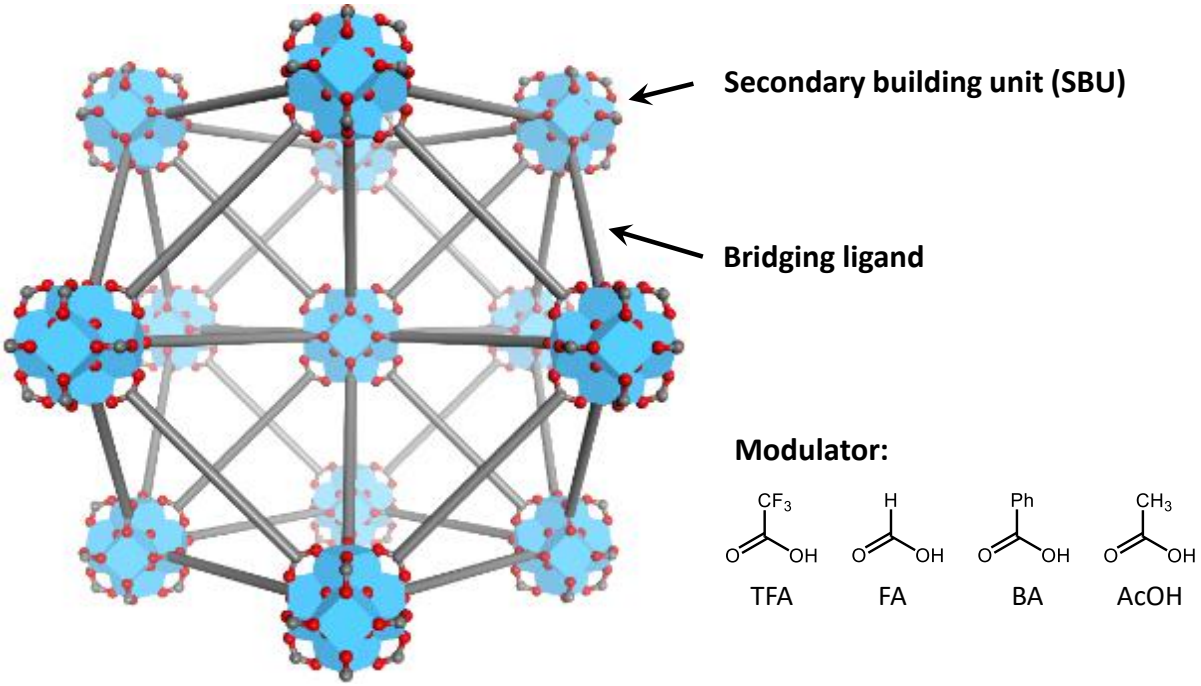

Figure 1-1. Schematic illustrating the structures and fundamental components of MOFs.

Classically, the synthesis of MOFs is driven by the interactions of metal ions and synthetic modulators (e.g., trifluoroacetic acid (TFA), formic acid (FA), benzoic acid (BA), and acetic acid (AcOH), **Figure 1-1**) which form incipient SBUs, often through the formation of metal-

carboxylate bonds.[2, 3] These incipient SBUs are subsequently interlinked by the aforementioned bridging organic ligands in entropically-favorable processes to generate MOF structures.[4] A variety of MOF structures have been realized through this general strategy, engendering the field of reticular chemistry.[5] This synthetic strategy leverages four distinct components: (1) various metal ions (e.g. Zr, Hf, Zn, Cu, Al) can be utilized to form SBUs; (2) For a particular metal, various SBUs can be formed by tuning modulators and synthetic conditions; (3) For a particular SBU, MOFs with different topological structures can be generated by employing bridging ligands with varying geometries (i.e., the geometry of terminal coordination sites); (4) For bridging ligands of the same geometry, MOFs with the same topological structures can form to provide different functionalities by tuning the length or attendant functional groups of these bridging ligands.

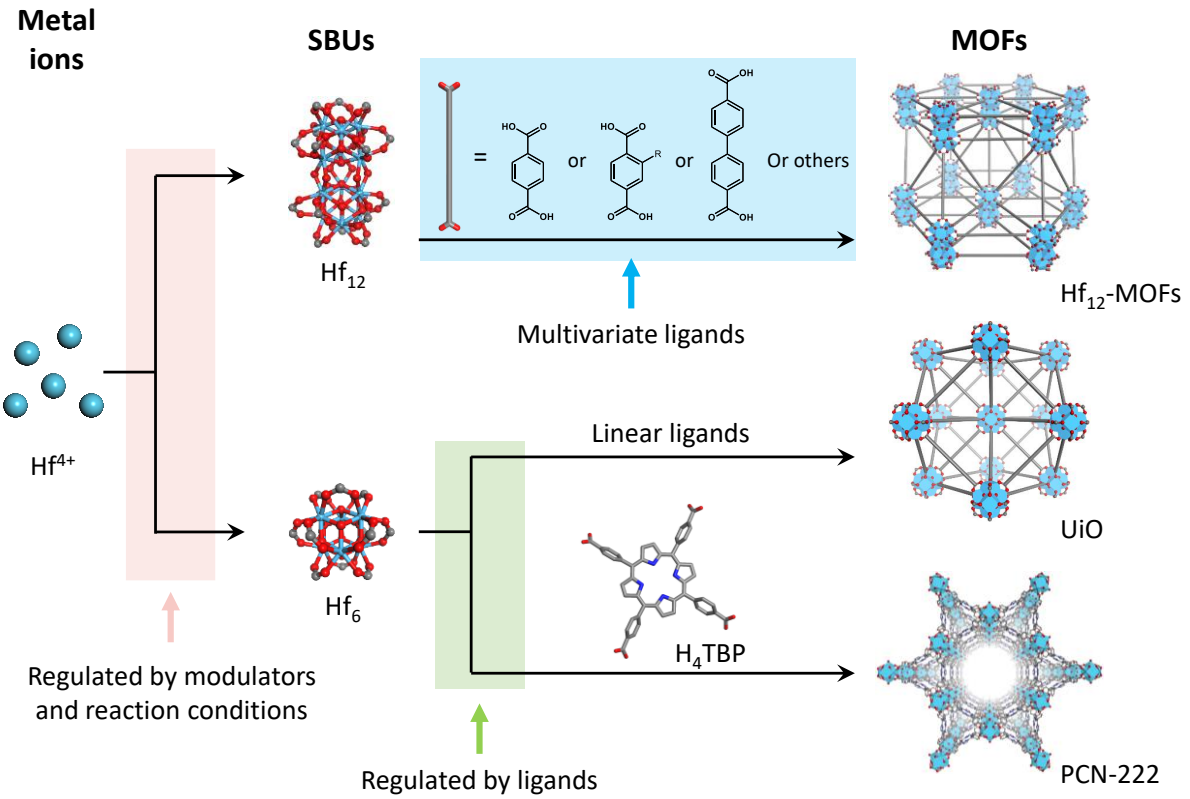

Figure 1-2. Schematic showing the SBU-directed pathway toward MOF synthesis.

This strategy is outlined in **Figure 1-2** where, for example: (1) Hf^{4+} is selected to initiate the MOF synthesis; (2) two distinct Hf-oxo SBUs, Hf_{12} and Hf_6, with formulations of $[Hf_{12}(\mu_3\text{-}O)_8(\mu_3\text{-}OH)_8(\mu_2\text{-}OH)_6(TFA)_{18}]$ and $[Hf_6(\mu_3\text{-}O)_4(\mu_3\text{-}OH)_4(CH_3COO)_{12}]$, respectively, are formed from modulators of TFA and AcOH, respectively; (3) Hf_6 SBUs can form different topological structures, UiO and PCN-222, by choosing ligands of linear and cruciform geometries, respectively; (4) Hf_{12}-MOFs constructed from Hf_{12} SBUs and linear ligands can afford various functionalities by tuning the lengths of (e.g., by connected additional phenyl rings) and by installing functional groups onto bridging ligands.

Although over 10,000 MOF structures have been generated through this strategy, the requisite initial formation of SBUs demands strong interactions between metal ions and modulators, preventing certain metals (e.g. soft metal ions and noble metals) from being incorporated into MOFs within these metal nodes entirely. To overcome these limitations and further expand the versatility and scope of MOFs, a new and distinct ligand-directed pathway for MOF synthesis is proposed in **Chapter 12**.

The diversity in structures emerging from reticular chemistry engenders two properties unique to MOFs in comparison to other materials. First, numerous combinations of SBUs and bridging ligands have provided MOFs with high yet tunable porosities. MOFs have thus shown tremendous potential in gas storage and separation. Second, their diversity in components yet regularity in structure has allowed MOFs to incorporate varied and multifunctional subunits, making MOFs themselves multifunctional materials. In particular, MOFs present unique opportunities for driving energy-converting photoreactions, which will be discussed in details in **section 1.3**.

1.2 Metal-Organic Layers (MOLs)

2D materials, exemplified by graphene and transition metal dichalcogenides, have been intensively studied owing to their favorable electronic and optical properties.[6-8] For applications in catalysis and photocatalysis, 2D materials can in principle obviate diffusion barriers to enhance activities. The intrinsically high surface areas of such 2D materials allow for the installation of various functionalities via surface modification to further augment activity.[9, 10] To date, however, the performance of 2D materials in photoreactions has been underwhelming, often limited by poor light-harvesting efficiency or/and low catalytic activity due to the difficulty of installing these functionalities in a controlled manner.[11, 12] It is thus of great importance to develop molecular 2D materials with synthetic flexibility and molecular tunability, to allow for the hierarchical installation of such functionalities, further enhancing photocatalytic activity over homogeneous analogues.[13-15]

As a dispersible monolayer version of MOFs, metal-organic layers (MOLs) have recently emerged as a novel class of molecular 2D materials with tremendous potential for catalytic and photocatalytic applications.[16-18] MOLs not only retain many of the advantages offered by MOFs (e.g., structural regularity/tunability and compositional diversity) but also possess the aforementioned strengths of 2D materials (e.g., high surface areas, no diffusion barriers, etc.). MOLs thus hold even greater potential in energy-converting photoreactions.

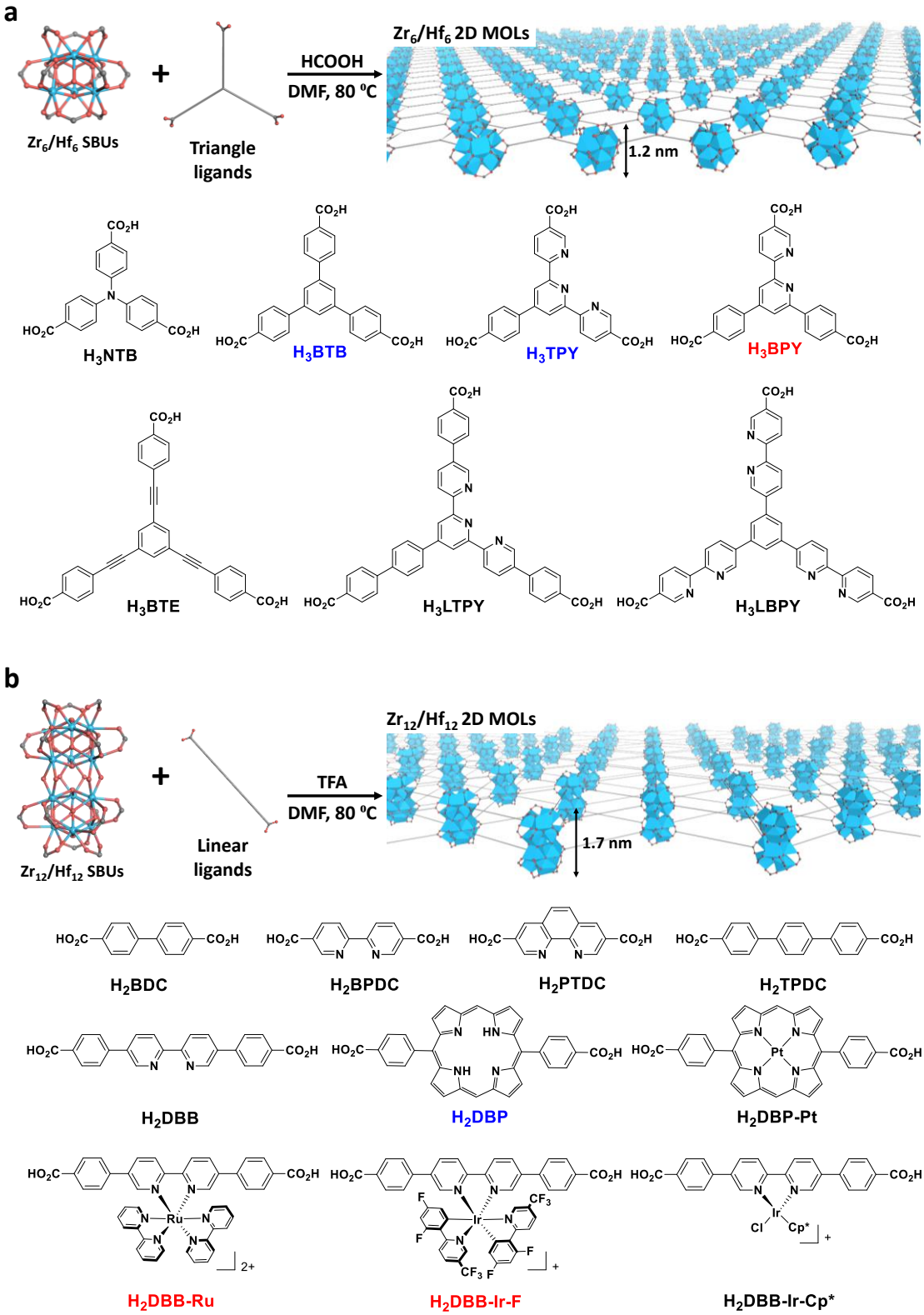

Figure 1-3. Schematic showing the synthesis and possible ligands for incorporation of Zr_6/Hf_6-MOLs (a) and Zr_{12}/Hf_{12}-MOLs (b). MOLs with the ligands highlighted in red (H_3BPY in **Chapter 4**, H_2DBB-Ru in **Chapter 7** and **9**, and H_2DBB-Ir-F in **Chapter 5**, **10**, and **11**) were reported in this thesis. MOLs with the ligands highlighted in blue (H_3BTB,[18] H_3TPY,[19] and H_2DBP[20]) were reported in other works from the Lin lab. Ligands in black are potential components for MOL synthesis, but have not been explored yet.

Compared to 2D coordination polymers, MOLs similarly exhibit high surface energies (σS). Many high index face nanoparticles (with high surface energies) have been successfully prepared via supersaturation of crystallization,[21] which reduces the energy difference ($\Delta\mu$) between the solution species (μ_l) and the crystallized ones (μ_c) as described by the Thomson-Gibbs equation $\Delta\mu = \mu_l - \mu_c = \sigma S$. We rationalized that by (1) introducing small capping molecules to reduce this surface energy, (2) creating a supersaturation of SBUs during MOL synthesis, and (3) taking advantage of differences in binding energy between lateral and vertical coordination sites of SBUs, we could realize anisotropic coordination of ligands to SBUs to afford 2D networks of MOLs. In our preliminary studies, we successfully explored two classes of free-standing MOLs: (1) the (3,6)-connected M_6-MOLs (M = Zr or Hf) with $[M_6(\mu_3\text{-}O)_4(\mu_3\text{-}OH)_4(HCO_2)_6]$ SBUs linked by triangular ligands (**Figure 1-3a**) and (2) the (2,12)-connected M_{12}-MOLs (M = Zr or Hf) with $[M_{12}(\mu_3\text{-}O)_8(\mu_3\text{-}OH)_8(\mu_2\text{-}OH)_6(CF_3CO_2)_6]$ SBUs doubly bridged by linear ligands (**Figure 1-3b**).

Here, we offer Hf_{12}-MOLs as an example to illustrate the synthetic strategy of MOLs (**Figure 1-4**). Through a solvothermal synthesis, Hf_{12} SBUs with a formulation of $[M_{12}(\mu_3\text{-}O)_8(\mu_3\text{-}OH)_8(\mu_2\text{-}OH)_6(TFA_V)_6(TFA_L)_{12}]$ (n.b., *V* and *L* describe vertically and laterally coordinating ligands, respectively) were first formed from Hf^{4+} ions and TFA and water as modulators. The increased positive charge distributed over the six interior Hf atoms of this Hf_{12} SBU relative to the six axial Hf atoms, directed the replacement of laterally coordinated TFA (TFA_L) with the carboxylate groups of linear bridging ligands, rather than of the vertically coordinated TFA (TFA_V), owing to more favorable exchange. As a result, epitaxial growth on these Hf_{12} SBU is far faster in the lateral direction than in the vertical direction, leading to the

2D nanoplate morphology of Hf_{12} SBU-based MOFs, as previously reported (**Figure 1-5c**). There exist, furthermore, specific linear ligands which *only* undergo lateral epitaxial growth on Hf_{12} SBUs, allowing monolayered Hf_{12} MOLs to be generated with a general formula of $[M_{12}(\mu_3\text{-}O)_8(\mu_3\text{-}OH)_8(\mu_2\text{-}OH)_6(TFA_V)_6(ligand)_6]$ (**Figure 1-5a,b**). These ligands, including, but not limited to, H_2DBB-Ru and H_2DBB-Ir-F, generally have electron-deficient carboxylate groups, deriving from attendant electron-withdrawing metal centers. These carboxylate groups have only weak coordination affinity for the Hf_{12} SBUs and can only replace the laterally-coordinated TFA, thus generating a MOL. These MOLs generally have a diameter of several hundreds of nanometers and a thickness of ~1.7 nm, which corresponds to the modeled height of Hf_{12} SBUs capped by TFA. As a comparison, MOF nanoplates (rather than MOLs) was synthesized from the H_2DBB-Ir ligand as H_2DBB-Ir has relatively electron-rich carboxylate groups compared to those of H_2DBB-Ir-F (**Figure 1-5c**).

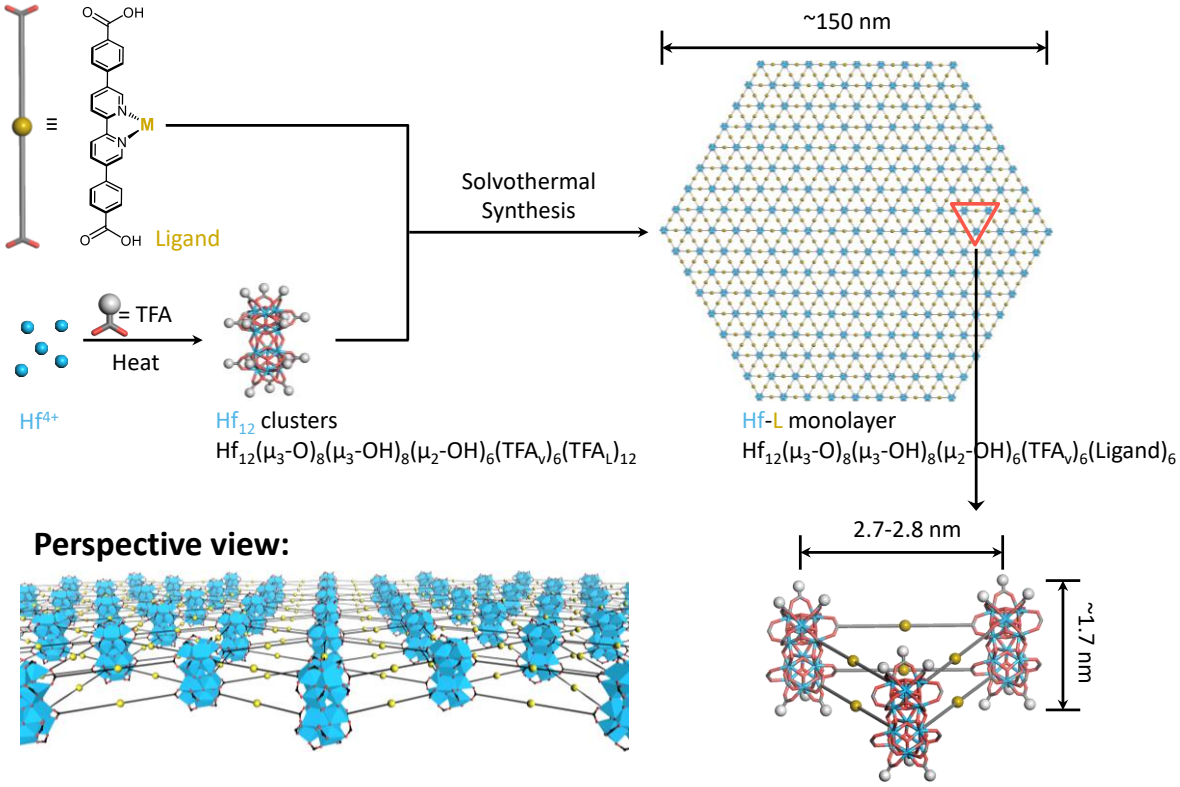

Figure 1-4. Schematic showing the synthetic route and proposed structures of Hf_{12}-MOLs.

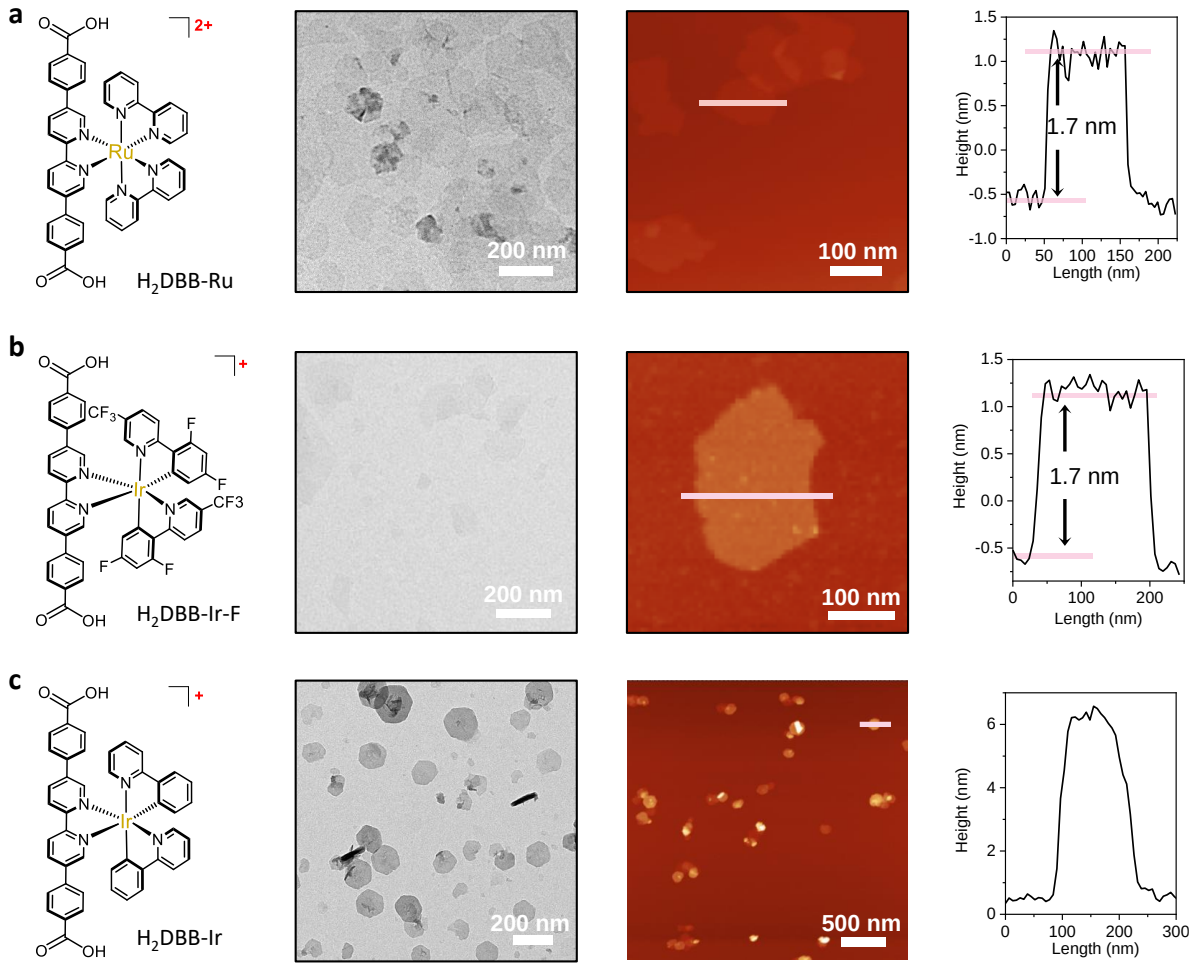

Figure 1-5. Ligands selection for Hf_{12}-MOLs. The ligand H_2DBB-Ru (a) and H_2DBB-Ir-F (b) accommodate MOL growth, while the ligand H_2DBB-Ir (c) instead affords MOF nanoplates.

MOLs can be further functionalized by replacing the remaining monocarboxylate capping groups (formate in M_6-MOLs and TFA in M_{12}-MOLs) with functional capping agents possessing monocarboxylate groups (**Figure 1-6**). By taking advantage of differences in pKa values (0.23, 3.75, 4.20, 4.76 for TFA, HCOOH, BA, and AcOH, respectively), carboxylate exchange reactions can proceed under mild conditions (from room temperature to 60 °C). Post-synthetic carboxylate exchange on MOLs can install functionalities that are difficult to incorporate into bridging ligands due to size or symmetry restriction or that are unstable under the conditions used to synthesize MOLs (viz., 80+ °C with high water and acid concentrations), allowing for the hierarchical incorporation of diverse functional moieties into both the bridging

ligands and capping agents. These functionalities (e.g. sensitizers, catalysts) can be installed onto the surfaces of MOLs in a spatially controlled manner by modifying the distinct functional groups of their SBUs and bridging ligands and so may accomplish synergistic functions, making MOLs an ideal platform for energy-converting photoreactions.

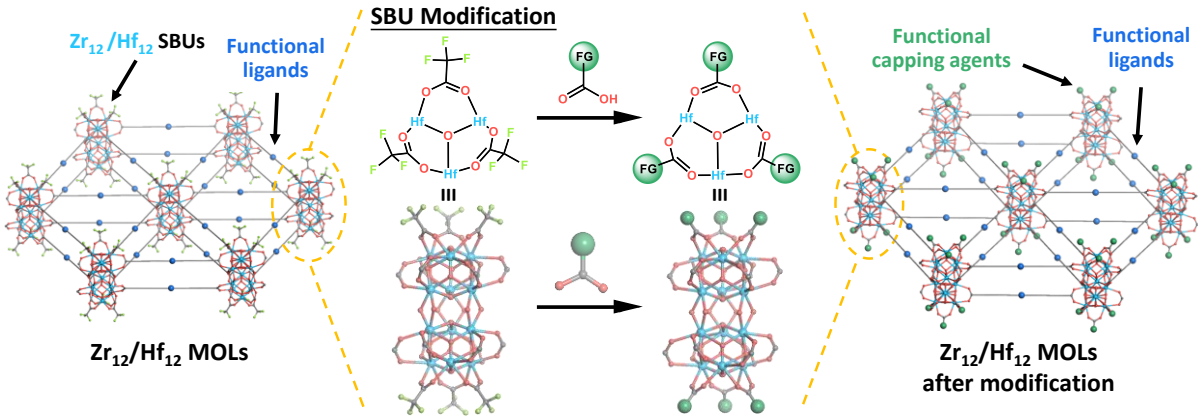

Figure 1-6. Schematic showing surface modification of MOLs.

1.3 Energy-converting photoreactions

Energy-converting systems for photoreactions generally contain two components: sensitizers and catalysts. The former can harvest the energy from the energy source (e.g. visible-light photons and X-ray photons) and transfer it to the catalyst. The later can convert and use this energy to generate high-energy molecules, such as reactive oxygen species (ROSs), fine chemicals, or solar fuels (**Figure 1-7**).

Due to their compositional diversity and structural regularity, MOFs and MOLs provide unique opportunities for energy-converting photoreactions. First, multifunctional sensitizers and catalysts can be incorporated within different subunits of MOFs/MOLs (e.g., within SBUs, bridging ligands, and capping agents). Second, the proximity of these incorporated components (<2 nm) within MOFs allows for facile energy transfer in the form of electromagnetic waves or moving particles (electrons or reactive intermediates), leading to efficient energy-converting

reactions and, in certain instances, unparalleled synergy between functional subunits (**Figure 1-7**).[22] Through combining various sensitizers and catalysts into MOFs/MOLs, these rationally-designed systems can effect energy-converting photoreactions of: visible light to generate ROSs and realize photodynamic therapy (PDT) as shown in **Chapters 2** and **3**; X-rays to generate ROSs and realize radiotherapy and radiodynamic therapy (RT-RDT) as shown in **Chapters 4**, **5**, and **6**; visible light to generate solar fuels and realize artificial photosynthesis as shown in **Chapters 8**, **9**, and **11**; and visible light to generate fine chemicals and realize photocatalysis as shown in **Chapter 10**.

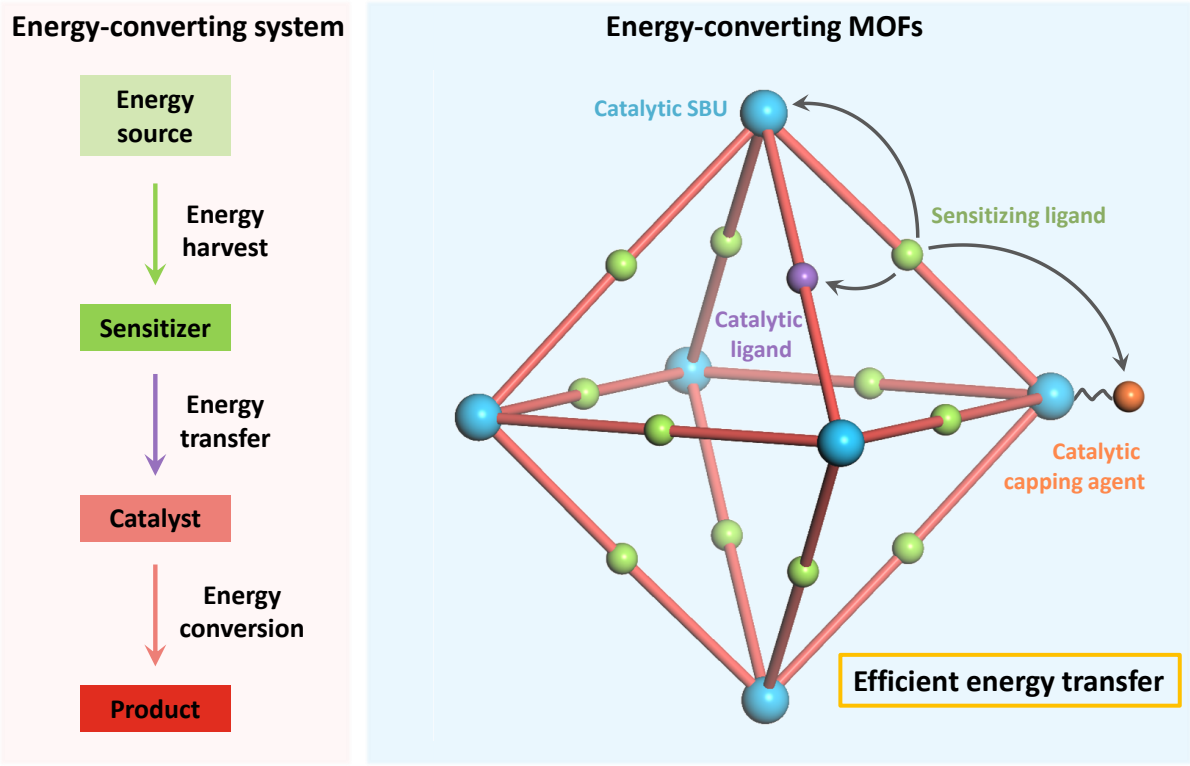

Figure 1-7. MOFs and MOLs present a unique platform for designing energy-converting systems with efficient energy transfer between their different subunits.

1.4 References

1. Furukawa, H.; Cordova, K. E.; O'Keeffe, M.; Yaghi, O. M., The Chemistry and Applications of Metal-Organic Frameworks. *Science* **2013,** *341* (6149), 1230444.
2. Eddaoudi, M.; Moler, D. B.; Li, H.; Chen, B.; Reineke, T. M.; O'Keeffe, M.; Yaghi, O. M., Modular Chemistry: Secondary Building Units as a Basis for the Design of Highly Porous and Robust Metal−Organic Carboxylate Frameworks. *Acc. Chem. Res.* **2001,** *34* (4), 319-330.
3. Rood, J. A.; Boggess, W. C.; Noll, B. C.; Henderson, K. W., Assembly of a Homochiral, Body-Centered Cubic Network Composed of Vertex-Shared Mg12 Cages: Use of Electrospray Ionization Mass Spectrometry to Monitor Metal Carboxylate Nucleation. *J. Am. Chem. Soc.* **2007,** *129* (44), 13675-13682.
4. Deng, H.; Doonan, C. J.; Furukawa, H.; Ferreira, R. B.; Towne, J.; Knobler, C. B.; Wang, B.; Yaghi, O. M., Multiple Functional Groups of Varying Ratios in Metal-Organic Frameworks. *Science* **2010,** *327* (5967), 846.
5. Yaghi, O. M., Reticular Chemistry in All Dimensions. *ACS Central Science* **2019,** *5* (8), 1295-1300.
6. Manzeli, S.; Ovchinnikov, D.; Pasquier, D.; Yazyev, O. V.; Kis, A., 2D transition metal dichalcogenides. *Nature Reviews Materials* **2017,** *2*, 17033.
7. Expanding our 2D vision. *Nature Reviews Materials* **2016,** *1*, 16089.
8. Yang, Y.; Yang, X.; Liang, L.; Gao, Y.; Cheng, H.; Li, X.; Zou, M.; Ma, R.; Yuan, Q.; Duan, X., Large-area graphene-nanomesh/carbon-nanotube hybrid membranes for ionic and molecular nanofiltration. *Science* **2019,** *364* (6445), 1057.
9. Luo, B.; Liu, G.; Wang, L., Recent advances in 2D materials for photocatalysis. *Nanoscale* **2016,** *8* (13), 6904-6920.
10. Low, J.; Cao, S.; Yu, J.; Wageh, S., Two-dimensional layered composite photocatalysts. *Chem. Commun.* **2014,** *50* (74), 10768-10777.
11. Hasani, A.; Tekalgne, M.; Le, Q. V.; Jang, H. W.; Kim, S. Y., Two-dimensional materials as catalysts for solar fuels: hydrogen evolution reaction and CO2 reduction. *Journal of Materials Chemistry A* **2019,** *7* (2), 430-454.
12. Butler, S. Z.; Hollen, S. M.; Cao, L.; Cui, Y.; Gupta, J. A.; Gutiérrez, H. R.; Heinz, T. F.; Hong, S. S.; Huang, J.; Ismach, A. F.; Johnston-Halperin, E.; Kuno, M.; Plashnitsa, V. V.; Robinson, R. D.; Ruoff, R. S.; Salahuddin, S.; Shan, J.; Shi, L.; Spencer, M. G.; Terrones, M.; Windl, W.; Goldberger, J. E., Progress, Challenges, and Opportunities in Two-Dimensional Materials Beyond Graphene. *ACS Nano* **2013,** *7* (4), 2898-2926.
13. Berardi, S.; Drouet, S.; Francàs, L.; Gimbert-Suriñach, C.; Guttentag, M.; Richmond, C.; Stoll, T.; Llobet, A., Molecular artificial photosynthesis. *Chem. Soc. Rev.* **2014,** *43* (22), 7501-7519.
14. McDaniel, N. D.; Bernhard, S., Solar fuels: thermodynamics, candidates, tactics, and figures of merit. *Dalton Trans.* **2010,** *39* (42), 10021-10030.
15. Duan, L.; Bozoglian, F.; Mandal, S.; Stewart, B.; Privalov, T.; Llobet, A.; Sun, L., A molecular ruthenium catalyst with water-oxidation activity comparable to that of photosystem II. *Nat. Chem.* **2012,** *4*, 418.

16. Lan, G.; Ni, K.; Xu, R.; Lu, K.; Lin, Z.; Chan, C.; Lin, W., Nanoscale Metal–Organic Layers for Deeply Penetrating X-ray-Induced Photodynamic Therapy. *Angew. Chem.* **2017,** *129* (40), 12270-12274.
17. Lan, G.; Li, Z.; Veroneau, S. S.; Zhu, Y.-Y.; Xu, Z.; Wang, C.; Lin, W., Photosensitizing Metal–Organic Layers for Efficient Sunlight-Driven Carbon Dioxide Reduction. *J. Am. Chem. Soc.* **2018,** *140* (39), 12369-12373.
18. Cao, L.; Lin, Z.; Peng, F.; Wang, W.; Huang, R.; Wang, C.; Yan, J.; Liang, J.; Zhang, Z.; Zhang, T.; Long, L.; Sun, J.; Lin, W., Self-Supporting Metal–Organic Layers as Single-Site Solid Catalysts. *Angewandte Chemie International Edition* **2016,** *55* (16), 4962-4966.
19. Lin, Z.; Thacker, N. C.; Sawano, T.; Drake, T.; Ji, P.; Lan, G.; Cao, L.; Liu, S.; Wang, C.; Lin, W., Metal–organic layers stabilize earth-abundant metal–terpyridine diradical complexes for catalytic C–H activation. *Chemical Science* **2018,** *9* (1), 143-151.
20. Ni, K.; Lan, G.; Chan, C.; Duan, X.; Guo, N.; Veroneau, S. S.; Weichselbaum, R. R.; Lin, W., Ultrathin Metal-Organic-Layer Mediated Radiotherapy-Radiodynamic Therapy. *Matter* **2019,** *1* (5), 1331-1353.
21. Lin, H. X.; Lei, Z. C.; Jiang, Z. Y.; Hou, C. P.; Liu, D. Y.; Xu, M. M.; Tian, Z. Q.; Xie, Z. X., Supersaturation-dependent surface structure evolution: from ionic, molecular to metallic micro/nanocrystals. *J. Am. Chem. Soc.* **2013,** *135* (25), 9311-4.
22. Zhang, T.; Lin, W., Metal–organic frameworks for artificial photosynthesis and photocatalysis. *Chem. Soc. Rev.* **2014,** *43* (16), 5982-5993.

Chapter 2. Nanoscale Metal-Organic Framework Overcomes Hypoxia for Photodynamic Therapy Primed Cancer Immunotherapy

2.1 Introduction

Cancer immunotherapy has recently emerged as a highly effective treatment strategy for several cancers. Checkpoint blockade immunotherapy, which uses antibodies to block negative immune regulatory pathways,[1] has enjoyed clinical success for several advanced diseases, such as melanoma, non-small-cell lung cancer, and renal cell carcinoma.[2, 3] However, due to insufficient activation of host immune systems, checkpoint blockade immunotherapy elicits limited rates of systemic antitumor responses for most cancers.[4] Combining checkpoint blockade immunotherapy with other immunogenic treatments is thus of great importance for increasing response rates of non-inflamed tumors.[5] In contrast to surgery, radiotherapy, and chemotherapy, which are mostly immunosuppressive, PDT causes acute inflammatory responses to alter the immunosuppressive tumor microenvironment to prime the host immune system.[6-9] Hence, PDT holds enormous potential for enhancing checkpoint blockade immunotherapy. Synergistic combination of PDT and checkpoint blockade immunotherapy, however, is rarely explored.[10, 11]

With the rapid development of molecular nanotechnology, a new class of nanophotosensitizers (nPSs) based on nMOFs have emerged as highly effective PSs for PDT. nMOF-based nPSs directly incorporate PSs as the building units rather than delivering photosensitizing cargos, allowing for unprecedentedly high PS loadings without deleterious self-quenching.[20] The porous structures of nMOF-based nPSs also facilitate the diffusion of ROS, improving the PDT efficacy of nMOFs over other nPSs. The efficacy of nPS-mediated

PDT, however, is also limited by tumor hypoxia. New nPSs are needed to function in hypoxic environments that are often encountered in human tumors.

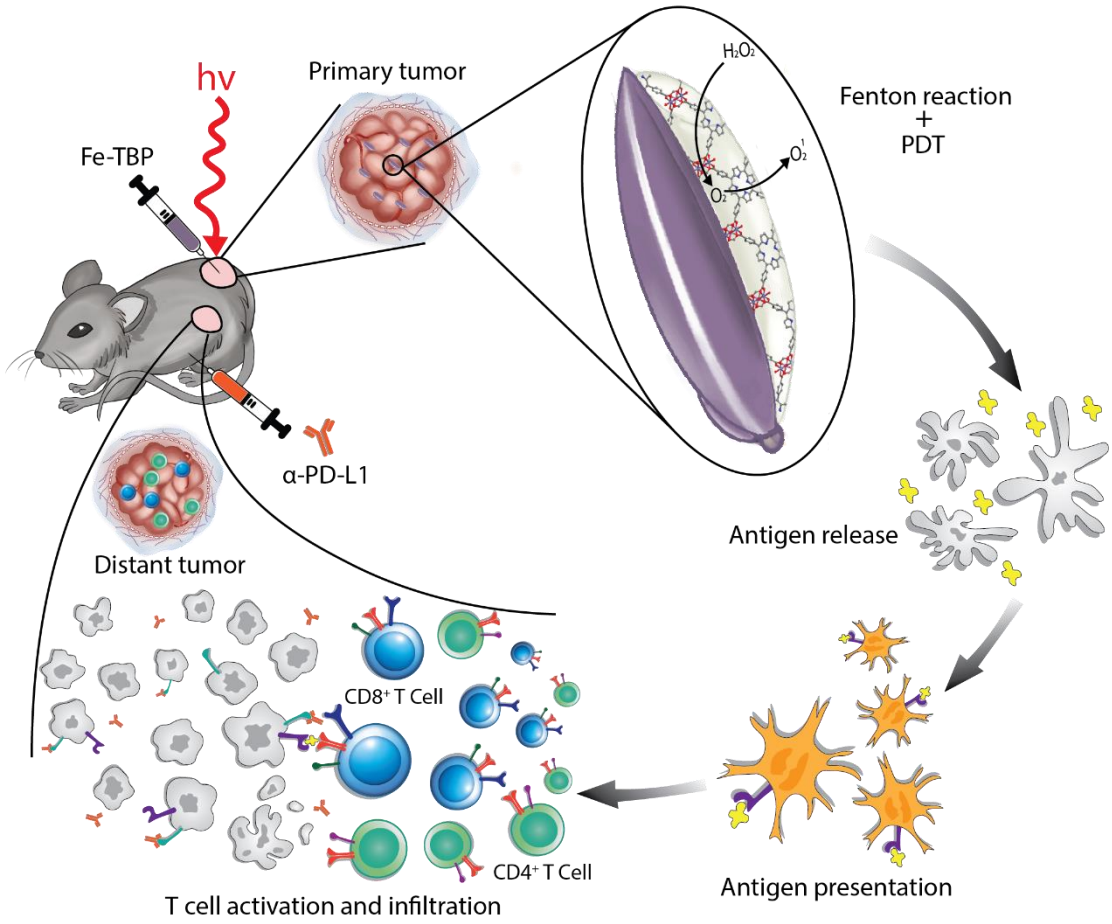

Figure 2-1. Schematic illustration of using Fe-TBP to overcome hypoxia for PDT primed cancer immunotherapy. The Fe_3O clusters in Fe-TBP decompose H_2O_2 to produce O_2 which is converted to cytotoxic $^1O_2$ by photo-excited TBP ligands to mediate immunogenic PDT. Tumor associated antigens released by PDT are presented to effector T cells to prime anti-PD-L1 checkpoint blockade immunotherapy, thereby eliciting abscopal effects.

In this Chapter, we report the design of a novel nMOF-based nPS, Fe-TBP, to overcome hypoxia and enhance cancer immunotherapy. Fe-TBP was constructed from Fe_3O clusters and TBP ligands, and, when irradiated under hypoxic conditions, catalyzed a cascade reaction in which intracellular H_2O_2 was decomposed by the Fe_3O clusters to produce O_2 through a Fenton-like reaction whereas the generated O_2 was converted to cytotoxic $^1O_2$ by photo-excited porphyrin moieties. We demonstrated that Fe-TBP mediated PDT elicited systemic antitumor

response to improve the α-PD-L1 checkpoint blockade immunotherapy, leading to the regression of both treated primary tumors and untreated distant tumors via abscopal effects (**Figure 2-1**).

2.2 Result and discussion

2.2.1 Synthesis and characterization

Fe-TBP was synthesized through a solvothermal reaction between $[Fe_3O(OAc)_6(H_2O)_3]OAc$ (OAc = acetate) and 5,10,15,20-tetra(*p*-benzoato)porphyrin (H_4TBP) with formic acid as the modulator. As-synthesized Fe-TBP showed a uniform nanorice morphology (**Figure 2-2a**). The crystallinity of Fe-TBP was confirmed by the lattice structure and fast Fourier transform (FFT) pattern in high-resolution transmission electron microscopy (HRTEM images (**Figure 2-2b**). To achieve more effective tumor accumulation of Fe-TBP, we precisely controlled the size and morphology of the Fe-TBP by tuning the concentrations of the precursors and the modulator and optimized the Fe-TBP particles to the nanorice morphology of 100 nm in length (**Figure 2-2c**), an ideal size for nanocarriers.[21]

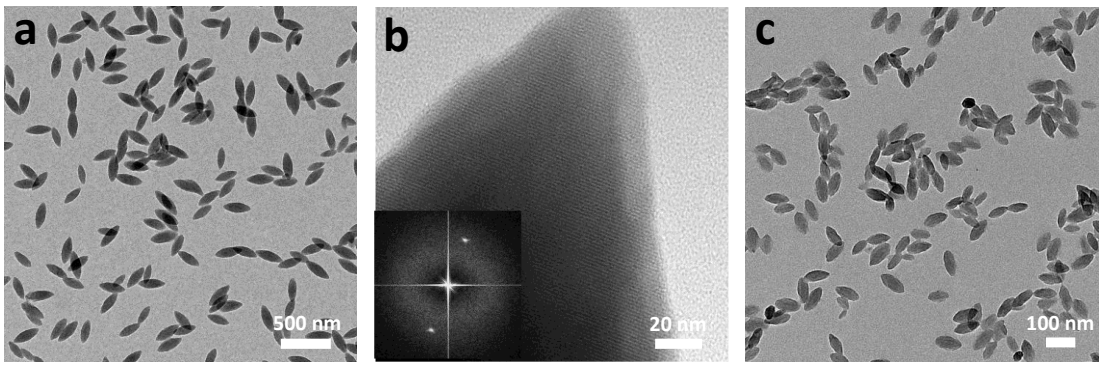

Figure 2-2. TEM images of Fe-TBP. (a) TEM image of Fe-TBP. (b) HRTEM image and FFT (inset) of Fe-TBP. (c) TEM image of optimized 100-nm Fe-TBP.

The **stp-a** topological structure of Fe-TBP was confirmed by its powder X-ray diffraction (PXRD) pattern, which is consistent with the reported PCN-600 structure (**Figure 2-3a**).[22] Fe-

TBP was formulated as $Fe_3(\mu_3\text{-}O)TBP_{1.5}(H_2O)_3(OAc)$ based on the **stp-a** topology of PCN-600. The UV-Vis spectra of Fe-TBP indicated the presence of TBP ligands (**Figure 2-3b**) whereas extended X-ray absorption fine structure (EXAFS) analysis verified the Fe coordination environments of $Fe_3O(carboxylate)_6(H_2O)_3^+$ in Fe-TBP (**Figure 2-3c**). The trivalent Fe centers were identified by X-ray absorption near edge spectroscopy (XANES). Moreover, the Fe to TBP ratio was determined to be 2.13 or 2.21 by ICP-MS and TGA respectively. The slightly higher Fe to TBP ratio is due to the nano-size of Fe-TBP and the likely presence of defects in Fe-TBP.

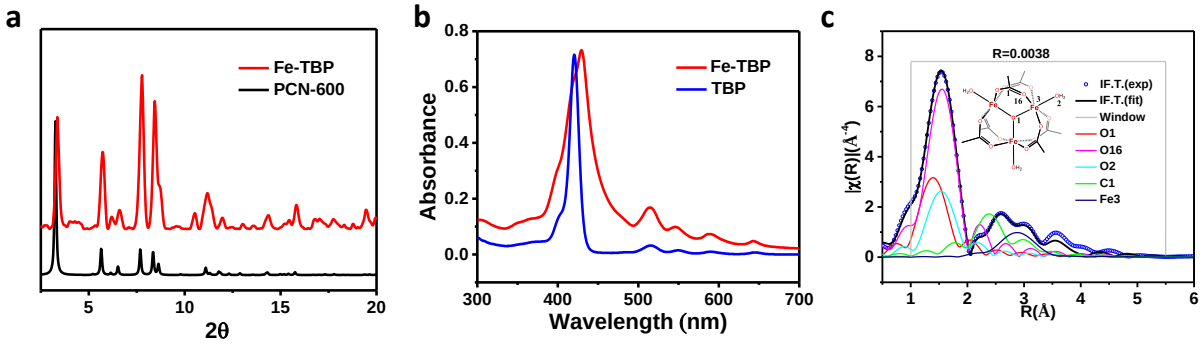

Figure 2-3. Structure characterization of Fe-TBP. (a) PXRD pattern of Fe-TBP in comparison to PCN-600. (b) UV-visible spectra of Fe-TBP and H_4TBP. (c) EXAFS fitting of Fe-TBP, showing the Fe coordination environment as $Fe_3O(carboxylate)_6(H_2O)_3^+$.

2.2.2 Fenton reaction

Because hypoxic cancer cells usually have higher H_2O_2 concentrations than normal cells, converting intracellular H_2O_2 into O_2 through a Fenton reaction is an effective way to overcome hypoxia.[23] To establish whether Fe-TBP can overcome hypoxia, we conducted several studies to determine the ability of Fe-TBP in catalyzing the decomposition of H_2O_2 to generate O_2. First, H_2O_2 at an intracellular concentration of 100 μM with or without Fe-TBP was added to an oxygen-free PBS at 37 °C. The time-dependent O_2 concentration was then detected by an oxygen sensor. As expected, a significant amount of O_2 was produced in the presence of Fe-

TBP (**Figure 2-4**).

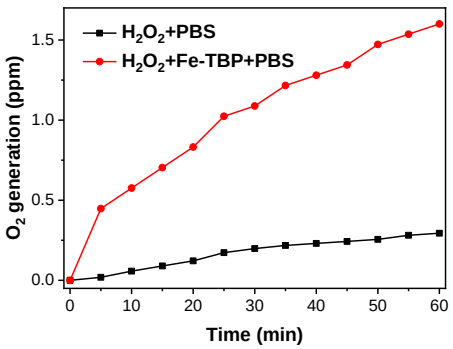

Figure 2-4. Time-dependent O_2 generation detected by an oxygen sensor.

To demonstrate the catalytic effect of Fe-TBP at the cellular level, the intracellular H_2O_2 concentration was assessed using a fluorescent peroxide assay kit. Under hypoxic conditions, strong green fluorescence was observed, indicating a high H_2O_2 level. The fluorescence intensity decreased dramatically after treatment with Fe-TBP, confirming that Fe-TBP decomposed intracellular H_2O_2, while no fluorescence decrease was observed in the H_4TBP control group (**Figure 2-5**).

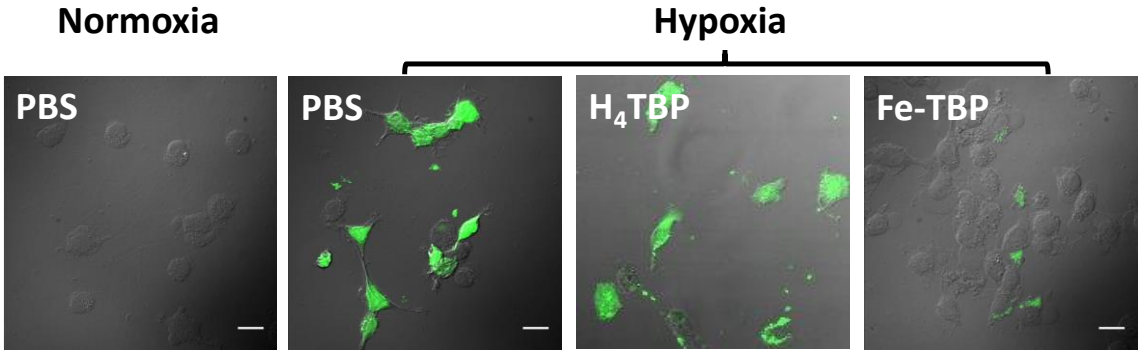

Figure 2-5. Confocal laser scanning microscope (CLSM) images of green fluorescence detecting intracellular H_2O_2 in cells. Scale bar = 20 μm.

We further proved the ability of Fe-TBP in reducing hypoxia by evaluating the expression of hypoxia-inducible factor (HIF-1α) protein, which is typically upregulated under hypoxic condition. Incubation of cells under low oxygen conditions induced the accumulation of HIF-1α. When treated with Fe-TBP, a significant reduction in the fluorescence intensity representing

HIF-1α was observed (**Figure 2-6**).

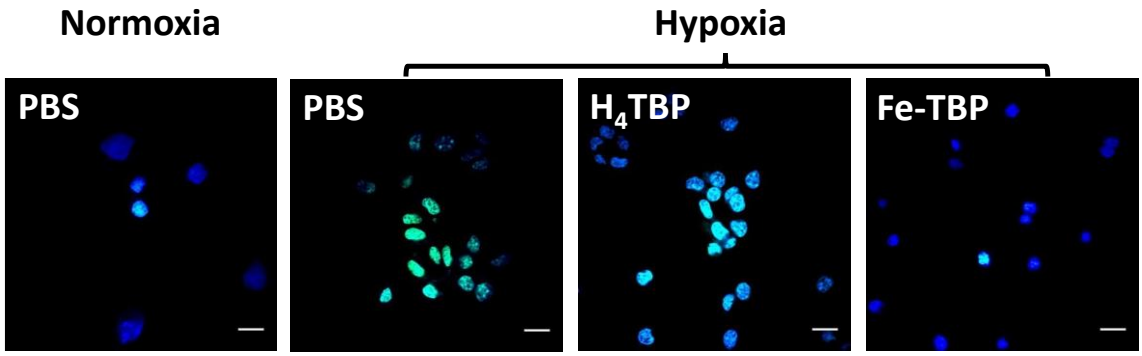

Figure 2-6. CLSM images of green fluorescent intranuclear HIF-α expression in cells. Scale bar = 20 μm.

More importantly, immunohistochemistry staining of HIF-1α further confirmed that Fe-TBP highly alleviated hypoxia in tumor tissues (**Figure 2-7**). Taken together, these data demonstrate that Fe-TBP can effectively overcome hypoxia at cellular to tumor levels.

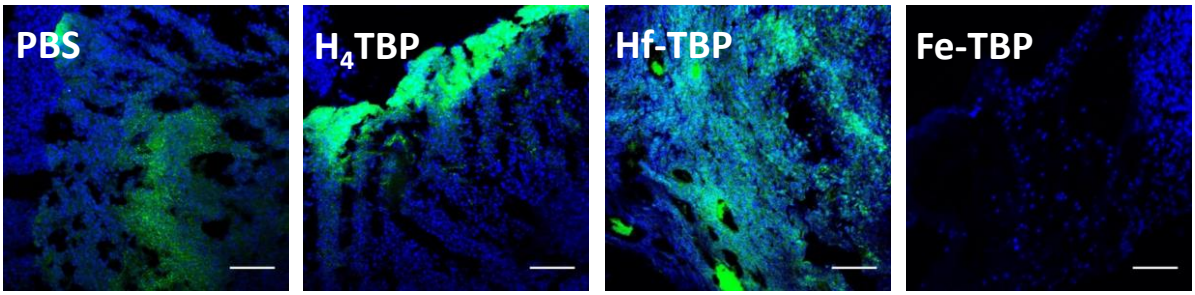

Figure 2-7. In vivo HIF-α expression was evaluated on sectioned tumor slides of CT26-bearing mice. Scale bar=100 μm.

2.2.3 PDT under hypoxic condition

We next sought to determine whether Fe-TBP could effectively mediate PDT under hypoxic condition. Hf-TBP, another nMOF constructed from Hafnium-based clusters and the same TBP ligand with similar size and morphology, was used as a control. First, the $^1O_2$ generation efficacy of Fe-TBP was determined by the Singlet Oxygen Sensor Green (SOSG). Fe-TBP effectively generated $^1O_2$ in irradiation-dependent manner in PBS under normoxic condition (**Figure 2-8a**). In oxygen-free PBS, Fe-TBP showed almost no $^1O_2$ generation upon

irradiation. However, upon the addition of H_2O_2 to oxygen-free PBS, Fe-TBP exhibited similar $^1O_2$ generation efficiency to the normoxic condition. In contrast, upon irradiation, both H_4TBP and Hf-TBP generated only trace amounts of $^1O_2$ in oxygen-free, H_2O_2-containing PBS (**Figure 2-8b**).

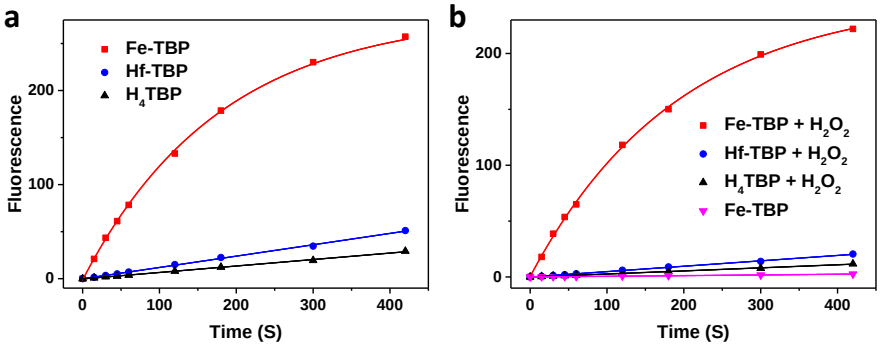

Figure 2-8. Fe-TBP-mediated $^1O_2$ generation. (a) $^1O_2$ generation by Fe-TBP, Hf-TBP, and H_4TBP under normoxic condition with 650 nm LED irradiation at 100 mW/cm^2, detected by SOSG assay. (b) $^1O_2$ generation by Fe-TBP, Hf-TBP, and H_4TBP in oxygen-free, H_2O_2-conatining PBS.

The *in vitro* PDT efficacy was evaluated by cytotoxicity tests. Under normoxic condition, Hf-TBP and H_4TBP showed slightly inferior PDT efficacy to Fe-TBP with IC_{50} values of 2.60 ± 1.59, 11.33 ± 6.75, and 25.13 ± 6.83 μM for Fe-TBP, Hf-TBP, and H_4TBP, respectively (**Figure 2-9a**). Under hypoxic condition, Fe-TBP exhibited comparable PDT efficacy with an IC_{50} of 3.10 ± 1.66 μM while Hf-TBP and H4TBP were totally ineffective with IC_{50} values much greater than 50 μM (**Figure 2-9b**). Our data confirm that Fe-TBP mediates effective PDT under both normoxic and hypoxic conditions.

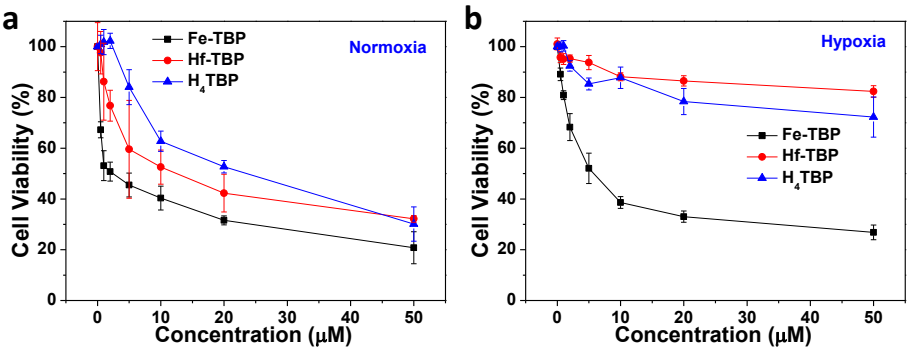

Figure 2-9. Cytotoxicity test of Fe-TBP. Cytotoxicity tests of Fe-TBP, Hf-TBP and H_4-TBP under (a) normoxia condition or (b) hypoxic condition.

2.2.4 Anti-cancer efficacy

We investigated whether Fe-TBP could improve cancer immunotherapy. First, we studied the cell death pathway of Fe-TBP mediated PDT to evaluate whether Fe-TBP can provide sufficient activation of the host immune system. After PDT treatment, significant amounts of Fe-TBP treated cells underwent apoptosis/necrosis with only 18.8% of cells remaining healthy. The ICD induced by PDT treatment was investigated by detecting cell-surface exposure of calreticulin (CRT). Strong green fluorescence representing expression of CRT was observed in Fe-TBP treated cells and quantified by flow cytometry (**Figure 2-10**). The mean fluorescence intensities were 1447, 1124, 215 and 154 for the cells treated with Fe-TBP, Hf-TBP, H_4-TBP and with light irradiation only, respectively. Immunostaining analysis confirmed high CRT expression in Fe-TBP treated tumors as indicated by strong green fluorescence (**Figure 2-11**).

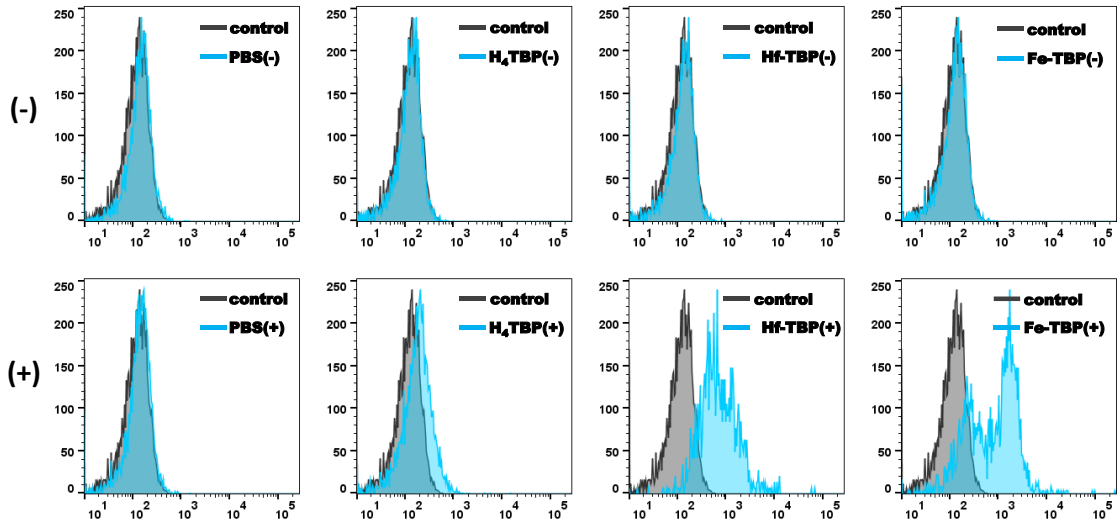

Figure 2-10. CRT exposure determined by flow cytometry. CRT exposure of CT26 was assessed after incubation with PBS, H_4TBP, Hf-TBP, or Fe-TBP with (+) or without (-) light irradiation by in vitro flow cytometry analysis. Grey histogram (control) and blue histogram show the difference of CRT exposure level on the cell surfaces. From left to right: PBS control, H_4TBP, Hf-TBP, or Fe-TBP, respectively.

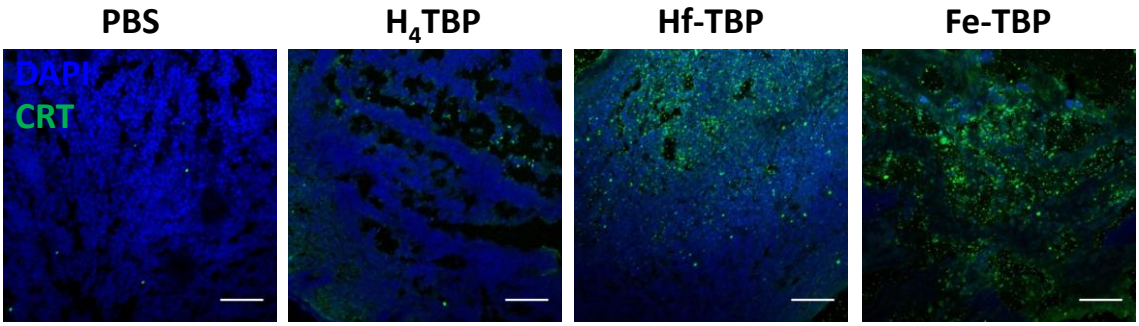

Figure 2-11. In vivo immunofluorescence of CRT exposure.

We then tested the anti-cancer effect on a bilateral model of murine colorectal CT26 tumors on BALB/c mice. One of the tumors (primary) was treated with Fe-TBP and irradiated, while the other tumor (distant) remained untreated. The mice then underwent α-PD-L1 treatment. The mice treated with either light irradiation only, Fe-TBP plus light irradiation, or α-PD-L1 plus light irradiation served as controls. The immunotherapeutic efficacy and the induction of abscopal effects of different treatment regimens were assessed by the growth rates of both the primary and distant tumors. We found that Fe-TBP mediated PDT significantly

improved the α-PD-L1 treatment by eliciting consistent abscopal effects, leading to >90% regression of both tumors at a low Fe-TBP dose of 0.2 μmol based on TBP and light dose of 45 J/cm^2 (**Figure 2-12**). Histological analysis of the tumors confirmed that Fe-TBP plus α-PD-L1 group showed necrotic tumor histology in the untreated distant tumor as observed by a lower density of tumor cells. In contrast, only a slight abscopal effect was observed in the mice treated with Fe-TBP and no abscopal effect was observed for mice treated with α-PD-L1 only. The body weights of mice remained consistent, regardless of treatment, suggesting no systemic toxicity.

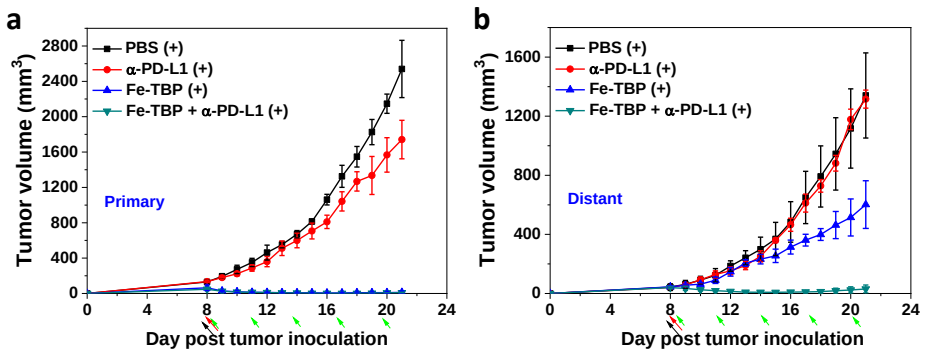

Figure 2-12. Tumor growth curves. Tumor growth curves of (a) primary tumors and (b) distant tumors of bilateral CT26 tumor-bearing mice treated with Fe-TBP with or without anti-PD-L1 antibody, anti-PD-L1 antibody, or PBS with LED irradiation (+). N=6. Black, red, and green arrows refer to the times Fe-TBP injections, X-ray irradiation, and antibody administration, respectively.

To confirm the long-term antitumor immune response, we carried out a tumor challenge study, wherein the cured mice successfully rejected tumor re-challenge (injection of 2 × 10^6 CT26 cells) thirty days post tumor eradication (**Figure 2-13**). Our results demonstrate that Fe-TBP improves the checkpoint blockade immunotherapy and promotes abscopal effects.

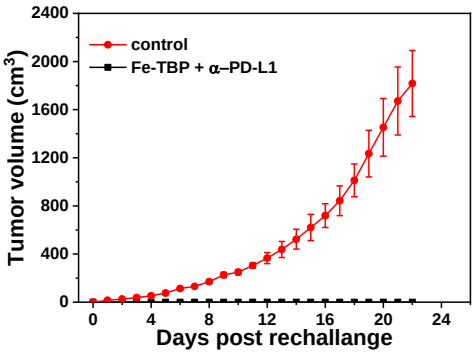

Figure 2-13. Tumor growth curves after rechallenge with CT26 cells. N=6.

2.2.4 Fe-TBP-enhanced immunotherapy

We next determined the mechanism by which Fe-TBP-mediated PDT enhances the efficacy of cancer immunotherapy. We first found that Fe-TBP plus α-PD-L1 treatment lost the immunotherapeutic efficacy after depletion of either B cells or $CD4^+$ or $CD8^+$ T cells on single tumor model, indicating the involvement of these cells in our treatments (**Figure 2-14**).

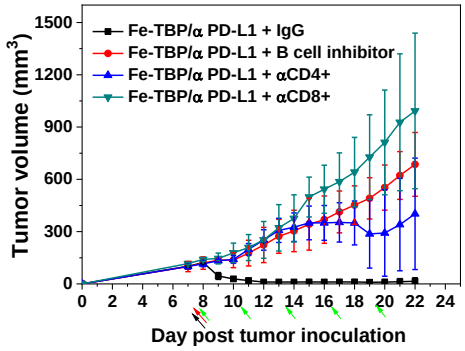

Figure 2-14. T cell or B cell depletion. Tumor growth curves of CT26 tumor bearing mice with T cell or B cell depletion and treatment with Fe-TBP, anti-PD-L1 antibody and LED irradiation. N=6. Black, red, and green arrows refer to the times Fe-TBP injections, X-ray irradiation, and antibody administration, respectively.

We then tested the anti-tumor immunity of CT26-bearing mice treated with Fe-TBP plus α-PD-L1 by ELISPOT and immune cells profiling. We determined the presence of tumor-antigen specific cytotoxic T cells with an IFN-γ ELISPOT assay. At day 10 after the PDT treatment, splenocytes were harvested from CT26-bearing mice and stimulated with

SPSYVYHQF, a tumor associated antigen peptide, for 42 hours and the IFN-γ spot forming cells were counted. The number of antigen-specific IFN-γ producing T cells significantly increased in tumor-bearing mice treated with Fe-TBP plus α-PD-L1 (96.9 ± 20.9 compared to 16.3 ± 4.1 for PBS or 63.9 ± 36.7 for Fe-TBP, **Figure 2-15a**), suggesting that Fe-TBP plus α-PD-L1 treatment induces tumor-specific T cell response. We further profiled infiltrating leukocytes in both the primary and distant tumors. The Fe-TBP plus α-PD-L1 group showed significant increase of tumor-infiltrating $CD4^+$ and $CD8^+$ T cells in both primary and distant tumors (**Figure 2-15c,d**). The infiltration of $CD8^+$ T cells was further confirmed by immunostaining. The Fe-TBP with or without antibody treated groups showed significant increase of tumor-infiltrating $CD45^+$ T cells as well as B cells in the primary tumors (**Figure 2-15b**). Interestingly, the distant tumors of Fe-TBP plus α-PD-L1 treated group shows significant increase of dendritic cell infiltration. Also, we found significant decrease of monocytes in the primary tumors in Fe-TBP with or without α-PD-L1 groups. In addition, significant decrease of regulatory T cells from both distant and primary sides of lymph nodes. Taken together, Fe-TBP-mediated PDT plus α-PD-L1 checkpoint blockade immunotherapy alleviated the immunosuppression and increase the infiltration of effector T cells.

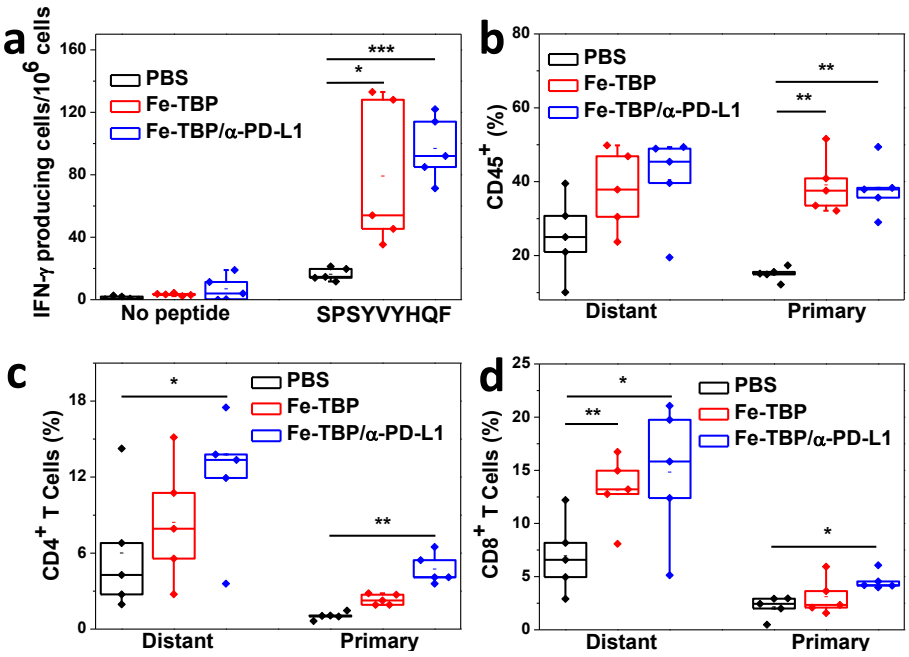

Figure 2-15. Tumor-specific immune responses. (a) ELISPOT assay was performed to detect IFN-γ producing T cells. The percentage of tumor-infiltrating $CD45^+$ cells (b), $CD4^+$ T cells (c), and $CD8^+$ T cells (d) with respect to the total tumor of cells. Data are expressed as means±s.d. (N=5). *P<0.05, **P<0.01, and ***P<0.001 from control.

2.3 Conclusion

In this work, we developed a novel nMOF-based nPS to overcome tumor hypoxia in PDT and improve cancer immunotherapy. We have shown that Fe-TBP plus α-PD-L1 treatment induces significant expansions of both $CD4^+$ and $CD8^+$ cytotoxic T cells, which can infiltrate distant tumors to elicit abscopal effects. In clinic, patients whose tumors are non-immunogenic would receive combinatorial therapies containing an immune checkpoint inhibitor plus an agent designed to create an immunogenic tumor microenvironment for clinical benefit. Our study herein presents a novel strategy to combining PDT with checkpoint blockage immunotherapy. Moreover, PDT is generally a local treatment that is ineffective for treating metastatic cancer. Our work provides a new strategy to overcome such limitation by combining PDT with checkpoint blockage immunotherapy to elicit systemic antitumor immunity via abscopal effects.

2.4 Methods

Preparation of Fe-TBP. To a 4 mL glass vial was added 0.5 mL of $Fe_3O(OAc)_6(H_2O)_3(OAc)$ solution (2.2 mg/mL in DMF), 0.5 mL of H_4TBP solution (1.32 mg/mL in DMF), and 100 μL of formic acid. The reaction mixture was kept in an 80 °C oven for 24 hours. The purple precipitate was collected by centrifugation and washed with DMF and ethanol. Fe-TBP of different size was synthesized by tuning the overall reaction concentration, including $Fe_3O(OAc)_6(H_2O)_3(OAc)$, H_4TBP, and formic acid. Fe-TBP of 100 nm in length was obtained by halving the reagent concentrations.

Oxygen generaton. 150 μM of H_2O_2 was incubated with 50 μM of Fe-TBP in oxygen-free PBS at 37 °C, followed by measuring the dissolved O_2 concentration with an oxygen meter at 5 minute intervals for one hour.

Singlet oxygen generation under normoxic condition. Fe-TBP, Hf-TBP, or H_4TBP suspension was prepared with an equivalent ligand dose of 5 μM in PBS. To 2 mL each of these suspensions, SOSG stock solution (5 μL at 5 mM) was added (final concentration=12.5 μM) before fluorescence measurements. The mixed solution was exposed to LED light (100 mW, 650 nm) for 0, 10, 20, 30, 60, 120, 180, 300, and 420 seconds and the fluorescence at different time points was measured by a fluorimeter.

Singlet oxygen generation under hypoxic condition. Fe-TBP, Hf-TBP, or H_4TBP suspension was prepared at an equivalent ligand dose of 5 μM in PBS. To 2 mL each of these three suspensions, SOSG stock solution and H_2O_2 was added to afford a final SOSG concentration of 12.5 μM and H_2O_2 concentration of 100 μM. Another control group was prepared by adding only SOSG stock solution to Fe-TBP suspension without H_2O_2. Oxygen was then removed

from these four mixtures by bubbling in nitrogen for 20 mins. These mixtures were subsequently exposed to an LED (100 mW, 650 nm) for 0, 10, 20, 30, 60, 120, 180, 300, and 420 seconds. The fluorescence at different time points was measured by a fluorimeter.

Hypoxia treatment. CT26 cells were subjected to hypoxia as described previously with modifications.[23] Briefly, CT26 cells were seeded on 6-well plate at 2×10^5 cells per well on the day before treatment. The medium was then exchanged for fresh medium and placed in an anaerobic chamber filled with 94.5% N_2, 5% CO_2 and 0.5 % O_2 to induce hypoxia. The control cells were incubated in a normoxic condition containing 5% CO_2 and 95% air (about 20% O_2).

Intracellular H_2O_2 assay. Intracellular H_2O_2 was detected by a MAK164 intracellular H_2O_2 kit. For hypoxic condition, cells were cultured in the hypoxic chamber for 12 hours and further incubated with PBS, H_4TBP, or Fe-TBP at an equivalent ligand dose of 10 μM for 4 hours. Then the medium was replaced by assay buffer and incubated for another 1 hour. After washing with PBS, intracellular H_2O_2 was observed by CLSM. For the normoxic condition, cells were treated with 100 μM of H_2O_2 for 12 hours and then further incubated with PBS, H_4TBP, or Fe-TBP at an equivalent ligand dose of 10 μM for 4 hours. Then the medium was replaced by assay buffer and incubated for another 1 hour. After washing with PBS, intracellular H_2O_2 was observed through fluorescent imaging.

HIF-1α immunostaining. Hypoxia levels were evaluated with the ab190197 antibody that has been conjugated with Alexa Fluor 488 fluorochrome against HIF-1α both in vitro and in vivo. For in vitro studies, CT26 cells were incubated in normoxic and hypoxic conditions and further incubated with PBS, H_4TBP, or Fe-TBP at an equivalent ligand dose of 10 μM for 4 hours. The hypoxic PDT treatment was performed inside the anaerobic chamber. Cells were then stained

with the antibody against HIF-1α and DAPI subsequently then observed by CLSM. For in vivo immunofluorescence imaging, CT26 tumor bearing mice were treated with H_4TBP, Hf-TBP, or Fe-TBP at a dose of 0.2 μmol TBP intratumorally. Mice treated with PBS served as a control. Tumors were excised and the sections were air-dried for at least 1 h and then fixed in acetone for 10 min at 20 °C. After stained with Alexa Fluor 488-HIF-1α and DAPI, the sections were then washed twice with PBS and observed under CLSM.

In vitro singlet oxygen generation. A LED array with peak emission at 650 nm was used as the light source for singlet oxygen generation tests. The irradiance of this LED is 20 mW/cm^2. SOSG reagent was employed for the detection of singlet oxygen under dark and light irradiation in hypoxic or normoxic conditions, respectively. CT26 cells were seeded on cover slides in 6-well plate at 2×10^5 cells per well and further cultured for 12 hours. H_4TBP, Hf-TBP, or Fe-TBP was added to the cells at an equivalent ligand dose of 10 μM. Cells incubated with PBS served as a control. After incubation of 4 hours, cells were irradiated by LED for 15 minutes. The slides were then washed with PBS and observed under CLSM.

Cytotoxicity. The cytotoxicity of H_4TBP, Hf-TBP, or Fe-TBP was evaluated with MTS assay under dark and light irradiation in hypoxic or normoxic conditions, respectively. Dark cytotoxicity was first tested without LED irradiation. CT26 cells were seeded on 96-well plates at 2×10^4 cells per well and further cultured for 12 hours. H_4TBP, Hf-TBP, or Fe-TBP were added to the cells at an equivalent ligand dose of 0, 0.2, 0.5, 1, 2, 5, 10, 20, and 50 μM. The cells were further incubated for 72 hours before determining the cell viability by MTS assay. To determine the cytotoxicity under light irradiation in the hypoxic condition, cells were seeded on 96-well plates at 2×10^4/well and cultured for 12 hours. Then cells were transferred into the

anaerobic chamber and further incubated for 6 hours. H_4TBP, Hf-TBP or Fe-TBP were added to the cells at an equivalent ligand dose of 0, 0.2, 0.5, 1, 2, 5, 10, 20, and 50 μM. Cells were then irradiated by LED for 15 minutes after incubation of 4 hours. The cells were further incubated for 72 hours before determining the cell viability by MTS assay. To determine the cytotoxicity with light irradiation under normoxic condition, cells were seeded on 96-well plates at 2×10^4 cells per well and further cultured for 18 hours. H_4TBP, Hf-TBP, or Fe-TBP was added to the cells at an equivalent ligand dose of 0, 0.2, 0.5, 1, 2, 5, 10, 20, and 50 μM. Cells were then irradiated by LED for 15 minutes after incubation of 4 hours. The cells were further incubated for 72 hours before determining the cell viability by MTS assay.

CRT assay. The ICD induced by PDT treatment was investigated by detecting cell-surface expression of CRT both in vitro and in vivo. For in vitro studies, CT26 cells were seeded in 6-well plates on cover slides overnight and incubated with H_4TBP, Hf-TBP, or Fe-TBP at 10 μM based on TBP ligand concentration for 4 hours followed by light irradiation for 0 or 15 minutes. Cells were then cultured in the incubator for another 4 hours to induce CRT exposure. For confocal imaging, cells were stained with AlexaFluor 488-CRT and DAPI, and observed under CLSM. For flow cytometry, cells were stained with AlexaFluor 488-CRT for cytometry analysis. For in vivo immunofluorescence imaging, CT26 tumor bearing mice were intratumorally treated with H_4TBP, Hf-TBP, or Fe-TBP at a TBP dose of 0.2 μmol. Mice treated with PBS served as a control. Tumors were excised and the sections were air-dried for at least 1 h and then fixed in acetone for 10 min at 20 °C. After stained with AlexaFluor 488-CRT and DAPI, the sections were then washed twice with PBS and observed under CLSM.

In vivo anticancer efficacy. For the evaluation of Fe-TBP-enabled PDT combined with

checkpoint blockade immunotherapy, 2×10^6 and 1×10^6 CT26 cells were injected into the right and left flank subcutaneous tissues of Balb/c mice on day 0 to mimic primary and distant tumors, respectively, in this bilateral syngeneic CT26 model. When the primary tumors reached 100-150 mm^3 in volume, Fe-TBP at TBP dose of 0.2 μmol or PBS was injected intratumorally. 4 hours after injection, mice were anaesthetized with 2% (v/v) isoflurane and the primary tumors were irradiated once with LED lamp at a dose of 20 mW/cm^2 for 7.5 minutes. Anti-PD-L1 antibody was given every three days by intraperitoneal injection at a dose of 75μg/mouse. Mice treated with PBS with light irradiation or antibody with light irradiation served as controls. Mice were euthanized on Day 21 and the excised tumors were photographed and weighed.

$CD4^+$ T cell, $CD8^+$ T cell, and B cell depletion. The anticancer efficacy of combined Fe-TBP-enabled PDT and anti-PD-L1 checkpoint blockade immunotherapy was evaluated using the single tumor subcutaneous CT26 model in BALB/c mice with T cell or B cell depletion. For T cell depletion, mice were injected intraperitoneally with 250 mg anti-CD4, anti-CD8, or rat IgG antibody twice every five days (days 7 and 12 after tumor inoculation). For B cell depletion, mice were injected intraperitoneally with 1 mg Ibrutinib for a total of 5 fractions on consecutive days.

Tumor rechallenge studies. The immune memory effect was evaluated with tumor rechallenge studies. 2×10^6 CT26 cells were inoculated on the right flanks of mice and treated with Fe-TBP-enabled PDT and anti-PD-L1 antibody as described in the efficacy test. Six out of ten mice had their tumors completely eradicated after treatment. On day 30 post tumor eradication, the cured Balb/c mice were challenged with 2×10^6 CT26 cells on their contralateral flanks. Healthy mice were simultaneously inoculated as control. The tumor size was measured with a caliper every

day and the tumor volume equals (width^2 × length)/2. Statistical analysis for all of the rechallenges was performed using the log-rank Kaplan-Meier estimation. The mice were sacrificed when the size of the right tumors in the PBS group exceeded 2 cm^3.

ELISPOT assay. Tumor-specific immune responses to IFN-γ were measured *in vitro* by ELISPOT assay (Mouse IFN-γ ELISPOT Ready-SET-Go!; Cat. No. 88-7384-88; eBioscience). A Millipore Multiscreen HTS-IP plate was coated overnight at 4 °C with anti-Mouse IFN-γ capture antibody. Single-cell suspensions of splenocytes were obtained from CT26 tumor-bearing mice treated with Fe-TBP-enabled PDT and anti-PD-L1 antibody or PBS control and seeded onto the antibody-coated plate at 2×10^5 cells per well. Cells were incubated with or without SPSYVYHQF stimulation (10 mg/ml; in purity >95%; PEPTIDE 2.0) at 37 °C for 42 h and then the suspension was discarded. The plate was then incubated with biotin-conjugated anti-IFN-γ detection antibody at r.t. for 2 h, followed by incubation with Avidin-HRP at r.t. for 2 h. 3-amino-9-ethylcarbazole substrate solution was added for cytokine spot detection.

2.5 References

1. Pardoll, D. M., The blockade of immune checkpoints in cancer immunotherapy. *Nat. Rev. Cancer* **2012,** *12* (4), 252-264.
2. Brahmer, J. R.; Tykodi, S. S.; Chow, L. Q.; Hwu, W.-J.; Topalian, S. L.; Hwu, P.; Drake, C. G.; Camacho, L. H.; Kauh, J.; Odunsi, K., Safety and activity of anti–PD-L1 antibody in patients with advanced cancer. *N Engl J Med* **2012,** *2012* (366), 2455-2465.
3. Topalian, S. L.; Hodi, F. S.; Brahmer, J. R.; Gettinger, S. N.; Smith, D. C.; McDermott, D. F.; Powderly, J. D.; Carvajal, R. D.; Sosman, J. A.; Atkins, M. B., Safety, activity, and immune correlates of anti–PD-1 antibody in cancer. *N Engl j Med* **2012,** *2012* (366), 2443-2454.
4. Sharma, P.; Allison, J. P., The future of immune checkpoint therapy. *Science* **2015,** *348* (6230), 56-61.
5. Min, Y.; Roche, K. C.; Tian, S.; Eblan, M. J.; McKinnon, K. P.; Caster, J. M.; Chai, S.; Herring, L. E.; Zhang, L.; Zhang, T., Antigen-capturing nanoparticles improve the abscopal effect and cancer immunotherapy. *Nat. nanotechno.* **2017,** *12* (9), 877.
6. Spring, B. Q.; Sears, R. B.; Zheng, L. Z.; Mai, Z.; Watanabe, R.; Sherwood, M. E.; Schoenfeld, D. A.; Pogue, B. W.; Pereira, S. P.; Villa, E., A photoactivable multi-

inhibitor nanoliposome for tumour control and simultaneous inhibition of treatment escape pathways. *Nat. nanotechnol.* **2016,** *11* (4), 378-387.
7. Lovell, J. F.; Jin, C. S.; Huynh, E.; Jin, H.; Kim, C.; Rubinstein, J. L.; Chan, W. C.; Cao, W.; Wang, L. V.; Zheng, G., Porphysome nanovesicles generated by porphyrin bilayers for use as multimodal biophotonic contrast agents. *Nat. Mater.* **2011,** *10* (4), 324-332.
8. Huang, P.; Lin, J.; Wang, X.; Wang, Z.; Zhang, C.; He, M.; Wang, K.; Chen, F.; Li, Z.; Shen, G., Light-triggered theranostics based on photosensitizer-conjugated carbon dots for simultaneous enhanced-fluorescence imaging and photodynamic therapy. *Adv. Mater.* **2012,** *24* (37), 5104-5110.
9. Marrache, S.; Choi, J. H.; Tundup, S.; Zaver, D.; Harn, D. A.; Dhar, S., Immune stimulating photoactive hybrid nanoparticles for metastatic breast cancer. *Integr. Biol.* **2013,** *5* (1), 215-223.
10. Lu, K.; He, C.; Guo, N.; Chan, C.; Ni, K.; Weichselbaum, R. R.; Lin, W., Chlorin-Based Nanoscale Metal–Organic Framework Systemically Rejects Colorectal Cancers via Synergistic Photodynamic Therapy and Checkpoint Blockade Immunotherapy. *J. Am. Chem. Soc.* **2016,** *138* (38), 12502-12510.
11. He, C.; Duan, X.; Guo, N.; Chan, C.; Poon, C.; Weichselbaum, R. R.; Lin, W., Core-shell nanoscale coordination polymers combine chemotherapy and photodynamic therapy to potentiate checkpoint blockade cancer immunotherapy. *Nat. Commun.* **2016,** *7*.
12. Lu, K.; He, C.; Lin, W., Nanoscale metal–organic framework for highly effective photodynamic therapy of resistant head and neck cancer. *J. Am. Chem. Soc.* **2014,** *136* (48), 16712-16715.
13. Fateeva, A.; Chater, P. A.; Ireland, C. P.; Tahir, A. A.; Khimyak, Y. Z.; Wiper, P. V.; Darwent, J. R.; Rosseinsky, M. J., A Water-Stable Porphyrin-Based Metal–Organic Framework Active for Visible-Light Photocatalysis. *Angew. Chem.* **2012,** *124* (30), 7558-7562.
14. Xu, H.; Liu, F.; Cui, Y.; Chen, B.; Qian, G., A luminescent nanoscale metal–organic framework for sensing of nitroaromatic explosives. *Chem. Commun.* **2011,** *47* (11), 3153-3155.
15. Park, J.; Jiang, Q.; Feng, D.; Mao, L.; Zhou, H.-C., Size-controlled synthesis of porphyrinic metal–organic framework and functionalization for targeted photodynamic therapy. *J. Am. Chem. Soc* **2016,** *138* (10), 3518-3525.
16. Furukawa, H.; Cordova, K. E.; O'Keeffe, M.; Yaghi, O. M., The chemistry and applications of metal-organic frameworks. *Science* **2013,** *341* (6149), 1230444.
17. Levine, D. J.; Runčevski, T. e.; Kapelewski, M. T.; Keitz, B. K.; Oktawiec, J.; Reed, D. A.; Mason, J. A.; Jiang, H. Z.; Colwell, K. A.; Legendre, C. M., Olsalazine-Based Metal–Organic Frameworks as Biocompatible Platforms for H2 Adsorption and Drug Delivery. *J. Am. Chem. Soc.* **2016,** *138* (32), 10143-10150.
18. Morris, W.; Briley, W. E.; Auyeung, E.; Cabezas, M. D.; Mirkin, C. A., Nucleic acid–metal organic framework (MOF) nanoparticle conjugates. *J. Am. Chem. Soc.* **2014,** *136* (20), 7261-7264.
19. An, J.; Geib, S. J.; Rosi, N. L., Cation-triggered drug release from a porous zinc− adeninate metal− organic framework. *J. Am. Chem. Soc.* **2009,** *131* (24), 8376-8377.
20. Lan, G.; Ni, K.; Lin, W., Nanoscale metal–organic frameworks for phototherapy of cancer. *Coord. Chem. Rev.* **2017**. *379*, 65-81.
21. Panyam, J.; Labhasetwar, V., Biodegradable nanoparticles for drug and gene delivery to

cells and tissue. *Adv. Drug Deliv. Rev.* **2003,** *55* (3), 329-347.
22. Wang, K.; Feng, D.; Liu, T.-F.; Su, J.; Yuan, S.; Chen, Y.-P.; Bosch, M.; Zou, X.; Zhou, H.-C., A series of highly stable mesoporous metalloporphyrin Fe-MOFs. *J. Am. Chem. Soc.* **2014,** *136* (40), 13983-13986.
23. Kim, J.; Cho, H. R.; Jeon, H.; Kim, D.; Song, C.; Lee, N.; Choi, S. H.; Hyeon, T., Continuous O_2-evolving $MnFe_2O_4$ nanoparticle-anchored mesoporous silica nanoparticles for efficient photodynamic therapy in hypoxic cancer. *J. Am. Chem. Soc.* **2017,** *139* (32), 10992-10995.

Chapter 3. Titanium-Based Nanoscale Metal-Organic Framework for Type I Photodynamic Therapy

3.1 Introduction

Although PDT is an efficient anti-cancer treatment,[1-4] this modality largely relies upon an oxygen-dependent type II mechanism through energy transfer from excited PSs to O_2 to generate $^1O_2$.[5] Therapeutic efficacy of type II PDT is diminished in hypoxic environments found in many solid tumors.[6] In contrast, type I PDT is more hypoxia-tolerant by generating cytotoxic radicals via electron transfer (ET) from excited PSs to O_2 and organic molecules.[7-9] We hypothesized that the tunability of nMOFs can be harnessed to enable type I PDT. In this Chapter, we report the synthesis of a novel nMOF, Ti-TBP, and its use in the first type I PDT mediated by nMOFs. In addition to sensitizing $^1O_2$ generation, Ti-TBP produces O_2^-, H_2O_2, and $^{\bullet}OH$ via transferring electrons from excited TBP* species to Ti^{4+}-based SBUs to form $TBP^{\bullet+}$ ligands and Ti^{3+} centers (**Figure 3-1**). The generation of four distinct ROSs leads to superb anticancer efficacy with >98% tumor regression and 60% cure rate.

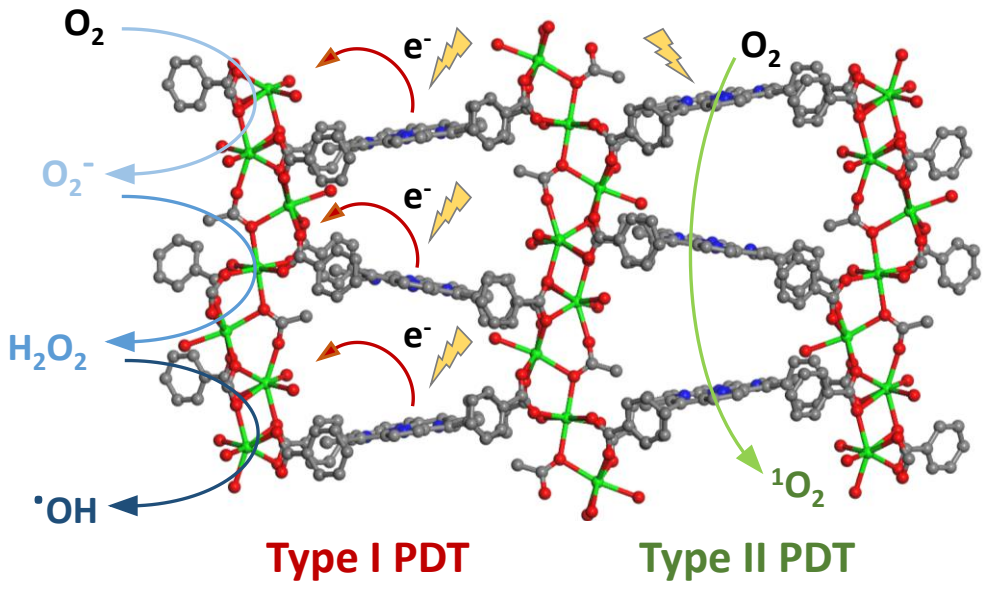

Figure 3-1. Schematic showing both type I and type II PDT enabled by Ti-TBP.

3.2 Result and discussion

3.2.1 Synthesis and characterization

Violet square-shaped crystals of Ti-(Ti·TBP) were synthesized through a solvothermal reaction between $TiCl_4$·2THF and H_4TBP in DMF with AcOH as the modulator at 120 ºC for 7 days. Single crystal X-ray diffraction studies revealed that the TBP ligands were metalated with Ti during crystal growth and the Ti-coordinated TBP (Ti·TBP) ligands were linked by infinite Ti-oxo chain SBUs to form a 3D framework of the new topology with the point symbol of $\{4^{18}.6^{22}.8^4.10\}\{4^2.6\}_2\{4^6.6^9\}_2\{4\}_2$ (**Figure 3-2** and **Table 3-1**). Each repeat unit of the Ti-oxo chain has five Ti^{4+} ions that are bridged by carboxylate groups from TBP or acetate ligands and terminated by hydroxyl groups (**Figure 3-2b**). Negligible Cl was detected in Ti-(Ti·TBP) by X-ray fluorescence (Cl:Ti = 0.0016:1), leading to a formula of $[Ti_5(Ti{\cdot}TBP)_2(OAc)_2(OH)_6](OAc)_8$.

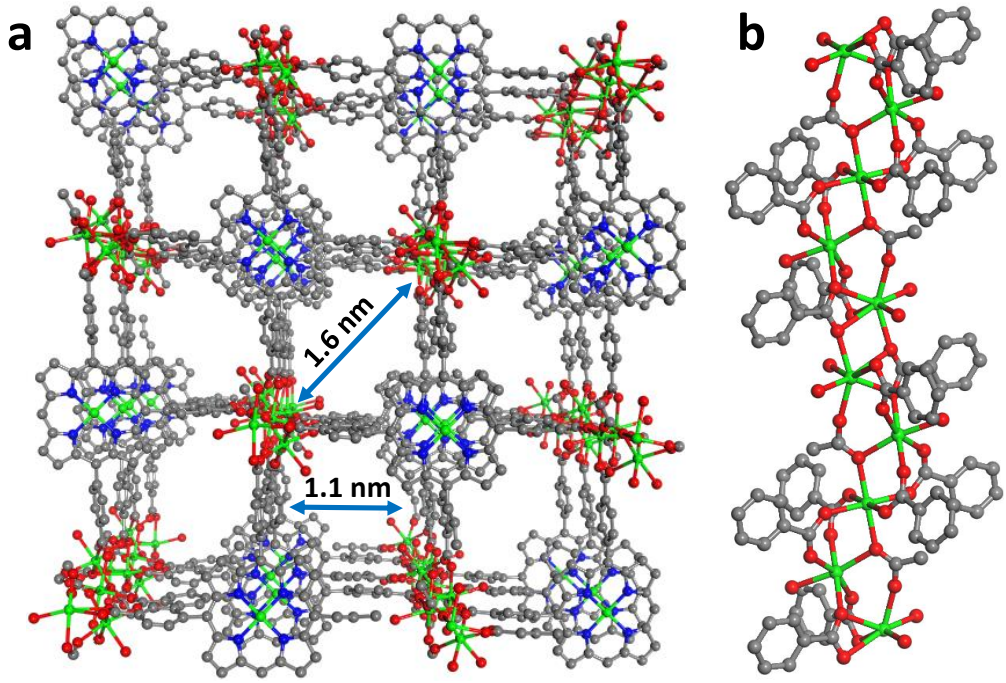

Figure 3-2. Crystal structure of Ti-(Ti·TBP). (a) Perspective view of Ti-(Ti·TBP) structure along the (010) direction. (b) Coordination environments of Ti-oxo chain SBUs.

Table 3-1. Crystallographic information of Ti-(Ti·TBP)

Name	Ti-(Ti·TBP)
Formula	$Ti_{3.5}C_{50}H_{27}N_4O_{13}$
Fw	1059.40
Temperature (K)	100
Wavelength (Å)	0.41328
Crystal system	Monoclinic
Space group	$P2_1/c$
***a* (Å)**	16.496(3)
***b* (Å)**	16.181(3)
***c* (Å)**	34.167(5)
***α* (º)**	90
***β* (º)**	92.685(2)
***γ* (º)**	90
***V* (Å^3)**	9110(2)
Z	4
Density (calcd. g/cm^3)	0.772
Absorption coeff. (mm^{-1})	0.079
F(000)	2144
θ range data collection	2.19-11.88
Limiting indices	-16 <= h <= 16 -16 <= k <= 16 -34 <= l <= 34
Reflection collected	112970
Independent reflection	9554
R (int)	0.0743
Data/restraints/parameters	9554/0/626
Goodness-of-fit on F^2	1.062
Final R indices [I>σ2(I)]	R1 = 0.1439, wR2 = 0.3692
R indices (all data)	R1 = 0.1532, wR2 = 0.3767
CCDC	1887074

Lowering the reaction temperature to 80 ºC led to the synthesis of Ti-TBP nMOF with non-metalated TBP ligands of the composition $[Ti_5(TBP)_2(OAc)_2(OH)_6](OAc)_4$. UV-Vis spectrum of Ti-TBP showed four characteristic Q-bands for non-metalated TBP ligands (**Figure 3-3a**). TGA of Ti-TBP showed a weight loss of 82.9% in the 300 to 600 °C range, matching the expected value of 82.4%, corresponding to decomposition of $[Ti_5(TBP)_2(AcO)_2(OH)_6](AcO)_4$ to $5TiO_2$ (**Figure 3-3b**). By combining ICP-MS analysis of Ti and UV-Vis analysis of TBP in digested Ti-TBP, we determined the Ti:TBP ratio as 2.67 ± 0.16, which is close to 2.5 expected for Ti-TBP but much lower than 3.5 expected for Ti-(Ti·TBP).

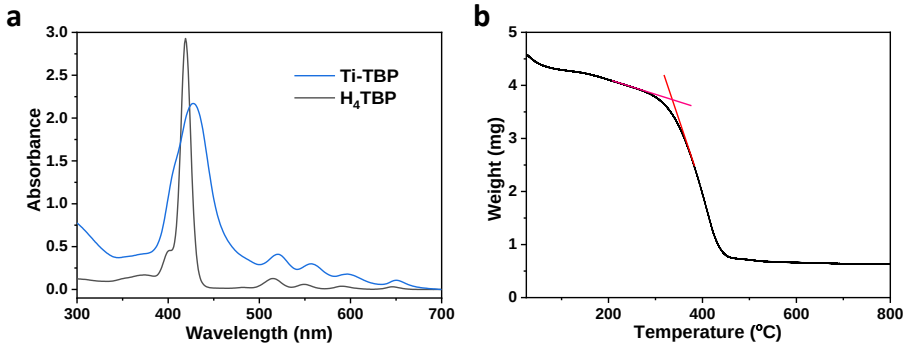

Figure 3-3. Composition analysis of Ti-TBP. (a) UV-vis spectra of Ti-TBP and H_4TBP. (b) TGA of freshly prepared Ti-TBP.

TEM imaging of Ti-TBP revealed square nanoplates with a diameter of ~150 nm (**Figure 3-4a**) while AFM topography of Ti-TBP gave a plate thickness of ~20 nm (**Figure 3-4c**). DLS measurements gave a diameter of 100.1 ± 4.0 nm for Ti-TBP (**Figure 3-4e**). The porous structure of Ti-TBP was confirmed by nitrogen adsorption isotherms at 77 K with a BET surface area of 527.7 m^2/g (**Figure 3-4d**). HRTEM imaging and FFT patterns of Ti-TBP revealed a 4-fold symmetry, consistent with the Ti-TBP structure projected in the (010) direction (**Figure 3-4b**). The distance between two adjacent lattice points in HRTEM was measured to be ~1.6 nm, matching the distance between the centers of two adjacent Ti-chain

SBUs. Moreover, PXRD pattern of Ti-TBP matched well with that simulated from its idealized structure (**Figure 3-4f**).

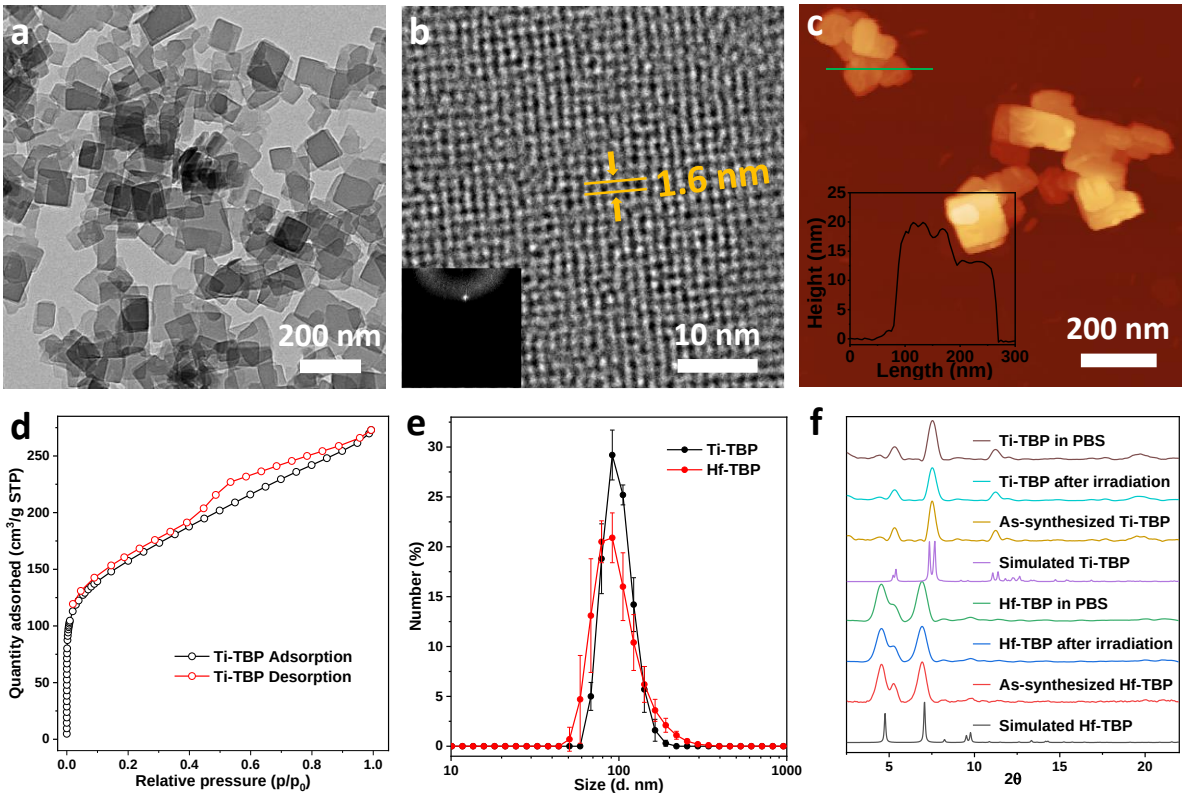

Figure 3-4. Characterization of Ti-TBP. TEM image (a), HRTEM image and FFT pattern (inset) (b), AFM topography and height profile (inset), and nitrogen sorption isotherms (d) of Ti-TBP nMOFs. (e) Number-averaged diameters of Ti-TBP and Hf-TBP in water. (f) PXRD patterns of Ti-TBP and Hf-TBP after soaking in 0.6 mM PBS for 8 h. Hf-TBP was synthesized as reported previously.[10]

3.2.2 ROS generation

We hypothesized that upon light irradiation, Ti^{4+} centers in the SBUs of Ti-TBP could be reduced to Ti^{3+} centers ($Ti^{4+} \rightarrow Ti^{3+}$, E = -0.50 V vs. NHE)[11] via ET from the photo-excited TBP* to form $TBP^{\bullet+}$, in addition to energy transfer from TBP* to O_2 to generate $^1O_2$ (type II PDT). The generated Ti^{3+} further reduces O_2 to generate $O_2^{\bullet-}$, H_2O_2, and $^{\bullet}OH$ to enable type I PDT (**Figure 3-1**). A well-studied nMOF based on redox-inert Hf_6 SBUs ($Hf^{4+} \rightarrow Hf^{3+}$, E = -1.55 V vs. NHE)[10] and TBP ligands was used as a control. PXRD and DLS measurements

showed that crystalline Hf-TBP exhibited a diameter of 100.0 ± 8.3 nm (**Figure 3-4e,f**). Upon light irradiation, Ti-TBP, Hf-TBP, and H_4TBP effected Type II PDT via $^1O_2$ generation as determined by SOSG assays (**Figure 3-5a**). Only Ti-TBP enabled type I PDT by generating a series of distinct ROSs, including O_2^- as determined by EPR with BMPO as a spin trap (**Figure 3-5b**), H_2O_2 as determined with a hydrogen peroxide assay kit (**Figure 3-5c**), and $^{\bullet}$OH as determined by APF assay (**Figure 3-5d**).

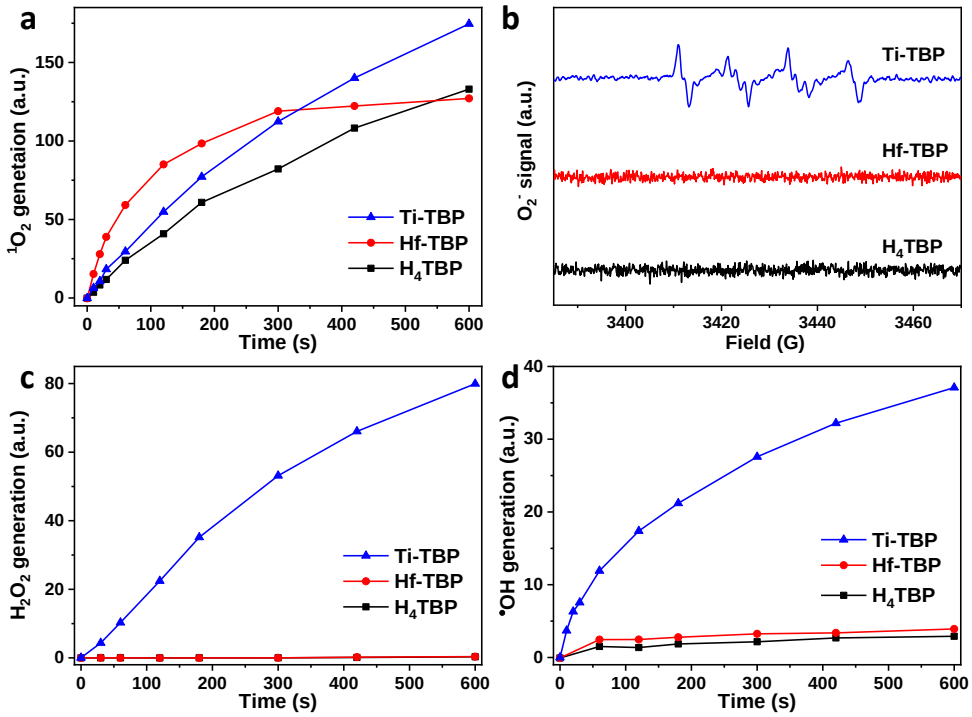

Figure 3-5. ROS generation by Ti-TBP. Time-dependent $^1O_2$ generation (a), O_2^- generation (b), and time-dependent H_2O_2 generation (c) and $^{\bullet}$OH generation (d) upon light irradiation under oxygenated conditions.

To demonstrate that Ti-TBP-enabled type I PDT can tolerate hypoxia of solid tumors, we mimicked hypoxic cancer cell environments with an oxygen-free aqueous solution containing either H_2O_2 (in high concentration in hypoxic cancer cells)[6] or GSH (a ubiquitous antioxidant in cells).[12] Upon light irradiation, Ti-TBP effectively reduced H_2O_2 through Ti^{3+} to generate highly cytotoxic $^{\bullet}$OH, while Hf-TBP and H_4TBP or Ti-TBP without light irradiation did not

enhance •OH generation (**Figure 3-6a**). Furthermore, $TBP^{\bullet+}$ elicited oxidative stress by oxidizing GSH to GSSG as determined by high performance liquid chromatography (**Figure 3-6b**).

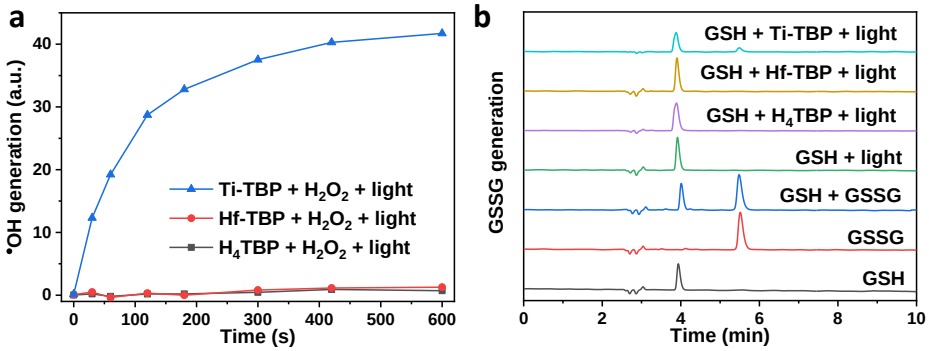

Figure 3-6. ROS generation under oxygen-free condition by Ti-TBP. Time-dependent enhanced •OH generation from H_2O_2 (a) and GSSG generation from GSH (b) upon light irradiation under oxygen-free conditions.

3.2.3 Mechanistic studies

The mechanism of Ti-TBP-enabled type I PDT was next investigated. The oxidative quenching of excited H_4TBP by $TiCl_4$·2THF was supported by fitting the luminescence quenching of H_4TBP to the concentration of added $TiCl_4$·2THF using the Stern-Völmer equation:

$$\frac{I_0}{I} = 1 + K_{SV}C_{Ti}$$

where K_{SV} is the Stern-Völmer constant, and I_0/I is the ratio of luminescence intensity in the absence and presence of $TiCl_4$·2THF. I_0/I showed a good linear relationship with respect to the concentration of $TiCl_4$·2THF (C_{Ti}) with $R^2 = 0.999$ and $K_{SV} = 0.108 \pm 0.002$ mL·μg^{-1} (36.05 ± 0.67 mM^{-1}) (**Figure 3-7**). This efficient luminescence quenching of H_4TBP by $TiCl_4$·2THF suggests efficient ET from TBP* to Ti^{4+}.

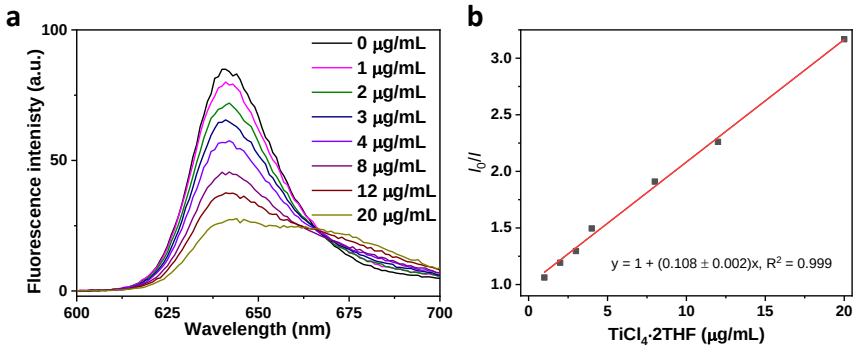

Figure 3-7. Luminescence quenching. (a) Emission spectra of 20 μM H_4TBP with addition of different amounts of $TiCl_4$·2THF. (b) Plots of I_0/I as a function of the concentration of $TiCl_4$·2THF.

EPR spectra of Ti-TBP upon light irradiation showed a sharp peak with a *g*-value of 2.001 that is attributable to $TBP^{\bullet+}$[13] and a weak broad peak with a *g*-value of 1.941 that is assignable to Ti^{3+} species (**Figure 3-8**).[14] No EPR signals were observed with Ti-TBP in dark, and only faint EPR signals corresponding to $TBP^{\bullet+}$ were observed in Hf-TBP and H_4TBP upon light irradiation. The EPR results thus directly prove ET in Ti-TBP.

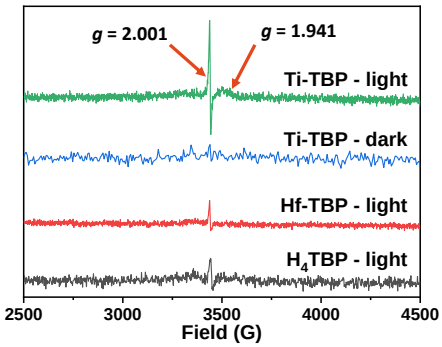

Figure 3-8. EPR spectra. EPR spectra showed the generation of Ti^{3+} (*g* = 1.941) and $TBP^{\bullet+}$ (g = 2.001) upon light irradiation under oxygen-free condition at 20 K.

To understand Ti^{3+}-mediated ROS generation, O_2^- was scavenged by benzoquinone to evaluate its influence on other ROSs.[15] $^1O_2$ generation of Ti-TBP decreased at the same proportion as the emission of H_4TBP (**Figure 3-9a**) due to luminescence quenching by benzoquinone. Negligible amounts of H_2O_2 (**Figure 3-9b**) and $^{\bullet}OH$ (**Figure 3-9c**) were detected in the presence of benzoquinone, demonstrating that both H_2O_2 and $^{\bullet}OH$ are generated

from $O_2^{\bullet-}$. We have thus shown that Ti^{3+} can propagate the generation of $O_2^{\bullet-}$, H_2O_2, and $^{\bullet}OH$ under light irradiation.

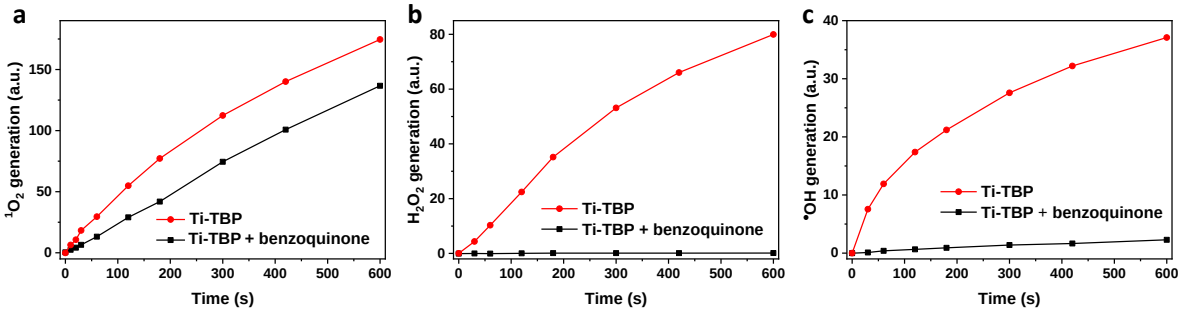

Figure 3-9. ROS generation with or without benzoquinone. Time-dependent $^1O_2$ (a), H_2O_2 (b) and $^{\bullet}OH$ (c) generation by Ti-TBP with or without benzoquinone upon light irradiation.

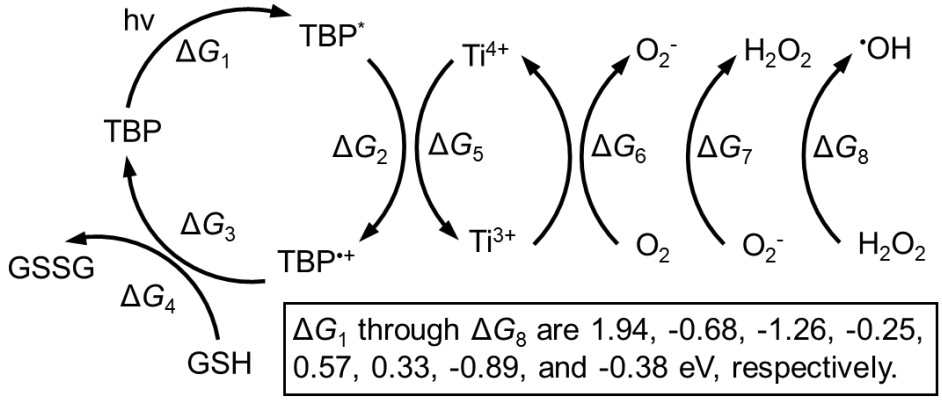

$TBP^* + Ti^{4+} \longrightarrow TBP^{\bullet+} + Ti^{3+}$ $\quad \Delta G = \Delta G_2 + \Delta G_5 = -0.11$ eV

$TBP^{\bullet+} + GSH \longrightarrow TBP + \frac{1}{2}GSSG + H^+$ $\quad \Delta G = \Delta G_3 - \Delta G_5 = -1.51$ eV

$Ti^{3+} + O_2 \longrightarrow Ti^{4+} + O_2^{\bullet-}$ $\quad \Delta G = \Delta G_6 - \Delta G_5 = -0.22$ eV

$Ti^{3+} + O_2^{\bullet-} + 2H^+ \longrightarrow Ti^{4+} + H_2O_2$ $\quad \Delta G = \Delta G_7 - \Delta G_5 = -1.46$ eV

$Ti^{3+} + H_2O_2 + H^+ \longrightarrow Ti^{4+} + {}^{\bullet}OH + H_2O$ $\quad \Delta G = \Delta G_8 - \Delta G_5 = -0.95$ eV

Figure 3-10. Proposed mechanism for Ti-TBP enabled type I PDT at pH 7.

We propose the mechanism of Ti-TBP enabled type I PDT in **Figure 3-10**. Photoexcitation of TBP to TBP* (ΔG_1, calculated from the emission peak of H_4TBP at 641 nm) generates Ti^{3+} and $TBP^{\bullet+}$ via ET. The Ti^{3+} centers generate $O_2^{\bullet-}$, H_2O_2, and $^{\bullet}OH$ whereas $TBP^{\bullet+}$ oxidizes GSH to GSSG. The energy difference between TBP* to $TBP^{\bullet+}$ ($\Delta G_2 = -\Delta G_1 - \Delta G_3$) is enough to drive the reduction of Ti^{4+} to Ti^{3+} (ΔG_5, determined by the CV of $TiCl_4 \cdot 2THF$). The Ti^{3+} centers sequentially reduce O_2 to generate $O_2^{\bullet-}$ (ΔG_6), H_2O_2 (ΔG_7), and $^{\bullet}OH$ (ΔG_8).[16] The oxidation

potential of $TBP^{\bullet+}$ to TBP (ΔG_3), determined by cyclic voltammogram (CV) of H_4TBP, is sufficient to oxidize GSH to GSSG (ΔG_4).

3.2.4 Anti-cancer efficacy

The cytotoxicity of Ti-TBP-mediated PDT was investigated in vitro on CT26 cells. Time-dependent ICP-MS analysis of Hf demonstrated efficient uptake of Ti-TBP and Hf-TBP by CT26 cells. Although H_4TBP, Hf-TBP, and Ti-TBP can all generate $^1O_2$, O_2^- was only detected in cells treated with Ti-TBP (**Figure 3-11**).

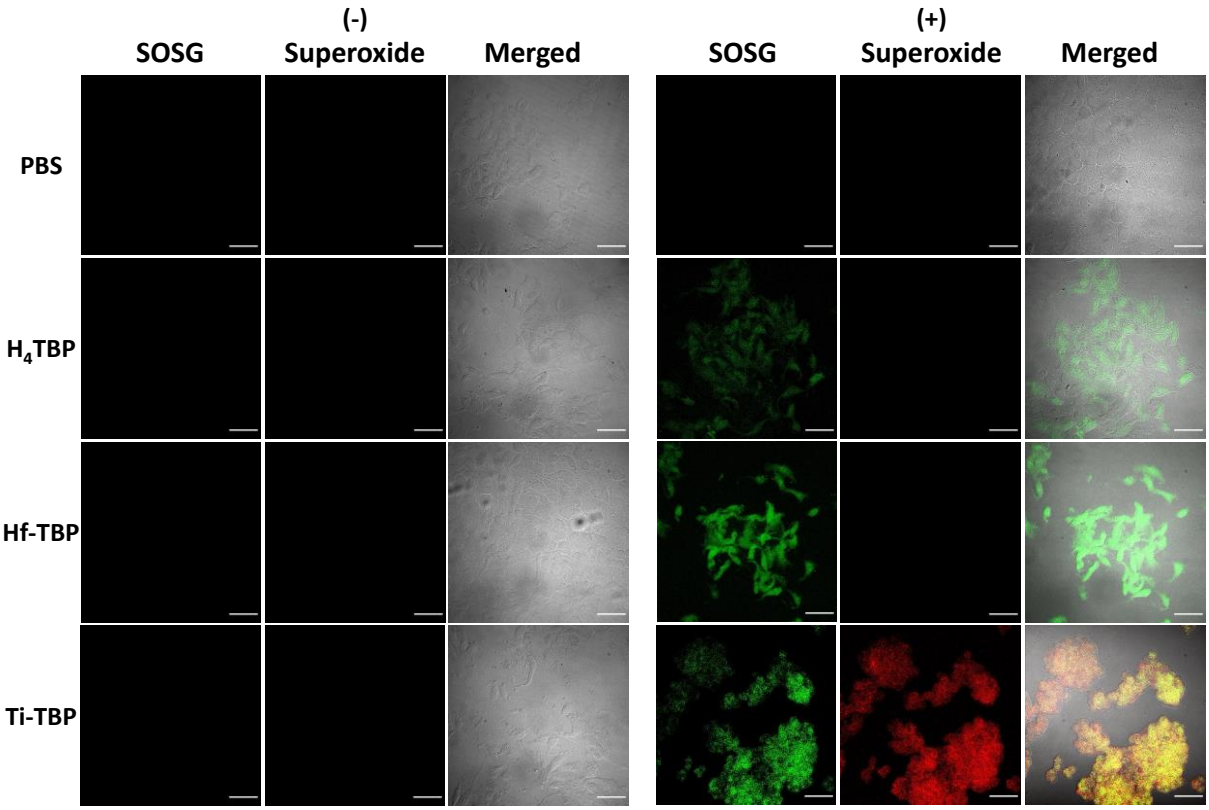

Figure 3-11. Intracellular $^1O_2$ and O2$^-$generation. Intracellular $^1O_2$ and O_2^-generation with (+) or without (-) light irradiation detected by SOSG and superoxide kit. Green and red fluorescence represent SOSG or superoxide signal, respectively. Green and red fluorescence merge to give yellow fluorescence. Scale bar = 50 μm.

The in vitro generation of $^{\bullet}OH$ was verified by direct $^{\bullet}OH$ detection via coumarin-3-carboxylic acid assay (**Figure 3-12**) and by DNA DSB quantification with γ-H2AX assay (**Figure 3-13**), both of which showed that $^{\bullet}OH$ was only detected in Ti-TBP treated cells.

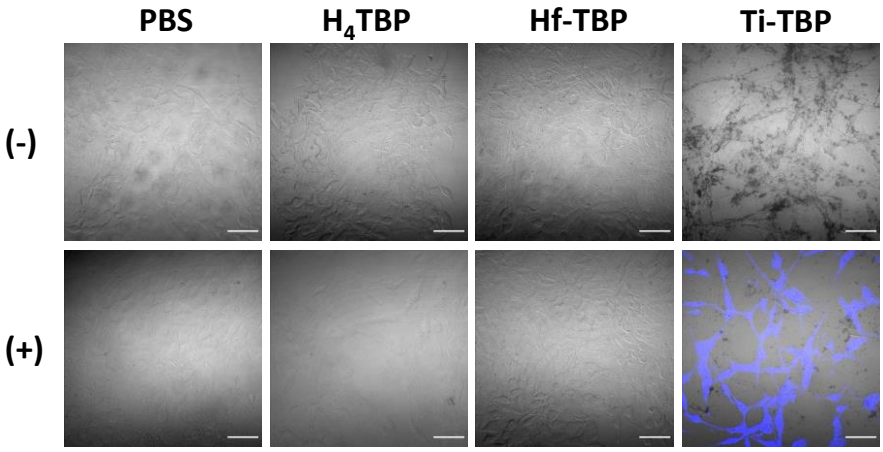

Figure 3-12. Intracellular •OH generation. Intracellular •OH generation with (+) or without (-) light irradiation detected by coumarin-3-carboxylic acid assay. Blue fluorescence represents •OH signal. Scale bar = 50 μm.

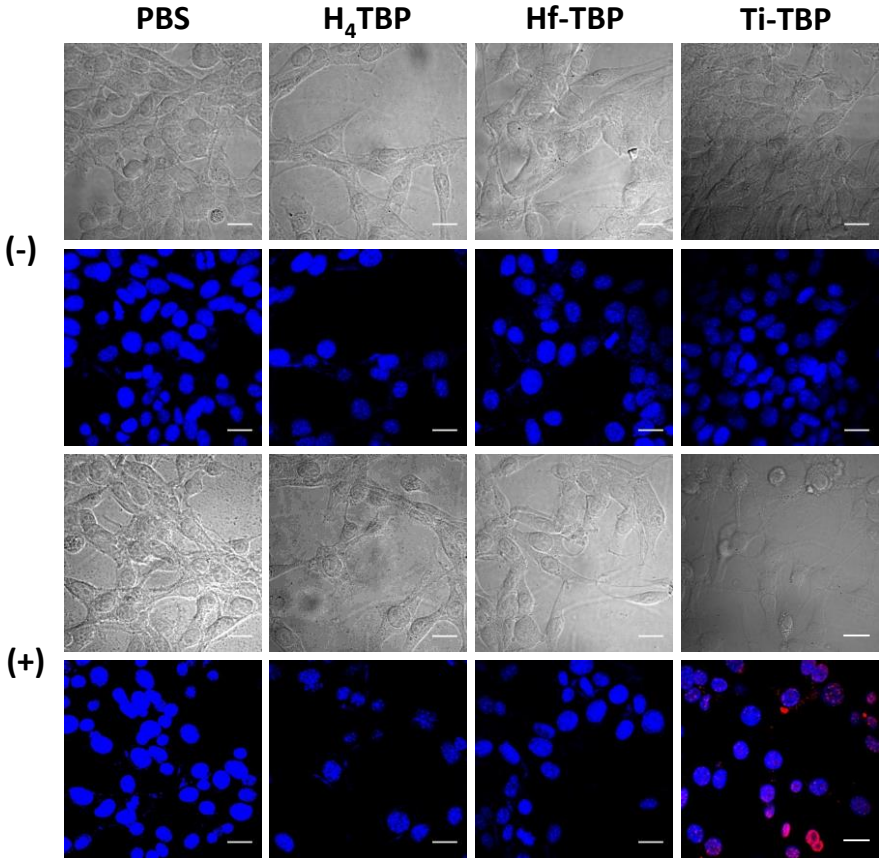

Figure 3-13. γ-H2AX assay. γ-H2AX assays showing DNA DSBs in CT26 cells treated with Ti-TBP, Hf-TBP, H_4TBP or PBS with (+) or without (-) light irradiation. Blue and red fluorescence represent nuclei and DSB signals, respectively. Scale bar = 20 μm.

Confocal imaging and flow cytometry using an Annexin V/dead cell apoptosis kit showed that significant numbers of cells underwent apoptosis when treated with Ti-TBP (**Figure 3-14**).

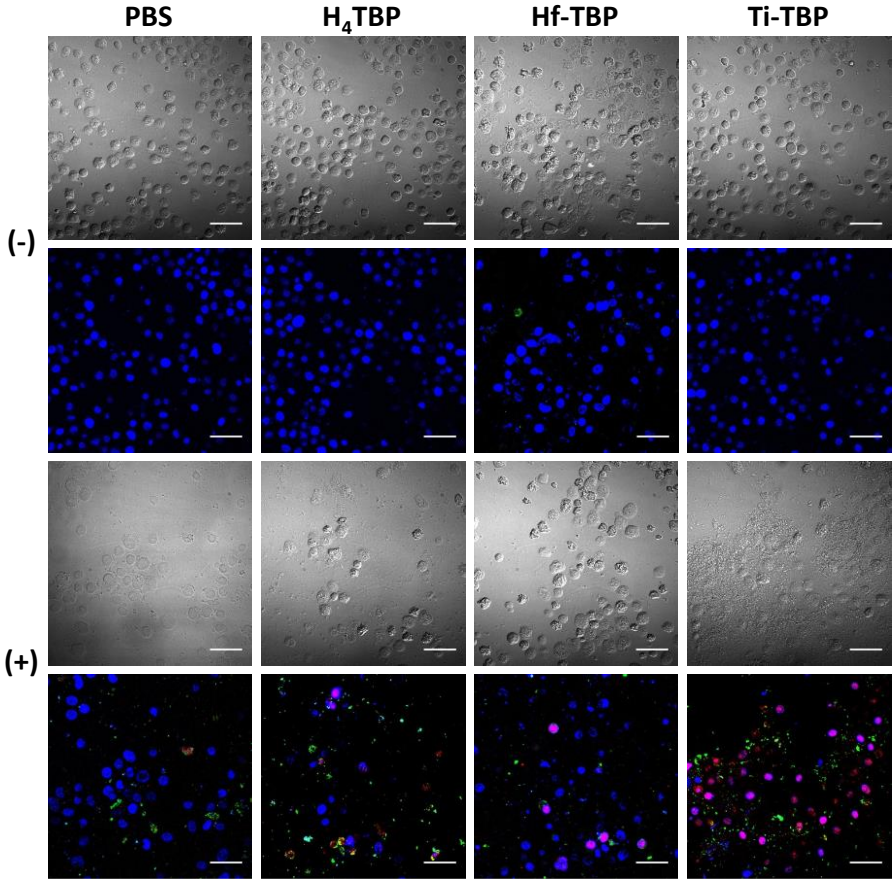

Figure 3-14. Annexin V assay. Annexin V assay to probe apoptotic cell death process of CT26 cells treated with Ti-TBP, Hf-TBP, H_4TBP or PBS with light irradiation. DAPI (blue), FITC-Annexin-V (green), and PI (red) indicate nucleus, apoptotic and dead cells, respectively. Scale bar = 50 μm

MTS assay (**Figure 3-15**) and live/dead cell confocal microscopic images (**Figure 3-16**) showed that Ti-TBP outperformed Hf-TBP with IC_{50} values of 3.4 ± 0. 7 and 7.8 ± 2.4 μM, respectively.

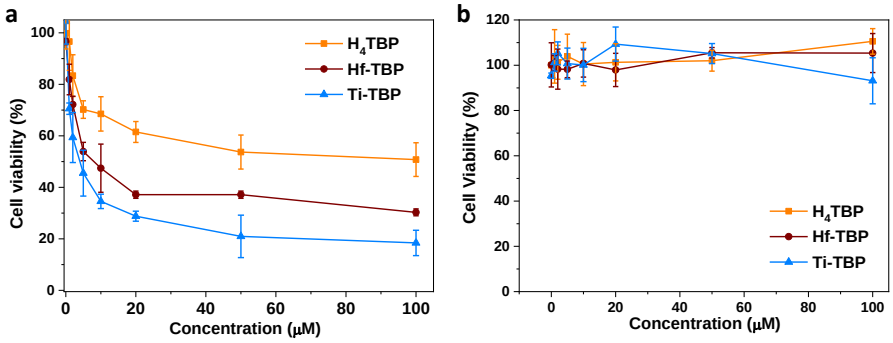

Figure 3-15. MTS assay. MTS assay showing the cytotoxicity of Ti-TBP, Hf-TBP, and H_4TBP with (a) or without (b) light irradiation. N=6.

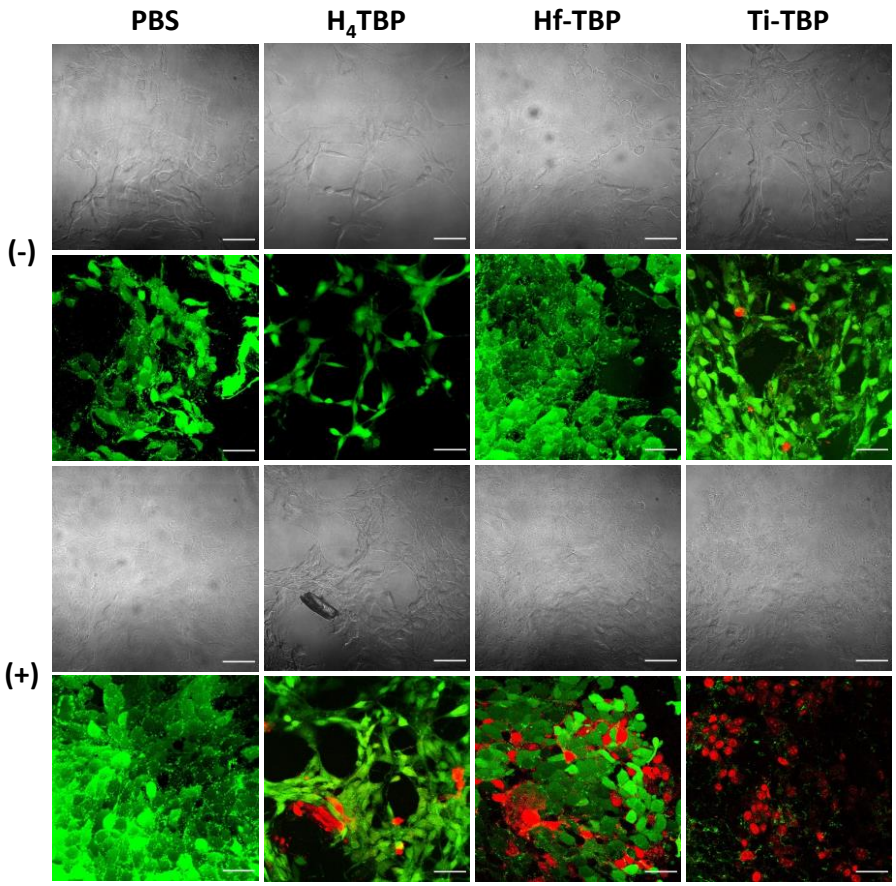

Figure 3-16. Live/dead cell analysis. Live/dead cell analysis with (+) or without (-) light irradiation on CT26 cells. Green fluorescence and red fluorescence represent calcein AM or EtBr signals, respectively, for live or dead cells. Scale bar = 50 μm

The therapeutic effects of Ti-TBP-mediated PDT were next evaluated in vivo on a colorectal adenocarcinoma model of CT26-tumor bearing BALB/c mice. When the tumors reached 100-150 mm^3, Ti-TBP, Hf-TBP, H_4TBP or PBS was injected intratumorally at a TBP doses of 0.2 μmol following by light irradiation (650 nm, 180 J/cm^2). Ti-TBP treatment led to effective tumor regression of 98.4% in volume with a cure rate of 60% (3 out of 5), when compared to that of the PBS dark control on Day 20. Hf-TBP and H_4TBP treatment showed moderate and slight tumor inhibition, respectively (**Figure 3-17a**). The averaged weights of excised tumors on Day 20 treated with Ti-TBP, Hf-TBP, H_4TBP or PBS were 0.027 ± 0.037 g, 0.127 ± 0.03 g, 0.617 ± 0.168 g, or 1.734 ± 0.291 g, respectively. Steady body weights, similar

weight gain patterns, and no difference in behaviors and organ functions were observed in all groups, indicating lack of systemic toxicity for Ti-TBP treatment (**Figure 3-17b**).

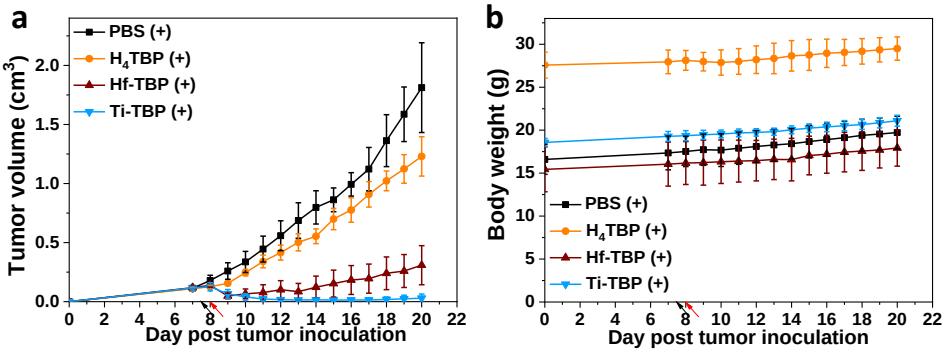

Figure 3-17. In vivo anti-cancer efficacy. Tumor growth (a) and bodyweight (b) for CT26 tumor-bearing mice treated with Ti-TBP, Hf-TBP, H_4TBP, or PBS with light irradiation (+). N = 5. Black and red arrows refer to intratumoral injection of Ti-TBP, Hf-TBP, H_4TBP, or PBS and light irradiation, respectively.

3.3 Conclusion

In this Chapter, we report the synthesis of a new MOF, Ti-TBP, and its use in hypoxia-tolerant type I PDT with superb anti-cancer efficacy. Upon light irradiation, the proximity of Ti-oxo chain SBUs to TBP ligands (~1.1 nm) facilitates ET to generate $TBP^{\bullet+}$ and Ti^{3+}, propagating the generation of O_2^-, H_2O_2, and $^{\bullet}OH$. Our work presents a new strategy to implement and understand type I PDT using nMOFs.

3.4 Methods

Synthesis of Ti-(Ti-TBP) single crystals. H_4TBP was synthesized as described previously.[10] To a 4 mL glass vial was added 0.5 mL of $TiCl_4 \cdot 2THF$ solution (6.0 mg/mL in DMF), 0.5 mL of H_4TBP solution (4.0 mg/mL in DMF), 140 μL of AcOH. The reaction mixture was kept in a 120 °C oven for 7 days to afford violet square-shaped single crystals (0.5 mg, 7.8% yield).

Synthesis of Ti-TBP nMOFs. To a 4 mL glass vial was added 0.5 mL of $TiCl_4 \cdot 2THF$ solution (2.0 mg/mL in DMF), 0.5 mL of H_4TBP solution (2.0 mg/mL in DMF), 50 μL of AcOH. The reaction mixture was kept in an 80 °C oven for 24 hours. The violet precipitate was collected

by centrifugation and washed with DMF and ethanol. The yield was 31% (0.66 mg) based on Ti as determined by ICP-MS.

$^1O_2$ generation with SOSG assay. SOSG reacts with $^1O_2$ to give bright green fluorescence (excitation/emission maxima 504/525 nm). H_4TBP, Hf-TBP, or Ti-TBP was suspended in 2 mL water at equivalent TBP concentrations of 20 μM in the presence of 12.5 μM SOSG. The mixed suspension was exposed to LED light (100 mW/cm^2, 650 nm) for 0, 10, 20, 30, 60, 120, 180, 300, 420, and 600 seconds and the fluorescence at different time points was measured with a fluorimeter.

O_2^- generation determined by EPR with BMPO. BMPO is a nitrone spin trap, which forms distinct adducts with O_2^- (BNPO-O_2^-) with a long half-life ($t_{1/2}$) of 23 minutes. H_4TBP, Hf-TBP, or Ti-TBP was suspended in benzyl alcohol at equivalent TBP concentrations of 100 μM in the presence of 25 mM BMPO. 500 μL of each suspension was added to EPR tubes and irradiated by light for 10 mins. The EPR signal of each sample was then collected on a Bruker Elexsys 500 X-band EPR (frequency = 9.6315 GHz) spectrometer at 298 K.

H_2O_2 generation with a hydrogen peroxide assay kit. The hydrogen peroxide assay kit reacts with H_2O_2 to give bright green fluorescence (excitation/emission maxima 490/520 nm). H_4TBP, Hf-TBP, or Ti-TBP was suspended in 2 mL water at equivalent TBP concentrations of 20 μM in the presence of 1 μL suspension of the hydrogen peroxide assay kit. The mixed suspension was exposed to LED light (100 mW/cm^2, 650 nm) for 0, 10, 20, 30, 60, 120, 180, 300, 420, and 600 seconds and the fluorescence at different time points was measured with a fluorimeter.

$^{\bullet}$OH generation with APF assay. APF reacts with $^{\bullet}$OH to give bright green fluorescence (excitation/emission maxima 490/515 nm). H_4TBP, Hf-TBP, or Ti-TBP was suspended in 2 mL water at equivalent TBP concentrations of 20 μM in the presence of 5 μM APF. The mixed suspension was exposed to LED light (100 mW/cm^2, 650 nm) for 0, 30, 60, 120, 180, 300, 420, and 600 seconds and the fluorescence at different time points was measured with a fluorimeter.

$^{\bullet}$OH generation from H_2O_2 enabled by Ti^{3+} under oxygen-free condition. Because hypoxic cancer cells usually have high H_2O_2 concentrations, converting intracellular H_2O_2 into highly cytotoxic $^{\bullet}$OH is an effective way to kill cancer cells. H_4TBP, Hf-TBP, or Ti-TBP was suspended in oxygen-free water at equivalent TBP concentrations of 20 μM in the presence of 150 μM H_2O_2 and 5 μM APF. An oxygen-free aqueous solution of 150 μM H_2O_2 and 5 μM APF served as control. The mixed suspension was exposed to LED light (100 mW/cm^2, 650 nm) for 0, 30, 60, 120, 180, 300, 420, and 600 seconds. Another dark control group was prepared by repeating the aforementioned Ti-TBP suspension without light irradiation. The fluorescence at different time points was measured with a fluorimeter.

Oxidizing GSH to GSSG by TBP$^{\bullet+}$ under oxygen-free condition. GSH is present at high concentration (1-10 mM) in cells and serves as an important antioxidant via oxidation to GSSG in cells to alleviate oxidative stress. The HPLC analysis of GSH and GSSG was performed using isocratic elution with a reversed phase C18 column, a mobile phase's composition of water/acetonitrile (95/5, v/v), trifluoroacetic acid (TFA: 0.1%) and sodium perchlorate (12 mg·mL^{-1}), and a flow rate of 1 mL·min^{-1}. The detection wavelength was set at 200 nm on the UV detector. The column oven temperature was kept at room temperature while the auto-sampler temperature was maintained at 4°C. A volume of 10 μL of sample solutions (aqueous solution of GSH or GSSG) was directly injected to the HPLC equipment and further analyzed. Under these conditions, the GSH and GSSG were simultaneous determined with retention times of 3.93 min and 5.51 min, respectively. H_4TBP, Hf-TBP, or Ti-TBP was suspended in oxygen-free water at equivalent TBP concentrations of 20 μM in the presence of 1 mM GSH. An oxygen-free aqueous solution of only 1 mM GSH served as a control group. The mixed suspension was exposed to LED light (100 mW/cm^2, 650 nm) for 40 mins, filtered through a 220-nm filter, and analyzed by HPLC. GSSG was only detected in Ti-TBP group with a concentration of 98.8 μM.

EPR of Ti-TBP under oxygen-free condition upon light irradiation. H_4TBP, Hf-TBP, or Ti-TBP was suspended in oxygen-free toluene at an equivalent TBP concentrations of 500 μM and transferred into EPR tubes. EPR spectra were recorded on a Bruker Elexsys 500 X-band EPR spectrometer under irradiation of a white-light lamp (Fiber-Lite MI-150) by focusing the lamp on the sample cell in the EPR cavity at 20 K. Frequency = 9.6315 GHz.

$^1O_2$ generation by Ti-TBP in the presence of benzoquinone. Ti-TBP was suspended in 2 mL water with a TBP concentration of 20 μM, a SOSG concentration of 12.5 μM, and a benzoquinone concentration of 0 or 500 μM. The mixed suspension was exposed to LED light (100 mW/cm^2, 650 nm) for 0, 10, 20, 30, 60, 120, 180, 300, 420, and 600 seconds and the fluorescence at different time points was measured with a fluorimeter. In the presence of 500 μM benzoquinone, Ti-TBP retained ~70% of its intrinsic $^1O_2$ generation (without benzoquinone). As the reduction of $^1O_2$ generation is similar to the quenching of TBP photoluminescence, we conclude that the loss of $^1O_2$ production in the presence of benzoquinone is due to the quenching of TBP* by benzoquinone

H_2O_2 generation by Ti-TBP in the presence of benzoquinone. Ti-TBP was suspended in 2 mL water with a TBP concentrations of 20 μM, followed by the addition of 1 μL of the hydrogen peroxide assay kit and benzoquinone to afford a concentration of 0 or 500 μM. The mixed suspension was exposed to LED light (100 mW/cm^2, 650 nm) for 0, 30, 60, 120, 180, 300, 420, and 600 seconds and the fluorescence at different time points was measured with a fluorimeter.

$^{\bullet}$OH generation by Ti-TBP in the presence of benzoquinone. Ti-TBP was suspended in 2 mL water with a TBP concentrations of 20 μM with the addition of APF at a concentration of 5 μM and benzoquinone at a concentration of 0 or 500 μM. The mixed suspension was exposed to LED light (100 mW/cm^2, 650 nm) for 0, 30, 60, 120, 180, 300, 420, and 600 seconds and the fluorescence at different time points was measured with a fluorimeter.

Cellular uptake. The cellular uptake of Ti-TBP and Hf-TBP was compared in CT26 cells. CT26 cells were seeded on 6-well plates at 1×10^6/well and cultured for 12 h. Ti-TBP and Hf-TBP were added to the cells at a TBP concentration of 20 μM. After incubation of 1, 2, 4, and 8 hours, the cells were collected and counted with a hemocytometer. The cells were digested with concentrated nitric acid in a microwave reactor and the metal concentrations were determined by ICP-MS.

In vitro $^1O_2$ and O_2^- generation. $^1O_2$ and O_2^- generation in live cells was detected by SOSG and superoxide anion assay kit, respectively. CT26 cells were seeded in a 3.5-cm petri dish and cultured for 12 h. The culture medium was then replaced with fresh medium containing 1 μM SOSG and 1 μM superoxide anion assay kit to preload the cells with SOSG and superoxide anion assay kit. After incubating for 30 min, the cells were washed by PBS three times to remove excess SOSG and superoxide anion assay kit. The cells were incubated with Ti-TBP, Hf-TBP, H_4TBP or PBS at a TBP concentration of 20 μM for 8 h, then washed with PBS three times to remove excess Ti-TBP, Hf-TBP, or H_4TBP. The cells were irradiated with LED light (650 nm, 100 mW/cm^2, 15 min). CLSM was used to visualize the $^1O_2$ and O_2^- generated in the live cells by detecting the green and red fluorescence inside the cells, respectively.

In vitro $^{\bullet}$OH generation with a coumarin-3-carboxylic acid assay. CT26 cells were seeded in a 3.5-cm petri dish and cultured for 12 h. The cells were incubated with Ti-TBP, Hf-TBP, H_4TBP or PBS at a TBP concentration of 20 μM for 8 h, then washed with PBS three times to remove excess Ti-TBP, Hf-TBP, or H_4TBP. The cells were irradiated with LED light (650 nm, 100 mW/cm^2, 15 min). Cells were stained immediately with the 20 μM coumarin-3-carboxylic acid. After incubating for 20 min, the cells were washed with PBS three times to remove excess coumarin-3-carboxylic acid. CLSM was used to visualize the $^{\bullet}$OH generated in the live cells by detecting the blue fluorescence inside the cells.

In vitro $^{\bullet}$OH generation with γ-H2AX assay. γ-H2AX, a protein that is phosphorylated after DNA damage by hydroxyl radicals to induce DNA damage repair, has been used as a sensitive

biomarker for probing DNA DSBs. CT26 cells were cultured in 35 mm tissue culture dishes overnight and incubated with Ti-TBP, Hf-TBP, H_4TBP or PBS at a TBP concentration of 20 μM for 8 h, followed by light irradiation (650 nm, 100 mW/cm^2, 15 min). Cells were stained immediately with the HCS DNA damage kit for CLSM.

Apoptosis. CT26 cells were cultured in 35 mm tissue culture dishes overnight and incubated with Ti-TBP, Hf-TBP, H_4TBP or PBS at an equivalent TBP concentration of 20 μM for 8 h followed by light irradiation (650 nm, 100 mW/cm^2, 15 min). 24 h later, the cells were stained with the AlexaFluor 488 Annexin V/dead cell apoptosis kit for CLSM. DAPI (blue), FITC-Annexin-V (green), and PI (red) indicate nucleus, apoptotic and dead cells, respectively.

MTS assay. The cytotoxicity of Ti-TBP, Hf-TBP, and H_4TBP was evaluated MTS assay with or without light irradiation. CT26 cells were seeded on 96-well plates at 1×10^5/well and further cultured for 12 h. Ti-TBP, Hf-TBP, or H_4TBP was added to the cells at an equivalent TBP-based ligand dose of 0, 1, 2, 5, 10, 20, 50 and 100 μM and incubated for 8 h, followed by light irradiation (650 nm, 100 mW/cm^2, 15 min). The cells were further incubated for 72 h before determining the cell viability by MTS assay.

Live/dead cell analysis. The live/dead cell analysis of Ti-TBP, Hf-TBP, and H_4TBP was evaluated with cell permeable dye calcein AM and EtBr with and without light irradiation. CT26 cells were seeded on 96-well plates at 1×10^5/well and further cultured for 12 h. Ti-TBP, Hf-TBP, and H_4TBP, or PBS were added to the cells at an equivalent TBP concentration of 20 μM and incubated for 8 h. The cells were then irradiated with light (650 nm, 100 mW/cm^2, 15 min). The cells were then washed with PBS gently and stained with calcein AM (green) for visualization of live cells and with EtBr (red) for visualization of dead cells.

In vivo anti-cancer efficacy. For the evaluation of PDT efficacy of Ti-TBP, Hf-TBP, and H_4TBP, a syngeneic model was established by subcutaneously inoculating 2×10^6 CT26 cells into the right flank subcutaneous tissues of BALB/c mice on day 0 as the CT26 model. When

the tumors reached 100-150 mm^3 in volume, Ti-TBP, Hf-TBP, and H_4TBP at a TBP dose of 0.2 μmol or PBS was injected intratumorally. 12 h after injection, mice were anaesthetized with 2% (v/v) isoflurane and the tumors were irradiated by light (650 nm, 100 mW/cm^2, 15 min). The tumor sizes were measured with a caliper daily where tumor volume equals ($width^2$ × length)/2. Body weight of each group was monitored daily. Mice were sacrificed on Day 20 and the excised tumors were photographed and weighed.

3.5 References

1. Spring, B. Q.; Bryan Sears, R.; Zheng, L. Z.; Mai, Z.; Watanabe, R.; Sherwood, M. E.; Schoenfeld, D. A.; Pogue, B. W.; Pereira, S. P.; Villa, E.; Hasan, T., A photoactivable multi-inhibitor nanoliposome for tumour control and simultaneous inhibition of treatment escape pathways. *Nat. Nanotech.* **2016,** *11*, 378.
2. Lovell, J. F.; Jin, C. S.; Huynh, E.; Jin, H.; Kim, C.; Rubinstein, J. L.; Chan, W. C. W.; Cao, W.; Wang, L. V.; Zheng, G., Porphysome nanovesicles generated by porphyrin bilayers for use as multimodal biophotonic contrast agents. *Nat. Mater.* **2011,** *10*, 324.
3. Huang, P.; Lin, J.; Wang, X.; Wang, Z.; Zhang, C.; He, M.; Wang, K.; Chen, F.; Li, Z.; Shen, G.; Cui, D.; Chen, X., Light-Triggered Theranostics Based on Photosensitizer-Conjugated Carbon Dots for Simultaneous Enhanced-Fluorescence Imaging and Photodynamic Therapy. *Adv. Mater.* **2012,** *24* (37), 5104-5110.
4. Zhang, Y.; Jeon, M.; Rich, L. J.; Hong, H.; Geng, J.; Zhang, Y.; Shi, S.; Barnhart, T. E.; Alexandridis, P.; Huizinga, J. D.; Seshadri, M.; Cai, W.; Kim, C.; Lovell, J. F., Non-invasive multimodal functional imaging of the intestine with frozen micellar naphthalocyanines. *Nat. Nanotech.* **2014,** *9*, 631.
5. Dolmans, D. E. J. G. J.; Fukumura, D.; Jain, R. K., Photodynamic therapy for cancer. *Nat. Rev. Cancer* **2003,** *3*, 380.
6. Kim, J.; Cho, H. R.; Jeon, H.; Kim, D.; Song, C.; Lee, N.; Choi, S. H.; Hyeon, T., Continuous O2-Evolving MnFe2O4 Nanoparticle-Anchored Mesoporous Silica Nanoparticles for Efficient Photodynamic Therapy in Hypoxic Cancer. *J. Am. Chem. Soc.* **2017,** *139* (32), 10992-10995.
7. Gilson, R. C.; Black, K. C. L.; Lane, D. D.; Achilefu, S., Hybrid TiO2–Ruthenium Nano-photosensitizer Synergistically Produces Reactive Oxygen Species in both Hypoxic and Normoxic Conditions. *Angew. Chem. Int. Ed.* **2017,** *56* (36), 10717-10720.
8. Vakrat-Haglili, Y.; Weiner, L.; Brumfeld, V.; Brandis, A.; Salomon, Y.; McLlroy, B.; Wilson, B. C.; Pawlak, A.; Rozanowska, M.; Sarna, T.; Scherz, A., The Microenvironment Effect on the Generation of Reactive Oxygen Species by Pd−Bacteriopheophorbide. *J. Am. Chem. Soc.* **2005,** *127* (17), 6487-6497.
9. Castano, A. P.; Demidova, T. N.; Hamblin, M. R., Mechanisms in photodynamic therapy: part one—photosensitizers, photochemistry and cellular localization. *Photodiagnosis and Photodynamic Therapy* **2004,** *1* (4), 279-293.

10. Lu, K.; He, C.; Guo, N.; Chan, C.; Ni, K.; Weichselbaum, R. R.; Lin, W., Chlorin-Based Nanoscale Metal–Organic Framework Systemically Rejects Colorectal Cancers via Synergistic Photodynamic Therapy and Checkpoint Blockade Immunotherapy. *J. Am. Chem. Soc.* **2016,** *138* (38), 12502-12510.
11. Guang-sen, C.; Okido, M.; Oki, T., Electrochemical studies of titanium ions (Ti4+) in equimolar KCl NaCl molten salts with 1 wt% K2TiF6. *Electrochim. Acta* **1987,** *32* (11), 1637-1642.
12. Trachootham, D.; Alexandre, J.; Huang, P., Targeting cancer cells by ROS-mediated mechanisms: a radical therapeutic approach? *Nat. Rev. Drug Discov.* **2009,** *8*, 579.
13. Lan, M.; Zhao, H.; Yuan, H.; Jiang, C.; Zuo, S.; Jiang, Y., Absorption and EPR spectra of some porphyrins and metalloporphyrins. *Dyes Pigm.* **2007,** *74* (2), 357-362.
14. Ji, P.; Song, Y.; Drake, T.; Veroneau, S. S.; Lin, Z.; Pan, X.; Lin, W., Titanium(III)-Oxo Clusters in a Metal–Organic Framework Support Single-Site Co(II)-Hydride Catalysts for Arene Hydrogenation. *J. Am. Chem. Soc.* **2018,** *140* (1), 433-440.
15. Samoilova, R. I.; Crofts, A. R.; Dikanov, S. A., Reaction of Superoxide Radical with Quinone Molecules. *J. Phys. Chem. A* **2011,** *115* (42), 11589-11593.
16. Wood, P. M., The potential diagram for oxygen at pH 7. *Biochem. J* **1988,** *253* (1), 287.

Chapter 4. Nanoscale Metal-Organic Layers for Deeply Penetrating X-ray Induced Photodynamic Therapy

4.1 Introduction

We and others reported a series of porphyrin- and chlorin-based nMOFs as efficient PSs for light-trigged ROS generation, thus leading to effective PDT.[1-6] However, it is not feasible for all the species generated to diffuse out of the 3D structure of nMOFs to exert cytotoxicity on cellular organelles, since the lifetime of ROS is short, thus limiting the overall efficacy of PDT. We hypothesized that the PDT efficacy of nMOFs could be further improved by reducing the dimensionality to afford 2D MOL. The 2D structure of MOLs allows ROS to diffuse freely, thus presenting an ideal platform for designing nanoscale PSs for efficient PDT.

$Ir[bpy(ppy)_2]^+$ (bpy = 2,2'-bipyridine, ppy = 2-phenyl-pyridine) and $Ru(bpy)_3^{2+}$ are two efficient PSs with the very high $^1O_2$ quantum yields (Φ_Δ) of 0.97 and 0.73, respectively.[7-9] However, due to large Stokes shifts, they can only be excited with photons at short wavelengths, ~355 nm for $Ir[bpy(ppy)_2]^+$ and ~450 nm for $Ru(bpy)_3^{2+}$. Such UV-Vis photons cannot penetrate human tissue (penetration depth <0.1 mm),[10] which severely limits their application in PDT. Our previous work demonstrated that a Hf-based nMOF can absorb X-rays and transfer energy to coordinated anthracene-based ligands to luminesce in the visible spectrum.[11] We believe that coordination between $Ir[bpy(ppy)_2]^+$- or $Ru(bpy)_3^{2+}$-derived tricarboxylate ligands and heavy Hf-based SBUs would enable direct excitation of the PSs by X-rays to achieve X-ray induced PDT (X-PDT).[12] In this Chapter, we report the rational design of two MOLs, composed of $[Hf_6O_4(OH)_4(HCO_2)_6]$ SBUs and $Ir[bpy(ppy)_2]^+$- or $Ru(bpy)_3^{2+}$-derived tricarboxylate ligands, as potent PSs. The Hf-MOLs achieve greatly enhanced PDT efficacy

both in vitro and in vivo upon X-ray irradiation (**Figure 4-1**).

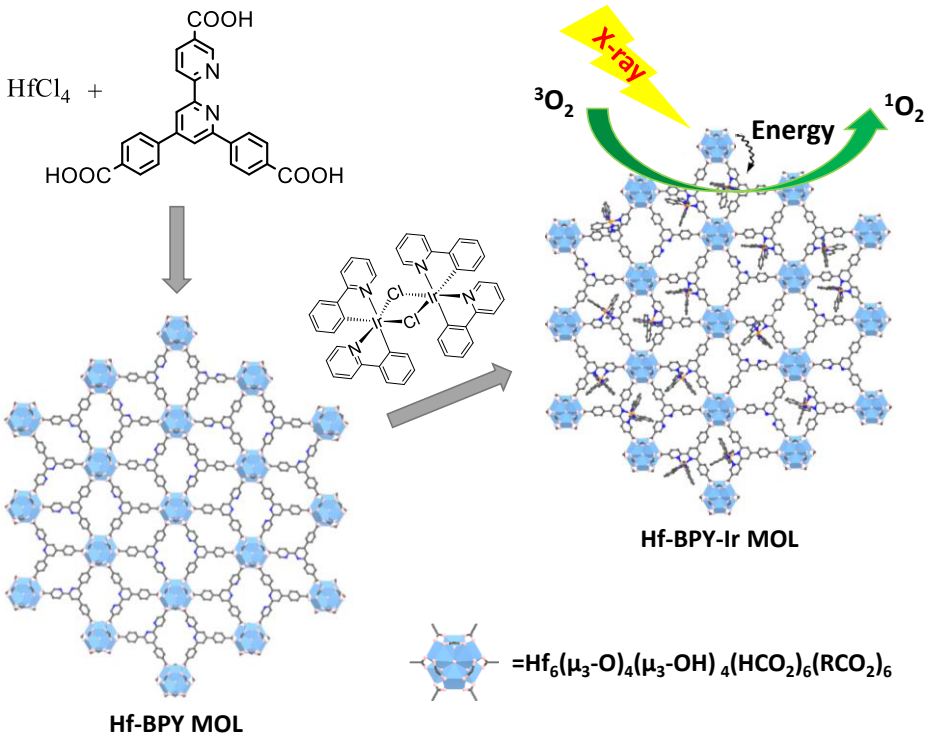

Figure 4-1. Schematic showing the synthesis of Hf-based MOLs and MOL-enabled X-PDT to generate $^1O_2$.

4.2 Result and discussion

4.2.1 Synthesis and characterization

Hf-BPY-Ir and Hf-BPY-Ru MOLs were generated through a two-step synthesis: a solvothermal synthesis to afford Hf-BPY MOL and a postsynthetic metalation to afford Hf-BPY-Ir and Hf-BPY-Ru MOLs. H_3BPY was synthesized as shown in **Figure 4-2** and treated with $HfCl_4$ in DMF, formic acid, and H_2O to afford Hf-BPY MOL as a white precipitate. By optimizing the amounts of formic acid and H_2O, the size of Hf-BPY could be controlled to a diameter of ~500 nm, as verified by TEM (**Figure 4-3a**). Hf-BPY was treated with $[Ir(ppy)_2Cl]_2$/$Ru(bpy)_2Cl_2$ to afford Hf-BPY-Ir/Hf-BPY-Ru MOL as an orange/brown participate. Due to the 2D structure of Hf-BPY, the bpy coordination sites are highly accessible,

resulting in efficient metalation. The Ir and Ru loadings were determined to be 67% and 59% for Hf-BPY-Ir and Hf-BPY-Ru, respectively, by inductively coupled plasma-mass spectrometry (ICP-MS).

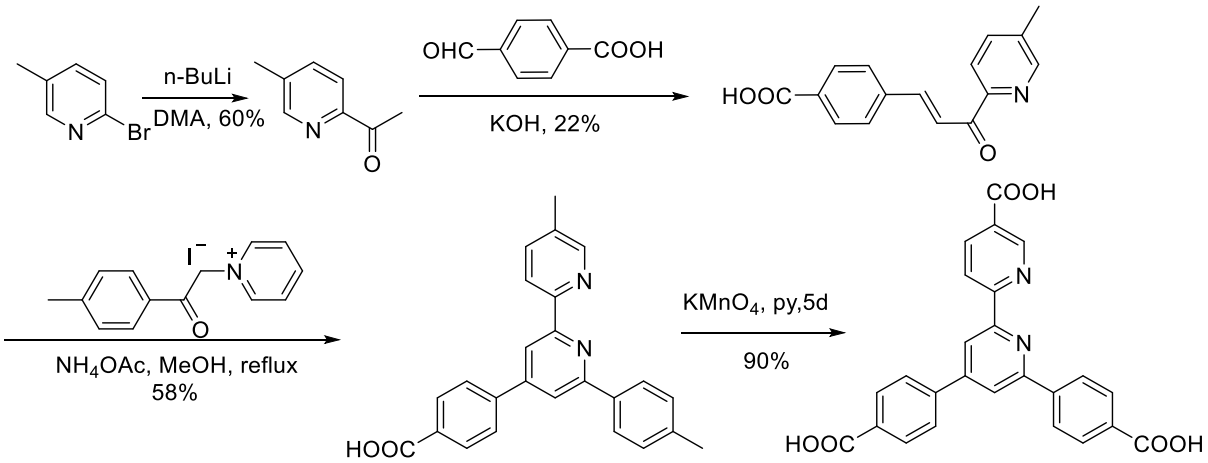

Figure 4-2. Synthesis route of H_3BPY.

In Hf-BPY, each Hf_6 cluster of 12-connectivity was capped by 6 formate groups (three at the top and three at the bottom), leaving the remaining six sites coordinated to 3-connected BPY ligands to form a 3,6-connected 2D network of $Hf_6(\mu_3\text{-}O)_4(\mu_3\text{-}OH)_4(HCO_2)_6(BPY)_2$ of **kgd** topology (**Figure 4-1**). HRTEM images of Hf-BPY, where Hf_6 clusters appear as dark spots, and FFT patterns (**Figure 4-3b**) of Hf-BPY were consistent with the **kgd** topology. The distance between two adjacent dark spots in the HRTEM was 2.0 nm, which matched the distance between two adjacent SBUs. The PXRD pattern of Hf-BPY was identical to that of the Hf-BTB MOL (**Figure 4-3c**),[20] which further confirmed the **kgd** structure of Hf-BPY. AFM images (**Figure 4-3d,e**) of Hf-BPY showed a 1.2 nm thickness, which is very close to the van der Waals size of the Hf_6 cluster capped by formate groups, indicating the monolayer structure of Hf-BPY. A nitrogen sorption study of Hf-BPY gave a BET surface are of 346 m^2/g (**Figure 4-3f**), indicating its porous structure.

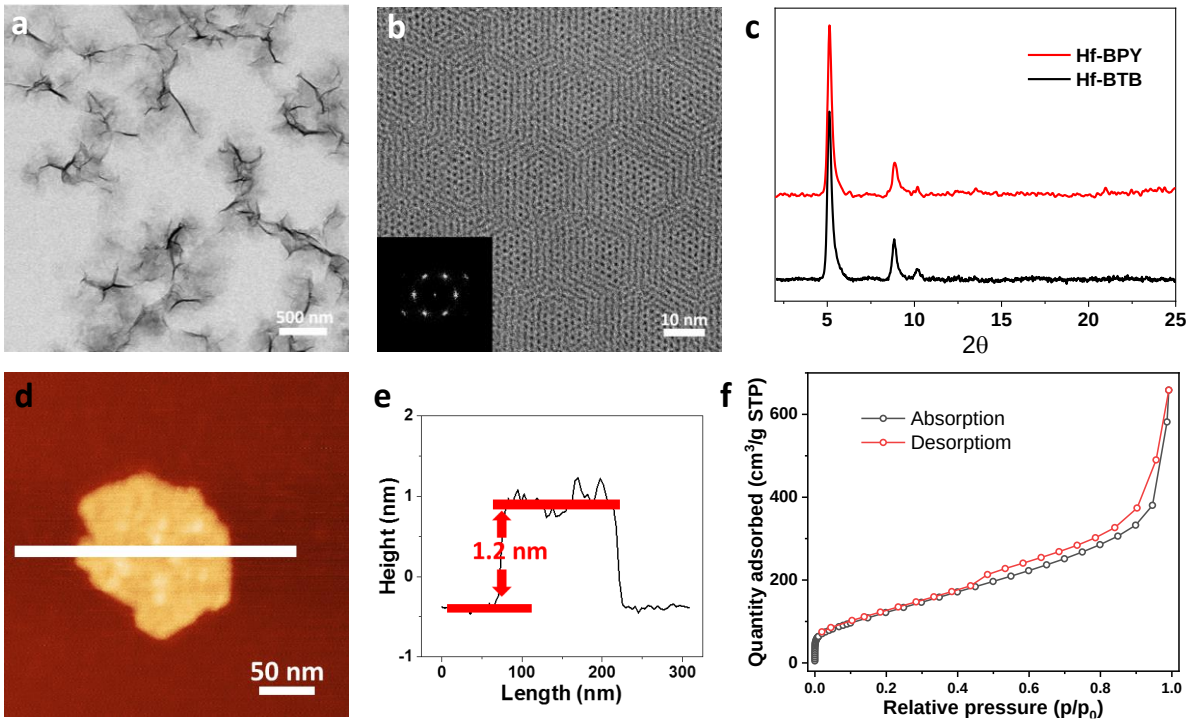

Figure 4-3. Characterization of Hf-BPY. TEM image (a), HRTEM image and FFT pattern (insert) (b), PXRD pattern (c), AFM topography (d) and its height profile (e), and nitrogen sorption isotherms of Hf-BPY.

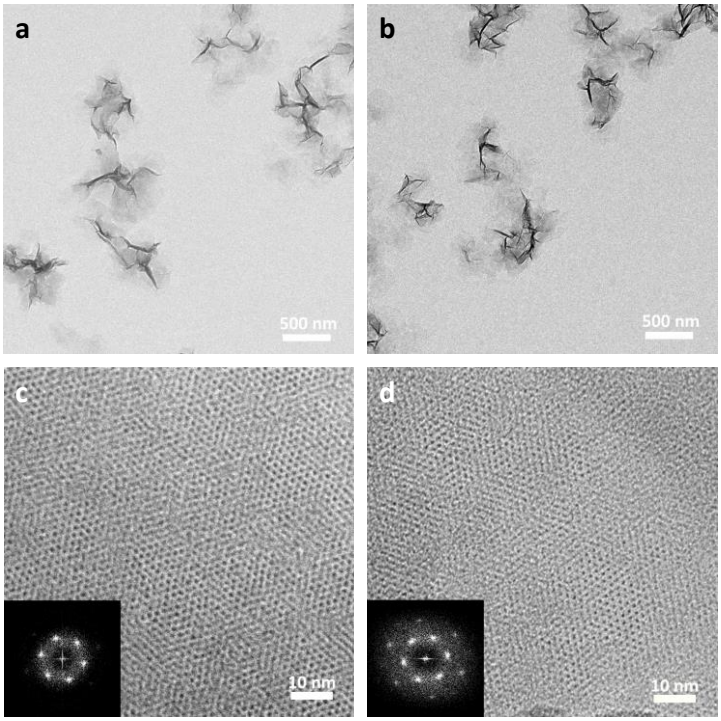

Figure 4-4. TEM images of Hf-BPY-Ir and Hf-BPY-Ru. TEM image (a), HRTEM image and FFT pattern (insert) (c) of Hf-BPY-Ir. TEM image (b), HRTEM image and FFT pattern (insert) (d) of Hf-BPY-Ru.

TEM imaging showed that Hf-BPY-Ir (**Figure 4-4a**) and Hf-BPY-Ru (**Figure 4-4b**) have similar morphologies and sizes as Hf-BPY. In addition, the HRTEM images and FFT patterns of Hf-BPY-Ir and Hf-BPY-Ru (**Figure 4-4c,d**) were identical to those of Hf-BPY. The retention of the MOL structure after metalation was supported by the similarity among the PXRD patterns of Hf-BPY-Ir, Hf-BPY-Ru, and Hf-BPY (**Figure 4-5**). PXRD patterns of the MOLs remained unchanged after incubation in DMEM media for 12 h, suggesting that the MOLs are stable for biomedical applications.

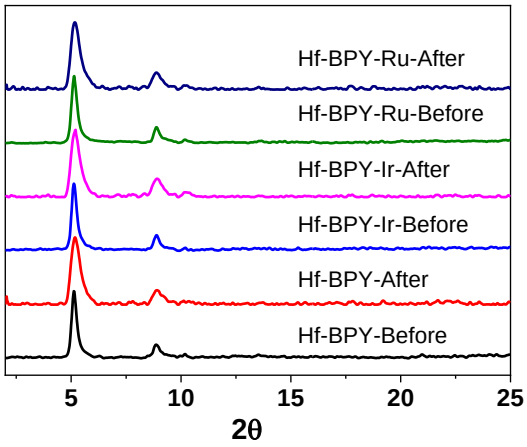

Figure 4-5. PXRD patterns of Hf-MOLs before and after incubation in DMEM media for 12 h.

To further confirm the metalation of Hf-BPY and to understand the coordination environments of Ir and Ru centers in Hf-MOLs, we synthesized $[(H_3BPY)Ir(ppy)_2]Cl$ (H_3BPY-Ir) and $[(H_3BPY)Ru(bpy)_2]Cl_2$ (H_3BPY-Ru) as ligand controls. The UV-vis absorption spectra of Hf-based MOLs exhibit similar MLCT bands as their corresponding ligands (**Figure 4-6**). Importantly, XAS indicated that Zr-BPY-Ir and Hf-BPY-Ru have the same Ir and Ru coordination environments as H_3BPY-Ir and H_3BPY-Ru, respectively (**Figure 4-7**). Due to similar energy between Ir L_3-edge (11215 eV) and Hf L_1-edge (11271 eV), XAS data was collected for Zr-BPY-Ir instead of Hf-BPY-Ir.

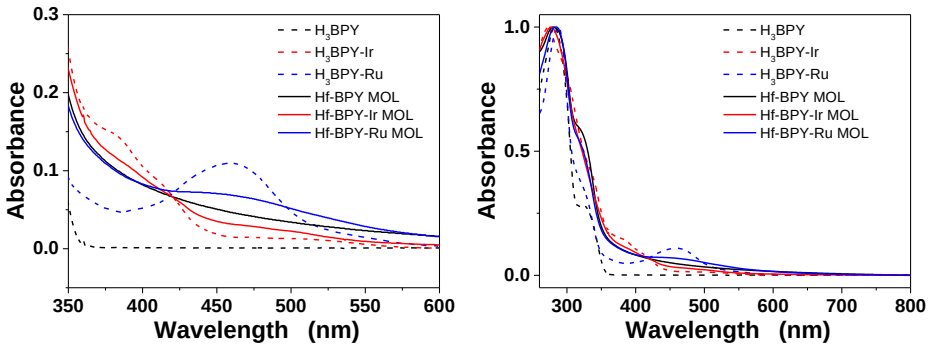

Figure 4-6. UV-vis absorption spectra of Hf-MOLs and their corresponding ligands.

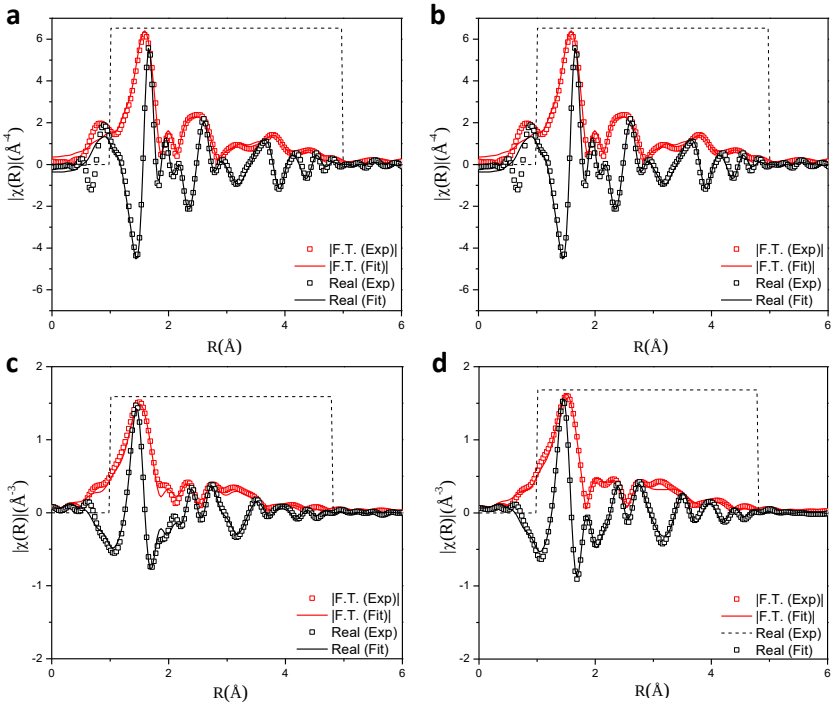

Figure 4-7. EXAFS spectra. Experimental EXAFS spectra and fits of Zr-BPY-Ir (a), H_3BPY-Ir (b), Hf-BPY-Ru (c), and H_3BPY-Ru (d) in R space showing the magnitude of Fourier Transform (hollow red squares, solid red line) and real components (hollow squares, dashed line).

4.2.2 Singlet oxygen generation

We next examined singlet oxygen generation efficiencies of MOLs using RNO assay. We also synthesized Zr-MOLs (Zr-BPY-Ir and Zr-BPY-Ru) using similar processes and used them for comparison. Upon irradiation with a Xe lamp using a 400 nm long-pass filter or X-rays (225 KVp, 13 mA), the $^1O_2$ generated by MOLs reacted with RNO in the presence of histidine, leading to a decrease of absorbance at 440 nm in the UV-visible spectra (**Figure 4-8**).

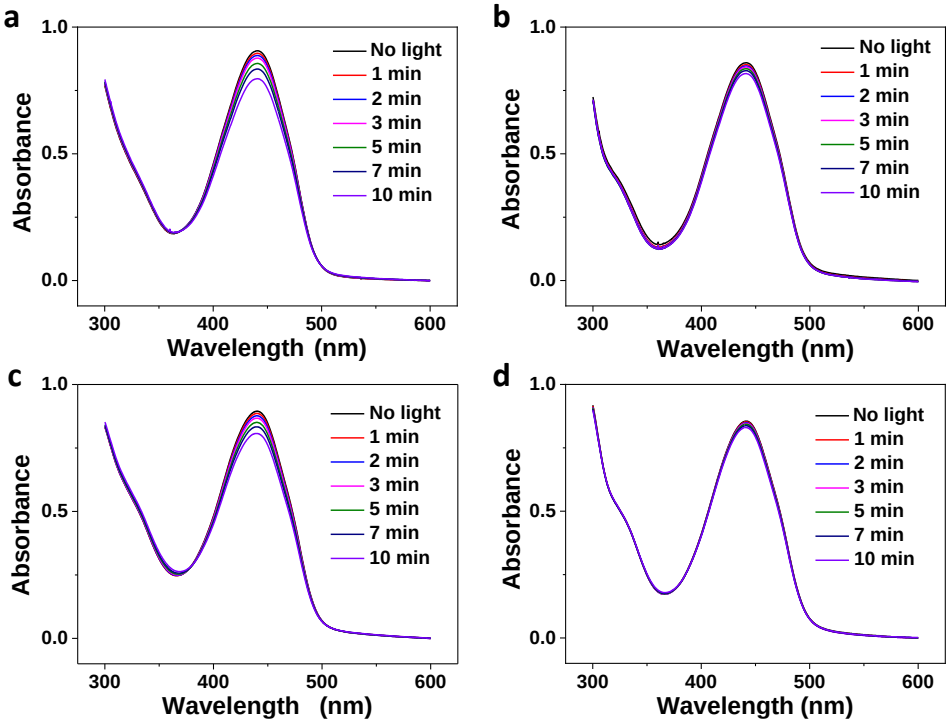

Figure 4-8. Singlet oxygen generation upon light irradiation. Singlet oxygen generation of Hf-BPY-Ir (a), Hf-BPY-Ru (b), Zr-BPY-Ir (c), and Zr-BPY-Ru (d) upon irradiation with a Xe lamp.

By linearly fitting difference in RNO peak absorbance [Δ(OD)] against irradiation doses (which scale linearly with exposure times upon visible light or X-ray dose, Y = Ax + B), the RNO assay provides a quantitative measure of $^1O_2$ generation efficiencies, with a more positive slope indicating more efficient $^1O_2$ generation. Upon visible light irradiation, the linear fitting results showed that Ir-based Zr- and Hf-MOLs generated $^1O_2$ more efficiently than Ru-based Zr- and Hf-MOLs (**Figure 4-9**), consistent with the difference in $^1O_2$ generation quantum yields between $[Ir(bpy)(ppy)_2]^+$ (Φ_Δ = 0.97) and $[Ru(bpy)_3]^{2+}$ (Φ_Δ = 0.73). Furthermore, only very slight differences were observed between two Ir-based MOLs (A = 1.09×10^{-2} for Hf-BPY-Ir and A = 0.88×10^{-2} for Zr-BPY-Ir) or two Ru-based MOLs (A = 4.1×10^{-3} for Hf-BPY-Ru and A = 2.4×10^{-3} for Zr-BPY-Ru), suggesting minor effects of the SBUs in the $^1O_2$ generation efficiency through spin-orbit coupling.

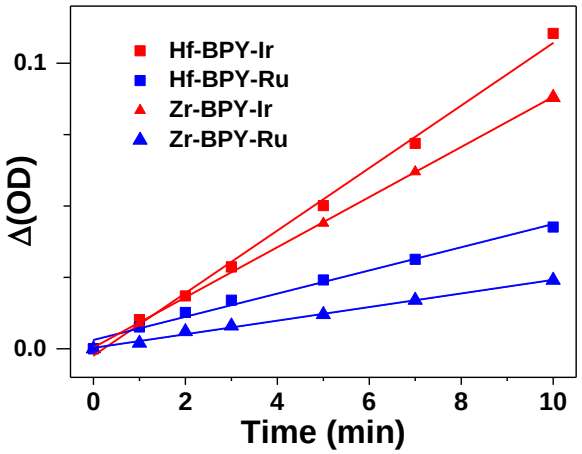

Figure 4-9. Linear fit of Δ(OD) against light irradiation dose.

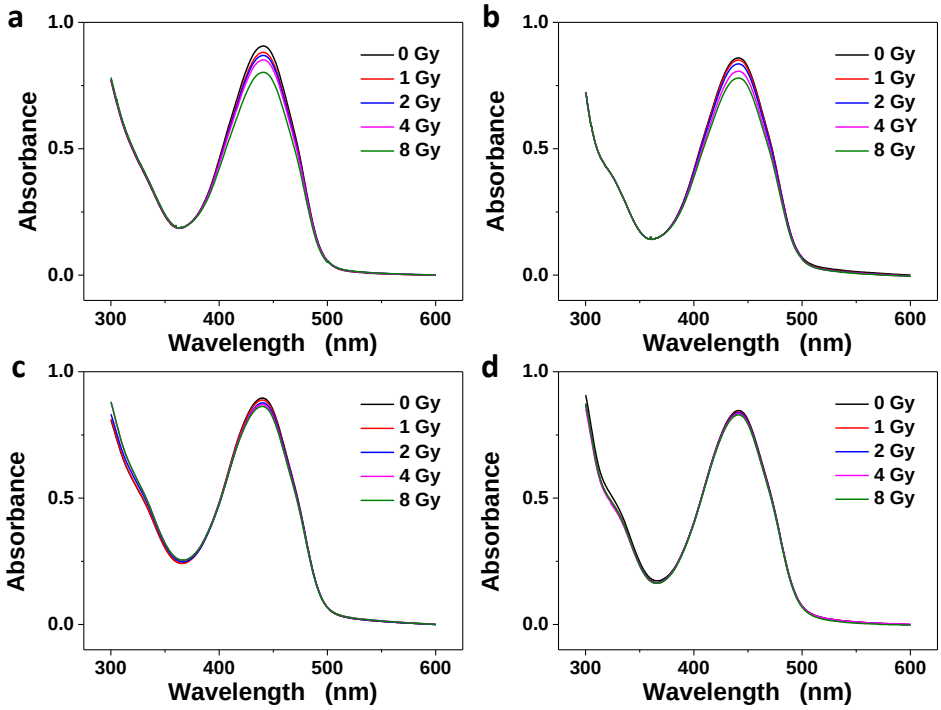

Figure 4-10. Singlet oxygen generation upon X-ray irradiation. Singlet oxygen generation of Hf-BPY-Ir (a), Hf-BPY-Ru (b), Zr-BPY-Ir (c), and Zr-BPY-Ru (d) upon X-ray irradiation.

However, upon X-ray irradiation, there was a drastic difference in $^1O_2$ generation efficiencies in Zr- and Hf-MOLs (**Figure 4-10**). Both Hf-MOLs ($A = 1.22\times10^{-2}$ for Hf-BPY-Ir and $A = 1.0\times10^{-2}$ for Hf-BPY-Ru) possessed much higher $^1O_2$ generation efficiency than their corresponding Zr-MOLs ($A = 0.39\times10^{-2}$ for Hf-BPY-Ir and $A = 0.19\times10^{-2}$ for Zr-BPY-Ir) (**Figure 4-11**), supporting our hypothesis that the X-ray energy was first absorbed by SBUs and then transferred to the PSs in the bridging ligands to lead to the X-PDT effect. Because the

heavier Hf atoms absorb X-rays more efficiently than the Zr atoms, the Hf-MOLs are expected to be more effective at X-PDT. Additionally, Ir-based MOLs showed only slightly better X-PDT efficiency than Ru-based MOLs, suggesting different energy transfer processes involved in X-PDT and PDT.

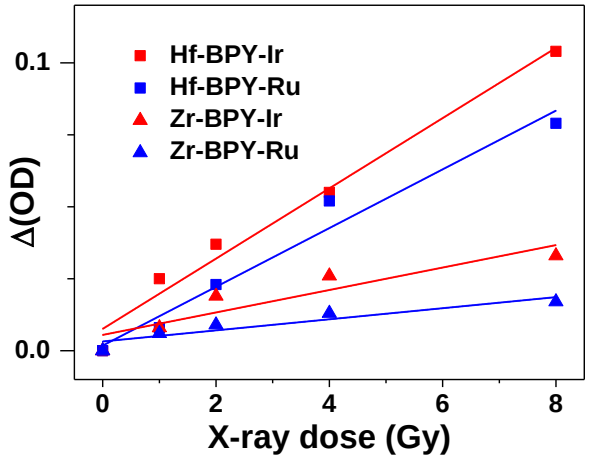

Figure 4-11. Liner fit of Δ(OD) against X-ray irradiation dose.

4.2.3 Anti-cancer efficacy

In the clinic, PDT is typically applied to superficial malignant tumors such as skin lesions and esophageal cancer due to the limited penetration of light (~3 mm at 800 nm). We sought to examine the potential of MOL-mediated X-PDT in the treatment of deeply seated tumors. Two types of murine colon adenocarcinoma cells, CT26 and MC38, were used for *in vitro* and *in vivo* studies. The cellular uptake was evaluated on CT26 cells incubated with Hf-BPY-Ir, Hf-BPY-Ru, or Hf-BPY at a Hf concentration of 50 μM for 1, 4, 8, and 24 h. At each time point, cells were digested and the Hf contents were determined by ICP-MS. Hf-BPY-Ru showed higher uptake (6580 ± 1770 ng/10^5 cells) than Hf-BPY-Ir (3317 ± 665 ng/10^5 cells) and Hf-BPY (1930 ± 716 ng/10^5 cells), presumably because of the higher positive charge of Hf-BPY-Ru, which favors interacting with the negatively charged cell membrane to facilitate endocytosis (**Figure 4-12**).

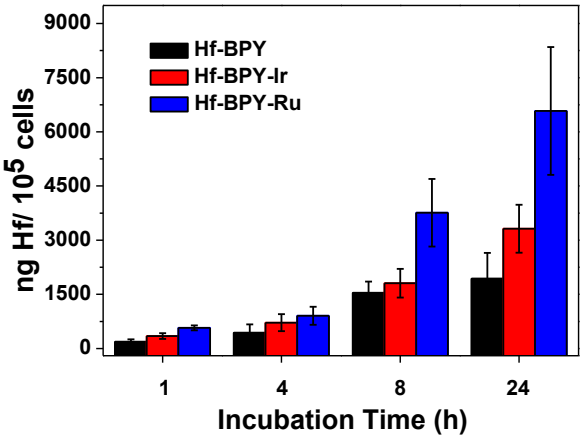

Figure 4-12. Cellular uptake of Hf-MOLs. Cellular uptake of Hf-MOLs after 4, 8, or 24 hour incubation based on Hf concentrations. The Hf concentrations were determined by ICP-MS (N = 3).

We next investigated the in vitro anticancer efficacy of three different Hf-based MOLs against CT26 and MC38 cells (**Figure 4-13**). To elucidate the key role of Hf in efficient absorption of X-rays, three corresponding Zr-MOLs were used as controls. MOLs were incubated with cells at various concentrations for 8 h, followed by irradiation with an X-ray irradiator at a dose of 2 Gy. Hf-BPY-Ir and Hf-BPY-Ru outperformed Hf-BPY and three Zr-MOLs. The IC_{50} values for Hf-BPY-Ir, Hf-BPY-Ru, and Hf-BPY against CT26 cells were calculated to be 3.82 ± 1.80, 3.63 ± 2.75, and 24.90 ± 7.87 μM, respectively. Against MC38 cells, the IC_{50} values were 11.66 ± 1.84, 10.72 ± 2.92, and 37.80 ± 6.57 μM, respectively. IC_{50} values exceeded 100 μM for Zr-BPY-Ir, Zr-BPY-Ru, and Zr-BPY in both CT26 and MC38 cell lines. No cytotoxicity was observed in dark control groups.

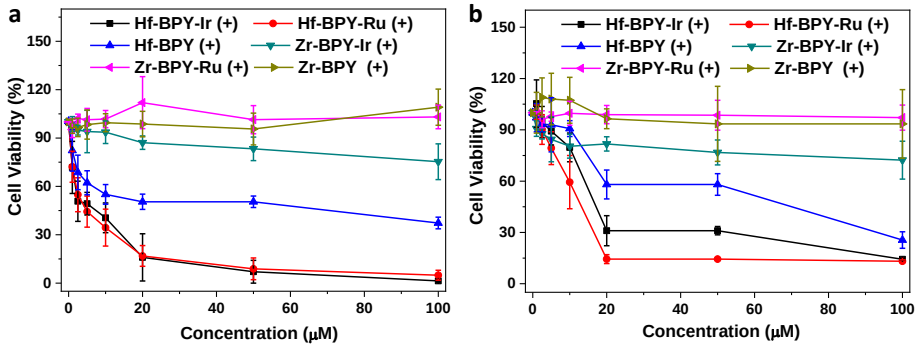

Figure 4-13. Cytotoxicity. Cytotoxicity of MOLs in CT26 cells (a) and MC38 cells (b).

Importantly, X-ray induced cytotoxicity of Hf-BPY-Ir and Hf-BPY-Ru remained essentially unchanged when the cells were covered with a beef block of 1 cm in thickness during X-ray irradiation (**Figure 4-14b**). In contrast, light induced cytotoxicity of Hf-BPY-Ir and Hf-BPY-Ru was completely lost when the cells were covered with the same beef block during light irradiation (**Figure 4-14a**). These results support our hypothesis that MOL-mediated X-PDT can be used to treat deeply seated tumors.

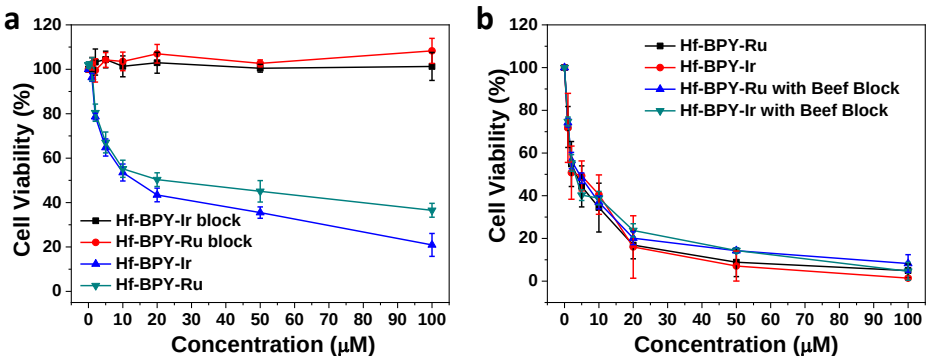

Figure 4-14. Cytotoxicity with beef block. Cytotoxicity of Hf-BPY-Ir and Hf-BPY-Ru in CT26 cells with or without beef block upon light (a) or X-ray (b) irradiation.

Interestingly, control experiments with Hf-QPDC-Ir nMOF, a UiO nMOF built from $Hf_6(\mu_3\text{-}O)_4(\mu_3\text{-}OH)_4$ SBUs and $[Ir(bpy)(ppy)_2]^+$-derivated QPDC-Ir bridging ligands, further support the enhanced X-PDT efficacy of the MOLs due to facile ROS diffusion; upon X-ray irradiation, Hf-QPDC-Ir nMOF exhibited much higher IC_{50} values of 32.85 ± 3.02μM for CT26 cells and 26.08 ± 2.38 μM for MC38 cells, respectively (**Figure 4-15**).

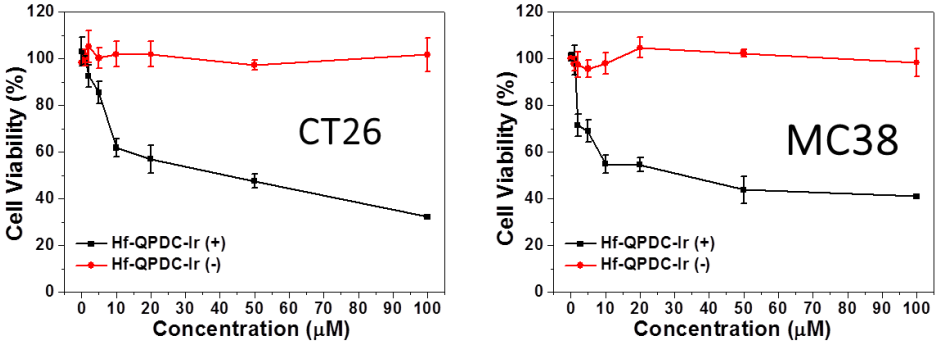

Figure 4-15. Cytotoxicity of Hf-QPDC-Ir.

We then explored the mechanism of X-ray induced cytotoxicity on CT26 cells. $^1O_2$ generation in live cells was examined by SOSG and detected by CLSM (**Figure 4-16**). Both Hf-BPY-Ir- and Hf-BPY-Ru-treated cells showed strong green SOSG fluorescence, indicating the efficient generation of $^1O_2$ in the MOLs upon X-ray irradiation. In contrast, PBS, Hf-BPY and H_3BPY ligand-treated groups showed no SOSG signal after X-ray induced $^1O_2$ generation, which supported our proposed X-PDT process using Hf-BPY-Ir and Hf-BPY-Ru MOLs.

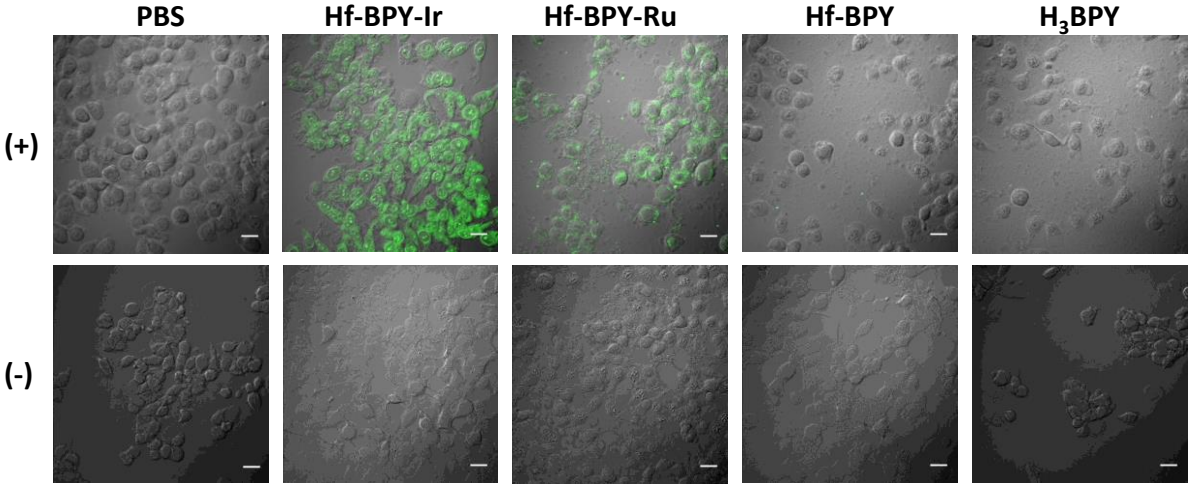

Figure 4-16. Intracellular $^1O_2$ generation. Intracellular $^1O_2$ generation with (+) or without (-) irradiation detected by SOSG. CT26 cells were preloaded with SOSG, incubated with PBS, Hf-MOLs or H_3BPY ligands and irradiated at 2 Gy. From left to right: PBS control, Hf-BPY-Ir, Hf-BPY-Ru, Hf-BPY, and H_3BPY ligand, respectively. Green fluorescence shows SOSG signal. Scale bar = 50 μm.

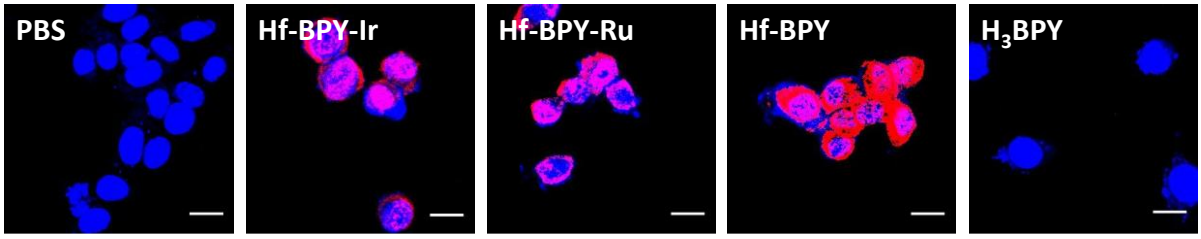

Figure 4-17. γ-H2AX assays. γ-H2AX assays showing the DNA DSBs in CT26 cells treated with the MOLs with X-ray irradiation at 2 Gy. Blue and red fluorescence show DAPI-stained nucleus and antibody-labeled γ-H2AX in the cells, respectively. Scale bar = 20 μm.

We also performed γ-H_2AFX assay on CT26 cells to determine DNA DSBs caused by MOLs upon X-ray irradiation. As shown in **Figure 4-17**, CT26 cells treated with three Hf-based MOLs showed significant red fluorescence, indicating DSBs induced by hydroxyl

radical from X-ray irradiation. This result suggests that Hf_6 SBUs are capable of radiosensitization to further enhance cytotoxicity of MOL-mediated X-PDT.

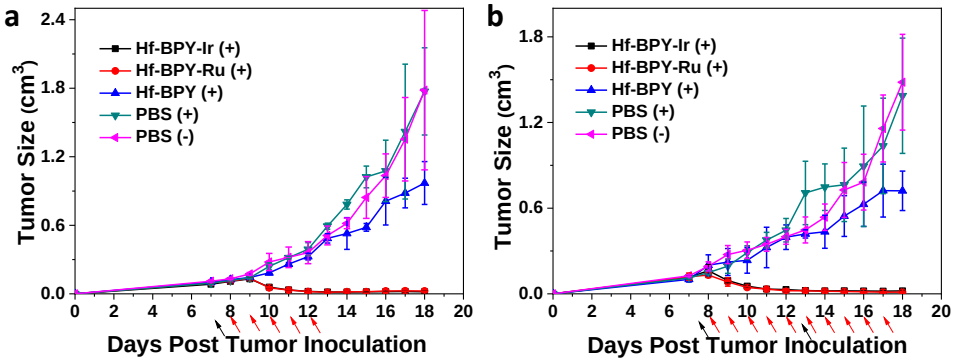

Figure 4-18. In vivo anti-cancer efficacy. Tumor growth inhibition curves after X-PDT treatment in the CT26 (a) and MC38 (b) models. Black arrows refer to injection of MOLs and red arrows refer to X-ray irradiation. N = 5.

Encouraged by the in vitro results, we carried out in vivo anticancer efficacy experiments on subcutaneous flank tumor-bearing mouse models of CT26 and MC38. When tumors reached 100-150 mm^3 in volume, Hf-BPY-Ir, Hf-BPY-Ru, or Hf-BPY with amount of 0.5 nmol based on Ir, Ru or BPY, respectively, or PBS was intratumorally injected followed by daily X-ray irradiation at a dose of 1 Gy/fraction (120 kVp, 20 mA, 2 mm-Cu filter) for a total of 5 fractions on the CT26 model (**Figure 4-18a**) or 10 fractions on the MC38 model (**Figure 4-18b**) on consecutive days. Tumor sizes and body weights were measured every day. To rule out any radiotherapy effects from the low dose X-ray, we used PBS-treated mice without X-ray irradiation as a dark control. The PBS groups with or without irradiation did not show any difference in tumor growth curves, indicating that low dose X-rays alone had no radiotherapeutic effects. The Hf-BPY groups appeared to show slight inhibition of tumor growth (P=0.047 or 0.048 for CT26 or MC38, respectively), consistent with the radiosensitization effects of the Hf_6 SBUs. In stark contrast, Hf-BPY-Ir and Hf-BPY-Ru treatments led to effective tumor regression in CT26 with 5 fractions of X-ray irradiation (5 Gy

total; total volume reduction of 83.6% or 77.3%, respectively) and in MC38 with 10 fractions of X-ray irradiation (10 Gy; total total volume reduction of 82.3% or 90.1%, respectively). The lack of systemic toxicity was further supported by steady body weights and similar weight gain patterns in all groups.

4.3 Conclusion

In this work, we rationally designed and synthesized two Hf-MOLs as powerful PSs for effective X-PDT of colon cancer models. Upon X-ray irradiation, Hf atoms in the SBUs absorb X-rays and transfer energy to $Ir[bpy(ppy)_2]^+$ or $[Ru(bpy)_3]^{2+}$ in the ligands to generate $^1O_2$, demonstrated by both RNO assay and in vitro $^1O_2$ detection as well as cytotoxicity studies. As a result of deep tissue penetration of X-rays, high $^1O_2$ quantum yields of $Ir[bpy(ppy)_2]^+$ or $[Ru(bpy)_3]^{2+}$, and efficient ROS diffusion through ultrathin MOLs, X-PDT treatment led to an impressive 90% reduction in tumor volumes. MOLs thus represent a novel class of 2-D materials with great potential for cancer treatment and other biomedical applications.

4.4 Methods

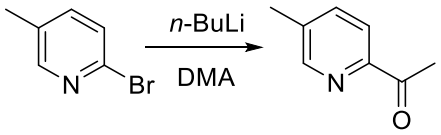

1-(5-methylpyridin-2-yl)ethanone. The synthesis of 1-(5-methylpyridin-2-yl)ethanone was modified from a reported protocol.[13] 2-bromo-5-methylpyridine (20 g, 116 mmol) was dissolved in 220 mL of dry Et_2O and cooled to -78 ºC. n-BuLi (47 mL, 2.5 M in hexanes) was added dropwise over 1h. The mixture was stirred at -78 ºC for 90 min before dimethylacetamide (12 mL) was added dropwise and stirred for another 3h. Sat. NH_4Cl (aq.) was added to quench

the reaction. The aqueous layer was washed with Et_2O twice and all the organic parts were combined, dried over anhydrous Mg_2SO_4, and filtered. After evaporation of the solvent, the residue was subjected to flash column chromatography on silica gel (10:90 EtOAc/CH_2Cl_2 as eluent), affording 1-(5-methylpyridin-2-yl)ethanone (9.4 g, 68.6 mmol, 59% yield) as a colorless oil. ^{1}H NMR (500 MHz, $CDCl_3$): δ 8.50 (s, 1 H), 7.95 (d, 1 H, J = 8.0 Hz), 6.21 (m, 1 H), 2.70 (s, 3 H), 2.42 (s, 3 H).

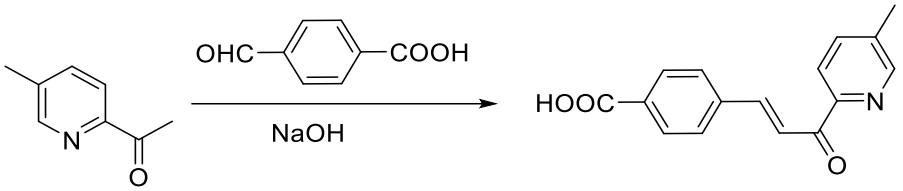

4-(5-methylpyridin-2-yl)formylvinyl benzoic acid. 1-(5-methylpyridin-2-yl)ethanone (10.65 g, 71 mmol) was dissolved in EtOH (35 mL) and then added dropwise to a mixed solution of 4-carboxybenzaldehyde (9.38 g, 69.6 mmol) and NaOH (3.76 g, 94 mmol) in EtOH/H_2O (1:1 v/v, 105 mL). The reaction mixture was stirred at room temperature overnight. The precipitate was separated via filtration and dissolved in MeOH/H_2O (1:1 v/v). 1M HCl was added to adjust the pH to 3 to afford white precipitate, which was collected via filtration and washed with MeOH/H_2O. This procedure produced 4-(5-methylpyridin-2-yl)-formylvinyl benzoic acid in 22% yield (4.09 g, 15.3 mmol). ^{1}H NMR (500 MHz, DMSO-d_6): δ 13.15 (br, 1H), 8.65 (s, 1H), 8.35 (d, 1H, J = 16.0 Hz), 7.8 – 8.1 (m, 7H), 2.43 (s, 3H).

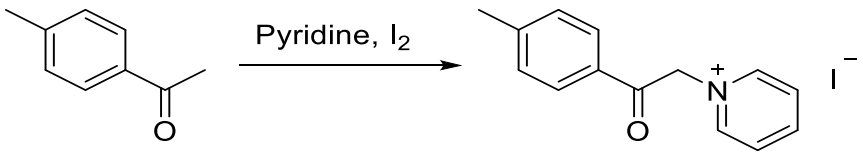

1-(2-oxo-2-(p-tolyl)ethyl)pyridin-1-ium. 4'-methylacetonphenone (1.336 mL, 10 mmol), pyridine (10 mL), and I_2 (2.54 g, 10 mmol) were stirred and heated at 120 ºC overnight. After

cooling to 0 °C, brown crystals precipitated. The crystals were filtered and washed with cold pyridine, $CHCl_3$, and Et_2O, then dried in vacuo to afford 1-(2-oxo-2-(p-tolyl)ethyl)pyridin-1-ium (2.50 g, 7.4 mmol, 74% yield). ^1H NMR (500 MHz, DMSO-d_6) δ 8.99 (d, 2 H, J = 6.5 Hz), 9.74 (t, 1 H, J = 8.0 Hz), 8.28 (t, 2 H, J = 7.0 Hz), 7.98 (d, 2 H, J = 7.0 Hz), 7.49 (d, 2 H, J = 8.0 Hz), 6.43 (s, 2 H), 2.46 (s, 3 Hz).

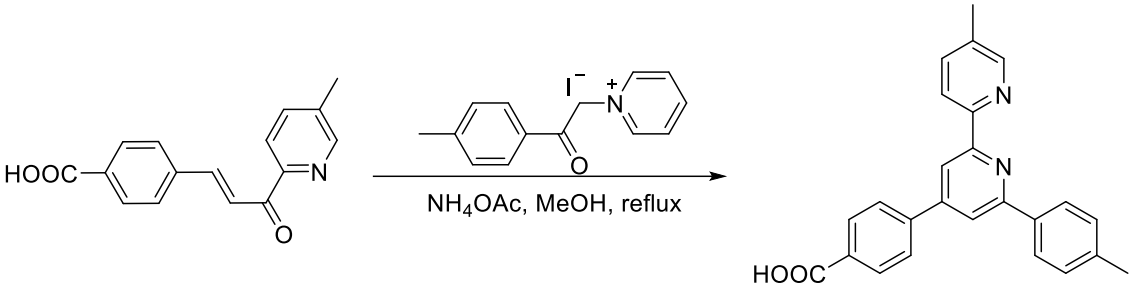

4-[2-(4-methylphenyl)-6-(5-methylpyridin-2-yl)pyridin-4-yl]benzoic acid. 4-(5-methylpyridin-2-yl)formylvinyl benzoic acid (4.00 g, 15.0 mmol) and 1-[2-(4-methylphenyl)-2-oxoethyl]-pyridinium iodide (5.60 g, 16.5 mmol) were dissolved in 90 mL MeOH, followed by the addition of NH_4OAc (11.5 g, 106 mmol). The reaction mixture was stirred under reflux for 6 h. After cooling to 0 °C, the precipitate was filtered and washed with cold MeOH and Et_2O to obtain 4-[2-(4-methylphenyl)-6-(5-methylpyridin-2-yl) pyridin-4-yl]benzoic acid (3.4 g, 8.94 mmol, 60% yield) as a white solid. ^1H NMR (500 MHz, DMSO-d_6): δ 8.60-8.58 (2H), 8.53 (d, 1H, J = 8.0 Hz), 8.33-8.25 (m, 3H), 8.14-8.08 (m, 4H), 7.84 (d, 1H, J = 7.0 Hz), 7.38 (d, 2H, J = 8.0 Hz), 2.40 (s, 6H).

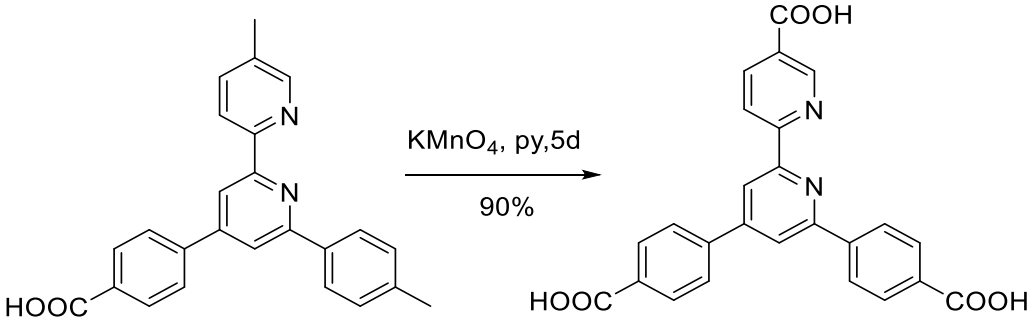

4',6'-dibenzoato-[2,2'-bipyridine]-4-carboxylic acid (H_3BPY). 4-[2-(4-methylphenyl)-6-(5-methylpyridin-2-yl)pyridin-4-yl]benzoic acid (3.4 g, 8.94 mmol) was dissolved in pyridine/H_2O (3:1 v/v, 240 mL), followed by the addition of $KMnO_4$ (5.00 g, 31.6 mmol). The reaction mixture was heated at 90 °C overnight. More $KMnO_4$ (5 g × 5, 46.8 mmol) was added to the reaction mixture to ensure complete oxidation. After refluxing for 5 d, the reaction mixture was cooled to room temperature, and EtOH was added to react with residual $KMnO_4$. The mixture was filtered, and the filtrate was put into a rotovap to remove most of the solvent. 1M HCl was added to the concentrated filtrate to adjust the pH to 3. White precipitates were collected via filtration, washed with copious amounts of water, and dried in vacuo to afford 4',6'-dibenzoato-[2,2'-bipyridine]-4-carboxylic acid (3.54 g, 8.05 mmol, 90% yield). ^{1}H NMR (500 MHz, DMSO-d_6): δ 12.23 (br, 3H), 9.24 (s, 1H), 8.79-8.76 (m, 2H), 8.53-8.49 (m, 4H), 8.18 - 8.11 (m, 6H).

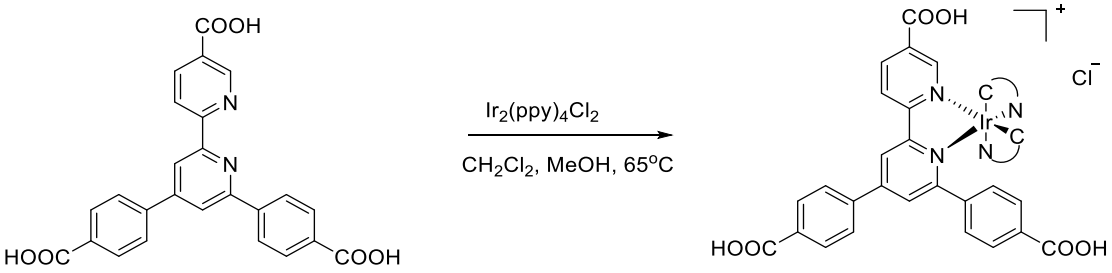

Synthesis of [(H_3BPY)-Ir(ppy)$_2$]Cl. H_3BPY (202 mg, 0.459 mmol) in CH_2Cl_2 (15 mL) was added to a stirred suspension of $[Ir(ppy)_2Cl]_2$ (246 mg, 0.230 mmol) in MeOH (25mL). The reaction mixture was stirred overnight at 68 °C. After cooling to room temperature, the solvent was removed by a rotovap. The residue was dissolved in MeOH and subjected to filtration. The filtrate was collected and concentrated. After adding a large amount of Et_2O, orange precipitate formed and was collected by filtration, then washed with Et_2O/MeOH and Et_2O, to afford

[(H_3BPY)Ir(ppy)$_2$]Cl (H_3BPY-Ir) as an orange solid (328 mg, 0.335 mmol, 73% yield). ^{1}H NMR (500 MHz, DMSO-d_6): δ 12.85 (br, 3H), 9.35 (d, 2H), 8.63 (d, 2H, J = 8.0 Hz), 8.35 (d, 2H, J = 8.5Hz), 8.25 (s, 1H), 8.15-8.11 (m, 5H), 8.05-8.01 (m, 2H), 7.94-7.86 (m, 3H), 7.72 (s, 1H, J = 7.5Hz), 7.35-7.23 (m, 4H), 7.17 (t, 1H), 6.91 (t, 1H), 6.80 (t, 1H), 6.44 (t, 1H), 6.25 (t, 1H), 5.82 (d, 1H), 5.41 (d,1H). ESI-MS: m/z = 941.4 ([M-Cl]$^+$).

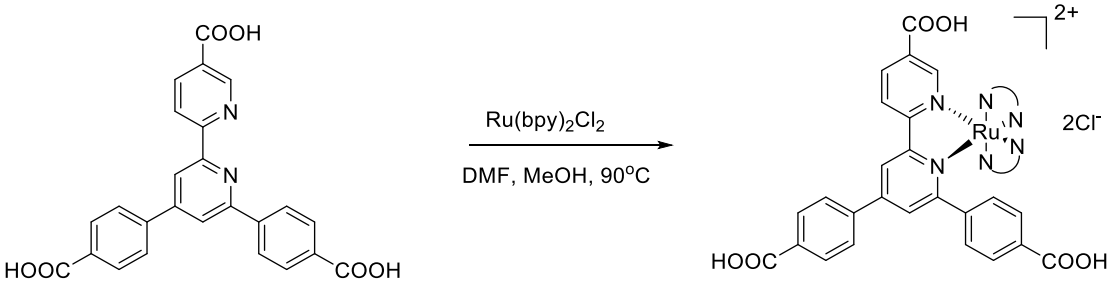

Synthesis of [(H_3BPY)Ru(bpy)$_2$]Cl$_2$. H_3BPY (22 mg, 0.050 mmol) in DMF (15 mL) was added to a stirred suspension of Ru(bpy)$_2$Cl$_2$ (28.8 mg, 0.058 mmol) in MeOH (15mL). The reaction mixture was stirred overnight at 90 °C. After cooling to room temperature, the solvent was removed by a rotovap. The residue was dissolved in MeOH and subjected to filtration. The filtrate was collected and concentrated. After adding a large amount of Et_2O, brown precipitate formed and was collected by filtration, then washed with Et_2O/MeOH and Et_2O, to afford [(H_3BPY)Ru(bpy)$_2$]Cl$_2$ (H_3BPY-Ru) as brown solid (22.6 mg, 0.025 mmol, 49 % yield). ^{1}H NMR (500 MHz, DMSO-d_6): δ 9.29 (s, 1H), 9.20 (d, 1H), 8.75 (t, 2H), 8.69 (d, 1H), 8.38 (d, 1H), 8.33-8.30 (m, 4H), 8.25 (t, 1H), 8.18 (t, 1H), 8.11 (d, 2H), 8.10-8.07 (m, 1H), 7.89 (s, 2H), 7.83 (d, 1H), 7.65-7.53 (m, 5H), 7.42-7.40 (m, 2H), 7.21 (s, 1H), 6.95 (d, 1H), 6.84 (t, 1H), 6.32 (s, 1H). ESI-MS: m/z = 427.2([M-2Cl]$^{2+}$).

Preparation of Hf-BPY or Zr-BPY MOL. To a 20 mL glass vial was added 2.5 mL of $HfCl_4$ solution (5.60 mg/mL in DMF) or 2.5 mL of $ZrCl_4$ solution (4.07 mg/mL in DMF), 2.5 mL of

the H_3BPY solution (5 mg/mL in DMF), 0.5 mL of formic acid, and 0.75 mL of water. The reaction mixture was kept in a 120 °C oven for 24 hours. The white precipitate was collected by centrifugation and washed with DMF and ethanol.

Preparation of Hf-BPY-Ir or Zr-BPY-Ir MOL. To a 2.5 mL methanol suspension of Hf-BPY MOL (15 mg) or Zr-BPY MOL (11 mg) was added 2.5 mL $[Ir(ppy)_2Cl]_2$ solution (6 mg/mL in DMF). The reaction mixture was kept in a 70 °C oven for 3 days. The orange precipitate was collected by centrifugation and washed with DMF and ethanol.

Preparation of Hf-BPY-Ru MOL or Zr-BPY-Ru MOL. To a 2.5 mL methanol suspension of Hf-BPY MOL (15 mg) or Zr-BPY MOL (11 mg) was added 2.5 mL $Ru(bpy)_2Cl_2$ solution (5.4 mg/mL in DMF). The reaction mixture was kept in a 70 °C oven for 3 days. The brown precipitate was collected by centrifugation and washed with DMF and ethanol.

EXAFS fitting. Fits of the EXAFS region were performed using the Artemis program of the IFEFFIT package. Fits were performed in R space, with a k-weight of 3 for the Ir samples and a k-weight of 2 for the Ru samples. Refinement was performed by optimizing an amplitude factor S_0^2 and energy shift ΔE_0, which are common to all paths, in addition to parameters for bond length (ΔR) and Debye-Waller factor (σ^2). The fitting models for Zr-BPY-Ir and H_3BPY-Ir were based on the crystal structure TEGVEI obtained from the Cambridge Crystallographic Database. The fitting models for Hf-BPY-Ru MOL and BPY-Ru homogeneous analog were based on the crystal structure ICITOD obtained from the Cambridge Crystallographic Database.

Singlet generation by RNO. The MOL samples (Hf-BPY-Ir, Hf-BPY-Ru, Zr-BPY-Ir and Zr-BPY-Ru) were suspended in water in the presence of 25 μM of RNO and 10 mM of histidine. The concentration of each MOL suspension was 10μM, based on Ir or Ru. The solutions were

transferred to 1-dram vials for visible light irradiation or X-ray irradiation. For visible light irradiation, the MOLs were irradiated by a 450 W Xe lamp with a 400 nm cut-off (long pass) filter (350 mW/cm^2) for 1, 2, 3, 5, 7, and 10 mins. For X-ray irradiation, MOLs were given X-ray doses (225 KVp, 13 mA) of 1, 2, 4, or 8 Gy. The UV-vis absorption spectra of the solutions were taken by a spectrophotometer. The difference in the RNO peak absorbance [Δ(OD)] at 440 nm was calculated by subtracting the readout in the sample curve from that of the control curve (no irradiation).

Cellular uptake. The cellular uptakes of Hf-BPY, Hf-BPY-Ir, and Hf-BPY-Ru were evaluated in CT26 cells. CT26 cells were seeded on 6-well plates at 5×10^5/well and then cultured for 24 h. Hf-BPY-Ir, Hf-BPY-Ru, and Hf-BPY were added to the cells at a Hf concentration of 50 μM. After incubation of 1, 4, 8, and 24 hours, the cells were collected and counted with a hemocytometer. The cells were digested with concentrated nitric acid in a microwave reactor and the metal concentrations were determined by ICP-MS.

Cytotoxicity. The cytotoxicity of Hf-BPY-Ir, Hf-BPY-Ru, Hf-BPY, Zr-BPY-Ir, Zr-BPY-Ru and Zr-BPY upon X-ray irradiation was evaluated against two different murine colorectal adenocarcinoma cell lines, CT26 and MC38. Dark cytotoxicity was first tested without X-ray irradiation. MOLs were incubated with the cells at various concentrations, ranging from 0-100 μM based on Ir, Ru, or BPY, respectively, for 8 h. The cell culture medium was then replaced with fresh medium, and the cells were incubated another 72 h before determining the cell viability by MTS assay. We then investigated cell viability with a fixed X-ray irradiation dose of 2 Gy. An X-ray beam with 250 kVp and 15 mA current were used for the irradiation. We

also tested the cell viability with the fixed Hf- MOLs concentration of 20μM based on Ir, Ru or BPY and various X-ray doses.

Intracellular $^1O_2$ generation. $^1O_2$ generation in live cells was detected by SOSG. CT26 cells were seeded in a 3.5-cm petri dish and cultured for 12 h. The culture medium was then replaced with fresh medium containing 1 μM SOSG to preload the cells with SOSG. After incubating for 30 min, the cells were washed by PBS three times to remove excess SOSG. The cells were incubated with PBS, Hf-MOLs or ligands at a ligand concentration of 20 μM for 8 h, then washed with PBS three times to remove excess MOLs or ligands. X-ray irradiation was applied to cells at a dose of 2 Gy (250 kVp, 15 mA, 1-mm Cu filter). CLSM was used to visualize the $^1O_2$ generated in the live cells by detecting the green fluorescence inside the cells.

γ-H_2AFX assay. The DNA DSB caused by MOLs upon X-ray irradiation was investigated by γ-H_2AFX assay in CT26 cells. Cells were incubated with the MOL at a ligand concentration of 20 μM for 8 h followed by X-ray irradiation at 2 Gy dose. CT26 cells incubated with PBS with 2 Gy X-ray irradiation served as a control. γ-H_2AFX assays were carried out immediately after X-ray irradiation. The nuclei were stained with DAPI. Red fluorescence indicated the DSBs stained with antibody-labeled γ-H_2AFX. The cells were imaged with CLSM. Groups treated with three Hf-based MOL showed red fluorescence, indicating DSB induced by hydroxyl radical from irradiation. As a negative control, group treated with PBS did not show obvious red fluorescence.

In vivo efficacy. We evaluated the in vivo anticancer efficacy of Hf-BPY-Ir and Hf-BPY-Ru through intratumoral injections on CT26 or MC38 tumor-bearing mice. When the tumors reached 100-150 mm^3 in volume, MOLs with a photosensitizer concentration of 10 μM were

intratumorally injected, followed by daily X-ray irradiation at a dose of 1 Gy/fraction (120 kVp, 20 mA, 2 mm-Cu filter), for a total of 5 fractions on CT26 models or 10 fractions on MC38 models on consecutive days. Tumor sizes were measured with a caliper every day, estimating tumor volume at (width^2 × length)/2. All mice were sacrificed on day 18 and the excised tumors were photographed and weighed. Body weights of each group were monitored as an indication of systemic toxicity.

4.5 References

1. Lu, K.; He, C.; Lin, W., Nanoscale Metal–Organic Framework for Highly Effective Photodynamic Therapy of Resistant Head and Neck Cancer. *J. Am. Chem. Soc.* **2014,** *136* (48), 16712-16715.
2. Lu, K.; He, C.; Lin, W., A Chlorin-Based Nanoscale Metal–Organic Framework for Photodynamic Therapy of Colon Cancers. *J. Am. Chem. Soc.* **2015,** *137* (24), 7600-7603.
3. Lu, K.; He, C.; Guo, N.; Chan, C.; Ni, K.; Weichselbaum, R. R.; Lin, W., Chlorin-Based Nanoscale Metal–Organic Framework Systemically Rejects Colorectal Cancers via Synergistic Photodynamic Therapy and Checkpoint Blockade Immunotherapy. *J. Am. Chem. Soc.* **2016,** *138* (38), 12502-12510.
4. Park, J.; Jiang, Q.; Feng, D.; Mao, L.; Zhou, H.-C., Size-Controlled Synthesis of Porphyrinic Metal–Organic Framework and Functionalization for Targeted Photodynamic Therapy. *J. Am. Chem. Soc.* **2016,** *138* (10), 3518-3525.
5. Liu, J.; Yang, Y.; Zhu, W.; Yi, X.; Dong, Z.; Xu, X.; Chen, M.; Yang, K.; Lu, G.; Jiang, L.; Liu, Z., Nanoscale metal−organic frameworks for combined photodynamic & radiation therapy in cancer treatment. *Biomaterials* **2016,** *97*, 1-9.
6. Lismont, M.; Dreesen, L.; Wuttke, S., Metal-Organic Framework Nanoparticles in Photodynamic Therapy: Current Status and Perspectives. *Adv. Funct. Mater.* **2017,** *27* (14), 1606314.
7. Takizawa, S.-y.; Aboshi, R.; Murata, S., Photooxidation of 1,5-dihydroxynaphthalene with iridium complexes as singlet oxygen sensitizers. *Photochem. Photobiol. Sci.* **2011,** *10* (6), 895-903.
8. Djurovich, P. I.; Murphy, D.; Thompson, M. E.; Hernandez, B.; Gao, R.; Hunt, P. L.; Selke, M., Cyclometalated iridium and platinum complexes as singlet oxygen photosensitizers: quantum yields, quenching rates and correlation with electronic structures. *Dalton Trans.* **2007,** (34), 3763-3770.
9. Garcìa-Fresnadillo, D.; Georgiadou, Y.; Orellana, G.; Braun, A. M.; Oliveros, E., Singlet-Oxygen (1Δg) Production by Ruthenium(II) complexes containing polyazaheterocyclic ligands in methanol and in water. *Helv. Chim. Acta* **1996,** *79* (4), 1222-1238.
10. Smith, A. M.; Mancini, M. C.; Nie, S., Second window for in vivo imaging. *Nat.*

Nanotechnol. **2009,** *4* (11), 710-711.
11. Wang, C.; Volotskova, O.; Lu, K.; Ahmad, M.; Sun, C.; Xing, L.; Lin, W., Synergistic Assembly of Heavy Metal Clusters and Luminescent Organic Bridging Ligands in Metal–Organic Frameworks for Highly Efficient X-ray Scintillation. *J. Am. Chem. Soc.* **2014,** *136* (17), 6171-6174.
12. Chen, H.; Wang, G. D.; Chuang, Y.-J.; Zhen, Z.; Chen, X.; Biddinger, P.; Hao, Z.; Liu, F.; Shen, B.; Pan, Z.; Xie, J., Nanoscintillator-Mediated X-ray Inducible Photodynamic Therapy for In Vivo Cancer Treatment. *Nano Lett.* **2015,** *15* (4), 2249-2256.
13. Cao, L.; Lin, Z.; Peng, F.; Wang, W.; Huang, R.; Wang, C.; Yan, J.; Liang, J.; Zhang, Z.; Zhang, T., Self-Supporting Metal–Organic Layers as Single-Site Solid Catalysts. *Angewandte Chemie International Edition* **2016,** *55* (16), 4962-4966.

Chapter 5. Nanoscale Metal-Organic Layers for Radiotherapy-Radiodynamic Therapy

5.1 Introduction

2D nanomaterials exhibit distinct biobehaviors from 3D systems due to their high specific surface areas as well as anisotropic physical and chemical properties.[1-5] In this regard, nMOLs, monolayer nanomaterials formed by reducing the dimensionality of nMOFs,[6, 7] present an interesting opportunity to study unique biobehaviors of low-dimensional nanomaterials. However, nMOLs have rarely been explored in biomedical applications owing to the difficulty in the synthesis of stable, functional, and non-aggregated nMOLs.

Radiotherapy (RT) is an efficient anti-cancer treatment and provides a curative therapy for many types of tumors.[8-11] However, high X-ray doses (50-75 Gy) often cause debilitating side effects. We recently discovered that nMOFs containing heavy metal SBUs display superb RT efficacy in tumor models.[12] The incorporation of photosensitizing porphyrin ligands into nMOFs further enhances therapeutic efficacy by simultaneously enhancing RT via generating $^{\bullet}OH$ on the heavy metal SBUs and enabling RDT via energy transfer from SBUs to porphyrin ligands to generate $^1O_2$.[13, 14] Thin plate nMOF morphologies facilitate the diffusion of ROS to cell milieu to exert cytotoxic effects. In this Chapter, we report the design of Hf_{12}-Ir and Hf_6-Ir nMOLs with $Ir(bpy)[dF(CF_3)ppy]_2^+$ [bpy = 2,2′-bipyridine; dF(CF3)ppy = 2-(2,4-difluorophenyl)-5-(trifluoromethyl)pyridine] derived ligands for highly effective RT-RDT of colorectal cancer (**Figure 5-1**). Upon X-ray irradiation, electron-dense Hf_{12} and Hf_6 SBUs efficiently absorb X-rays to generate $^{\bullet}OH$ and transfer energy to $Ir(bpy)[dF(CF_3)ppy]_2^+$ to generate $^1O_2$ and O_2^- anions. The generated ROS diffuse out of ultrathin nMOLs to exert

cytotoxic effects and afford an effective X-ray triggered cancer treatment.

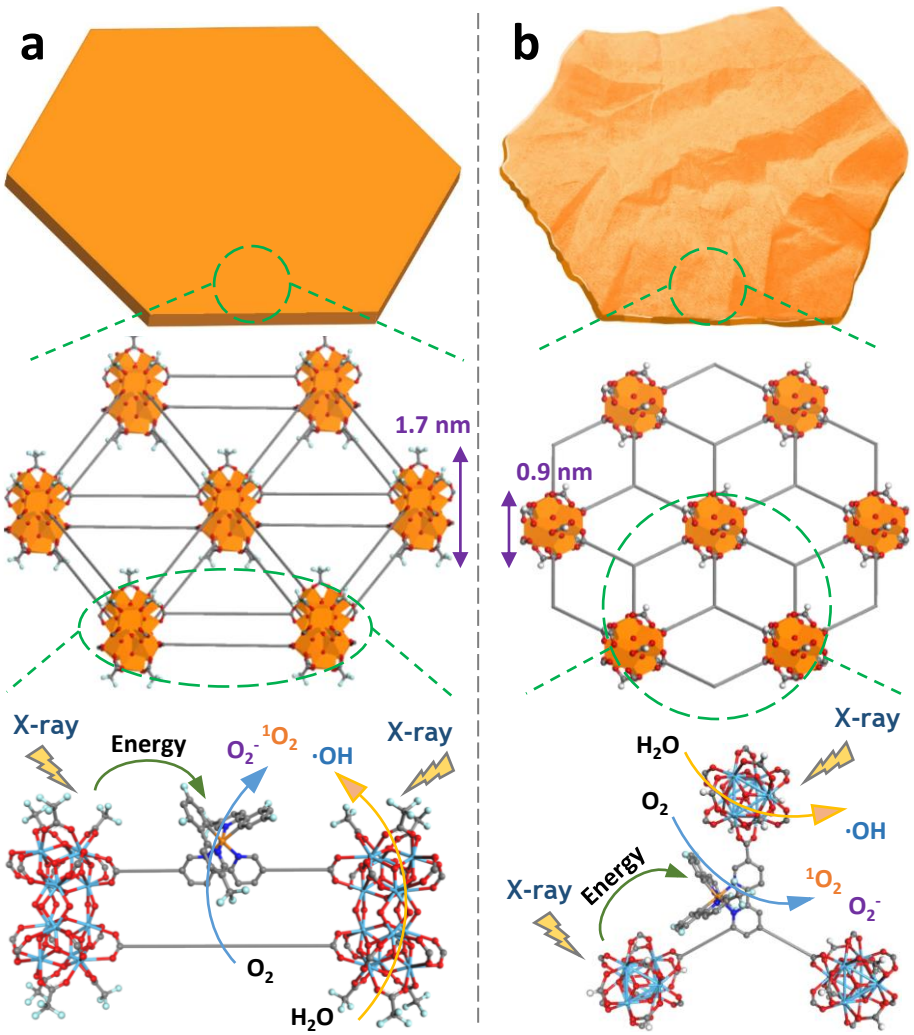

Figure 5-1. Schematic showing the morphologies and topological structures of and X-ray triggered ROS generation by Hf_{12}-Ir (a) and Hf_6-Ir (b).

5.2 Result and discussion

5.2.1 Synthesis and characterization

Hf_{12}-Ir was synthesized through a solvothermal reaction between $HfCl_4$ and $Ir(DBB)[dF(CF_3)ppy]_2^+$ (H_2**L**-Ir,) in DMF at 80 °C with TFA and water as modulators. Hf_{12}-Ir is an infinite 2D network of **kgd** topology with $Hf_{12}(\mu_3\text{-}O)_8(\mu_3\text{-}OH)_8(\mu_2\text{-}OH)_6$ SBUs and **L**-Ir bridging ligands (**Figure 5-2a-c**). Hf_{12}-Ir monolayers are vertically capped by TFA groups to afford a molecular formula of $Hf_{12}(\mu_3\text{-}O)_8(\mu_3\text{-}OH)_8(\mu_2\text{-}OH)_6(TFA)_6$(**L**-Ir)$_6$. $Hf_6(\mu_3\text{-}O)_4(\mu_3\text{-}$

$OH)_4(BPY)_2(HCO_2)_6$ (Hf_6-BPY) of **kgd** topology was first synthesized through a solvothermal reaction between $HfCl_4$ and H_3BPY in DMF at 120 °C with HCOOH and water as modulators.[6] Treatment of Hf_6-BPY with $Ir[dF(CF_3)ppy]_2Cl_2$ afforded Hf_6-Ir containing $Ir(BPY)[dF(CF_3)ppy]_2^+$ (BPY-Ir) photosensitizers. The Ir metalation yield in Hf_6-Ir was determined to be 71% by ICP-MS. Hf_6-Ir exhibits a monolayer structure with formate capping ligands and possess a molecular formulation of $Hf_6(\mu_3\text{-}O)_4(\mu_3\text{-}OH)_4(BPY\text{-}Ir)_{1.42}(BPY)_{0.58}(HCO_2)_6$ (**Figure 5-2d-f**).

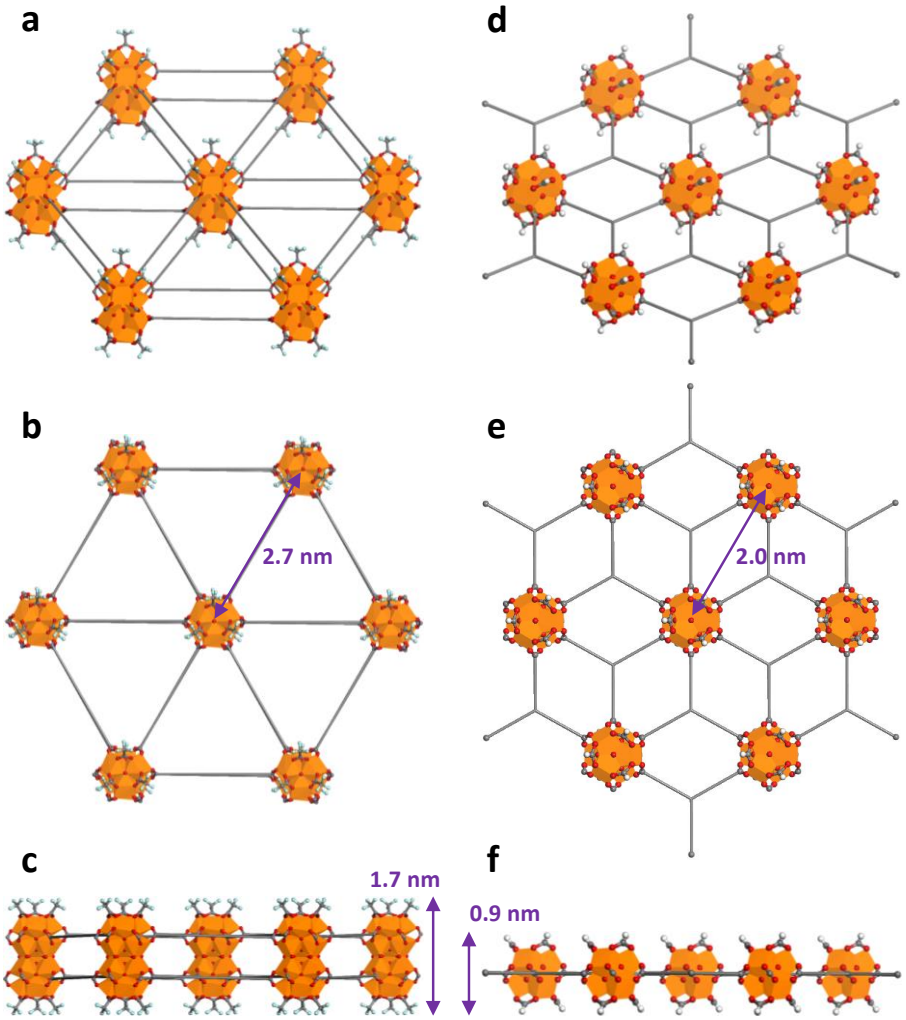

Figure 5-2. Modeled structures of Hf12-Ir and Hf6-Ir MOL. Diagonal (a), vertical (b), and lateral (c) perspective views of Hf_{12}-Ir. The **L**-Ir ligands are simplified as linear gray rods. Diagonal (d), vertical (e), and lateral (f) perspective views of Hf_6-Ir. The BPY-Ir or BPY ligands are simplified as trigonal gray rods. The distance between two adjacent SBUs is measured to

(Figure 5-2 continued) be 2.7 nm for Hf_{12}-Ir and 2.0 nm for Hf_6-Ir, respectively. The heights of Hf_{12}-Ir and Hf_6-Ir, as determined by the height of SBUs, are 1.7 nm and 0.9 nm, respectively.

TEM imaging showed flat monolayer morphology for Hf_{12}-Ir (**Figure 5-3a**) with rigid dual linear linkers between two adjacent Hf_{12} SBUs and wrinkled monolayer morphology for Hf_6-Ir (**Figure 5-3d**) with flexible single triangle linkers between three adjacent Hf_6 SBUs. AFM measurements supported the monolayer structures: Hf_{12}-Ir displayed a flat monolayer structure with a thickness of 1.7 nm (**Figure 5-3b,c**), which is consistent with the modeled height of Hf_{12} SBUs capped with TFA groups, while Hf_6-Ir showed a wrinkled monolayer structure with edge-thickness of 1.2 nm (**Figure 5-3e,f**), which is consistent with the height of Hf_6 SBUs capped with formate groups. DLS measurements gave number-averaged sizes of 91.3 ± 1.1 and 295.3 ± 2.7 nm for Hf_{12}-Ir and Hf_6-Ir, respectively.

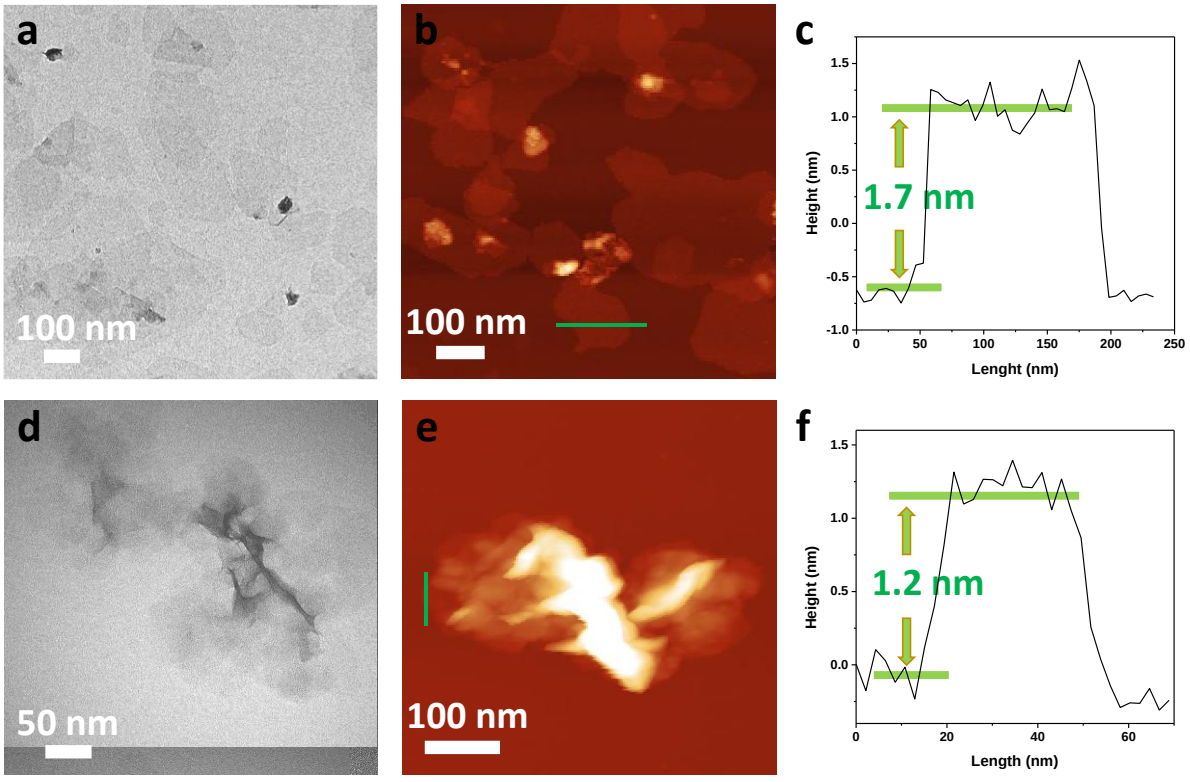

Figure 5-3. Morphology characterization. TEM image (a), AFM topography (b), and height profile (c) of Hf_{12}-Ir. TEM image (d), AFM topography (e), and height profile (f) of Hf_6-Ir.

HRTEM images of Hf_{12}-Ir and Hf_6-Ir, in which Hf_{12} and Hf_6 SBUs appear as black spots, and their FFT patterns revealed six-fold symmetry that is consistent with the **kgd** topology (**Figure 5-4**). The distance between two adjacent spots was measured to be 2.7 nm and 2.0 nm for Hf_{12}-Ir and Hf_6-Ir, respectively, matching the modeled Hf_{12}-Hf_{12} and Hf_6-Hf_6 SBU distances (**Figure 5-2**). Moreover, PXRD patterns of Hf_{12}-Ir and Hf_6-Ir matched well with those simulated from the proposed Hf_{12} and Hf_6 MOL structures (**Figure 5-5**).[15]

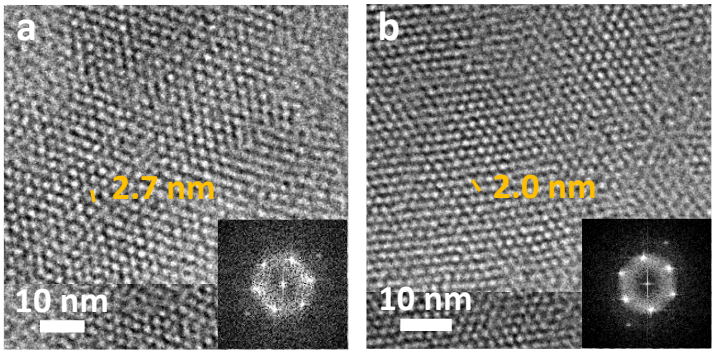

Figure 5-4. HRTEM images. HRTEM image and FFT pattern (insert) of Hf_{12}-Ir (a) and Hf_6-Ir (b).

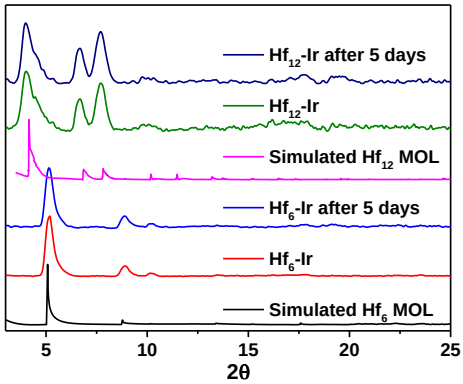

Figure 5-5. PXRD patterns. PXRD patterns of Hf_{12}-Ir and Hf_6-Ir, freshly prepared or incubated in 0.6 mM PBS for 5 days, in comparison to their simulated patterns.[15]

^{1}H NMR spectrum of digested Hf_{12}-Ir showed aromatic signals corresponding to H_2**L**-Ir. Hf_6-Ir showed similar EXAFS to its homogeneous analogue, $Ir(H_3BPY)[dF(CF_3)ppy]_2^+$ (H_3BPY-Ir), which were well fitted with their molecular model (**Figure 5-6a**). Hf_{12}-Ir and Hf_6-

Ir showed similar UV-Vis absorption and emission characteristics to their homogeneous analogues, H_2**L**-Ir and H_3BPY-Ir (**Figure 5-6b**), respectively.

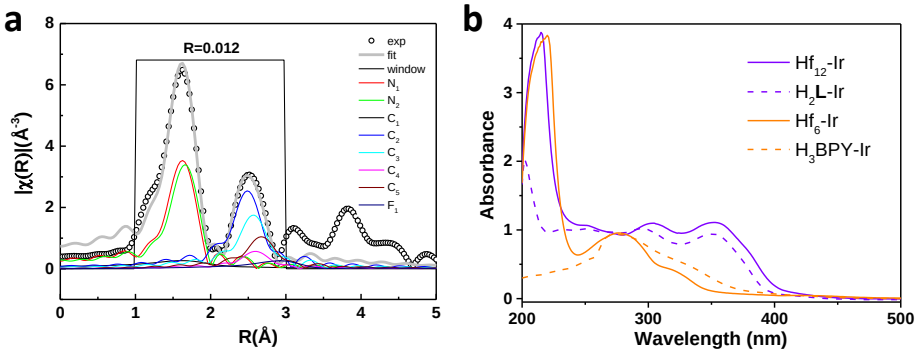

Figure 5-6. Composition analysis. (a) EAXFS fitting of Hf_6-Ir. (b) UV-Vis spectra of Hf_{12}-Ir, Hf_6-Ir, H_2**L**-Ir, and H_3BPY-Ir.

5.2.2 ROS generation

RT enhancement abilities of Hf_{12}-Ir and Hf_6-Ir were studied through detecting •OH upon X-ray irradiation. •OH generation was first confirmed by APF whose fluorescence is turned on when reacting with •OH. A linear increase of •OH generation was observed with increasing X-ray dose in aqueous APF suspensions of H_2**L**-Ir, Hf_{12}-Ir, and Hf_6-Ir, affording relative enhancement of 12.6%, 124.6%, and 125.4%, respectively (**Figure 5-7**).

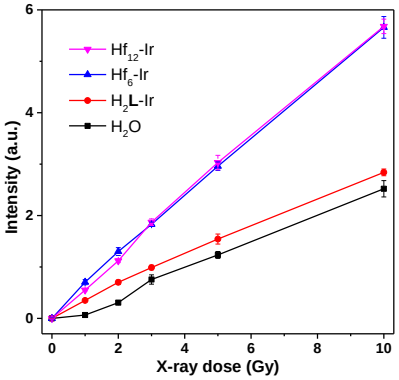

Figure 5-7. •OH generation determined by APF assay.

The in vitro generation of ˙OH was verified by DNA DSB quantification with a γ-H2AX assay in which a histone protein is phosphorylated to repair DNA DSBs caused by direct ionization or hydroxyl radicals. After X-ray irradiation, significant red γ-H2AX fluorescence indicating DSBs was observed in the cells treated with Hf_{12}-Ir and Hf_6-Ir by confocal microscopy, while no signal was observed in cells treated with PBS or without X-ray irradiation (**Figure 5-8**).

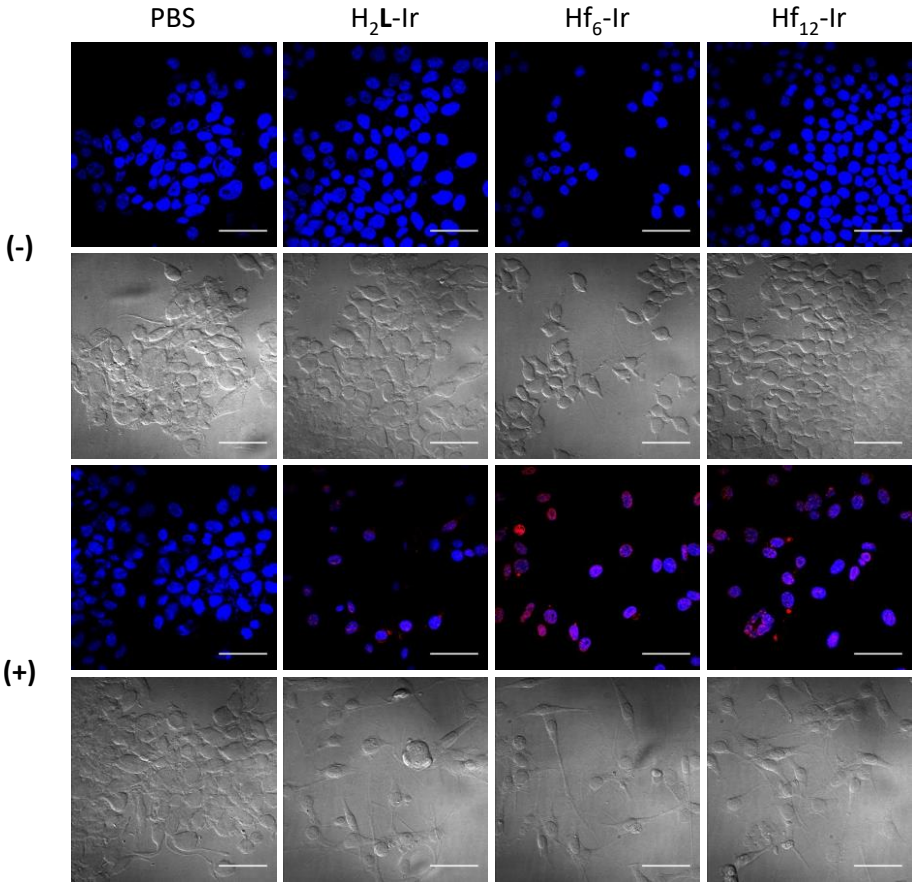

Figure 5-8. ˙OH generation determined by γ-H2AX assay. γ-H2AX assays showing DSBs in MC38 cells treated with PBS, H_2**L**-Ir, Hf_6-Ir or Hf_{12}-Ir with (+) or without (-) X-ray irradiation. Blue and red fluorescence represent nuclei and DSB signals, respectively. Scale bar = 50 μm.

RDT capabilities of Hf_{12}-Ir and Hf_6-Ir were studied via detecting $^1O_2$ and O_2^- generated by X-ray irradiation. X-ray dose dependent $^1O_2$ generation of Hf_{12}-Ir, Hf_6-Ir, H_2**L**-Ir and blank control was determined by SOSG. While Hf_6-Ir and H_2**L**-Ir showed some $^1O_2$ generation, Hf_{12}-

Ir was highly efficient in $^1O_2$ generation that saturates at an X-ray dose of ~5 Gy (**Figure 5-9a**). O_2^- generation was detected by EPR with BMPO as a spin trap.[16] As shown in **Figure 5-9b**, the characteristic signals from BMPO-O_2^- were detected in Hf_{12}-Ir and Hf_6-Ir upon X-ray irradiation, while no signals was observed in either H_2**L**-Ir or a blank control.

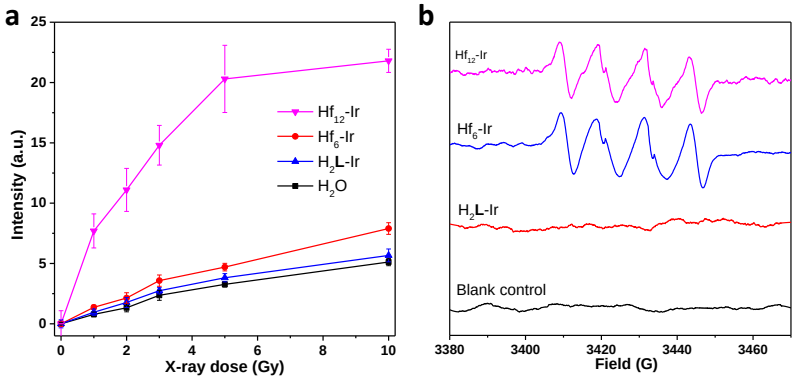

Figure 5-9. $^1O_2$ and O_2^- generation. (a) $^1O_2$ generation determined by SOSG assay. (b) O_2^- generation determined by BMPO assay.

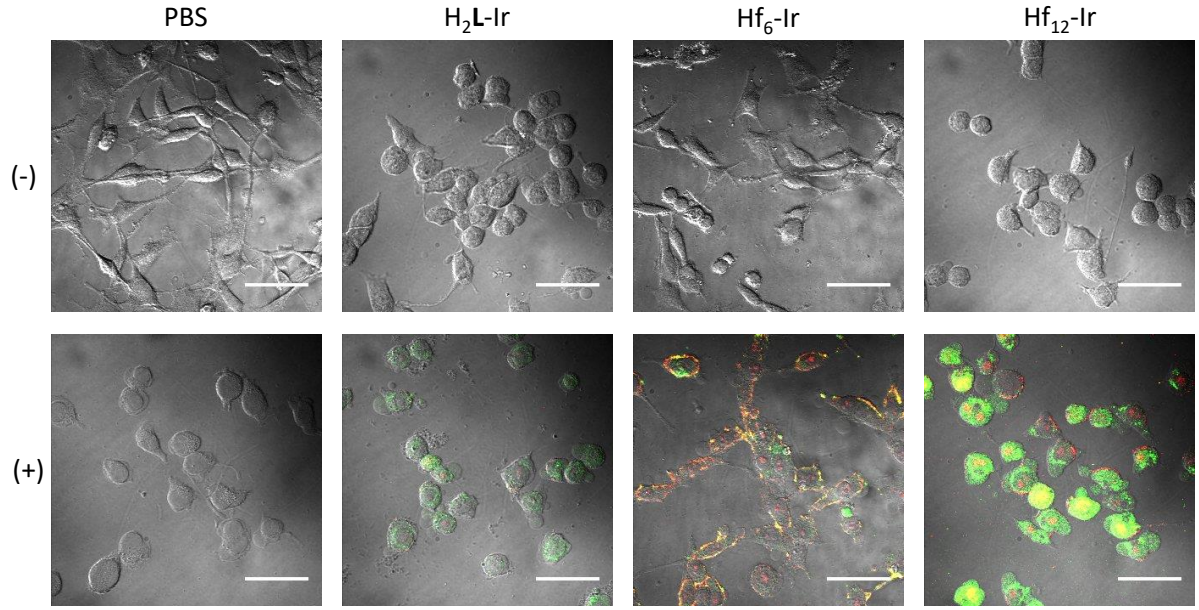

Figure 5-10. Intracellular $^1O_2$ and O_2^- generation. Intracellular $^1O_2$ and O_2^-generation with (+) or without (-) X-ray irradiation detected by SOSG and superoxide kit. Green and red fluorescence represent SOSG or superoxide signal, respectively. Green and red fluorescence merges to yellow fluorescence. Scale bar = 50 μm.

The in vitro generation of $^1O_2$ and O_2^- was confirmed by confocal imaging with SOSG, which displays green fluorescence after reacting with $^1O_2$, and with a superoxide kit, which

displays red fluorescence after reacting with O_2^-. As shown in **Figure 5-10**, both $^1O_2$ and O_2^- signals were detected in cells treated with Hf_{12}-Ir and Hf_6-Ir, only $^1O_2$ signals was detected in the cells treated with H_2**L**-Ir, and no signal was observed in cells treated with PBS or without X-ray irradiation. SOSG and EPR studies as well as in vitro confocal imaging thus demonstrate the ability of Hf_{12}-Ir and Hf_6-Ir to elicit RDT by generating $^1O_2$ and O_2^- upon X-ray irradiation. Heavy metal SBUs absorb X-rays and transfer energy to Ir-based ligand to sensitize the generation of $^1O_2$ and O_2^-.

5.2.3 Anti-cancer efficacy

RT-RDT therapeutic effects of Hf_{12}-Ir and Hf_6-Ir were evaluated in vitro using MC38 cells. First, the stability of Hf_{12}-Ir and Hf_6-Ir in vitro was confirmed by the maintenance of PXRD patterns after the MOLs were incubated in PBS for 5 days (**Figure 5-5**). Time-dependent ICP-MS analysis of Hf (1 to 8 h) demonstrated efficient uptake of Hf_{12}-Ir and Hf_6-Ir by MC38 cells. Colony assay showed that Hf_{12}-Ir and Hf_6-Ir elicited effective cell reproductive death (RT) with REF_{10} values of 2.07 and 2.21, respectively (**Figure 5-11a**). MTS assay (**Figure 5-11b**) showed that Hf_{12}-Ir and Hf_6-Ir caused effective cell instant death (RDT) with IC_{50} values of 7.8 ± 1.5 and 15.5 ± 3.1 μM, respectively. No dark cytotoxicity was observed in Hf_{12}-Ir or Hf_6-Ir treated cells.

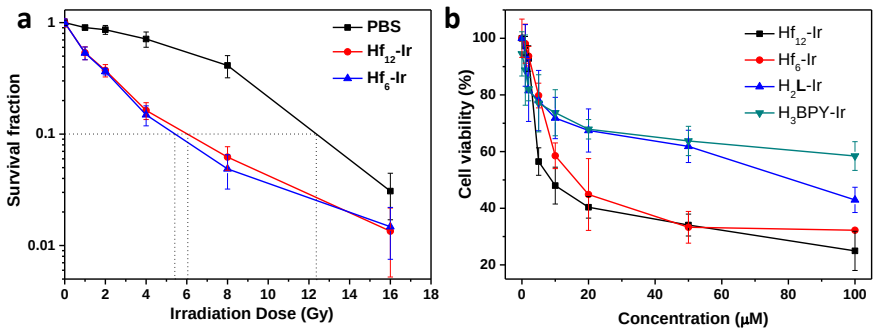

Figure 5-11. Cytotoxicity. Clonogenic (a) and MTS (b) assays of Hf_{12}-Ir and Hf_6-Ir on MC38 cells. N=6.

Both apoptosis and immunogenic cell death (ICD) contributed to the RT-RDT efficacy of Hf_{12}-Ir and Hf_6-Ir. The apoptosis induced by RT-RDT was determined by flow cytometry using an Annexin V/dead cell apoptosis kit. No apoptosis or necrosis was observed for cells treated with PBS or without X-ray irradiation. In contrast, significant numbers of cells underwent apoptosis when treated with Hf_{12}-Ir or Hf_6-Ir and X-ray irradiation (**Figure 5-12**).

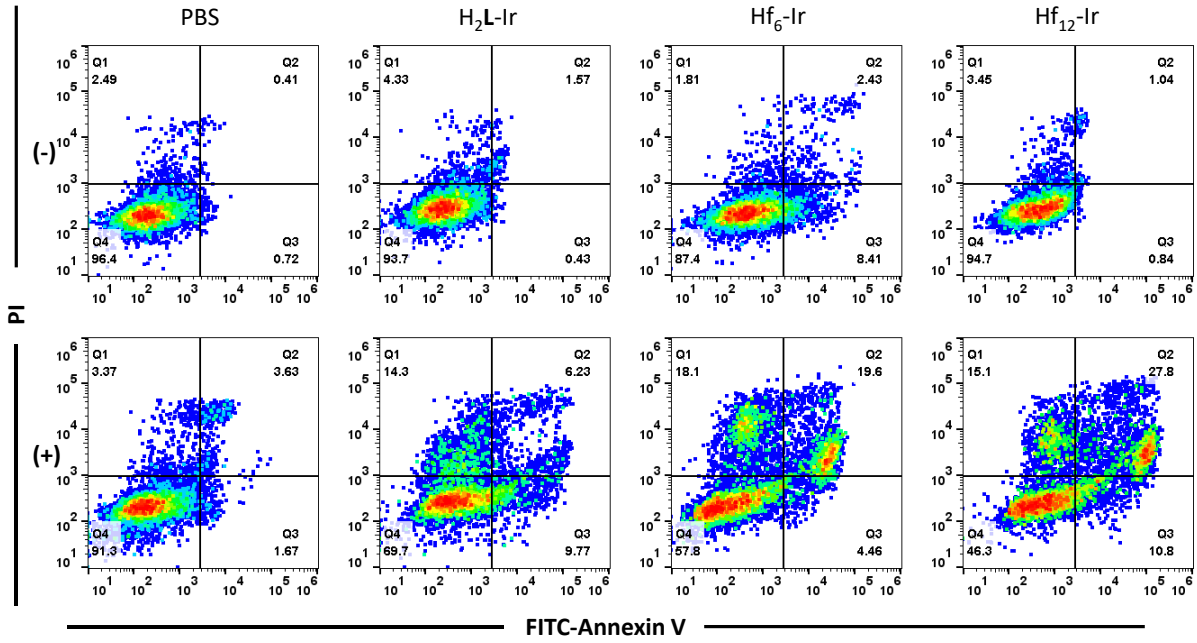

Figure 5-12. Apoptosis. Annexin V/PI cell apoptosis/death analysis of MC38 cells with (+) or without (-) X-ray irradiation. The quadrants from lower left to upper left (counter clockwise) represent healthy, early apoptotic, late apoptotic, and necrotic cells, respectively.

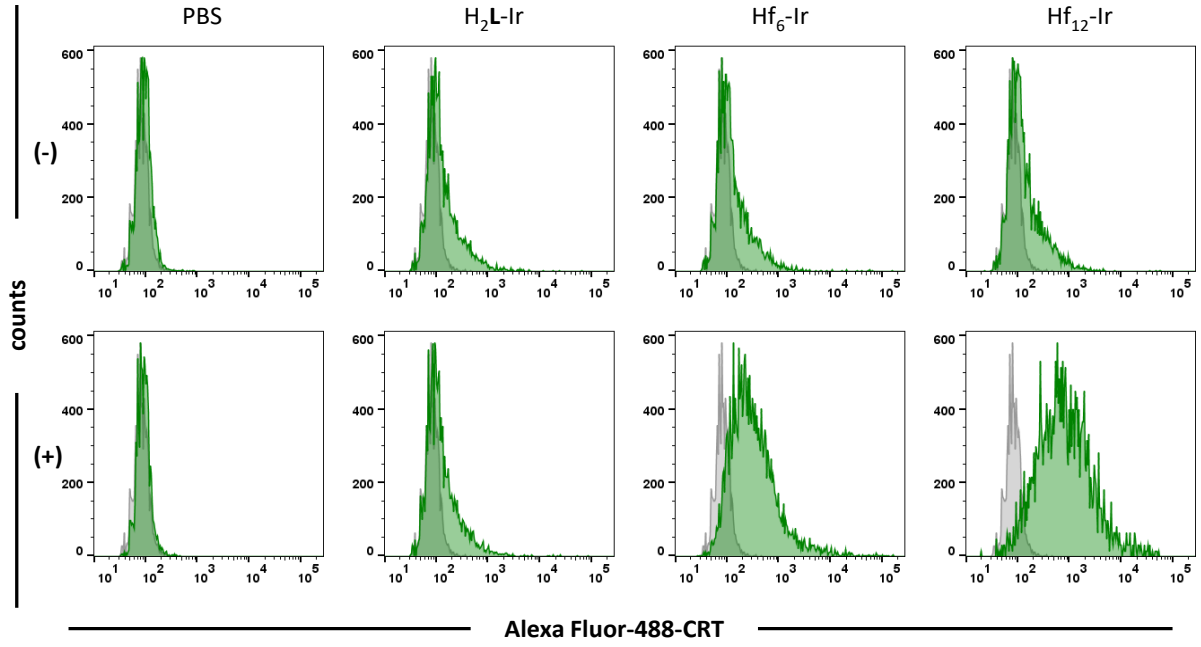

Figure 5-13. CRT exposure. CRT exposure on the cell surface of MC38 cells was assessed after incubation with Hf_{12}-Ir, Hf_6-Ir, H_2**L**-Ir or PBS with flow cytometry with (+) or without (-) X-ray irradiation.

ICD induced by RT-RDT was evaluated via determining calreticulin (CRT) expression by flow cytometry using Alexa Fluor 488 conjugated-CRT antibody. CRT is a distinct biomarker exposed on the surface of cells undergoing ICD. Cells treated with H_2**L**-Ir or without X-ray irradiation showed no surface CRT expression, while significant amounts of CRT were detected on the surfaces of cells treated with Hf_{12}-Ir or Hf_6-Ir and X-ray irradiation (**Figure 5-13**).

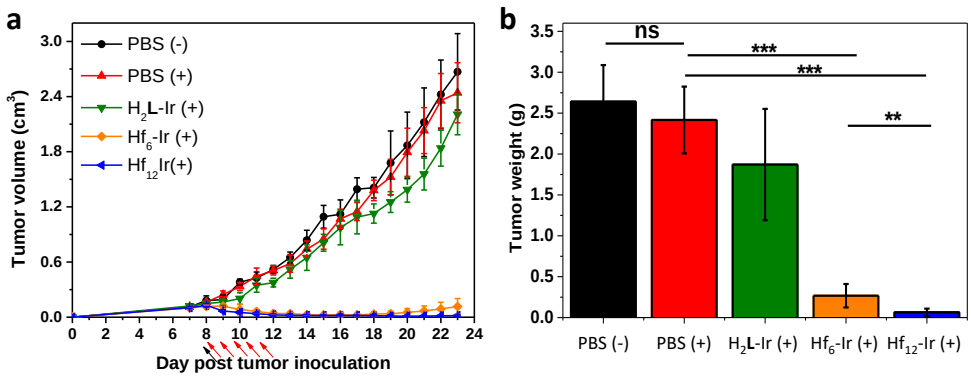

Figure 5-14. In vivo efficacy. Tumor growth inhibition/regression curves (a) and excised tumor weights on day 23 (b) for MC38 tumor-bearing mice treated with PBS, H_2**L**-Ir, Hf_6-Ir, or Hf_{12}-Ir upon X-ray irradiation or PBS without X-ray irradiation. Black arrows refer to intratumoral injection and red arrows refer to X-ray irradiation. N=6.

A colorectal adenocarcinoma model of MC38-tumor bearing C57BL/6 mice was employed to evaluate the RT-RDT anti-tumor efficacy of Hf_{12}-Ir and Hf_6-Ir in vivo. When the tumors reached 100-150 mm^3 in volume, Hf_{12}-Ir, Hf_6-Ir, H_2**L**-Ir or PBS was injected intratumorally at a Hf/Ir dose of 0.2 μmol followed by 5 daily X-ray fractions at a dose of 0.5 Gy/fraction. All mice were sacrificed 23 days after tumor inoculation. Both Hf_{12}-Ir and Hf_6-Ir treatment led to effective tumor regression, while H_2**L**-Ir treatment showed only slight tumor inhibition (**Figure 5-14a**). The average tumor volume of the Hf_{12}-Ir and Hf_6-Ir treatment group was only 0.7% and 4.3% of that of the PBS dark control on Day 23. The tumor growth inhibition/regression results were confirmed by the weights of excised tumors on Day 23. The tumor weights of mice treated with Hf_{12}-Ir, Hf_6-Ir, H_2**L**-Ir or PBS upon X-ray irradiation and PBS without X-ray irradiation were 0.065 ± 0.045 g, 0.267 ± 0.143 g, 1.871 ± 0.651 g, 2.415 ± 0.408 g, or 2.640 ± 0.447 g, respectively (**Figure 5-14b**). A TdT-mediated dUTP nick end labeling (TUNEL) assay showed significant in vivo apoptosis of RT-RDT treatment of Hf_{12}-Ir or Hf_6-Ir (**Figure 5-15**). Steady body weights, similar weight gain patterns, and no difference in behaviors and organ functions were observed in all groups, indicating lack of systemic toxicity for Hf_{12}-Ir or Hf_6-Ir administration.

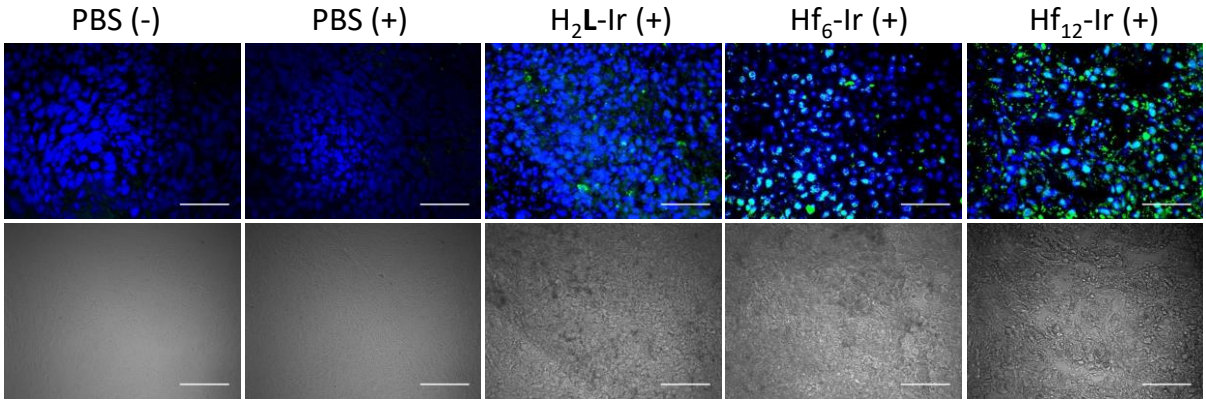

Figure 5-15. TUNEL immunofluorescence staining. TUNEL immunofluorescence staining of excised tumor slices for MC38 tumor-bearing mice treated with PBS, H_2**L**-Ir, Hf_6-Ir or Hf_{12}-Ir

with X-ray irradiation (+) or PBS without X-ray irradiation (-). Scale bar = 50 μm.

5.3 Conclusion

In this work, we have synthesized two novel nMOLs based on electron-dense Hf_{12} or Hf_6 SBUs and strongly photosensitizing Ir(bpy)[dF(CF_3)ppy]$_2^+$ bridging ligands for highly effective RT-RDT. Upon X-ray irradiation, Hf_{12} or Hf_6 SBUs strongly absorb X-rays to generate hydroxyl radicals for the RT effect and transfer energy to Ir(bpy)[dF(CF_3)ppy]$_2^+$ to generate $^1O_2$ and O_2^- for the RDT effect. X-ray triggered ROS generation by nMOLs enables a highly effective cancer treatment modality via the unique RT-RDT mechanism, with an order of magnitude reduction of X-ray doses. nMOLs thus represent a novel class of 2D materials with great potential for cancer treatment and other biomedical applications.

5.4 Methods

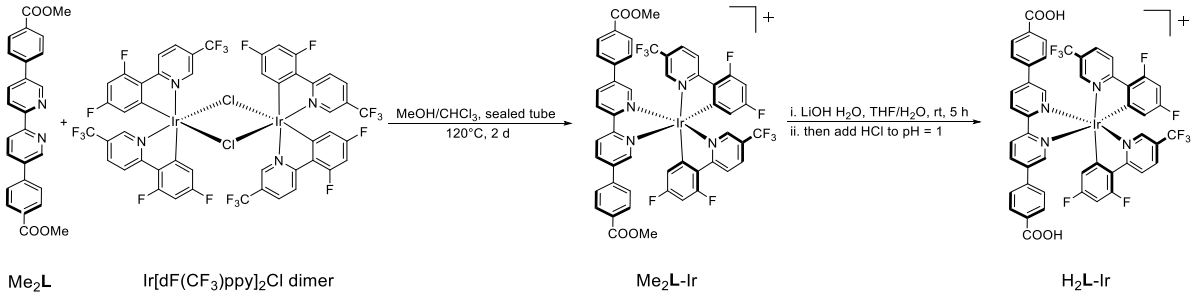

Synthesis of H_2L-Ir. Ir(DBB)[dF(CF_3)ppy]$_2^+$ [H_2**L**-Ir, DBB = 4,4'-di(4-benzoato)-2,2'-bipyridine; dF(CF_3)ppy = 2-(2,4-difluorophenyl)-5-(trifluoromethyl)pyridine] was synthesized as described previously as shown above.[17] ^{1}H NMR (500 MHz, DMSO-d_6): δ 9.08 (d, 2 H), 8.75 (d, 2 H), 8.48 (d, 2 H), 8.43 (d, 2 H), 8.14 (s, 2 H), 8.02 (d, 4 H), 7.81 (s, 2 H), 7.63 (d, 4 H), 7.10 (t, 2 H), 5.89 (t, 2 H).

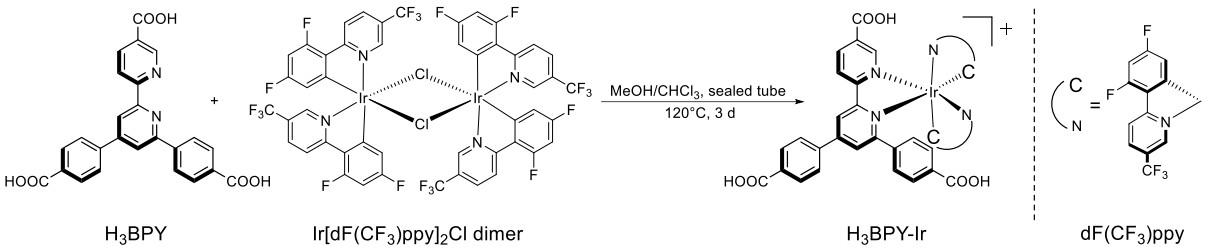

Synthesis of H_3BPY-Ir. H_3BPY was synthesized as described previously.[18] Ir[dF(CF_3)ppy]$_2$Cl dimer (148.8 mg, 0.1 mmol), H_3BPY (88.1 mg, 0.2 mmol), methanol (5 mL), and chloroform (5 mL) were added to a 25 mL thick-walled sealed tube. The tube was sealed and heated at 120 °C for 3 days. After cooling to ambient temperature, the solvent was removed under reduced pressure to afford the crude product. The crude product was then suspended into 5 mL ethanol and filtrated under vacuum. 5 mL ether was then added to the above filtrate to precipitate the product as a light yellow solid (87.8 mg, 37%). ^{1}H NMR (500 MHz, DMSO-d_6): δ 9.28 (s, 1 H), 9.19 (d, 1 H), 8.60 (d, 1 H), 8.53 (d, 1 H), 8.43–8.26 (m, 9 H), 8.15-8.13 (m, 4 H), 7.69 (s, 1 H), 7.02 (m, 1 H), 6.43 (m, 1 H), 5.53 (d d, 1 H), 5.01 (d d, 1 H). HR-MS (ESI-FT) *m*/*z* Calcd. for $C_{49}H_{26}F_{10}IrN_4O_6^+$([M − Cl^-]$^+$) 1149.13, Found: 1149.13.

Synthesis of Hf_{12}-Ir. To a 4 mL glass vial was added 0.5 mL of $HfCl_4$ solution (2.0 mg/mL in DMF), 0.5 mL of H_2**L**-Ir solution (4.4 mg/mL in DMF), 2 μL of TFA, and 5μL of water. The reaction mixture was kept in an 80 °C oven for 24 hours. The yellow precipitate was collected by centrifugation and washed with DMF and ethanol. The yield was 48% based on Hf as determined by ICP-MS.

Digestion of Hf_{12}-Ir. 1.0 mg Hf_{12}-Ir was dried under vacuum. The resulting solid was then digested in a solution of 500 μL DMSO-d_6 and 50 μL D_3PO_4 and sonicated for 10 min. The mixture was then added to 50 μL D_2O and analyzed by ^{1}H NMR. The digested Hf_{12}-Ir showed all signals corresponding to H_2**L**-Ir without any other aromatic signals, which confirms the

presence of only **L**-Ir ligands in Hf_{12}-Ir.

Synthesis of Hf_6-Ir. To a 20 mL glass vial was added 2.5 mL of $HfCl_4$ solution (5.60 mg/mL in DMF), 2.5 mL of the H_3BPY solution (5 mg/mL in DMF), 0.5 mL of formic acid, and 0.75 mL of water. The reaction mixture was kept in a 120 °C oven for 24 hours. The white precipitate (Hf_6-BPY) was collected by centrifugation and washed with DMF and ethanol. To a 1 mL methanol suspension of Hf_6-BPY (1 mg) was added 2 mg $Ir[dF(CF_3)ppy]_2Cl$ dimer. The reaction mixture was kept in an 80 °C oven for 2 days. The yellow precipitate (Hf_6-Ir) was collected by centrifugation and washed with methanol and ethanol. The metalation yield was determined to be 71% by ICP-MS.

EXAFS Fitting: Fitting of the EXAFS region was performed using the Artemis program of the IFEFFIT package. Fitting was performed in R space, with a *k*-weight of 2 for iridium samples. Refinement was performed by optimizing an amplitude factor S_0^2 and energy shift ΔE_0 which are common to all paths, in addition to parameters for bond length (ΔR) and Debye-Waller factor (σ^2). The fitting model for H_3-BPY-Ir was based on the DFT optimized structure.

$^{\bullet}$OH generation with APF assay. APF reacts with $^{\bullet}$OH to give bright green fluorescence (excitation/emission maxima 490/515 nm). Hf_{12}-Ir, Hf_6-Ir, and H_2**L**-Ir were suspended in water at equivalent Hf or Ir concentrations of 20 μM in the presence of 5 μM APF. A water solution of 5 μM APF was used as blank control. 100 μL of each suspension was added to a 96-well plate and then irradiated with 0, 1, 2, 3, 5, or 10 Gy X-ray (Philips RT250 X-ray generator, Philips, USA, 250 KVp, 15 mA, 1 mm Cu filter). The fluorescence signal was immediately collected with a Xenogen IVIS 200 imaging system.

In vitro ·OH generation with γ-H2AX assay. γ-H2AX, a protein that can be phosphorylated after generated hydroxyl radicals oxidation to induce DNA damage repair, has been used as a sensitive biomarker for probing DSBs. MC38 cells were cultured in 35 mm tissue culture dishes overnight and incubated with particles/ligands at a Hf/Ir concentration of 20 μM for 4 h followed by irradiation at 0 or 2 Gy X-ray (Philips RT250 X-ray generator, Philips, 250 kVp, 15 mA, 1 mm Cu filter). Cells were stained immediately with the HCS DNA damage kit (Life Technology, USA) for CLSM.

$^1O_2$ generation with SOSG assay. Hf_{12}-Ir, Hf_6-Ir, and H_2**L**-Ir were suspended in water at equivalent Hf/Ir concentrations of 20 μM in the presence of 12.5 μM SOSG. A water solution of 12.5 μM SOSG was used as a blank control. 100 μL of each suspension was added to a 96-well plate and then irradiated with 0, 1, 2, 3, 5, or 10 Gy X-ray (Philips RT250 X-ray generator, Philips, USA, 250 KVp, 15 mA, 1 mm Cu filter). The fluorescence signal was immediately collected with a Xenogen IVIS 200 imaging system.

O_2^- generation determined by BMPO. BMPO is a nitrone spin trap, which can form distinguishable adducts with O_2^- (BNPO- O_2^-) with a long half lifetime ($t_{1/2}$ = 23 minutes).[16] Hf_{12}-Ir, Hf_6-Ir, and H_2**L**-Ir were suspended in MeCN at equivalent Hf/Ir concentrations of 100 μM in the presence of 25 mM BMPO. A MeCN solution of 25 mM BMPO was used as a blank control. 500 μL of each suspension was added to a 2 mL vial and then irradiated with 5 Gy X-ray (225 kVp, 13 mA, 0.3 mm-Cu filter). The EPR signal was then collected by a Bruker Elexsys 500 X-band EPR.

In vitro $^1O_2$ and O_2^- generation. $^1O_2$ and O_2^- generation in live cells was detected by SOSG and superoxide anion assay kit, respectively. MC38 cells were seeded in a 3.5-cm petri dish

and cultured for 12 h. The culture medium was then replaced with fresh medium containing 1 μM SOSG and 1 μM superoxide anion assay kit to preload the cells with SOSG and superoxide anion assay kit. After incubating for 30 min, the cells were washed by PBS three times to remove excess SOSG and superoxide anion assay kit. The cells were incubated with Hf_{12}-Ir, Hf_6-Ir, H_2**L**-Ir, or PBS at a Hf/Ir concentration of 20 μM for 8 h, then washed with PBS three times to remove excess Hf_{12}-Ir, Hf_6-Ir, or H_2**L**-Ir. X-ray irradiation was applied to cells at a dose of 0 or 2 Gy (250 kVp, 15 mA, 1-mm Cu filter). CLSM was used to visualize the $^1O_2$ and O_2^- generated in the live cells by detecting the green and red fluorescence inside the cells.

Cellular uptake. The cellular uptakes of Hf_{12}-Ir and Hf_6-Ir were compared in MC38 cells. MC38 cells were seeded on 6-well plates at 1×10^6/well and then cultured for 12 h. Hf_{12}-Ir and Hf_6-Ir were added to the cells at a Hf concentration of 20 μM. After incubation of 1, 2, 4, and 8 hours, the cells were collected and counted with a hemocytometer. The cells were digested with concentrated nitric acid in a microwave reactor and the metal concentrations were determined by ICP-MS.

Clonogenic assay. MC38 cells were cultured in a 6-well plate overnight and incubated with Hf_{12}-Ir or Hf_6-Ir at a Hf concentration of 20 μM for 4 h followed by irradiation with 0, 1, 2, 4, 8 and 16 Gy X-ray (Philips RT250 X-ray generator, Philips, USA, 250 KVp, 15 mA, 1 mm Cu filter). Cells were trypsinized and counted immediately. 200-2000 cells were seeded in a 6-well plate and cultured with 2 mL medium for 14 days. Once colony formation was observed, the culture medium was discarded. The plates were rinsed twice with PBS, then stained with 500 μL of 0.5% w/v crystal violet in 50% methanol/H_2O. The wells were rinsed with water for three times and the colonies were counted manually.

MTS assay. The cytotoxicity of Hf_{12}-Ir, Hf_6-Ir, H_2**L**-Ir and H_3BPY-Ir was evaluated with MTS assay with or without X-ray irradiation. MC38 cells were seeded on 96-well plates at 1×10^5/well and further cultured for 12 h. Hf_{12}-Ir, Hf_6-Ir, H_2**L**-Ir and H_3BPY-Ir were added to the cells at an equivalent Ir-based ligand dose of 0, 1, 2, 5, 10, 20, 50 and 100 μM and incubated for 4 h. The cells were then irradiated with X-rays at a dose of 0 or 2 Gy (Philips RT250 X-ray generator, Philips, USA, 250 KVp, 15 mA, 1 mm Cu filter). The cells were further incubated for 72 h before determining the cell viability by MTS assay.

Apoptosis/necrosis. MC38 cells were cultured in 35 mm tissue culture dishes overnight and incubated with Hf_{12}-Ir, Hf_6-Ir, H_2**L**-Ir or PBS at an equivalent Hf/Ir dose of 20 μM for 4 h followed by irradiation with 0 or 2 Gy X-ray (250 kVp, 15 mA, 1 mm Cu filter). 24 h later, the cells were stained according to the AlexaFluor 488 Annexin V/dead cell apoptosis kit and quantified by flow cytometry with three different runs for statistical analysis.

ICD. MC38 cells were cultured in a 6-well plate overnight and incubated with Hf_{12}-Ir, Hf_6-Ir, H_2**L**-Ir or PBS at a Hf/Ir concentration of 20 μM for 4 h followed by irradiation with 0 or 2 Gy X-ray (250 kVp, 15 mA, 1 mm Cu filter). After incubation for 4 h, the cells were washed three times with PBS, fixed with 4% paraformaldehyde, incubated with AlexaFluor 488-CRT (Enzo Life Sciences, USA) for 2 h at room temperature and analyzed by flow cytometry.

In vivo anti-cancer efficacy. For the evaluation of RT-RDT efficacy of Hf_{12}-Ir, Hf_6-Ir, H_2**L**-Ir or PBS, a syngeneic model was established by subcutaneously inoculating 2×10^6 MC38 cells onto the right flank subcutaneous tissues of C57Bl/6 mice on day 0 as the MC38 model. When the tumors reached 100-150 mm^3 in volume, Hf_{12}-Ir, Hf_6-Ir or H_2**L**-Ir at a Hf/Ir dose of 0.2 μmol or PBS was injected intratumorally. 12 h after injection, mice were anaesthetized with 2%

(v/v) isoflurane and the primary tumors were irradiated with 0.5 Gy X-ray per fraction (225 kVp, 13 mA, 0.3 mm-Cu filter) for a total of 5 daily fractions. The tumor sizes were measured with a caliper every day where tumor volume equals (width^2 × length)/2. Body weight of each group was monitored every day. Mice were sacrificed on Day 23 and the excised tumors were photographed and weighed. Tumors and major organs were sectioned for immunofluorescent TUNEL analysis.

5.5 References

1. Tan, C.; Cao, X.; Wu, X.-J.; He, Q.; Yang, J.; Zhang, X.; Chen, J.; Zhao, W.; Han, S.; Nam, G.-H.; Sindoro, M.; Zhang, H., Recent Advances in Ultrathin Two-Dimensional Nanomaterials. *Chem. Rev.* **2017,** *117* (9), 6225-6331.
2. Chimene, D.; Alge, D. L.; Gaharwar, A. K., Two-dimensional nanomaterials for biomedical applications: emerging trends and future prospects. *Adv. Mater.* **2015,** *27* (45), 7261-7284.
3. Chen, Y.; Tan, C.; Zhang, H.; Wang, L., Two-dimensional graphene analogues for biomedical applications. *Chem. Soc. Rev.* **2015,** *44* (9), 2681-2701.
4. Wang, Z.; Zhu, W.; Qiu, Y.; Yi, X.; von dem Bussche, A.; Kane, A.; Gao, H.; Koski, K.; Hurt, R., Biological and environmental interactions of emerging two-dimensional nanomaterials. *Chem. Soc. Rev.* **2016,** *45* (6), 1750-1780.
5. Butler, S. Z.; Hollen, S. M.; Cao, L.; Cui, Y.; Gupta, J. A.; Gutiérrez, H. R.; Heinz, T. F.; Hong, S. S.; Huang, J.; Ismach, A. F.; Johnston-Halperin, E.; Kuno, M.; Plashnitsa, V. V.; Robinson, R. D.; Ruoff, R. S.; Salahuddin, S.; Shan, J.; Shi, L.; Spencer, M. G.; Terrones, M.; Windl, W.; Goldberger, J. E., Progress, Challenges, and Opportunities in Two-Dimensional Materials Beyond Graphene. *ACS Nano* **2013,** *7* (4), 2898-2926.
6. Lan, G.; Ni, K.; Xu, R.; Lu, K.; Lin, Z.; Chan, C.; Lin, W., Nanoscale Metal–Organic Layers for Deeply Penetrating X-ray-Induced Photodynamic Therapy. *Angew. Chem.* **2017,** *129* (40), 12270-12274.
7. Lan, G.; Li, Z.; Veroneau, S. S.; Zhu, Y.-Y.; Xu, Z.; Wang, C.; Lin, W., Photosensitizing Metal-Organic Layers for Efficient Sunlight-Driven Carbon Dioxide Reduction. *J. Am. Chem. Soc.* **2018**.
8. Thariat, J.; Hannoun-Levi, J.-M.; Myint, A. S.; Vuong, T.; Gérard, J.-P., Past, present, and future of radiotherapy for the benefit of patients. *Nat. Rev. Clin. Oncol.* **2013,** *10* (1), 52.
9. Schaue, D.; McBride, W. H., Opportunities and challenges of radiotherapy for treating cancer. *Nat. Rev. Clin. Oncol.* **2015,** *12* (9), 527.
10. Chen, W.; Zhang, J., Using nanoparticles to enable simultaneous radiation and photodynamic therapies for cancer treatment. *J. Nanosci. Nanotechnol.* **2006,** *6* (4), 1159-1166.
11. Chen, H.; Wang, G. D.; Chuang, Y.-J.; Zhen, Z.; Chen, X.; Biddinger, P.; Hao,

Z.; Liu, F.; Shen, B.; Pan, Z.; Xie, J., Nanoscintillator-Mediated X-ray Inducible Photodynamic Therapy for In Vivo Cancer Treatment. *Nano Lett.* **2015,** *15* (4), 2249-2256.
12. Ni, K.; Lan, G.; Chan, C.; Quigley, B.; Lu, K.; Aung, T.; Guo, N.; La Riviere, P.; Weichselbaum, R. R.; Lin, W., Nanoscale metal-organic frameworks enhance radiotherapy to potentiate checkpoint blockade immunotherapy. *Nat. Commun.* **2018,** *9* (1), 2351.
13. Lu, K.; He, C.; Guo, N.; Chan, C.; Ni, K.; Lan, G.; Tang, H.; Pelizzari, C.; Fu, Y.-X.; Spiotto, M. T.; Weichselbaum, R. R.; Lin, W., Low-dose X-ray radiotherapy–radiodynamic therapy via nanoscale metal–organic frameworks enhances checkpoint blockade immunotherapy. *Nature Biomedical Engineering* **2018,** *2* (8), 600-610.
14. Ni, K.; Lan, G.; Veroneau, S. S.; Duan, X.; Song, Y.; Lin, W., Nanoscale metal-organic frameworks for mitochondria-targeted radiotherapy-radiodynamic therapy. *Nat. Commun.* **2018,** *9* (1), 4321.
15. PXRD pattern was simulated by complete integrating method in real space.
16. Zhao, H.; Joseph, J.; Zhang, H.; Karoui, H.; Kalyanaraman, B., Synthesis and biochemical applications of a solid cyclic nitrone spin trap: a relatively superior trap for detecting superoxide anions and glutathiyl radicals. *Free Radical Biol. Med.* **2001,** *31* (5), 599-606.
17. Zhu, Y.-Y.; Lan, G.; Fan, Y.; Veroneau, S.; Song, Y.; Micheroni, D.; Lin, W., Merging Photoredox and Organometallic Catalysts in a Metal-Organic Framework Significantly Boosts Photocatalytic Activities. *Angew. Chem.* **2018**.
18. Lan, G.; Ni, K.; Xu, R.; Lu, K.; Lin, Z.; Chan, C.; Lin, W., Nanoscale Metal–Organic Layers for Deeply Penetrating X-ray-Induced Photodynamic Therapy. *Angew. Chem.* **2017,** *129* (40), 12270-12274.

Chapter 6. Nanoscale Metal-Organic Framework Hierarchically Combines High-Z Components for Multifarious Radio-Enhancement

6.1 Introduction

Compared to conventional nanomaterials, nMOFs provide a unique platform to simultaneously incorporate multiple components not only onto the framework as metal-oxo SBUs and bridging ligands but also within the cavities in the forms of functional molecules and nanoparticles/clusters.[1-6] Moreover, the proximity of these components (usually < 2 nm) allows for efficient transfer of energy, electrons, and reactive intermediates, leading to unparalleled synergy between the functional subunits.[7-9]

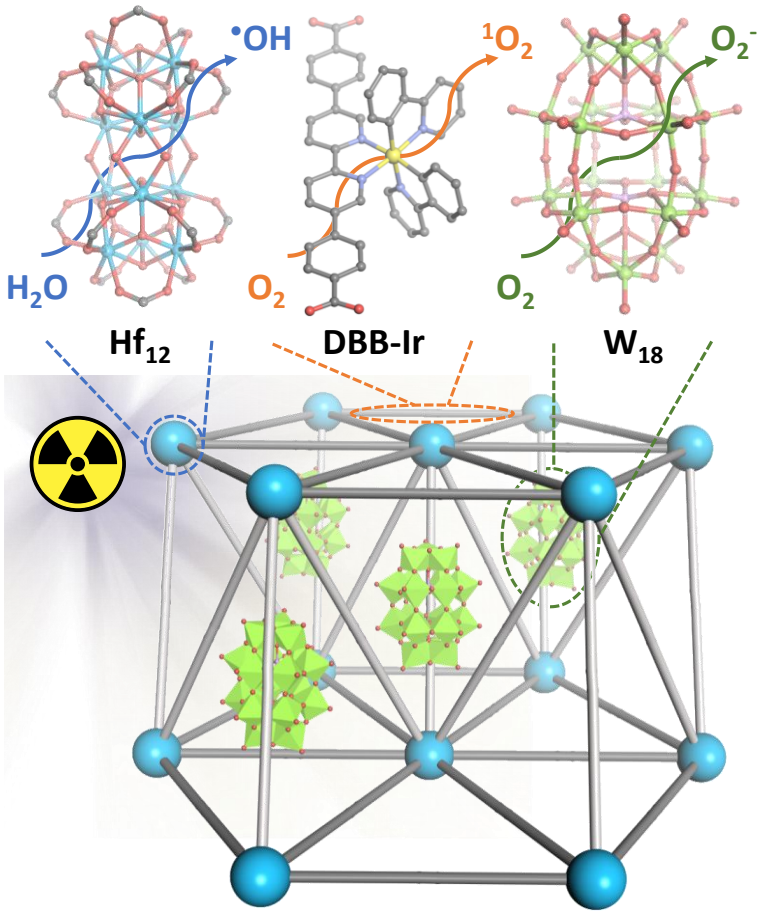

Figure 6-1. Schematic showing the hierarchical assembly of Hf_{12}, DBB-Ir, and W_{18} subunits in W_{18}@Hf_{12}-DBB-Ir and the generation of three distinct ROSs upon X-ray irradiation.

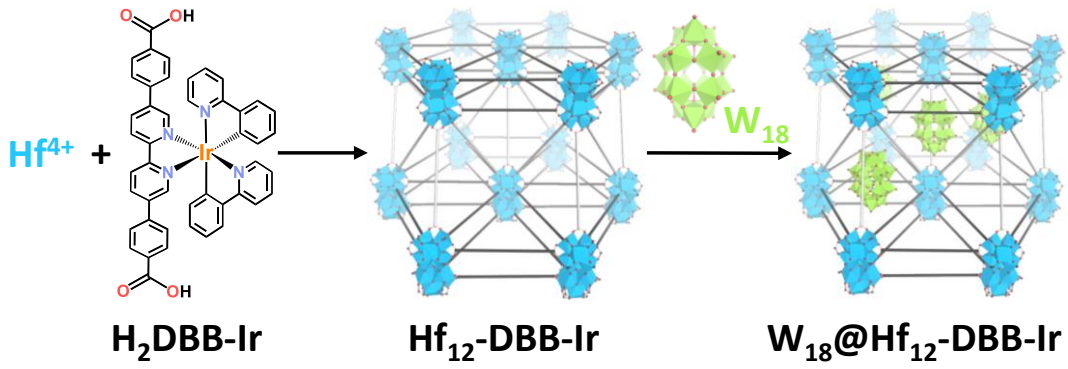

Figure 6-2. Schematic showing the two-step synthesis of W_{18}@Hf_{12}-DBB-Ir

RT using X-rays and other ionizing radiations has been in clinical use for over a century.[10] Despite decades of intensive search for molecules/materials to augment the therapeutic effects of radiation,[11-13] there are currently no Food and Drug Administration-approved radioenhancers that can increase RT efficacy without incurring unwanted side effects. Some high-Z nanoparticles (e.g. Au or HfO_2), nanoclusters, and metal-organic complexes have been shown to enhance RT with modest radioenhancement.[14-19] In this Chapter, we report the first nMOF-based multifarious radioenhancer, W_{18}@Hf_{12}-DBB-Ir, that simultaneously incorporates three high-Z components for efficient ROS generation (**Figure 6-1**). Constructed from Hf-oxo SBUs (Hf_{12}) and $Ir(DBB)(ppy)_2^+$ (DBB-Ir) bridging ligands, the cationic framework of $[Hf_{12}(\mu_3\text{-}O)_8(\mu_3\text{-}OH)_8(\mu_2\text{-}OH)_6(DBB\text{-}Ir)_9]^{9+}$ (Hf_{12}-DBB-Ir) efficiently encapsulates Wells–Dawson-type $[P_2W_{18}O_{62}]^{6-}$ (W_{18}) POM through electrostatic attractions to afford W_{18}@Hf_{12}-DBB-Ir (**Figure 6-2**). The hierarchical assembly of these high-Z components in W_{18}@Hf_{12}-DBB-Ir not only enhances the absorption of radiation to significantly increase $^{\bullet}OH$ generation through water radiolysis, but also enables synergistic interactions to generate $^1O_2$ through photosensitizing DBB-Ir and O_2^- through redox-active W_{18}, leading to superb anti-cancer efficacy in MC38 and CT26 tumor models of colon cancer.

6.2 Result and discussion

6.2.1 Synthesis and characterization

Hf_{12}-DBB-Ir was synthesized through a solvothermal reaction between $HfCl_4$ and H_2DBB-Ir in DMF at 80 °C with TFA and water as modulators. Hf_{12}-DBB-Ir displayed a hexagonal nanoplate morphology with a diameter of ~150 nm as shown by TEM (**Figure 6-3a**) and a thickness of ~10 nm as determined by AFM (**Figure 6-3b**). DLS studies gave a number-averaged size of 114.8 ± 5.8 nm (**Figure 6-3c**).

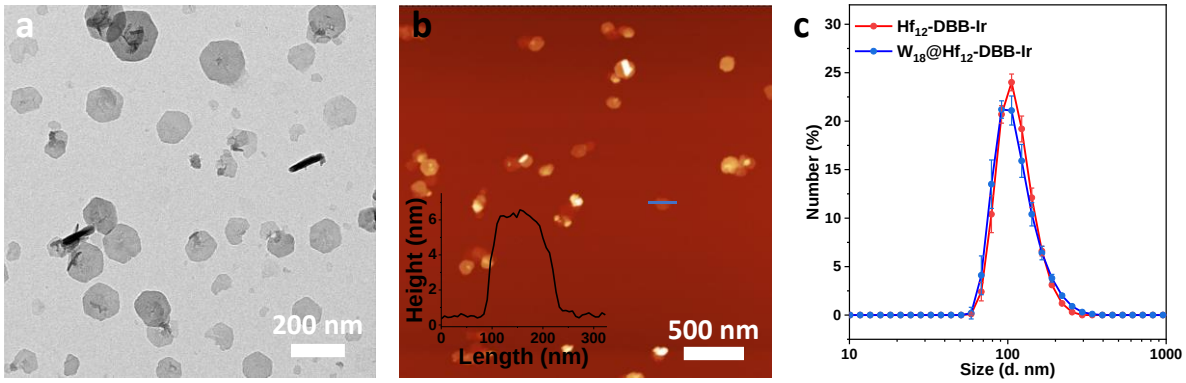

Figure 6-3. Morphology characterization of Hf_{12}-DBB-Ir. TEM image (a) and AFM topography and height profile along the blue line (inset, b) of Hf_{12}-DBB-Ir. (c) Number-averaged diameters of Hf_{12}-DBB-Ir and W_{18}@Hf_{12}-DBB-Ir in water.

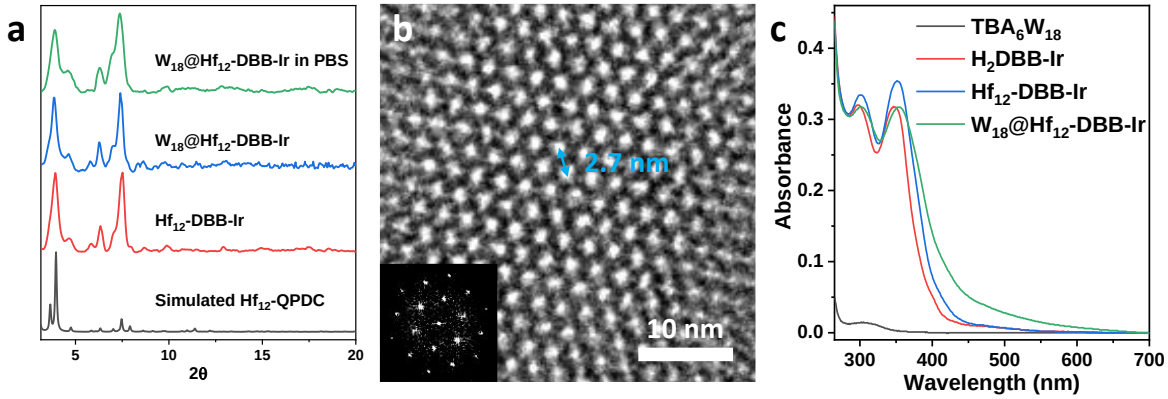

Figure 6-4. Structure characterization of Hf_{12}-DBB-Ir. (a) PXRD patterns of freshly prepared Hf_{12}-DBB-Ir and W_{18}@Hf_{12}-DBB-Ir and after incubation in 0.6 mM PBS for 5 days, in comparison to that simulated from the structure of Zr_{12}-QPDC.[20] (b) HRTEM image, where Hf_{12} SBUs appear as white spots, and its FFT pattern (inset). (c) UV-Vis spectra of W_{18}@Hf_{12}-DBB-Ir and Hf_{12}-DBB-Ir, in comparison to H_2DBB-Ir and TBA_6W_{18}. The concentration is 10 μM based on Ir for W_{18}@Hf_{12}-DBB-Ir and Hf_{12}-DBB-Ir and W for TBA_6W_{18}.

Hf_{12}-DBB-Ir had the same **hcp** topological structure as previously reported Zr_{12}-QPDC,[20] as demonstrated by PXRD (**Figure 6-4a**). HRTEM image and its FFT pattern of Hf_{12}-DBB-Ir displayed a six-fold symmetry and a Hf_{12}-Hf_{12} SBU distance of 2.7 nm, matching the modeled distance (**Figure 6-4b**). Moreover, the UV-vis spectrum of Hf_{12}-DBB-Ir (**Figure 6-4c**) confirmed the presence of DBB-Ir ligands in Hf_{12}-DBB-Ir. The determined topological and chemical structures of Hf_{12}-DBB-Ir are shown in **Figure 6-5**.

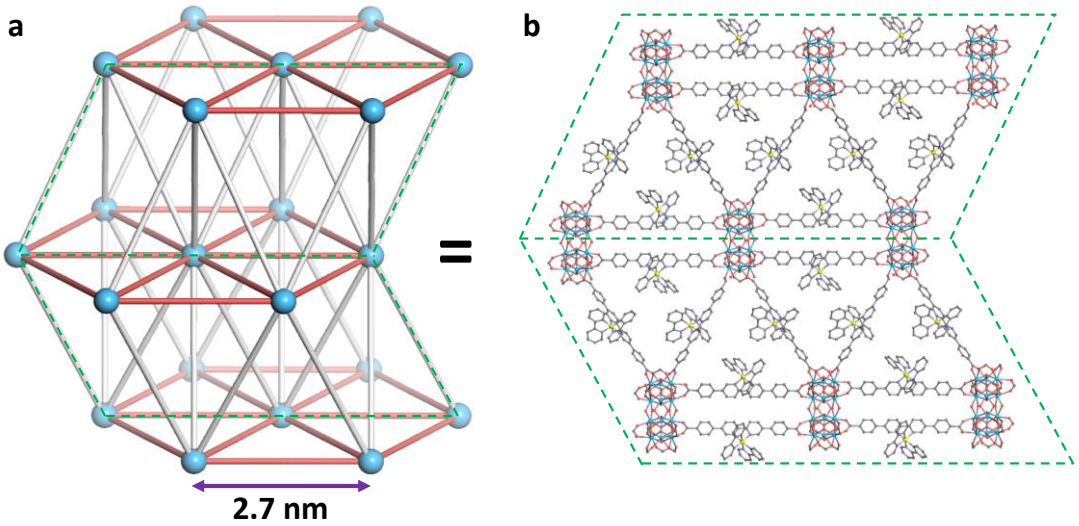

Figure 6-5. Topological and chemical structure of Hf_{12}-DBB-Ir. (a) Topological structure (**hcp**) of Hf_{12}-DBB-Ir. Blue balls represent $Hf_{12}(\mu_3\text{-}O)_8(\mu_3\text{-}OH)_8(\mu_2\text{-}OH)_6(RCOO)_9$ SBUs; red rods represent dual DBB-Ir ligands that laterally coordinated to Hf_{12} SBUs; gray rods represent single DBB-Ir ligands that vertically coordinated to Hf_{12} SBUs. The distance between the centers of the adjacent Hf_{12} SBUs is ~2.7 nm. (b) Chemical structure of Hf_{12}-DBB-Ir corresponding to the selected area in **Figure 6-5a**.

W_{18}@Hf_{12}-DBB-Ir was next synthesized by heating a mixture of Hf_{12}-DBB-Ir and TBA_6W_{18} [TBA = $(n\text{-}Bu)_4N^+$] in ethanol at 70 °C. Due to the electrostatic attraction between anionic W_{18} and cationic Hf_{12}-DBB-Ir, W_{18} was successfully loaded into W_{18}@Hf_{12}-DBB-Ir, as demonstrated by the IR spectra, which displayed characteristic peaks of both Hf_{12}-DBB-Ir and W_{18} (**Figure 6-6**). The ratio of W to Hf was determined to be 0.77 ± 0.05 by ICP-MS and confirmed by TGA. The formulation of W_{18}@Hf_{12}-DBB-Ir was thus determined to be

$[P_2W_{18}O_{62}]_{0.513}@Hf_{12}(\mu_3\text{-}O)_8(\mu_3\text{-}OH)_8(\mu_2\text{-}OH)_6(DBB\text{-}Ir)_9$.

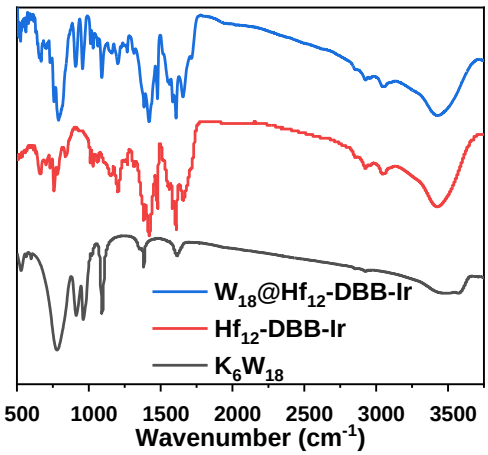

Figure 6-6. IR spectra. IR spectra of $W_{18}@Hf_{12}$-DBB-Ir, Hf_{12}-DBB-Ir, and K_6W_{18}.

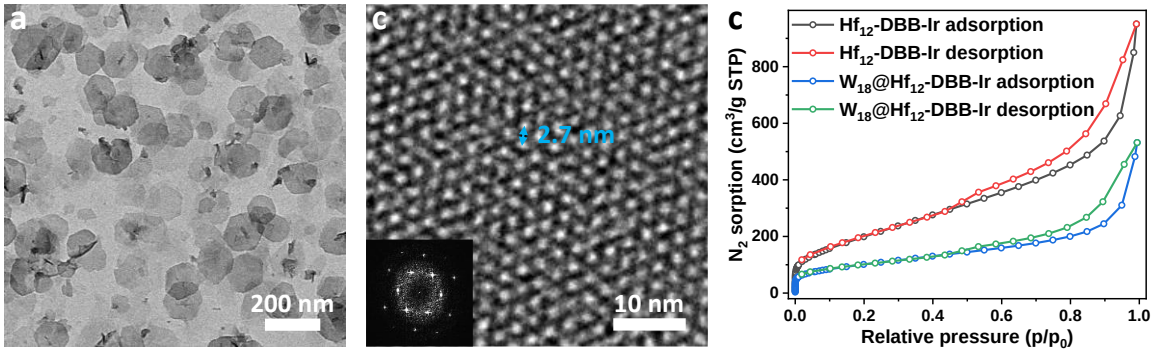

Figure 6-7. Characterization of $W_{18}@Hf_{12}$-DBB-Ir. TEM image (a) and HRTEM image (b) of $W_{18}@Hf_{12}$-DBB-Ir. (c) Nitrogen sorption isotherms of Hf_{12}-DBB-Ir and $W_{18}@Hf_{12}$-DBB-Ir at 77 K.

$W_{18}@Hf_{12}$-DBB-Ir maintained the same hexagonal nanoplate morphology and size (115.5 ± 2.8 nm) as Hf_{12}-DBB-Ir, as shown by TEM (**Figure 6-7a**) and DLS (**Figure 6-3c**), respectively. Upon W_{18} loading, the ζ potential of the nMOF decreased from 9.6 mV to 5.4 mV, consistent with the partial neutralization of positive surface charge of Hf_{12}-DBB-Ir by the anionic W_{18}. Similar PXRD patterns (**Figure 6-4a**) and HRTEM images (**Figure 6-7b**) between Hf_{12}-DBB-Ir and $W_{18}@Hf_{12}$-DBB-Ir demonstrated the maintenance of the MOF structure after W_{18} loading. The presence of DBB-Ir in $W_{18}@Hf_{12}$-DBB-Ir was demonstrated by its characteristic UV-Vis absorption peaks (**Figure 6-4c**) and by its ^{1}H NMR signals in digested $W_{18}@Hf_{12}$-DBB-Ir. As shown in **Figure 6-7c**, $W_{18}@Hf_{12}$-DBB-Ir exhibited a smaller BET

surface area of 345.5 m^2/g than that of Hf_{12}-DBB-Ir (662.3 m^2/g).

6.2.2 ROS generation

The radio-enhancement effect of W_{18}@Hf_{12}-DBB-Ir was next investigated by measuring ·OH generation from water radiolysis and detecting DNA DSBs caused by ·OH upon X-ray irradiation. APF assay, in which the probe fluorescence is turned on when reacting with ·OH, showed that W_{18}@Hf_{12}-DBB-Ir and Hf_{12}-DBB-Ir generated significantly more ·OH than water upon X-ray irradiation, affording relative enhancements of 55.1% and 48.7%, respectively (**Figure 6-8**). Confocal microscopy (**Figure 6-9**) and flow cytometry (**Figure 6-10**) with a γ-H2AX assay kit, which detects the phosphorylation of the histone protein H2AX for DNA DSB repair via fluorescence turn-on, showed significant DNA DSBs in MC38 cells treated with W_{18}@Hf_{12}-DBB-Ir and Hf_{12}-DBB-Ir. In contrast, negligible enhancement of ·OH generation and minimal DNA DSBs were observed in both H_2DBB-Ir and W_{18} groups, indicating the importance of hierarchically assembling high-Z components in the nMOF platform for radio-enhancement effects. To test this hypothesis, a physical mixture of W_{18} and Hf_{12}-DBB-Ir was also examined, which showed no enhancement in ·OH generation over Hf_{12}-DBB-Ir and much lower ·OH generation than W_{18}@Hf_{12}-DBB-Ir (**Figure 6-8**).

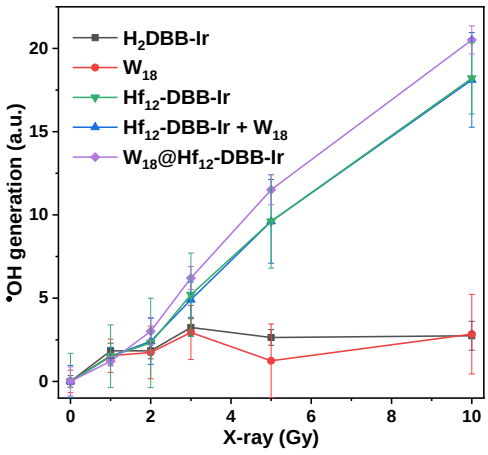

Figure 6-8. ·OH generation determined by APF assay.

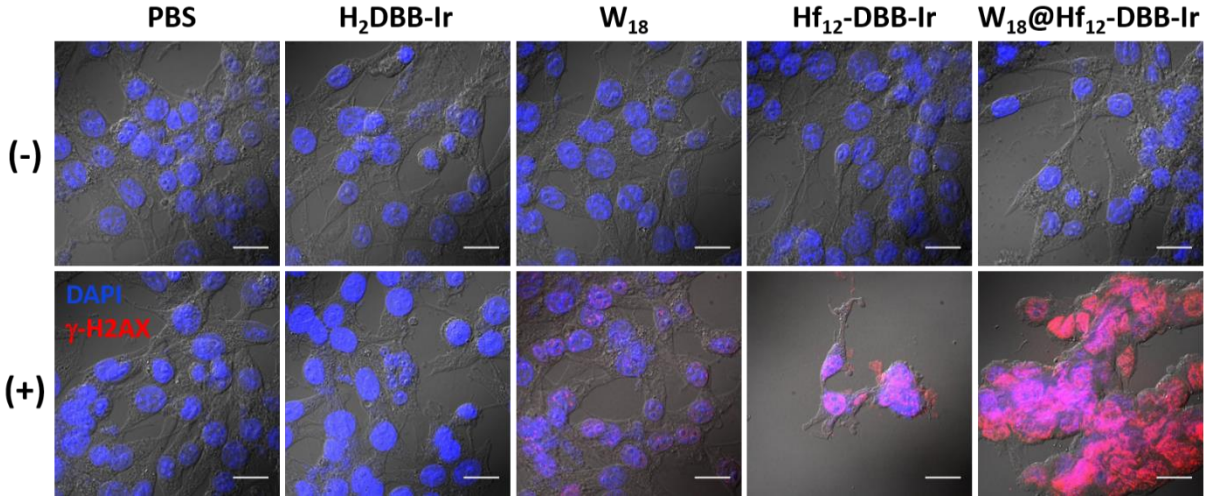

Figure 6-9. ˙OH generation determined by γ-H2AX assays. γ-H2AX assay showing DNA DSBs in MC38 cells treated with PBS, H_2DBB-Ir, W_{18}, Hf_{12}-DBB-Ir, or W_{18}@Hf_{12}-DBB-Ir with (+) or without (-) X-ray irradiation. Blue and red fluorescence represent nuclei and DSB signals, respectively. Scale bar = 20 μm.

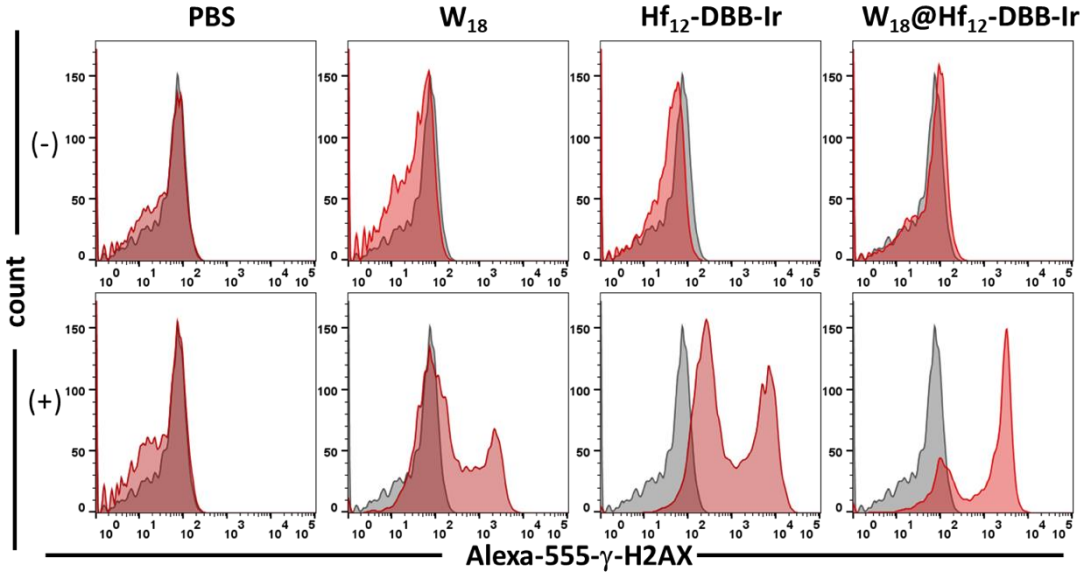

Figure 6-10. DNA DSBs quantified by flow cytometry. DNA DSBs of MC38 cells were assessed after incubation with PBS, H_2DBB-Ir, W_{18}, Hf_{12}-DBB-Ir, or W_{18}@Hf_{12}-DBB-Ir and irradiated with X-ray at 0 (-) or 2 (+) Gy by flow cytometry analysis. Grey histogram (control) and red histogram show the difference of γ-H2AX level in the cells.

We next used SOSG, a turn-on fluorescent probe upon reacting with $^1O_2$, and BMPO, a spin trap for O_2^- to form paramagnetic BMPO-O_2^- adducts, to determine the generation of $^1O_2$ and O_2^- upon irradiation of W_{18}@Hf_{12}-DBB-Ir and control samples with X-rays. While W_{18}@Hf_{12}-DBB-Ir displayed significant generation of both $^1O_2$ and O_2^- (**Figure 6-11**),

H_2DBB-Ir and W_{18} controls showed minimal generation of $^1O_2$ and O_2^-, respectively. In addition, only $^1O_2$ but no O_2^- signal was detected in Hf_{12}-DBB-Ir, confirming that $^1O_2$ and O_2^- were generated by DBB-Ir and W_{18}, respectively. Moreover, the physical mixture of Hf_{12}-DBB-Ir and W_{18} showed much lower $^1O_2$ and O_2^- generation than W_{18}@Hf_{12}-DBB-Ir and no enhancement of $^1O_2$ and O_2^- generation over Hf_{12}-DBB-Ir and W_{18}, respectively. Hierarchical assembly of the high-Z components in W_{18}@Hf_{12}-DBB-Ir is thus critical for the generation of both $^1O_2$ and O_2^-.

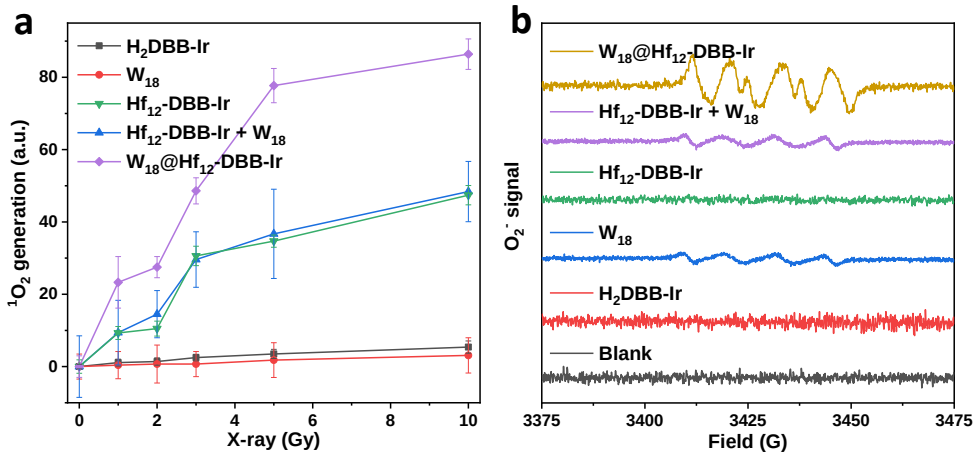

Figure 6-11. $^1O_2$ and O_2^- generation. (a) $^1O_2$ generation determined by SOSG assay. (b) O_2^- generation determined by BMPO assay.

The in vitro generation of $^1O_2$, as determined by the SOSG assay, and O_2^-, as determined by the superoxide kit assay, confirmed these results: H_2DBB-Ir and W_{18} generated minimal amounts of $^1O_2$ and O_2^-, respectively, while Hf_{12}-DBB-Ir only generated $^1O_2$ and W_{18}@Hf_{12}-DBB-Ir enhanced the generation of both $^1O_2$ and O_2^- (**Figure 6-12**).

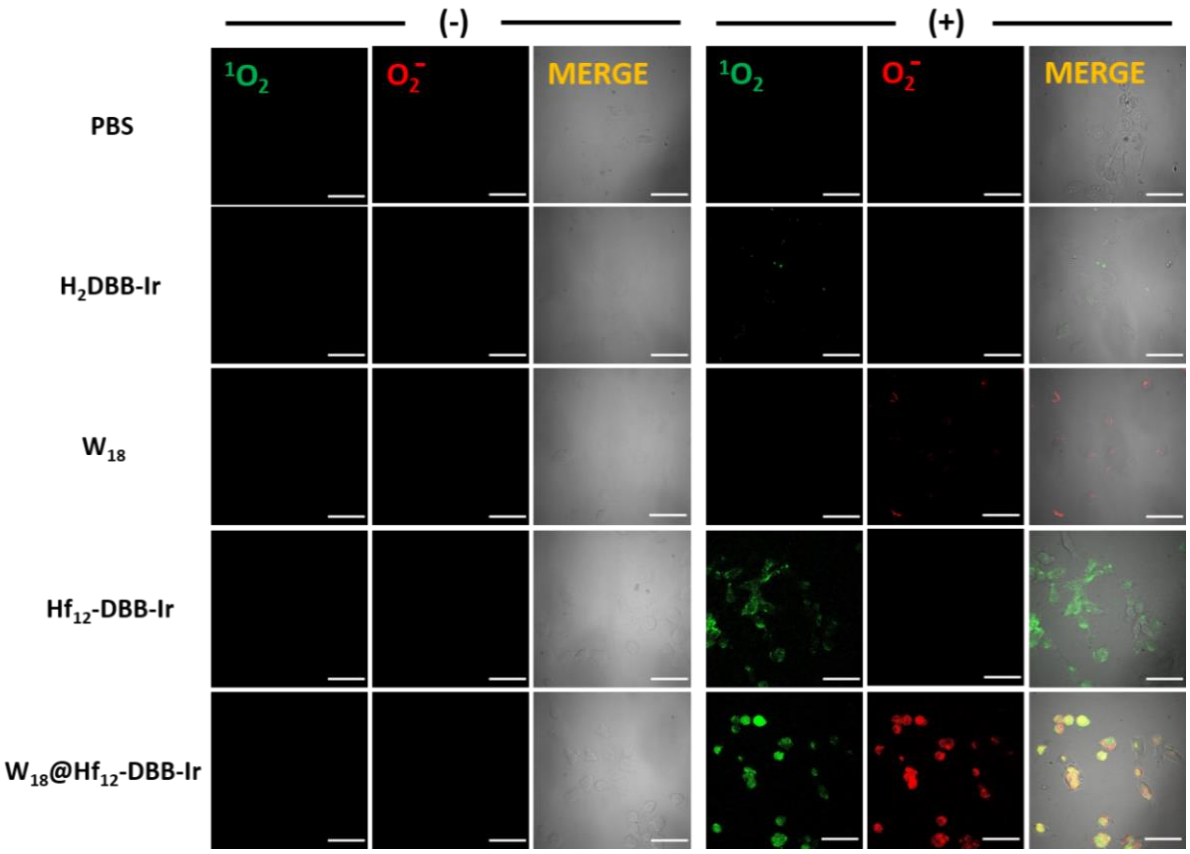

Figure 6-12. Intracellular $^1O_2$ and O_2^- generation. Intracellular $^1O_2$ and O_2^- generation with (+) or without (-) X-ray irradiation detected by SOSG and superoxide kit. Green and red fluorescence represent SOSG or superoxide signal, respectively. Green and red fluorescence merges to yellow fluorescence. Scale bar = 50 μm.

We believe that the proximity of high-Z components (< 2 nm) in W_{18}@Hf_{12}-DBB-Ir significantly increases the capture of secondary radiation, particularly photoelectrons and Auger electrons with short travel distances (~10 nm), to elicit increased radio-enhancement by generating $^{\bullet}OH$, $^1O_2$, and O_2^-. In contrast to conventional nanoparticle-based radioenhancers (e.g. Au and HfO_2) that can only generate $^{\bullet}OH$, W_{18}@Hf_{12}-DBB-Ir not only enhanced $^{\bullet}OH$ generation by Hf_{12} SBUs but also sensitized $^1O_2$ generation through photosensitizing DBB-Ir and O_2^- generation through redox-active W_{18} upon X-ray irradiation (**Figure 6-13**), to afford RT-RDT. The porous structure of W_{18}@Hf_{12}-DBB-Ir facilitates the diffusion of generated ROSs for DNA DSBs and other cell killing processes.

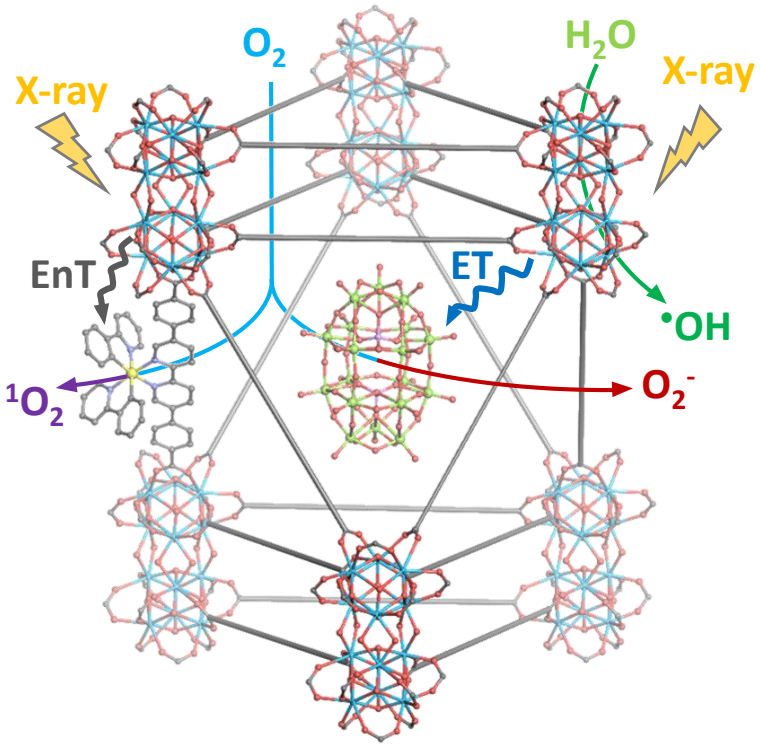

Figure 6-13. Schematic showing key ROS generation mechanisms for W_{18}@Hf_{12}-DBB-Ir: Hf_{12} enhances $^{\bullet}OH$ generation, DBB-Ir sensitizes $^1O_2$ generation, and W_{18} enables O_2^- generation. The arrows with EnT and ET represent energy and electron transfer, respectively.

6.2.3 Anti-cancer efficacy

We next examined if W_{18}@Hf_{12}-DBB-Ir could exert cytotoxicity on cancer cells via RT-RDT. W_{18}@Hf_{12}-DBB-Ir was stable in 0.6 mM PBS for 5 days as demonstrated by PXRD (**Figure 6-4a**) and <5% leaching of W_{18} by ICP-MS. Time-dependent Hf and W ICP-MS analyses (1 to 8 h) demonstrated efficient uptake of W_{18}@Hf_{12}-DBB-Ir and Hf_{12}-DBB-Ir by MC38 cells. In contrast, MC38 cells showed negligible uptake of W_{18} under the same conditions (**Figure 6-14**), likely due to the repulsion between negatively charged cell membrane and anionic W_{18}. The encapsulation of W_{18} in W_{18}@Hf_{12}-DBB-Ir allows for its efficient uptake by cells.

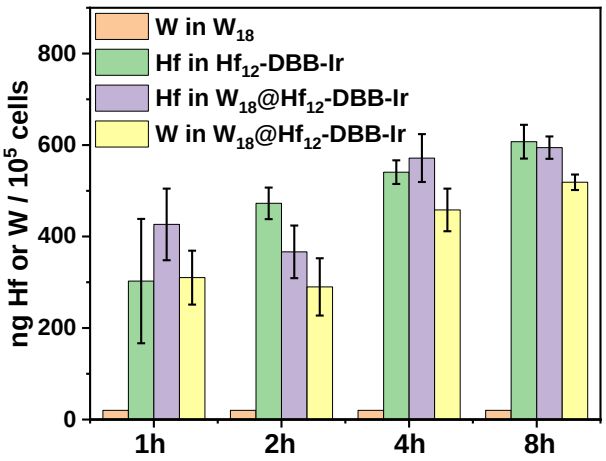

Figure 6-14. Cellular uptake. Cellular uptake by MC38 cells after 4, 8, or 24 hour incubation based on Hf concentrations. The Hf concentrations were determined by ICP-MS (N = 3).

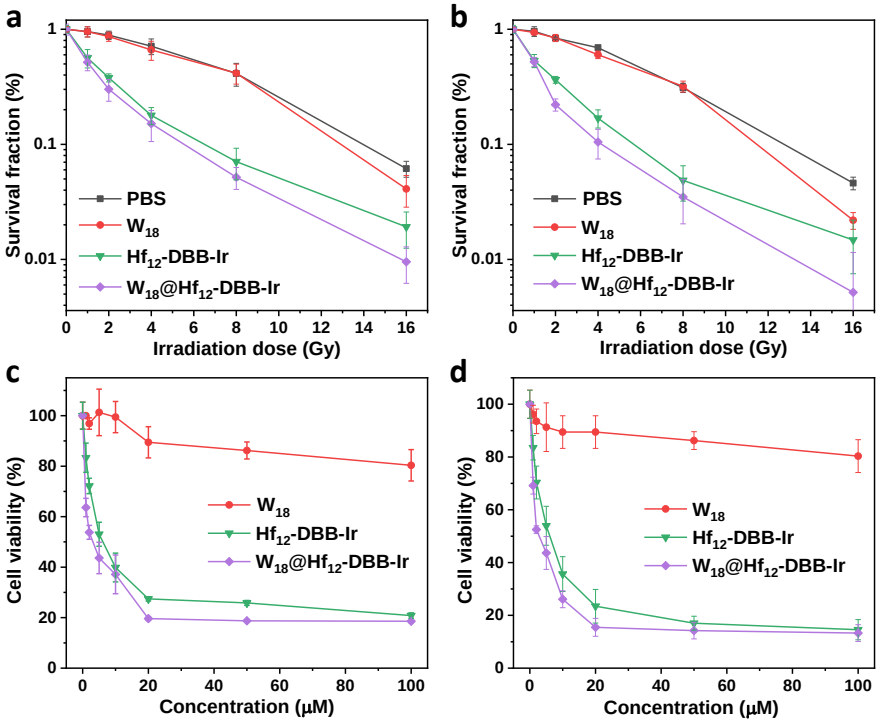

Figure 6-15. Cytotoxicity. Clonogenic assay on MC38 (a) and CT26 cells cells (b). MTS assay on MC38 (c) and CT26 cells cells (d). N = 6.

Upon X-ray irradiation, W_{18}@Hf_{12}-DBB-Ir elicited strong in vitro cytotoxicty with effective cell reproductive death, as determined by clonogenic assay (**Figure 6-15a,b**) with REF_{10} of 2.51 and 3.09 on MC38 and CT26 cells, respectively, and efficient cell instant death, as determined by MTS assay (**Figure 6-15c,d**). The IC_{50} values of W_{18}@Hf_{12}-DBB-Ir with X-ray radiation were 2.51 and 3.12 μM for MC38 cells and CT26 cells, respectively, by MTS

assay. As controls, Hf_{12}-DBB-Ir and W_{18} treatment showed appreciable and weak in vitro cytotoxicity, respectively. No dark toxicity was observed in any of these groups. Confocal microscopy (**Figure 6-16**) and flow cytometry (**Figure 6-17**) using an Annexin V/dead cell apoptosis kit showed that significant numbers of MC38 cells treated with W_{18}@Hf_{12}-DBB-Ir and X-rays underwent apoptosis/necrosis, while moderate and little apoptosis/necrosis was observed for cells treated with Hf_{12}-DBB-Ir and W_{18}, respectively.

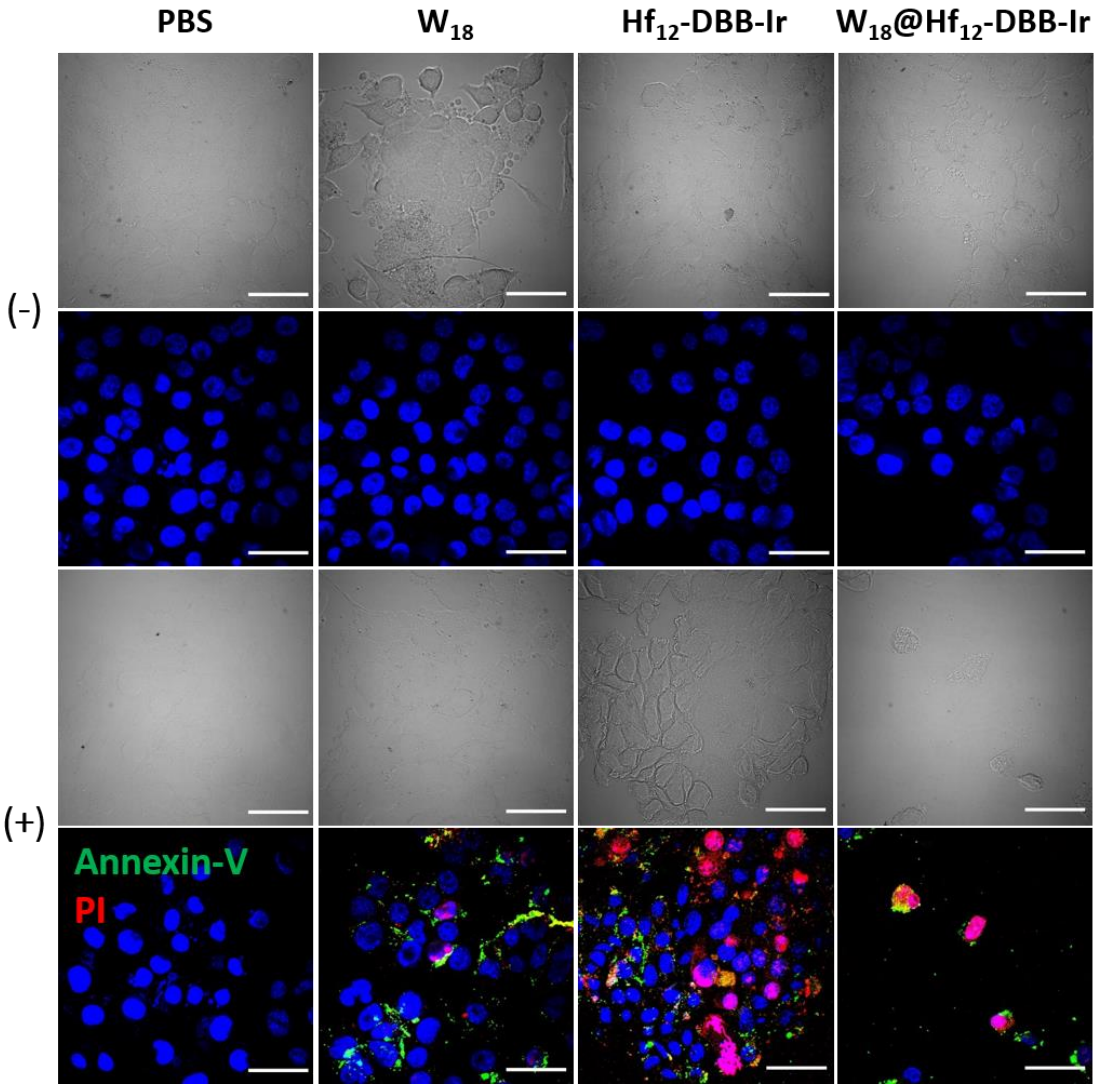

Figure 6-16. Apoptosis determined by CLSM. Annexin-V assay to probe apoptotic cell death process of CT26 cells treated with (+) or without (-) X-ray irradiation. DAPI (blue), FITC-Annexin-V (green), and PI (red) indicate nuclei, apoptotic cells, and dead cells, respectively. Scale bar = 50 μm.

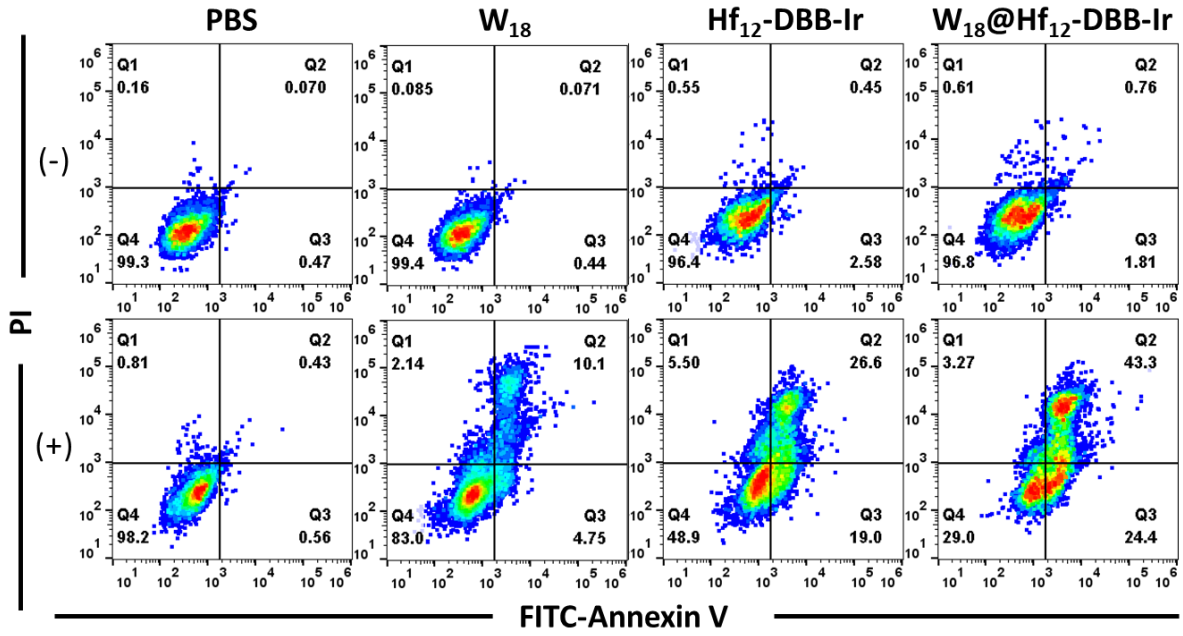

Figure 6-17. Apoptosis determined by flow cytometry. Annexin V/PI cell apoptosis/death analysis of MC38 cells with (+) or without (-) X-ray irradiation. The quadrants from lower left to upper left (counter clockwise) represent healthy, early apoptotic, late apoptotic, and necrotic cells, respectively. The percentage of cells in each quadrant is shown on the graphs.

The therapeutic effects of W_{18}@Hf_{12}-DBB-Ir were further evaluated in vivo on two murine colorectal adenocarcinoma models of MC38-tumor bearing C57BL/6 mice and CT26-tumor bearing Balb/c mice. When the tumors reached 100-150 mm^3, W_{18}@Hf_{12}-DBB-Ir, Hf_{12}-DBB-Ir, W_{18}, or PBS was intratumorally (i.t.) injected into both MC38-tumor and CT26-tumor bearing mice at a Hf/W dose of 0.2 μmol on day 7 followed by 5 daily X-ray fractions of 1 Gy/fraction. W_{18}@Hf_{12}-DBB-Ir or PBS was also intravenously (i.v.) injected into MC38-tumor bearing mice on day 7 and day 11 at a Hf dose of 1 μmol followed by 2.5 Gy irradiation after each injection. W_{18}@Hf_{12}-DBB-Ir showed superb anti-cancer efficacy on both tumor models, while Hf_{12}-DBB-Ir treatment exhibited weaker tumor regression and W_{18} treatment showed only moderate tumor inhibition. The tumor growth inhibition (TGI) indices were 99.3%, 98.7%, 95.1%, and 64.3% for W_{18}@Hf_{12}-DBB-Ir (i.t.), W_{18}@Hf_{12}-DBB-Ir (i.v.), Hf_{12}-DBB-Ir, and

W_{18} treatments, respectively, on MC38-tumor bearing mice (**Figure 6-18a**). TGI indices were 99.7%, 96.7%, and 55.5% on CT26-tumor bearing mice for W_{18}@Hf_{12}-DBB-Ir, Hf_{12}-DBB-Ir and W_{18} treatments, respectively (**Figure 6-18b**). These TGI results were confirmed by the weights of excised tumors on day 22. Steady body weights and lack of abnormalities on histological images of frozen major organ slices demonstrated no systemic toxicity for W_{18}@Hf_{12}-DBB-Ir.

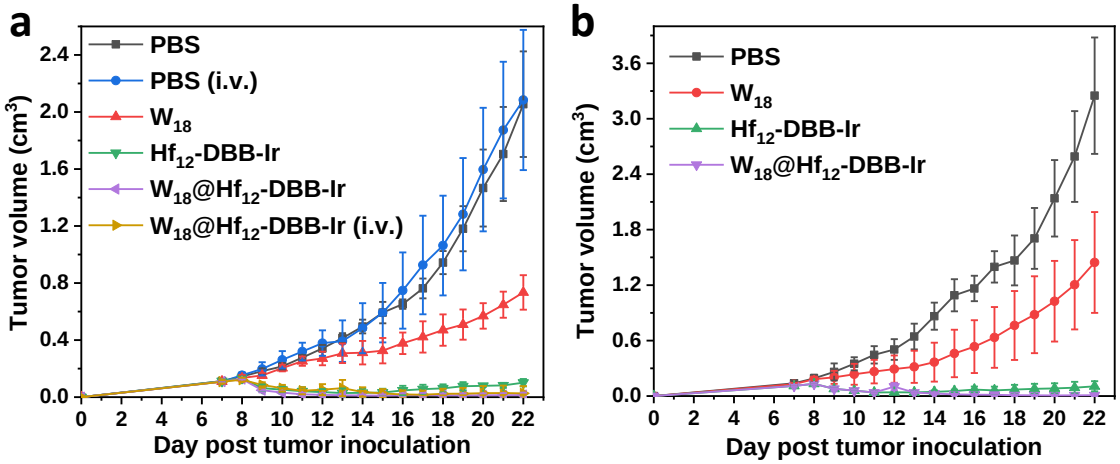

Figure 6-18. In vivo efficacy. Tumor growth inhibition/regression curves for MC38 (a) and CT26 (b) tumor-bearing mice. The doses and irradiation schedules are described in methods.

6.3 Conclusion

In this work, we synthesized a novel nMOF-based radioenhancer, W_{18}@Hf_{12}-DBB-Ir, with superb anti-cancer efficacy. We demonstrated that the composition tunability, structural regularity, and porosity of nMOFs allow for hierarchical assembly of three different high-Z components (Hf_{12}, DBB-Ir, and W_{18}) in W_{18}@Hf_{12}-DBB-Ir to harvest X-ray energy and facilitate synergistic interactions between the high-Z components to generate three distinct ROSs. Our work provides a novel strategy to exploit the unique structural advantages of MOFs to realize complex functions for biomedical applications.

6.4 Methods

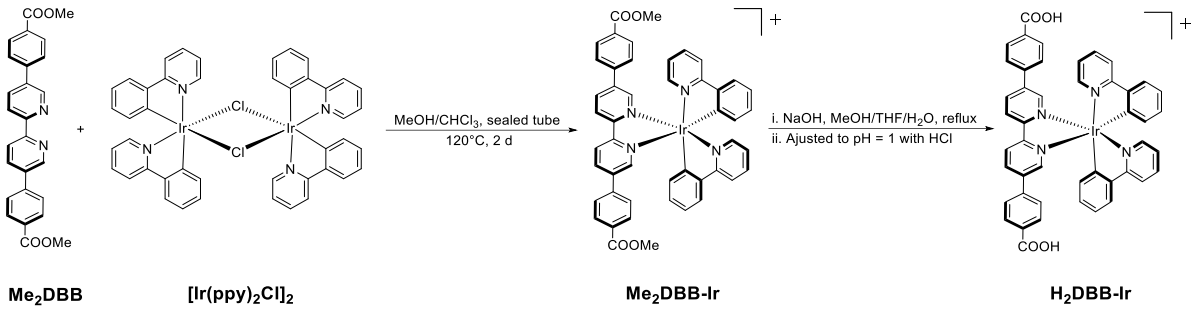

Synthesis of H_2DBB-Ir. [Ir(H_2DBB)(ppy)$_2$]Cl (H_2DBB-Ir) was synthesized through a modified protocol as shown in above.[21] [Ir(ppy)$_2$Cl]$_2$ (1.07 g, 1.0 mmol), Me_2DBB (0.85 g, 2.0 mmol), methanol (25 mL), and chloroform (25 mL) were added to a 200 mL heavy-walled tube. The tube was degassed with N_2, sealed, and heated at 120 °C for 2 days. After cooling to ambient temperature, the solvents were removed under reduced pressure to afford pure Me_2DBB-Ir as an orange solid (1.92 g, 2.0 mmol, 100%). Me_2DBB-Ir (0.96 g, 1.0 mmol), THF (50 mL), MeOH (50 mL), NaOH (1.5 g), and H_2O (20 mL) were added to a 250 mL flask. The solution was stirred under reflux overnight. After THF and MeOH were removed under reduced pressure, the solution was acidified by adding concentrated HCl until pH = 1 was reached and a yellow precipitate formed. The solid was collected by centrifugation, washed with H_2O and MeOH, and finally dried under vacuum to afford H_2DBB-Ir (0.85 g, 0.91 mmol, 91%) as a fine yellow powder. ^{1}H NMR (500 MHz, DMSO-d_6): δ 9.05 (d, 2 H), 8.66 (d d, 2 H), 8.27 (d, 2 H), 8.06 (d, 2 H), 7.94 (m, 8 H), 7.88 (d, 2 H), 7.53 (d, 4 H), 7.16 (t, 2 H), 7.08 (t, 2 H), 6.97 (t, 2 H), 6.32 (d, 2 H).

Synthesis of Hf_{12}-DBB-Ir. To a 4 mL glass vial was added 0.5 mL of $HfCl_4$ solution (2.0 mg/mL in DMF), 0.5 mL of H_2DBB-Ir solution (4.0 mg/mL in DMF), 1 μL of TFA, and 5μL of water. The reaction mixture was kept in an 80 °C oven for 24 hours. The yellow precipitate

was collected by centrifugation and washed with DMF and ethanol. The yield was 56% based on Hf as determined by ICP-MS.

Digestion of Hf_{12}-DBB-Ir. 1.0 mg Hf_{12}-DBB-Ir was dried under vacuum. The resulting solid was then digested in a solution of 500 μL DMSO-d_6 and 50 μL D_3PO_4 and sonicated for 10 min. The mixture was then added to 50 μL D_2O and analyzed by ^1H NMR. The digested Hf_{12}-DBB-Ir showed all signals corresponding to H_2DBB-Ir without any other aromatic signals, which confirms the presence of only DBB-Ir ligands in Hf_{12}-DBB-Ir

Synthesis of organic-soluble TBA_6W_{18}.[22] The Wells-Dawson POM, $K_6[P_2W_{18}O_{62}]\cdot 14H_2O$ (K_6W_{18}), was first synthesized as previously described.[23] To the solution of K_6W_{18} (10.0 g, 2.06 mmol, in 60 mL H_2O) an aqueous solution of $(n\text{-}C_4H_9)_4NBr$ (TBABr) (4.0 g, 12.40 mmol in 40 mL H_2O) was added dropwise under vigorous stirring. After stirring for 10 min, 2 M HNO_3 was added to adjust the pH value to 2.0 to afford a light-yellow precipitate. The precipitate was then collected by centrifugation, washed with water (20 mL) five times, and dried at 70°C for 24 h to afford pure $[(n\text{-}C_4H_9)_4N]_6[P_2W_{18}O_{62}]$ (TBA_6W_{18}) as a white powder (12.0 g, 1.79 mmol, 87%).

Synthesis of W_{18}@Hf_{12}-DBB-Ir. To a 4 mL glass vial was added 0.5 mL of Hf_{12}-DBB-Ir suspension (2 mM based on Hf in EtOH) and 0.5 mL of TBA_6W_{18} solution (2.0 mg/mL in EtOH). The reaction mixture was stirred at 70 °C overnight. The yellow precipitate was collected by centrifugation and washed with ethanol three times. The ratio of W to Hf was determined to be 0.77 ± 0.05 by ICP-MS.

$^{\bullet}$OH generation with APF assay. APF reacts with $^{\bullet}$OH to give bright green fluorescence (excitation/emission maxima 490/515 nm). H_2DBB-Ir, W_{18}, Hf_{12}-DBB-Ir, a mixture of Hf_{12}-

DBB-Ir and W_{18}, and W_{18}@Hf_{12}-DBB-Ir were suspended in water at equivalent Hf (Hf_{12}-DBB-Ir and W_{18}@Hf_{12}-DBB-Ir), Ir (H_2DBB-Ir), or W (W_{18}) concentrations of 20 μM in the presence of 5 μM APF. The mixture of Hf_{12}-DBB-Ir and W_{18} contained 20 μM Hf_{12}-DBB-Ir and 20 μM W_{18}. A water solution of 5 μM APF was used as blank control. 100 μL of each suspension was added to a 96-well plate and then irradiated with X-rays at 0, 1, 2, 3, 5, or 10 Gy (Philips RT250 X-ray generator, Philips, USA, 250 KVp, 15 mA, 1 mm Cu filter). The fluorescence signal was immediately collected with a Xenogen IVIS 200 imaging system.

In vitro DNA DSB with γ-H2AX assay. γ-H2AX, a protein that is phosphorylated to induce DNA damage repair after oxidation by hydroxyl radicals, has been used as a sensitive biomarker for probing DNA DSBs. MC38 cells were cultured in 35 mm tissue culture dishes overnight and incubated with H_2DBB-Ir, W_{18}, Hf_{12}-DBB-Ir, and W_{18}@Hf_{12}-DBB-Ir at an equivalent concentration of 20 μM for 4 h followed by X-ray irradiation at either 0 or 2 Gy (Philips RT250 X-ray generator, Philips, 250 kVp, 15 mA, 1 mm Cu filter). Cells were stained immediately with the HCS DNA damage kit for CLSM.

$^1O_2$ generation with SOSG assay. SOSG reacts with $^1O_2$ to give bright green fluorescence (excitation/emission maxima 504/525 nm). H_2DBB-Ir, W_{18}, Hf_{12}-DBB-Ir, mixture of Hf_{12}-DBB-Ir and W_{18}, and W_{18}@Hf_{12}-DBB-Ir were suspended in water at equivalent Hf (Hf_{12}-DBB-Ir and W_{18}@Hf_{12}-DBB-Ir), Ir (H_2DBB-Ir), or W (W_{18}) concentrations of 20 μM in the presence of 12.5 μM SOSG. The mixture of Hf_{12}-DBB-Ir and W_{18} contained 20 μM Hf_{12}-DBB-Ir and 20 μM W_{18}. A water solution of 12.5 μM SOSG was used as a blank control. 100 μL of each suspension was added to a 96-well plate and then irradiated with X-rays at 0, 1, 2, 3, 5, or 10

Gy (Philips RT250 X-ray generator, Philips, USA, 250 KVp, 15 mA, 1 mm Cu filter). The fluorescence signal was immediately collected with a Xenogen IVIS 200 imaging system.

O_2^- generation determined by BMPO assay. BMPO is a nitrone spin trap, which can form adducts with O_2^- (BMPO-O_2^-) with a half-life ($t_{1/2}$) of 23 minutes. H_2DBB-Ir, W_{18}, Hf_{12}-DBB-Ir, a mixture of Hf_{12}-DBB-Ir and W_{18}, and W_{18}@Hf_{12}-DBB-Ir were suspended in toluene at equivalent Hf (Hf_{12}-DBB-Ir and W_{18}@Hf_{12}-DBB-Ir), Ir (H_2DBB-Ir), or W (W_{18}) concentrations of 200 μM in the presence of 25 mM BMPO. The mixture of Hf_{12}-DBB-Ir and W_{18} contained 200 μM Hf_{12}-DBB-Ir and 200 μM W_{18}. A toluene solution of 25 mM BMPO was used as a blank control. 500 μL of each suspension was added to a 2 mL vial and then irradiated with X-ray at 5 Gy (225 kVp, 13 mA, 0.3 mm-Cu filter). The EPR signal was immediately collected by a Bruker Elexsys 500 X-band EPR.

In vitro $^1O_2$ and O_2^- generation. $^1O_2$ and O_2^- generation in live cells was detected by SOSG and superoxide anion assay kit, respectively. MC38 cells were seeded in a 3.5-cm petri dish and cultured for 12 h. The culture medium was then replaced with fresh medium containing 1 μM SOSG and 1 μM superoxide anion assay kit to preload the cells with SOSG and superoxide anion assay kit. After incubating for 30 min, the cells were washed by PBS three times to remove excess SOSG and superoxide anion assay kit. The cells were incubated with H_2DBB-Ir, W_{18}, Hf_{12}-DBB-Ir, and W_{18}@Hf_{12}-DBB-Ir at a Hf/W/Ir concentration of 20 μM for 4 h, then washed with PBS three times to remove excess nMOF/POM/ligands. X-ray irradiation was applied to cells at a dose of either 0 or 2 Gy (250 kVp, 15 mA, 1-mm Cu filter). CLSM was used to visualize the $^1O_2$ and O_2^- generated in the live cells by detecting the green and red fluorescence inside the cells.

Cellular uptake. The cellular uptakes of K_6W_{18}, Hf_{12}-DBB-Ir, and W_{18}@Hf_{12}-DBB-Ir were compared in MC38 cells. MC38 cells were seeded on 6-well plates at 1×10^6/well and then cultured for 12 h. K_6W_{18}, Hf_{12}-DBB-Ir, and W_{18}@Hf_{12}-DBB-Ir were added to the cells at a Hf/W concentration of 20 μM. After incubation of 1, 2, 4, and 8 hours, the cells were collected and counted with a hemocytometer. The cells were digested with concentrated nitric acid in a microwave reactor and the metal concentrations were determined by ICP-MS.

Clonogenic assay. MC38 or CT26 cells were cultured in a 6-well plate overnight and incubated with W_{18}, Hf_{12}-DBB-Ir, or W_{18}@Hf_{12}-DBB-Ir at a Hf/W concentration of 20 μM for 4 h followed by irradiation with X-rays at 0, 1, 2, 4, 8 or 16 Gy (Philips RT250 X-ray generator, Philips, USA, 250 KVp, 15 mA, 1 mm Cu filter). Cells were trypsinized and counted immediately. 200-2000 cells were seeded in a 6-well plate and cultured with 2 mL medium for 14 days. Once colony formation was observed, the culture medium was discarded. The plates were rinsed twice with PBS, then stained with 500 μL of 0.5% w/v crystal violet in 50% methanol/H_2O. The wells were rinsed with water for three times and the colonies were counted manually. The REF_{10} values of W_{18}, Hf_{12}-DBB-Ir, and W_{18}@Hf_{12}-DBB-Ir were 1.08, 2.14, and 2.51, respectively, on MC38 cells, and 1.11, 2.24, and 3.09, respectively, on CT26 cells.

MTS assay. The cytotoxicity of W_{18}, Hf_{12}-DBB-Ir, or W_{18}@Hf_{12}-DBB-Ir was evaluated with MTS assay with and without X-ray irradiation. MC38 and CT26 cells were seeded on 6-well plates at 1×10^5/well and further cultured for 12 h. W_{18}, Hf_{12}-DBB-Ir, or W_{18}@Hf_{12}-DBB-Ir was added to the cells at an equivalent Hf/W dose of 0, 1, 2, 5, 10, 20, 50 and 100 μM and incubated for 4 h. The cells were then irradiated with X-rays at a dose of either 0 or 2 Gy (Philips RT250 X-ray generator, Philips, USA, 250 KVp, 15 mA, 1 mm Cu filter). The cells were further

incubated for 72 h before determining the cell viability by MTS assay. The IC_{50} values of Hf_{12}-DBB-Ir or W_{18}@Hf_{12}-DBB-Ir were 6.07 or 2.51 μM on MC38 cells, and 6.16 or 3.12 μM on CT26 cells.

Apoptosis. MC38 cells were cultured in 35 mm tissue culture dishes overnight and incubated with W_{18}, Hf_{12}-DBB-Ir, and W_{18}@Hf_{12}-DBB-Ir or PBS at an equivalent dose of 20 μM for 4 h followed by irradiation with X-rays at either 0 or 2 Gy (250 kVp, 15 mA, 1 mm Cu filter). 24 h later, the cells were stained according to the AlexaFluor 488 Annexin V/dead cell apoptosis kit for CLSM and quantified by flow cytometry.

In vivo anti-cancer efficacy. For the evaluation of RT-RDT efficacy of W_{18}, Hf_{12}-DBB-Ir, W_{18}@Hf_{12}-DBB-Ir or PBS, two syngeneic models were established by subcutaneously inoculating 2×10^6 MC38 cells onto the right flank subcutaneous tissues of C57Bl/6 mice on day 0 as the MC38 model or subcutaneously inoculating 2×10^6 CT26 cells onto the right flank subcutaneous tissues of Balb/c mice on day 0 as the CT26 model. When the tumors reached 100-150 mm^3 in volume on day 7, mice bearing MC38 or CT26 were intratumorally injected with W_{18}, Hf_{12}-DBB-Ir, W_{18}@Hf_{12}-DBB-Ir at a Hf/W dose of 0.2 μmol or PBS. 12 h after injection, mice were anaesthetized with 2% (v/v) isoflurane and the tumors were irradiated with X-rays at 1 Gy per fraction (225 kVp, 13 mA, 0.3 mm-Cu filter) for a total of 5 daily fractions. When the tumors reached 100-150 mm^3 in volume, mice bearing MC38 tumors were intravenously injected with W_{18}@Hf_{12}-DBB-Ir at a Hf dose of 1 μmol per mouse or with PBS twice on days 7 and 11. 8 h after each intravenous (i.v.) injection, the tumors were irradiated with 2.5 Gy X-ray. Tumor sizes were measured with a caliper every day, where tumor volume

equals (width^2 × length)/2. The body weight of each group was monitored every day. Mice were sacrificed on Day 22 and the excised tumors were photographed and weighed.

6.5 References

1. Ni, K.; Lan, G.; Chan, C.; Quigley, B.; Lu, K.; Aung, T.; Guo, N.; La Riviere, P.; Weichselbaum, R. R.; Lin, W., Nanoscale metal-organic frameworks enhance radiotherapy to potentiate checkpoint blockade immunotherapy. *Nat. Commun.* **2018,** *9* (1), 2351.
2. Lu, K.; He, C.; Guo, N.; Chan, C.; Ni, K.; Lan, G.; Tang, H.; Pelizzari, C.; Fu, Y.-X.; Spiotto, M. T.; Weichselbaum, R. R.; Lin, W., Low-dose X-ray radiotherapy–radiodynamic therapy via nanoscale metal–organic frameworks enhances checkpoint blockade immunotherapy. *Nature Biomedical Engineering* **2018,** *2* (8), 600-610.
3. Cui, Y.; Yue, Y.; Qian, G.; Chen, B., Luminescent Functional Metal–Organic Frameworks. *Chem. Rev.* **2012,** *112* (2), 1126-1162.
4. Lovell, J. F.; Jin, C. S.; Huynh, E.; Jin, H.; Kim, C.; Rubinstein, J. L.; Chan, W. C. W.; Cao, W.; Wang, L. V.; Zheng, G., Porphysome nanovesicles generated by porphyrin bilayers for use as multimodal biophotonic contrast agents. *Nat. Mater.* **2011,** *10*, 324.
5. Zhang, Y.; Jeon, M.; Rich, L. J.; Hong, H.; Geng, J.; Zhang, Y.; Shi, S.; Barnhart, T. E.; Alexandridis, P.; Huizinga, J. D.; Seshadri, M.; Cai, W.; Kim, C.; Lovell, J. F., Non-invasive multimodal functional imaging of the intestine with frozen micellar naphthalocyanines. *Nat. Nanotechnol.* **2014,** *9*, 631.
6. Zheng, X.; Wang, L.; Pei, Q.; He, S.; Liu, S.; Xie, Z., Metal–Organic Framework@Porous Organic Polymer Nanocomposite for Photodynamic Therapy. *Chem. Mater.* **2017,** *29* (5), 2374-2381.
7. Lan, G.; Ni, K.; Xu, Z.; Veroneau, S. S.; Song, Y.; Lin, W., Nanoscale Metal–Organic Framework Overcomes Hypoxia for Photodynamic Therapy Primed Cancer Immunotherapy. *J. Am. Chem. Soc.* **2018,** *140* (17), 5670-5673.
8. Lan, G.; Ni, K.; Veroneau, S. S.; Feng, X.; Nash, G. T.; Luo, T.; Xu, Z.; Lin, W., Titanium-Based Nanoscale Metal–Organic Framework for Type I Photodynamic Therapy. *J. Am. Chem. Soc.* **2019,** *141* (10), 4204-4208.
9. Wang, C.; Volotskova, O.; Lu, K.; Ahmad, M.; Sun, C.; Xing, L.; Lin, W., Synergistic Assembly of Heavy Metal Clusters and Luminescent Organic Bridging Ligands in Metal–Organic Frameworks for Highly Efficient X-ray Scintillation. *J. Am. Chem. Soc.* **2014,** *136* (17), 6171-6174.
10. Skliarenko, J.; Warde, P., Practical and clinical applications of radiation therapy. *Medicine (Baltimore)* **2016,** *44* (1), 15-19.
11. Kuncic, Z.; Lacombe, S., Nanoparticle radio-enhancement: principles, progress and application to cancer treatment. *Phys. Med. Biol.* **2018,** *63* (2), 02TR01.
12. Schaue, D.; McBride, W. H., Opportunities and challenges of radiotherapy for treating cancer. *Nat. Rev. Clin. Oncol.* **2015,** *12*, 527.
13. Thariat, J.; Hannoun-Levi, J.-M.; Sun Myint, A.; Vuong, T.; Gérard, J.-P., Past, present, and future of radiotherapy for the benefit of patients. *Nat. Rev. Clin. Oncol.* **2012,** *10*,

52.
14. Bonvalot, S.; Le Pechoux, C.; De Baere, T.; Kantor, G.; Buy, X.; Stoeckle, E.; Terrier, P.; Sargos, P.; Coindre, J. M.; Lassau, N.; Ait Sarkouh, R.; Dimitriu, M.; Borghi, E.; Levy, L.; Deutsch, E.; Soria, J.-C., First-in-Human Study Testing a New Radioenhancer Using Nanoparticles (NBTXR3) Activated by Radiation Therapy in Patients with Locally Advanced Soft Tissue Sarcomas. *Clin. Cancer Res.* **2017,** *23* (4), 908.
15. Hainfeld, J. F.; Slatkin, D. N.; Smilowitz, H. M., The use of gold nanoparticles to enhance radiotherapy in mice. *Phys. Med. Biol.* **2004,** *49* (18), N309-N315.
16. Yong, Y.; Zhang, C.; Gu, Z.; Du, J.; Guo, Z.; Dong, X.; Xie, J.; Zhang, G.; Liu, X.; Zhao, Y., Polyoxometalate-Based Radiosensitization Platform for Treating Hypoxic Tumors by Attenuating Radioresistance and Enhancing Radiation Response. *ACS Nano* **2017,** *11* (7), 7164-7176.
17. Chen, H.; Wang, G. D.; Chuang, Y.-J.; Zhen, Z.; Chen, X.; Biddinger, P.; Hao, Z.; Liu, F.; Shen, B.; Pan, Z.; Xie, J., Nanoscintillator-Mediated X-ray Inducible Photodynamic Therapy for In Vivo Cancer Treatment. *Nano Lett.* **2015,** *15* (4), 2249-2256.
18. Lee, H.-Y.; Li, Z.; Chen, K.; Hsu, A. R.; Xu, C.; Xie, J.; Sun, S.; Chen, X., PET/MRI dual-modality tumor imaging using arginine-glycine-aspartic (RGD)–conjugated radiolabeled iron oxide nanoparticles. *J. Nucl. Med.* **2008,** *49* (8), 1371-1379.
19. Kim, J.-K.; Seo, S.-J.; Kim, H.-T.; Kim, K.-H.; Chung, M.-H.; Kim, K.-R.; Ye, S.-J., Enhanced proton treatment in mouse tumors through proton irradiated nanoradiator effects on metallic nanoparticles. *Phys. Med. Biol.* **2012,** *57* (24), 8309-8323.
20. Dai, R.; Peng, F.; Ji, P.; Lu, K.; Wang, C.; Sun, J.; Lin, W., Electron Crystallography Reveals Atomic Structures of Metal–Organic Nanoplates with M12(μ3-O)8(μ3-OH)8(μ2-OH)6 (M = Zr, Hf) Secondary Building Units. *Inorg. Chem.* **2017,** *56* (14), 8128-8134.
21. Wang, C.; deKrafft, K. E.; Lin, W., Pt Nanoparticles@Photoactive Metal–Organic Frameworks: Efficient Hydrogen Evolution via Synergistic Photoexcitation and Electron Injection. *J. Am. Chem. Soc.* **2012,** *134* (17), 7211-7214.
22. Zhang, Z.-M.; Zhang, T.; Wang, C.; Lin, Z.; Long, L.-S.; Lin, W., Photosensitizing Metal–Organic Framework Enabling Visible-Light-Driven Proton Reduction by a Wells–Dawson-Type Polyoxometalate. *J. Am. Chem. Soc.* **2015,** *137* (9), 3197-3200.
23. Graham, C. R.; Finke, R. G., The Classic Wells−Dawson Polyoxometalate, K6[α-P2W18O62]·14H2O. Answering an 88 Year-Old Question: What Is Its Preferred, Optimum Synthesis? *Inorg. Chem.* **2008,** *47* (9), 3679-3686.

Chapter 7. Multifunctional Nanoscale Metal-Organic Layers for Ratiometric pH and Oxygen Sensing

7.1 Introduction

The development of biosensors to probe physiological processes and pathobiological factors is of great importance to early disease diagnosis.[1-4] Among many forms of biosensors, optical probes are the most commonly used in cellular sensing and imaging as they permit direct, real-time, and label-free detection of many biological and chemical analytes.[5-8] In particular, nanoparticle-based optical biosensors have afforded powerful tools for minimally invasive analyte monitoring in live cells.[9-15] They provide the foundation to develop multifunctional ratiometric biosensors to precisely monitor a number of biological and chemical factors underlying various pathobiologies.

In the past decade, nMOFs have shown great potential for biological sensing and related applications.[16-28] By simultaneously incorporating molecular sensors and reference probes as well as ensuring their spatial isolation to avoid self-quenching in the frameworks, nMOFs have provided a novel crystalline molecular nanomaterial platform for designing ratiometric sensors with high sensitivity and resolution.[29, 30] However, due to the strict symmetry requirement of bridging ligands and relatively small pores/channels of most nMOFs, only simple molecular sensors can be incorporated into nMOFs and accessible to small analytes, severely limiting the universality of nMOFs in biosensing. We propose that nMOLs,[31] a monolayered version of nMOFs, can overcome these limitations of nMOFs to afford the next generation of two-dimensional nanobiosensors. nMOLs not only retain molecular nature, structural regularity, and compositional diversity of nMOFs, but also possess high densities of open sites to allow

covalent installation of complex molecular sensors and ready access to large analytes. In this Chapter, we report the design of a proof-of-concept nMOL-based biosensor, Hf_{12}-Ru-F/R, for ratiometric pH and oxygen sensing in mitochondria (**Figure 7-1**).

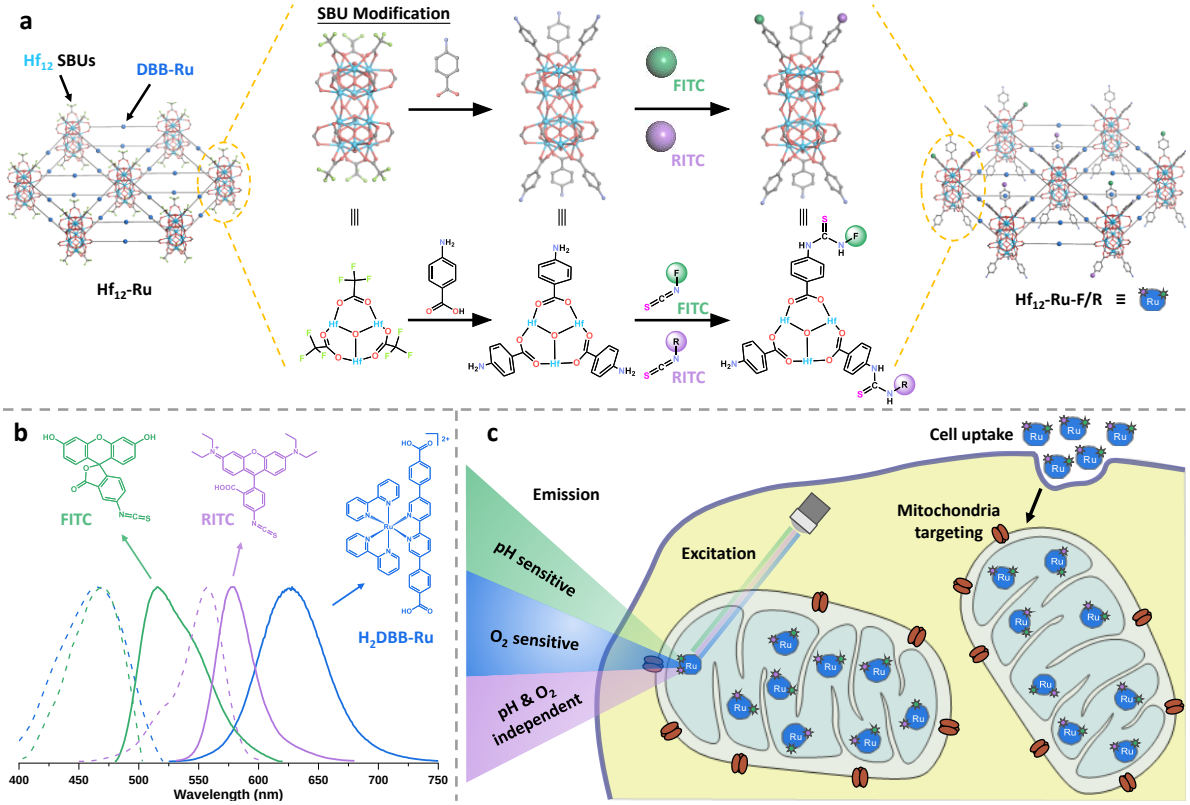

Figure 7-1. Schematic showing the synthesis of multifunctional Hf_{12}-Ru-F/R. (a) Surface modification of Hf_{12}-Ru by exchanging TFA capping groups on Hf_{12} SBUs with *para*-aminobenzoate groups and covalent conjugation of FITC and RITC to Hf_{12} SBUs by forming thiourea linkages. (b) Chemical structures and excitation/emission spectra of FITC, RITC, and H_2DBB-Ru. (c) Positively charged Hf_{12}-Ru-F/R targets mitochondria and allows ratiometric sensing of intra-mitochondrial pH and oxygen via the luminescence ratios of pH-sensitive FITC to pH-independent RITC and O_2-sensitive DBB-Ru to O_2-independent RITC, respectively.

7.2 Result and discussion

7.2.1 Synthesis and characterization

The Hf_{12}-Ru nMOL was synthesized solvothermally between $HfCl_4$ and $Ru(H_2DBB)(bpy)_2^{2+}$ (H_2DBB-Ru) in DMF at 80 ºC with TFA and water as modulators. Hf_{12}-Ru was proposed as an infinite 2D network of **kgd** topology, where Hf_{12} SBUs were vertically

terminated by TFA groups and laterally bridged by DBB-Ru ligands to afford the formula of $Hf_{12}(\mu_3\text{-}O)_8(\mu_3\text{-}OH)_8(\mu_2\text{-}OH)_6(DBB\text{-}Ru)_6(TFA)_6$. The monolayer structure of Hf_{12}-Ru was demonstrated by TEM (**Figure 7-2a**) showing a diameter of ~150 nm and AFM (**Figure 7-2b,c**) giving a thickness of ~1.7 nm. This thickness is consistent with the modeled height of Hf_{12} clusters capped with TFA groups. DLS measurements gave a number-averaged diameter of 98.5 ± 2.2 nm for Hf_{12}-Ru (**Figure 7-2f**). The proposed topological structure of Hf_{12}-Ru was further confirmed by its similar PXRD pattern to that simulated from a Hf_{12} MOL (**Figure 7-2d**)[31] and HRTEM image along with its FFT (**Figure 7-2e**), which revealed a six-fold symmetry and a Hf_{12}-Hf_{12} distance of ~2.7 nm that matches the modeled structure well. The formulation of Hf_{12}-Ru was further supported by TGA.

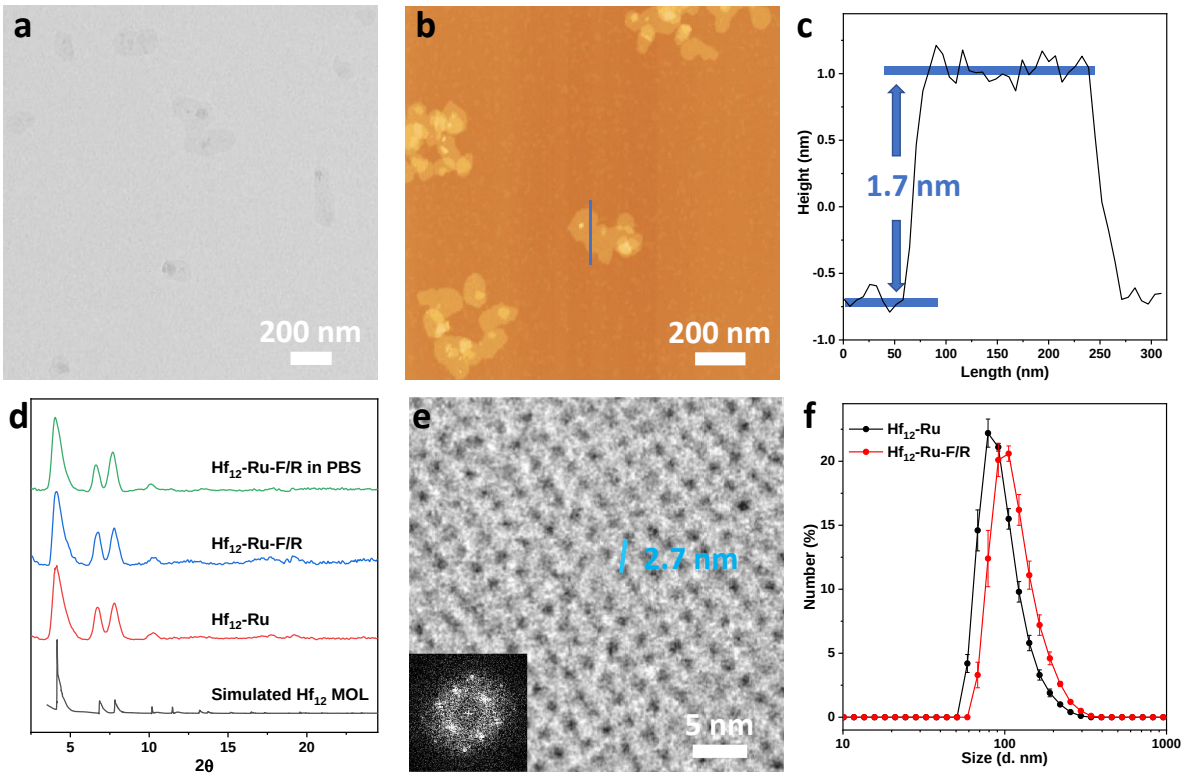

Figure 7-2. Characterization of Hf_{12}-Ru. TEM image (a), AFM topography (b) and height profile (c), HRTEM image with the FFT pattern in the inset (e) of Hf_{12}-Ru. (d) PXRD patterns of Hf_{12}-Ru and Hf_{12}-Ru-F/R, freshly prepared or after 4 h incubation in 0.6 mM PBS, in comparison to the simulated pattern for the Hf_{12} MOL. (f) Number-averaged diameters of Hf_{12}-Ru and Hf_{12}-Ru-F/R in EtOH.

The ratiometric sensor Hf_{12}-Ru-F/R was synthesized by covalently attaching FITC and RITC to Hf_{12}-Ru (**Figure 7-1**). Vertically capped TFA groups on Hf_{12} SBUs were first replaced by *para*-aminobenzoate (ABA) to afford Hf_{12}-Ru-ABA with the formula of $Hf_{12}(\mu_3\text{-}O)_8(\mu_3\text{-}OH)_8(\mu_2\text{-}OH)_6(DBB\text{-}Ru)_6(ABA)_6$ based on the ^1H NMR analysis of digested Hf_{12}-Ru-ABA. FITC and RITC were then covalently conjugated to ABA-capped Hf_{12} SBUs by forming the ABA-F (between ABA and FITC) and ABA-R (between ABA and RITC) thiourea linkages to generate Hf_{12}-Ru-F/R with the formula of $Hf_{12}(\mu_3\text{-}O)_8(\mu_3\text{-}OH)_8(\mu_2\text{-}OH)_6(DBB\text{-}Ru)_6(ABA)_{6\text{-}x\text{-}y}(ABA\text{-}F)_x(ABA\text{-}R)_y$, where x and y represent FITC and RITC loadings, respectively. The ABA-F and ABA-R moieties in Hf_{12}-Ru-F/R were confirmed by the observation of $[ABA\text{-}F + H]^+$ and $[ABA\text{-}R]^+$ peaks in addition to the $[H_2DBB\text{-}Ru/2]^+$ peaks in the HRMS of digested Hf_{12}-Ru-F/R (**Figure 7-3**). No signal corresponding to free FITC and RITC was detected, confirming their covalent attachment to the MOL via the thiourea linkages.

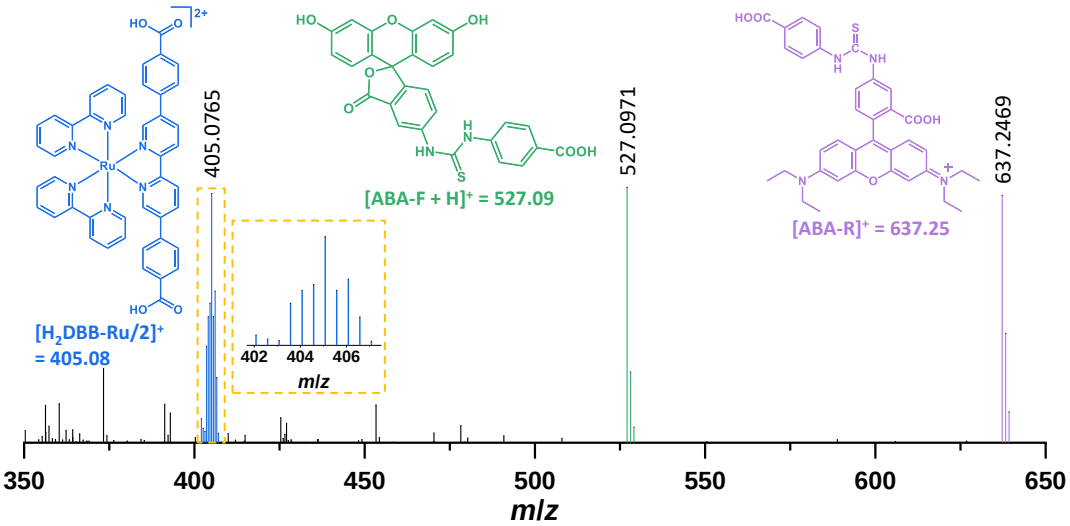

Figure 7-3. HRMS spectrum of digested Hf_{12}-Ru-F/R.

Compared to Hf_{12}-Ru, Hf_{12}-Ru-F/R displayed similar morphology by TEM (**Figure 7-4a**), identical topological structure by HRTEM (**Figure 7-4b**) and PXRD (**Figure 7-2d**), and a slightly increased number-averaged size of 119.1 ± 2.3 nm by DLS (**Figure 7-2f**).

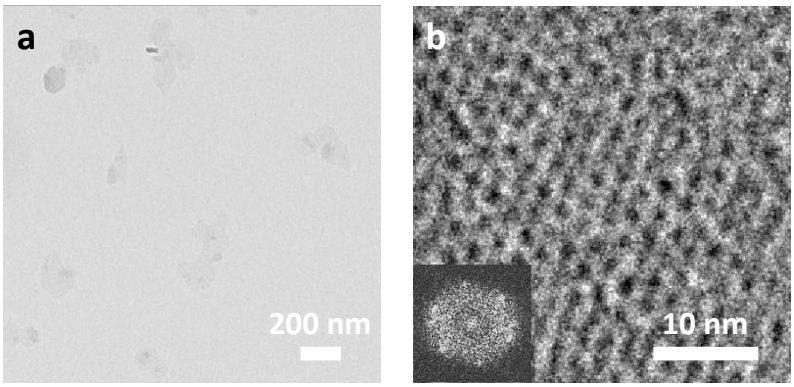

Figure 7-4. Characterization of Hf_{12}-Ru-F/R. TEM image (a) and HRTEM image with the FFT pattern in the inset (b) of Hf_{12}-Ru-F/R.

7.2.2 Luminescence analysis

We hypothesized that Hf_{12}-Ru-F/R could allow ratiometric pH sensing based on the fluorescence ratio of pH-sensitive FITC to pH-independent RITC and O_2 sensing based on the luminescence ratio of O_2-sensitive DBB-Ru to O_2-independent RITC. The loadings of FITC and RITC in Hf_{12}-Ru-F/R were optimized to be 1.1 mol% and 5.6 mol%, respectively, to achieve comparable luminescence intensities for FITC, RITC, and DBB-Ru (**Figure 7-5**). Hf_{12}-Ru-F/R with this composition was used in subsequent studies.

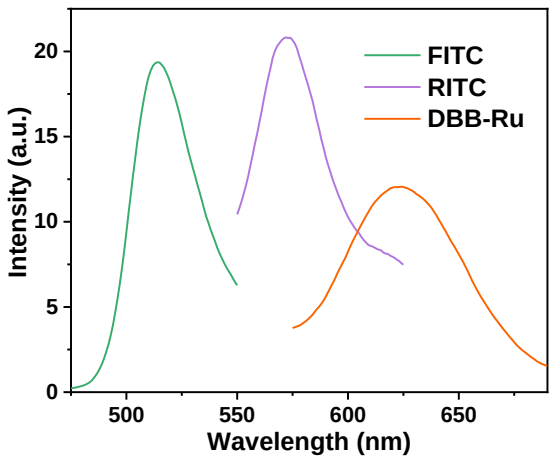

Figure 7-5. Luminescence spectra of Hf_{12}-Ru-F/R. Luminescence spectra of Hf_{12}-Ru-F/R with 1.1 mol% FITC and 5.6 mol% RITC showing emissions corresponding to FITC, RITC, and DBB-Ru, respectively.

Calibration curves and *in vitro* sensing studies were performed using excitation/emission wavelengths of 430/620, 465/500, and 535/600 nm for DBB-Ru, FITC, and RITC, respectively

(**Figure 7-6**).

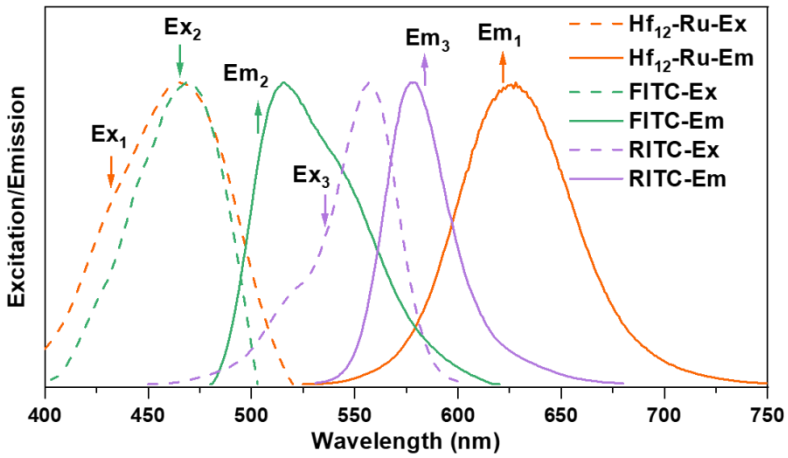

Figure 7-6. Normalized excitation and emission spectra of Hf_{12}-Ru, FITC, and RITC. The excitation and emission wavelengths used for following quantification were (Ex_1 = 430 nm, Em_1 = 620 nm) for DBB-Ru, (Ex_2 = 465 nm, Em_2 = 500 nm) for FITC, and (Ex_3 = 535 nm, Em_3 = 600 nm) for RITC, for both free dye solutions and Hf_{12}-Ru-F/R suspensions

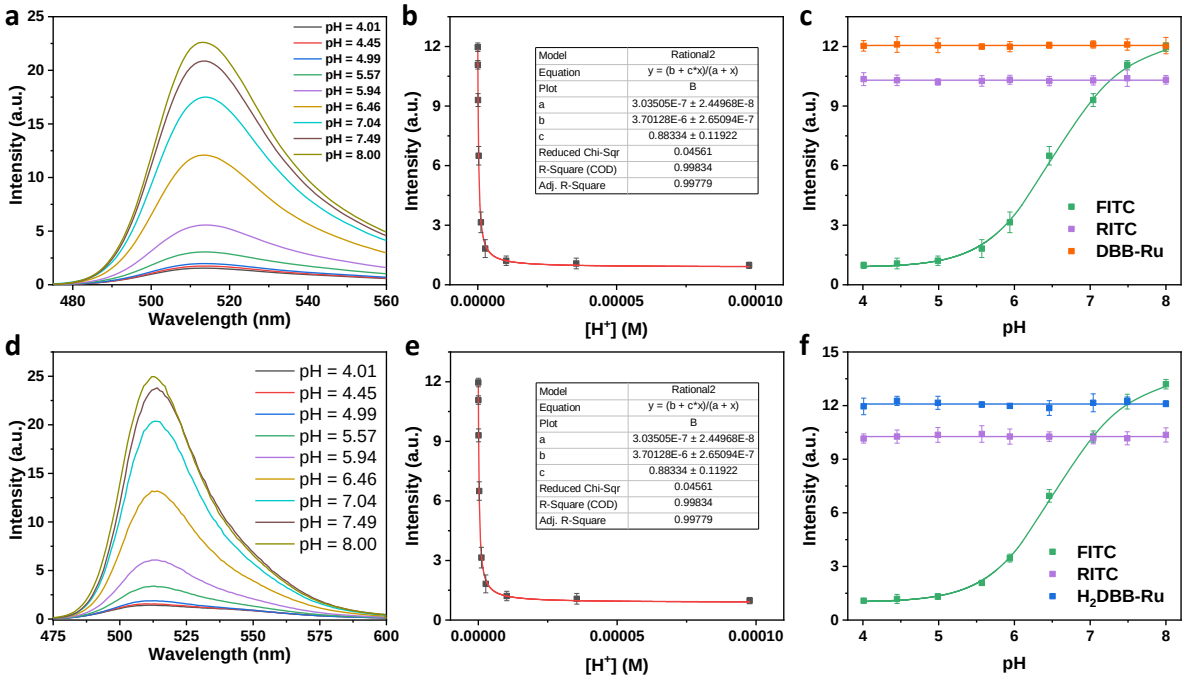

Figure 7-7. pH response of Hf_{12}-Ru-F/R. Emission spectra of 0.11 μM FITC in Hf_{12}-Ru-F/R suspensions (a) or 0.11 μM free FITC (d) in PBS at different pH with excitation at 465 nm under normoxia. Fitting of its luminescence intensity (Ex = 465 nm, Em = 500 nm) of Hf_{12}-Ru-F/R (b) or free FITC (e) against [H^+] based on Eq. 7-1. (c) Plots of luminescence intensities of Hf_{12}-Ru-F/R at different pHs under normoxia. (f) Plots of luminescence intensities of 0.11 μM free FITC, 0.56 μM free RITC, and 10.0 μM free H2DBB-Ru at different pHs under normoxia. The luminescence intensity of FITC in (c) and (f) fitted well with Eq. 7-2.

The response of Hf_{12}-Ru-F/R to pH and O_2 was first studied by fluorimetry. In PBS with pH values of 4.0-8.0 and under normoxia, Hf_{12}-Ru-F/R showed significantly different FITC fluorescence intensities but constant RITC and DBB-Ru signals (**Figure 7-7a-c**). The pH response of Hf_{12}-Ru-F/R is similar to that of free FITC (**Figure 7-7d-f**) and well fitted with Eq. 7-1 ($R^2 = 0.998$).

On the other hand, Hf_{12}-Ru-F/R showed different DBB-Ru luminescence intensities but constant FITC and RITC signals under varied O_2 partial pressures (**Figure 7-8**). The O_2 responses of both Hf_{12}-Ru-F/R and H_2DBB-Ru were well fitted to the Stern-Völmer equation (Eq. 7-5, $R^2 = 1$) with similar fitting parameters.

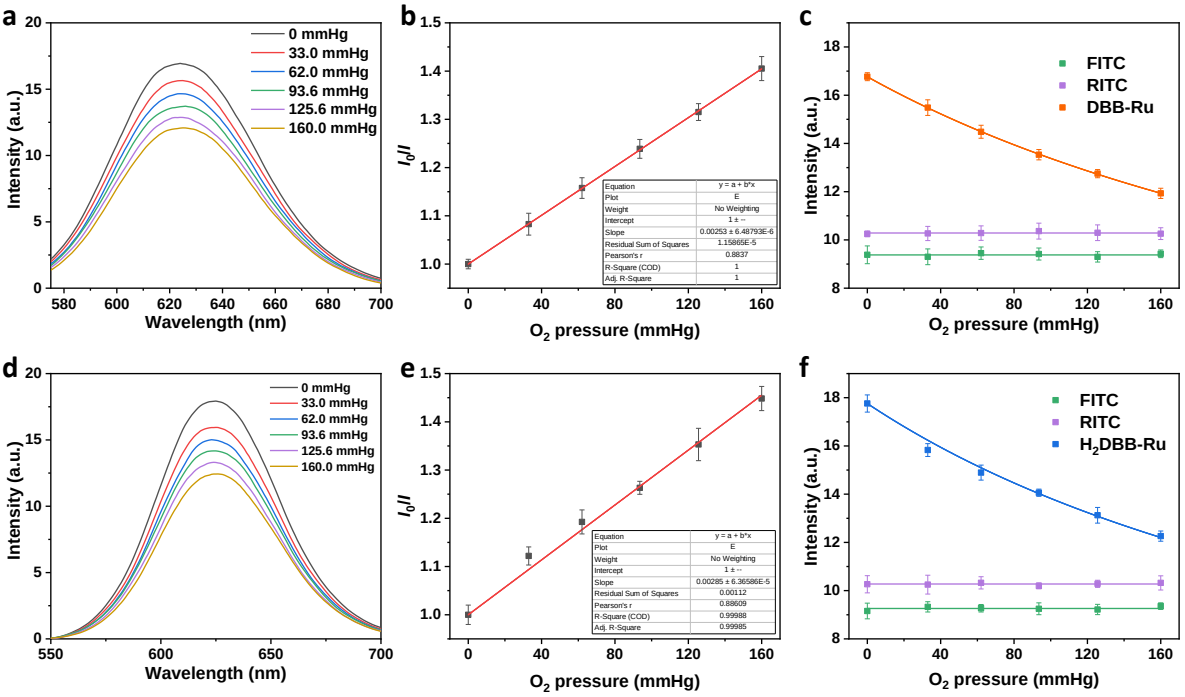

Figure 7-8. O_2 response of Hf_{12}-Ru-F/R. Emission spectra of 10.0 μM DBB-Ru in Hf_{12}-Ru-F/R suspension (a) or 10.0 μM free H_2DBB-Ru (d) in PBS (pH = 7.04) under different O_2 pressures with excitation at 430 nm. Fitting of its luminescence intensity ratio I_0/I (Ex = 430 nm, Em = 620 nm) of DBB-Ru in Hf_{12}-Ru-F/R (b) or free H_2DBB-Ru (e) against O_2 pressure based on Eq. 7-5. (c) Plots of luminescence intensities of Hf_{12}-Ru-F/R under different O_2 pressures at pH 7.04. (f) Plots of luminescence intensities of 0.11 μM free FITC, 0.56 μM free RITC, and 10.0 μM free H_2DBB-Ru in PBS (pH = 7.04) under different O_2 pressures. The luminescence intensity of DBB-Ru in (c) and (f) fitted well with Eq. 7-6.

Based on Eqs 7-1 and 7-5, Hf_{12}-Ru-F/R accurately determined the pH and O_2 values of a random series of samples (**Figure 7-9**). These fluorimetric study results suggest the potential of Hf_{12}-Ru-F/R in ratiometric pH and O_2 sensing.

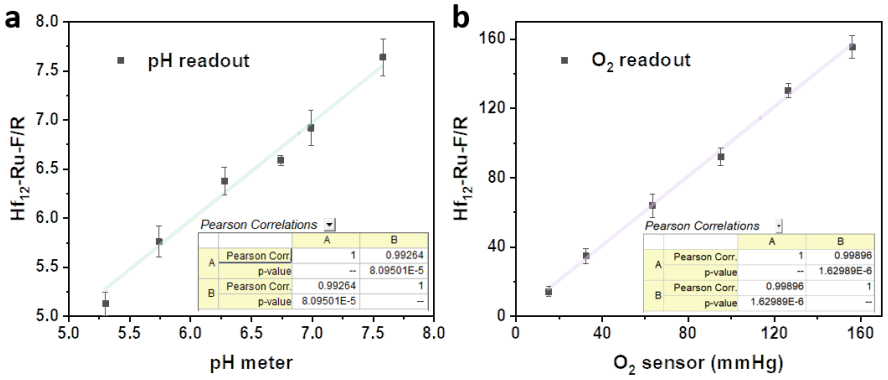

Figure 7-9. Validation of Hf_{12}-Ru-F/R in pH and O_2 sensing. Hf_{12}-Ru-F/R showed pH (a) and O_2 (b) readouts corresponding to those from a pH meter and an O_2 sensor with Pearson correlation coefficients (r) of 0.992 and 0.999, respectively.

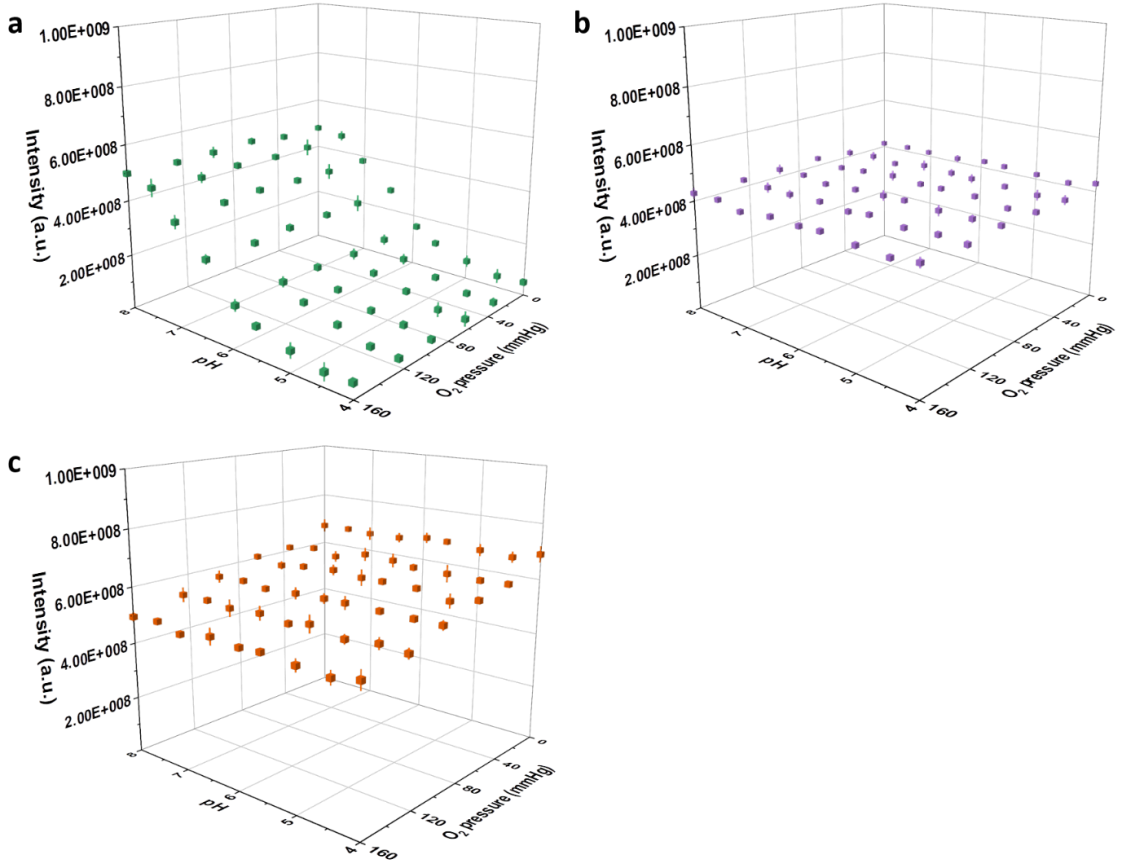

Figure 7-10. pH and O_2 response of Hf_{12}-Ru-F/R by IVIS imaging. Plots of the luminescence intensities of FITC (a), RITC (b), and DBB-Ru (c) at different pH and O_2 pressure as measured by a Xenogen IVIS 200 imaging system.

We next constructed pH and O_2 calibration curves for Hf_{12}-Ru-F/R using an IVIS imaging system. Hf_{12}-Ru-F/R was incubated in PBS at pH values of 4.01, 4.45, 4.99, 5.57, 5.94, 6.46, 7.04, 7.49, and 8.00 under O_2 pressures of 0, 34.1, 63.5, 95.8, 124.2, and 160.0 mmHg and the luminescence signals of FITC, DBB-Ru, and RITC in Hf_{12}-Ru-F/R were collected separately. As shown in **Figure 7-10**, FITC only responded to pH, DBB-Ru only responded to O_2, and RITC did not respond to either pH or O_2. The ratiometric calibration curves for pH and O_2 were then established by fitting the dependence of the fluorescence ratio of FITC to RITC ($r_{F/R}$) on pH according to Eq. 7-9 (R^2 = 0.996, **Figure 7-11a**) and the dependence of the luminescence ratio of DBB-Ru to RITC ($r_{Ru/R}$) on O_2 pressure (P_{O_2}) according to Eq. 7-10 (R^2 = 0.999, **Figure 7-11b**), respectively.

$$r_{F/R} = \frac{0.119e^{-2.303pH} + 3.91 \times 10^{-7}}{e^{-2.303pH} + 3.28 \times 10^{-7}} \qquad (Eq.\ 7-9)$$

$$r_{Ru/R} = \frac{1.613}{1 + 0.00237P_{O_2}} \qquad (Eq.\ 7-10)$$

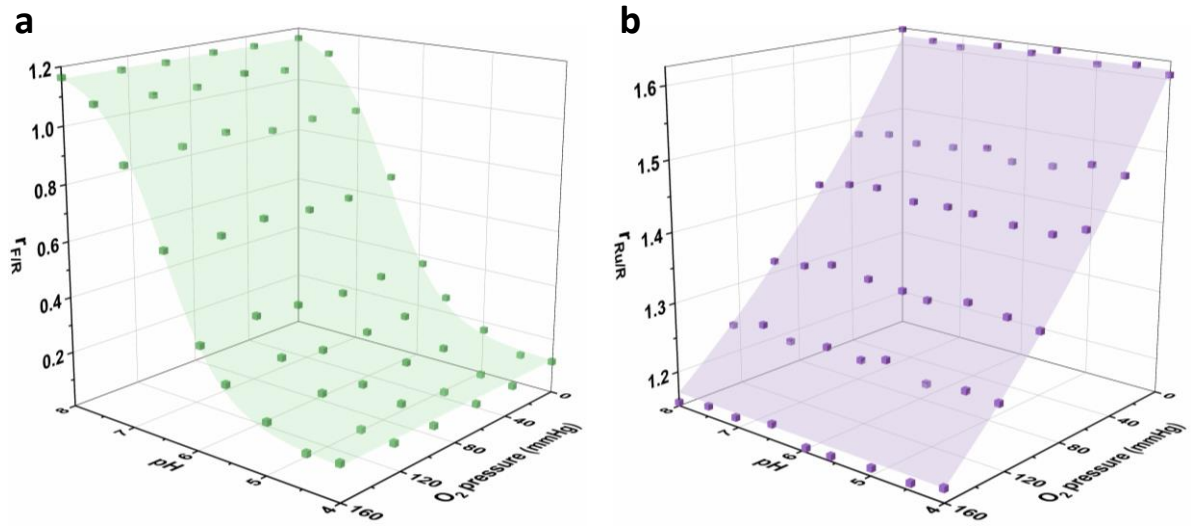

Figure 7-11. Calibration curves. Calibration curves for pH (a, Eq. 1) and O_2 (b, Eq. 2) of Hf_{12}-Ru-F/R acquired by IVIS imaging.

7.2.3 In vitro pH and O_2 sensing

The stability of Hf_{12}-Ru-F/R under physiological conditions was demonstrated by the unchanged PXRD pattern after incubation in 0.6 mM PBS for 4 h (**Figure 7-2d**). We then evaluated uptake of Hf_{12}-Ru-F/R in mouse colon carcinoma CT26 cells. The highly positive zeta potentials of Hf_{12}-Ru (37.7 ± 1.6 mV) and Hf_{12}-Ru-F/R (26.9 ± 2.2 mV) facilitated their cellular uptake as quantified by ICP-MS (**Figure 7-12**).

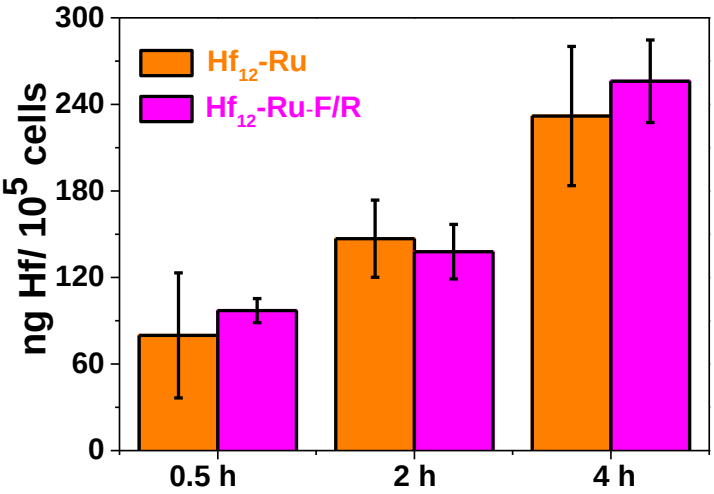

Figure 7-12. Cellular uptake of Hf_{12}-Ru and Hf_{12}-Ru-F/R. Cellular uptake of Hf_{12}-Ru and Hf_{12}-Ru-F/R after 0.5, 2 or 4 h incubation with equivalent Hf concentrations of 20 μM (N = 3). The Hf concentrations were determined by ICP-MS.

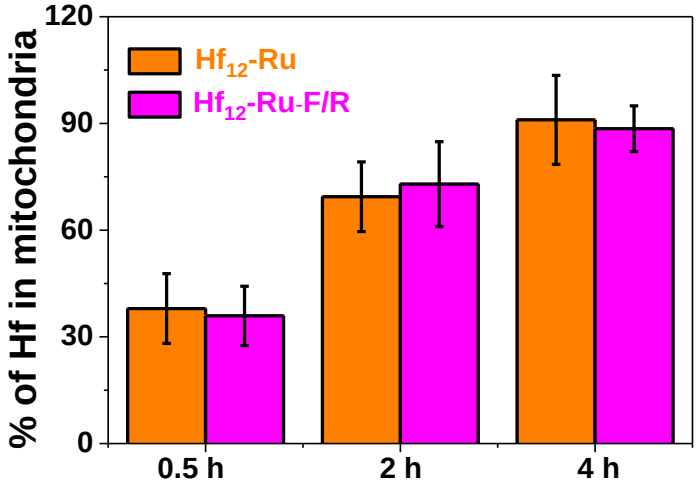

Figure 7-13. Time-dependent enrichment of Hf_{12}-Ru or Hf_{12}-Ru-F/R in mitochondria. Mitochondria were isolated from nMOL treated cells and the nMOL amounts quantified by ICP-MS. N = 3.

We then extracted mitochondria after incubating CT26 cells with Hf_{12}-Ru or Hf_{12}-Ru-F/R

and determined the percentages of internalized particles in mitochondria by ICP-MS. Both Hf_{12}-Ru and Hf_{12}-Ru-F/R were quickly enriched in mitochondria and reached saturation after 4 h incubation (**Figure 7-13**). Localization of Hf_{12}-Ru in mitochondria was also visualized by CLSM.[32] After incubating CT26 cells with Hf_{12}-Ru for 0, 0.5, 2, and 4 h, CLSM images were captured for co-localization analysis (**Figure 7-14**).

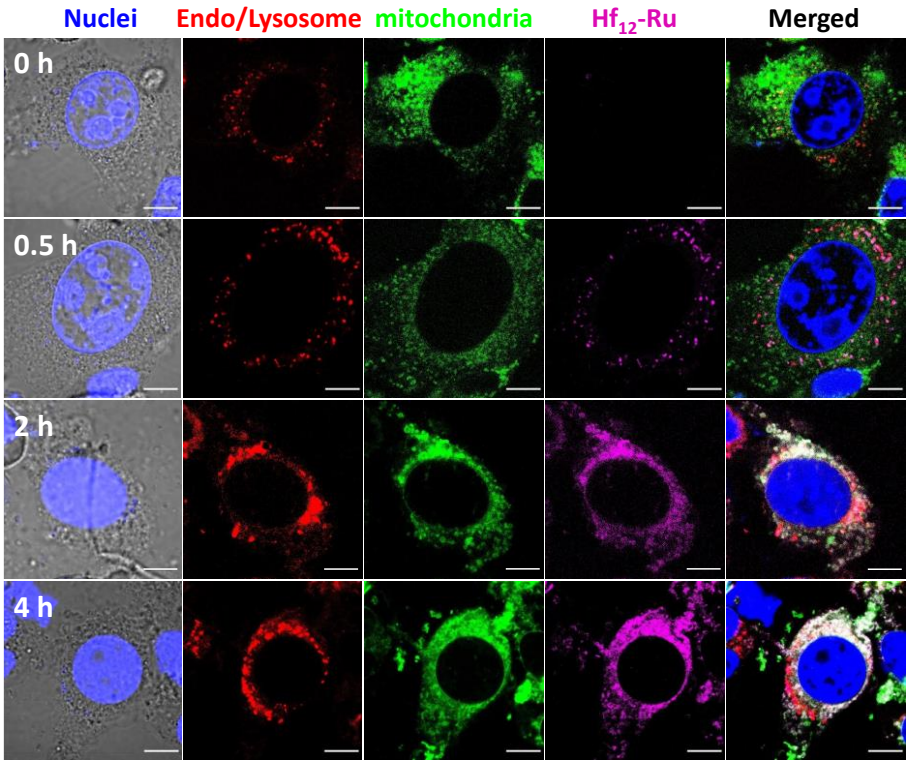

Figure 7-14. Time-dependent subcellular localization of Hf_{12}-Ru in CT26 cells. Blue, red, green and magenta colors represent DAPI-stained cell nuclei, endo/lysotracker-stained endo/lysosomes, mitotracker-stained mitochondria, and Hf_{12}-Ru, respectively. Scale bar = 5 μm.

0.5 h post incubation, enhanced magenta signals of Hf_{12}-Ru were mostly co-localized with red signals representing endo/lysosomes, indicating fast endocytosis of positively charged Hf_{12}-Ru. At the 2 h time point, the majority of Hf_{12}-Ru co-localized with mitochondria, proving its ability to effectively escape from endosomes and simultaneously enrich itself within mitochondria. At the 4 h time point, Hf_{12}-Ru accumulated in mitochondria with no co-

localization with endo/lysosomes. CLSM co-localization analysis could not be performed on Hf_{12}-Ru-F/R due to spectral overlap between RITC and Mitotracker Red as well as FITC and Lysotracker Green. These results demonstrate the mitochondria-targeting property of both Hf_{12}-Ru and Hf_{12}-Ru-F/R.

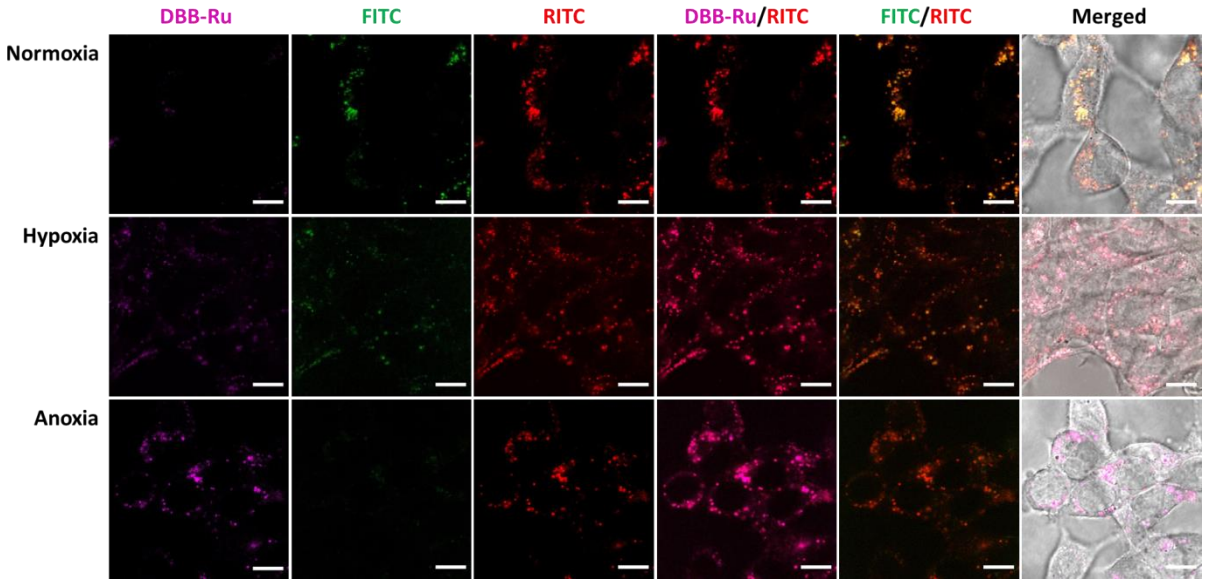

Figure 7-15. Representative low-res CLSM images. Representative low-res CLSM images showing luminescence intensities of DBB-Ru (magenta), FITC (green), and RITC (red) at different O_2 pressures as sensed by Hf_{12}-Ru-F/R. Scale bar = 10 μm.

With low background autofluorescence, CT26 cells were used to evaluate the applicability of Hf_{12}-Ru-F/R as a ratiometric sensor in live cells by CLSM. Hf_{12}-Ru-F/R at a concentration of 20 μM based on Hf was incubated with CT26 cells seeded on a 35 mm glass bottom dish for live cell imaging. After removing the supernatant and refilling with air, N_2/air mixture, and N_2 to mimic normoxic, hypoxic, and anoxic conditions, respectively, dishes were sealed tightly and scanned under a confocal microscope with different objective lens. At both low (**Figure 7-15**) and high (**Figure 7-16**) magnifications, cells under anoxic conditions presented bright magenta signal of DBB-Ru and dim green signal of FITC, consistent with low P_{O_2} and pH values. In contrast, under normoxic conditions, cells showed high FITC signals and low DBB-

Ru signals, consistent with high P_{O_2} and pH values.

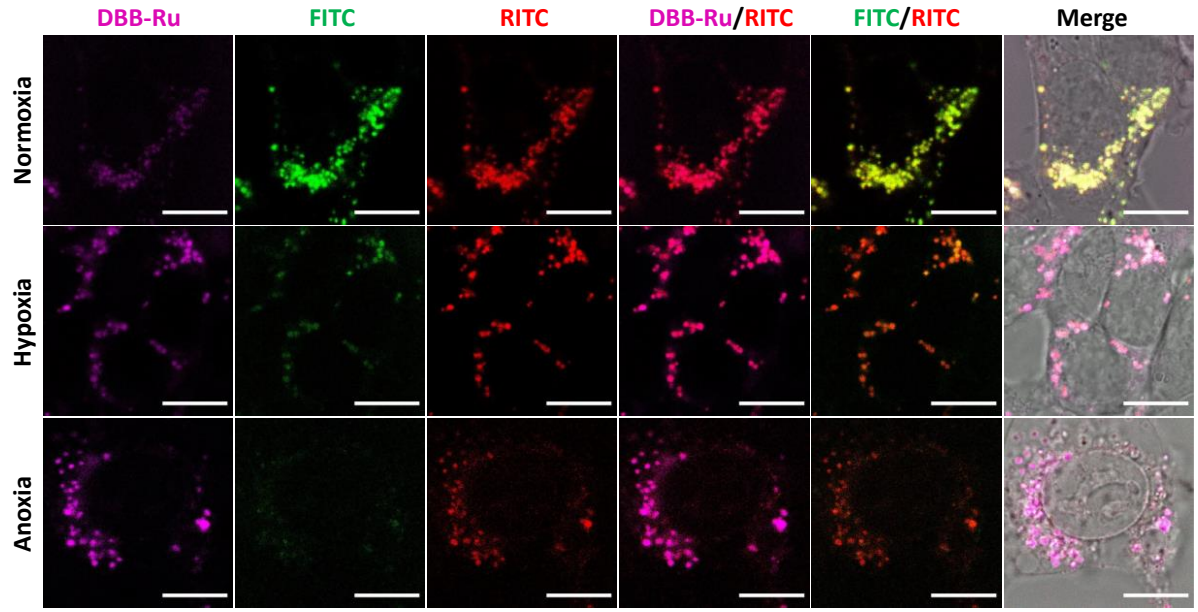

Figure 7-16. Representative high-res CLSM images. Representative high-res CLSM images showing luminescence intensities of DBB-Ru (magenta), FITC (green), and RITC (red) at different O_2 pressures as sensed by Hf_{12}-Ru-F/R. Scale bar = 10 μm.

We randomly picked regions of interest (ROIs) in each high resolution CLSM image (**Figure 7-17**) to obtain intensity readouts from ImageJ. Analysis of over 300 ROIs showed a positive correlation between pH and local O_2 concentration inside mitochondria (**Figure 7-18**). This conclusion matches the previously qualitative studies.[33, 34] Our work presents the first quantitative study to establish the correlation between pH and O_2 in mitochondria.

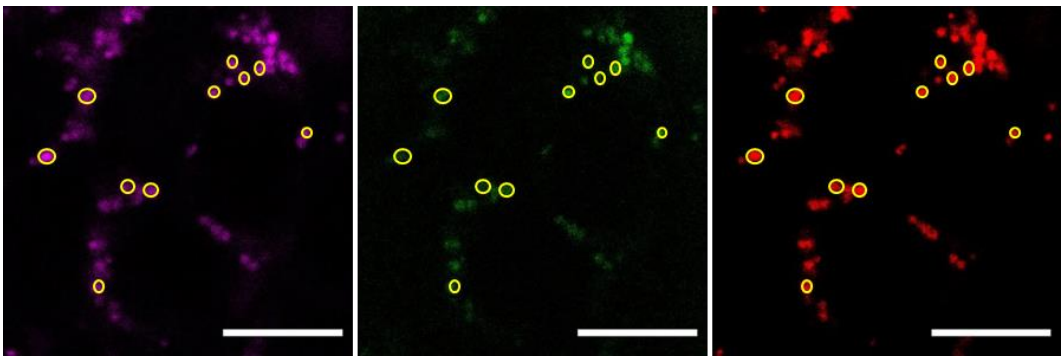

Figure 7-17. Representative case for randomly picked 10 ROIs on one set of high-res CLSM image. Scale bar = 10 μm.

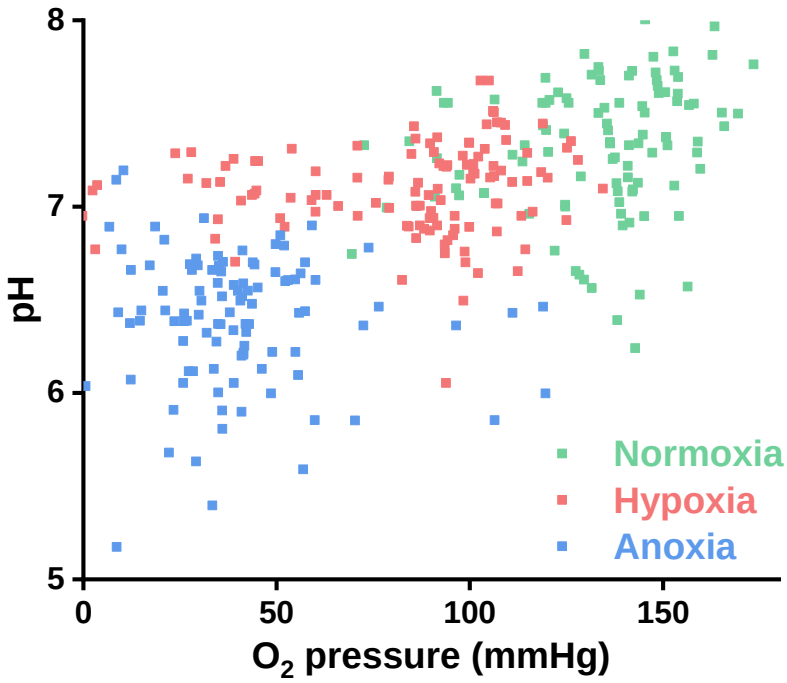

Figure 7-18. Positive correlation between pH and P_{O_2} in mitochondria as sensed by Hf_{12}-Ru-F/R. Statistical analysis gave a Pearson correlation coefficient (r) of 0.66.

7.3 Conclusion

In this work, we have demonstrated the first biological sensing using multifunctional nMOLs. Covalent conjugation of FITC and RITC on the surface of the Hf_{12}-Ru MOL afforded Hf_{12}-Ru-F/R as a mitochondria-targeted ratiometric sensor for real-time monitoring of pH and O_2 in live cells. High-resolution confocal microscope imaging using Hf_{12}-Ru-F/R as a ratiometric sensor provided the first quantitative evidence for a positive correlation between pH and local O_2 concentration in mitochondria. This study establishes the potential of nMOL-based ratiometric biosensors in sensing and imaging of biologically important analytes in order to reveal new insights into physiological processes in live cells.

7.4 Methods

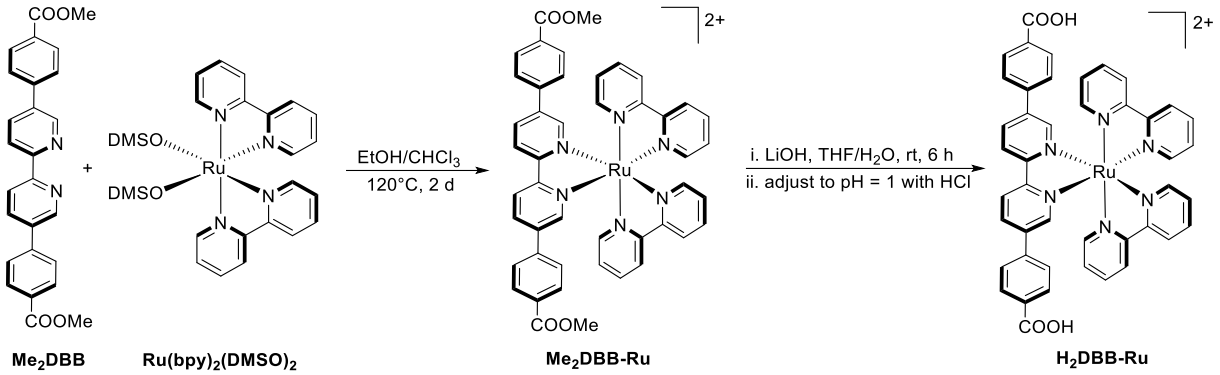

Synthesis of H_2DBB-Ru. Ru(DBB)$(bpy)_2^{2+}$ [H_2DBB-Ru, bpy = 2,2'-bipyridine, DBB = 4,4'-di(4-benzoato)-2,2'-bipyridine] was synthesized as shown above according to the literature.[35] ^{1}H NMR (500 MHz, DMSO-d_6): δ 9.05 (d, 2 H), 8.88 (d, 2 H), 8.85 (d, 2 H), 8.59 (d, 2 H), 8.23 (t, 2 H), 8.18 (t, 2 H), 8.00 (d, 4 H), 7.96 (d, 2 H), 7.85 (d, 2 H), 7.81 (s, 2 H), 7.64-7.55 (m, 8 H).

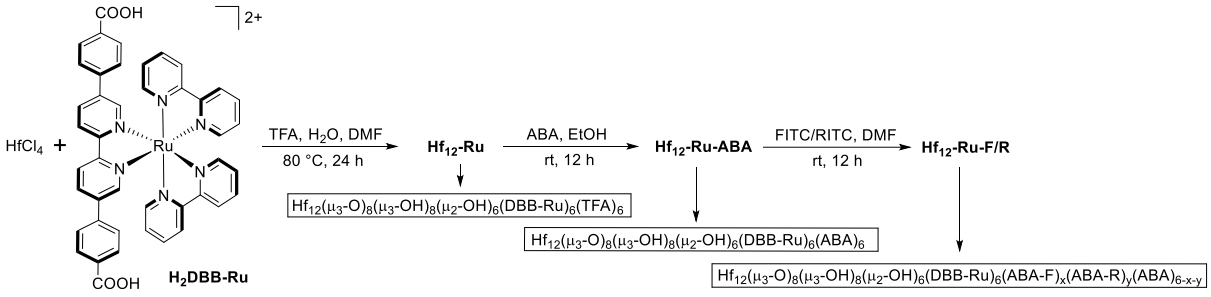

Synthesis of Hf_{12}-Ru. To a 4 mL glass vial was added 0.5 mL of $HfCl_4$ solution (2.0 mg/mL in DMF), 0.5 mL of H_2DBB-Ru solution (4.0 mg/mL in DMF), 2 μL TFA, and 5μL of water. The reaction mixture was kept in an 80 °C oven for 24 hours. The orange precipitate was collected by centrifugation and washed with DMF and ethanol. The yield was 45% based on Hf as determined by ICP-MS.

Synthesis of Hf_{12}-Ru-ABA. To a 4 mL glass vial was added 1 mL of Hf_{12}-Ru suspension (2 mM based on Hf in EtOH) and 0.5 mg of ABA. The reaction mixture was stirred overnight at

room temperature. The orange precipitate was collected by centrifugation and washed with ethanol twice. The yield was 89% based on Hf as determined by ICP-MS.

Analysis of digested Hf_{12}-Ru-ABA by ^{1}H NMR. To determine the ratio of the ABA ligands and DBB-Ru ligands in Hf_{12}-Ru-ABA, 2.0 mg of Hf_{12}-Ru-ABA was dried under vacuum and then digested in a solution of 500 μL DMSO-d_6 and 50 μL D_3PO_4. The mixture was then sonicated for 10 min, to which 50 μL D_2O was added, and analyzed by ^{1}H NMR. The ratio of ABA ligand and DBB-Ru ligand was approximately 1:1 as determined by comparing the peaks corresponding to each ligand in ^{1}H NMR, which is consistent with the formulation of $Hf_{12}(\mu_3\text{-}O)_8(\mu_3\text{-}OH)_8(\mu_2\text{-}OH)_6(DBB\text{-}Ru)_6(ABA)_6$ and indicates complete carboxylate exchange between ABA and trifluoroacetate.

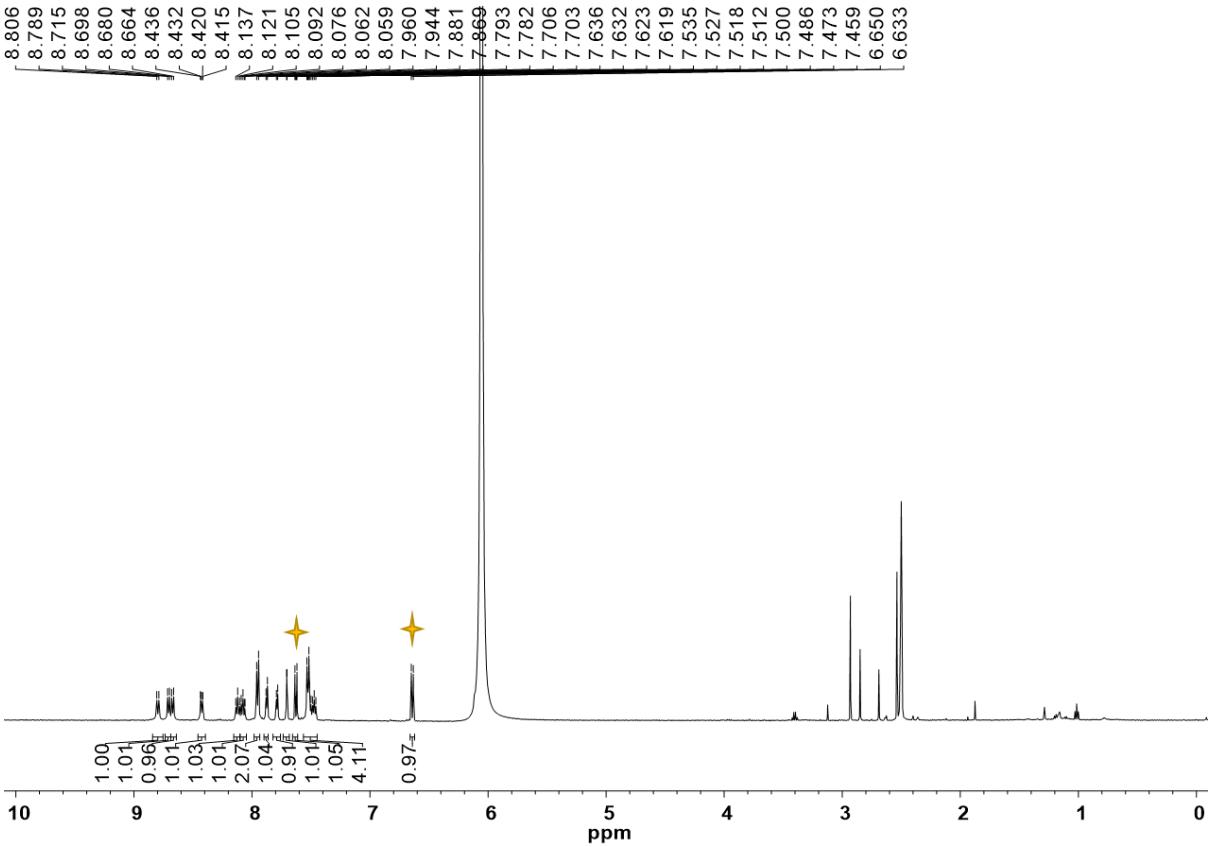

Synthesis of Hf_{12}-Ru-F/R. To a 4 mL glass vial was added 1 mL of Hf_{12}-Ru-ABA suspension (2.0 mM based on Hf and 1.0 mM based on Ru in DMF), 500 or 20 μM FITC, and 500 or 200 μM RITC. The reaction mixture was stirred at room temperature overnight. The orange precipitate was collected by centrifugation and washed with DMF and ethanol.

UV-Vis determination. When the feed concentrations of FITC and RITC were 500 μM and 500 μM, the FITC and RITC loadings were ~31.5% and ~10.1%, based on the absorbance ratio between FITC and RITC to DBB-Ru as determined by UV-Vis spectroscopy, respectively. When the concentration of DBB-Ru in Hf_{12}-Ru-F/R was 10.0 μM as determined by ICP-MS, the readout of its UV-Vis absorbance at 489 nm and 565 nm were 0.181 and 0.063, respectively.

FITC: (0.181-0.00659*10)/0.03652 = 3.15 μM, 3.15/10.0 = 31.5%

RITC: (0.063-0.00135*10)/0.04923 = 1.01 μM, 1.01/10.0 = 10.1%

Luminescence determination. When the feed concentrations of FITC and RITC were 20 μM and 200 μM, the FITC and RITC loadings were ~1.1% and ~5.6%, based on the ratio between FITC and RITC to DBB-Ru as determined by luminescence intensity, respectively. When the concentration of DBB-Ru in Hf_{12}-Ru-F/R was 10.0 μM as determined by ICP-MS, the readouts of fluorescence signals at 514 nm and 576 nm were 19.37 and 20.46, respectively.

FITC: 19.37/175.9 = 0.11 μM, 0.11/10.0 = 1.1%

RITC: 20.46/36.5 = 0.56 μM, 0.56/10.0 = 5.6%

HRMS analysis of digested Hf_{12}-Ru-F/R. To demonstrate covalent modification of FITC and RITC through thiourea linkage in Hf_{12}-Ru-F/R, 0.1 mg of Hf_{12}-Ru-F/R (FITC: 31.5%, RITC: 10.1%) was dried under vacuum and then digested in a solution of 500 μL DMSO and 50 μL D_3PO_4. The mixture was then sonicated for 10 min and analyzed by HRMS.

Fitting equation for pH as measured by FITC. HA and A were used herein to refer to mono- and di-anionic forms of FITC, respectively.[36] The concentration of each species is:

$$[HA] = c_{\mathrm{F}} \frac{[H^+]}{[H^+] + K}$$
$$[A^-] = c_{\mathrm{F}} \frac{K}{[H^+] + K}$$

Where c_{F} is the total concentration of FITC, and K is the dissociation constant of the aforementioned step.

The luminescence intensity (I_{f}) is linearly correlated to FITC species concentrations:

$$I_f = I_0 \phi_f \varepsilon l c = kc$$

where I_0, ϕ_{f}, ε, l, and c are incident light intensity, quantum yield, extinction coefficient, path length, and the FITC species concentrations, respectively.

The luminescence intensity of FITC is:

$$I_{\mathrm{F}} = k_1[HA] + k_2[A^-] = k_1 c_{\mathrm{F}} \frac{[H^+]}{[H^+] + K} + k_2 c_{\mathrm{F}} \frac{K}{[H^+] + K} = c_{\mathrm{F}} \frac{k_1[H^+] + k_2 K}{[H^+] + K}$$

Therefore, the luminescence intensity of FITC against proton activity fits a rational function in a form of:

$$I_{\mathrm{F}} = \frac{\mathrm{A}_1[H^+] + \mathrm{B}_1}{[H^+] + \mathrm{C}_1} \ (Eq.\ 7-1)$$
$$= \frac{\mathrm{A}_1 e^{-2.303pH} + \mathrm{B}_1}{e^{-2.303pH} + \mathrm{C}_1} \ (Eq.\ 7-2)$$

where

$$\mathrm{A}_1 = c_{\mathrm{F}} k_1$$

$$\mathrm{B}_1 = c_{\mathrm{F}} k_2 K$$

$$\mathrm{C}_1 = K$$

Based on this hypothesis, we fitted the FITC luminescence intensity with different pH values, which gave the following results:

(1) For 0.11 μM free FITC solution measured by fluorimeter:

$$I_{\mathrm{F}} = \frac{1.00[H^+] + 3.91 \times 10^{-6}}{[H^+] + 2.88 \times 10^{-7}} = \frac{1.00e^{-2.303pH} + 3.91 \times 10^{-6}}{e^{-2.303pH} + 2.88 \times 10^{-7}}$$

(2) For 0.11 μM FITC on Hf_{12}-Ru-F/R suspension measured by fluorimeter:

$$I_{\mathrm{F}} = \frac{0.88[H^+] + 3.70 \times 10^{-6}}{[H^+] + 3.03 \times 10^{-7}} = \frac{0.88e^{-2.303pH} + 3.70 \times 10^{-6}}{e^{-2.303pH} + 3.03 \times 10^{-7}}$$

The luminescence intensity of RITC (I_{R}) is linearly correlated to RITC concentrations:

$$I_{\mathrm{R}} = k_3 c_{\mathrm{R}}$$

Where c_{R} is the total concentration of RITC

The luminescence intensity ratio between FITC and RITC is:

$$r_{\mathrm{F/R}} = \frac{I_{\mathrm{F}}}{I_{\mathrm{R}}} = \frac{c_{\mathrm{F}}}{k_3 c_{\mathrm{R}}} \frac{k_1[H^+] + k_2 K}{[H^+] + K}$$

Therefore, the luminescence intensity ratio between FITC and RITC against proton activity fits a rational function of the form:

$$r = \frac{\mathrm{A}_2[H^+] + \mathrm{B}_2}{[H^+] + \mathrm{C}_2} \ (\mathrm{Eq.}\,7-3) = \frac{\mathrm{A}_2 e^{-2.303pH} + \mathrm{B}_2}{e^{-2.303pH} + \mathrm{C}_2} \ (\mathrm{Eq.}\,7-4)$$

where

$$\mathrm{A}_2 = \frac{c_{\mathrm{F}} k_1}{k_3 c_{\mathrm{R}}}$$

$$\mathrm{B}_2 = \frac{c_{\mathrm{F}} k_2 K}{k_3 c_{\mathrm{R}}}$$

$$\mathrm{C}_2 = K$$

Based on this hypothesis, we fitted the luminescence intensity ratio between FITC and RITC at different pH values, which gave the following results:

(3) For 0.11 μM FITC and 0.56 μM RITC in Hf_{12}-Ru-F/R suspension measured by

Xenogen IVIS 200 imaging:

$$r_{\mathrm{F/R}} = \frac{0.119[H^+] + 3.91 \times 10^{-7}}{[H^+] + 3.28 \times 10^{-7}} = \frac{0.119e^{-2.303pH} + 3.91 \times 10^{-7}}{e^{-2.303pH} + 3.28 \times 10^{-7}}$$

Fitting equation for O_2 as measured by DBB-Ru. The luminescence quenching of DBB-Ru (in both H_2DBB-Ru and Hf_{12}-Ru-F/R) was fitted to the Stern-Völmer equation:

$$\frac{I_0}{I_{\mathrm{Ru}}} = 1 + K_{\mathrm{SV}} P_{\mathrm{O_2}} \ (\mathrm{Eq.}\ 7-5)$$

where I_0, I_{Ru}, P_{O2} and K_{SV} are the luminescence intensity of DBB-Ru in the absence of O_2, the luminescence intensity of DBB-Ru in the presence of O_2, the O_2 pressure, and the Stern-Völmer constant, respectively.

Therefore, the luminescence intensity of DBB-Ru against O_2 pressure fits a rational function in a form of:

$$I_{\mathrm{Ru}} = \frac{I_0}{1 + K_{\mathrm{SV}} P_{\mathrm{O_2}}} = \frac{\mathrm{A_3}}{1 + \mathrm{B_3} P_{\mathrm{O_2}}} \ (\mathrm{Eq.}\ 7-6)$$

where

$$\mathrm{A_3} = I_0$$

$$\mathrm{B_3} = K_{\mathrm{SV}}$$

Based on this hypothesis, we fitted the DBB-Ru luminescence intensity ratio under different O_2 pressures, which gave the following results:

(4) For 10.0 μM free H_2DBB-Ru solution measured by fluorimeter:

$$\frac{I_0}{I_{\mathrm{Ru}}} = 1 + 0.00285 P_{\mathrm{O_2}}$$

$$I_{\mathrm{Ru}} = \frac{17.760}{1 + 0.00285 P_{\mathrm{O_2}}}$$

(5) For 10.0 μM Hf_{12}-Ru-F/R suspension measured by fluorimeter:

$$\frac{I_0}{I_{\mathrm{Ru}}} = 1 + 0.00285 P_{\mathrm{O_2}}$$

$$I_{\mathrm{Ru}} = \frac{16.767}{1 + 0.00253P_{\mathrm{O_2}}}$$

The luminescence intensity ratio between DBB-Ru and RITC in Hf_{12}-Ru-F/R was also fitted to the Stern-Völmer equation:

$$\frac{(r_{Ru/R})_0}{r_{Ru/R}} = 1 + K_{\mathrm{SV}}P_{\mathrm{O_2}} \ (\mathrm{Eq.}\ 7-7)$$

where $(r_{Ru/R})_0$ and $r_{Ru/R}$ are the luminescence intensity ratios between DBB-Ru and RITC in the absence and presence of O_2, respectively.

Therefore, the luminescence intensity ratio between DBB-Ru and RITC against O_2 pressure fits a rational function of the form:

$$r_{\mathrm{Ru/R}} = \frac{I_{\mathrm{Ru}}}{I_{\mathrm{R}}} = \frac{I_0}{k_3 c_{\mathrm{R}}(1 + K_{\mathrm{SV}}P_{\mathrm{O_2}})} = \frac{\mathrm{A_4}}{1 + \mathrm{B_4}P_{\mathrm{O_2}}} \ (\mathrm{Eq.}\ 7-8)$$

$$\mathrm{A_4} = \frac{I_0}{k_3 c_{\mathrm{R}}}$$

$$\mathrm{B_4} = K_{\mathrm{SV}}$$

Based on this hypothesis, we fitted the luminescence intensity ratio between DBB-Ru and RITC at different O_2 partial pressures, which gave the following results:

(6) For 10.0 μM DBB-Ru and 0.56 μM RITC in Hf_{12}-Ru-F/R suspension measured by Xenogen IVIS 200 imaging:

$$\frac{(r_{Ru/R})_0}{r_{Ru/R}} = 1 + 0.00237P_{\mathrm{O_2}}$$

$$r_{Ru/R} = \frac{1.613}{1 + 0.00237P_{\mathrm{O_2}}}$$

pH adjustment. To a 0.6 mM PBS was added 1M NaOH or HCl to adjust the pH to 4.0-8.0. The pH value of these PBS was determined ot be 4.01, 4.45, 4.99, 5.57, 5.94, 6.46, 7.04, 7.49, and 8.00, respectively, by an accumet AB150 pH meter.

O_2 pressure adjustment. Into a glove box was blown the mixture of N_2 and Air with the Air

percentages of 0, 20%, 40%, 60%, 80%, and 100% to afford the O_2 pressure of ~0, ~32, ~64, ~96, ~128, and ~160 mmHg, respectively. The exact O_2 pressure at each condition was measured by a commercial oxygen sensor (YSI ProODO 626279).

Luminescence spectra and quantification. The luminescence spectra of DBB-Ru, FITC, and RITC at different pH and O_2 pressure were measured by an RF-5301PC fluorimeter (Shimadzu, Japan) at spectrum mode with excitation wavelength at 430 nm, 465 nm, and 535 nm, respectively. The intensity quantification of DBB-Ru, FITC, and RITC at different pH and O_2 pressure was measured at quantitative mode and each quantitative measurement was repeated three times.

Standard curves as determined by Xenogen IVIS 200 imaging Hf_{12}-Ru-F/R suspension (DBB-Ru = 10.0 μM, FITC = 0.11 μM, and RITC = 0.56 μM) in PBS with different pH (4.01, 4.45, 4.99, 5.57, 5.94, 6.46, 7.04, 7.49, and 8.00) was added to a 96-well plate with 6 wells for each pH point and 100 μL of Hf_{12}-Ru-F/R suspension for each well. These 96-well plates were then incubated in a glove box under different O_2 pressure (0, 34.1, 63.5, 95.8, 124.2, and 160.0 mmHg). The luminescence signals of DBB-Ru, FITC, and RITC were collected with a Xenogen IVIS 200 imaging system.

Cellular uptake of Hf_{12}-Ru and Hf_{12}-Ru-F/R. The cellular uptakes of Hf_{12}-Ru and Hf_{12}-Ru-F/R were evaluated on CT26 cells. Cells were seeded on 6-well plates at 1.5×10^6/well and further cultured overnight. Particles were added to the cells at a Hf concentration of 20 μM. After incubation of 0.5, 2 and 4 hours, the cells were collected, and the cell numbers were counted by a hemocytometer. Cells were digested with 1% hydrofluoric acid and concentrated nitric acid in a microwave reactor (CEM, USA) and the Hf concentrations were determined by

ICP-MS. Results were expressed as the amount of Hf (ng) per 10^5 cells.

Colocalization of Hf_{12}-Ru with MitoTracker. Mitochondria-targeting property of Hf_{12}-Ru-F/R (Hf_{12}-Ru) was evaluated on CT26 cells. Cells were seeded on 35 mm glass bottom dishes (MatTek, USA) at 5×10^5/well and further cultured overnight. Particles were added to the cells at a Hf concentration of 20 μM. MitoTracker™ green was pre-loaded with a dilution of 1:2000 10 mins before the stop of particle incubation. 0.5, 2 and 4 hours post incubation, supernatant was removed and the dishes were transferred and cultured in hypoxic chamber for 30 mins. The samples were then rinsed with 1 mL PBS three times gently for directly scanning under SP8 LIGHTENING confocal microscope. Cells without particle incubation were used as control of incubation for 0 h. To quantitatively analyze the mitochondria targeting property, extraction of mitochondria was conducted according to a previously reported protocol.[32] CT26 cells were washed twice in mitochondrial extraction buffer containing mannitol (200 mM), sucrose (70 mM), HEPES (10 mM), and EDTA (1.0 mM) at pH 7.2 and 4 °C and then re-suspended for homogenization. The homogenate was spun for 10 min at 600 g to recover the supernatant. The supernatant was further spun for 10 min at 11,000 g to recover the mitochondrial fraction for ICP-MS quantification.

In Vitro pH and O_2 sensing with Hf_{12}-Ru-F/R. CT26 cells were seeded on 35 mm glass bottom dishes (MatTek, USA) at 5×10^5/well and further cultured overnight. Particles were added to the cells at a Hf concentration of 20 μM. After incubation for 4 h, the supernatant was removed and the dishes were transferred and cultured under normoxic, hypoxic or anoxic conditions for 30 mins. The normoxic, hypoxic or anoxic conditions were achieved in glove box with the flowing of a mixture of N_2 and Air. The samples were then rinsed with 1 mL PBS

three times gently for directly scanning under SP8 LIGHTENING confocal microscope (Leica, Germany). Representative low-res and high-res CLSM images were harvested with 200× magnification or 400×magnification, respectively. Data to study the relation between pH and O_2 were read from high-res CLSM images. 10 ROIs were randomly chosen from each figure and over 100 ROIs were analyzed for each condition. The imaging studies under normoxic condition were repeated to confirm the reproducibility.

7.5 References

1. Casey, J. R.; Grinstein, S.; Orlowski, J., Sensors and regulators of intracellular pH. *Nat. Rev. Mol. Cell Biol.* **2010,** *11* (1), 50-61.
2. Webb, B. A.; Chimenti, M.; Jacobson, M. P.; Barber, D. L., Dysregulated pH: a perfect storm for cancer progression. *Nat. Rev. Cancer* **2011,** *11* (9), 671-677.
3. Harris, A. L., Hypoxia — a key regulatory factor in tumour growth. *Nat. Rev. Cancer* **2002,** *2*, 38.
4. Yu, M.; Xu, J.; Zheng, J., Renal Clearable Luminescent Gold Nanoparticles: From the Bench to the Clinic. *Angew. Chem.* **2019,** *131* (13), 4156-4172.
5. Clark, H. A.; Hoyer, M.; Philbert, M. A.; Kopelman, R., Optical Nanosensors for Chemical Analysis inside Single Living Cells. 1. Fabrication, Characterization, and Methods for Intracellular Delivery of PEBBLE Sensors. *Anal. Chem.* **1999,** *71* (21), 4831-4836.
6. Benjaminsen, R. V.; Sun, H.; Henriksen, J. R.; Christensen, N. M.; Almdal, K.; Andresen, T. L., Evaluating Nanoparticle Sensor Design for Intracellular pH Measurements. *ACS Nano* **2011,** *5* (7), 5864-5873.
7. Cooper, M. A., Optical biosensors in drug discovery. *Nat. Rev. Drug Discovery* **2002,** *1* (7), 515-528.
8. Chung, C. Y.-S.; Posimo, J. M.; Lee, S.; Tsang, T.; Davis, J. M.; Brady, D. C.; Chang, C. J., Activity-based ratiometric FRET probe reveals oncogene-driven changes in labile copper pools induced by altered glutathione metabolism. *Proceedings of the National Academy of Sciences* **2019,** *116* (37), 18285.
9. Buck, S. M.; Xu, H.; Brasuel, M.; Philbert, M. A.; Kopelman, R., Nanoscale probes encapsulated by biologically localized embedding (PEBBLEs) for ion sensing and imaging in live cells. *Talanta* **2004,** *63* (1), 41-59.
10. Koo, Y.-E. L.; Cao, Y.; Kopelman, R.; Koo, S. M.; Brasuel, M.; Philbert, M. A., Real-Time Measurements of Dissolved Oxygen Inside Live Cells by Organically Modified Silicate Fluorescent Nanosensors. *Anal. Chem.* **2004,** *76* (9), 2498-2505.
11. Wu, C.; Bull, B.; Christensen, K.; McNeill, J., Ratiometric Single-Nanoparticle Oxygen Sensors for Biological Imaging. *Angew. Chem. Int. Ed.* **2009,** *48* (15), 2741-2745.
12. Zhao, Q.; Zhou, X.; Cao, T.; Zhang, K. Y.; Yang, L.; Liu, S.; Liang, H.; Yang, H.; Li, F.; Huang, W., Fluorescent/phosphorescent dual-emissive conjugated polymer dots

for hypoxia bioimaging. *Chemical Science* **2015,** *6* (3), 1825-1831.
13. Chojnacki, P.; Mistlberger, G.; Klimant, I., Separable Magnetic Sensors for the Optical Determination of Oxygen. *Angew. Chem. Int. Ed.* **2007,** *46* (46), 8850-8853.
14. Chen, S.; Hong, Y.; Liu, Y.; Liu, J.; Leung, C. W. T.; Li, M.; Kwok, R. T. K.; Zhao, E.; Lam, J. W. Y.; Yu, Y.; Tang, B. Z., Full-Range Intracellular pH Sensing by an Aggregation-Induced Emission-Active Two-Channel Ratiometric Fluorogen. *J. Am. Chem. Soc.* **2013,** *135* (13), 4926-4929.
15. Medintz, I. L.; Stewart, M. H.; Trammell, S. A.; Susumu, K.; Delehanty, J. B.; Mei, B. C.; Melinger, J. S.; Blanco-Canosa, J. B.; Dawson, P. E.; Mattoussi, H., Quantum-dot/dopamine bioconjugates function as redox coupled assemblies for in vitro and intracellular pH sensing. *Nat. Mater.* **2010,** *9* (8), 676-684.
16. Furukawa, H.; Cordova, K. E.; O'Keeffe, M.; Yaghi, O. M., The Chemistry and Applications of Metal-Organic Frameworks. *Science* **2013,** *341* (6149), 1230444.
17. Kreno, L. E.; Leong, K.; Farha, O. K.; Allendorf, M.; Van Duyne, R. P.; Hupp, J. T., Metal–Organic Framework Materials as Chemical Sensors. *Chem. Rev.* **2012,** *112* (2), 1105-1125.
18. Hu, Z.; Deibert, B. J.; Li, J., Luminescent metal–organic frameworks for chemical sensing and explosive detection. *Chem. Soc. Rev.* **2014,** *43* (16), 5815-5840.
19. Cui, Y.; Yue, Y.; Qian, G.; Chen, B., Luminescent Functional Metal–Organic Frameworks. *Chem. Rev.* **2012,** *112* (2), 1126-1162.
20. Wu, P.; Wang, J.; He, C.; Zhang, X.; Wang, Y.; Liu, T.; Duan, C., Luminescent Metal-Organic Frameworks for Selectively Sensing Nitric Oxide in an Aqueous Solution and in Living Cells. *Adv. Funct. Mater.* **2012,** *22* (8), 1698-1703.
21. Foucault-Collet, A.; Gogick, K. A.; White, K. A.; Villette, S.; Pallier, A.; Collet, G.; Kieda, C.; Li, T.; Geib, S. J.; Rosi, N. L.; Petoud, S., Lanthanide near infrared imaging in living cells with Yb³⁺ nano metal organic frameworks. *Proceedings of the National Academy of Sciences* **2013,** *110* (43), 17199.
22. Rabone, J.; Yue, Y. F.; Chong, S. Y.; Stylianou, K. C.; Bacsa, J.; Bradshaw, D.; Darling, G. R.; Berry, N. G.; Khimyak, Y. Z.; Ganin, A. Y.; Wiper, P.; Claridge, J. B.; Rosseinsky, M. J., An Adaptable Peptide-Based Porous Material. *Science* **2010,** *329* (5995), 1053.
23. Morris, W.; Briley, W. E.; Auyeung, E.; Cabezas, M. D.; Mirkin, C. A., Nucleic Acid–Metal Organic Framework (MOF) Nanoparticle Conjugates. *J. Am. Chem. Soc.* **2014,** *136* (20), 7261-7264.
24. Levine, D. J.; Runčevski, T.; Kapelewski, M. T.; Keitz, B. K.; Oktawiec, J.; Reed, D. A.; Mason, J. A.; Jiang, H. Z. H.; Colwell, K. A.; Legendre, C. M.; FitzGerald, S. A.; Long, J. R., Olsalazine-Based Metal–Organic Frameworks as Biocompatible Platforms for H2 Adsorption and Drug Delivery. *J. Am. Chem. Soc.* **2016,** *138* (32), 10143-10150.
25. Zeng, J.-Y.; Zou, M.-Z.; Zhang, M.; Wang, X.-S.; Zeng, X.; Cong, H.; Zhang, X.-Z., π-Extended Benzoporphyrin-Based Metal–Organic Framework for Inhibition of Tumor Metastasis. *ACS Nano* **2018,** *12* (5), 4630-4640.
26. Zheng, X.; Wang, L.; Pei, Q.; He, S.; Liu, S.; Xie, Z., Metal–Organic Framework@Porous Organic Polymer Nanocomposite for Photodynamic Therapy. *Chem. Mater.* **2017,** *29* (5), 2374-2381.

27. Park, J.; Jiang, Q.; Feng, D.; Mao, L.; Zhou, H.-C., Size-Controlled Synthesis of Porphyrinic Metal–Organic Framework and Functionalization for Targeted Photodynamic Therapy. *J. Am. Chem. Soc.* **2016,** *138* (10), 3518-3525.
28. Lan, G.; Ni, K.; Lin, W., Nanoscale metal–organic frameworks for phototherapy of cancer. *Coord. Chem. Rev.* **2019,** *379*, 65-81.
29. Xu, R.; Wang, Y.; Duan, X.; Lu, K.; Micheroni, D.; Hu, A.; Lin, W., Nanoscale Metal–Organic Frameworks for Ratiometric Oxygen Sensing in Live Cells. *J. Am. Chem. Soc.* **2016,** *138* (7), 2158-2161.
30. He, C.; Lu, K.; Lin, W., Nanoscale Metal–Organic Frameworks for Real-Time Intracellular pH Sensing in Live Cells. *J. Am. Chem. Soc.* **2014,** *136* (35), 12253-12256.
31. Lan, G.; Ni, K.; Veroneau, S. S.; Song, Y.; Lin, W., Nanoscale Metal–Organic Layers for Radiotherapy–Radiodynamic Therapy. *J. Am. Chem. Soc.* **2018,** *140* (49), 16971-16975.
32. Ni, K.; Lan, G.; Veroneau, S. S.; Duan, X.; Song, Y.; Lin, W., Nanoscale metal-organic frameworks for mitochondria-targeted radiotherapy-radiodynamic therapy. *Nat. Commun.* **2018,** *9* (1), 4321.
33. Chacon, E.; Reece, J. M.; Nieminen, A. L.; Zahrebelski, G.; Herman, B.; Lemasters, J. J., Distribution of electrical potential, pH, free Ca2+, and volume inside cultured adult rabbit cardiac myocytes during chemical hypoxia: a multiparameter digitized confocal microscopic study. *Biophys. J.* **1994,** *66* (4), 942-952.
34. Solaini, G.; Baracca, A.; Lenaz, G.; Sgarbi, G., Hypoxia and mitochondrial oxidative metabolism. *Biochimica et Biophysica Acta (BBA) - Bioenergetics* **2010,** *1797* (6), 1171-1177.
35. Zhang, Z.-M.; Zhang, T.; Wang, C.; Lin, Z.; Long, L.-S.; Lin, W., Photosensitizing Metal–Organic Framework Enabling Visible-Light-Driven Proton Reduction by a Wells–Dawson-Type Polyoxometalate. *J. Am. Chem. Soc.* **2015,** *137* (9), 3197-3200.
36. Martin, M. M.; Lindqvist, L., The pH dependence of fluorescein fluorescence. *J. Lumin.* **1975,** *10* (6), 381-390.

Chapter 8. Electron Injection from Photoexcited MOF Ligands to Ru_2 Secondary Building Units for Visible-Light-Driven Hydrogen Evolution

8.1 Introduction

Because photo-driven water splitting is recognized as a pathway to convert solar energy into chemical energy,[1-4] MOFs have been examined for photocatalytic HER via hierarchical assembly of PSs and catalytic centers.[5-9] Photo-excited or photo-reduced PSs in MOFs can efficiently inject multi-electrons to adjacent catalytic centers to enable HER. For instance, by loading Pt NPs or POMs as HER catalysts into the cavities of photosensitizing MOFs, Lin and coworkers observed facile electron injection from photosensitizing frameworks to Pt NPs or POMs for photocatalytic HER.[5-7] Direct incorporation of HER catalysts in the SBUs of photosensitizing MOFs should provide an even more efficient system, but, due to the kinetic inertness of catalytically relevant precious metals such as Ru, Pd, Ph, Pt, and Ir, their incorporation as SBUs into photosensitizing MOFs has not been achieved. In this Chapter, we report the design of two novel MOFs, Ru-TBP and Ru-TBP-Zn, built from Ru_2 paddlewheel SBUs and porphyrin-derived tetracarboxylate ligands for efficient visible-light-driven HER (**Figure 8-1**). Upon visible-light ($\lambda > 400$ nm) irradiation, the excited porphyrin ligands inject electrons into adjacent Ru_2 SBUs to produce hydrogen from water.

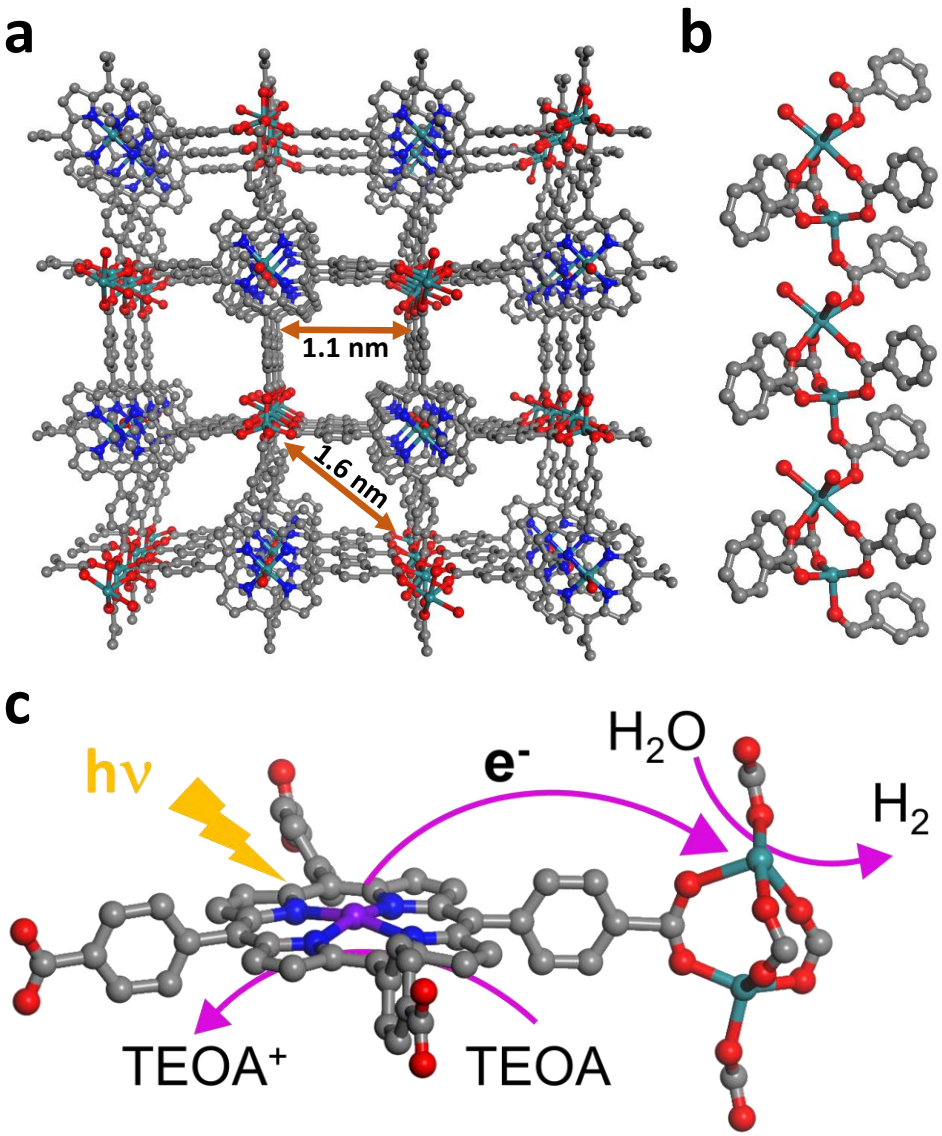

Figure 8-1. Schematic showing the HER catalyzed by Ru-TBP. (a) Perspective view of Ru-TBP crystal structure down the (100) direction. The distance between adjacent porphyrin centers and Ru_2 SBUs is ~1.1 nm, whereas the distance between adjacent Ru_2 SBUs is ~1.6 nm. (b) Coordination environment of Ru_2 paddlewheel SBUs. (c) Schematic showing visible-light-driven HER catalyzed by Ru-TBP or Ru-TBP-Zn. Photoexicted porphyrin ligands inject electrons to adjacent Ru_2 SBUs to reduce protons to hydrogen. The oxidized porphyrin ligands are then reduced by sacrificial TEOA to regenerate the photocatalytic system.

8.2 Result and discussion

8.2.1 Synthesis and characterization

Plate-shaped single crystals of Ru-TBP were synthesized through a solvothermal reaction between $RuCl_3 \cdot xH_2O$ and H_4TBP in DMF with acetic acid as the modulator at 120 °C. X-ray

single crystal diffraction studies revealed the coordination of Ru^{III} ions to the nitrogen atoms of TBP during the MOF synthesis, with a DMF molecule occupying the axial positions. The metalated TBP ligands are linked by Ru_2 paddlewheel SBUs to form a 3D framework of **sql** topology (**Figure 8-1a**). The two Ru^{III} centers in each Ru_2 SBUs are bridged by three benzoate groups whereas adjacent Ru_2 SBUs are linked by one benzoate group to form a 1D chain (**Figure 8-1b**). In each Ru_2 SBU, one Ru^{III} is tetrahedrally coordinated to four carboxylate oxygen atoms and the other Ru^{III} is octahedrally coordinated to four carboxylate oxygen atoms and two water molecules. Ru-TBP thus has a framework formula of $[Ru_2(TBP\text{-}Ru\text{-}DMF)(H_2O)_2]^{2+}$ based on the crystal structure.

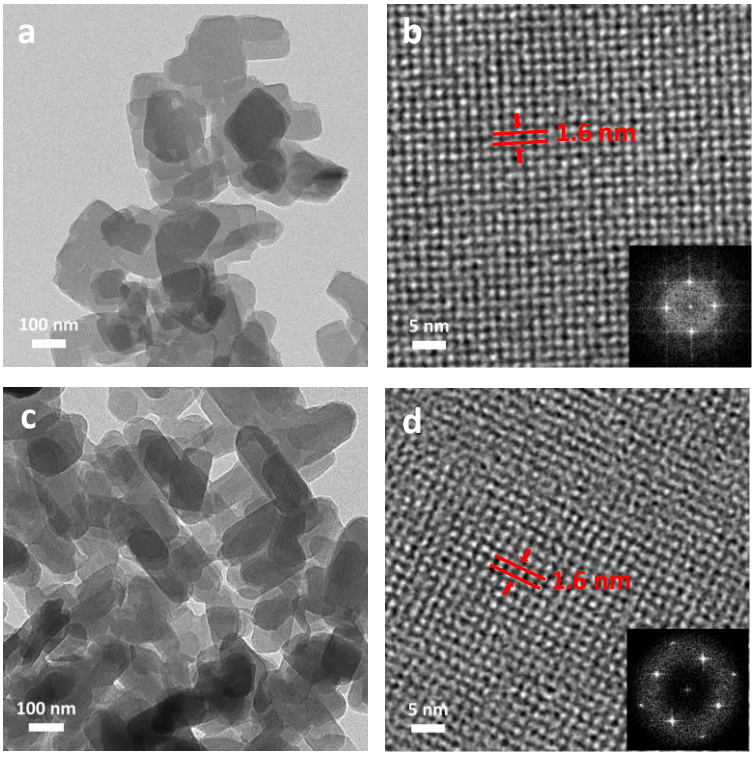

Figure 8-2. Morphological structures of Ru-TBP and Ru-TBP-Zn. TEM image (a) and HRTEM image and FFT pattern (inset) (b) of Ru-TBP. TEM image (c) and HRTEM image and FFT pattern (inset) (d) of Ru-TBP-Zn.

By decreasing the concentration of acetic acid modulator, we optimized the synthesis of Ru-TBP to produce nanoplates of ~500 nm in diameter as shown by TEM (**Figure 8-2a**).

HRTEM image of Ru-TBP nanoplates showed lattice points corresponding to Ru_2 SBUs with the FFT revealing a four-fold symmetry (**Figure 8-2b**), which is consistent with the projection of Ru-TBP crystal structure in the (100) direction. The distance between two adjacent lattice points in the HRTEM image was measured to be 1.6 nm, matching the distance between two adjacent Ru_2 SBUs.

The analogous MOF with Zn^{II}-metalated TBP ligands, Ru-TBP-Zn, was similarly synthesized from $RuCl_3 \cdot xH_2O$ and H_4TBP-Zn and exhibited similar size and morphology to Ru-TBP (**Figure 8-2c**). Ru-TBP-Zn is isostructural to Ru-TBP as demonstrated by HRTEM imaging (**Figure 8-2d**) and PXRD studies (**Figure 8-3a**). The porous structures of Ru-TBP and Ru-TBP-Zn were confirmed by type I nitrogen adsorption isotherms at 77 K (**Figure 8-3b**) with BET surface areas of 441 m^2/g and 422 m^2/g, respectively. These BET surface areas are similar to those reported for MOFs constructed from Cu_2 or Zn_2 paddlewheels and TBP ligands.[10, 11]

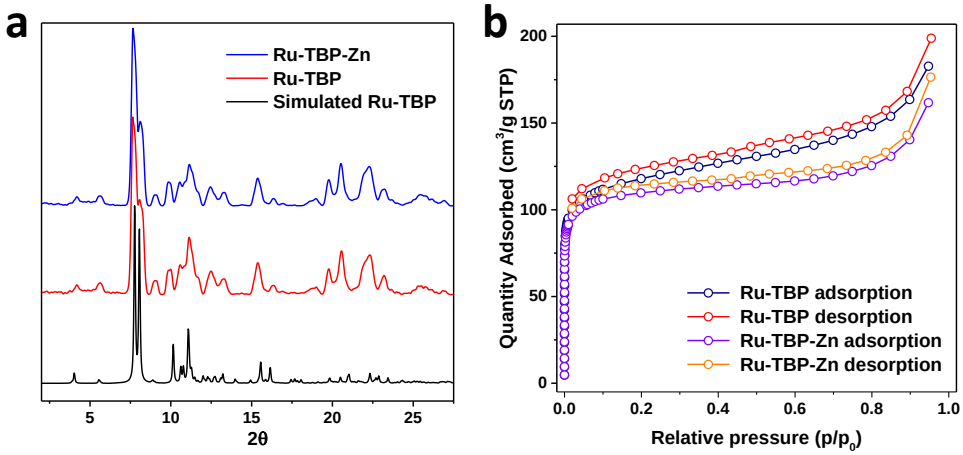

Figure 8-3. Topological structures of Ru-TBP and Ru-TBP-Zn. PXRD patterns (a) and nitrogen sorption isotherms (b) of Ru-TBP and Ru-TBP-Zn.

The Ru oxidation states in Ru-TBP and Ru-TBP-Zn were studied by XPS. The Ru $3p_{3/2}$ peak of Ru-TBP and Ru-TBP-Zn exhibited binding energies of 462.7 eV and 462.6 eV (**Figure**

8-4a), respectively, indicating the Ru^{III} oxidation state.[12] Additionally, XANES spectra of Ru-TBP and Ru-TBP-Zn showed a similar energy edge to $RuCl_3$, confirming the Ru^{III} centers in the MOFs (**Figure 8-4c,d**).

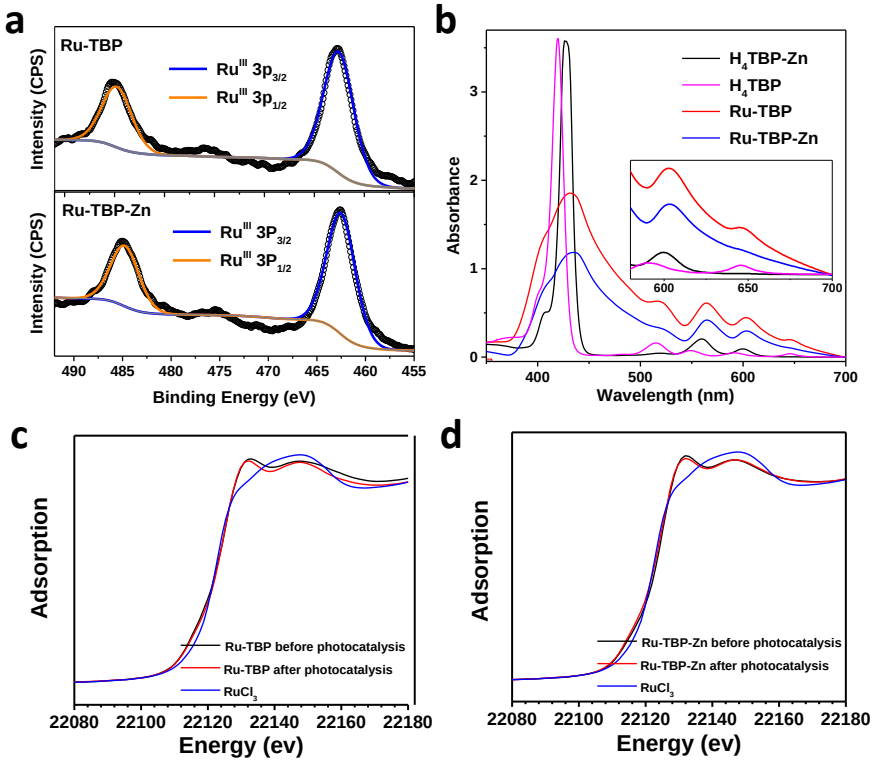

Figure 8-4. Chemical structures of Ru-TBP and Ru-TBP-Zn. Ru 3p XPS spectra (a), and UV-visible absorption spectra (b) of Ru-TBP and Ru-TBP-Zn. XANES analyses show +3 oxidation state for Ru-TBP (c) and Ru-TBP-Zn (d) before and after light irradiation as the edge features are similar to $RuCl_3$ control sample.

The Ru^{III} and Zn^{II} occupancies in the metalated porphyrin ligands in the Ru-TBP and Ru-TBP-Zn nanoplates were investigated by a combination of UV-visible spectroscopy, TGA, and ICP-MS. The UV-visible absorption spectra of Ru-TBP showed a small peak at 648 nm (**Figure 8-4b**), which corresponds to the last Q-band of free TBP ligand, indicating incomplete metalation of TBP ligand in Ru-TBP nanoplates. The ratio of TBP-Ru ligand to TBP ligand in Ru-TBP nanoplates was calculated to be 0.71:0.29 by TGA, affording a formula of Ru_2(TBP-Ru-DMF)$_{0.71}$(TBP)$_{0.29}$)(H_2O)$_2$]$Cl_{2.71}$. For Ru-TBP-Zn nanoplates, the UV-visible absorption

spectra showed the same Q bands as H_4TBP-Zn (**Figure 8-4b**), indicating complete metalatiom of TBP ligands by Zn^{II}. ICP-MS analysis gave a Ru to Zn ratio of 1.92 ± 0.09, supporting the formulation of Ru-TBP-Zn. These Ru-TBP and Ru-TBP-Zn nanoplates were used for subsequent HER and mechanistic studies.

8.2.2 Visible light-driven HER

We hypothesized that the integration of photosensitizing porphyrin ligands and Ru_2 SBUs in the MOFs could facilitate multielectron injection from the excited ligands to catalytic SBUs to drive HER. The discrete Ru_2 paddlewheel (Ru_2-PD) with a formula of $Ru^{II}Ru^{III}(CH_3COO)_4(DMF)Cl$ was synthesized and used as a homogeneous control (**Figure 8-5**).

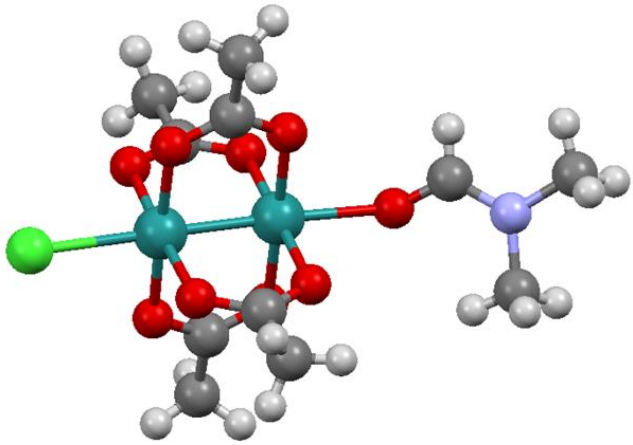

Figure 8-5. Crystal structure of Ru_2-PD.

The visible-light driven (λ > 400 nm) HER catalytic activities of Ru-TBP, Ru-TBP-Zn, and the homogenous control (Ru_2-PD + H_4TBP-Zn) were studied in an oxygen-free CH_3CN solution with H_2O as proton source and triethanolamine (TEOA) as sacrificial electron donor (CH_3CN:H_2O:TEOA = 20:1:5, V:V:V). The amount of generated H_2 was quantified by gas chromatography (GC) analysis of the headspace gas in the reactor. H_2 production increased linearly with time at a rate of 0.13 $mmol \cdot h^{-1} \cdot g^{-1}$ for Ru-TBP and 0.24 $mmol \cdot h^{-1} \cdot g^{-1}$ for Ru-TBP-

Zn, with respect to the Ru_2 moieties (or the porphyrin derivatives). The higher HER catalytic activity of Ru-TBP-Zn than that of Ru-TBP is likely due to the better photosensitizing ability of the TBP-Zn ligand than the TBP-Ru or the TBP ligand. The TON [defined as $n(1/2H_2)$] reached 21.2 for Ru-TBP and 39.4 for Ru-TBP-Zn after 72 h irradiation (**Figure 8-6a**). In comparison, the Ru_2-PD + H_4TBP-Zn homogenous control exhibited a modest TON of 1.4. The significantly enhanced catalytic activity of Ru-TBP-Zn over the homogenous control confirmed that the important role played by hierarchical organization of photosensitizing ligands and catalytic SBUs in facilitating multi-electron transfer processes to drive photocatalytic HER.

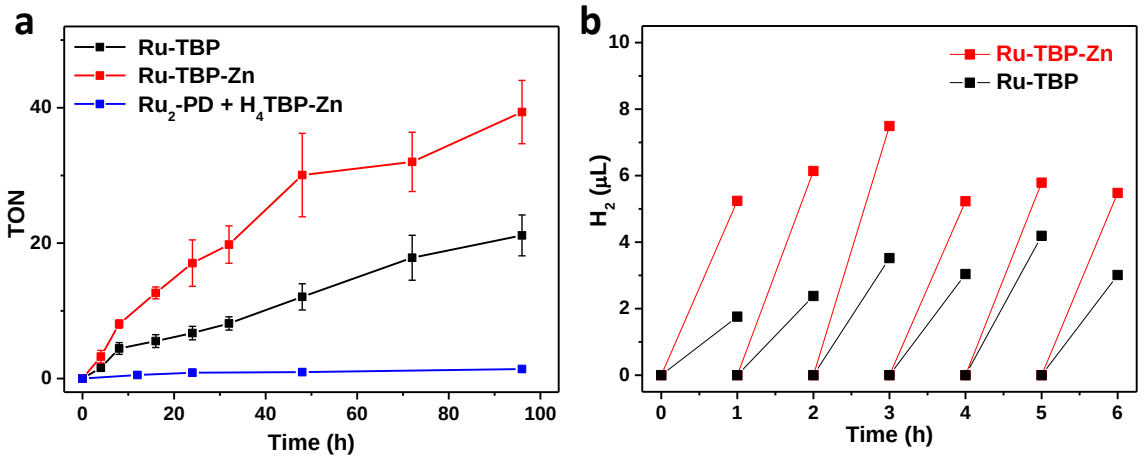

Figure 8-6. Photocatalytic HER of Ru-TBP and Ru-TBP-Zn. (a) Time-dependent HER TONs of Ru-TBP and Ru-TBP-Zn along with the homogeneous control. N = 3. (b) Time-dependent H_2 generation of Ru-TBP and Ru-TBP-Zn for six consecutive reactions.

To confirm the catalytic activity of Ru_2 SBUs in MOFs and rule out the involvement of Ru NPs, H_2 generation was measured hourly for six consecutive reactions (**Figure 8-6b**). Both Ru-TBP and Ru-TBP-Zn showed similar H_2 generation in six reactions, arguing against the role of Ru NPs in HER, which would have afforded increasing HER rates over time. In addition, the XANES spectra of Ru-TBP and Ru-TBP-Zn also showed no change of Ru valence states or formation of Ru NPs after photocatalysis (**Figure 8-4a,b**). After photocatalysis, both Ru-

TBP and Ru-TBP-Zn showed the same PXRD patterns as freshly prepared MOFs (**Figure 8-7**), indicating their structural stability during HER.

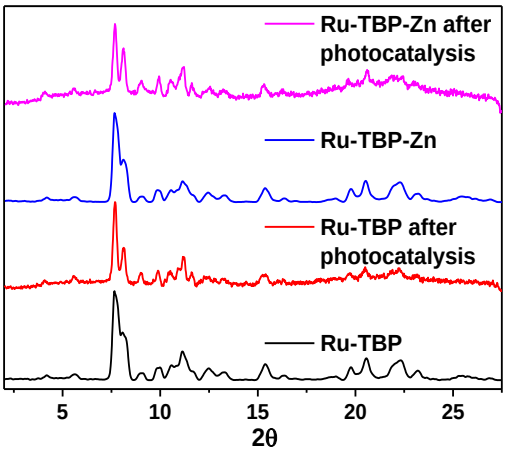

Figure 8-7. PXRD patterns of Ru-TBP and Ru-TBP-Zn after photocatalysis.

8.2.3 Mechanistic studies

The HER mechanism was investigated by photophysical and electrochemical studies on Ru-TBP-Zn and Ru_2-PD + Me_4TBP-Zn homogenous control. To establish whether the excited TBP-Zn was quenched reductively by TEOA as electron donor or oxidatively by Ru_2 moieties as electron acceptor, the luminescence spectra of Me_4TBP-Zn were measured with addition of TEOA or Ru_2-PD. As shown in **Figure 8-8a** and **Figure 8-8b**, the luminescence of Me_4TBP-Zn was efficiently quenched by Ru_2-PD but not TEOA, indicating that the photocatalytic HER in Ru-TBP-Zn occurred via electron transfer from the excited TBP-Zn to Ru_2 SBUs. The luminescence quenching of Me_4TBP-Zn was fitted to the Stern-Völmer equation to afford a K_{SV} value of 6.03 $mL \cdot mg^{-1}$ (**Figure 8-8c**). In addition, time-resolved photoluminescence measurements showed a shorter lifetime of TBP-Zn in Ru-TBP-Zn (τ = 1.98 ns) than that in Me_4TBP-Zn (τ = 2.13 ns) in CH_3CN solution (**Figure 8-8d**), consistent to the oxidative quenching mechanism.

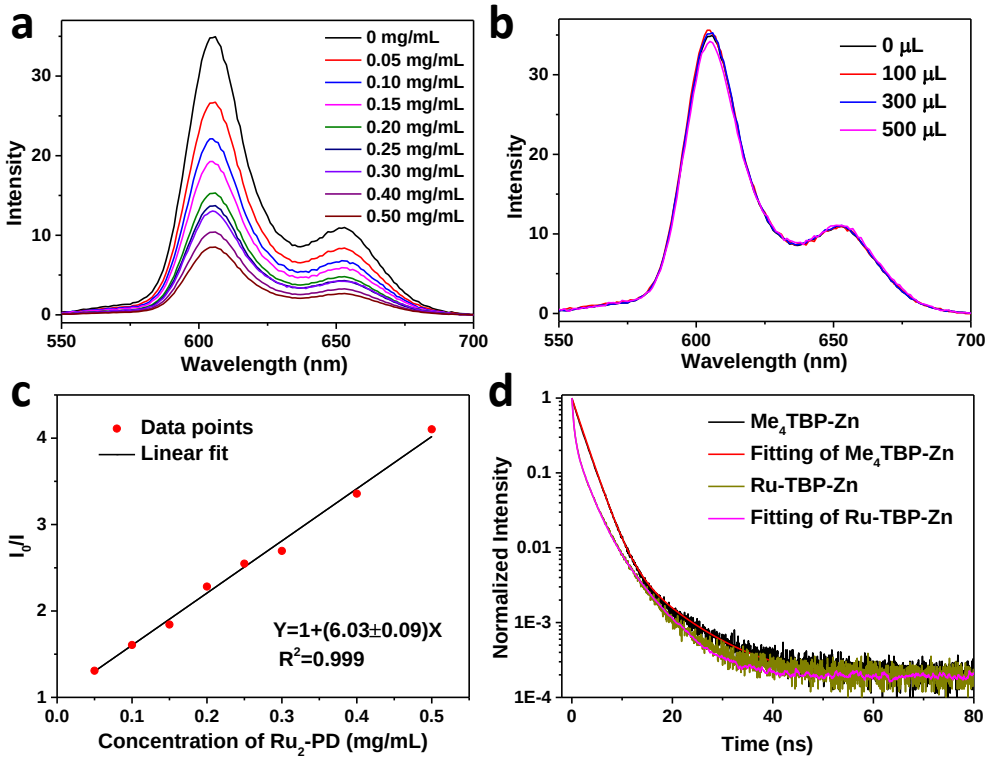

Figure 8-8. Physical characterization. Emission spectra of Me_4TBP-Zn (0.1 mg/mL) after the addition of different amounts of Ru_2-PD (a) and TEOA (b) in 2 mL CH_3CN with 410 nm excitation. (c) Plots of I_0/I as a function of the concentration of Ru_2-PD. (d) Normalized luminescence decay traces of Me4TBP-Zn and Ru-TBP-Zn.

CVs of Ru_2-PD and Ru-TBP-Zn were then studied to provide additional insight into the HER process. Ru_2-PD showed a reversible reduction peak at 0.08 V vs. NHE in CH_3CN, corresponding to the reduction of $Ru^{II}Ru^{III}$ to $Ru^{II}Ru^{II}$, and an irreversible catalytic peak with an onset potential of -0.47 V (**Figure 8-9a**). Similar CV pattern was observed for Ru-TBP-Zn, suggesting that the Ru_2 SBUs in Ru-TBP-Zn were first reduced to $Ru^{II}Ru^{II}$ before catalyzing proton reduction. The onset potential of catalytic peak of Ru-TBP-Zn was -0.50 V vs. NHE in CH_3CN solution with H_2O and TFA as proton source (CH_3CN:H_2O:TFA = 20:0.5:0.5, V:V:V), where the proton concentration is $10^{7.23}$ higher than the photocatalytic HER condition (CH_3CN:H_2O = 20:1, V:V). The energy to drive HER by Ru_2 SBUs in Ru-TBP-Zn under photocatalytic condition was estimated to be 0.93 eV (ΔE') by the Nernst equation.

Based on the photophysical and electrochemical data, we propose the photocatalytic HER mechanism of Ru-TBP-Zn as shown in **Figure 8-10**. Under visible-light irradiation, the ligand TBP-Zn is excited to the $(TBP\text{-}Zn)^*$ state, which can transfer one electron to the Ru_2 SBU to generate $(TBP\text{-}Zn)^+$. After each Ru_2 SBU first accepting two electrons to form $Ru^{II}Ru^{II}$, further electron injections to the Ru_2 SBU drive the proton reduction to generate H_2. The $(TBP\text{-}Zn)^+$ is reduced back to the TBP-Zn by the TEOA sacrificial donor to complete the catalytic cycle. DPV showed that Me_4TBP-Zn displayed first oxidation peak at 0.93V (**Figure 8-9b**), indicating the energy change from $(TBP\text{-}Zn)^+$ to TBP-Zn was -0.93 eV (ΔE_3). As shown in **Figure 8-8a**, Me_4TBP-Zn exhibited luminescence emission peak at 605 nm, corresponding to the energy increase from TBP-Zn ground state to $(TBP\text{-}Zn)^*$ excited state and of 2.05 eV (ΔE_1). Based on the proposed catalytic cycle, the energy loss from $(TBP\text{-}Zn)^*$ to $(TBP\text{-}Zn)^+$ is 2.05 – 0.93 = 1.12 eV ($-\Delta E_2$), which is larger than the 0.93 eV needed for photocatalytic HER by Ru_2 SBUs in Ru-TBP-Zn.

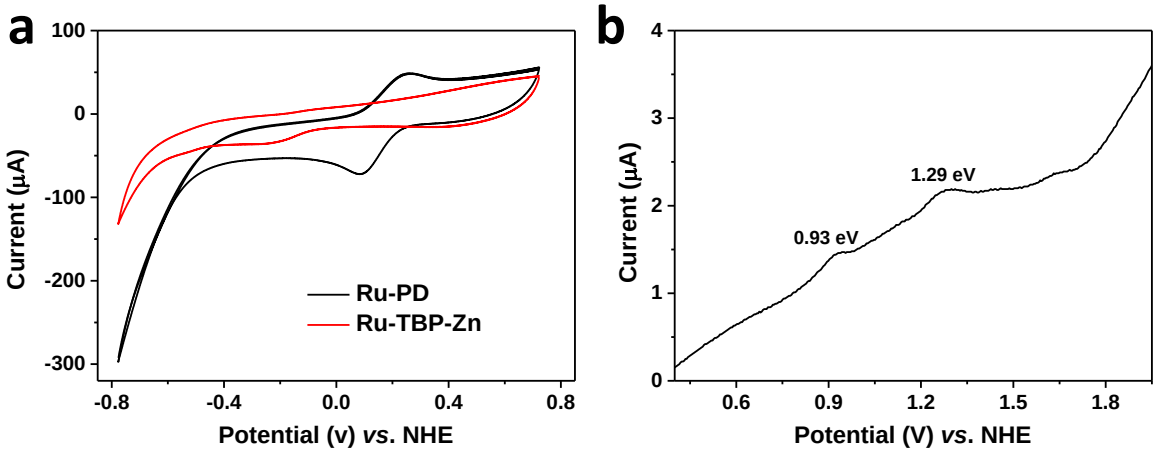

Figure 8-9. Electrochemical characterization. (a) CVs of 5 mM Ru_2-PD and 0.5 mg Ru-TBP-Zn coated on electrode surface in a 20 mL 0.1 M TBAH/CH_3CN solution with 500 μL H_2O and 500 μL TFA. (b) DPV of Me_4TBP-Zn.

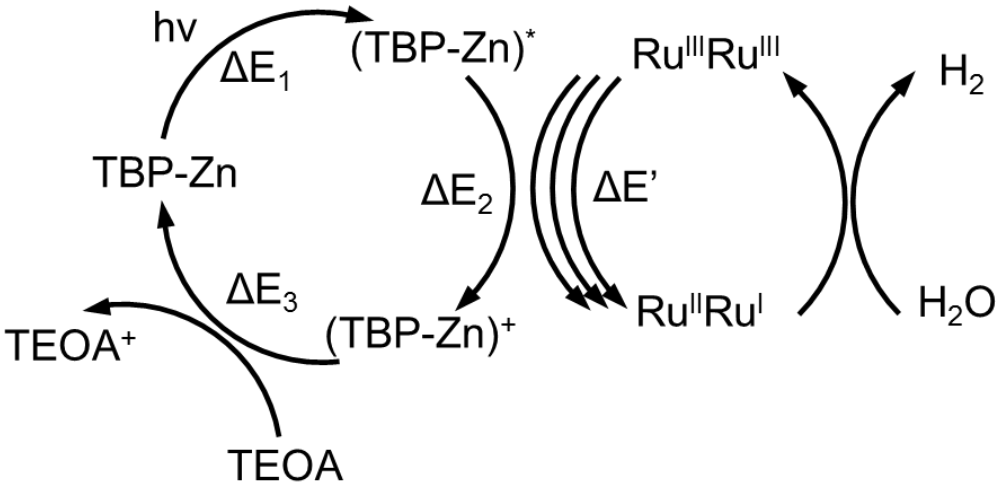

Figure 8-10. Proposed catalytic cycle. Proposed catalytic cycle for visible-light-driven hydrogen evolution catalyzed by Ru-TBP-Zn. ΔE_1 = 2.05 eV, ΔE_2 = -1.12 eV, ΔE_3 = -0.93 eV and ΔE' = 0.93 eV.

8.3 Conclusion

In this work, we designed two novel MOFs built from Ru_2 SBUs and porphyrin-derived ligands and realized photocatalytic HER by directly incorporating HER catalysts as the SBUs into photosensitizing MOFs. The proximity of photosensitizing porphyrin ligands to the catalytic Ru_2 SBUs in the MOFs facilitated multi-electron transfer, leading to 28 times higher HER activity than the homogeneous control. Photophysical and electrochemical studies established the oxidative quenching of the $(TBP\text{-}Zn)^*$ excited states by Ru_2 SBUs as the initiating step of HER and revealed the energetics of key intermediates in the catalytic cycle. This work provides a blueprint for designing multifunctional MOFs with catalytic SBUs and photosensitizing ligands for photocatalytic and other applications.

8.4 Methods

Synthesis of Ru-TBP single crystals. H_4TBP was synthesized as described previously.[13] To a 4 mL glass vial was added 0.5 mL of $RuCl_3 \cdot xH_2O$ (40-43% Ru) solution (1.2 mg/mL in DMF),

0.5 mL of H_4TBP solution (2.0 mg/mL in DMF) and 80 μL of acetic acid. The reaction mixture was kept in a 120 °C oven for 7 days to afford dark purple square-shaped single crystal.

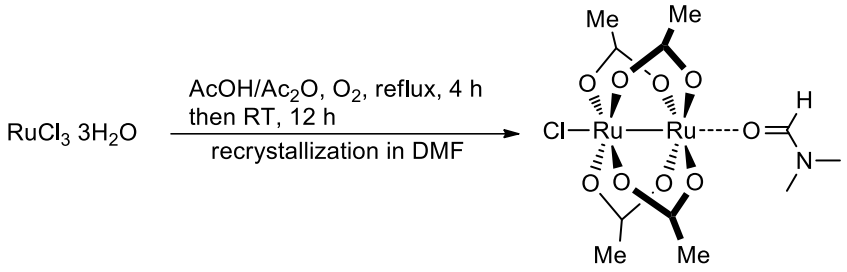

Synthesis of Ru_2-PD single crystals. $RuCl_3 \cdot 3H_2O$ (1.0 g) and anhydrous LiCl (1.0 g) were added to a mixture of glacial acetic acid (35 mL) and acetic anhydride (7 mL). The solution was refluxed for 4 hours in a stream of oxygen. After cooling to ambient temperature for 12 hours the precipitate was filtered under reduced pressure, washed successively with acetic acid, methanol and ether, and dried in vacuum to give product as a red brown solid (0.76 g, 85%).[14] The solid was dissolved in DMF. Evaporation of the DMF solution in ambient atmosphere gave red brown crystals of Ru_2-PD.

Single crystal X-ray diffraction. Single crystal X-ray diffraction of Ru-TBP and Ru_2-PD was performed with a Bruker APEX II CCD based detector at ChemMatCARS (Sector 15), Advanced Photon Source (APS), Argonne National Laboratory. Data were scaled and corrected for absorption effects using the multi-scan procedure as implemented in SADABS (Bruker AXS, version 2014/5, 2015, part of Bruker APEX3 software package). The structure was solved by SHELXT (Version 2014/5)[15] and refined by a full-matrix least-squares procedure using OLEX23[16] software packages (XL refinement program version 2014/7)[17]. Crystallographic data and details of the data collection and structure refinement are listed in **Table 8-1**.

Table 8-1. Crystallographic information of Ru-TBP and Ru_2-PD.

	Ru-TBP	**Ru_2-PD**
Formula	$C_{51}H_{31}N_5O_{11}Ru_3$	$C_{11}H_{19}ClNO_9Ru_2$
formula weight	1193.02	546.86
crystal system	triclinic	monoclinic
space group	*P*-1	$P2_1/n$
a, Å	8.7321(11)	8.1385(2)
b, Å	21.947(3)	11.9075(4)
c, Å	22.807(3)	18.1107(6)
α, deg	90.743(2)	90
β, deg	93.980(3)	95.2950(10)
γ, deg	92.211(3)	90
V, Å^3	4356.6(9)	1747.60(9)
Z	2	4
T, K	100(2)	100(2)
F(000)	1184	1076
D_C, g cm^{-3}	0.909	2.078
μ, mm^{-1}	0.713	2.393
λ, Å	0.41328	0.41328
crystal size, mm^3	0.05 × 0.04 × 0.03	0.02 × 0.02 × 0.02
no. total reflns.	47931	47449
no. uniq. reflns, R_{int}	7561, 0.1882	3848, 0.1142
no. obs. [$I \geq 2\sigma$(I)]	6127	3806
no. params	543	224
*R*1 [$I \geq 2\sigma$(I)]	0.1478	0.0279
*wR*2 (all data)	0.4295	0.0744
S	1.937	1.106
$\Delta\rho^a$, *e* / Å^3	1.832, –1.370	0.657, –1.147
max. and mean Δ/σ^b	0.001, 0.000	0.004, 0.000
CCDC	1822737	1822738

Synthesis of Ru-TBP nanoplates. To a 4 mL glass vial was added 0.5 mL of $RuCl_3 \cdot xH_2O$ (40-43% Ru) solution (1.2 mg/mL in DMF), 0.5 mL of H_4TBP solution (2.0 mg/mL in DMF) and 50 μL of acetic acid. The reaction mixture was kept in a 120 °C oven for 2 days. The purple precipitate was collected by centrifugation and washed with DMF and ethanol. The yield of Ru-TBP was 33% based on Ru.

Synthesis of Ru-TBP-Zn nanoplates. To a 4 mL glass vial was added 0.5 mL of $RuCl_3 \cdot xH_2O$ (40-43% Ru) solution (1.2 mg/mL in DMF), 0.5 mL of H_4TBP-Zn solution (2.2 mg/mL in DMF)

and 50 μL of acetic acid. The reaction mixture was kept in a 120 °C oven for 2 days. The purple precipitate was collected by centrifugation and washed with DMF and ethanol. The yield of Ru-TBP-Zn was 35% based on Ru.

TGA of Ru-TBP nanoplates. The first weight loss (5.71%) in the 25-250 °C temperature range corresponds to removal of weakly boned water to SBUs and adsorbed solvents in the pores. The second weight loss (70.11%) in the 250-600 °C temperature range corresponds to decomposition of the $[Ru_2(TBP\text{-}Ru\text{-}DMF)_x(TBP)_{1-x}]Cl_{2+x}$ to $(2+x)RuO_2$, based on which the percentage of TBP-Ru (x) was determined to be 71%. The formulation of Ru-TBP was then determined to be $[Ru_2(TBP\text{-}Ru\text{-}DMF)_{0.71}(TBP)_{0.29}(H_2O)_2]Cl_{2.71}$.

TGA of Ru-TBP-Zn nanoplates. The first weight loss (5.88%) in the 25-250 °C temperature range corresponds to removal of weakly boned water to SBUs and adsorbed solvents in the pores. The second weight loss (68.93%) in the 250-600 °C temperature range corresponds to decomposition of the $[Ru_2(TBP\text{-}Zn)]Cl_2$ to $(2\cdot RuO_2 + ZnO)$, which was calculated to be 69.04%. The formulation of Ru-TBP-Zn was then determined to be $[Ru_2(TBP\text{-}Zn)(H_2O)_2]Cl_2$.

Photocatalytic HER. Photocatalytic HER was carried out in an external illumination type reaction vessel with a magnetic stirrer. Samples were prepared in 4.5 mL septum-sealed glass vials. Each sample was made up to a volume of 2.6 mL of 2.0 mL CH_3CN, 0.1 mL H_2O, and 0.5 mL TEOA. Samples contained 0.1 mg Ru-TBP or Ru-TBP-Zn. Sample vials were capped and deoxygenated by bubbling nitrogen through for 20 min to ensure complete air removal. The solution was irradiated by a 230 W solid state light source with a 400 nm filter. After the hydrogen evolution reaction, the gas in the headspace of the vial was analyzed by GC to determine the amount of hydrogen generated.

X-ray absorption spectroscopy. X-ray absorption data were collected at Beamline 10-BM-A, B at the Advanced Photon Source (APS) at Argonne National Laboratory. Spectra were collected at the ruthenium K-edge (22117 eV) in transmission mode. The X-ray beam was monochromatized by a Si(111) monochromater and detuned by 50% to reduce the contribution of higher-order harmonics below the level of noise. A metallic ruthenium foil standard was used as a reference for energy calibration and was measured simultaneously with experimental samples. The incident beam intensity (I_0), transmitted beam intensity (I_t), and reference (I_r) were measured by 20 cm ionization chambers with gas compositions of 44% N_2 and 56% Ar, 5% N_2 and 95% Ar, and 100% N_2, respectively. Data were collected over six regions: -250 to -30 eV (10 eV step size, dwell time of 0.25 s), -30 to -12 eV (5 eV step size, dwell time of 0.5 s), -12 to 30 eV (1.1 eV step size, dwell time of 1 s), 30 eV to 6 $Å^{-1}$, (0.05 $Å^{-1}$ step size, dwell time of 2 s), 6 $Å^{-1}$ to 12 $Å^{-1}$, (0.05 $Å^{-1}$ step size, dwell time of 4 s), 12 $Å^{-1}$ to 15 $Å^{-1}$, (0.05 $Å^{-1}$ step size, dwell time of 8 s). Multiple X-ray absorption spectra were collected at room temperature for each sample. Samples were ground and mixed with polyethyleneglycol (PEG) and packed in a 6-shooter sample holder to achieve adequate absorption length. Data was processed using the Athena and Artemis programs of the IFEFFIT package based on FEFF 6.[18, 19] Prior to merging, spectra were calibrated against the reference spectra and aligned to the first peak in the smoothed first derivative of the absorption spectrum, the background noise was removed, and the spectra were processed to obtain a normalized unit edge step. The Ru oxidation states of Ru-TBP and Ru-Zn-TBP before and after light irradiation were determined by comparing the edge feature with $RuCl_3$. They all show adsorption peak at around 22125 eV.

Fitting of the luminescence quenching of Me_4TBP-Zn by Ru_2-PD. The oxidative quenching mechanism was supported by fitting the data of luminescence quenching of Me_4TBP-Zn by Ru_2-PD to the Stern-Volmer equation,

$$\frac{I_0}{I} = K_{SV} C_{Ru2-PD}$$

where K_{SV} is the Stern-Völmer constant, and I_0/I is the ratio of luminescence intensity in the absence and presence of Ru_2-RD. I_0/I showed a good linear relationship with respect to the concentration of Ru-PD ($C_{Ru\text{-}PD}$) with $R^2 = 0.999$ and $K_{SV} = 6.03$ mL·mg^{-1}.

Lifetimes of Ru-TBP-Zn and Me_4TBP-Zn. Time-domain lifetimes were measured on a ChronosBH lifetime fluorimeter (ISS, Inc.) using Time-Correlated Single Photon Counting (TCSPC) methods. The fluorimeter contained Becker-Hickl SPC-130 detection electronics and an HPM-100-40 Hybrid PMT detector. Excitation was provided by a 405 nm picosecond pulsed laser source (Hamamatsu PLP-10). Emission wavelengths were selected with interference filters (Semrock Brightline FF01-641/75). The Instrument Response Function (IRF) was measured to be approximately 0.13 ns (full width at half maximum, FWHM) in a 1% scattering solution of Ludox LS colloidal silica. Multi-component exponential decay lifetimes were fit using a forward convolution method in the Vinci control and analysis software.

CV. CVs of 5 mM Ru_2-PD (dissolved in solution) and 0.5 mg Ru-TBP-Zn (coated on electrode surface) were tested in 20 mL 0.1 M TBAH/CH_3CN solution with 500 μL H_2O and 500 μL TFA with a scan rate of 100 mV/s. Working, reference, and counter electrodes were glassy carbon (3 mm diameter disk), Ag/AgCl, and Pt, respectively. Upon scanning to negative potential, the large and irreversible reductive wave, corresponding to catalytic water reduction, was -0.47 V vs. NHE for Ru_2-PD and -0.50 V vs. NHE for Ru-TBP-Zn, respectively.

Estimation of the energy to drive photocatalytic HER by Ru_2 SBUs in Ru-TBP-Zn. Based on Nernst equation, the proton reduction potential (E) is calculated as follows:

$$E = E_0 + 0.059\log\,[\mathrm{H}^+]$$

In the condition of CV test (25 μL TFA and 25 μL H_2O per 1 mL CH_3CN):

$$E_1 = -0.50\ \mathrm{V} = E_0 + 0.059\log\,[\mathrm{H}^+]_1$$

In the condition of photocatalytic HER (50 μL H_2O per 1 mL CH_3CN):

$$E_2 = E_0 + 0.059\log\,[\mathrm{H}^+]_2$$

The ratio of $[H^+]_2$ to $[H^+]_1$ is approximately equals to the proton concentration of 50 μL H_2O to solution of 25 μL TFA and 25 μL H_2O, which is calculated to be $10^{-7.23}$.

$$E_2 - E_1 = 0.059\log\left(\frac{[\mathrm{H}^+]_2}{[\mathrm{H}^+]_1}\right) = -0.43\ \mathrm{V}, E_2 = -0.93\ \mathrm{V}$$

The energy to drive the photocatalytic HER (ΔE') is then calculated to be 0.93 eV.

DPV. DPV of Me_4TBP-Zn (0.1 mg/mL) was tested in 20 mL 0.1 M TBAH/CH_3CN solution with a scan rate of 100 mV/s. Working, reference, and counter electrodes were glassy carbon (3 mm diameter disk), Ag/AgCl, and Pt, respectively. The first oxidative peak at 0.93 V vs. NHE corresponded to the oxidation of TBP-Zn to TBP-Zn^+.

8.5 References

1. Gao, Y.; Ding, X.; Liu, J.; Wang, L.; Lu, Z.; Li, L.; Sun, L., Visible light driven water splitting in a molecular device with unprecedentedly high photocurrent density. *Journal of the American Chemical Society* **2013,** *135* (11), 4219-4222.
2. Meyer, T. J., Catalysis: the art of splitting water. *Nature* **2008,** *451* (7180), 778.
3. Sakai, K.; Ozawa, H., Homogeneous catalysis of platinum (II) complexes in photochemical hydrogen production from water. *Coordination Chemistry Reviews* **2007,** *251* (21-24), 2753-2766.
4. Sala, X.; Romero, I.; Rodríguez, M.; Escriche, L.; Llobet, A., Molecular catalysts that oxidize water to dioxygen. *Angewandte Chemie International Edition* **2009,** *48* (16), 2842-2852.
5. Wang, C.; DeKrafft, K. E.; Lin, W., Pt nanoparticles@ photoactive metal–organic

frameworks: efficient hydrogen evolution via synergistic photoexcitation and electron injection. *Journal of the American Chemical Society* **2012,** *134* (17), 7211-7214.
6. Zhang, Z.-M.; Zhang, T.; Wang, C.; Lin, Z.; Long, L.-S.; Lin, W., Photosensitizing metal–organic framework enabling visible-light-driven proton reduction by a Wells–Dawson-type polyoxometalate. *Journal of the American Chemical Society* **2015,** *137* (9), 3197-3200.
7. Kong, X. J.; Lin, Z.; Zhang, Z. M.; Zhang, T.; Lin, W., Hierarchical Integration of Photosensitizing Metal–Organic Frameworks and Nickel-Containing Polyoxometalates for Efficient Visible-Light-Driven Hydrogen Evolution. *Angewandte Chemie International Edition* **2016,** *55* (22), 6411-6416.
8. Fateeva, A.; Chater, P. A.; Ireland, C. P.; Tahir, A. A.; Khimyak, Y. Z.; Wiper, P. V.; Darwent, J. R.; Rosseinsky, M. J., A Water-Stable Porphyrin-Based Metal–Organic Framework Active for Visible-Light Photocatalysis. *Angewandte Chemie* **2012,** *124* (30), 7558-7562.
9. Pullen, S.; Fei, H.; Orthaber, A.; Cohen, S. M.; Ott, S., Enhanced photochemical hydrogen production by a molecular diiron catalyst incorporated into a metal–organic framework. *Journal of the American Chemical Society* **2013,** *135* (45), 16997-17003.
10. Ohmura, T.; Usuki, A.; Fukumori, K.; Ohta, T.; Ito, M.; Tatsumi, K., New Porphyrin-Based Metal− Organic Framework with High Porosity: 2-D Infinite 22.2-Å Square-Grid Coordination Network. *Inorganic chemistry* **2006,** *45* (20), 7988-7990.
11. Choi, E.-Y.; Wray, C. A.; Hu, C.; Choe, W., Highly tunable metal–organic frameworks with open metal centers. *CrystEngComm* **2009,** *11* (4), 553-555.
12. Opre, Z.; Grunwaldt, J.-D.; Maciejewski, M.; Ferri, D.; Mallat, T.; Baiker, A., Promoted Ru–hydroxyapatite: designed structure for the fast and highly selective oxidation of alcohols with oxygen. *Journal of Catalysis* **2005,** *230* (2), 406-419.
13. Lu, K.; He, C.; Guo, N.; Chan, C.; Ni, K.; Weichselbaum, R. R.; Lin, W., Chlorin-based nanoscale metal–organic framework systemically rejects colorectal cancers via synergistic photodynamic therapy and checkpoint blockade immunotherapy. *Journal of the American Chemical Society* **2016,** *138* (38), 12502-12510.
14. Mitchell, R. W.; Spencer, A.; Wilkinson, G., Carboxylato-triphenylphosphine complexes of ruthenium, cationic triphenylphosphine complexes derived from them, and their behaviour as homogeneous hydrogenation catalysts for alkenes. *Journal of the Chemical Society, Dalton Transactions* **1973,** (8), 846-854.
15. Sheldrick, G. M., Crystal structure refinement with SHELXL. *Acta Crystallographica Section C: Structural Chemistry* **2015,** *71* (1), 3-8.
16. Dolomanov, O. V.; Bourhis, L. J.; Gildea, R. J.; Howard, J. A.; Puschmann, H., OLEX2: a complete structure solution, refinement and analysis program. *Journal of Applied Crystallography* **2009,** *42* (2), 339-341.
17. Sheldrick, G. M., A short history of SHELX. *Acta Crystallographica Section A: Foundations of Crystallography* **2008,** *64* (1), 112-122.
18. Rehr, J. J.; Albers, R. C., Theoretical approaches to x-ray absorption fine structure. *Reviews of modern physics* **2000,** *72* (3), 621.
19. Ravel, B.; Newville, M., ATHENA, ARTEMIS, HEPHAESTUS: data analysis for X-ray absorption spectroscopy using IFEFFIT. *Journal of synchrotron radiation* **2005,** *12* (4), 537-541.

Chapter 9. Photosensitizing Metal-Organic Layers for Highly Efficient Sunlight-Driven Carbon Dioxide Reduction

9.1 Introduction

Structural regularity and synthetic tunability of MOFs allow hierarchical integration of multiple functional moieties, including PSs and catalytic centers, to facilitate multi-electron or radical transfer in photoreactions.[1, 2] However, due to intrinsically high absorptivity of most PSs, only superficial layers of MOFs are involved in photoreactions. Light scattering by MOF particles also reduces photon utilization. Furthermore, photocatalytic efficiency of MOFs is limited by restricted diffusion of radicals and other energetic intermediates through MOF channels. By reducing one dimension of MOFs to a single layer, MOLs have recently emerged as a new class of functionalizable 2D materials for many potential applications.[3-6] We believe that MOLs can overcome the aforementioned issues for MOFs due to their thinness and hold great promise for applications in artificial photosynthesis and photocatalysis.

Sunlight-driven CO_2 reduction to energy-rich compounds represents a promising approach to overcome the shortage of fossil fuels and to mitigate climate change.[7-15] Among many photocatalytic systems for CO_2 reduction, combinations of $[Ru(bpy)_3]^{2+}$ (bpy = 2,2′-bipyridine) as a PS and $Re^{I}(bpy)(CO)_3Cl$ as a CO_2 reduction catalyst have been most extensively studied due to their ability to generate CO with high selectivity and efficiency.[16-20] Previous studies have demonstrated an improvement of photocatalytic CO_2 reduction efficiency by linking $[Ru(bpy)_3]^{2+}$ and $Re^{I}(bpy)(CO)_3Cl$ moieties in supramolecular systems.[21, 22] In this Chapter, we report the design of the first photosensitizing MOL, Hf_{12}-Ru, built from Hf_{12} secondary building units (SBUs) and $[Ru(bpy)_3]^{2+}$ derived linear dicarboxylate ligands.

SBUs surface capping of Hf_{12}-Ru with $Re^{I}(bpy)(CO)_3Cl$ or $Mn^{I}(bpy)(CO)_3Br$ derived monocarboxylic acids afforded multifunctional Hf_{12}-Ru-Re and Hf_{12}-Ru-Mn MOLs for highly efficient photocatalytic CO_2 reduction. The proximity of photosensitizing Hf_{12}-Ru MOL skeleton to the capping monocarboxylate ligands (1-2 nm) facilitates multi-electron transfer from photoexcited $[Ru(bpy)_3]^{2+*}$ to $M^{I}(bpy)(CO)_3X$ (M = Re, Mn) catalytic centers, reaching 24-hour turnover numbers (TONs) of 3,849 and 1,347, respectively (**Figure 9-1**). Remarkably, Hf_{12}-Ru-Re catalyzed sunlight-driven CO_2 reduction with a TON of 670 in 6 hours of daylight.

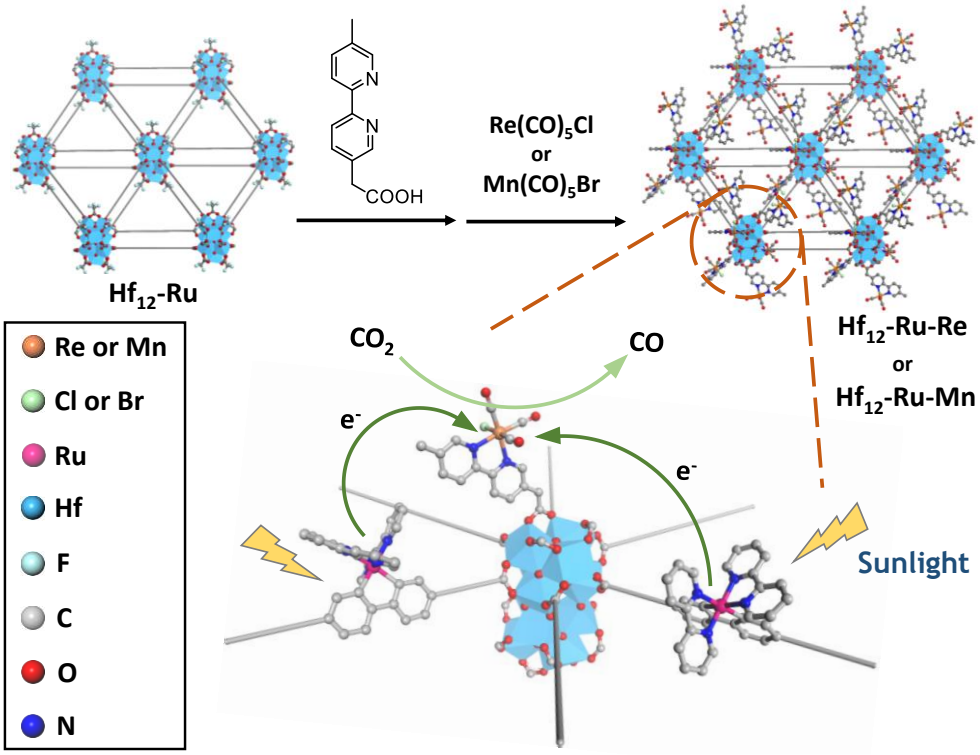

Figure 9-1. Schematic showing the modification of Hf_{12}-Ru to afford Hf_{12}-Ru-Re or Hf_{12}-Ru-Mn and sunlight-driven CO_2 reduction. Photoexcited **L**-Ru ligands in the MOL inject multi-electrons to surface-capped $Re(MeMBA)(CO)_3Cl$ or $Mn(MeMBA)(CO)_3Br$ to reduce CO_2 to CO.

9.2 Result and discussion

9.2.1 Synthesis and characterization

Hf_{12}-Ru MOLs were synthesized through a solvothermal reaction between $HfCl_4$ and bis(2,2'-bipyridine)(5,5'-di(4-carboxyl-phenyl)-2,2'-bipyridine)-ruthenium (II) dichloride (H_2**L**-Ru) in DMF at 80 °C with TFA and water as modulators. Hf_{12}-Ru is proposed as the first MOL constructed from Hf_{12} SBUs and laterally connected linear **L**-Ru linkers to form an infinite 2D network of kagome dual (**kgd**) topology. Each Hf_{12} SBU is also vertically capped by six TFA groups. Hf_{12}-Ru thus has a formula of $Hf_{12}(\mu_3\text{-}O)_8(\mu_3\text{-}OH)_8(\mu_2\text{-}OH)_6(TFA)_6$(**L**-Ru)$_6$. 2D Hf_{12}-Ru MOL forms in part due to stronger Hf-carboxylate bonds in the lateral direction than those in the vertical direction as we recently observed in Hf_{12}-based MOFs.[23]

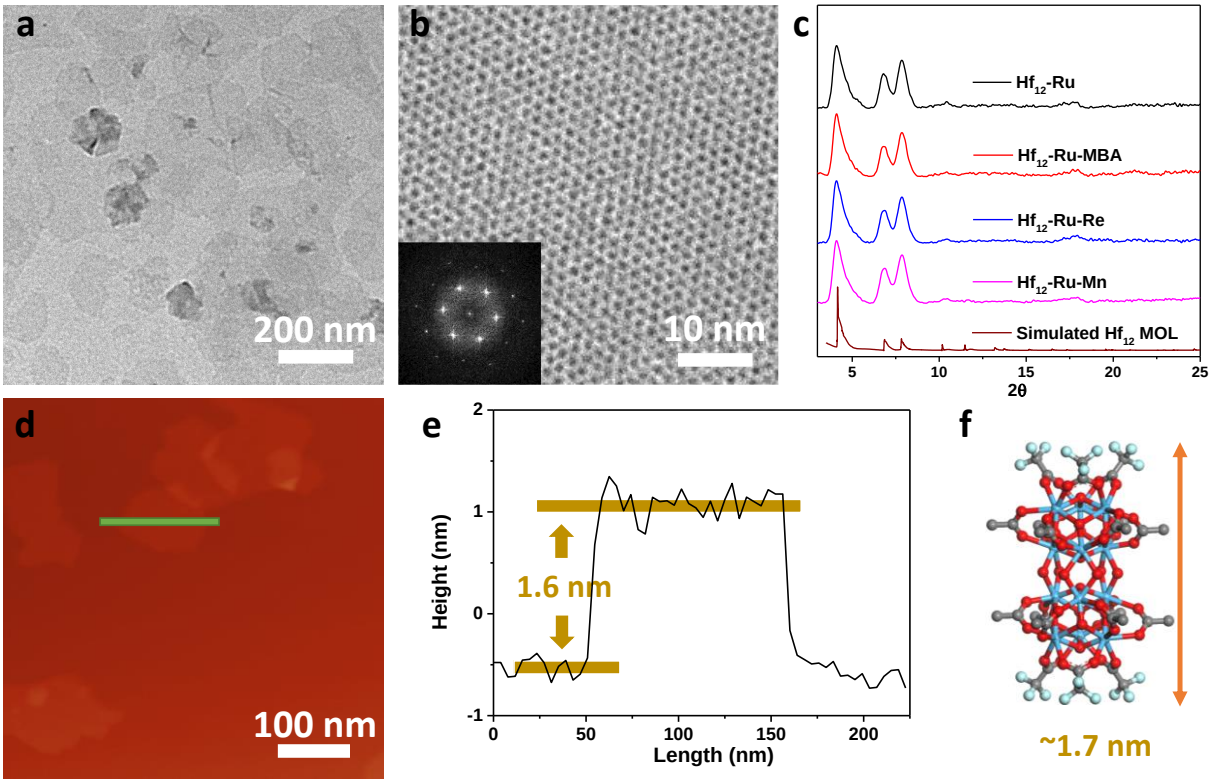

Figure 9-2. Characterization of Hf_{12}-Ru. TEM (a) and HRTEM (b) of Hf_{12}-Ru. (c) PXRD pattern of Hf_{12} MOLs in comparison to the simulated pattern.[24] AFM topography (d) and height profile (e) of Hf_{12}-Ru. (f) Schematic showing a Hf_{12} cluster capped by TFA groups with a height of ~1.7 nm.

TEM imaging showed Hf_{12}-Ru as flat nanoplates of ~100 nm in diameter (**Figure 9-2a**). The low contrast of the TEM images is consistent with the monolayer nature of Hf_{12}-Ru, which is confirmed by a nanoplate thickness of ~1.6 nm observed by AFM (**Figure 9-2d,e**). This thickness is consistent with the modeled height of Hf_{12} clusters capped with TFAs (~1.7 nm, **Figure 9-2f**). HRTEM imaging confirmed the topological structure of Hf_{12}-Ru with lattice points corresponding to Hf_{12} SBUs and FFT revealing a six-fold symmetry (**Figure 9-2b**) that is consistent with the projection of Hf_{12}-Ru structure along the vertical direction. The distance between adjacent lattice points in HRTEM images was measured to be 2.7 nm, matching the distance between adjacent Hf_{12} SBUs. Moreover, the PXRD pattern of Hf_{12}-Ru matched well with that simulated from the proposed Hf_{12} MOL structure (**Figure 9-2c**).[24] All of these data support the proposed monolayer structure of Hf_{12}-Ru. Furthermore, the ^{1}H NMR spectrum of digested Hf_{12}-Ru showed all signals corresponding to H_2**L**-Ru without any other aromatic signals, which confirms the presence of only **L**-Ru ligands in Hf_{12}-Ru. Finally, Hf_{12}-Ru showed similar absorption and emission spectra as H_2**L**-Ru (**Figure 9-3**), suggesting photosensitizing ability of Hf_{12}-Ru.

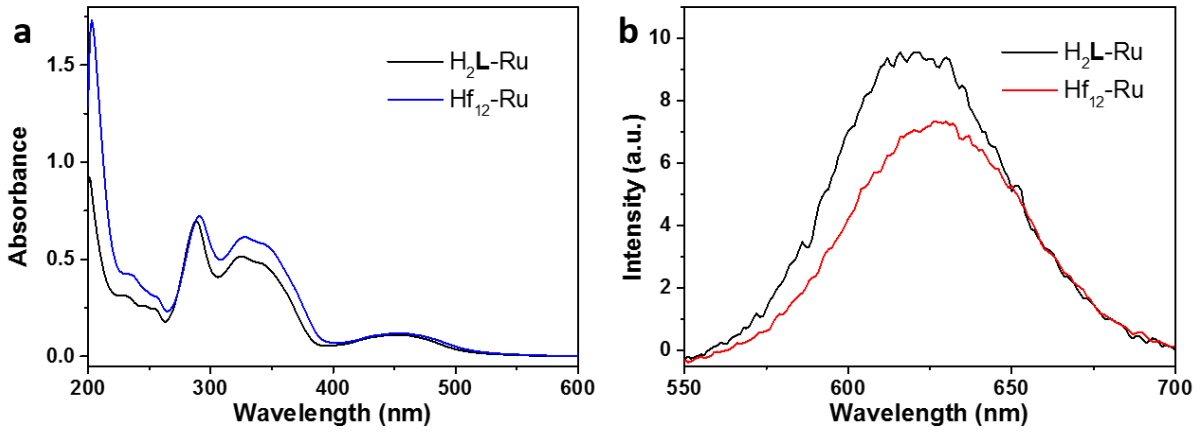

Figure 9-3. UV-visible spectra (a) and luminescence spectra (b) of Hf_{12}-Ru in comparison to H_2**L**-Ru.

Hf_{12}-Ru was modified with 2-(5'-methyl-[2,2'-bipyridin]-5-yl)acetic acid (H-MBA) ligands on the surface to afford Hf_{12}-Ru-MBA by replacing weakly coordinating TFAs on SBUs with MBA ligands. The ^{1}H NMR spectrum of digested Hf_{12}-Ru-MBA gave an MBA to **L**-Ru ratio of ~1:1 (**Figure 9-4**), indicating complete replacement of TFAs in Hf_{12}-Ru-MBA to give a formula of $Hf_{12}(\mu_3\text{-}O)_8(\mu_3\text{-}OH)_8(\mu_2\text{-}OH)_6(MBA)_6(\mathbf{L}\text{-}Ru)_6$. Additionally, no signal corresponding to TFA was detected in the ^{19}F NMR spectrum of digested Hf_{12}-Ru-MBA. PXRD studies indicated that Hf_{12}-Ru-MBA exhibited the same structure as Hf_{12}-Ru (**Figure 9-2c**).

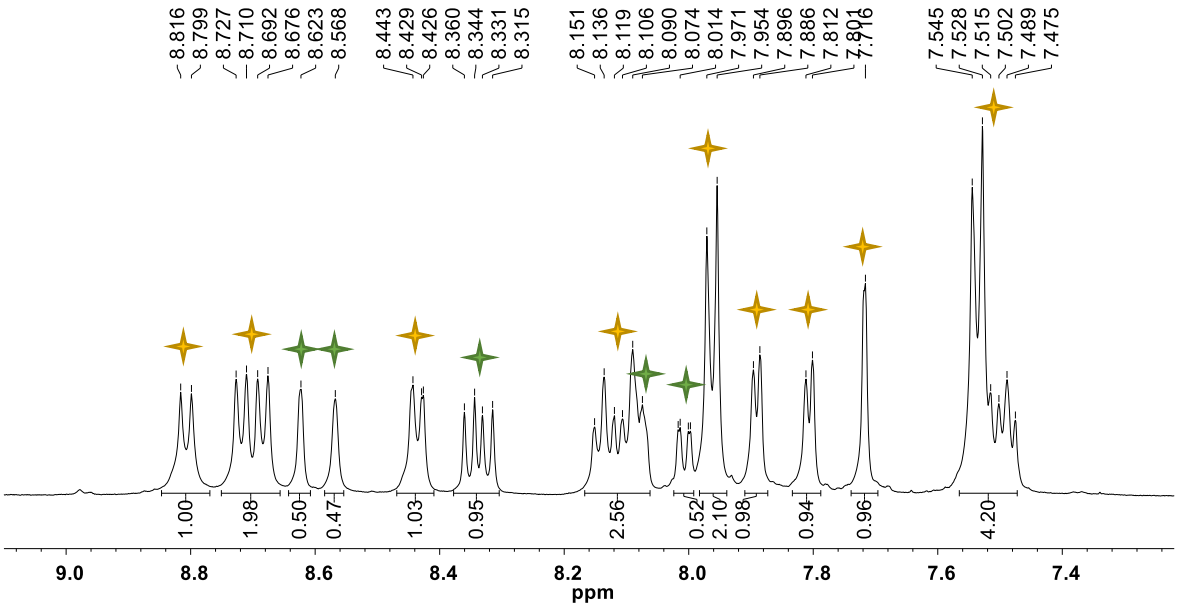

Figure 9-4. NMR spectrum of digested Hf_{12}-Ru-MBA. Yellow and green stars correspond to **L**-Ru ligands and MBA ligands, respectively.

Hf_{12}-Ru-MBA was then metalated with $Re(CO)_5Cl$ or $Mn(CO)_5Br$ to afford Hf_{12}-Ru-Re with the catalytic center $Re(MBA)(CO)_3Cl$ that is an analogue of $Re^{I}(bpy)(CO)_3Cl$ or Hf_{12}-Ru-Mn with the catalytic center $Mn(MBA)(CO)_3Br$ that is an analogue of $Mn^{I}(bpy)(CO)_3Br$. Hf_{12}-Ru-Re and Hf_{12}-Ru-Mn showed similar sizes and morphologies to Hf_{12}-Ru by TEM (**Figure 9-5a,d**) and maintained the same structure as Hf_{12}-Ru as indicated by PXRD (**Figure 9-2c**).

AFM studies showed that the thickness of Hf_{12}-Ru-Re and Hf_{12}-Ru-Mn increased to ~3.7 nm (**Figure 9-5b,c,e,f**), which is consistent with the height of Hf_{12} clusters capped with MBA ligands (3.2-4.0 nm) (**Figure 9-6**).

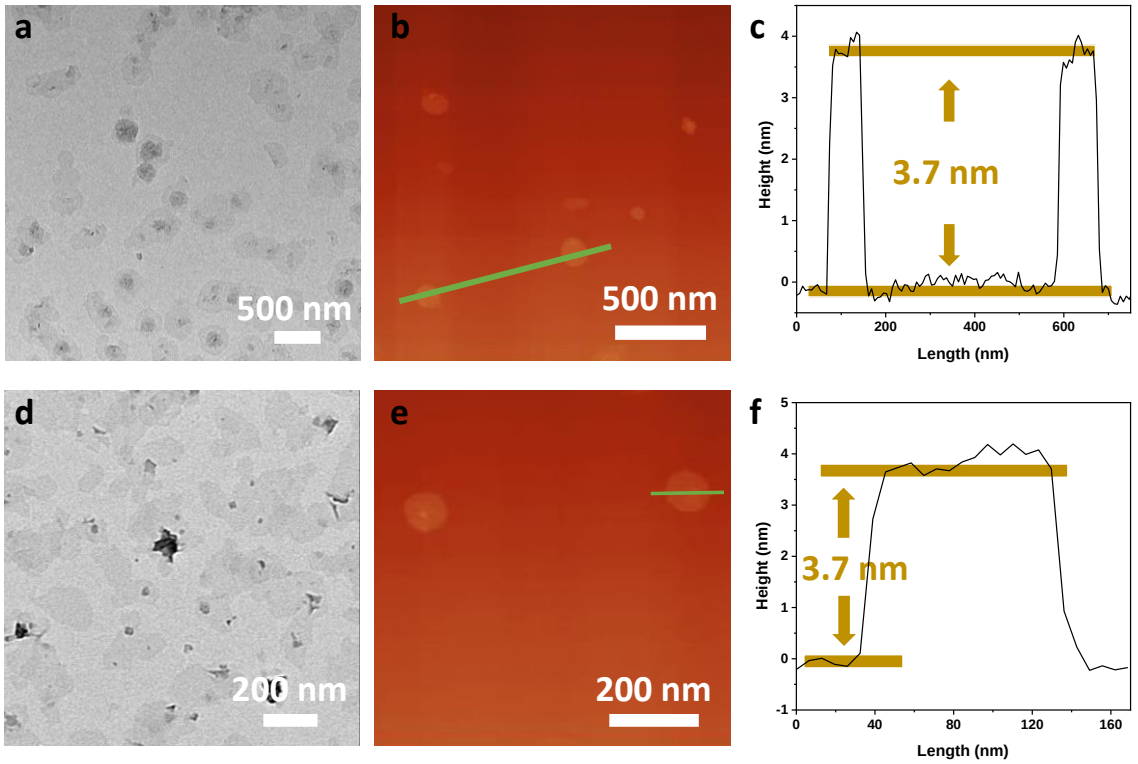

Figure 9-5. Morphology characterization of Hf_{12}-Ru-Re and Hf_{12}-Ru-Mn. TEM (a), AFM topography (b) and height profile (c) of Hf_{12}-Ru-Re. TEM (d), AFM topography (e) and height profile (f) of Hf_{12}-Ru-Re.

In Hf_{12}-Ru-Re and Hf_{12}-Ru-Mn, each catalytic center is adjacent to six **L**-Ru ligands, which enables multi-electron transfer from **L**-Ru to Re(MBA)$(CO)_3$Cl or Mn(MBA)$(CO)_3$Br. Electron transfer was further facilitated by a short distance of 1.3 nm between each catalytic center and its nearest **L**-Ru ligand (**Figure 9-7**).

Re and Mn coordination environments of Hf_{12}-Ru-Re, Hf_{12}-Ru-Mn, and Re(MeMBA)$(CO)_3$Cl and Mn(MeMBA)$(CO)_3$Br {MeMBA = methyl 2-(5'-methyl-[2,2'-bipyridin]-5-yl)acetate} were determined by X-ray absorption spectroscopy. Hf_{12}-Ru-Re and Hf_{12}-Ru-Mn showed similar EXAFS profiles to Re(MeMBA)$(CO)_3$Cl and

Mn(MeMBA)$(CO)_3$Br, which were well fitted with their corresponding molecular models (Re(bpy)$(CO)_3$Cl for Hf_{12}-Ru-Re and Mn(bpy)$(CO)_3$Br for Hf_{12}-Ru-Mn) (**Figure 9-8**).

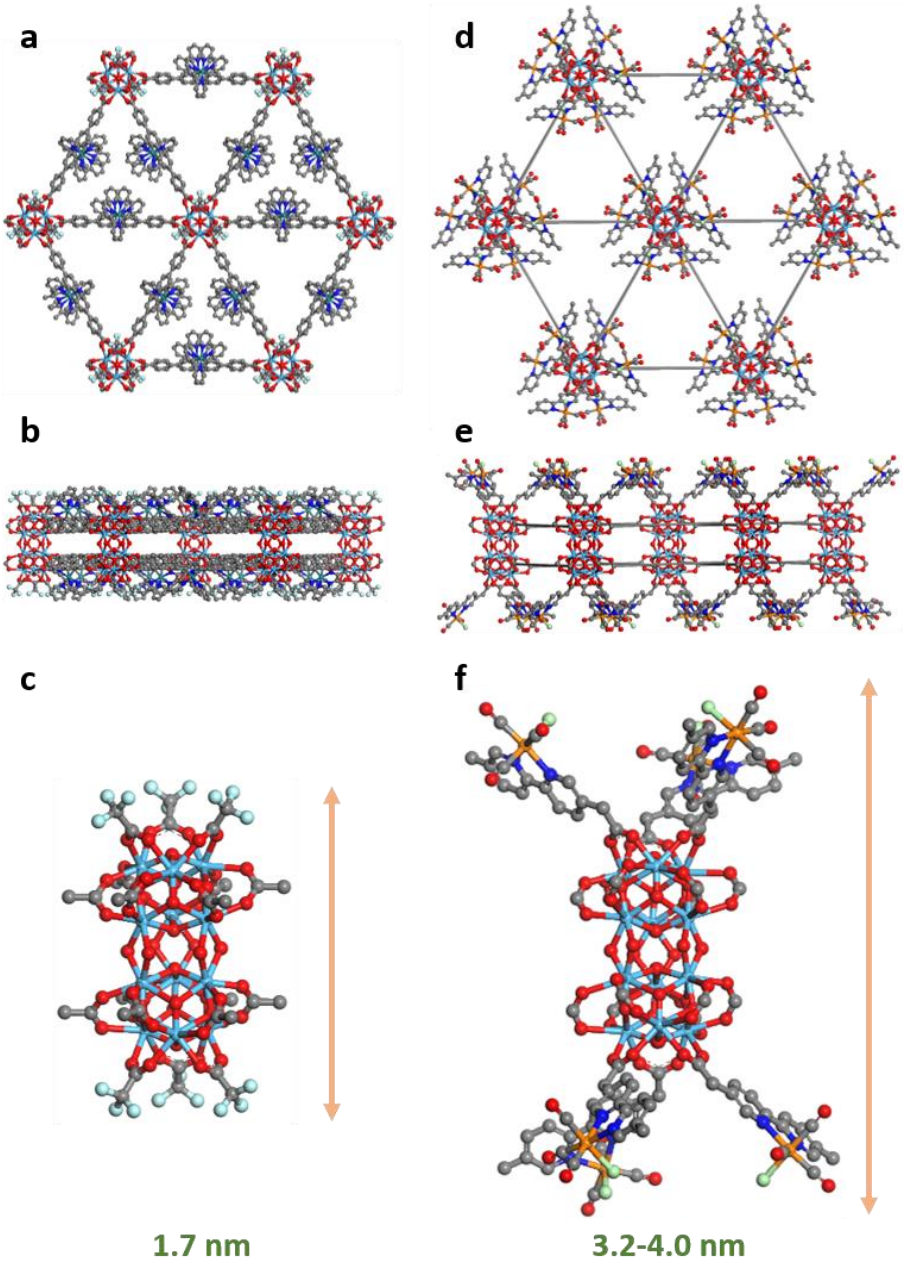

Figure 9-6. Modeled structures of Hf_{12}-Ru and Hf_{12}-Ru-Re (or Hf_{12}-Ru-Mn). Vertical (a) and lateral perspective (b) views of Hf_{12}-Ru. (c) A view of the Hf_{12} cluster. The height of the Hf_{12} cluster capped by trifluoroacetate is measured to be ~1.7 nm. Vertical (d) and lateral perspective (e) views of of Hf_{12}-Ru-Re or Hf_{12}-Ru-Mn. The **L**-Ru ligands are simplified as gray rods. (f) A view of the Hf_{12} cluster. The height of Hf_{12} cluster capped by Re(MBA)$(CO)_3$Cl or Mn(MBA)$(CO)_3$Br is measured to be 3.2-4.0 nm, depending on the rotation angle of the MBA ligands relative to the MOL plane.

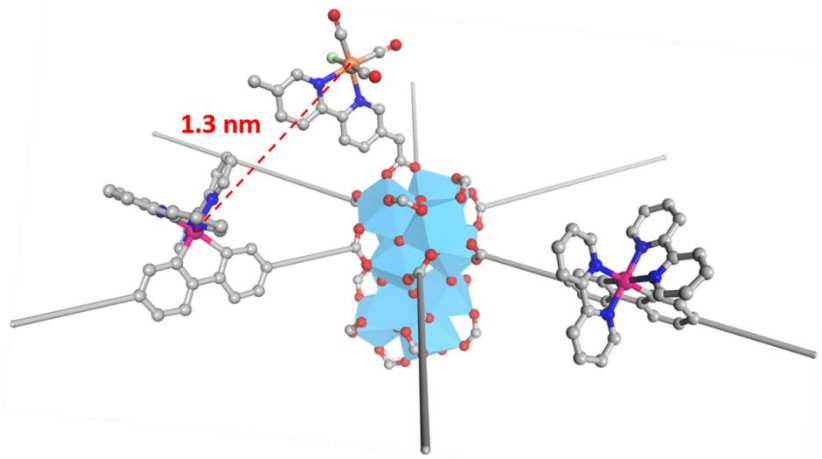

Figure 9-7. Modeled structure of catalytic center. The distance between the centers of Re(MBA)(CO)$_3$Cl or Mn(MBA)(CO)$_3$Br to the center of the nearest **L**-Ru ligand was measured to be 1.3 nm.

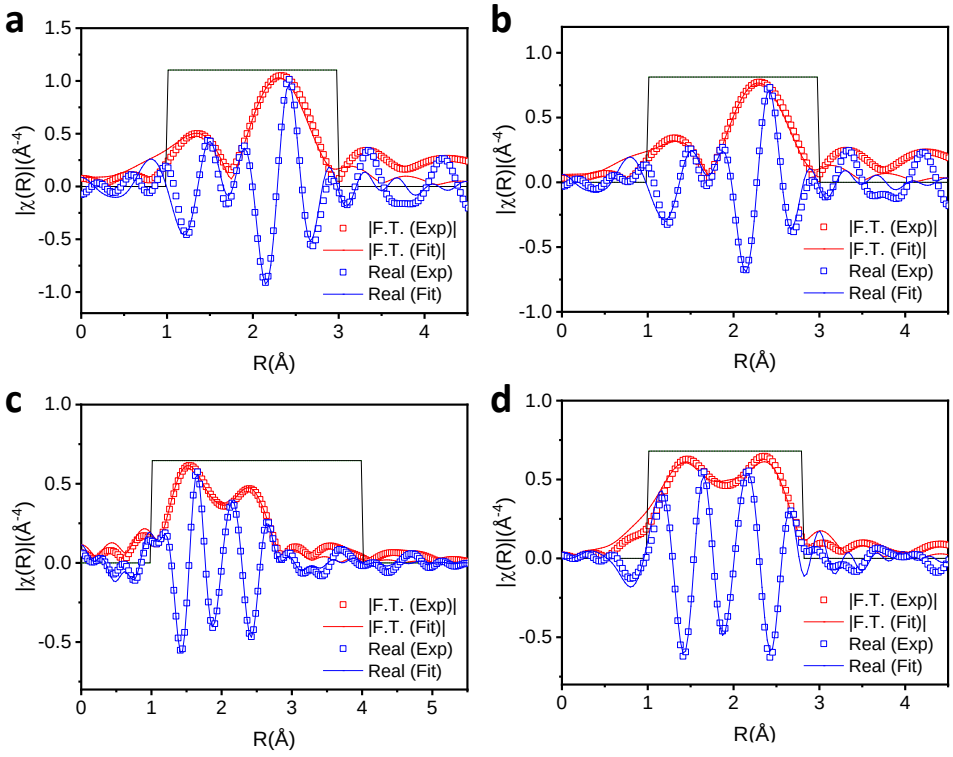

Figure 9-8. EXAFS fitting of Hf$_{12}$-Ru-Re and Hf$_{12}$-Ru-Mn. Experimental EXAFS spectra and fits of Hf$_{12}$-Ru-Re (a), Re(MeMBA)(CO)$_3$Cl (b), Hf$_{12}$-Ru-Mn (c), and Mn(MeMBA)(CO)$_3$Br (d) in R space showing the magnitude of Fourier Transform (red hollow squares, red solid line) and real components (blue hollow squares, blue solid line).

Moreover, Hf$_{12}$-Ru-Re and Hf$_{12}$-Ru-Mn showed similar CO stretching vibrations in comparison to Re(MeMBA)(CO)$_3$Cl and Mn(MeMBA)(CO)$_3$Br, respectively (**Figure 9-9**). These results indicate that Hf$_{12}$-Ru-Re and Hf$_{12}$-Ru-Mn exhibit the same Re and Mn

coordination environments as molecular photocatalytic CO_2 reduction catalysts $Re^{I}(bpy)(CO)_3Cl$ and $Mn^{I}(bpy)(CO)_3Br$, respectively.

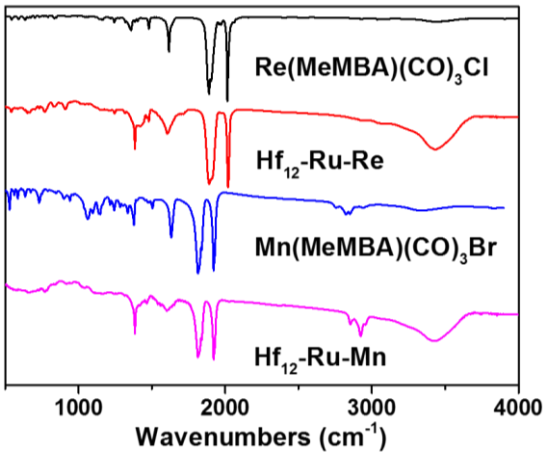

Figure 9-9. IR spectra of Hf_{12}-Ru-Re and Hf_{12}-Ru-Mn. IR spectra of Hf_{12}-Ru-Re and Hf_{12}-Ru-Mn in comparison to homogenous Mn and Re compounds.

9.2.2 Photocatalytic CO_2 reduction

Hf_{12}-Ru-Re and Hf_{12}-Ru-Mn provide an excellent opportunity to test whether capping the surface of photosensitizing Hf_{12}-Ru with $Re(MBA)(CO)_3Cl$ or $Mn(MBA)(CO)_3Br$ catalyst could facilitate multi-electron transfer from photoexcited Hf_{12}-Ru to catalytic Re or Mn centers to drive efficient CO_2 reduction (**Figure 9-1**). The catalytic activities for visible-light driven ($\lambda > 400$ nm) CO_2 reduction of Hf_{12}-Ru-Re, Hf_{12}-Ru-Mn, and homogenous controls H_2**L**-Ru plus $Re(MeMBA)(CO)_3Cl$, or H_2**L**-Ru plus $Mn(MeMBA)(CO)_3Br$) were studied in an oxygen-free CH_3CN solution with saturated CO_2, TEOA, and BNAH or BIH as sacrificial electron donor. The amount of generated CO was quantified by GC analysis of the headspace gas. The TON reached 3849 (BIH) or 2092 (BNAH) for Hf_{12}-Ru-Re and 1367 (BIH) or 240 (BNAH) for Hf_{12}-Ru-Mn after 24 h irradiation (**Figure 9-10a,b**). In comparison, H_2**L**-Ru plus $Re(MeMBA)(CO)_3Cl$ and H_2**L**-Ru plus $Mn(MeMBA)(CO)_3Br$ exhibited modest TONs of <54 under same conditions. Greater than 70-fold increase in catalytic activity for Hf_{12}-Ru-Re and

Hf_{12}-Ru-Mn over their homogenous controls confirms the important role of hierarchical organization of PSs and Re or Mn catalytic centers in the MOLs in facilitating multi-electron transfer processes to drive photocatalytic CO_2 reduction. Furthermore, Hf_{12}-Ru-Re outperformed Hf_{12}-Ru-Mn in CO generation due to the intrinsically higher catalytic CO_2 reduction activity of Re(bpy)$(CO)_3$Cl than that of Mn(bpy)$(CO)_3$Br. The CO_2 reduction product selectivity for Hf_{12}-Ru-Re and Hf_{12}-Ru-Mn was examined by quantifying the amounts of HCOOH generated using HPLC. Similar to previously reported molecular systems,[22, 25] Hf_{12}-Ru-Re showed a ~98% selectivity for CO, while Hf_{12}-Ru-Mn generated more HCOOH with a 82% selectivity for CO.

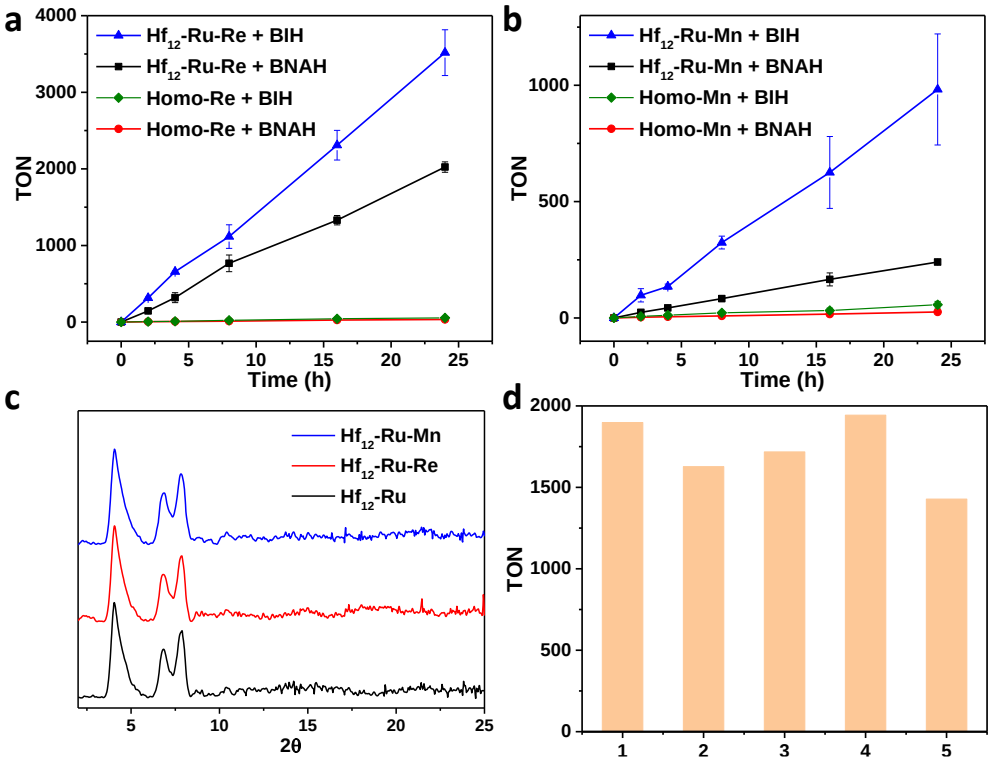

Figure 9-10. Photocatalytic CO_2 reduction. Time-dependent CO_2 reduction TONs of Hf_{12}-Ru-Re (a) and Hf_{12}-Ru-Mn (b) along with their homogeneous controls H_2**L**-Ru plus Re(MeMBA)$(CO)_3$Cl and H_2**L**-Ru plus Mn(MeMBA)$(CO)_3$Br. N = 3. (c) PXRD patterns of Hf_{12}-Ru, Hf_{12}-Ru-Re, and Hf_{12}-Ru-Mn after photocatalysis. (d) Plots of TONs of CO_2 reduction catalyzed by recovered Hf_{12}-Ru-Re in five consecutive runs.

To confirm the structural stability of the MOLs following 24-hour CO_2 reduction, Hf_{12}-Ru, Hf_{12}-Ru-Re, and Hf_{12}-Ru-Mn were centrifuged from the reaction suspensions. The recovered MOLs showed the same PXRD patterns as freshly prepared MOLs (**Figure 9-10c**) with <1% leaching of Hf by ICP-MS. To further confirm the photocatalytic durability of these MOLs, Hf_{12}-Ru-Re was used in 5 consecutive cycles of CO_2 reduction, showing consistent catalytic activity with a total TON of 8,613 (**Figure 9-10d**).

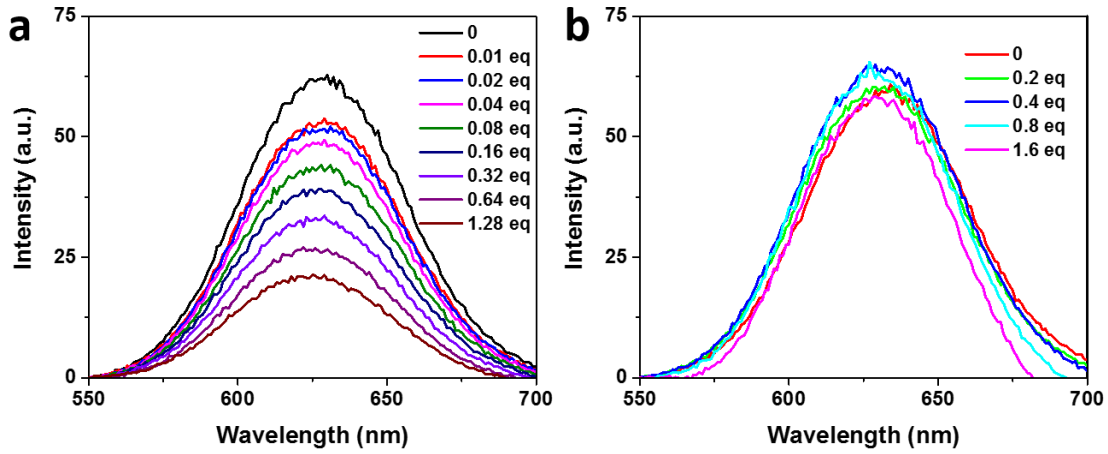

Figure 9-11. Luminescence quenching. Emission spectra of Hf_{12}-Ru (50 μM) after the addition of different equivalents of BIH (a) and Re(MeMBA)$(CO)_3$Cl (b) in 2 mL of CH_3CN with 450 nm excitation.

The CO_2 reduction mechanism was investigated by photophysical and electrochemical studies. The phosphorescence spectra of Hf_{12}-Ru were measured with the addition of different equivalence of BIH or Re(MeMBA)$(CO)_3$Cl. As shown in the **Figure 9-11**, the phosphorescence of Hf_{12}-Ru was efficiently quenched by BIH but not by Re(MeMBA)$(CO)_3$Cl, indicating that the excited Hf_{12}-Ru was reductively quenched by BIH to generate $[Hf_{12}\text{-Ru}]^-$. CV and DPV studies demonstrated that Hf_{12}-Ru had similar reduction potential to H_2**L**-Ru ($E^{red}_{1/2}$ = -0.89 V vs SCE, corresponding to Hf_{12}-Ru to $[Hf_{12}\text{-Ru}]^-$), which is negative enough to reduce Re(MeMBA)$(CO)_3$Cl ($E^{red}_{1/2}$ = -0.34 V vs SCE, **Figure 9-12**).

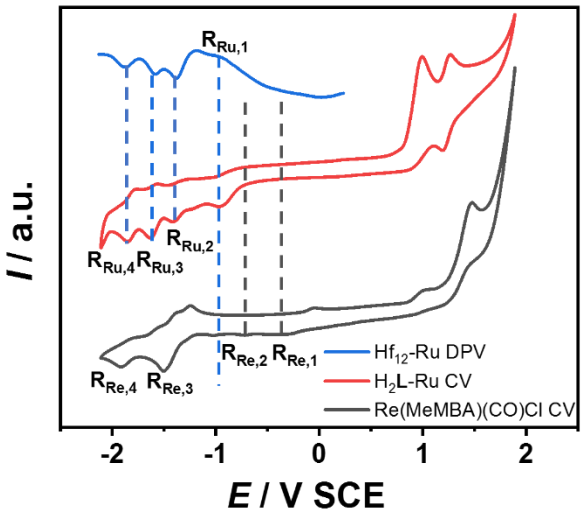

Figure 9-12. Electrochemical characterization. CV of H_2**L**-Ru, Re(MeMBA)(CO)Cl, and DPV of Hf_{12}-Ru in 0.1 M TBAH/DMF (TBAH = tetrabutylammonium hexafluorophosphate). Potential sweep rate was 100 mV/s.

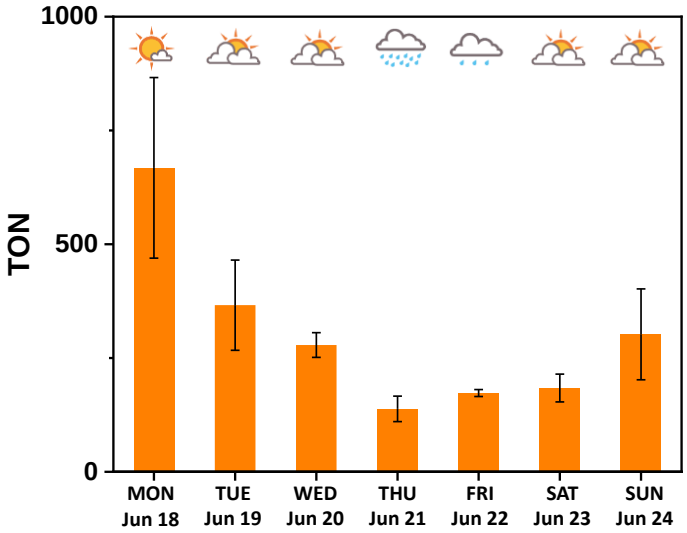

Figure 9-13. Sunlight-driven CO_2 reduction TONs of Hf_{12}-Ru-Re in 6 hours.

We next examined Hf_{12}-Ru-Re catalyzed CO_2 reduction upon sunlight irradiation. The Hf_{12}-Ru-Re reaction suspension was prepared as above and placed near a window inside a chemistry laboratory at the University of Chicago. This suspension was stirred from 11:00 am to 5:00 pm on Jun. 18th to Jun. 24th in 2018. Remarkably, Hf_{12}-Ru-Re catalyzed CO_2 reduction under sunlight irradiation with unprecedented efficiency, reaching a TON of 670 in 6 h (**Figure 9-13**). The effectiveness of Hf_{12}-Ru-Re catalyzed sunlight-driven CO_2 reduction was understandably weather dependent, with the highest TON of 670 achieved on sunny Jun. 18th,

2018 and the lowest TON of 138 observed on rainy Jun. 22nd, 2018. To the best of our knowledge, this work presents the first study of sunlight-driven CO_2 reduction using a combination of $[Ru(bpy)_3]^{2+}$ as a PS and $Re^{I}(bpy)(CO)_3Cl$ as a CO_2 reduction catalyst.

9.3 Conclusion

In this work, we synthesized the first MOL based on readily functionalizable linear dicarboxylate ligands. The post-synthetic functionalization of photosensitizing Hf_{12}-Ru MOL with $M(bpy)(CO)_3X$ (M = Re or Mn) moieties via carboxylate exchange reactions afforded Hf_{12}-Ru-Re and Hf_{12}-Ru-Mn MOLs that possess both $[Ru(bpy)_3]^{2+}$ PSs and $M(bpy)(CO)_3X$ catalysts for efficient photocatalytic CO_2 reduction. We showed that multi-electron transfer from photoexcited $[Ru(bpy)_3]^{2+*}$ to $M^{I}(bpy)(CO)_3X$ (M = Re, Mn) catalytic centers is greatly facilitated by the proximity of the photosensitizing MOL skeleton to the capping CO_2 reduction catalysts. The Hf_{12}-Ru-Re system exhibited high CO_2 reduction TONs of 8,613 under artificial visible light and of 670 under sunlight. This work thus provides a versatile synthetic strategy to multifunctional MOLs for studying artificial photosynthesis.

9.4 Methods

Synthesis of Hf_{12}-Ru. bis(2,2'-bipyridine)(5,5'-di(4-carboxyl-phenyl)-2,2'-bipyridine)-ruthenium(II) dichloride (H_2**L**-Ru) was synthesized as described previously.[26] To a 4 mL glass vial was added 0.5 mL of $HfCl_4$ solution (2.0 mg/mL in DMF), 0.5 mL of H_2**L**-Ru solution (4 mg/mL in DMF), 2 μL of TFA, and 5μL of water. The reaction mixture was kept in an 80 °C oven for 24 hours. The orange precipitate was collected by centrifugation and washed with DMF and ethanol. The yield was 52% based on Hf.

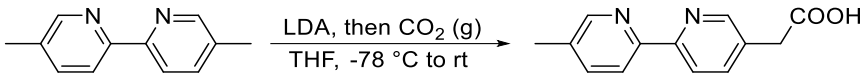

Synthesis of 2-(5'-methyl-[2,2'-bipyridin]-5-yl)acetic acid (H-MBA). H-MBA was synthesized by a modified literature method.[27] Di-isopropylamine (0.8 mL, 6.5 mmol) was dissolved in THF (3 mL) and cooled to –78 °C before the dropwise addition of *n*-BuLi (3.5 mL 5.6 mmol). The resulting solution was stirred for 30 mins at –78 °C before the quick addition of a solution of 5,5'-dimethyl-2,2'-bipyridine (1.0 g, 5.5 mmol) in THF (12 mL) and the resultant mixture was stirred for 2 additional hours at this temperature. Dry CO_2 was then bubbled through at the same temperature for 1 h and the mixture was warmed to ambient temperature with CO_2 still being bubbled through. Ether (100 mL) was added to the resulting semisolid white mass, and the mixture was extracted with 1 M NaOH aqueous solution (20 mL × 3). The alkaline layer was acidified to pH 1 with concentrated HCl and then extracted with ether (20 mL × 3). The acidic solution was buffered to pH 5 with sodium acetate. After removing the solvent, the crude product was subjected to column chromatography (SiO_2, *i*-PrOH/H_2O, 8:1). After removal of the solvent under reduced pressure, the resulting solid was extracted into MeOH (50 mL), dried in vacuo and recrystallized from EtOH with the addition of hexanes to yield pure product as a white solid (0.92 g, 74%). ^{1}H NMR (500 MHz, DMSO-d_6): δ 8.49 (d, J = 2.0 Hz, 2 H), 8.24 (d, J = 8.0 Hz, 1 H), 8.23 (d, J = 8.0 Hz, 1 H), 7.75 (d d, J_1 = 8.0 Hz, J_2 = 2.0 Hz, 1 H), 7.72 (d d, J_1 = 8.0 Hz, J_2 = 2.0 Hz, 1 H), 3.45 (s, 2 H), 2.34 (s, 3 H). ^{13}C NMR (125 MHz, DMSO-d_6): δ 173.2, 153.1, 152.9, 149.8, 149.4, 137.8, 137.5, 134.0, 133.1, 119.7, 119.4, 41.0, 17.8.

Synthesis of Hf_{12}-Ru-MBA. To a 4 mL glass vial was added 1 mL of Hf_{12}-Ru suspension (2 mM based on Hf in EtOH) and 1 mg of H-MBA. The reaction mixture was stirred overnight at

room temperature. The orange precipitate was collected by centrifugation and washed with ethanol twice.

Analysis of digested Hf_{12}-Ru-MBA by ^{1}H NMR and ^{19}F NMR. To determine the ratio of the MBA ligands and **L**-Ru ligands in Hf_{12}-Ru-MBA, 2.0 mg of Hf_{12}-Ru-MBA was dried under vacuum and then digested in a solution of 500 μL DMSO-d_6 and 50 μL D_3PO_4. The mixture was then sonicated for 10 min, added 50 μL D_2O, and analyzed by ^{1}H NMR and ^{19}F NMR.

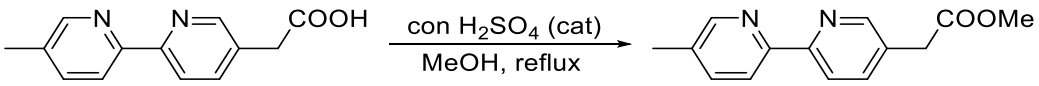

Synthesis of MeMBA. To H-MBA (456 mg, 2 mmol) in methanol (20 mL) was added conc. H_2SO_4 (0.5 mL) dropwise and slowly, and the solution was stirred at reflux for 24 hours. After being cooled to room temperature, the solution was neutralized with saturated $NaHCO_3$ aqueous solution and then concentrated under reduced pressure. The crude product was dissolved in EtOAc (30 mL) and washed with deionized H_2O (10 mL × 2) and brine (10 mL) and dried over anhydrous sodium sulfate. After removing the solvent, the crude product was subjected to column chromatography (SiO_2, CH_2Cl_2/MeOH, 20:1) to give the pure product as a white powder (460 mg, 95%). ^{1}H NMR (500 MHz, $CDCl_3$): δ 8.56 (d, J = 2.0 Hz, 1 H), 8.50 (d, J = 2.0 Hz, 1 H), 8.33 (d, J = 8.0 Hz, 1 H), 8.27 (d, J = 8.0 Hz, 1 H), 7.75 (d d, J_1 = 8.0 Hz, J_2 = 2.0 Hz, 1 H), 7.62 (d d, J_1 = 8.2 Hz, J_2 = 2.0 Hz, 1 H), 3.72 (s, 2 H), 3.69 (s, 2 H), 2.39 (s, 4 H). ^{13}C NMR (125 MHz, $CDCl_3$): δ 171.1, 155.2, 153.3, 149.6, 149.6, 137.7, 137.4, 133.4, 129.4, 120.5, 120.5, 77.4, 77.2, 76.9, 52.2, 38.1, 18.3.

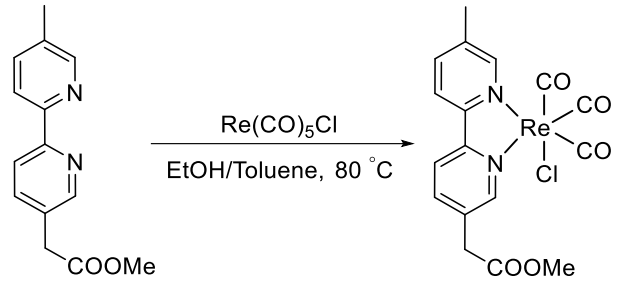

Synthesis of Re(MeMBA)(CO)$_3$Cl. MeMBA (45.6 mg, 0.2 mmol) and $Re(CO)_5Cl$ (72 mg, 0.2 mmol) were mixed in a 20 mL dry ethanol/toluene (1:1) solution and added to a 50 mL high-pressure tube. The tube was sealed and heated at 80 ºC for two days. After removal of most of the solvent, the crude product was filtrated and then washed with toluene to afford a yellow powder. Yield: 102 mg, 91%. ^{1}H NMR (DMSO-d_6, 500 MHz): δ 8.90 (s, 1H), 8.88 (s, 1H), 8.10 (d, 1H), 8.06 (m, 2H), 7.85 (s, 1H), 3.79-3.80 (m, 5H), 2.52 (s, 3H). IR, ν(CO): 2015, 1902, 1889 cm^{-1} (**Figure 9-9**).

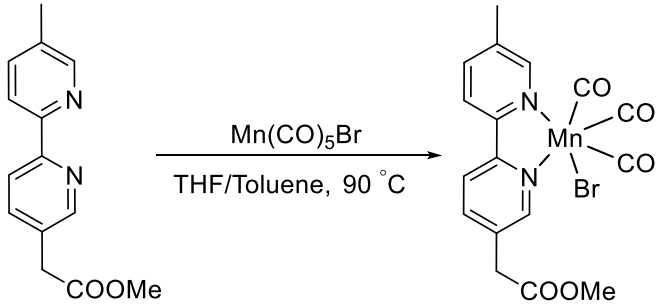

Synthesis of Mn(MeMBA)(CO)$_3$Br. MeMBA (45.6 mg, 0.2 mmol) and $Mn(CO)_5Br$ (0.2 mmol, 56.4 mg) were dissolved in 40 mL of tetrahydrofuran and toluene (1:1). The solution was transferred to a 100 mL round bottom flask and heated at 90 ºC under N_2 for 2 h. After removing most of the solvent, the crude product was filtrated and then washed with toluene to afford a brown powder. Yield: 67.4 mg, 71%. NMR spectra were uninformative due to the paramagnetic nature of Mn(MeMBA)(CO)$_3$Br. IR, ν(CO): 2021, 1940, 1915 cm^{-1} (**Figure 9-9**).

Synthesis of Hf_{12}-Ru-Re. To a 4 mL glass vial was added 1 mL of Hf_{12}-Ru-MBA suspension (2.0 mM based on Hf in EtOH) and 1 mg of 1.0 mg of $Re(CO)_5Cl$. The reaction mixture was stirred overnight at 70 ºC. The orange precipitate was collected by centrifugation and washed with ethanol twice. The yield for metalation of MBA was ~100% based on the ratio between Re and Hf (Re:Hf = 1:1), as determined by ICP-MS.

Synthesis of Hf_{12}-Ru-Mn. To a 4 mL glass vial was added 1 mL of Hf_{12}-Ru-MBA suspension (2.0 mM based on Hf in ether) and 1 mg of 1.0 mg of $Mn(CO)_5Br$. The reaction mixture was stirred overnight at room temperature. The orange precipitate was collected by centrifugation and washed with ether, THF, and ethanol. The yield for metalation of MBA was 82% based on the ratio between Mn and Hf, (Mn:Hf = 0.82:1), as determined by ICP-MS.

Photocatalytic CO_2 reduction reaction. Photocatalytic CO_2 reduction reaction was carried out in an external illumination type reaction vessel with a magnetic stirrer. Samples were prepared in 4.5 mL septum-sealed glass vials. Each sample was made up to a total volume of 2 mL of 1.9 mL CH_3CN, 0.1 mL TEOA, and 0.1M sacrificial agent (BIH: 45.0 mg or BNAH: 42.9 mg). Hf_{12}-Ru-Re or Hf_{12}-Ru-Mn was added to the solution to make the final concentration of 0.1 μM based on Re or Mn. Vials were capped and CO_2 was bubbled through for 5-10 min to ensure complete air removal and replacement by CO_2. The solution was irradiated by a 230 W Xenon lamp light (300 mW/cm^2) with a 400 nm filter. After the CO_2 reduction reaction, the gas in the headspace of the vial was analyzed by GC with FID and TCD detector to determine the amount of CO generated. To detect the amount of HCOOH generated by HPLC, a HCOOH calibration curve was made based on the concentration range between 0 μM and10 μM. Each sample was prepared by dissolving pure HCOOH in MeCN to make the final concentration

from 1 μM to 10 μM. All of the samples were run three times to get the average of the peak areas. After detection of CO by GC, reaction solutions were filtered to remove the residual solid and further analyzed by HPLC to determine the amount of HCOOH.

Recycle experiment. Recycle experiment was carried out in an external illumination type reaction vessel with a magnetic stirrer. Sample was prepared in 4.5 mL septum-sealed glass vial. A mixture of 1.9 mL CH_3CN, 0.1 mL TEOA, 0.1M sacrificial agent (BIH: 45.0mg) and Hf_{12}-Ru-Re was added to the solution to make the final concentration of 0.1 μM based on Re. Vial was capped and CO_2 was bubbled through for 5-10 min to ensure complete air removal and replacement by CO_2. The solution was irradiated by a 230 W Xenon lamp light (300 mW/cm^2) with a 400 nm filter. After reacting for 12 h, the gas in the headspace of the vial was analyzed and additional BIH was added into the vial to make saturated BIH solution. The mixture was again bubbled with CO_2 and the reaction was repeated for a total of 5 runs.

Phosphorescence quenching. Phosphorescence quenching of Hf_{12}-Ru. To establish whether the excited Hf_{12}-Ru was quenched reductively by BIH or oxidatively by $Re(MeMBA)(CO)_3Cl$, the phosphorescence spectra of Hf_{12}-Ru were measured with addition of different equivalent of BIH or $Re(MeMBA)(CO)_3Cl$.

Sunlight-driven CO_2 reduction reaction. Photocatalytic CO_2 reduction reaction was carried out in an external illumination type reaction vessel with a magnetic stirrer. Samples were prepared in 4.5 mL septum-sealed glass vials. Each sample was made up to a volume of 2 mL of 1.9 mL CH_3CN, 0.1 mL TEOA, and 0.1 M sacrificial agent (BIH: 45.0 mg). Hf_{12}-Ru-Re was added to the solution to make the final concentration of 0.1 μM based on Re Vials were capped and CO_2 was bubbled through for 5-10 min to ensure complete air removal and replacement

by CO_2. The vial was placed next to the laboratory window which faces the sun for 6 h (from 11 am to 5 pm). After the CO_2 reduction reaction, the gas in the headspace of the vial was analyzed by GC with FID and TCD detector to determine the amount of CO generated.

9.5 References

1. Zhang, T.; Lin, W., Metal–organic frameworks for artificial photosynthesis and photocatalysis. *Chem. Soc. Rev.* **2014,** *43* (16), 5982-5993.
2. Cui, Y.; Yue, Y.; Qian, G.; Chen, B., Luminescent functional metal–organic frameworks. *Chem. Rev.* **2011,** *112* (2), 1126-1162.
3. Cao, L.; Lin, Z.; Peng, F.; Wang, W.; Huang, R.; Wang, C.; Yan, J.; Liang, J.; Zhang, Z.; Zhang, T., Self-Supporting Metal–Organic Layers as Single-Site Solid Catalysts. *Angew. Chem. Int. Ed.* **2016,** *55* (16), 4962-4966.
4. Lan, G.; Ni, K.; Xu, R.; Lu, K.; Lin, Z.; Chan, C.; Lin, W., Nanoscale Metal–Organic Layers for Deeply Penetrating X-ray-Induced Photodynamic Therapy. *Angew. Chem.* **2017,** *129* (40), 12270-12274.
5. Lin, Z.; Thacker, N. C.; Sawano, T.; Drake, T.; Ji, P.; Lan, G.; Cao, L.; Liu, S.; Wang, C.; Lin, W., Metal–organic layers stabilize earth-abundant metal–terpyridine diradical complexes for catalytic C–H activation. *Chem. Sci.* **2018,** *9* (1), 143-151.
6. Zhao, M.; Wang, Y.; Ma, Q.; Huang, Y.; Zhang, X.; Ping, J.; Zhang, Z.; Lu, Q.; Yu, Y.; Xu, H., Ultrathin 2D metal–organic framework nanosheets. *Adv. Mater.* **2015,** *27* (45), 7372-7378.
7. Berardi, S.; Drouet, S.; Francas, L.; Gimbert-Suriñach, C.; Guttentag, M.; Richmond, C.; Stoll, T.; Llobet, A., Molecular artificial photosynthesis. *Chem. Soc. Rev.* **2014,** *43* (22), 7501-7519.
8. Appel, A. M.; Bercaw, J. E.; Bocarsly, A. B.; Dobbek, H.; DuBois, D. L.; Dupuis, M.; Ferry, J. G.; Fujita, E.; Hille, R.; Kenis, P. J., Frontiers, opportunities, and challenges in biochemical and chemical catalysis of CO2 fixation. *Chem. Rev.* **2013,** *113* (8), 6621-6658.
9. Roy, S. C.; Varghese, O. K.; Paulose, M.; Grimes, C. A., Toward solar fuels: photocatalytic conversion of carbon dioxide to hydrocarbons. *Acs Nano* **2010,** *4* (3), 1259-1278.
10. Sakimoto, K. K.; Wong, A. B.; Yang, P., Self-photosensitization of nonphotosynthetic bacteria for solar-to-chemical production. *Science* **2016,** *351* (6268), 74-77.
11. Yu, J.; Low, J.; Xiao, W.; Zhou, P.; Jaroniec, M., Enhanced photocatalytic CO2-reduction activity of anatase TiO2 by coexposed {001} and {101} facets. *J. Am. Chem. Soc.* **2014,** *136* (25), 8839-8842.
12. Kumar, B.; Llorente, M.; Froehlich, J.; Dang, T.; Sathrum, A.; Kubiak, C. P., Photochemical and photoelectrochemical reduction of CO2. *Annu. Rev. Phys. Chem.* **2012,** *63*, 541-569.
13. Diercks, C. S.; Liu, Y.; Cordova, K. E.; Yaghi, O. M., The role of reticular chemistry in the design of CO 2 reduction catalysts. *Nat. Mater.* **2018**, 1.
14. McDaniel, N. D.; Bernhard, S., Solar fuels: Thermodynamics, candidates, tactics, and figures of merit. *Dalton Trans.* **2010,** *39* (42), 10021-10030.

15. Hou, J.; Cao, S.; Wu, Y.; Liang, F.; Ye, L.; Lin, Z.; Sun, L., Perovskite-based nanocubes with simultaneously improved visible-light absorption and charge separation enabling efficient photocatalytic CO2 reduction. *Nano Energy* **2016,** *30*, 59-68.
16. Hawecker, J.; Lehn, J.-M.; Ziessel, R., Efficient photochemical reduction of CO 2 to CO by visible light irradiation of systems containing Re (bipy)(CO) 3 X or Ru (bipy) 3 2+–Co 2+ combinations as homogeneous catalysts. *J. Chem. Soc., Chem. Commun.* **1983,** (9), 536-538.
17. Morris, A. J.; Meyer, G. J.; Fujita, E., Molecular approaches to the photocatalytic reduction of carbon dioxide for solar fuels. *Acc. Chem. Res.* **2009,** *42* (12), 1983-1994.
18. Takeda, H.; Ishitani, O., Development of efficient photocatalytic systems for CO2 reduction using mononuclear and multinuclear metal complexes based on mechanistic studies. *Coord. Chem. Rev.* **2010,** *254* (3-4), 346-354.
19. Windle, C. D.; Perutz, R. N., Advances in molecular photocatalytic and electrocatalytic CO2 reduction. *Coord. Chem. Rev.* **2012,** *256* (21-22), 2562-2570.
20. Won, D.-I.; Lee, J.-S.; Ji, J.-M.; Jung, W.-J.; Son, H.-J.; Pac, C.; Kang, S. O., Highly Robust Hybrid Photocatalyst for Carbon Dioxide Reduction: Tuning and Optimization of Catalytic Activities of Dye/TiO2/Re (I) Organic–Inorganic Ternary Systems. *J. Am. Chem. Soc.* **2015,** *137* (42), 13679-13690.
21. Gholamkhass, B.; Mametsuka, H.; Koike, K.; Tanabe, T.; Furue, M.; Ishitani, O., Architecture of Supramolecular Metal Complexes for Photocatalytic CO2 Reduction: Ruthenium− Rhenium Bi-and Tetranuclear Complexes. *Inorg. Chem.* **2005,** *44* (7), 2326-2336.
22. Tamaki, Y.; Ishitani, O., Supramolecular Photocatalysts for the Reduction of CO2. *ACS Catal.* **2017,** *7* (5), 3394-3409.
23. Dai, R.; Peng, F.; Ji, P.; Lu, K.; Wang, C.; Sun, J.; Lin, W., Electron crystallography reveals atomic structures of metal–organic nanoplates with M12 (μ3-O) 8 (μ3-OH) 8 (μ2-OH) 6 (M= Zr, Hf) secondary building units. *Inorg. Chem.* **2017,** *56* (14), 8128-8134.
24. PXRD pattern was simulated by complete integrating method in real space.
25. Grills, D. C.; Ertem, M. Z.; McKinnon, M.; Ngo, K. T.; Rochford, J., Mechanistic aspects of CO2 reduction catalysis with manganese-based molecular catalysts. *Coord. Chem. Rev.* **2018,** *374*, 173-217.
26. Zhang, Z.-M.; Zhang, T.; Wang, C.; Lin, Z.; Long, L.-S.; Lin, W., Photosensitizing metal–organic framework enabling visible-light-driven proton reduction by a Wells–Dawson-type polyoxometalate. *J. Am. Chem. Soc.* **2015,** *137* (9), 3197-3200.
27. Davis, H. J.; Genov, G. R.; Phipps, R. J., meta-Selective C− H Borylation of Benzylamine-, Phenethylamine-, and Phenylpropylamine-Derived Amides Enabled by a Single Anionic Ligand. *Angew. Chem.* **2017,** *129* (43), 13536-13540.

Chapter 10. Metal-Organic Layers as Multifunctional 2D Nanomaterials for Enhanced Photoredox Catalysis

10.1 Introduction

As a dispersible monolayered version of MOFs,[1-15] MOLs have recently emerged as a novel class of molecular 2D materials with tremendous potential for catalytic applications.[16-18] MOLs not only retain many of the advantages offered by MOFs such as structural regularity/tunability and compositional diversity but also possess the strengths of 2D materials such as graphene and transition metal dichalcogenides (TMDCs). Importantly, unlike graphene and TMDCs, disparate functionalities can be installed onto the surfaces of MOLs in a spatially controlled fashion by modifying distinct functional groups on their SBUs and bridging ligands to accomplish synergistic complex functions (**Figure 10-1**). In this Chapter, we report the design of a new multifunctional MOL, Hf_{12}-Ir-Ni, for highly efficient photoredox catalysis by taking advantage of the proximity between photosensitizing bridging ligands and Ni catalysts on the SBUs.

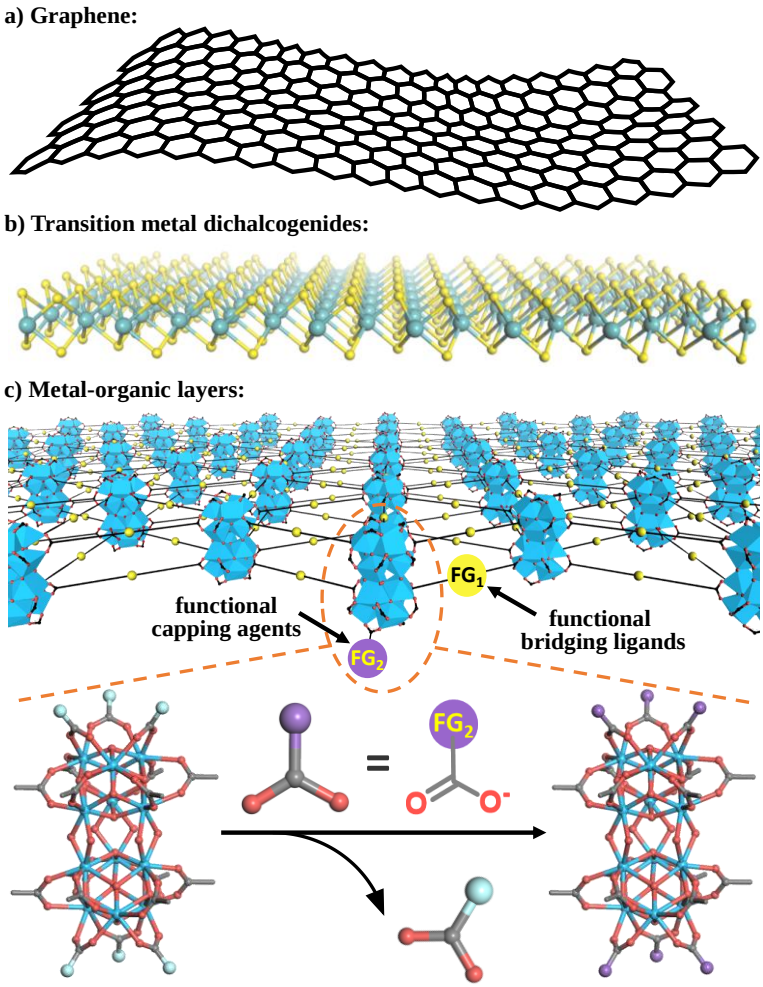

Figure 10-1. Schematic depiction of MOLs and postsynthetic surface modification. Schematic depiction of graphene (a), metal dichalcogenides (b), and MOLs (c), a new kind of 2D materials, in which disparate functional groups (FGs) can be hierarchically incorporated into laterally bridged linkers and vertically coordinated capping agents. Zoomed-in view of postsynthetic surface modification of MOLs with functional capping agents through carboxylate exchange.

10.2 Result and discussion

10.2.1 Synthesis and characterization

Hf_{12}-Ir-Ni is a 2D network built from Hf_{12} SBUs and photosensitizing $Ir(DBB)[dF(CF_3)ppy]_2^+$ (DBB-Ir-F bridging ligands). The SBUs are vertically terminated by catalytically active $Ni(MBA)Cl_2$ [MBA-Ni, MBA = 2-(4'-methyl-[2,2'-bipyridin]-4-yl)acetate] capping agents to afford a monolayer structure. Hf_{12}-Ir-Ni was synthesized in three steps (**Figure 10-2**).

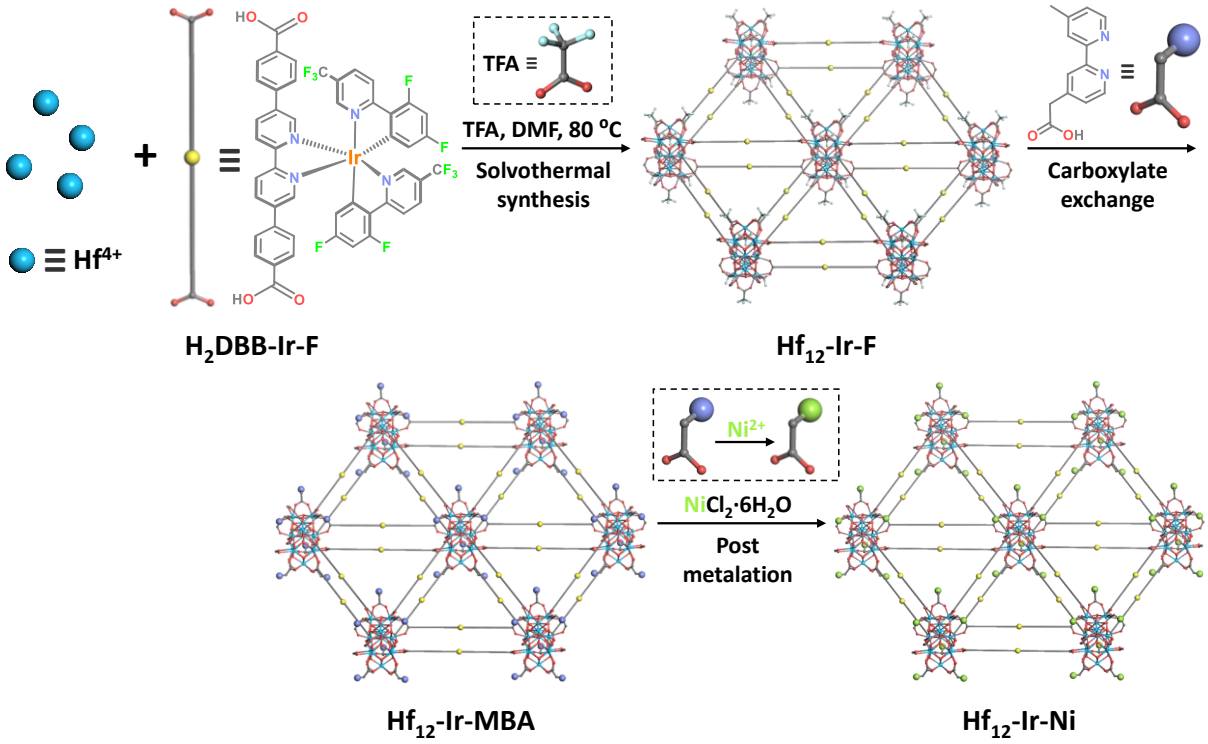

Figure 10-2. Schematic showing the synthetic route to Hf_{12}-Ir-Ni.

First, Hf_{12}-Ir-F was prepared through a solvothermal reaction between $HfCl_4$ and H_2DBB-Ir-F in DMF at 80 ºC with TFA and water as modulators. Hf_{12} SBUs were vertically terminated by TFA capping agents and laterally bridged by DBB-Ir-F ligands to afford an infinite 2D network of the formula $Hf_{12}(\mu_3\text{-}O)_8(\mu_3\text{-}OH)_8(\mu_2\text{-}OH)_6(DBB\text{-}Ir\text{-}F)_6(TFA)_6$. Second, MBA capping agents were installed on the surface of Hf_{12}-Ir-F by replacing TFA groups to afford Hf_{12}-Ir-MBA with the formula of $Hf_{12}(\mu_3\text{-}O)_8(\mu_3\text{-}OH)_8(\mu_2\text{-}OH)_6(DBB\text{-}Ir\text{-}F)_6(MBA)_6$. Finally, Hf_{12}-Ir-Ni was obtained by metalating the MBA capping agents on Hf_{12}-Ir-MBA to generate catalytically active MBA-Ni. Hf_{12}-Ir-Ni has a formula of $Hf_{12}(\mu_3\text{-}O)_8(\mu_3\text{-}OH)_8(\mu_2\text{-}OH)_6(DBB\text{-}Ir\text{-}F)_6(MBA\text{-}Ni)_6$ (**Figure 10-2**).

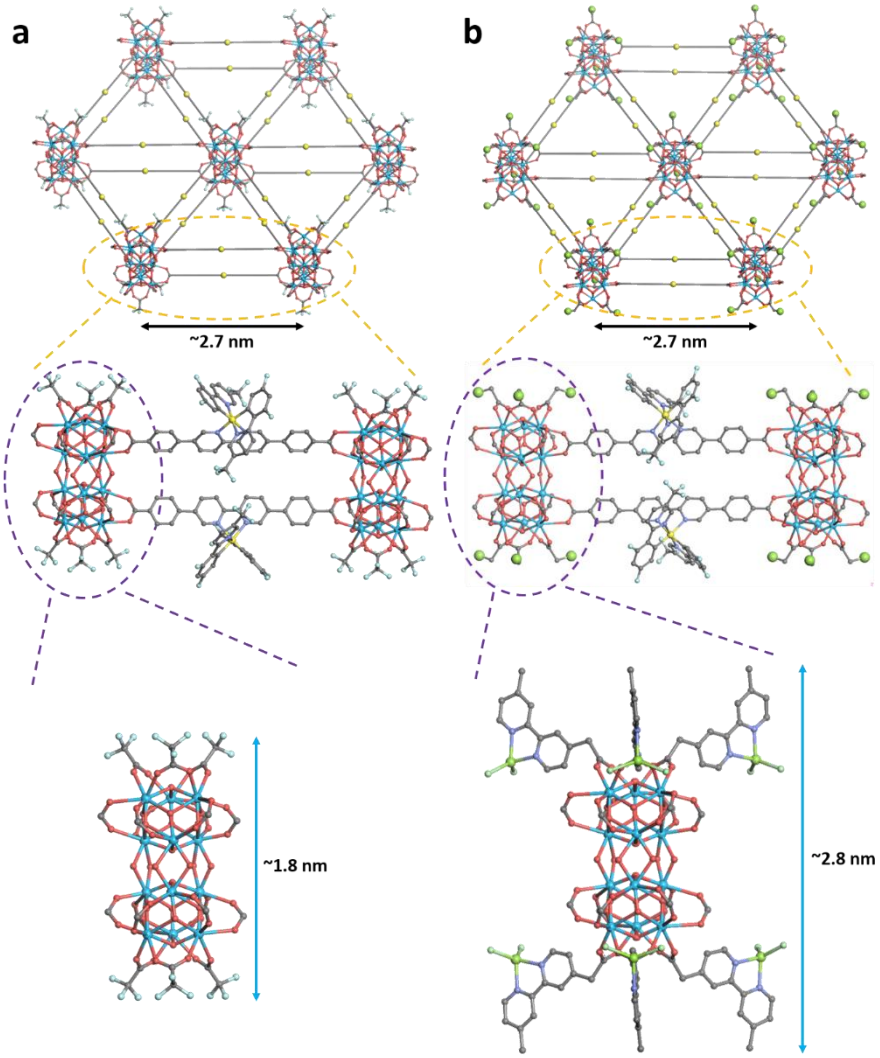

Figure 10-3. Modeled structures of Hf_{12}-Ir-F and Hf_{12}-Ir-Ni. Modeled structures of Hf_{12}-Ir-F (a) and Hf_{12}-Ir-Ni (b). The height of Hf_{12} clusters capped by trifluoroacetate in Hf_{12}-Ir-F and by MBA-Ni in Hf_{12}-Ir-Ni were measured to be ~1.8 nm and ~2.8 nm, respectively.

The monolayer structure of Hf_{12}-Ir-F was confirmed by a combination of TEM (**Figure 10-4a**) and AFM (**Figure 10-4d,e**), with a diameter of ~300 nm and a thickness of ~1.8 nm. This thickness is consistent with the modeled height of Hf_{12} clusters capped with TFA groups (~1.8 nm, **Figure 10-3a**). DLS measurements gave a number-averaged diameter of 116.2 ± 7.3 nm for Hf_{12}-Ir-F (**Figure 10-4f**). The proposed **kgd** topological structure of Hf_{12}-Ir-F was supported by PXRD studies and HRTEM imaging. Hf_{12}-Ir-F displayed a PXRD pattern similar to that simulated based on the structure model of the Hf_{12} MOL (**Figure 10-4c**) whereas

HRTEM and its FFT (**Figure 10-4b**) revealed a six-fold symmetry and a Hf_{12}-Hf_{12} distance of 2.7 nm, matching well with the modeled. In addition, the ^{1}H NMR spectrum of digested Hf_{12}-Ir-F showed only signals corresponding to DBB-Ir-F. TGA of Hf_{12}-Ir-F showed a weight loss of 62.4% in the 350-800 °C range, corresponding to its decomposition to (12 HfO_2 + 6 IrO_2) (61.5% expected). Finally, UV-Vis and luminescence (**Figure 10-5**) spectra showed that Hf_{12}-Ir-F displayed the same characteristic absorption, excitation, and emission spectra as Me_2DBB-Ir, suggesting the photosensitizing ability of Hf_{12}-Ir-F.

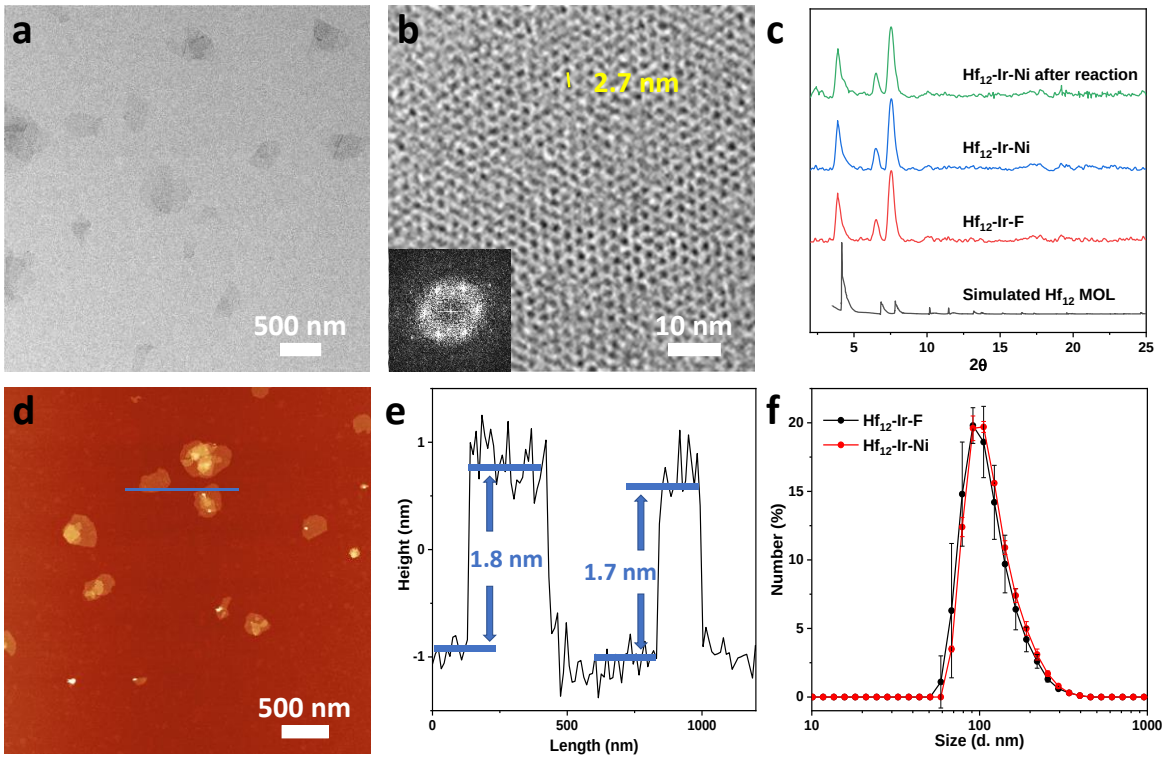

Figure 10-4. Characterization of Hf_{12}-Ir-F. TEM image (a), HRTEM image with the FFT pattern in the inset (b), AFM topography (d) and its height profile (e), and number-averaged diameter of Hf_{12}-Ir-F. (c) PXRD patterns of Hf_{12}-Ir-F and Hf_{12}-Ir-Ni, freshly prepared or after photoredox reaction, in comparison to the simulated pattern for the Hf_{12} MOL.

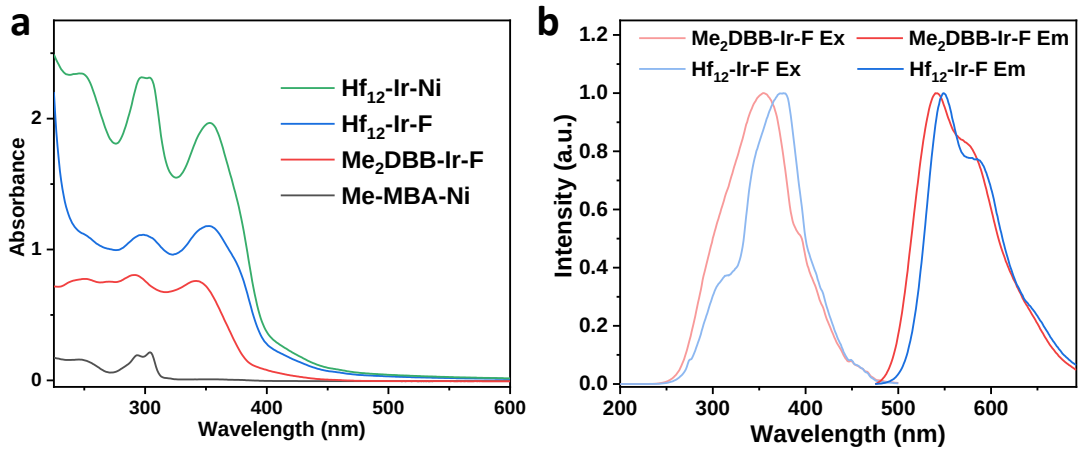

Figure 10-5. UV-Vis and luminescence spectra. (a) UV-Vis spectra of Hf_{12}-Ir-Ni, Hf_{12}-Ir-F, Me_2DBB-Ir-F, and Me-MBA-Ni. (b) Normalized excitation (Ex) and emission (Em) spectra of Hf_{12}-Ir-F in comparison to those of Me_2DBB-Ir-F.

Hf_{12}-Ir-F was further functionalized through exchanging weakly coordinating TFA groups on the SBUs with MBA capping agents to afford Hf_{12}-Ir-MBA. The ^{1}H NMR spectrum of digested Hf_{12}-Ir-MBA showed an MBA to DBB-Ir-F molar ratio of ~1:1 (**Figure 10-6**), indicating complete replacement of TFA groups.

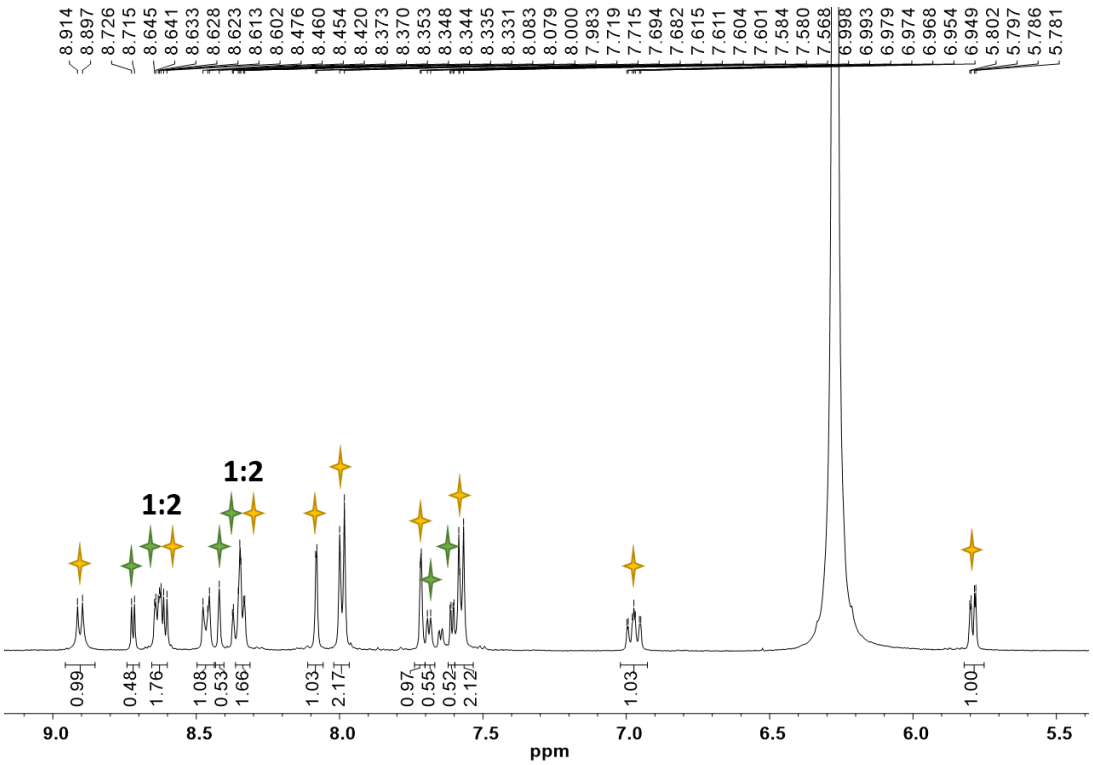

Figure 10-6. NMR spectrum of digested Hf_{12}-Ir-MBA. The peaks marked with yellow and green stars correspond to H_2DBB-Ir-F and H-MBA ligands, respectively.

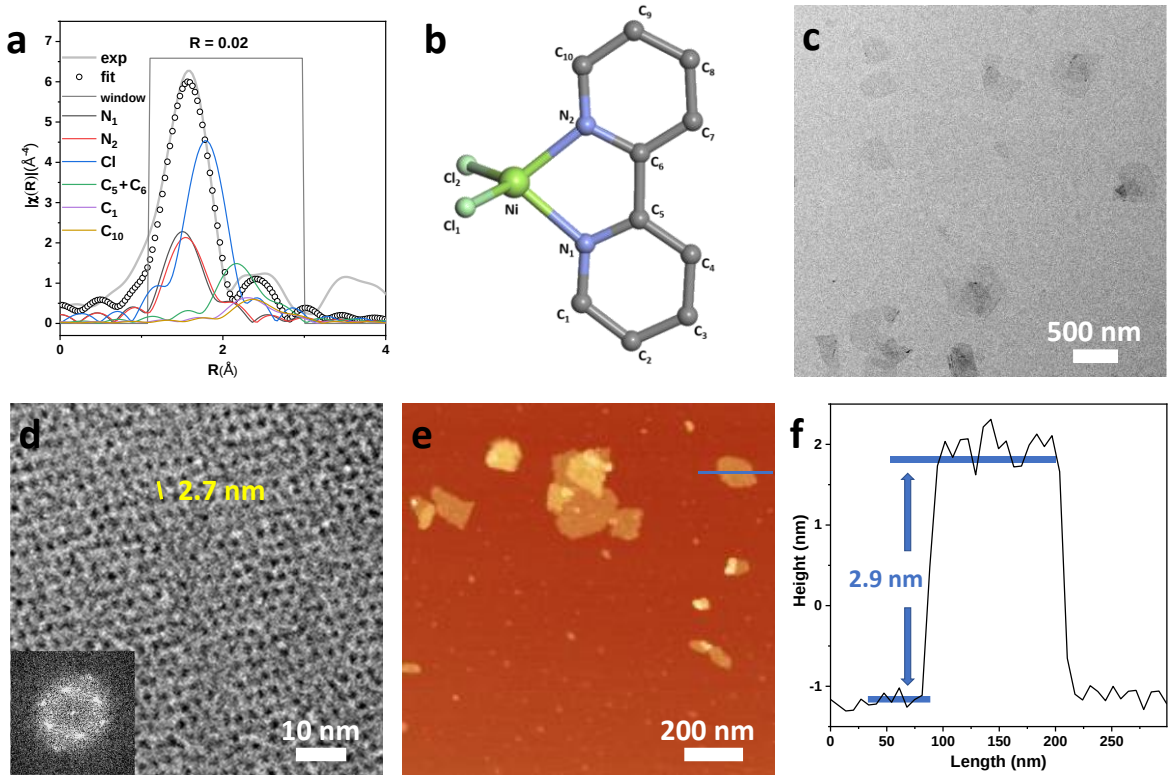

Figure 10-7. Characterization of Hf_{12}-Ir-Ni. EXAFS fitting (a), TEM image (c), HRTEM image with the FFT pattern in the inset (d), AFM topography (e) and its height profile (f) of Hf_{12}-Ir-F. (b) Molecular model of $Ni(bpy)Cl_2$ for EXAFS fitting of Hf_{12}-Ir-Ni.

After metalation of the MBA sites on Hf_{12}-Ir-MBA with $NiCl_2$, we used X-ray absorption spectroscopy to characterize the coordination environment of the MBA-Ni species. Hf_{12}-Ir-Ni showed similar EXAFS features as Me-MBA-Ni, both of which were well fit to the molecular model of tetrahedrally coordinated $Ni(bpy)Cl_2$ (**Figure 10-7a,b**). ICP-MS analysis indicated that Hf_{12}-Ir-Ni had a Ni to Hf molar ratio of ~1:2, matching the ratio expected for complete metalation of Hf_{12}-Ir-MBA by $NiCl_2$. The UV-Vis absorption spectrum of Hf_{12}-Ir-Ni displayed characteristic absorption peaks attributable to both Me_2DBB-Ir-F and Me-MBA-Ni (**Figure 10-5a**). TEM and AFM imaging indicated that Hf_{12}-Ir-Ni retained the monolayer structure and morphology of Hf_{12}-Ir-F, with a diameter of ~300 nm (**Figure 10-7c**) and a thickness of ~2.9 nm (**Figure 10-7e,f**). The increased thickness is consistent with the modeled height of the Hf_{12} cluster capped with MBA-Ni ligands (**Figure 10-3b**). DLS measurements also showed that

Hf_{12}-Ir-Ni exhibited a slightly increased size with the number-averaged diameter of 122.0 ± 2.3 nm (**Figure 10-4f**). Finally, Hf_{12}-Ir-Ni exhibited similar PXRD patterns (**Figure 10-4c**) and HRTEM images (**Figure 10-7d**) as Hf_{12}-Ir-F, indicating the retention of the **kgd** topological structure during postsynthetic capping ligand exchange and Ni coordination.

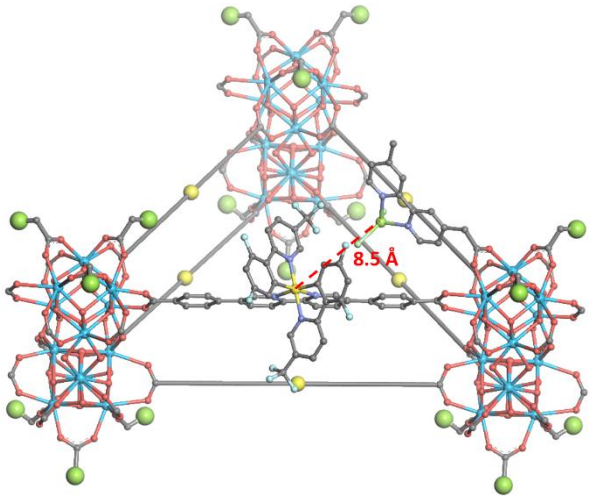

Figure 10-8. The distance between the centers of DBB-Ir-F to the center of the nearest MBA-Ni was measured to be 8.5 Å.

10.2.2 Photoredox reactions

On the basis of the proximity between photosensitizing DBB-Ir-F bridging ligands and catalytic MBA-Ni capping groups in Hf_{12}-Ir-Ni (~0.85 nm measured from the modeled structure, **Figure 10-8**), we proposed that electron transfer (ET) from photoexcited DBB-Ir-F to MBA-$NiCl_2$ could be greatly enhanced to promote efficiently photocatalytic reactions. The spatially isolated MBA-Ni sites on the MOL surface are also expected to prevent the formation of Ni^{I}-Ni^{II} dimers which were recently showed to lead to diminished photoredox reactivity.[19] Photocatalytic performance of Hf_{12}-Ir-Ni was evaluated in three important SET reactions, including C-S cross coupling between aryl iodides and thiols, C-O cross coupling between alcohols and aryl bromides, and C-C cross-coupling between potassium benzyltrifluoroborates and aryl bromides under mild conditions.[20-28]

Table 10-1. Hf_{12}-Ir-Ni catalyzed C-S, C-O, and C-C cross-coupling reactions. [a]Reactions were conducted at 0.50 mmol scale. [b]0.01 mol% catalyst was used. [c]Reactions were conducted at 0.25 mmol scale. [d] Reactions were conducted at 0.125 mmol scale.

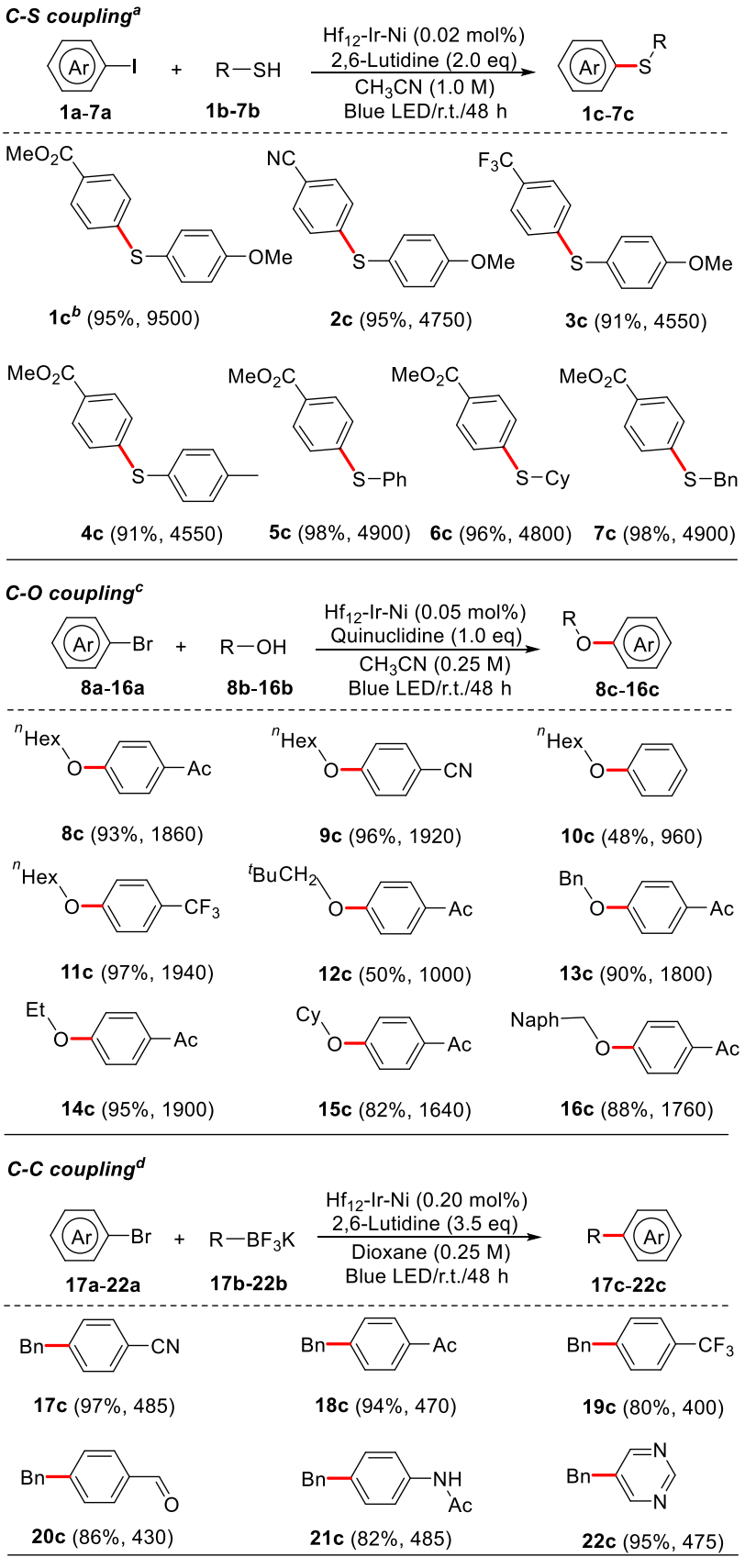

As shown in **Table 10-1**, Hf_{12}-Ir-Ni efficiently catalyzed all three SET reactions to afford C-S, C-O, and C-C coupling products in high yields. With very low loadings of Hf_{12}-Ir-Ni (0.02 mol%, 0.05 mol%, and 0.20 mol% based on Ni for C-S, C-O, and C-C couplings, respectively), the reactions proceeded smoothly to afford C-S, C-O, and C-C cross-coupled products with TONs of ~4500, ~1800, and ~450, respectively. In contrast, the homogenous control containing Me_2DBB-Ir-F and Me-MBA-Ni in a 1:1 molar ratio afforded low yields of cross-coupled products (**5c**: 7%, **15c**: 5%, and **20c**: 12% for C-S, C-O, and C-C cross-couplings, respectively) at the same catalyst loadings under identical conditions. 15-500 times more homogenous Ni catalysts than Hf_{12}-Ir-Ni were required to afford comparable yields of cross-coupling products.

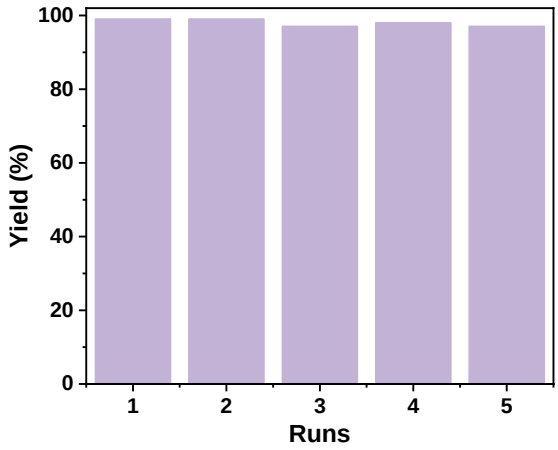

Figure 10-9. Yield of **5c** with recovered Hf_{12}-Ir-Ni in five consecutive runs.

Hf_{12}-Ir-Ni catalyzed cross-coupling reactions exhibit broad substrate scopes with good compatibility with a variety of functional groups including trifluoromethyl, cyano, carbonyl, esteryl, amidyl, naphthyl and pyrimidinyl groups. Neither acidic proton nor coordinating substituents on the substrates retarded the coupling reactions. Aryl halides bearing electron-withdrawing groups tended to afford coupling products in higher yields, due probably to their preference to undergo oxidative addition on the Ni(0) species. Hf_{12}-Ir-Ni was stable under photocatalytic reactions as demonstrated by the retention of PXRD pattern for the recovered

Hf_{12}-Ir-Ni (**Figure 10-4c**) and the leaching of <0.3% Hf, <0.6% Ir, and <0.1% Ni as determined by ICP-MS. We further showed that Hf_{12}-Ir-Ni could be recovered and used for at least five cycles without loss of catalytic activity (**Figure 10-9**). We have thus developed a versatile and recyclable MOL catalyst for C-C, C-O and C-S coupling reactions with broad substrate scopes.[20]

10.2.3 Mechanistic study

To understand how the proximity between DBB-Ir-F and MBA-Ni in Hf_{12}-Ir-Ni impacts the photocatalytic activities, we compared ET rates from photoexcited [DBB-Ir-F]* to NBA-Ni among three different systems: a homogenous solution of Me_2DBB-Ir-F and Me-MBA-Ni, a suspension of Hf_{12}-Ir-F and Me-MBA-Ni, and Hf_{12}-Ir-Ni. CV studies showed that [DBB-Ir-F]* could reduce MBA-Ni^{II} to MBA-Ni^{I} via ET. Upon light irradiation, ET from excited [DBB-Ir-F]* to MBA-Ni led to a decrease of luminescence intensity and lifetime of [DBB-Ir-F]*, which was determined by ET rates between [DBB-Ir-F]* and MBA-Ni. These luminescence quenching curves were fitted with the following Stern-Völmer equations with ET rates proportional to Stern-Völmer (K_{sv}) constants,

$$\frac{I_0}{I} = 1 + K_{SV}R_{Ni/Ir} \qquad \text{Eq } 10-1$$

$$\frac{\tau_0}{\tau} = 1 + K_{SV}R_{Ni/Ir} \qquad \text{Eq}10-2$$

where I_0/I and τ_0/τ are the ratios of luminescence intensity and lifetime of [DBB-Ir-F]* in the absence and presence of MBA-Ni compounds, respectively, and $R_{Ni/Ir}$ represents the ratio of MBA-Ni to DBB-Ir-F in each system.

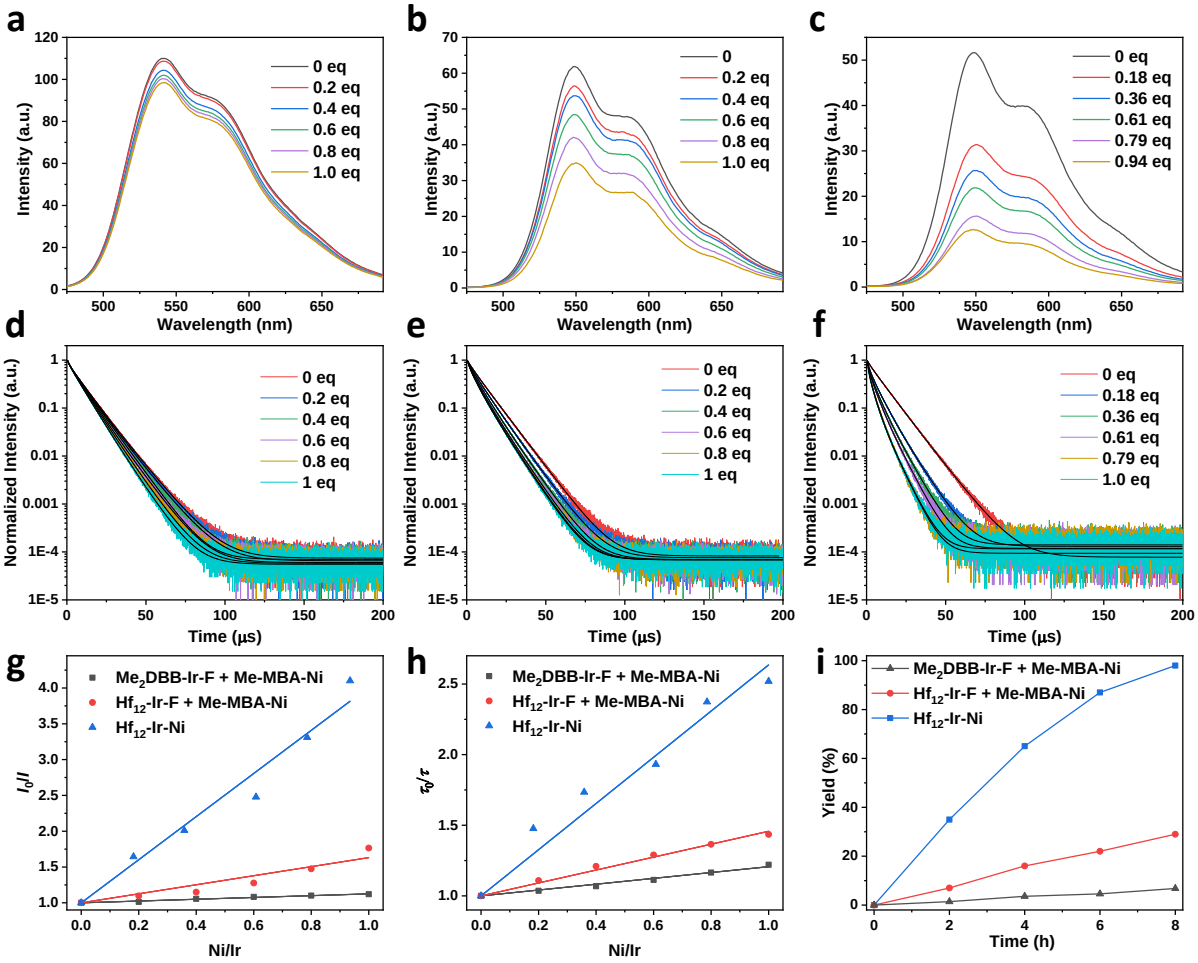

Figure 10-10. ET rate studies. Emission spectra (a) and normalized luminescence decay trace (d) of Me_2DBB-Ir-F with different amounts of added Me-MBA-Ni. Emission spectra (b) and normalized luminescence decay trace (e) of Hf_{12}-Ir-F with different amounts of added Me-MBA-Ni. Emission spectra (c) and normalized luminescence decay trace (f) of Hf_{12}-Ir-Ni with different Ni loading. Plots of I_0/I (g) and τ_0/τ (h) as a function of the ratio of MBA-Ni to DBB-Ir-F. (i) Time-dependent yields of **5c** with different catalytic systems.

While a drastic decrease in luminescence intensity was observed in Hf_{12}-Ir-Ni with increased loading of MBA-Ni, only moderate and minimal intensity decreases were observed when Me-MBA-Ni was added to Hf_{12}-Ir-F and Me_2DBB-Ir-F, respectively (**Figures 10-10a-c**). These luminescence intensity curves were well fitted with Eq 10-1 to afford K_{sv} values of 3.01 ± 0.15, 0.63 ± 0.06, and 0.12 ± 0.01 for Hf_{12}-Ir-Ni, Hf_{12}-Ir-F, and Me_2DBB-Ir-F, respectively (**Figure 10-10g**). Luminescence lifetimes showed similar behaviors and were fitted to Eq 10-2, affording K_{sv} values of 1.64 ± 0.09, 0.46 ± 0.01, and 0.21 ± 0.01 for Hf_{12}-Ir-Ni, Hf_{12}-Ir-F,

and Me_2DBB-Ir-F, respectively (**Figures 10-10d-f,h**). Hf_{12}-Ir-Ni thus shows a 25-fold increase in luminescence intensity quenching and an approximately 8-fold increase in luminescence lifetime quenching over the homogenous system (Me_2DBB-Ir-F + Me-MBA-Ni), suggesting an order of magnitude enhancement in intra-MOL ET from [DBB-Ir-F]* to MBA-Ni in Hf_{12}-Ir-Ni (**Figure 10-11**). Hf_{12}-Ir-F shows slightly enhanced ET from [DBB-Ir-F]* to Me_2MBA-Ni, likely due to attractive interactions between Hf_{12}-Ir-F and Me-MBA-Ni. To probe how enhanced ET affects the rates of photocatalytic reactions, we studied time-dependent yields of **5c** with the three catalytic systems: Hf_{12}-Ir-Ni and Hf_{12}-Ir-F + Me-MBA-Ni showed ~15-fold and ~4-fold increases in reaction rates over the homogenous control (Me_2DBB-Ir-F + Me-MBA-Ni), respectively (**Figure 10-10i**).

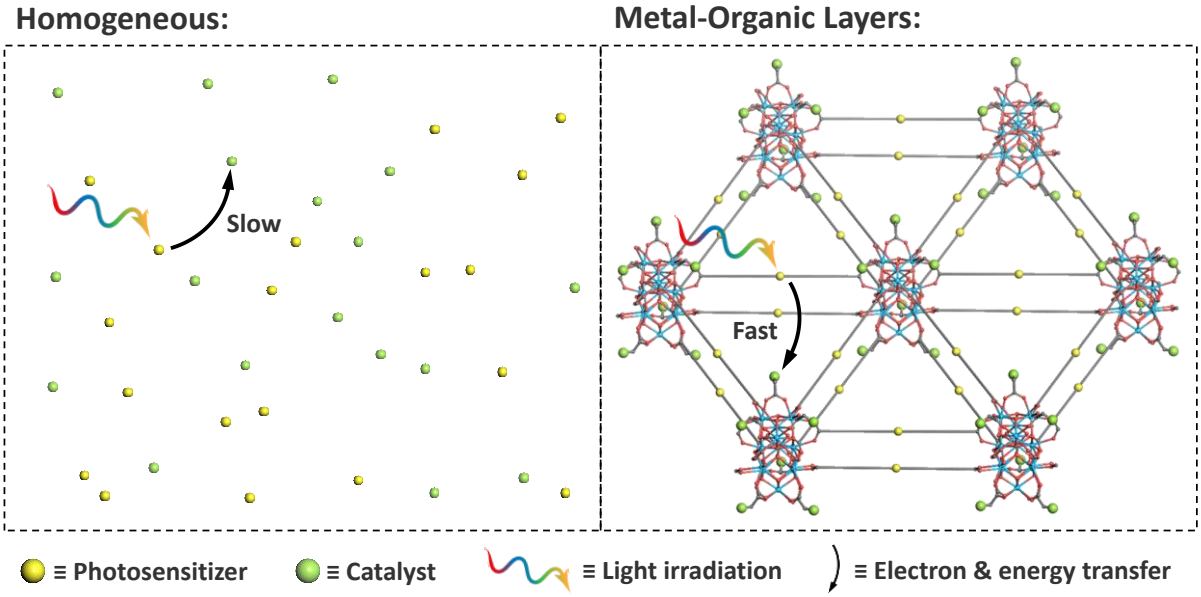

Figure 10-11. Schematic showing much enhanced SET process in Hf_{12}-Ir-Ni over the homogeneous system.

10.3 Conclusion

In this work, we developed a bottom-up approach to a new multifunctional MOL for efficient photoredox catalysis. Hierarchical installation of photosensitizing DBB-Ir-F bridging

ligands and catalytically active MBA-Ni capping agents in close proximity (~0.85 nm) on the Hf_{12}-Ir-Ni MOL significantly enhances electron transfer from [DBB-Ir-F]* to MBA-Ni^{II}, leading to a 15-fold increase in photoredox reactivity. Hf_{12}-Ir-Ni is highly effective in catalyzing important C-S, C-O, and C-C cross-coupling reactions with broad substrate scopes and TONs of ~4500, ~1900, and ~450, respectively. This work provides a general strategy for designing multifunctional MOLs for photocatalytic applications.

10.4 Methods

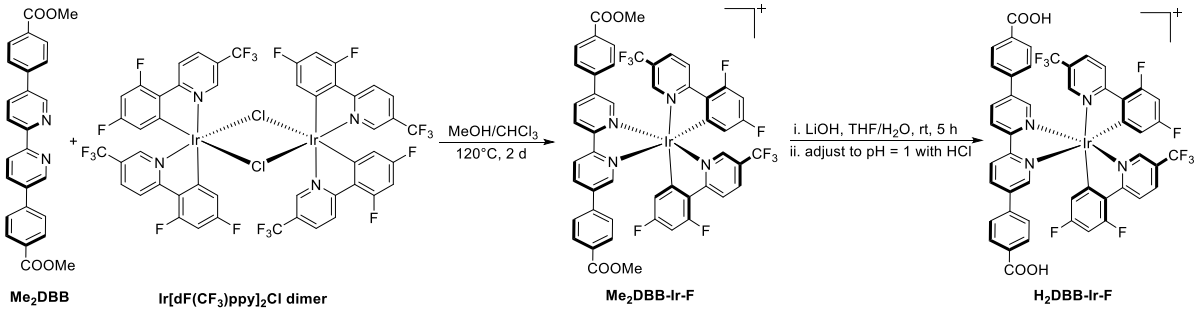

Synthesis of H_2DBB-Ir-F. $Ir(DBB)[dF(CF_3)ppy]_2^+$ [H_2DBB-Ir-F, DBB = 4,4'-di(4-benzoato)-2,2'-bipyridine; $dF(CF_3)ppy$ = 2-(2,4-difluorophenyl)-5-(trifluoromethyl)pyridine] was synthesized as shown above according to the literature report.[29] ^{1}H NMR (500 MHz, DMSO-d_6): δ 9.11 (d, 2 H), 8.77 (dd, 2 H), 8.48 (d, 2 H), 8.43 (d, 2 H), 8.15 (s, 2 H), 8.04 (d, 4 H), 7.81 (s, 2 H), 7.67 (d, 4 H), 7.11 (m, 2 H), 5.89 (dd, 2 H).

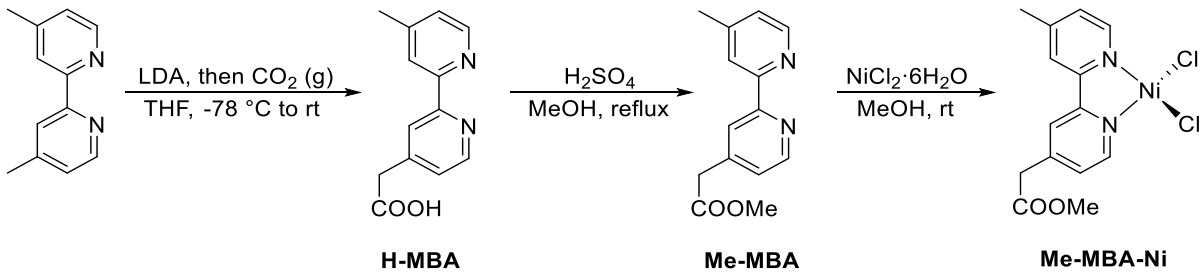

Synthesis of 2-(4'-methyl-[2,2'-bipyridin]-4-yl)acetic acid (H-MBA). Di-isopropylamine (0.8 mL, 6.5 mmol) was dissolved in THF (3 mL) and cooled to –78 °C before the dropwise

addition of *n*-BuLi (3.5 mL 5.6 mmol). The resulting solution was stirred for 30 mins at -78 °C before the quick addition of a solution of 4,4'-dimethyl-2,2'-bipyridine (1.0 g, 5.5 mmol) in THF (12 mL) and the resultant mixture was stirred for 2 additional hours at -78 °C. Dry CO_2 was then bubbled through at -78 °C for 1 h and the mixture was slowly warmed to ambient temperature with CO_2 still being bubbled through. Ether (100 mL) was added to the resulting semisolid white mass, and the mixture was extracted with 1 M NaOH aqueous solution (20 mL × 3). The alkaline layer was acidified to pH 1 with concentrated HCl and then extracted with ether (20 mL × 3). The acidic solution was buffered to pH 5 with sodium acetate. The resulting solid was extracted into MeOH (50 mL), dried in vacuo and recrystallized from EtOH with the addition of hexanes to yield the pure product as a white solid (0.85 g, 68%). ^{1}H NMR (500 MHz, DMSO-d_6): δ 8.51 (d, 1 H), 8.46 (d, 1 H), 8.25 (s, 1 H), 8.22(s,1 H), 7.25 (m, 2 H), 3.30 (s, 2 H), 2.41 (s, 3 H). HRMS (ESI-FT) *m*/*z* Calcd. for $C_{13}H_{13}N_2O_2^+$ ($[M + H^+]^+$) 229.0977, Found: 229.0980.

Synthesis of methy 2-(4'-methyl-[2,2'-bipyridin]-4-yl)acetate (Me-MBA). To H-MBA (912 mg, 4.0 mmol) in methanol (40 mL) was added conc. H_2SO_4 (1.0 mL) dropwise and slowly. The solution was stirred at reflux for overnight. After being cooled to room temperature, the solution was neutralized with saturated $NaHCO_3$ aqueous solution and then concentrated under reduced pressure. The crude product was dissolved in EtOAc (40 mL) and washed with deionized H_2O (20 mL × 2), and brine (20 mL) and dried over anhydrous sodium sulfate. The solvent was removed by rotary evaporation to yield the pure product as a white powder (890 mg, 92%). ^{1}H NMR (500 MHz, $CDCl_3$): δ 8.64 (d, 1 H), 8.55 (d, 1 H), 8.34 (s, 1 H), 8.25 (d, 1

H), 7.29 (d 1 H), 7.17 (d, 1 H), 3.75 (s, 2 H), 3.74 (s, 3 H), 2.46 (s, 3 H). HRMS (ESI-FT) *m/z* Calcd. for $C_{14}H_{15}N_2O_2^+$ ($[M + H^+]^+$) 243.1134, Found: 243.1127.

Synthesis of Ni(Me-MBA)Cl$_2$ (Me-MBA-Ni). MeMBA (60.5 mg, 0.25 mmol) and $NiCl_2 \cdot 6H_2O$ (59.4 mg, 0.25 mmol) were mixed in 5 mL ethanol. The mixture was stirred at room temperature for 4 hours. The solvent was then removed by rotary evaporation to afford Me-MBA-Ni as a green powder (68 mg, 96%).

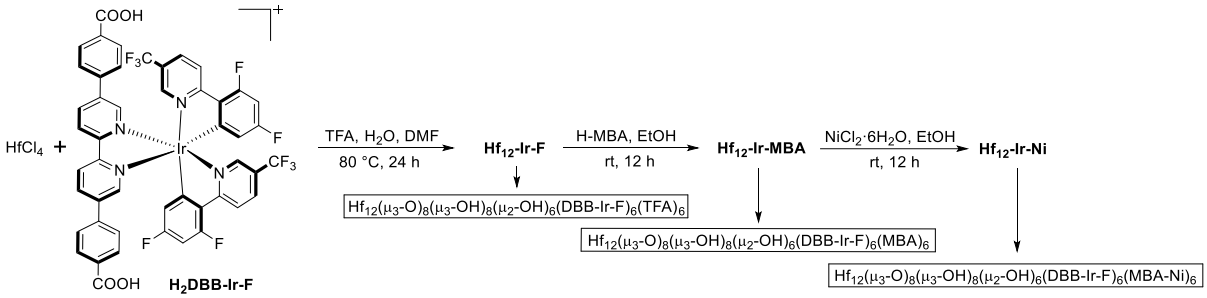

Synthesis of Hf$_{12}$-Ir-F. To a 4 mL glass vial was added 0.5 mL of $HfCl_4$ solution (2.0 mg/mL in DMF), 0.5 mL of H_2DBB-Ir-F solution (4.0 mg/mL in DMF), 2 μL of TFA, and 5μL of water. The reaction mixture was kept in an 80 °C oven for 24 hours. The yellow precipitate was collected by centrifugation and washed with DMF and ethanol. The yield was 52% based on Hf as determined by ICP-MS.

Digestion of Hf$_{12}$-Ir-F. 1.0 mg Hf_{12}-Ir-F was dried under vacuum. The resulting solid was then digested in a solution of 500 μL DMSO-d_6 and 50 μL D_3PO_4 and sonicated for 10 min. The mixture was then added 50 μL D_2O and analyzed by ^{1}H NMR.

Synthesis of Hf$_{12}$-Ir-MBA. To a 4 mL glass vial was added 1 mL of Hf_{12}-Ir-MBA suspension (2 mM based on Hf in EtOH) and 1 mg of H-MBA. The reaction mixture was stirred overnight at room temperature. The yellow precipitate was collected by centrifugation and washed with ethanol twice. The yield was 92% based on Hf as determined by ICP-MS.

Analysis of digested Hf_{12}-Ir-MBA by ^1H NMR. To determine the ratio of the MBA ligands and DBB-Ir-F ligands in Hf_{12}-Ir-MBA, 2.0 mg of Hf_{12}-Ir-MBA was dried under vacuum and then digested in a solution of 500 μL DMSO-d_6 and 50 μL D_3PO_4. The mixture was then sonicated for 10 min, added 50 μL D_2O, and analyzed by ^1H NMR.

Synthesis of Hf_{12}-Ir-Ni. To a 4 mL glass vial was added 1 mL of Hf_{12}-Ni-MBA suspension (2.0 mM based on Hf in EtOH) and 2 mg of $NiCl_2 \cdot 6H_2O$. The reaction mixture was stirred at room temperature overnight. The green-yellow precipitate was collected by centrifugation and washed with ethanol twice. The extent for MBA metalation was ~100% based on the ratio between Hf and Ni as determined by ICP-MS.

General procedure for C-S cross-coupling. Aryl iodide (0.50 mmol), thiophenol/thiol (0.75 mmol, 1.5 equiv), 2,6-lutidine (1.00 mmol, 2.0 equiv), and Hf_{12}-Ir-Ni (0.10 μmol, 0.02 mol%) were mixed in dry CH_3CN (0.5 mL) in a closable flask. The resulting mixture was stirred under blue LED irradiation at room temperature in an Ar atmosphere for 48 hours. After the reaction, the solvent was removed under vacuum. The residue was then subjected to column chromatography on silica gel using *n*-hexane and dichloromethane as eluent to give the products **1c**-**7c**.

General procedure for C-O cross-coupling. Aryl bromide (0.25 mmol), alcohol (0.50 mmol, 2.0 equiv), quinuclidine (0.25 mmol, 1.0 equiv), and Hf_{12}-Ir-Ni (0.125 μmol, 0.05 mol%) were mixed in dry CH_3CN (1.0 mL) in a closable flask. The resulting mixture was stirred under blue LED irradiation at room temperature in an Ar atmosphere for 48 hours. After the reaction, the solvent was removed under vacuum. The residue was then subjected to column

chromatography on silica gel using *n*-hexane and ethyl acetate as eluent to give the products **8c**-**16c**.

General procedure for C-C cross-coupling. Aryl bromide (0.125 mmol), benzylic trifluoroborate (0.25 mmol, 2.0 equiv), 2,6-lutidine (0.438 mmol, 3.5 equiv), and Hf_{12}-Ir-Ni (0.25 μmol, 0.20 mol%) were mixed in dry dioxane (0.5 mL) in a closable flask. The resulting mixture was stirred under blue LED irradiation at room temperature in an Ar atmosphere for 48 hours. After the reaction, the solvent was removed under vacuum. The residue was then subjected to column chromatography on silica gel using *n*-hexane and ethyl acetate as eluent to give the products **17c**-**22c**.

Recycle experiments. 4-(Methoxycarbonyl)phenyl iodide (131.0 mg, 0.50 mmol), benzenethiol (82.6 mg, 0.75 mmol, 1.5 equiv), 2,6-lutidine (107.2 mg, 1.00 mmol, 2.0 equiv), and Hf_{12}-Ir-Ni (250 μL, 4 mM in CH_3CN, 1.0 μmol, 0.2 mol%) were mixed in dry CH_3CN (0.5 mL) in a closable flask. The resulting mixture was stirred under blue LED irradiation at room temperature in an Ar atmosphere for 8 hours. After reaction, the MOL catalyst was recovered via centrifugation, and washed with dry CH_3CN (1.0 mL × 3) for subsequent cycles of reactions. The reaction mixture was subjected to GC-MS analysis. The aforementioned procedure was repeated four times.

Time-dependent experiment 1 (T1). 4-(Methoxycarbonyl)phenyl iodide (131.0 mg, 0.50 mmol), benzenethiol (82.6 mg, 0.75 mmol, 1.5 equiv), 2,6-lutidine (107.2 mg, 1.00 mmol, 2.0 equiv), and Hf_{12}-Ir-Ni (250 μL, 4 mM in CH_3CN, 1.0 μmol, 0.2 mol%) were mixed in dry CH_3CN (0.5 mL) in a closable flask. The resulting mixture was stirred under blue LED

irradiation at room temperature in an Ar atmosphere. The reaction progress was tracked by GC-MS every two hours.

Time-dependent experiment 2 (T2). The reaction procedure is similar to that of **T1**. The only difference is that Hf_{12}-Ir-Ni catalyst was replaced by a combination of Hf_{12}-Ir-F and Me-MBA-Ni.

Time-dependent experiment 3 (T3). The reaction procedure is similar to that of **T1**. The only difference is that Hf_{12}-Ir-Ni catalyst was replaced by a combination of Me_2DBB-Ir-F and Me-MBA-Ni.

Homogenous control experiments. The reaction procedures are similar to those Hf_{12}-Ir-Ni catalyzed C-C, C-O and C-S cross-couplings. The only difference is the replacement of Hf_{12}-Ir-Ni MOL catalyst by a combination of Me_2DBB-Ir-F and Me-MBA-Ni at the same loading or one hundred times higher loading.

CV. CVs of 5 mM Me_2DBB-Ir-F and 5 mM Me-MBA-Ni were tested in 20 mL 0.1 M TBAH/CH_3CN solution, respectively, with a scan rate of 100 mV/s (TBAH = Tetrabutylammonium hydroxide). Working, reference, and counter electrodes were glassy carbon (3 mm diameter disk), Ag/AgCl, and Pt, respectively. The peak corresponding to $[Me_2DBB\text{-}Ir\text{-}F]^+$/$Me_2$DBB-Ir-F ($O_1$), Me_2DBB-Ir-F/$[Me_2DBB\text{-}Ir\text{-}F]^-$ (R_1), and Me-MBA-Ni/$[Me\text{-}MBA\text{-}Ni]^-$ (R_2) were determined to be 1.37 V, -0.88 V, and -0.73 V vs SCE, corresponding to 1.61 V, -0.64 V, and -0.49 V vs NHE, respectively. The energy gap between $[Me_2DBB\text{-}Ir\text{-}F]^+$ and Me_2DBB-Ir-F (ΔG_1) was determined to be -1.61 eV. The energy gap between Me-MBA-Ni and $[Me\text{-}MBA\text{-}Ni]^-$ (ΔG_2) was determined to be 0.45 eV. Since excited $[Me_2DBB\text{-}Ir\text{-}F]^*$ show emission peak at 550 nm, the energy gap between Me_2DBB-Ir-F and

[Me_2DBB-Ir-F]* (ΔG_3) was calculated to be 2.26 eV. Therefore, the energy gap between [Me_2DBB-Ir-F]* and [Me_2DBB-Ir-F]$^+$ (ΔG_4) was calculated to be -0.65 eV ($\Delta G_4 = -\Delta G_1 - \Delta G_3$), which was enough to drive the reduction of Me-MBA-Ni to generate [Me-MBA-Ni]$^-$ (ΔG_2 = 0.45 eV).

Hf_{12}-Ir-Ni with different Ni loadings. To a 4 mL glass vial was added 1 mL EtOH suspension of Hf_{12}-Ni-MBA (1.0 μmol based on Ir) and $NiCl_2 \cdot 6H_2O$ of different amount (0.2, 0.4, 0.6, 0.8, and 1.0 μmol based on Ni). The reaction mixture was stirred overnight at room temperature. The green-yellow precipitate was collected by centrifugation and washed with ethanol twice. The ratio between Ni and Ir (loading of Ni) for these generated Hf_{12}-Ir-Ni was determined by ICP-MS to be 0.18, 0.36, 0.61, 0.79, and 0.94, respectively.

Luminescence quenching of Me_2DBB-Ir-F. To a 4 mL cuvette was added 3 mL MeCN solution of Me_2DBB-Ir-F (20 μM based on Ir). The solution was degassed with N_2 for 5 mins before luminescence intensity or lifetime test. Different amounts of Me-MBA-Ni were then dissolved into the solution to achieve the final concentration of 4, 8, 12, 16, and 20 μM (based on Ni), respectively. The luminescence intensity and lifetime of Me_2DBB-Ir-F in these mixed solutions were measured separately.

Luminescence quenching of Hf_{12}-Ir-F. To a 4 mL cuvette was added 3 mL MeCN suspension of Hf_{12}-Ir-F (20 μM based on Ir). The suspension was degassed with N_2 for 5 mins before luminescence intensity or lifetime test. Different amounts of Me-MBA-Ni were then dissolved into the suspension to achieve the final concentration of 4, 8, 12, 16, and 20 μM (based on Ni), respectively. The luminescence intensity and lifetime of Hf_{12}-Ir-F in these mixed suspensions were measured separately.

Luminescence quenching of Hf_{12}-Ir-Ni. To a 4 mL cuvette was added 3 mL MeCN suspension of Hf_{12}-Ir-Ni (20 μM based on Ir) with different Ni loadings. These suspensions was degassed with N_2 for 5 mins before luminescence intensity and lifetime test.

10.5 References

1. Furukawa, H.; Cordova, K. E.; O'Keeffe, M.; Yaghi, O. M., The Chemistry and Applications of Metal-Organic Frameworks. *Science* **2013,** *341* (6149), 1230444.
2. Fateeva, A.; Chater, P. A.; Ireland, C. P.; Tahir, A. A.; Khimyak, Y. Z.; Wiper, P. V.; Darwent, J. R.; Rosseinsky, M. J., A Water-Stable Porphyrin-Based Metal–Organic Framework Active for Visible-Light Photocatalysis. *Angew. Chem. Int. Ed.* **2012,** *51* (30), 7440-7444.
3. Mason, J. A.; Oktawiec, J.; Taylor, M. K.; Hudson, M. R.; Rodriguez, J.; Bachman, J. E.; Gonzalez, M. I.; Cervellino, A.; Guagliardi, A.; Brown, C. M.; Llewellyn, P. L.; Masciocchi, N.; Long, J. R., Methane storage in flexible metal–organic frameworks with intrinsic thermal management. *Nature* **2015,** *527*, 357.
4. Morris, W.; Briley, W. E.; Auyeung, E.; Cabezas, M. D.; Mirkin, C. A., Nucleic Acid–Metal Organic Framework (MOF) Nanoparticle Conjugates. *J. Am. Chem. Soc.* **2014,** *136* (20), 7261-7264.
5. Cui, Y.; Yue, Y.; Qian, G.; Chen, B., Luminescent Functional Metal–Organic Frameworks. *Chem. Rev.* **2012,** *112* (2), 1126-1162.
6. Zhang, Y.; Guo, J.; Shi, L.; Zhu, Y.; Hou, K.; Zheng, Y.; Tang, Z., Tunable chiral metal organic frameworks toward visible light–driven asymmetric catalysis. *Science Advances* **2017,** *3* (8), e1701162.
7. Johnson, J. A.; Zhang, X.; Reeson, T. C.; Chen, Y.-S.; Zhang, J., Facile Control of the Charge Density and Photocatalytic Activity of an Anionic Indium Porphyrin Framework via in Situ Metalation. *J. Am. Chem. Soc.* **2014,** *136* (45), 15881-15884.
8. Jiang, Y.; Park, J.; Tan, P.; Feng, L.; Liu, X.-Q.; Sun, L.-B.; Zhou, H.-C., Maximizing Photoresponsive Efficiency by Isolating Metal–Organic Polyhedra into Confined Nanoscaled Spaces. *J. Am. Chem. Soc.* **2019,** *141* (20), 8221-8227.
9. Yu, X.; Cohen, S. M., Photocatalytic Metal–Organic Frameworks for Selective 2,2,2-Trifluoroethylation of Styrenes. *J. Am. Chem. Soc.* **2016,** *138* (38), 12320-12323.
10. Liu, Y.; Howarth, A. J.; Hupp, J. T.; Farha, O. K., Selective Photooxidation of a Mustard-Gas Simulant Catalyzed by a Porphyrinic Metal–Organic Framework. *Angew. Chem. Int. Ed.* **2015,** *54* (31), 9001-9005.
11. Xu, H.-Q.; Hu, J.; Wang, D.; Li, Z.; Zhang, Q.; Luo, Y.; Yu, S.-H.; Jiang, H.-L., Visible-Light Photoreduction of CO2 in a Metal–Organic Framework: Boosting Electron–Hole Separation via Electron Trap States. *J. Am. Chem. Soc.* **2015,** *137* (42), 13440-13443.
12. Yaghi, O. M., Reticular Chemistry in All Dimensions. *ACS Central Science* **2019**.
13. Wang, H.; Zhu, Q.-L.; Zou, R.; Xu, Q., Metal-Organic Frameworks for Energy Applications. *Chem* **2017,** *2* (1), 52-80.
14. Chen, K.; Wu, C.-D., Transformation of Metal-Organic Frameworks into Stable Organic

Frameworks with Inherited Skeletons and Catalytic Properties. *Angew. Chem. Int. Ed.* **2019,** *58* (24), 8119-8123.
15. Moreau, F.; da Silva, I.; Al Smail, N. H.; Easun, T. L.; Savage, M.; Godfrey, H. G. W.; Parker, S. F.; Manuel, P.; Yang, S.; Schröder, M., Unravelling exceptional acetylene and carbon dioxide adsorption within a tetra-amide functionalized metal-organic framework. *Nat. Commun.* **2017,** *8*, 14085.
16. Lan, G.; Ni, K.; Xu, R.; Lu, K.; Lin, Z.; Chan, C.; Lin, W., Nanoscale Metal–Organic Layers for Deeply Penetrating X-ray-Induced Photodynamic Therapy. *Angew. Chem.* **2017,** *129* (40), 12270-12274.
17. Lan, G.; Li, Z.; Veroneau, S. S.; Zhu, Y.-Y.; Xu, Z.; Wang, C.; Lin, W., Photosensitizing Metal–Organic Layers for Efficient Sunlight-Driven Carbon Dioxide Reduction. *J. Am. Chem. Soc.* **2018,** *140* (39), 12369-12373.
18. Cao, L.; Lin, Z.; Peng, F.; Wang, W.; Huang, R.; Wang, C.; Yan, J.; Liang, J.; Zhang, Z.; Zhang, T.; Long, L.; Sun, J.; Lin, W., Self-Supporting Metal–Organic Layers as Single-Site Solid Catalysts. *Angew. Chem. Int. Ed.* **2016,** *55* (16), 4962-4966.
19. Sun, R.; Qin, Y.; Ruccolo, S.; Schnedermann, C.; Costentin, C.; Daniel, G. N., Elucidation of a Redox-Mediated Reaction Cycle for Nickel-Catalyzed Cross Coupling. *J. Am. Chem. Soc.* **2019,** *141* (1), 89-93.
20. Twilton, J.; Le, C.; Zhang, P.; Shaw, M. H.; Evans, R. W.; MacMillan, D. W. C., The merger of transition metal and photocatalysis. *Nature Reviews Chemistry* **2017,** *1*, 0052.
21. Tellis, J. C.; Primer, D. N.; Molander, G. A., Single-electron transmetalation in organoboron cross-coupling by photoredox/nickel catalysis. *Science* **2014,** *345* (6195), 433.
22. Terrett, J. A.; Cuthbertson, J. D.; Shurtleff, V. W.; MacMillan, D. W. C., Switching on elusive organometallic mechanisms with photoredox catalysis. *Nature* **2015,** *524*, 330.
23. Oderinde, M. S.; Frenette, M.; Robbins, D. W.; Aquila, B.; Johannes, J. W., Photoredox Mediated Nickel Catalyzed Cross-Coupling of Thiols With Aryl and Heteroaryl Iodides via Thiyl Radicals. *J. Am. Chem. Soc.* **2016,** *138* (6), 1760-1763.
24. Corcé, V.; Chamoreau, L.-M.; Derat, E.; Goddard, J.-P.; Ollivier, C.; Fensterbank, L., Silicates as Latent Alkyl Radical Precursors: Visible-Light Photocatalytic Oxidation of Hypervalent Bis-Catecholato Silicon Compounds. *Angew. Chem. Int. Ed.* **2015,** *54* (39), 11414-11418.
25. Nakajima, K.; Nojima, S.; Nishibayashi, Y., Nickel- and Photoredox-Catalyzed Cross-Coupling Reactions of Aryl Halides with 4-Alkyl-1,4-dihydropyridines as Formal Nucleophilic Alkylation Reagents. *Angew. Chem. Int. Ed.* **2016,** *55* (45), 14106-14110.
26. Welin, E. R.; Le, C.; Arias-Rotondo, D. M.; McCusker, J. K.; MacMillan, D. W. C., Photosensitized, energy transfer-mediated organometallic catalysis through electronically excited nickel(II). *Science* **2017,** *355* (6323), 380.
27. Tasker, S. Z.; Jamison, T. F., Highly Regioselective Indoline Synthesis under Nickel/Photoredox Dual Catalysis. *J. Am. Chem. Soc.* **2015,** *137* (30), 9531-9534.
28. Ackerman, L. K. G.; Martinez Alvarado, J. I.; Doyle, A. G., Direct C–C Bond Formation from Alkanes Using Ni-Photoredox Catalysis. *J. Am. Chem. Soc.* **2018,** *140* (43), 14059-14063.
29. Zhu, Y.-Y.; Lan, G.; Fan, Y.; Veroneau, S.; Song, Y.; Micheroni, D.; Lin, W., Merging Photoredox and Organometallic Catalysts in a Metal-Organic Framework Significantly Boosts Photocatalytic Activities. *Angew. Chem.* **2018**.

Chapter 11. Metal-Organic-Zyme Evolution for CO_2 to Methane Conversion

11.1 Introduction

Enzymes have evolved over billions of years to efficiently and selectively catalyze even the most challenging chemical transformations in nature. For example, the high reactivity and selectivity of metalloenzymes result from their complex active sites consisting of metal ions coordinated to amino acid (AA) side chains or a prosthetic group, secondary coordination to nearby AA side chains, and other cofactors (e.g., pigments, NAD(P)H, ATP) (**Figure 11-1A**).[1] Secondary coordination stabilizes specific transition states and reactive intermediates via non-covalent interactions whereas cofactors may provide electrons, hydrides, and other species to power the reaction pathways. Recapitulating the selectivity and activity of natural enzymes for industrially relevant or otherwise important transformations has gained significant attention, particularly via protein engineering [2] and directed evolution (**Figure 11-2**).[3] Still, the challenges associated with designing and scaling natural and engineered enzymes (i.e., high cost, low stability, difficulty in storage) have prompted the development of artificial enzymes in the forms of metal-clusters, [4-7] metal or metal-oxide nanoparticles,[8] supermolecules and polymers,[9] and MOFs,[10-13] among others.[14] However, current designs of artificial enzymes predominately mimic the active metal centers of enzymes without secondary coordination or additional cofactors. Thus, artificial analogues are currently limited to catalyzing simple reactions and lack the systematic tunability required to expand their scope. A general method to rationally design artificial enzymes with complex yet tunable active sites is needed to target increasingly challenging and relevant chemical transformations.

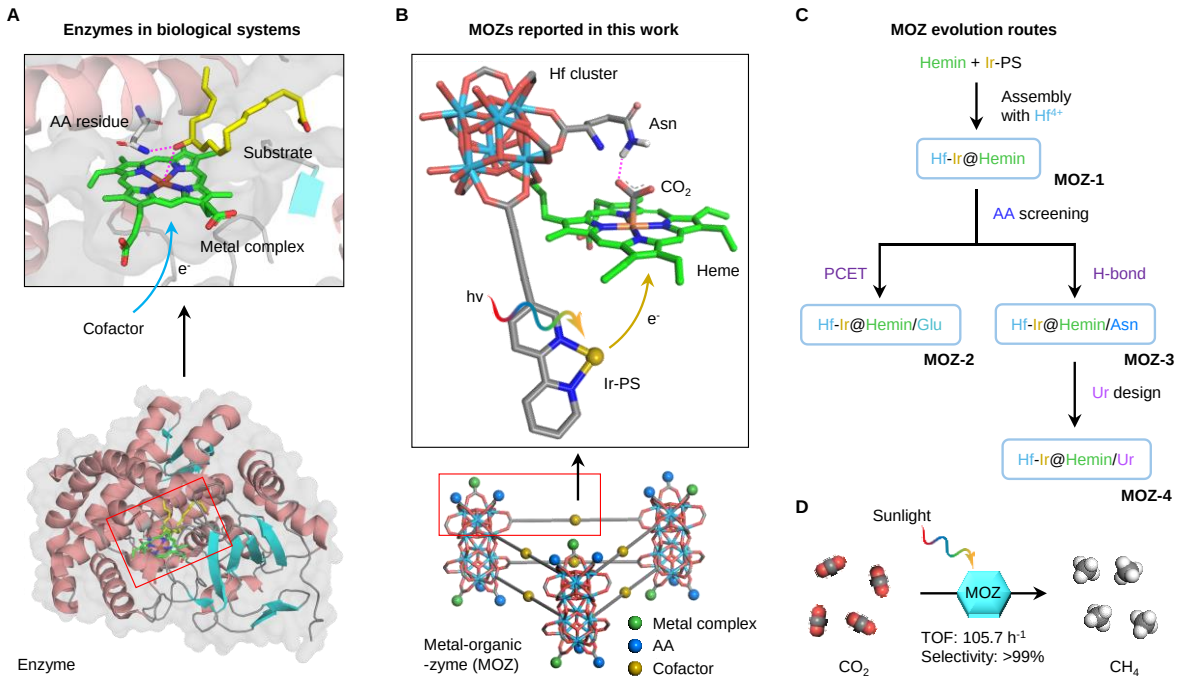

Figure 11-1. MOZ overview and evolution. (A) Schematic of the natural enzyme cytochrome P450 74A (bottom, PDB 3DSI) and its active-site (top) [1], where the substrate is bound to the heme site through stabilization of the secondary coordination sphere by an adjacent AA residue (Asn). The overall reaction is promoted by an NAD(P)H cofactor. (B) Schematic of a representative MOZ (bottom) reported in this work for CO_2 to methane conversion, with the binding of CO_2 by heme-iron active-sites stabilized by adjacent ligands (e.g., Asn, Ur) via H-bond interactions. The overall reaction is promoted by photoexcited Ir-PS cofactors. Hydrogen atoms bound to carbon are omitted for clarity. C atoms in heme are highlighted in green, with all other atoms labeled as follows: H, white; C, gray; O, red; N, blue; Fe, orange; Hf, light blue; Ir, yellow. (C) MOZ evolution route. (D) MOZ-catalyzed conversion of CO_2 to CH_4 with TOFs up to 150.7 h^{-1} with >99% selectivity under direct sunlight.

In this Chapter, we report a new form of artificial enzyme, a metal-organic-zyme (MOZ), that can be rationally designed to integrate metal complexes, AAs, and cofactors into a MOL (**Figure 11-1B**). We demonstrate the viability of MOZs by targeting CO_2 conversion: a class of chemical transformations ubiquitous in nature yet inefficient in artificial systems. The conversion of CO_2 into energy-rich products (e.g., methane) may realize new forms of sustainable energy while mitigating deleterious impacts of rapid fossil fuel consumption,[15-20] yet such conversion into useful and scalable products has proven challenging. In this work we rationally design and evolve a library of MOZs to optimize activity and selectivity for

photocatalytic CO_2 to methane (CH_4) conversion (**Figure 11-1C** and **Figure 11-3**). The underlying MOL of these MOZs presents Hf_{12} oxo-clusters laterally connected by photosensitizing Ir-based ligands, which serve as artificial pigments for light-driven electron transfer. The hemin, an iron-porphyrin complex with a potent activity for CO_2 reduction, is loaded onto this monolayer, and a library of MOZs is subsequently generated by further appending the 20 standard proteinogenic AAs to form unique active sites around each iron-center. Screening efficiencies for photocatalytic CO_2 to CH_4 conversion of these MOZs reveals a dependence on: (1) side chain pKa and (2) hydrogen bond (H-bond) interactions with appended AAs. The pKa dependence was attributed to accessing a proton coupled electron transfer (PCET) pathway as exemplified by Glu-modification, while H-bond interactions stabilized reactive intermediates as exemplified by Asn-modification. This mechanistic understanding inspired the design of a urea-based ligand (Ur) to provide greater stabilization of reactive intermediates via even stronger H-bond interactions, which afforded the unprecedented activity for the conversion of CO_2 to CH_4 with a TOF and selectivity of 150.7 h^{-1} and >99%, respectively, under direct sunlight (**Figure 11-1D**).

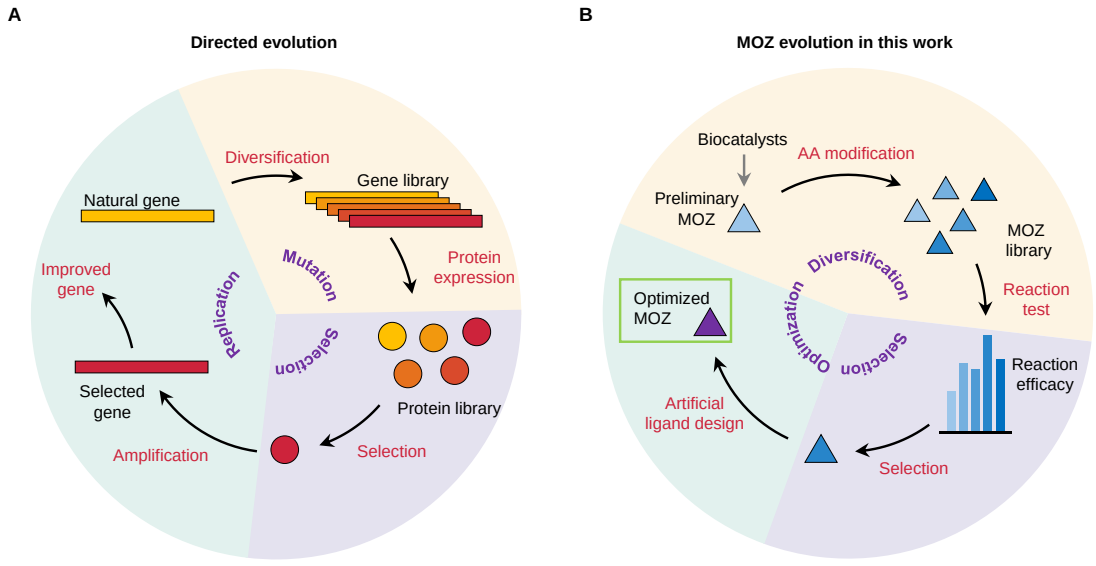

(Figure 11-2 continued) **Figure 11-2.** Comparison of directed evolution and MOZ evolution. (A) Schematic showing the process of directed evolution, which consists of subjecting a gene to iterative rounds of (1) *mutation* to create a library of variants, (2) *selection* to express those variants and isolate members with the desired function and (3) *replication* to generate a new template for subsequent rounds of evolution. (B) Schematic showing the process of MOZ evolution inspired by directed evolution and proposed in this work. MOZ evolution consists of (1) *diversification* and designing a progenitor MOZ inspired by biocatalysts to create a library of MOZs through AA modification to tune microenvironment, (2) *selection* and screening of MOZs for a specific function to select members with enhanced activity, and (3) *optimization* by elucidating how activity is enhanced by selected members and designing artificial ligands for further enhancement. In this work, these three steps correspond to (1) constructing **MOZ-1** from hemin and Ir-PS and separately appending proteinogenic amino acids, (2) testing activity of MOZs for photocatalytic CO_2 reduction to select **MOZ-2** (with Glu modification) and **MOZ-3** (with Asn modification), and (3) using DFT calculation to reveal the enhancement of **MOZ-3** activity by stabilizing intermediates through hydrogen-bonding and subsequently designing the Ur ligand to generate **MOZ-4** to further enhance activity through even stronger hydrogen-bonding interactions.

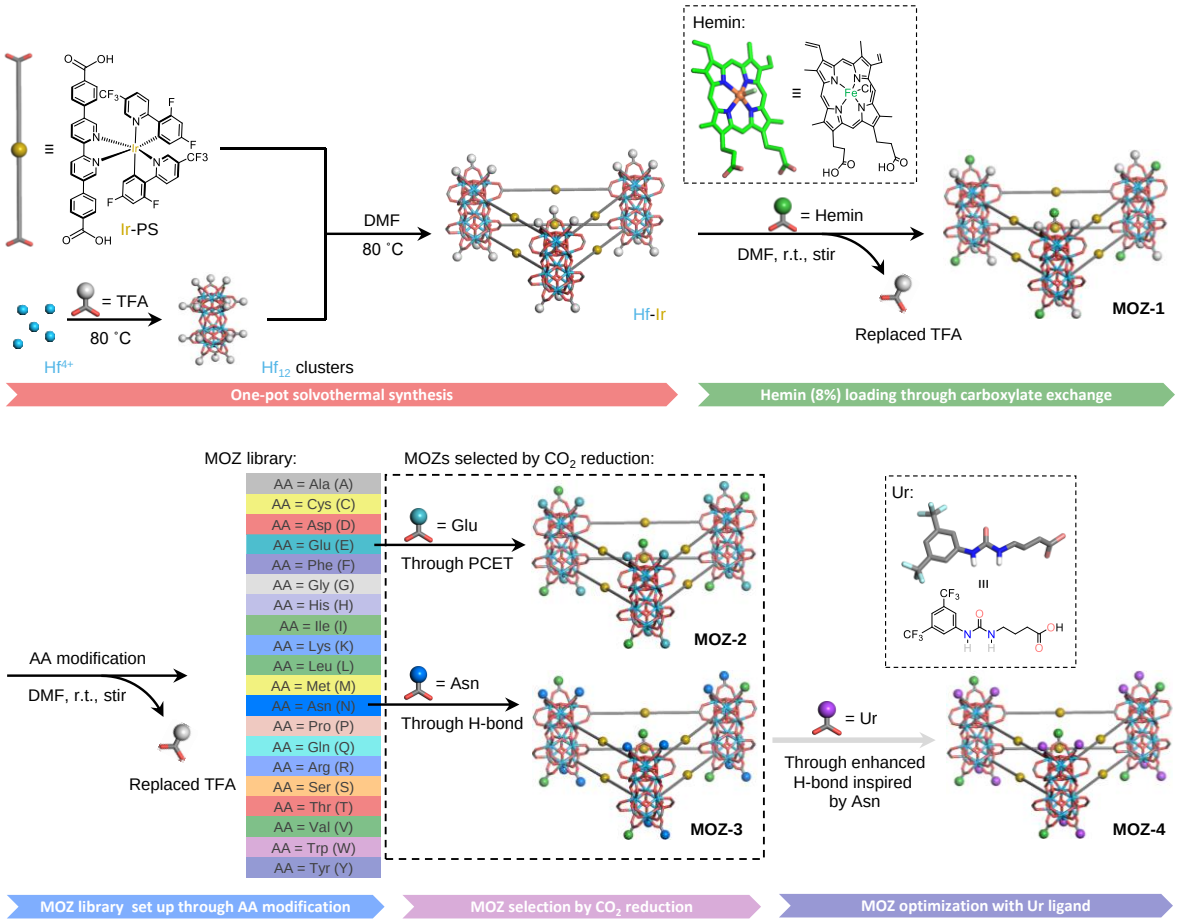

Figure 11-3. MOZ construction and evolution. (1) Hf-Ir monolayer was synthesized through a one-pot solvothermal synthesis to interlink Hf_{12} SBUs with Ir-PS. (2) **MOZ-1** was synthesized through post-synthetic modification of Hf-Ir monolayer with hemin, wherein weakly-coordinating TFA is replaced through carboxylate exchange. (3) The library of MOZs was

(Figure 11-3 continued) generated by separately appending 20 AAs on **MOZ-1**, whereby all remaining TFA was exchanged to generate 20 MOZ candidates with unique active sites. (4) **MOZ-2** (with Glu modification) and **MOZ-3** (with Asn modification) showed enhanced activity for photocatalytic CO_2 reduction by promoting proton coupled electron transfer (PCET) and stabilizing reactive intermediates through hydrogen-bond (H-bond), respectively. (5) Inspired by H-bond interactions in **MOZ-3**, the Ur ligand (capable of stronger H-bond) was designed and synthesized. The optimized **MOZ-4** was generated by appending this Ur ligand onto **MOZ-1** and subsequently revealed the highest activity for photocatalytic CO_2 reduction.

11.2 Result and discussion

The underlying MOL (Hf-Ir) of these MOZs was synthesized though a solvothermal reaction to afford previously reported Hf_{12} clusters $[Hf_{12}(\mu_3\text{-}O)_8(\mu_3\text{-}OH)_8(\mu_2\text{-}OH)_6]$ vertically capped by TFA and laterally connected by photosensitizing Ir(4,4'-di(4-benzoato)-2,2'-bipyridine)[2-(2,4-difluorophenyl)-5-(trifluoromethyl)pyridine]$_2^+$ (Ir-PS) ligands to afford a crystalline two-dimensional network with the formula $Hf_{12}(\mu_3\text{-}O)_8(\mu_3\text{-}OH)_8(\mu_2\text{-}OH)_6$(Ir-PS)$_6(TFA)_6$ (**Figure 11-4**) (see section 11**.4.1**). Each face of the Hf_{12} clusters coordinates to three labile TFA groups which could be exchanged for more strongly coordinating carboxylate groups such as those in hemin, AAs, and Ur, allowing for the installation of various functional groups on the MOZs (see section 11**.4.2**). Hemin was first installed on Hf-Ir via carboxylate exchange to afford the primary MOZ (**MOZ-1**). The ratio of hemin to Ir-PS was chosen to be <10% to facilitate the injection of multiple electrons from Ir-PSs to a hemin site during a single catalytic cycle of CO_2 reduction. The remaining TFA (~90%) accommodated further modification of **MOZ-1** with AAs or Ur, as described below.

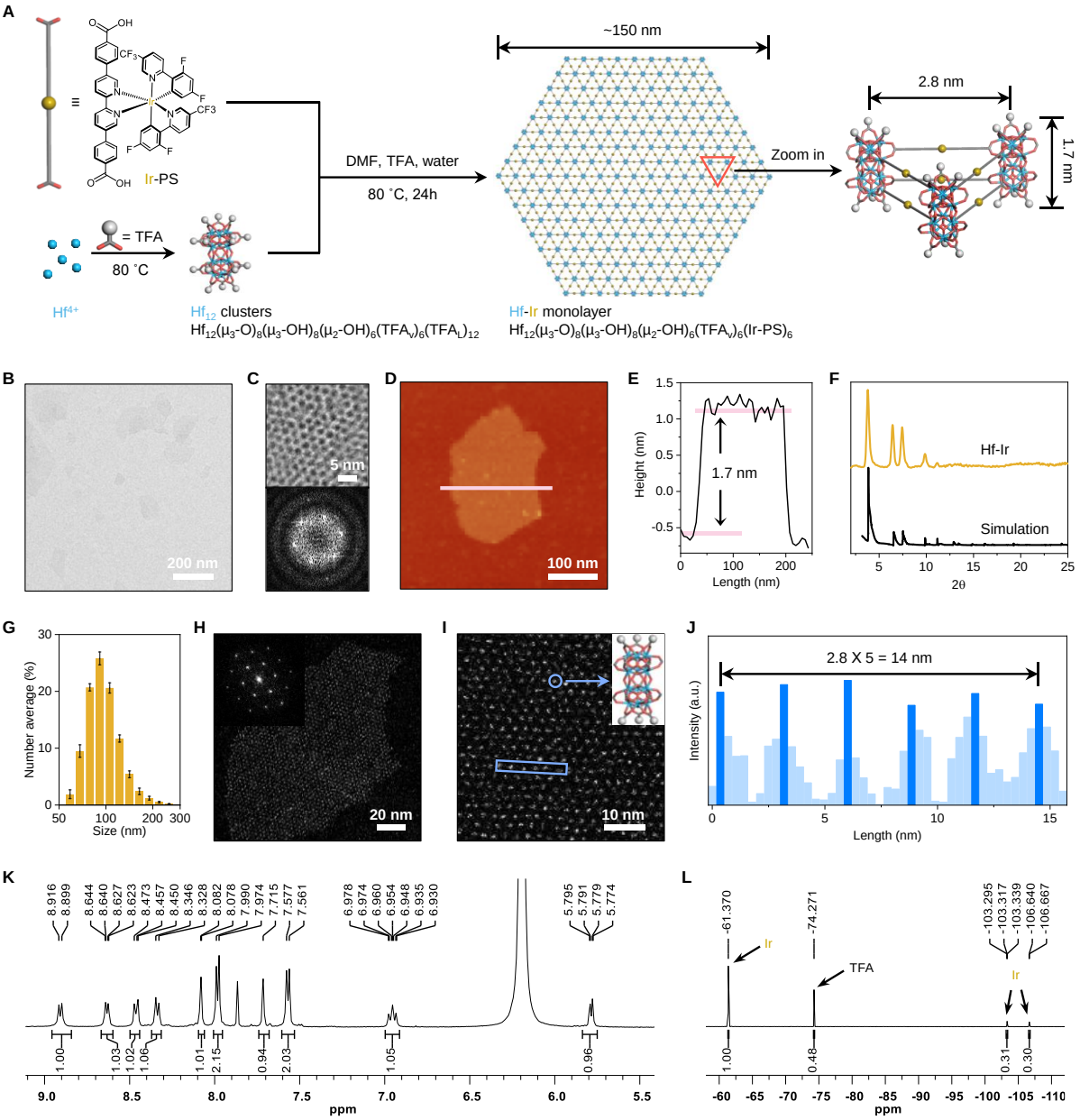

Figure 11-4. Hf-Ir monolayer. (A) Schematic showing the solvothermal synthesis and proposed structure and composition of Hf-Ir monolayer. A Hf_{12} cluster was first formed with TFA capping both vertically (TFA_v) and laterally (TFA_L). The TFA_L was further replaced by the Ir-PS and the Hf_{12} cluster was thus regularly connected to a 2D network. (B) TEM imaging, (C) HRTEM imaging (top) and fast Fourier transform (FFT) pattern (bottom), (D) AFM topography and (E) height profile, (F) PXRD pattern compared to that of simulated structure, (G) number-averaged diameters (99.1 ± 3.4 nm), (H) large-range HAADF imaging and FFT pattern (inset), and (I) small-range HAADF imaging and (J) intensity analysis of Hf-Ir monolayer. (K) ^{1}H NMR spectrum of digested Hf-Ir monolayer. (L) ^{19}F NMR spectrum of digested Hf-Ir monolayer, in which signals from left to right correspond to -CF_3 in Ir-PS, -CF_3 in TFA, -F in Ir-PS, and -F in Ir-PS.

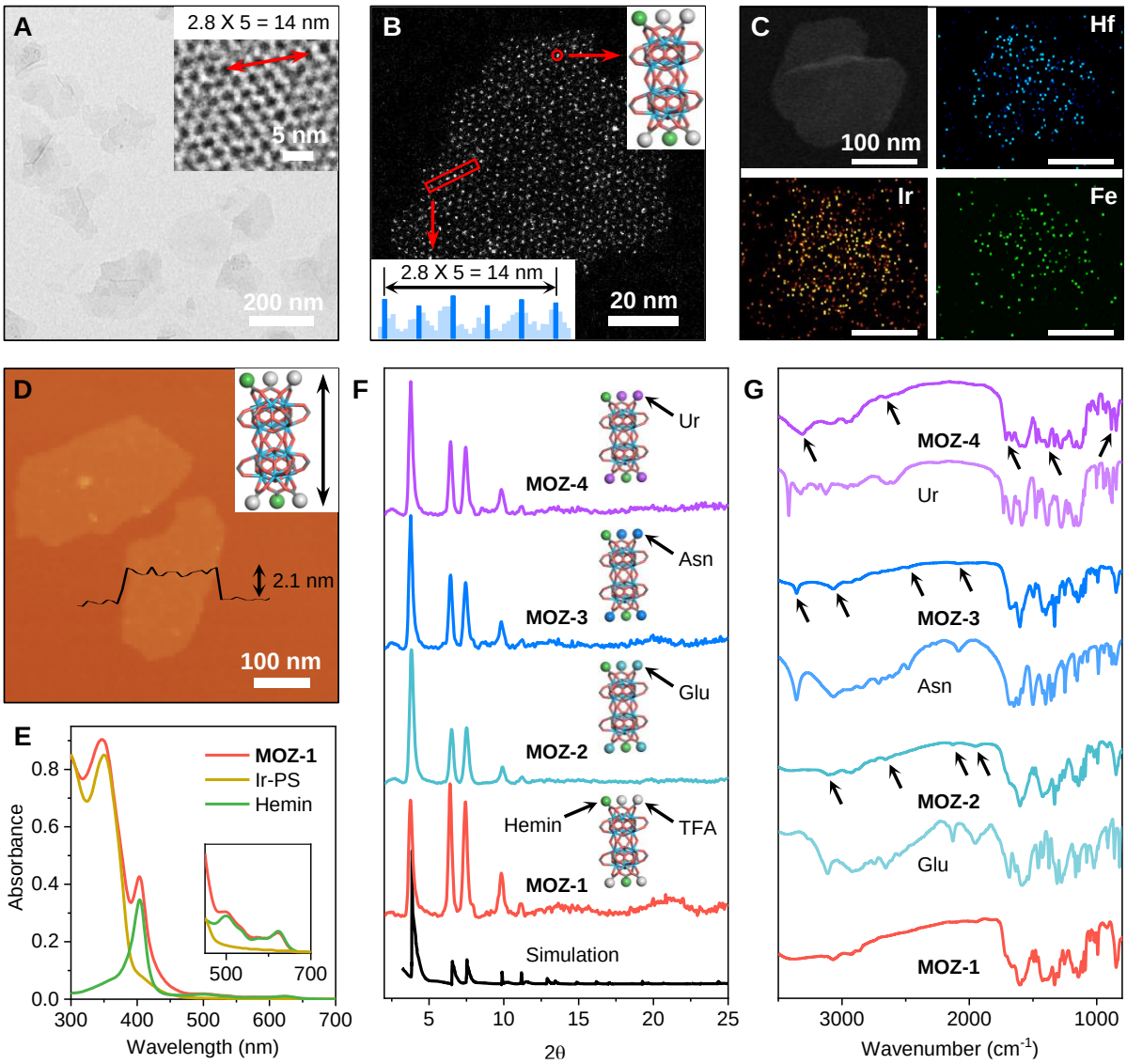

Figure 11-5. Characterization of MOZs. (A) TEM and HRTEM (inset) images, (B) HAADF image, (C) EDS mapping, and (D) AFM topography with height profile of **MOZ-1**. Hemin-capped Hf_{12} clusters appearing as black and white regions in (A) and (B), respectively. (E) UV-vis spectrum of digested **MOZ-1** and its deconvolution into hemin and Ir-PS absorptions. (F) PXRD patterns of MOZs compared to the simulated pattern based on the MOL structure. Hemin-capped Hf_{12} clusters with various capping groups (i.e., TFA, Glu, Asn, and Ur) are also shown to illustrate different MOZs. (G) IR spectra of MOZs compared to corresponding Glu, Asn, and Ur absorptions. Black arrows in **MOZ-2**, **MOZ-3**, and **MOZ-4** spectra label absorption corresponding to Glu, Asn, and Ur, respectively.

MOZ-1 retained the monolayer morphology of Hf-Ir with a diameter of ~150 nm and a thickness of ~2.1 nm, as determined by TEM (**Figure 11-5A**) and AFM (**Figure 11-5D**), respectively. The ~0.5 nm increase in thickness of **MOZ-1** over Hf-Ir matched the height

expected for Hf_{12} clusters modified with flexible hemin groups. HRTEM (inset in **Figure 11-5A**) and high-angle annular dark-field (HAADF) (**Figure 11-5B**) imaging of **MOZ-1** revealed the six-fold **kgd** topological structure and an expected Hf_{12}-Hf_{12} distance of ~2.8 nm. The topological structure of **MOZ-1** was further supported by the similarity of its PXRD pattern to that simulated from its model structure (**Figure 11-5F**). EDS mapping showed homogenous distribution of hemin groups with the signals of Hf, Ir, and Fe dispersed across the entire monolayer (**Figure 11-5C** and **Figure 11-6**). The loading of hemin was quantified to be ~8.0% per Ir-PS based on UV-vis absorptions (**Figure 11-5E** and **Figure 11-8**) by deconvoluting the spectrum of digested **MOZ-1** into absorptions from hemin and Ir-PS, affording an empirical formula of $Hf_{12}(\mu_3\text{-}O)_8(\mu_3\text{-}OH)_8(\mu_2\text{-}OH)_6(\text{Ir-PS})_6(\text{hemin})_{0.48}(TFA)_{5.52}$ for **MOZ-1** (see section 11.**4.4**).

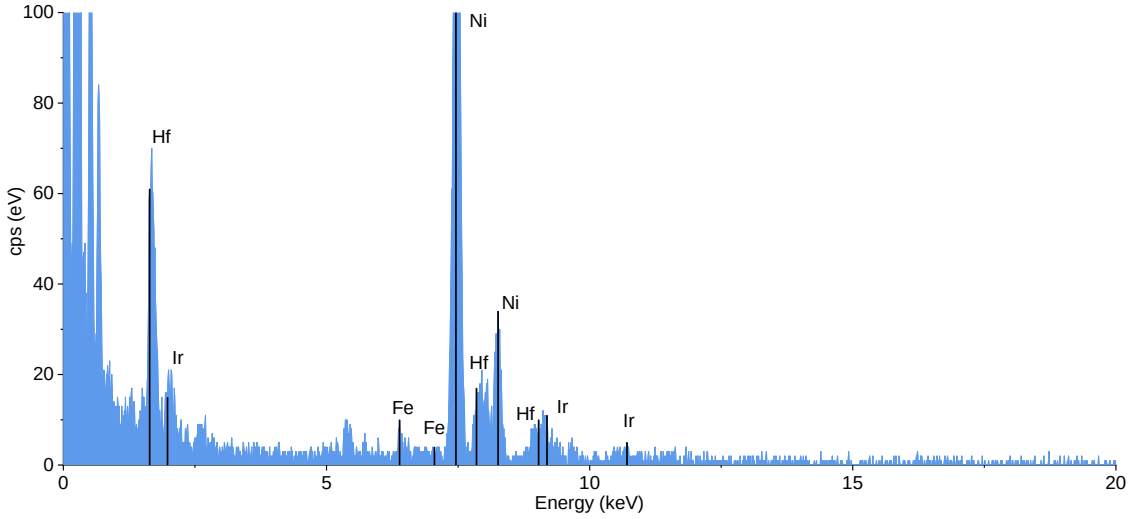

Figure 11-6. EDS spectrum of MOZ-1. Signals of Hf, Ir, Fe are clearly observed. Fe showed a relatively lower signal intensity due to both lower loading (Fe/Ir = 8% and Fe/Hf = 4%) and relatively lower sensitivity factor (counts) in EDS mode. Ni was observed as sample was drop-casted onto carbon coated nickel grids.

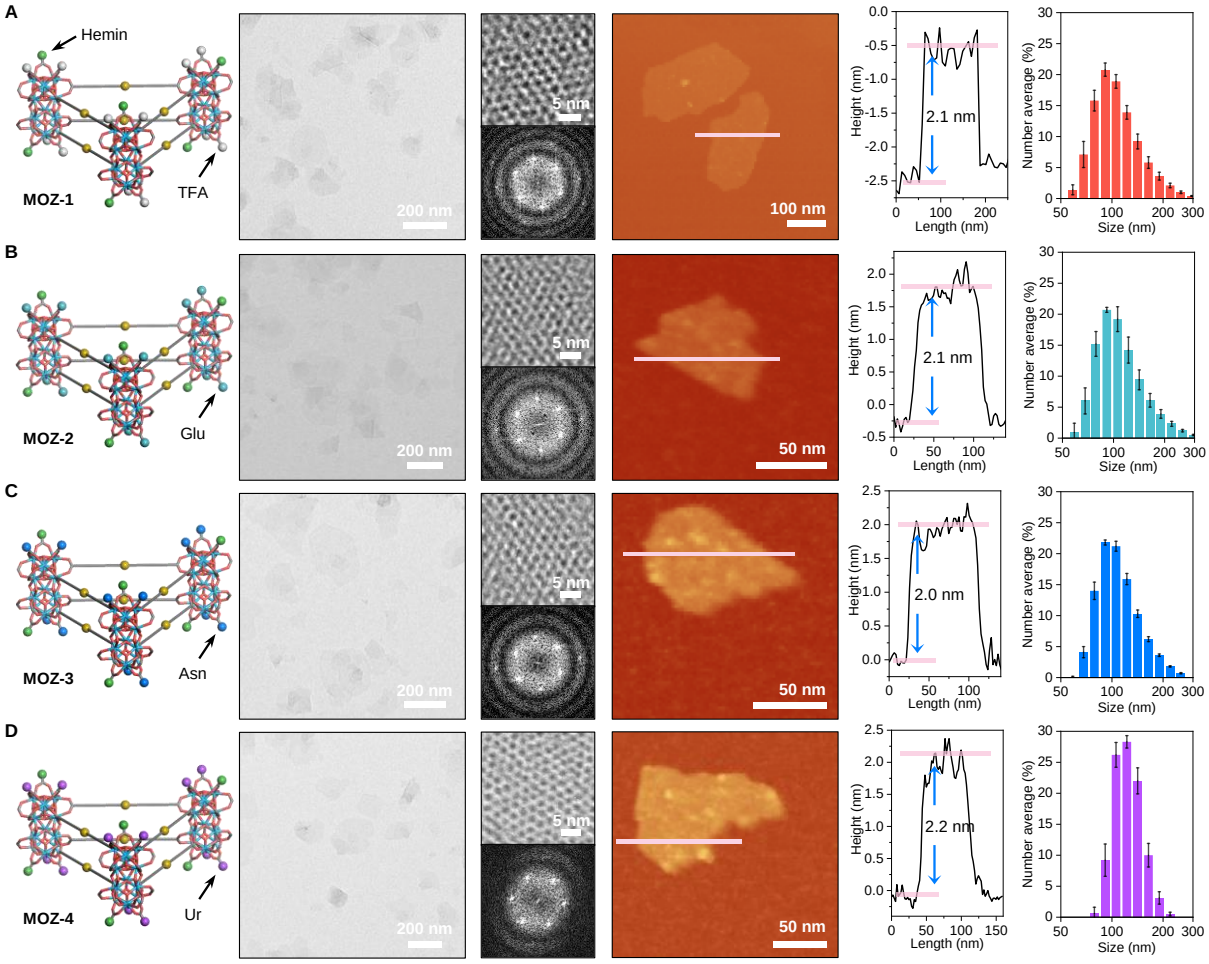

Figure 11-7. Morphological characterization of MOZs. Morphological characterization of (A) **MOZ-1**, (B) **MOZ-2**, (C) **MOZ-3**, and (D) **MOZ-4**. For each, from left to right: modeled structure, TEM imaging, HRTEM imaging (top) and its FFT pattern (bottom), AFM topography, height profile, and number-averaged diameter as measured by DLS. Number-averaged diameters were measured to be 112.5 ± 9.5 nm, 114.9 ± 5.7 nm, 113.9 ± 5.6 nm, and 125.5 ± 3.6 nm for **MOZ-1**, **MOZ-2**, **MOZ-3**, and **MOZ-4**, respectively.

A library of MOZs was subsequently evolved by replacing the remaining TFA on **MOZ-1** with proteinogenic AAs through carboxylate exchange reactions. The resultant MOZs, specifically those with Glu and Asn modifications, were characterized by TEM, AFM, and DLS, revealing a preserved monolayer morphology, with diameters of ~150 nm, thicknesses of 2.0-2.2 nm, and number-averaged sizes of 112-125 nm (**Figure 11-7**). These MOZs also maintained the topological structure of **MOZ-1**, as revealed by PXRD (**Figure 11-5F**) and HRTEM imaging (**Figure 11-7**). The incorporation of AAs was confirmed by IR spectroscopy in which

the absorptions of **MOZ-1** were consistently observed in all MOZs while the unique peaks of Glu or Asn were observed in corresponding MOZs (**Figure 11-5G**). The complete replacement of TFA was confirmed by NMR analysis of digested MOZs, with no TFA signal observed by ^{19}F NMR and a near 1:1 ratio of AA to Ir-PS signal by ^{1}H NMR (**Figure 11-9**). While weakly coordinating TFA groups could be completely replaced by AAs, strongly coordinating hemin groups remained unchanged, with hemin to Ir-PS ratios of 7.8% and 8.0% in Glu- and Asn-modified MOZs as quantified by UV-Vis analysis (**Figure 11-8**). The formulae of Glu- and Asn-modified MOZs (denoted **MOZ-2** and **MOZ-3**, respectively) were thus determined as $Hf_{12}(\mu_3\text{-}O)_8(\mu_3\text{-}OH)_8(\mu_2\text{-}OH)_6(\text{Ir-PS})_6(\text{hemin})_{0.47}(\text{Glu})_{5.53}$ and $Hf_{12}(\mu_3\text{-}O)_8(\mu_3\text{-}OH)_8(\mu_2\text{-}OH)_6(\text{Ir-PS})_6(\text{hemin})_{0.48}(\text{Asn})_{5.52}$, respectively (see section **11.4.4**).

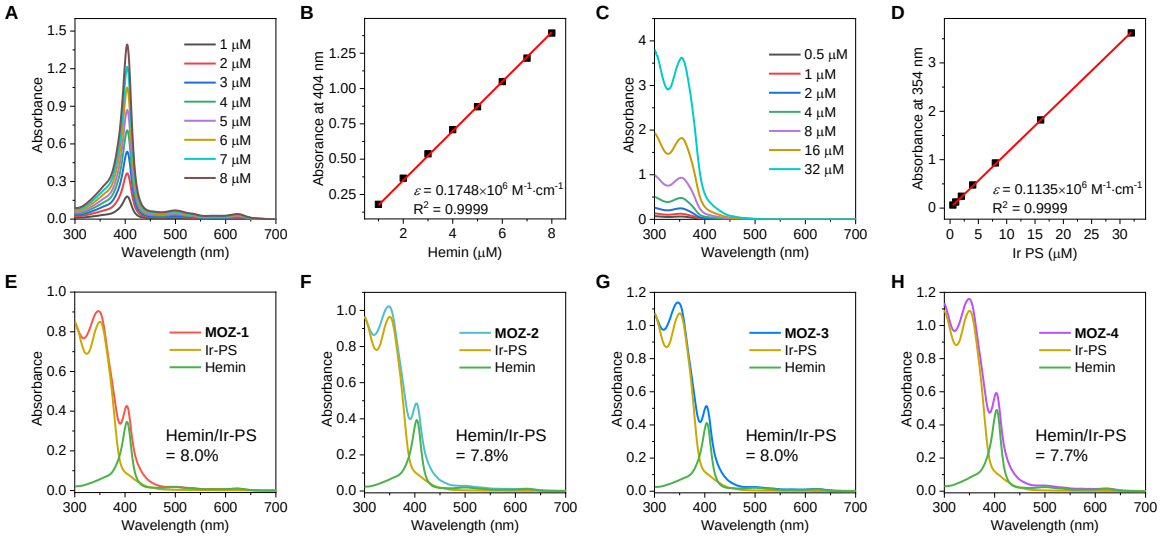

Figure 11-8. UV-vis analysis. (A) Standard absorption curves of hemin in DMF and (B) linear fit of absorption at 404 nm vs. concentration (ε = 0.1748 × 10^6 $M^{-1}\cdot cm^{-1}$, R^2 = 0.9999). (C) Standard absorption curves of Ir-PS in DMF and (D) linear fit of absorption at 354 nm vs. concentration (ε = 0.1135 × 10^6 $M^{-1}\cdot cm^{-1}$, R^2 = 0.9999). Absorption curves of digested (E) **MOZ-1**, (F) **MOZ-2**, (G) **MOZ-3**, and (H) **MOZ-4**. Each of these absorption spectra was quantitatively deconvoluted into the separate absorptions of hemin and Ir-PS. The concentration of hemin and Ir-PS in each MOZ was determined by their standard curves and the ratio of hemin to Ir-PS was thus calculated to be 8.0%, 7.8%, 8.0%, and 7.7% for **MOZ-1**, **MOZ-2**, **MOZ-3**, and **MOZ-4**, respectively. This is consistent with a hemin to Ir-PS ratio of ~8.0%, verifying that hemin is not exchanged with Glu, Asn, or Ur in **MOZ-2**, **MOZ-3**, or **MOZ-4**, respectively.

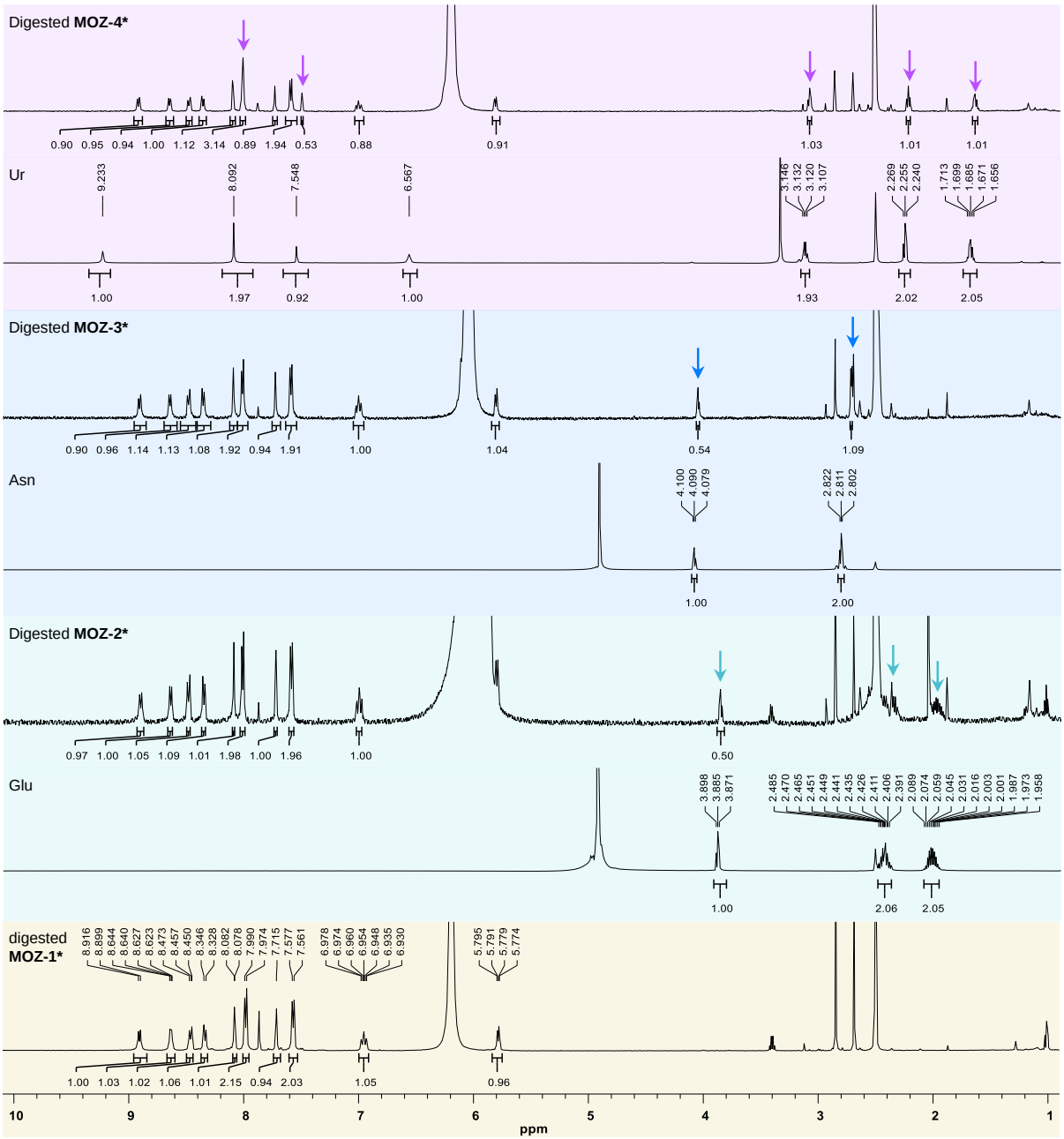

Figure 11-9. NMR analysis. From bottom to top: ^{1}H NMR spectra of digested **MOZ-1***, Glu, digested **MOZ-2***, Asn, digested **MOZ-3***, Ur, and digested **MOZ-4***. MOZ*s refer to a hemin-free analogues of MOZs to avoid the paramagnetic influence of hemin. Ir-PS signals were found in all the MOZs*, while Glu, Asn, and Ur signals were observed in MOZ-2*, **MOZ-3***, and **MOZ-4***, respectively. NMR signals of Ur ligand corresponding to amine protons (9.233 and 6.567 ppm) were not observed in the digested **MOZ-4*** due to a strong acidic digestion condition. A 1:2 NMR signal ratio of Ir-PS to Glu, Asn, or Ur was observed in **MOZ-2***, **MOZ-3***, and **MOZ-4***, respectively, corresponding to a 1:1 molar ratio of Glu, Asn, or Ur to Ir-PS. These results demonstrate that Glu, Asn, and Ur can fully replace the capped TFA during the synthesis of **MOZ-2**, **MOZ-3**, and **MOZ-4**.

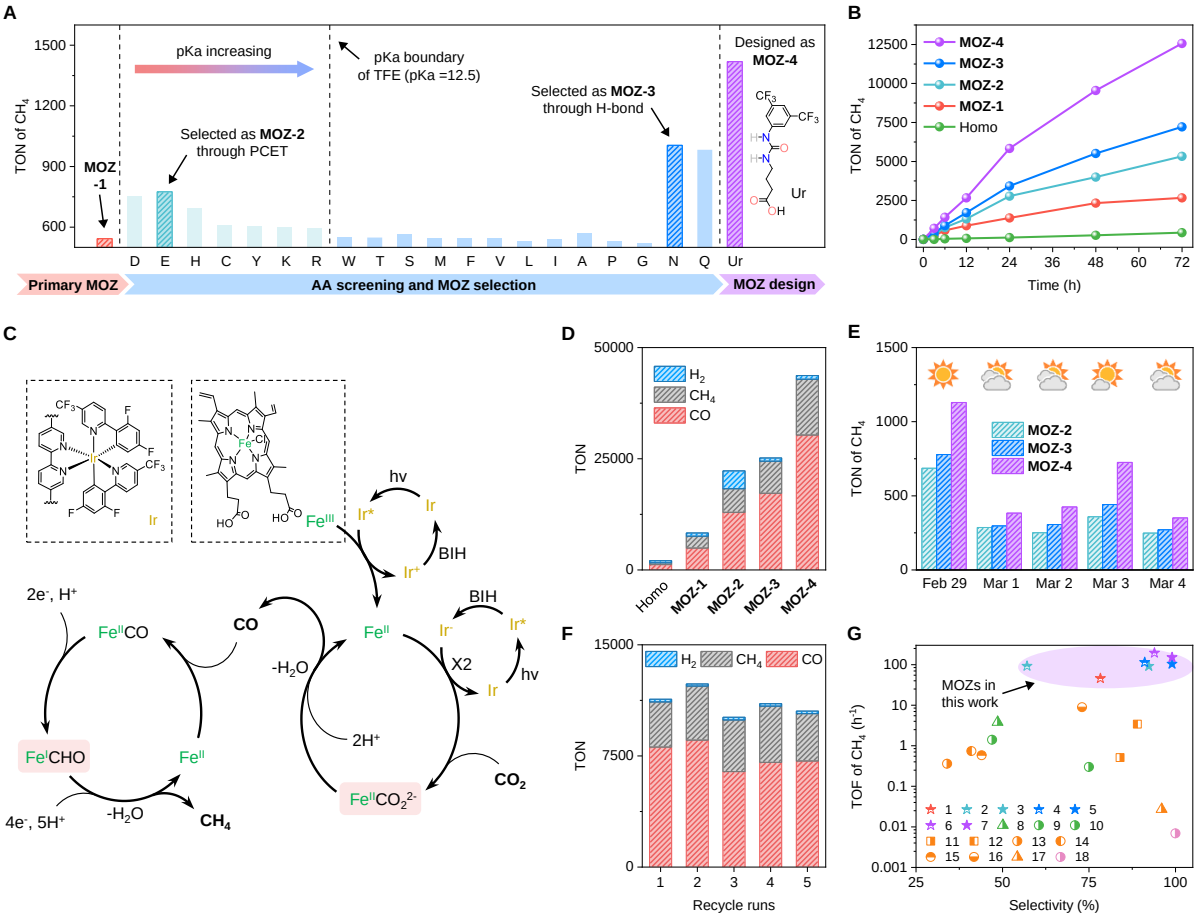

Figure 11-10. Photocatalytic conversion of CO_2 to CH_4 by MOZs. (A) TONs for CH_4 of MOZ-1, AA-modified MOZs, and Ur-modified MOZ. AAs are represented with one letter codes and inset shows the structure of Ur. (B) Time-dependent TONs of CH_4 for MOZs and homogeneous control (Homo) under visible-light irradiation (Xenon lamp). (C) The proposed two-step mechanism for photocatalytic conversion of CO_2 to CH_4, in which CO_2 is first reduced to CO, which is further reduced to CH_4. Hemin and Ir-PS are simplified as Fe^{III} and Ir, respectively. (D) TON summary of CO, CH_4, and H_2 for MOZs and homogeneous control under 72-h visible-light irradiation (Xenon lamp). (E) TONs of CH_4 for **MOZ-2**, **MOZ-3**, and **MOZ-4** over five consecutive days under direct sunlight. (F) TON summary of CO, CH_4, and H_2 for recycled **MOZ-4** over five consecutive trials. (G) Summary of activities for photocatalytic conversion of CO_2 to CH_4 by MOZs in this works compared to previously reported catalysts. Data points 1-7 refer to this work: 1, **MOZ-1**; 2, **MOZ-2**; 3, **MOZ-2** under direct sunlight; 4, **MOZ-3**; 5, **MOZ-3** under direct sunlight; 6, **MOZ-4**; and 7, **MOZ-4** under direct sunlight. Data points 8-10 refer to molecular catalysts: 8, homogeneous control in this work; 9, Fe-*p*-TMA with $Ir(ppy)_3$ [15]; 10, Fe-*p*-TMA with organic photosensitizer [21]. Data points 11-17 refer to metal and metal-oxide nanoparticle-based catalysts: 11, $Pt@Cu_2O/TiO_2$ [22]; 12, $(MgO,Pt)/TiO_2$ [23]; 13, Ag/TiO_2 [23]; 14, Pd/TiO_2 [23]; 15, Rh/TiO_2 [23]; 16, Pt/TiO_2 [24]; 17, Pd_7Cu_1/TiO_2 [25]. Data point 18 refers to metal-organic framework-based catalyst $Cu_3(BTC)_2@TiO_2$ [26]. All reactions were performed under artificial visible light, except where specifically noted. Detailed reaction conditions and additional catalysts are provided in **Table 11-1**.

Table 11-1. Summary of photocatalytic CO_2-to-CH_4 conversion with different systems

Name	**Reaction conditions***	**TOF (h^{-1}/ μmol·g^{-1}·h^{-1})**	**QYs**	**selectivity**	**References**
Metal-organic-zymes reported in this work					
Homo control	Xe lamp; DMA; r.t.; 1 atm	3.8/32.8	0.005%	48.6%	This work
MOZ-1	Xe lamp; DMA; r.t.; 1 atm	45.8/273.1	0.056%	78.3%	
MOZ-2	Xe lamp; DMA; r.t.; 1 atm	92.3/540.6	0.11%	57.1%	
	Sunlight; DMA; r.t.; 1 atm	91.5/535.9	1.1%	92.3%	
MOZ-3	Xe lamp; DMA; r.t.; 1 atm	114.0/673.1	0.14%	91.1%	
	sunlight; DMA; r.t.; 1 atm	103.8/612.9	1.2%	>99%	
MOZ-4	Xe lamp; DMA; r.t.; 1 atm	194.3/1021.7	0.24%	93.9%	
	Sunlight; DMA; r.t.;1 atm	150.8/793.0	1.8%	>99%	
Metal-organic complexes					
Fe-*p*-TMA and $Ir(ppy)_3$	AM 1.5 lamp; MeCN; r.t.; 1 atm	1.4/162	0.18%	47%	15
Fe-*p*-TMA and organic PS	AM 1.5 lamp; DMF; r.t.; 1 atm	0.30/35	0.47%	75%	21
Metal & metal oxide-based nanoparticles					
Cu/TiO_2	UV lamp; H_2O; r.t.; 1 atm	N.A./0.18	Not reported	Not reported	27
$Cu_{0.33}Pt_{0.67}@TiO_2$	AM 1.5 lamp; N.A.; r.t.; no report.	8.6/134	Not reported	Not reported	28
$Pt@Cu_2O/TiO_2$	Xe lamp; N.A.; 50; 0.2 MPa	0.51/33	Not reported	84%	22
Au/TiO_2	UV lamp; N.A.; 75; 1 atm	N.A./2.3	2.3%	Not reported	29
Pt/N-doped TiO_2	Xe lamp; N.A.; 45; 1 atm	4.5/5.7	Not reported	Not reported	30
$(MgO,Pt)/TiO_2$	Xe lamp; N.A.; 50; 0.2 MPa	3.4/11	Not reported	89%	23
Ag/TiO_2	Xe lamp; N.A.; 50; 0.2 MPa	0.36/2.1	Not reported	34%	23

Pd/TiO_2	Xe lamp; N.A.; 50; 0.2 MPa	0.74/4.3	Not reported	41%	23
Rh/TiO_2	Xe lamp; N.A.; 50; 0.2 MPa	0.58/3.5	Not reported	44%	23
Pt/TiO_2	Xe lamp; N.A.; 80; 0.4 MPa	8.9/60	Not reported	73%	24
In/TiO_2	Hg lamp; N.A.; 100; 2 kPa	6.2/675	Not reported	Not reported	31
TiO_2/MWCNT	UV lamp; N.A.; r.t.; no report	N.A./12	Not reported	Not reported	32
SEG-TiO_2	Hg lamp; N.A.; r.t.; no report	N.A./500	Not reported	Not reported	33
(N_3-dye,Cu,Fe)/ TiO_2	Hg lamp; N.A.; 75; 1 atm	0.040/0.85	0.045%	Not reported	34
$ZnPc/TiO_2$	Tungsten-Halogen lamp; H_2O; no report; no report	62/133	Not reported	Not reported	35
Pd_7Cu_1/TiO_2	Xe lamp; N.A.; no report; 0.2 MPa	0.027/19.6	Not reported	96%	25
(NiO,In_2O_3)/TiO_2	Hg lamp; N.A.; no report; 1 atm	7.9/240	Not reported	Not reported	36
WO_3	Xe lamp; N.A.; r.t.; 1 atm	N.A./1.0	Not reported	Not reported	37
Zn_2GeO_4	Xe lamp; N.A.; r.t.; 1 atm	N.A./1.5	Not reported	Not reported	38
Pt/(g-C_3N_4/$NaNbO_3$)	Xe lamp; N.A.; no report; 1 atm	N.A./6.4	Not reported	Not reported	39
$SrNb_2O_6$	Xe lamp; N.A.; 50; 0.2 MPa	N.A./0.33	0.065%	67%	40
Metal-organic frameworks					
$Cu_3(BTC)_2$@TiO_2	Xe lamp; N.A.; 40; 0.15 MPa	0.0069/2.63	Not reported	100%	26
MOF-525-Co	Xe lamp; MeCN; no report; 80 kPa	0.32/37	Not reported	Not reported	41
Perovskite					
$CsPbBr_3$ QD/GO	AM 1.5 lamp; EA; no report; no report	N.A./29.6	Not reported	99%	42

*Reaction conditions in the order of light source, reaction solvent, reaction temperature, and pressure of CO_2. N.A. refers to a gas-solid phase reaction without any solvent.

The MOZs in this library were next examined in photocatalytic CO_2 reduction. MOZs (0.1 nmol based on Hemin) were individually added to 1 mL DMA solutions of TFE (0.1 M, as proton resource) with BIH (50 mM, as sacrificial reductant) under 1 atm CO_2 and visible-light irradiation for 6 h (Xenon lamp, λ > 250nm). The coexistence of AAs and hemin formed unique active site on each Hf_{12} cluster, having two AA residues and side-chain functional groups within several angstroms of hemin iron-centers. The active sites in these MOZs have smaller footprints (sizes) than most natural enzymes (~30 vs. ~60 nm^3 per active site, see section 11**.4.3**). Upon light irradiation, photoexcited Ir-PS ligands injected electrons into these unique active sites of each MOZ to drive CO_2 reduction. As previously reported, the Fe-porphyrin catalyzed conversion of CO_2 to CH_4 proceeds through two-steps: (1) CO_2 is reduced to the stable intermediate CO through a two-electron and two-proton process and (2) thusly generated CO is further reduced to CH_4 through a six-electron and six-proton process (**Figure 11-10C**, see section 11**.4.6**) [15, 21, 43]. The only observed byproduct of this reaction is H_2, which is proposed to proceed through a competing reaction pathway (**Figure 11-15F**) [15, 21]. Thus, the activity of each MOZ for CO_2 reduction was evaluated by quantifying the generation of CH_4. **MOZ-1** showed a 7-fold enhancement over the homogeneous control (a molar-equivalent mixture of hemin and Ir-PS) owing to the accelerated electron transfer from excited Ir-PSs to the adjacent hemin (<2 nm distance) (**Figure 11-10B**). AA-modified MOZs further enhanced activities for CO_2 reduction owing to two distinct pathways: PCET and H-bond stabilization (**Figure 11-10A**).

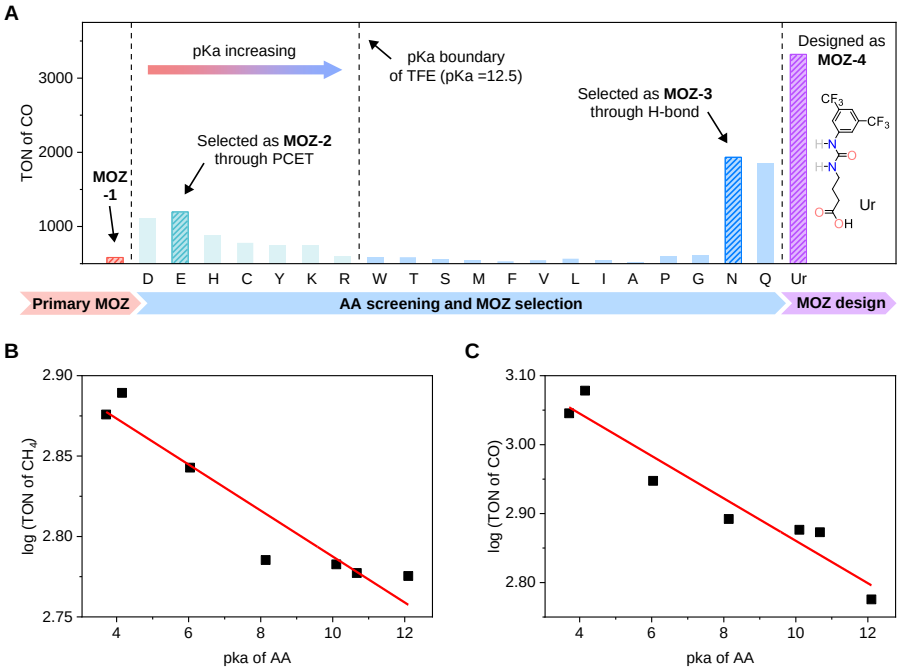

Figure 11-11. AA screening. (A) TON of CO for **MOZ-1**, AA-modified **MOZ-1**, and Ur-modified **MOZ-1**. Glu- and Asn-modified **MOZ-1** (**MOZ-2** and **MOZ-3**, respectively) were selected due to their enhanced activity. Ur-modified MOZ-1 was designed as **MOZ-4**. (B) log(TON of CH_4) and (C) log(TON of CO) both showed negative correlation with pKa values of modified AA with the Pearson correlation coefficient of -0.95 and -0.96, respectively.

First, as the generation of both CO and CH_4 requires protons and electrons, MOZs with amino acid side chains more acidic (i.e., lower pKa) than TFE (pKa = 12.5) could enhance activity through a PCET pathway [44]. This correlation was quantified by plotting TONs for both CH_4 and CO generation with the pKa values of AA side chains on individual MOZs, affording Pearson correlation coefficients of -0.95 and -0.96, respectively (**Figure 11-11**). The CO_2 reduction activity enhancement via the PCET pathway was maximized in **MOZ-2** with Glu modification, consistent with the lowest pKa for the Glu side chain among the 20 proteinogenic AAs. As MOZs modified with AAs whose side chains were less acidic than TFE were not expected to exhibit higher activity than **MOZ-1**, we were surprised to discover that Asn- and Gln-modified **MOZ-1** afforded much higher CO_2 reduction over **MOZ-2** (**Figure 11-10A**). We attributed this unexpected activity enhancement by Asn and Gln to the secondary-coordination

sphere stabilization through H-bond interactions between electron-deficient amide –NH_2 fragments and Fe-bound CO_2-reduction reactive intermediates (**Figure 11-1B**) [45]. The CO_2 reduction activity enhancement via the H-bond pathway was maximized in **MOZ-3** with Asn modification.

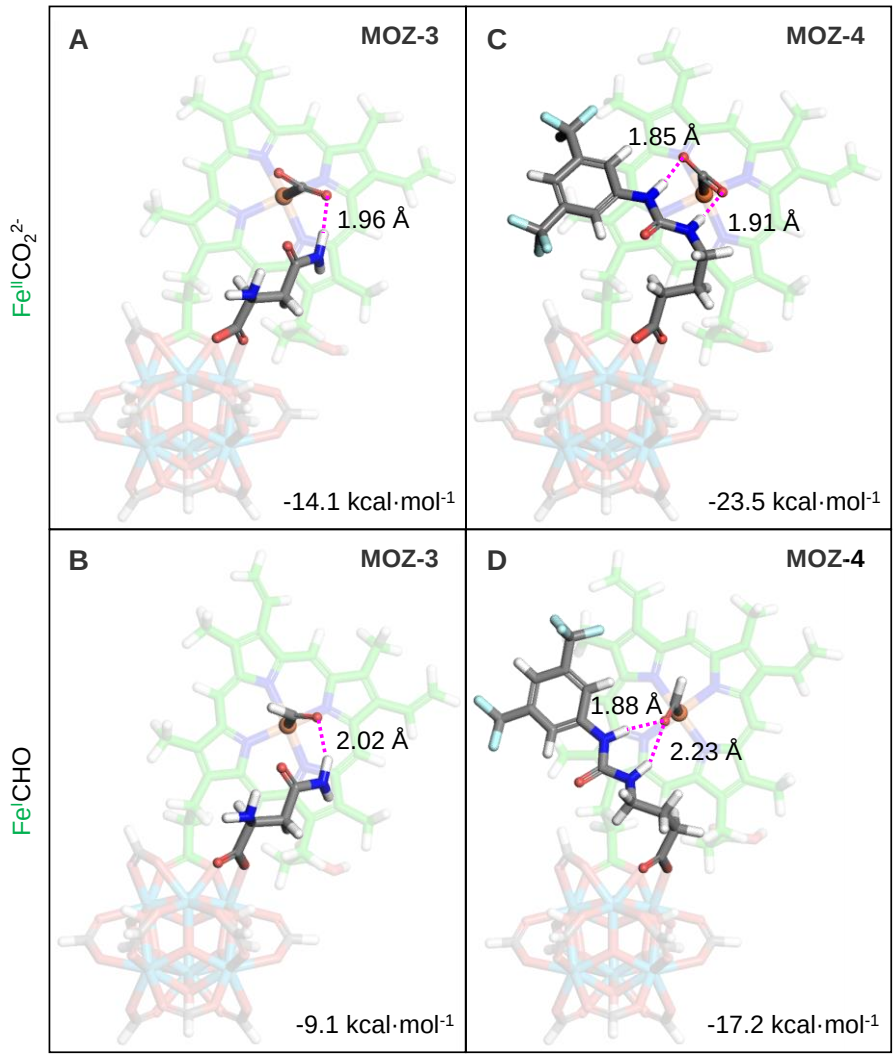

Figure 11-12. Hydrogen-bonding stabilization. Representative model structures of (A) $Fe^{II}CO_2^{2-}$ and (B) $Fe^{I}CHO$ in **MOZ-3** and (C) $Fe^{II}CO_2^{2-}$ and (D) $Fe^{I}CHO$ in **MOZ-4**, optimized by DFT calculation at UB3LYP-D3 level of theory with a simplified Zr_6 cluster. C atoms in Heme are labeled in green, with all other atoms are labeled as follows: H, white; C, gray; O, red; N, blue; F, cyan; Fe, orange; Zr, light blue. Fe-bound CO_2, Fe-bound CHO, Asn, and Ur are highlighted. H-bonds are presented as magenta dotted line with their bond distances labeled alongside and corresponding stabilized enthalpy (ΔH_{Stb}) detailed in the bottom right corners.

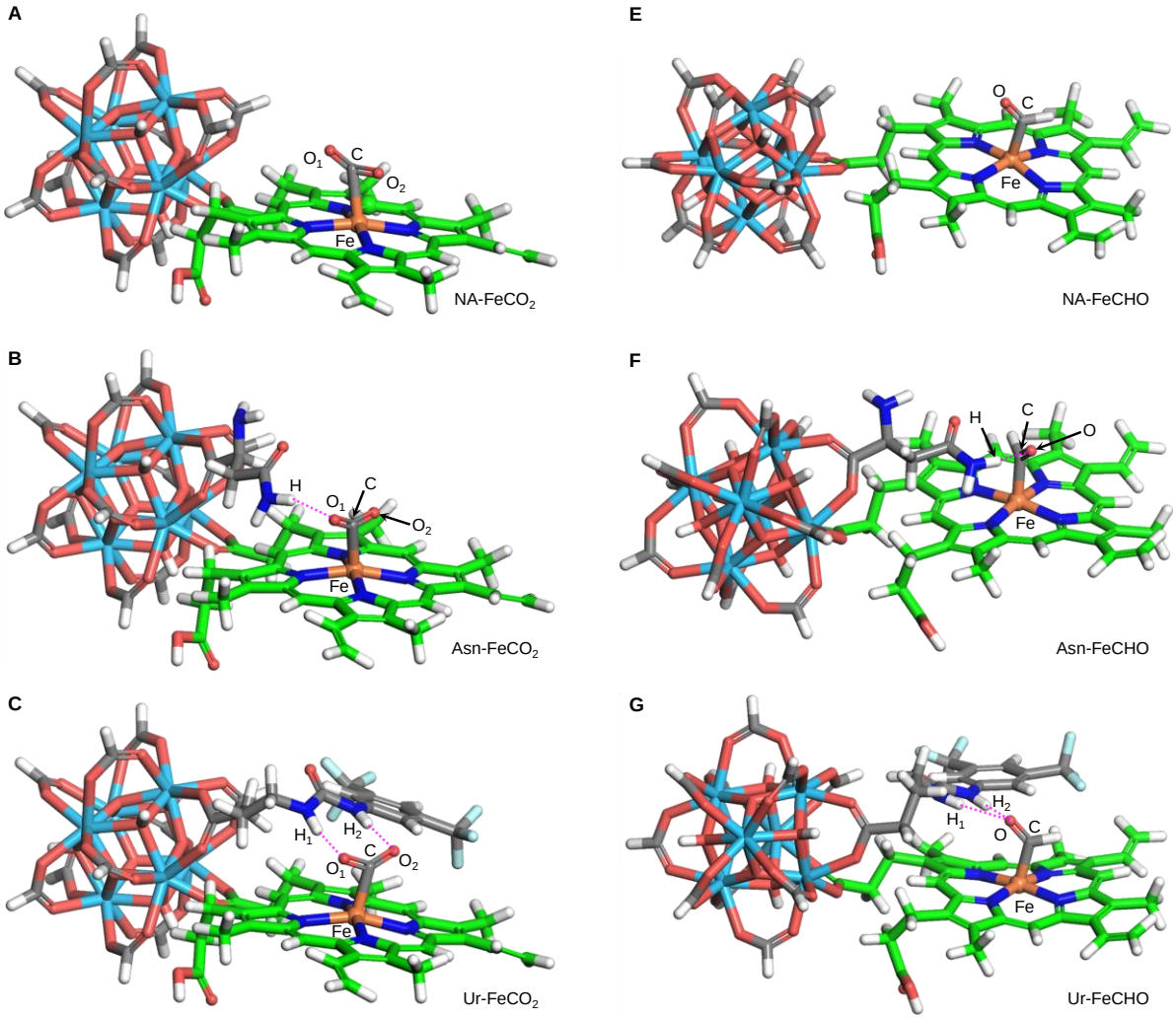

D

Parameters	NA-$FeCO_2$	Asn-$FeCO_2$	Ur-$FeCO_2$
d_{Fe-C} (Å)	2.19	2.10	2.04
d_{C-O} (Å)	1.21 ($C–O_1$) 1.23 ($C–O_2$)	1.22 ($C–O_1$) 1.23 ($C–O_2$)	1.24 ($C–O_1$) 1.23 ($C–O_2$)
$\angle O_1–C–O_2$ (°)	150.0	145.9	136.2
$d_{H\text{-}bond}$ (Å)	-	1.96 ($H\cdots O_1$)	1.91 ($H_1\cdots O_1$) 1.85 ($H_2\cdots O_2$)
NPA Charge (CO_2)	-0.29	-0.38	-0.56
ΔH_{stb} (kcal·mol^{-1})	0	-14.1	-23.5

H

Parameters	NA-FeCHO	Asn-FeCHO	Ur-FeCHO
d_{Fe-C} (Å)	2.02	1.88	1.86
d_{C-O} (Å)	1.20	1.21	1.22
$d_{H\text{-}bond}$ (Å)	-	2.02 ($H\cdots O$)	2.23 ($H_1\cdots O$) 1.88 ($H_2\cdots O$)
NPA Charge (CO_2)	-0.31	-0.36	-0.43
ΔH_{stb} (kcal·mol^{-1})	0	-9.1	-17.2

Figure 11-13. Optimized structures by DFT calculations. Optimized structures of (A) NA-$FeCO_2$ (as control), (B) Asn-$FeCO_2$ (in **MOZ-3**), and (C) Ur-$FeCO_2$ (in **MOZ-4**) with the crucial atoms labeled. (D) Summary of the geometries of the bound CO_2 in the above optimized structures. Optimized structures of (E) NA-FeCHO (as control), (F) Asn-FeCHO (in **MOZ-3**), and (G) Ur-FeCHO (in **MOZ-4**) with the crucial atoms labeled. (H) Summary of the geometries of the bound CHO in the above optimized structures.

This H-bond stabilization in **MOZ-3** was elucidated by DFT calculation. In the proposed two-step reduction of CO_2 and CO, $Fe^{II}CO_2^{2-}$ and $Fe^{I}CHO$ are recognized as crucial reactive intermediates (**Figure 11-10C**). DFT calculations were thus performed on each model compounds to investigate the possible geometry of $Fe^{II}CO_2^{2-}$ and $Fe^{I}CHO$, respectively (**Figure 11-12** and **Figure 11-13**, see section 11**.4.7**) [46]. **MOZ-3** revealed a moderate H-bond interaction between amide arms and Fe-boundCO_2 in $Fe^{II}CO_2^{2-}$ with (N)H···O donor–acceptor distances of 1.96 Å. This anchoring of CO_2 corresponded with a free enthalpy of stabilization (ΔH_{Stb}) of -14.1 kcal·mol^{-1} (**Figure 11-12A**). **MOZ-3** further revealed an additional moderate H-bond interaction between the amide arm and the Fe-bound CHO in $Fe^{I}CHO$ with (N)H···O donor–acceptor distances of 2.02 Å, corresponding to a ΔH_{Stb} of -9.1 kcal·mol^{-1} (**Figure 11-12B**).

The performance of the MOZs selected by these different reaction pathways were further evaluated in time-dependent reactions. Upon 72-h visible light irradiation, **MOZ-2** and **MOZ-3** significantly enhanced CO_2 reduction with the TONs for CH_4 generation reaching 4258 and 5773, respectively, compared to 2132 for **MOZ-1** and only 343 for the homogenous control (**Figure 11-10B**). These TONs showed a linear increase over time, indicating the stability of these MOZs in photocatalytic CO_2 reduction. The structural stability of these MOZs was further confirmed by PXRD of MOZs recovered after reactions (**Figure 11-14E**) and by ICP-MS analyses which showed the leaching of <1% Hf, <2% Ir, and <2% Fe into the supernatant. **MOZ-2**, however, was only moderately selective for CH_4 generation (57.1%), as the PCET pathway enabled by Glu also accelerated the generation of H_2 (**Figure 11-10D** and **Figure 11-14A,B**). In contrast, **MOZ-3** only accelerated the sequential generation of CO and CH_4 by

stabilizing their reactive intermediates while leaving the H_2 generation pathway unaltered, thus leading to an enhanced selectively of 91.1% (**Figure 11-10D** and **Figure 11-14A,B**). This proposed sequential generation of CO and CH_4 was experimentally demonstrated by the more efficient CH_4 generation with CO as substrate (**Figure 11-15A-C**).

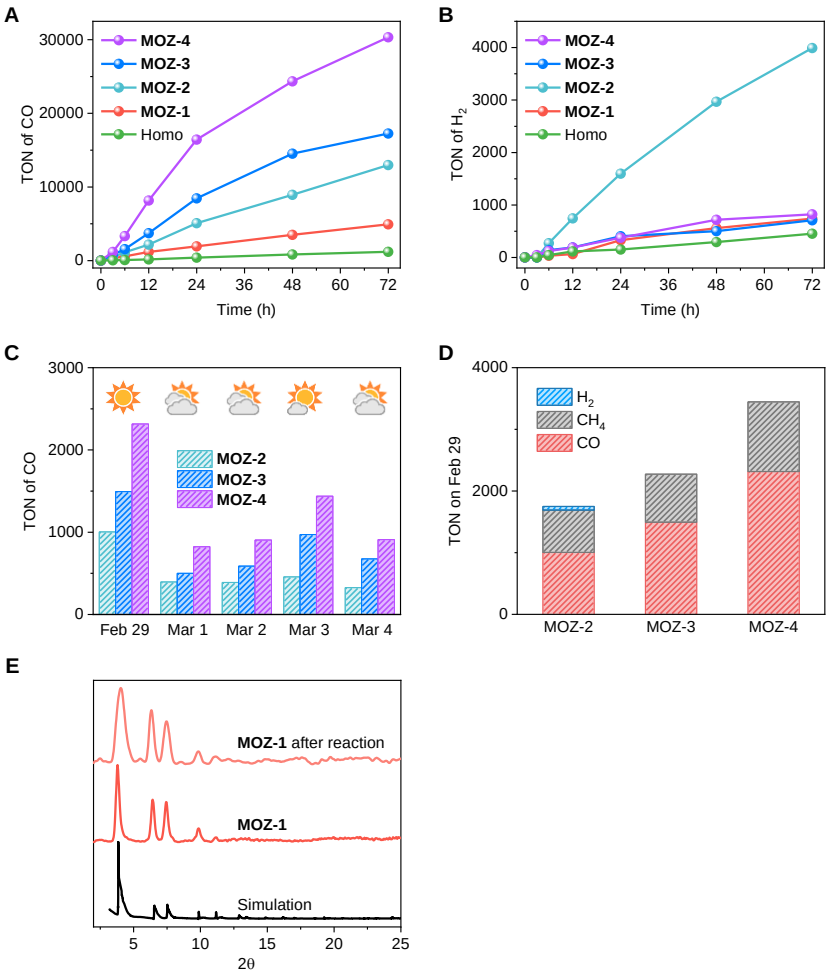

Figure 11-14. Photocatalytic CO_2 reduction. Time-dependent TONs of (A) CO and (B) H_2 for **MOZ-1**, **MOZ-2**, **MOZ-3**, **MOZ-4**, and homogeneous control (Homo, mixture of Ir-PS and hemin) under Xenon lamp irradiation. (C) TONs of CO for **MOZ-2**, **MOZ-3**, or **MOZ-4** over five consecutive days (Feb 29 to Mar 4, 2020) under direct sunlight. (D) TON of CO, CH_4, and H_2 for **MOZ-2**, **MOZ-3**, and **MOZ-4** under direct sunlight on Feb 29, 2020. (E) PXRD pattern of MOZ-1; after 72 h under reaction condition this pattern remained similar to those of simulated and freshly prepared **MOZ-1**, demonstrating stability of MOZs during photocatalytic reactions.

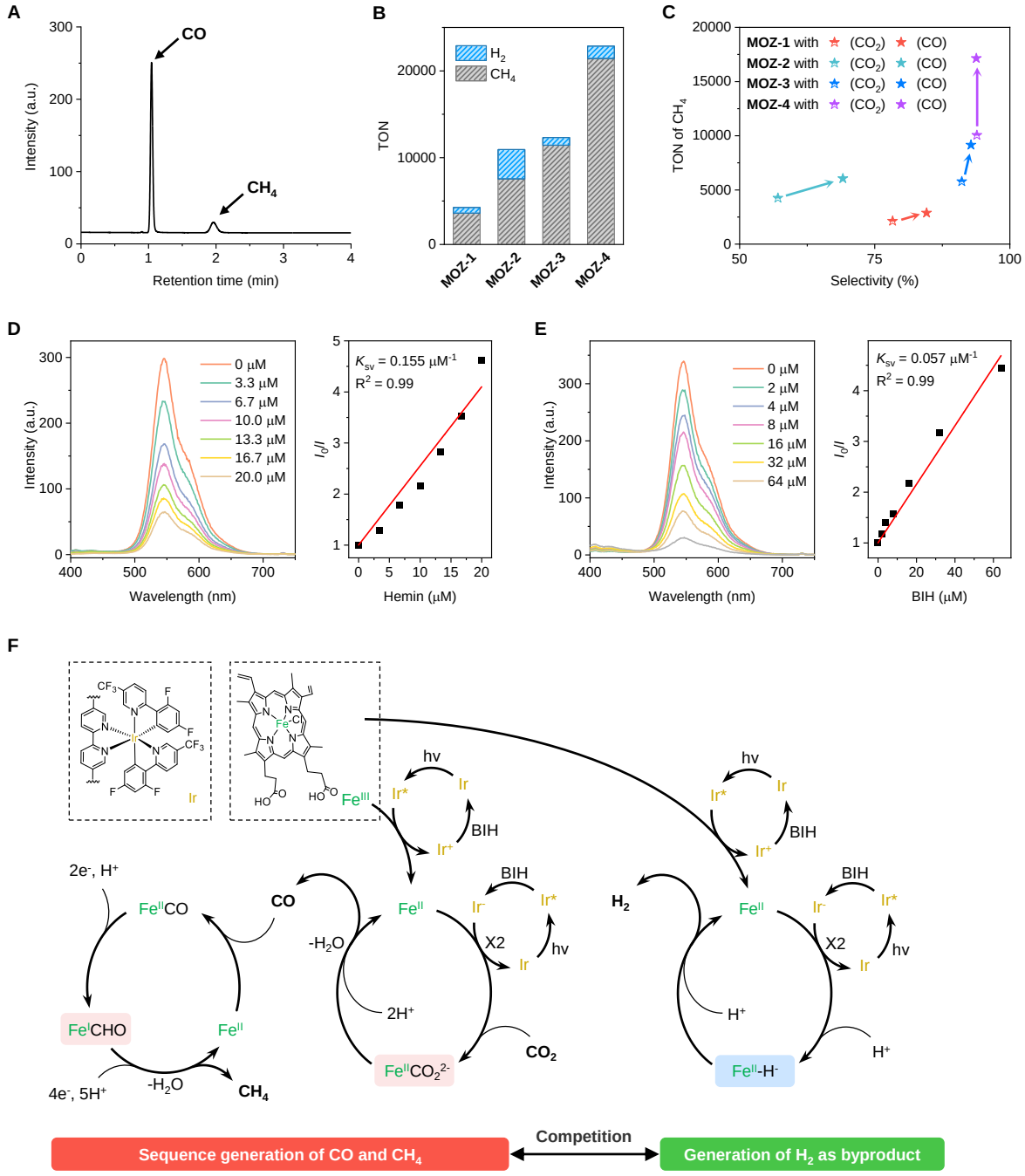

Figure 11-15. Mechanistic analysis. (A) Example gas chromatogram for observed gaseous products by FID detector. Retention times were 1.04 and 1.95 min for CO and CH_4, respectively. (B) TON of CH_4 and H_2 with CO/N_2 (1:9) atmosphere for **MOZ-1**, **MOZ-2**, **MOZ-3** or **MOZ-4** under 72 h visible-light irradiation (Xenon lamp). (C) Reaction summary (TON and selectivity) of CH_4 generation with both CO_2 and CO/N_2 (1:9) atmospheres, under 72 h visible-light irradiation (Xenon lamp). (D) Luminescence spectra upon excitation at 350 nm of 20 μM Ir-PS in DMF with varying concentrations of hemin (left) and its Stern-Volmer fitting (right, $R^2 = 0.99$ and $K_{SV} = 0.155\ \mu M^{-1}$). (E) Luminescence spectra upon excitation at 350 nm of 20 μM Ir-PS in DMF with varying concentrations of BIH (left) and its Stern-Volmer fitting (right, $R^2 = 0.99$ and $K_{SV} = 0.057\ \mu M^{-1}$). (F) The proposed complete mechanism for photocatalytic CO_2-to-CH_4 conversation, with competing H_2 generation as byproduct

Inspired by the outstanding catalytic performance of **MOZ-3** for both activity and selectivity, a urea-based ligand (Ur) was designed to provide even stronger H-bond stabilization. Ur incorporates a phenyl ring bearing two electron-withdrawing -CF_3 groups to enhance the electron-deficiency of the urea –NH fragment. Ur was modified onto **MOZ-1** in the same manner as proteinogenic AAs to afford **MOZ-4**, which was similarly characterized as **MOZ-2** and **MOZ-3** to reveal a conserved morphology, topography, and structure, with the formula $Hf_{12}(\mu_3\text{-}O)_8(\mu_3\text{-}OH)_8(\mu_2\text{-}OH)_6$(Ir-PS)$_6$(hemin)$_{0.46}(Ur)_{5.54}$ (**Figure 11-4F,G** and **Figure 11-7 to 9**). As expected, **MOZ-4** further enhanced selective reduction of CO_2 by 5-fold over **MOZ-1** and 29-fold over the homogeneous control, with a TON and selectivity for CH_4 of 10053 and 93.9%, respectively, over 72 h of visible-light irradiation (**Figure 11-10B,D**). This stable, heterogeneous **MOZ-4** was recycled at least five times without no apparent loss of activity (**Figure 11-10F**). This further enhancement in activity over **MOZ-3** was attributed to stronger H-bond stabilization, as elucidated by similar DFT calculations. Two strong H-bonds were modeled to $Fe^{II}CO_2^{2-}$ with (N)H···O donor–acceptor distances of 1.85 Å and 1.91 Å, respectively, corresponding to a ΔH_{Stb} of -23.5 kcal·mol^{-1} (**Figure 11-12C**). Two additional strong/moderate H-bonds was modeled to $Fe^{I}CHO$ with (N)H···O donor–acceptor distances of 1.88 Å and 2.23 Å, respectively, corresponding to a ΔH_{Stb} of -17.2 kcal·mol^{-1} (**Figure 11-12D**).

MOZ-4 was further examined for photocatalytic CO_2 conversion to CH_4 under direct sunlight. These photocatalytic CO_2 reduction studies were carried out under the same conditions as described above under natural sunlight for five consecutive winter days in Chicago, Illinois: Feb 29 to Mar 4, 2020 from 10 am to 4 pm (**Figure 11-10E** and **Figure 11-14C,D**). Reactivity was weather-dependent, but on a sunny day (Feb 29), **MOZ-4** catalyzed

CH_4 generation with a TON of 904, a TOF of 150.7 h^{-1}, a quantum yield of 1.8%, and a selectivity of over 99%. **MOZ-4** thus directly converted CO_2 to CH_4 with energy input from sunlight. The MOZs reported in this work showed higher activity (by over an order of magnitude) and selectivity than previously reported catalysts, including small molecules [15, 21], metal or metal oxide nanoparticles [22-25], metal-organic frameworks [26], and others (**Figure 11-10G** and **Table 11-1**), and are able to operate under ambient conditions and direct sunlight. We anticipate that the operating principles of our system may aid in the development of other MOZ systems for increasingly challenging reactions (e.g., N_2 reduction, complex molecule synthesis, etc) by readily integrating various metal complexes, amino acids, artificial ligands, and other cofactors into proper MOL templates.

11.3 Methods

Synthesis of Hf-Ir MOL. To a 4 mL glass vial was added 0.5 mL of a $HfCl_4$ solution (2.0 mg/mL in DMF), 0.5 mL of an Ir-PS solution (4.0 mg/mL in DMF), 2 μL of TFA, and 5μL of water. The reaction solution was kept in an 80 °C oven for 24 hours. The afforded yellow precipitate was collected by centrifugation and washed with DMF three times. Yield was 43% based on Hf as determined by ICP-MS.

Synthesis of 4-(3-(3,5-bis(trifluoromethyl)phenyl)ureido)butanoic acid (Ur). An aqueous solution of the 4-amino butanoic acid (0.83 g, 8.0 mmol) was heated to boiling and 1-isocyanato-3,5-bis(trifluoromethyl)benzene (2.1 g, 8.2 mmol) was added in five portions to the gently refluxing solution. This reaction mixture was refluxed for 20 min, cooled to room temperature, and treated with an equimolar amount of concentrated HCl (12 M, 0.7 mL) to pH ~1. This reaction mixture was then kept at room temperature for 7 h and precipitated crystals

were filtered off. The solid was further purified by column chromatography on silica gel using a 10:1 $CHCl_3$:MeOH solution as the eluent to give Ur ligand as white crystals. Yield: 81% (2.32 g). ^{1}H NMR (500 MHz, DMSO-d_6) δ 9.22 (s, 1H), 8.08 (s, 2H), 7.54 (s, 1H), 6.56 (s, 1H), 3.12 (q, J = 6.7 Hz, 2H), 2.24 (t, J = 7.4 Hz, 2H), 1.67 (p, J = 7.2 Hz, 2H). ^{13}C NMR (126 MHz, DMSO-d_6) δ 174.71, 155.3, 143.1, 131.01 (q, J = 32.76 Hz), 124.9, 122.7, 120.5, 39.1, 31.5, 25.5. HRMS: m/z calculated for $C_{13}H_{13}F_6N_2O_3$ $[M+H]^+$: 359.0910, found: 359.0838.

Synthesis of MOZ-1. To a 1 mL DMF suspension of Hf-Ir (4.1 μmol based on Ir) was added 0.267 mg (0.41 μmol) hemin. The reaction mixture was stirred for 3 hours at room temperature. The afforded dark yellow precipitate was collected by centrifugation and washed with DMF three times to generate **MOZ-1**.

AA modification and synthesis of MOZ-2, MOZ-3, and MOZ-4. To separate 1 mL DMF suspensions of **MOZ-1** (4.0 μmol based on Ir) was added 3 equivalents relative to iridium of each AA or Ur. Each reaction mixture was stirred overnight at room temperature. The afforded dark yellow precipitates were collected by centrifugation and washed with DMF three times to give modified MOZs. **MOZ-2** and **MOZ-3** were generated from Glu and Asn modification, respectively, and **MOZ-4** was generated from Ur modification.

MOZ screening for photocatalytic CO_2 reduction. To separate 4.6 mL vials were added 1 mL DMA, 11.2 mg BIH, 7.3 μL TFE, and 0.1 nmol based on hemin of each modified MOZ. Each vial was sealed with a septum and degassed with CO_2 for 10 min before being stirred under visible-light irradiation (Xenon lamp) for 6 hours. 200 μL of gaseous products from each vial were collected in gas-tight syringes for GC analysis.

Time-dependent photocatalytic CO_2 reduction. To separate 4.6 mL vials was added 1 mL

DMA, 11.2 mg BIH, and 7.3 μL TFE. **MOZ-1**, **MOZ-2**, **MOZ-3**, **MOZ-4** (0.1 nmol based on hemin), or a homogeneous control (0.1 nmol hemin and 1.25 nmol Ir-PS) was added to individual vials. Each vial was then sealed with a septum and degassed with CO_2 for 10 min and before being stirred under visible-light irradiation (Xenon lamp) for 3 h, 6 h, 12 h, 24 h, 48 h, and 72 h. 200 μL of gaseous products from each vial were collected at each time point in gas-tight syringes for GC analysis.

Sunlight-driven CO_2 reduction. To separate 4.6 mL vials was added 1 mL DMA, 11.2 mg BIH, and 7.3 μL TFE. **MOZ-2**, **MOZ-3**, and **MOZ-4** (0.1 nmol based on hemin) were added to individual vials. Each vial was then sealed with a septum and degassed with CO_2 for 10 min before being stirred under direct sunlight from 10:00 to 16:00 between Feb. 29 and Mar. 4, 2020. 200 μL of gaseous products from each vial were collected on each day in gas-tight syringes for GC analysis.

Recycling studies. To a 4.6 mL vial was added 1 mL DMA, 11.2 mg BIH, 7.3 μL TFE, and **MOZ-4** (0.1 nmol based on hemin). The vial was then sealed with a septum and degassed with CO_2 for 10 min before being stirred under visible-light irradiation (Xenon lamp) for 12 hours. 200 μL of gaseous products were collected in gas-tight syringes for GC analysis. **MOZ-4** was then recovered and reused in four repeated trials.

Photocatalytic CO reduction. To separate 4.6 mL vials was added 1 mL DMA, 11.2 mg BIH, and 7.3 μL trifluoro ethanol. **MOZ-1**, **MOZ-2**, **MOZ-3**, **MOZ-4** (0.1 nmol based on hemin) was added to individual vials. Each vial was then sealed with a septum and degassed with a CO/N_2 mixture (1:9) for 10 min before being stirred under visible-light irradiation (Xenon lamp) for 72 h. 200 μL of gaseous products from each vial were collected in gas-tight syringes for

GC analysis.

Luminescence quenching studies. Hemin was added incrementally to a 20 μM Ir-PS solution in DMF to afford hemin concentrations of 0, 3.3, 6.7, 10.0, 13.3, 16.7, and 20.0 μM. A luminescence spectrum was collected at each hemin concentration by a fluorimeter with an excitation wavelength of 350 nm (**Figure 11-15D**). The oxidative quenching of Ir-PS by hemin was supported by fitting the obtained intensities at 545 nm (I) to the concentration of hemin (C_{Hemin}) using the Stern-Völmer equation:

$$\frac{I_0}{I} = 1 + K_{\text{SV}} C_{\text{Hemin}}$$

where K_{SV} is the Stern-Völmer constant and I_0/I is the ratio of luminescence intensity of Ir-PS at 545 nm in the absence and presence of hemin. I_0/I revealed a strong linear correlation to the C_{Hemin} with $R^2 = 0.99$ and $K_{\text{SV}} = 0.155$ μM^{-1}.

The luminescence quenching of Ir-PS by BIH was studied under a similar condition (**Figure 11-15E**) with $R^2 = 0.99$ and $K_{\text{SV}} = 0.057$ μM^{-1}.

Quantum yield (QY) calculation. The quantum yields for the photocatalytic CO_2 reduction were determined by following equations:

$$QY_{\text{CO}} = \frac{\text{Number of generated CO molecules} \times 2}{\text{Numbers of incident photons}}$$

$$QY_{\text{CH}_4} = \frac{\text{Number of generated CH}_4\text{ molecules} \times 8}{\text{Numbers of incident photons}}$$

The number of incident photons were measured using $K_3Fe(C_2O_4)_3$ as chemical actinometer irradiated with Xenon lamp or sunlight with 350 ± 10 nm band-pass optical filter according to previously reported literature [37] and known parameters [47]. The number of generated CO or CH_4 was also measured under the same irradiation condition (Xenon lamp or sunlight with 350 ± 10 nm band-pass optical filter).

DFT calculation. DFT calculations utilized the density functional methods implemented in Gaussian 16 (revision C.01) [48]. We relied upon unrestricted B3LYP-D3 methods [46]. The 6-31G* basis set was used for light atoms (e.g. C, H, O, N, F) [49] while the LANL2DZ basis set was used for Fe with effective core potentials (ECPs) for preliminary screening of conformations and spin states [50, 51]. The self-consistent field was set to quadratically convergent with an extra step if the first order SCF would not converge (SCF=XQC). Geometries of all models were optimized in the gas phase on basis of experimental X-ray structures. Gibbs free energy was calculated using zero-point energy and thermal corrections. All conformations were geometrically optimized to the energy minimum. Frequency calculations and natural charge calculation were performed on the optimized structures with the same basis set and level of theory.

11.4 Supplementary text

11.4.1 Hf-Ir MOL

The Hf-Ir monolayer is proposed to be constructed from previously reported Hf_{12} clusters [52], which are vertically capped by TFA and laterally linked by Ir-PS to generate a 2D network with the **kgd** topology. This monolayer morphology of Hf-Ir was confirmed by TEM and AFM, revealing a diameter of ~150 nm (**Figure 11-4B**) and a thickness of ~1.7 nm, respectively, corresponding with the modeled structure of TFA capped Hf_{12} cluster (**Figure 11-4D,E**). The **kgd** topology was confirmed by both HRTEM (**Figure 11-4C**) and HAADF (**Figure 11-4H-J**) revealing a six-fold pattern and a Hf_{12}-Hf_{12} distance of ~2.8 nm, corresponding with the modeled structure of Hf-Ir. Additionally, Hf-Ir presented a similar PXRD pattern to that of its simulated structure (**Figure 11-4F**). The composition of Hf-Ir was thus proposed to be $Hf_{12}(\mu_3$-

$O)_8(\mu_3\text{-}OH)_8(\mu_2\text{-}OH)_6(Ir\text{-}PS)_6(TFA)_6$. This composition was further confirmed by ICP-MS which revealed the expected Hf:Ir ratio of approximately 1:2 and by NMR of digested Hf-Ir, where ^1H NMR confirmed the presence of Ir-PS (**Figure 11-4K**) and ^{19}F NMR revealed the expected 1:1 ratio of TFA to Ir-PS (**Figure 11-4L**). (Since each Ir-PS has two $-CF_3$ groups while each TFA only has one $-CF_3$ group, the 2:1 NMR signal ratio of Ir-PS to TFA in **Figure 11-4L** corresponds to a 1:1 molar ration of Ir-PS to TFA.)

11.4.2 Active sites in MOZs.

Each Hf_{12} cluster in the Hf-Ir monolayer is capped by six CF_3COO^- groups, with three on each the top and bottom face. (Each face of Hf_{12} clusters is defined as potentially active site after hemin and AA loading). The strongly electron withdrawing $-CF_3$ group in CF_3COO^- results in weak coordination to the Hf_{12} clusters (through Hf-O bonds). This weak coordination is reflected in the strong acidity of CF_3COOH with the pKa of 0.23, and enabled facile carboxylate exchange reactions with relatively electron-rich carboxylate group. This property makes the Hf-Ir monolayer a good template for building catalytic sites.

To build **MOZ-1**, electron-rich carboxylate groups of hemin, with the pKa of 3.2-3.5 [53], could efficiently replace the CF_3COO^- in Hf-Ir monolayer. 8.0% of TFA in Hf-Ir was replaced by hemin from a 0.10 molar equivalent hemin solution in DMF over a 3-h reaction, as determined by UV-vis analysis (**Figure 11-5E**). We propose this 8.0% hemin-loading is distributed homogenously over Hf_{12} sites, with 24% Hf_{12} sites having one hemin groups and the rest having none. Two hemin groups on the same Hf_{12} face is sterically unfavorable, and such binding was presumed to be negligible.

To construct more complex MOZs, AAs (3 equivalents to TFA) with relatively electron-

rich carboxylate groups and pKas of ~2.0 successfully replaced all the remaining TFA in **MOZ-1**, while did not replace hemin (see discussion later). To note, Glu is probably binding through the carboxylate group in the side chain rather than the main chain, but it would result in the same PCET this effect. Thus, ~24% Hf_{12} sites in these MOZs were composed of one hemin molecule and two AA molecules. The hemin and AA molecules were several angstroms apart and thus were active sites for CO_2 reduction, as described in the manuscript.

11.4.3 Active-site density in MOZs

As shown in **Figure 11-4A**, MOZs are composed of repeating triangular units of three Hf_{12} clusters. Considering the Hf_{12}-Hf_{12} distance of ~2.8 nm and Hf_{12} height of ~2.1 nm in MOZs, the volume of this unit, regarded as triangular prism, was estimated to be

$$0.5 \times 2.8 \times 1.4\sqrt{3} \times 2.1 = 7.1\ \text{nm}^3$$

Since each unit has three Hf_{12} clusters, each Hf_{12} cluster is shared by another adjacent 5 units, each Hf_{12} cluster has two Hf_{12} site, and 24% of these sites are active (with hemin), the average volume for each active site in these MOZs was estimated to be:

$$\frac{7.1}{3 \div 6 \times 2 \times 24\%} = 30\ \text{nm}^3$$

For enzymes, the volume (V) for each active-site/enzyme can be estimated from its mass (M) through the empirical equation [54]:

$$V(nm^3) = 1.212 \times 10^{-3}(\text{nm}^3/\text{Da}) \times M(\text{Da})$$

Since the majority of enzyme protein molecules have a molecular weight within the range of 20-160,000 kDa (average of ~50 kDa), the average volume for each active site in enzymes was estimated to be:

$$1.212 \times 10^{-3}(\text{nm}^3/\text{Da}) \times 50{,}000(\text{Da}) = 60\ \text{nm}^3$$

According to these estimation results, MOZs (~30 nm^3 per active-site) in this work thus have higher active-site density than the majority of enzymes (average ~60 nm^3 per active-site).

11.4.4 Composition analysis of MOZs

MOZ-1. The hemin to Ir-PS ratio in **MOZ-1** was determined to be 8.0% by UV-Vis analysis (**Figure 11-8E**), suggesting 8.0% of capped TFA is replaced by hemin through carboxylate exchange. The composition of **MOZ-1** was thus proposed to be $Hf_{12}(\mu_3\text{-}O)_8(\mu_3\text{-}OH)_8(\mu_2\text{-}OH)_6(\text{Ir-PS})_6(\text{Hemin})_{0.48}(\text{TFA})_{5.52}$.

MOZ-2, **MOZ-3**, and **MOZ-4**. **MOZ-2**, **MOZ-3**, and **MOZ-4** were synthesized from **MOZ-1**, where capping-TFA is fully replaced by Glu, Asn, and Ur, respectively. This replacement was confirmed by the NMR analysis of digested MOZs (**Figure 11-9**). The paramagnetic nature of hemin prevents NMR measurement, so hemin-free **MOZ-2***, **MOZ-3***, and **MOZ-4*** were alternatively synthesized directly from Hf-Ir. All digested hemin-free MOZs showed Ir-PS signal in ^1H NMR, and **MOZ-2***, **MOZ-3***, and **MOZ-4*** each presented the expected signals of Glu, Asn, and Ur, respectively. The ratios of Ir-PS to Glu, Asn or Ur were close to 1:1, confirming full replacement of TFA. The hemin to Ir-PS ratios for **MOZ-2**, **MOZ-3**, and **MOZ-4** were determined to be 7.8%, 8.0%, and 7.7%, respectively, by UV-vis analysis. Therefore, the compositions of **MOZ-2**, **MOZ-3**, and **MOZ-4** are proposed to be $Hf_{12}(\mu_3\text{-}O)_8(\mu_3\text{-}OH)_8(\mu_2\text{-}OH)_6(\text{Ir-PS})_6(\text{Hemin})_{0.47}(\text{Glu})_{5.53}$, $Hf_{12}(\mu_3\text{-}O)_8(\mu_3\text{-}OH)_8(\mu_2\text{-}OH)_6(\text{Ir-PS})_6(\text{Hemin})_{0.48}(\text{Asn})_{5.52}$, and $Hf_{12}(\mu_3\text{-}O)_8(\mu_3\text{-}OH)_8(\mu_2\text{-}OH)_6(\text{Ir-PS})_6(\text{Hemin})_{0.46}(\text{Ur})_{5.54}$, respectively.

11.4.5 Selectivity

CH_4, CO, and H_2 were the major products detected in this work, with no other gaseous or

liquidus products clearly observed. Based on the proposed mechanism, CO was produced as a stable intermediate product toward CH_4 generation (**Figure 11-10C**). This mechanism was confirmed by both a big amount of generated CO as detected by GC (**Figure 11-15**A) and the accelerated CH_4 generation when CO was instead used as substrate (**Figure 11-15B,C**). Therefore, as CO is a stable intermediate to CH_4, H_2 is the major byproduct in this process, which was also previously reported, and the selectivity of CH_4 is defined as:

$$\text{Selectivity} = \frac{\text{TON}\ (CH_4)}{\text{TON}\ (CH_4) + \text{TON}\ (H_2)}$$

11.4.6 Mechanism of photocatalytic CO_2-to-CH_4 Conversion

In MOZs, the reduction potentials of pigments (Ir-PS, simplified as Ir) were determined to be -0.52 V and -1.40 V (*vs*. SCE) for Ir^+/Ir^* and Ir/Ir^-, respectively [55]. The reductive potentials of catalytic centers in hemin (porphyrin-Fe^{III}, simplified as Fe^{III}) were measured to be -0.16 , -1.03 V, and -1.60 V (*vs*. SCE) for Fe^{III}/Fe^{II}, Fe^{II}/Fe^{I}, and Fe^{I}/Fe^{0}, respectively [56].

Luminescence quenching studies showed that the excited Ir* can be effectively quenched by both Fe^{III} and BIH (**Figure 11-15D,E**). Their quenching behaviors are both well fitted with Stern-Volmer equation, though quenching by Fe^{III} had a larger Stern-Volmer slope (K_{SV} = 0.155 μM^{-1}) than that by BIH (K_{SV} = 0.057 μM^{-1}). The faster quenching rate of Ir* by Fe^{III} is likely due to their proximity (<2 nm) in MOZs. Therefore, Fe^{III} is proposed to first be reduced by Ir* to generate Fe^{II} (known as heme) and Ir^+, upon which generated Ir^+ is reduced to Ir by BIH (only Fe-involving processes are listed in the following equations):

$$Fe^{III} + Ir^* \rightarrow Fe^{II} + Ir^+$$

Since Ir* (-0.52 V *vs.* SCE) is not powerful enough to reduce the Fe^{II} and generate Fe^{I} (-1.03 V *vs.* SCE), this reduction is proposed to be proceed via Ir^- (-1.40 V *vs.* SCE, generated

from BIH reduction of Ir*):

$$Fe^{II} + Ir^{-} \rightarrow Fe^{I} + Ir$$

Since Ir^{-} (-1.40 V *vs.* SCE) is not powerful to reduce Fe^{I} and generate Fe^{0} (-1.60 V *vs.* SCE), which combines with CO_2 to generate the reactive intermediate $Fe^{II}CO_2^{2-}$, this reduction and associated CO_2 binding is proposed to go through a synergistic pathway (The proposed PCET and H-bond stabilization pathways in this work may decrease the reduction potential needed for this synergistic process):

$$Fe^{I} + Ir^{-} + CO_2 \rightarrow Fe^{II}CO_2^{2-} + Ir$$

The generated reactive intermediate $Fe^{II}CO_2^{2-}$ is protonated by two H^{+} to release CO as a stable intermediate as well as H_2O while regenerating Fe^{II}:

$$Fe^{II}CO_2^{2-} + 2H^{+} \rightarrow Fe^{II} + CO + H_2O$$

Generated CO is next bound to Fe^{II} and undergoes a two-electron (from Ir^{-}) and one-proton reduction to generate the active intermediate $Fe^{I}CHO$:

$$Fe^{II} + CO \rightarrow Fe^{II}CO$$

$$Fe^{II}CO + 2Ir^{-} + H^{+} \rightarrow Fe^{I}CHO + 2Ir$$

Thusly generated $Fe^{I}CHO$ then undergoes a four-electron (from Ir^{-}) and five-proton reduction to release CH_4 as the target product alongside H_2O while regenerating Fe^{II}:

$$Fe^{I}CHO + 4Ir^{-} + 5H^{+} \rightarrow Fe^{II} + 4Ir + CH_4 + H_2O$$

11.4.7 DFT calculation

To simplify calculations, a Zr_6 cluster capped by formate modelled the active cites in **MOZ-3** and **MOZ-4**. This simplification had three justifications: (1) Each active site composes only one face of component Hf_{12} clusters in MOZs, and so Hf_{12} clusters could be simplified to

Hf_6 clusters [$Hf_6(\mu_3\text{-}O)_4(\mu_3\text{-}OH)_4$], half of the Hf_{12} clusters; (2) Hf has very similar chemical properties and electronic structures to Zr, and so Hf_6 cluster could be further simplified to the Zr_6 cluster [$Zr_6(\mu_3\text{-}O)_4(\mu_3\text{-}OH)_4$]; (3) The capping organic ligands on this Zr_6 cluster have minimal effect on the energy calculation as previously reported [57], and so the capping ligand of this Zr_6 cluster was simplified to formate with the formulation of $Zr_6(\mu_3\text{-}O)_4(\mu_3\text{-}OH)_4(HCOO)_{12}$ [58].

The geometries of hemin, Asn, and Ur were first optimized in the gas phase on the basis of their experimental X-ray structures. The hemin-capped Zr_6 cluster was chosen as the model to represent the starting coordination environment of the Fe catalytic site. The geometry of the two crucial reactive intimidates during the CO_2-to-CH_4 conversion ($Fe^{II}CO_2^{2-}$ and $Fe^{I}CHO$, as shown in **Figure 11-10** and **Figure 11-15F**) for **MOZ-3** (denoted by Asn-$FeCO_2$ and Asn-FeCHO) and **MOZ-4** (denoted by Ur-$FeCO_2$ and Ur-FeCHO) were optimized as quintets as previously reported [46] and triplets, respectively, by the B3LYP under unrestricted open-shell calculation (**Figure 11-12**). An AA-free version of these reactive intimidates (denoted by NA-$FeCO_2$ and NA-FeCHO) were optimized as controls. The stabilization enthalpy (ΔH_{stb}) by the H-bonds in **MOZ-3** or **MOZ-4** were thusly defined as the enthalpy difference between the reactive intermediates in **MOZ-3** (Asn-$FeCO_2$ and Asn-FeCHO) or **MOZ-4** (Ur-$FeCO_2$ and Ur-FeCHO) and their corresponding controls (NA-$FeCO_2$ and NA-FeCHO, respectively).

As shown in **Figure 11-13**, based on these optimized structures, the extent of interaction between Fe and bound CO_2 in $FeCO_2^{2-}$ reactive species can be ascertained by the length of Fe-C bond and the angle of ∠O-C-O. A shorter Fe-C bond length and a narrower ∠O-C-O angel indicated a stronger back bonding from Fe to bound CO_2, leading to a stronger interaction

between Fe and bound CO_2, corresponding to a better activation of CO_2. In the case of NA-$FeCO_2$, the CO_2 binds to the Fe center in an η_2-mode, with the Fe-C bond length computed to be 2.19 Å and the ∠O-C-O angle computed to 150.0°. This angle is substantially lower than that in free CO_2 (180°), suggesting substantial pi-backbonding from Fe to CO_2 in NA-$FeCO_2$. Asn-$FeCO_2$ presented a slightly stronger pi-backbonding from Fe to CO_2 with Fe-C bond length decreased to 2.10 Å and the ∠O-C-O angle decreases to 145.9°. This slightly stronger interaction between Fe and bound CO_2 in Asn-$FeCO_2$ was attributed to the moderate H-bond (1.96 Å) between the -NH fragment of Asn and oxygen atom of bound CO_2, leading to a ΔH_{stb} of -14.1 kcal·mol^{-1}. In the case of Ur-$FeCO_2$, due to two strong H-bonds between the -NH fragments of Ur and each oxygen atom of bound CO_2 (1.85 Å and 1.91 Å, ΔH_{stb} of -23.5 kcal·mol^{-1}), even stronger pi-backbonding from Fe to bound CO_2 was observed with the Fe-C bond length further decreased to 2.04 Å while the ∠O–C–O angle narrowed to 136.2°. Indeed, the natural population analysis (NPA) charge on bound CO_2 is -0.29, -0.38, and -0.56 in NA-$FeCO_2$, Asn-$Fe^{II}CO_2$, and Ur-$FeCO_2$, respectively. The more negative NPA charge on bound CO_2 in Asn-$FeCO_2$ and Ur-$FeCO_2^-$ was because that H-bonding from the Asn and Ur to the bound CO_2 promoted the electron density transfer from Fe to bound CO_2.

Similar trend of the interaction between Fe and bound CHO was also observed in the optimized structures of FeCHO, as mainly reflected by the Fe-C bond length. NA-FeCHO, Asn-FeCHO, and Ur-FeCHO presented a Fe-C length of 2.02 Å, 1.88 Å, and 1.86 Å, the NPA charge of the bound CHO is -0.31, -0.36 and -0.43 respectively. This decreasing Fe-C length was attributed to the H-bond stabilization between the oxygen in CHO and the -NH fragments in Asn (2.02 Å, ΔH_{stb} of -9.1 kcal·mol^{-1}) or in Ur (1.88 Å, 2.23 Å, ΔH_{stb} of-17.2 kcal·mol^{-1}).

11.5 References

1. Lee, D.-S.; Nioche, P.; Hamberg, M.; Raman, C. S., Structural insights into the evolutionary paths of oxylipin biosynthetic enzymes. *Nature* **2008,** *455* (7211), 363-368.
2. Ulmer, K. M., Protein engineering. *Science* **1983,** *219* (4585), 666.
3. Arnold, F. H., Directed Evolution: Bringing New Chemistry to Life. *Angewandte Chemie International Edition* **2018,** *57* (16), 4143-4148.
4. Berggren, G.; Adamska, A.; Lambertz, C.; Simmons, T. R.; Esselborn, J.; Atta, M.; Gambarelli, S.; Mouesca, J. M.; Reijerse, E.; Lubitz, W.; Happe, T.; Artero, V.; Fontecave, M., Biomimetic assembly and activation of [FeFe]-hydrogenases. *Nature* **2013,** *499* (7456), 66-69.
5. Helm, M. L.; Stewart, M. P.; Bullock, R. M.; DuBois, M. R.; DuBois, D. L., A Synthetic Nickel Electrocatalyst with a Turnover Frequency Above 100,000 s^{−1} for H₂ Production. **2011,** *333* (6044), 863-866.
6. Camara, J. M.; Rauchfuss, T. B., Combining acid–base, redox and substrate binding functionalities to give a complete model for the [FeFe]-hydrogenase. *Nature Chem.* **2012,** *4* (1), 26-30.
7. Ott, S.; Kritikos, M.; Åkermark, B.; Sun, L.; Lomoth, R., A Biomimetic Pathway for Hydrogen Evolution from a Model of the Iron Hydrogenase Active Site. *Angewandte Chemie International Edition* **2004,** *43* (8), 1006-1009.
8. Wu, J.; Wang, X.; Wang, Q.; Lou, Z.; Li, S.; Zhu, Y.; Qin, L.; Wei, H., Nanomaterials with enzyme-like characteristics (nanozymes): next-generation artificial enzymes (II). *Chem. Soc. Rev.* **2019,** *48* (4), 1004-1076.
9. Takezawa, H.; Shitozawa, K.; Fujita, M., Enhanced reactivity of twisted amides inside a molecular cage. *Nature Chem.* **2020**.
10. Rabone, J.; Yue, Y. F.; Chong, S. Y.; Stylianou, K. C.; Bacsa, J.; Bradshaw, D.; Darling, G. R.; Berry, N. G.; Khimyak, Y. Z.; Ganin, A. Y.; Wiper, P.; Claridge, J. B.; Rosseinsky, M. J., An Adaptable Peptide-Based Porous Material. *Science* **2010,** *329* (5995), 1053.
11. Deng, H.; Grunder, S.; Cordova, K. E.; Valente, C.; Furukawa, H.; Hmadeh, M.; Gándara, F.; Whalley, A. C.; Liu, Z.; Asahina, S.; Kazumori, H.; O'Keeffe, M.; Terasaki, O.; Stoddart, J. F.; Yaghi, O. M., Large-Pore Apertures in a Series of Metal-Organic Frameworks. *Science* **2012,** *336* (6084), 1018.
12. Xiao, D. J.; Bloch, E. D.; Mason, J. A.; Queen, W. L.; Hudson, M. R.; Planas, N.; Borycz, J.; Dzubak, A. L.; Verma, P.; Lee, K.; Bonino, F.; Crocellà, V.; Yano, J.; Bordiga, S.; Truhlar, D. G.; Gagliardi, L.; Brown, C. M.; Long, J. R., Oxidation of ethane to ethanol by N2O in a metal–organic framework with coordinatively unsaturated iron(II) sites. *Nature Chem.* **2014,** *6* (7), 590-595.
13. Nath, I.; Chakraborty, J.; Verpoort, F., Metal organic frameworks mimicking natural enzymes: a structural and functional analogy. *Chem. Soc. Rev.* **2016,** *45* (15), 4127-4170.
14. Marchetti, L.; Levine, M., Biomimetic Catalysis. *ACS Catalysis* **2011,** *1* (9), 1090-1118.
15. Rao, H.; Schmidt, L. C.; Bonin, J.; Robert, M., Visible-light-driven methane formation from CO2 with a molecular iron catalyst. *Nature* **2017,** *548* (7665), 74-77.
16. Mariano, R. G.; McKelvey, K.; White, H. S.; Kanan, M. W., Selective increase in

CO₂ electroreduction activity at grain-boundary surface terminations. *Science* **2017,** *358* (6367), 1187.
17. García de Arquer, F. P.; Dinh, C.-T.; Ozden, A.; Wicks, J.; McCallum, C.; Kirmani, A. R.; Nam, D.-H.; Gabardo, C.; Seifitokaldani, A.; Wang, X.; Li, Y. C.; Li, F.; Edwards, J.; Richter, L. J.; Thorpe, S. J.; Sinton, D.; Sargent, E. H., CO₂ electrolysis to multicarbon products at activities greater than 1 A cm^{−2}. **2020,** *367* (6478), 661-666.
18. Morales-Guio, C. G.; Cave, E. R.; Nitopi, S. A.; Feaster, J. T.; Wang, L.; Kuhl, K. P.; Jackson, A.; Johnson, N. C.; Abram, D. N.; Hatsukade, T.; Hahn, C.; Jaramillo, T. F., Improved CO2 reduction activity towards C2+ alcohols on a tandem gold on copper electrocatalyst. *Nature Catalysis* **2018,** *1* (10), 764-771.
19. Liu, C.; Colón, B. C.; Ziesack, M.; Silver, P. A.; Nocera, D. G., Water splitting–biosynthetic system with CO₂ reduction efficiencies exceeding photosynthesis. *Science* **2016,** *352* (6290), 1210.
20. Smith, P. T.; Kim, Y.; Benke, B. P.; Kim, K.; Chang, C. J., Supramolecular Tuning Enables Selective Oxygen Reduction Catalyzed by Cobalt Porphyrins for Direct Electrosynthesis of Hydrogen Peroxide. *Angewandte Chemie International Edition* **2020,** *59* (12), 4902-4907.
21. Rao, H.; Lim, C.-H.; Bonin, J.; Miyake, G. M.; Robert, M., Visible-Light-Driven Conversion of CO2 to CH4 with an Organic Sensitizer and an Iron Porphyrin Catalyst. *J. Am. Chem. Soc.* **2018,** *140* (51), 17830-17834.
22. Zhai, Q.; Xie, S.; Fan, W.; Zhang, Q.; Wang, Y.; Deng, W.; Wang, Y., Photocatalytic Conversion of Carbon Dioxide with Water into Methane: Platinum and Copper(I) Oxide Co-catalysts with a Core–Shell Structure. *Angewandte Chemie International Edition* **2013,** *52* (22), 5776-5779.
23. Xie, S.; Wang, Y.; Zhang, Q.; Deng, W.; Wang, Y., MgO- and Pt-Promoted TiO2 as an Efficient Photocatalyst for the Preferential Reduction of Carbon Dioxide in the Presence of Water. *ACS Catalysis* **2014,** *4* (10), 3644-3653.
24. Wang, Y.; Lai, Q.; Zhang, F.; Shen, X.; Fan, M.; He, Y.; Ren, S., High efficiency photocatalytic conversion of CO2 with H2O over Pt/TiO2 nanoparticles. *RSC Advances* **2014,** *4* (84), 44442-44451.
25. Long, R.; Li, Y.; Liu, Y.; Chen, S.; Zheng, X.; Gao, C.; He, C.; Chen, N.; Qi, Z.; Song, L.; Jiang, J.; Zhu, J.; Xiong, Y., Isolation of Cu Atoms in Pd Lattice: Forming Highly Selective Sites for Photocatalytic Conversion of CO2 to CH4. *J. Am. Chem. Soc.* **2017,** *139* (12), 4486-4492.
26. Li, R.; Hu, J.; Deng, M.; Wang, H.; Wang, X.; Hu, Y.; Jiang, H.-L.; Jiang, J.; Zhang, Q.; Xie, Y.; Xiong, Y., Integration of an Inorganic Semiconductor with a Metal–Organic Framework: A Platform for Enhanced Gaseous Photocatalytic Reactions. *Adv. Mater.* **2014,** *26* (28), 4783-4788.
27. Tan, J. Z. Y.; Fernández, Y.; Liu, D.; Maroto-Valer, M.; Bian, J.; Zhang, X., Photoreduction of CO2 using copper-decorated TiO2 nanorod films with localized surface plasmon behavior. *Chem. Phys. Lett.* **2012,** *531*, 149-154.
28. Zhang, X.; Han, F.; Shi, B.; Farsinezhad, S.; Dechaine, G. P.; Shankar, K., Photocatalytic Conversion of Diluted CO2 into Light Hydrocarbons Using Periodically

Modulated Multiwalled Nanotube Arrays. *Angewandte Chemie International Edition* **2012,** *51* (51), 12732-12735.
29. Hou, W.; Hung, W. H.; Pavaskar, P.; Goeppert, A.; Aykol, M.; Cronin, S. B., Photocatalytic Conversion of CO2 to Hydrocarbon Fuels via Plasmon-Enhanced Absorption and Metallic Interband Transitions. *ACS Catalysis* **2011,** *1* (8), 929-936.
30. Li, X.; Zhuang, Z.; Li, W.; Pan, H., Photocatalytic reduction of CO2 over noble metal-loaded and nitrogen-doped mesoporous TiO2. *Applied Catalysis A: General* **2012,** *429-430*, 31-38.
31. Tahir, M.; Amin, N. S., Indium-doped TiO2 nanoparticles for photocatalytic CO2 reduction with H2O vapors to CH4. *Applied Catalysis B: Environmental* **2015,** *162*, 98-109.
32. Xia, X.-H.; Jia, Z.-J.; Yu, Y.; Liang, Y.; Wang, Z.; Ma, L.-L., Preparation of multi-walled carbon nanotube supported TiO2 and its photocatalytic activity in the reduction of CO2 with H2O. *Carbon* **2007,** *45* (4), 717-721.
33. Liang, Y. T.; Vijayan, B. K.; Gray, K. A.; Hersam, M. C., Minimizing Graphene Defects Enhances Titania Nanocomposite-Based Photocatalytic Reduction of CO2 for Improved Solar Fuel Production. *Nano Letters* **2011,** *11* (7), 2865-2870.
34. Nguyen, T.-V.; Wu, J. C. S.; Chiou, C.-H., Photoreduction of CO2 over Ruthenium dye-sensitized TiO2-based catalysts under concentrated natural sunlight. *Catalysis Communications* **2008,** *9* (10), 2073-2076.
35. Zhao, Z.-H.; Fan, J.-M.; Wang, Z.-Z., Photo-catalytic CO2 reduction using sol–gel derived titania-supported zinc-phthalocyanine. *Journal of Cleaner Production* **2007,** *15* (18), 1894-1897.
36. Tahir, M.; Tahir, B.; Amin, N. A. S.; Muhammad, A., Photocatalytic CO2 methanation over NiO/In2O3 promoted TiO2 nanocatalysts using H2O and/or H2 reductants. *Energy Conversion and Management* **2016,** *119*, 368-378.
37. Chen, X.; Zhou, Y.; Liu, Q.; Li, Z.; Liu, J.; Zou, Z., Ultrathin, Single-Crystal WO3 Nanosheets by Two-Dimensional Oriented Attachment toward Enhanced Photocatalystic Reduction of CO2 into Hydrocarbon Fuels under Visible Light. *ACS Applied Materials & Interfaces* **2012,** *4* (7), 3372-3377.
38. Liu, Q.; Zhou, Y.; Kou, J.; Chen, X.; Tian, Z.; Gao, J.; Yan, S.; Zou, Z., High-Yield Synthesis of Ultralong and Ultrathin Zn2GeO4 Nanoribbons toward Improved Photocatalytic Reduction of CO2 into Renewable Hydrocarbon Fuel. *Journal of the American Chemical Society* **2010,** *132* (41), 14385-14387.
39. Shi, H.; Chen, G.; Zhang, C.; Zou, Z., Polymeric g-C3N4 Coupled with NaNbO3 Nanowires toward Enhanced Photocatalytic Reduction of CO2 into Renewable Fuel. *ACS Catalysis* **2014,** *4* (10), 3637-3643.
40. Xie, S.; Wang, Y.; Zhang, Q.; Deng, W.; Wang, Y., SrNb2O6 nanoplates as efficient photocatalysts for the preferential reduction of CO2 in the presence of H2O. *Chemical Communications* **2015,** *51* (16), 3430-3433.
41. Zhang, H.; Wei, J.; Dong, J.; Liu, G.; Shi, L.; An, P.; Zhao, G.; Kong, J.; Wang, X.; Meng, X.; Zhang, J.; Ye, J., Efficient Visible-Light-Driven Carbon Dioxide Reduction by a Single-Atom Implanted Metal–Organic Framework. *Angewandte Chemie International Edition* **2016,** *55* (46), 14310-14314.
42. Xu, Y.-F.; Yang, M.-Z.; Chen, B.-X.; Wang, X.-D.; Chen, H.-Y.; Kuang, D.-B.;

Su, C.-Y., A CsPbBr3 Perovskite Quantum Dot/Graphene Oxide Composite for Photocatalytic CO2 Reduction. *Journal of the American Chemical Society* **2017,** *139* (16), 5660-5663.
43. Ju, W.; Bagger, A.; Wang, X.; Tsai, Y.; Luo, F.; Möller, T.; Wang, H.; Rossmeisl, J.; Varela, A. S.; Strasser, P., Unraveling Mechanistic Reaction Pathways of the Electrochemical CO2 Reduction on Fe–N–C Single-Site Catalysts. *ACS Energy Letters* **2019,** *4* (7), 1663-1671.
44. Costentin, C.; Drouet, S.; Passard, G.; Robert, M.; Savéant, J.-M., Proton-Coupled Electron Transfer Cleavage of Heavy-Atom Bonds in Electrocatalytic Processes. Cleavage of a C–O Bond in the Catalyzed Electrochemical Reduction of CO2. *J. Am. Chem. Soc.* **2013,** *135* (24), 9023-9031.
45. Gotico, P.; Boitrel, B.; Guillot, R.; Sircoglou, M.; Quaranta, A.; Halime, Z.; Leibl, W.; Aukauloo, A., Second-Sphere Biomimetic Multipoint Hydrogen-Bonding Patterns to Boost CO2 Reduction of Iron Porphyrins. *Angewandte Chemie International Edition* **2019,** *58* (14), 4504-4509.
46. Davethu, P. A.; de Visser, S. P., CO2 Reduction on an Iron-Porphyrin Center: A Computational Study. *The Journal of Physical Chemistry A* **2019,** *123* (30), 6527-6535.
47. CRC handbook of chemistry and physics. **1977**.
48. Frisch, M. J.; Trucks, G. W.; Schlegel, H. B.; Scuseria, G. E.; Robb, M. A.; Cheeseman, J. R.; Scalmani, G.; Barone, V.; Petersson, G. A.; Nakatsuji, H.; Li, X.; Caricato, M.; Marenich, A. V.; Bloino, J.; Janesko, B. G.; Gomperts, R.; Mennucci, B.; Hratchian, H. P.; Ortiz, J. V.; Izmaylov, A. F.; Sonnenberg, J. L.; Williams; Ding, F.; Lipparini, F.; Egidi, F.; Goings, J.; Peng, B.; Petrone, A.; Henderson, T.; Ranasinghe, D.; Zakrzewski, V. G.; Gao, J.; Rega, N.; Zheng, G.; Liang, W.; Hada, M.; Ehara, M.; Toyota, K.; Fukuda, R.; Hasegawa, J.; Ishida, M.; Nakajima, T.; Honda, Y.; Kitao, O.; Nakai, H.; Vreven, T.; Throssell, K.; Montgomery Jr., J. A.; Peralta, J. E.; Ogliaro, F.; Bearpark, M. J.; Heyd, J. J.; Brothers, E. N.; Kudin, K. N.; Staroverov, V. N.; Keith, T. A.; Kobayashi, R.; Normand, J.; Raghavachari, K.; Rendell, A. P.; Burant, J. C.; Iyengar, S. S.; Tomasi, J.; Cossi, M.; Millam, J. M.; Klene, M.; Adamo, C.; Cammi, R.; Ochterski, J. W.; Martin, R. L.; Morokuma, K.; Farkas, O.; Foresman, J. B.; Fox, D. J. *Gaussian 16 Rev. C.01*, Wallingford, CT, 2016.
49. Hariharan, P. C.; Pople, J. A., The influence of polarization functions on molecular orbital hydrogenation energies. *Theoretica chimica acta* **1973,** *28* (3), 213-222.
50. Hay, P. J.; Wadt, W. R., Ab initio effective core potentials for molecular calculations. Potentials for the transition metal atoms Sc to Hg. *The Journal of Chemical Physics* **1985,** *82* (1), 270-283.
51. Hay, T. H. D. J. a. P. J., in Modern Theoretical Chemistry. *Ed. H. F. Schaefer III, Vol. 3 (Plenum, New York, 1977)*.
52. Dai, R.; Peng, F.; Ji, P.; Lu, K.; Wang, C.; Sun, J.; Lin, W., Electron Crystallography Reveals Atomic Structures of Metal–Organic Nanoplates with M12(μ3-O)8(μ3-OH)8(μ2-OH)6 (M = Zr, Hf) Secondary Building Units. *Inorg. Chem.* **2017,** *56* (14), 8128-8134.
53. Das, D. K.; Medhi, O. K., The role of heme propionate in controlling the redox potential of heme: Square wave voltammetry of protoporphyrinato IX iron(III) in aqueous surfactant micelles. *J. Inorg. Biochem.* **1998,** *70* (2), 83-90.

54. Erickson, H. P., Size and shape of protein molecules at the nanometer level determined by sedimentation, gel filtration, and electron microscopy. *Biol. Proced. Online* **2009,** *11*, 32-51.
55. Zhu, Y.-Y.; Lan, G.; Fan, Y.; Veroneau, S. S.; Song, Y.; Micheroni, D.; Lin, W., Merging Photoredox and Organometallic Catalysts in a Metal–Organic Framework Significantly Boosts Photocatalytic Activities. *Angewandte Chemie International Edition* **2018,** *57* (43), 14090-14094.
56. Bhugun, I.; Lexa, D.; Savéant, J.-M., Homogeneous Catalysis of Electrochemical Hydrogen Evolution by Iron(0) Porphyrins. *J. Am. Chem. Soc.* **1996,** *118* (16), 3982-3983.
57. Troya, D., Reaction Mechanism of Nerve-Agent Decomposition with Zr-Based Metal Organic Frameworks. *The Journal of Physical Chemistry C* **2016,** *120* (51), 29312-29323.
58. Moon, S.-Y.; Liu, Y.; Hupp, J. T.; Farha, O. K., Instantaneous Hydrolysis of Nerve-Agent Simulants with a Six-Connected Zirconium-Based Metal–Organic Framework. *Angewandte Chemie International Edition* **2015,** *54* (23), 6795-6799.

Chapter 12. Inverted Construction of Metal-Organic Frameworks

12.1 Introduction

Realizing the real-world applications of a material requires fine-tuning its underlying components and optimizing its intrinsic properties.[1] The emergence of reticular chemistry, a field exploring the concatenation of molecular building blocks to form repeating and defined structures, has allowed for the incorporation of various organic and inorganic subunits into an expansive catalogue of two and three-dimensional materials, introducing MOFs.[2-5] As an emerging class of crystalline porous materials, MOFs are examined for diverse applications in gas storage,[6-8] gas separation,[9-12] catalysis,[13, 14] and nanomedicine,[15, 16] among others.[17-21] This diversity in function and application largely derives from the variety of functional organic ligands which can be incorporated into MOFs. Emerging research, however, has begun focusing on metal nodes and their synergistic interactions with organic ligands, which has dramatically increased the versatility of MOFs. The ability to optimize MOFs around these metal nodes, however, is impeded by the conventional conception of MOF synthesis.

Classically, MOF synthesis is driven by interactions between metal ions and molecular modulators to form incipient SBUs, often through the formation of metal-carboxylate bonds.[22,23] The modulators of these incipient SBUs exchange with bridging organic ligands in an entropically-favorable process to crosslink SBUs and afford MOF structure.[24] This SBU-directed pathway, however, presents two distinct limitations: (1) as the formation of SBUs is restricted to metal ions that present favorable interactions with modulators, certain metals (e.g. soft metal ions and noble metals) cannot be incorporated into metal nodes, and their MOFs are difficult to obtain; and (2) as the formation of SBUs is driven by the unique coordination mode

preferred by each metal ion, MOFs synthesized from different metal ions cannot generate a single conserved architecture. A more generalizable, less constrained pathway to MOF synthesis is needed to accommodate a wider variety of metals, with more diverse physical and chemical properties.

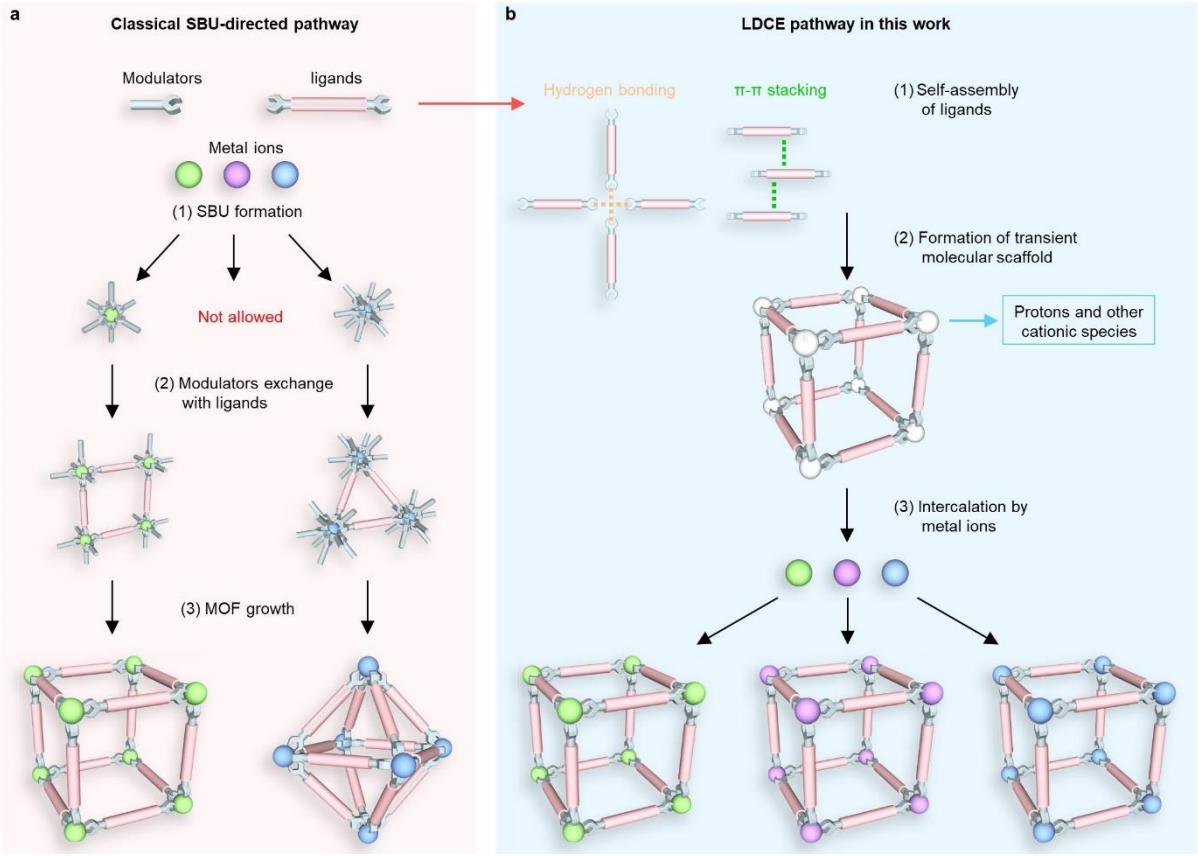

Figure 12-1. Conventional vs. inverted construction of MOFs. Schematic contrasting (a) classical SBU-directed pathway and (b) proposed LDCE pathway in this work for MOF growth.

We propose herein a conceptually new approach to MOF synthesis through a process of ligand-directed crystal engineering (LDCE) which is driven by the self-organization of organic ligands through π-π stacking and hydrogen bonding to form a transient molecular scaffold (**Figure 12-1b**). An array of metal ions can then intercalate such a molecular scaffold to form conserved SBUs and isostructural MOFs. We demonstrate this LDCE pathway by generating an H-TBP scaffold which accommodates the construction of an isostructural library of 23 M-

TBP MOFs incorporating each naturally occurring transition metal in Groups 5 through 12 (M = V, Cr, Mn, Fe, Co, Ni, Cu, Zn, Nb, Mo, Ru, Rh, Pd, Ag, Cd, Ta, W, Re, Os, Ir, Pt, Au, and Hg) (**Figure 12-2a**). These M-TBP MOFs present identical structures and by incorporating an array of metal ions each reveals a unique electronic structure, resulting in tunable photocatalytic properties across this library. The energy profile of this LDCE pathway and the electronic structures of M-TBP MOFs were analyzed using the Vienna Ab initio Simulation Package (VASP). We demonstrate the utility of the M-TBP library in optimizing MOF functions, systematically employing M-TBP MOFs in photocatalytic hydrogen evolution and radical coupling reactions.

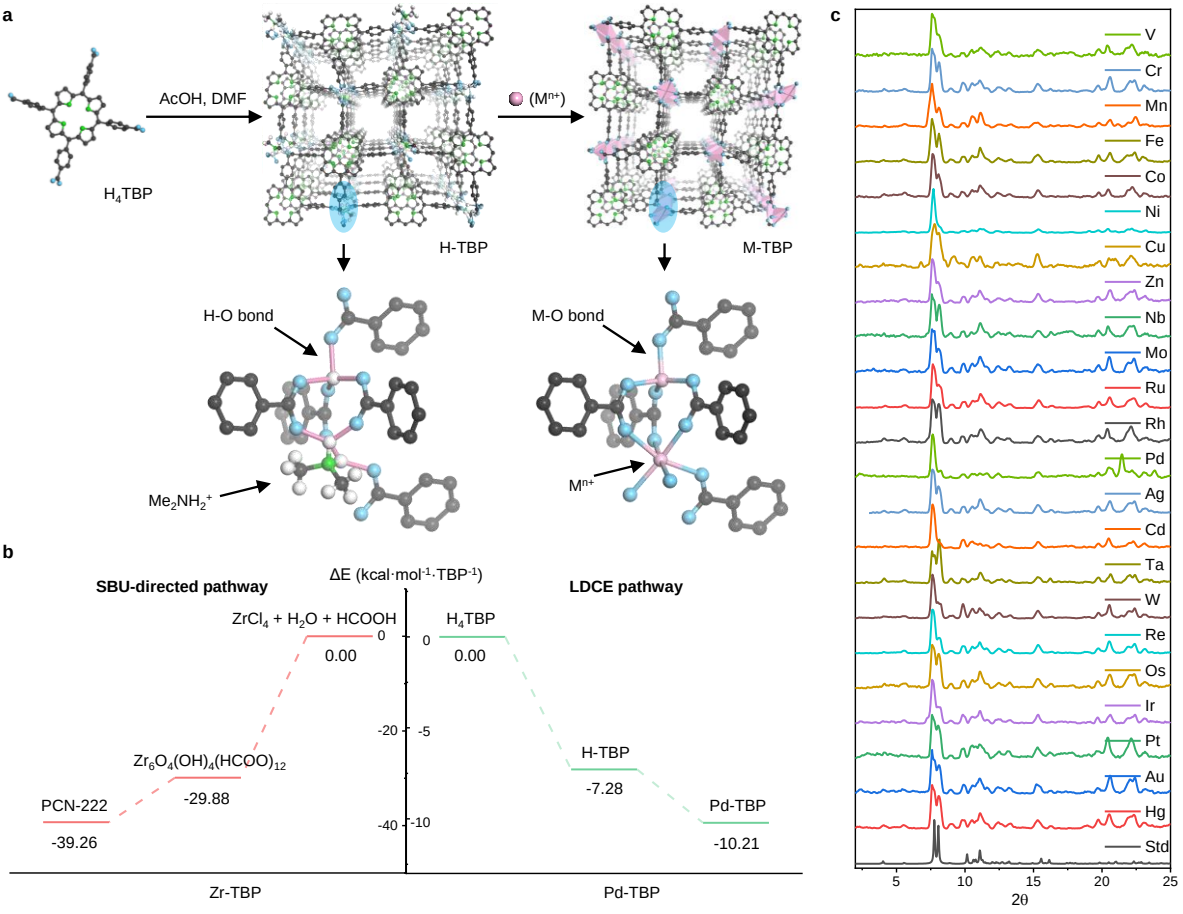

Figure 12-2. Synthesis of M-TBP through LDCE pathway. (a) Schematic showing the two-step synthesis of M-TBP through the proposed LDCE pathway. (b) Energy profiles of the SBU-directed pathway, as represented by Zr-TBP (left), and the LDCE pathway, as represented by

(Figure 12-2 continued) Pd-TBP (right). (c) PXRD patterns of isostructural M-TBP in comparison to that simulated from the M-TBP single crystal structures.

12.2 Result and discussion

12.2.1 Ligand-direct crystal engineering

The existence of this LDCE pathway was resolved through efforts to generate MOFs from transition metals and TBP ligands. Through similar solvothermal reactions of respective metal precursors with H_4TBP in DMF with AcOH as a modulator (**Table 12-1**), a series of 23 M-TBP MOFs incorporating each transition metal in Groups 5 through 12 (excluding radioactive Tc) were obtained. Surprisingly, the same topological structure and square-plate morphology was revealed for each M-TBP MOF by PXRD (**Figure 12-2c**) and TEM (**Figure 12-3**), respectively. The presence of respective metal ions in each M-TBP MOF was confirmed by ICP-MS and the yields of these M-TBP syntheses based on the incorporated metals were determined to range from 26% to 48% (**Table 12-1**). The oxidation states of these ions were confirmed to be the same as those of their respective precursors, as revealed by the XPS (**Figure 12-4**). The presence of free-based TBP was confirmed by characteristic TBP absorptions in UV-Vis spectra of digested M-TBP MOFs (**Figure 12-5a,b**). TGA confirmed the ligand-to-metal ratio to be approximately 1:2, and nitrogen gas sorption isotherms afforded BET surface areas of around 500 m^2/g for this M-TBP library (**Figure 12-5c,d**).

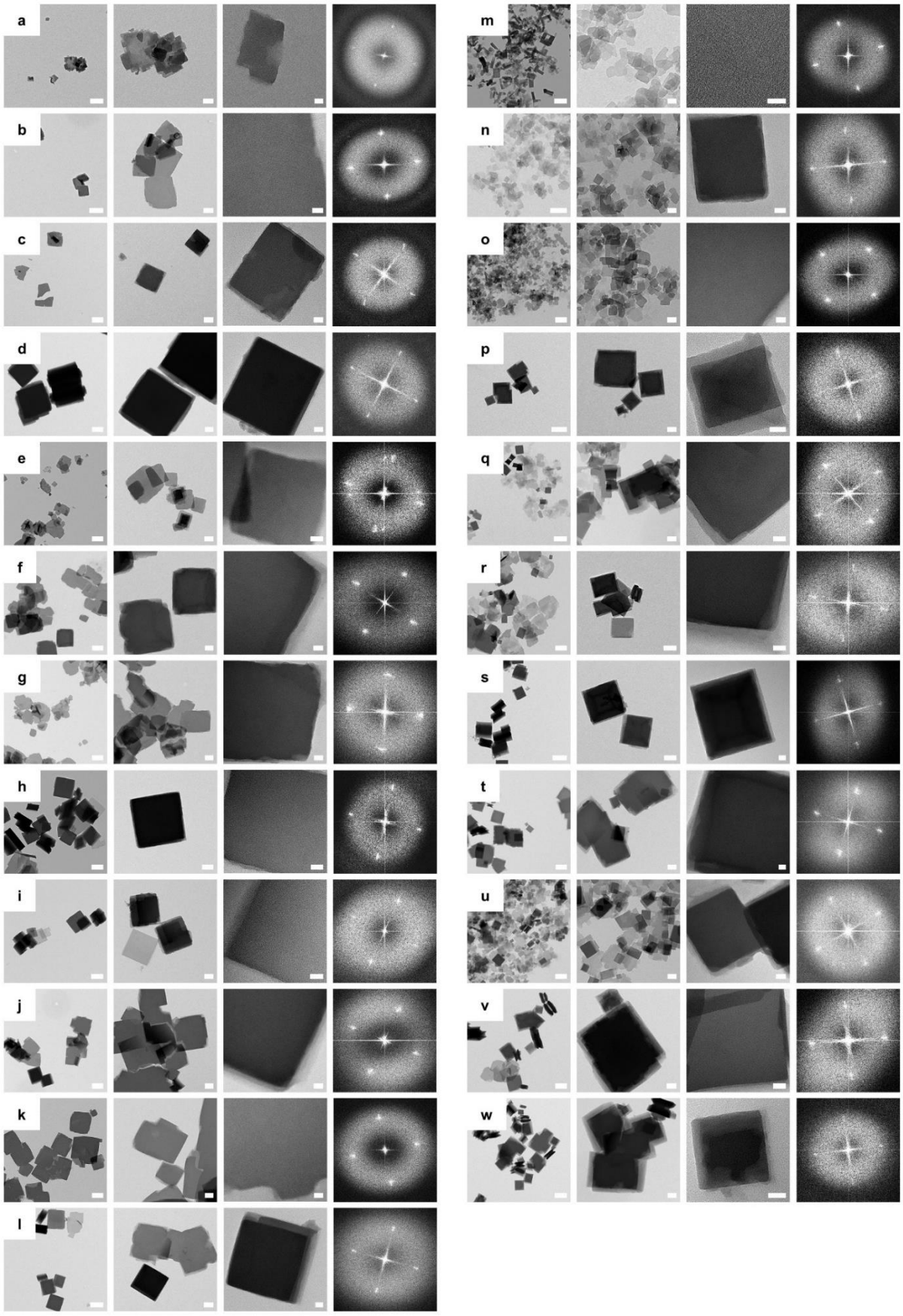

Figure 12-3. TEM images of M-TBP family. TEM images of V-TBP (a), Cr-TBP (b), Mn-TBP

(Figure 12-3 continued) (c), Fe-TBP (d), Co-TBP (e), Ni-TBP (f), Cu-TBP (g), Zn-TBP (h), Ni-TBP (i), Mo-TBP (j), Ru-TBP (k), Rh-TBP (l), Pd-TBP (m), Ag-TBP (n), Cd-TBP (o), Ta-TBP (p), W-TBP (q), Re-TBP (r), Os-TBP (s), Ir-TBP (t), Pt-TBP (u), Au-TBP (v), and Hg-TBP (w). From left to right: large-area TEM image (scale bar: 500 nm), small-area TEM image (scale bar: 100 nm), HRTEM image (scale bar: 100 nm), and respective FFT pattern.

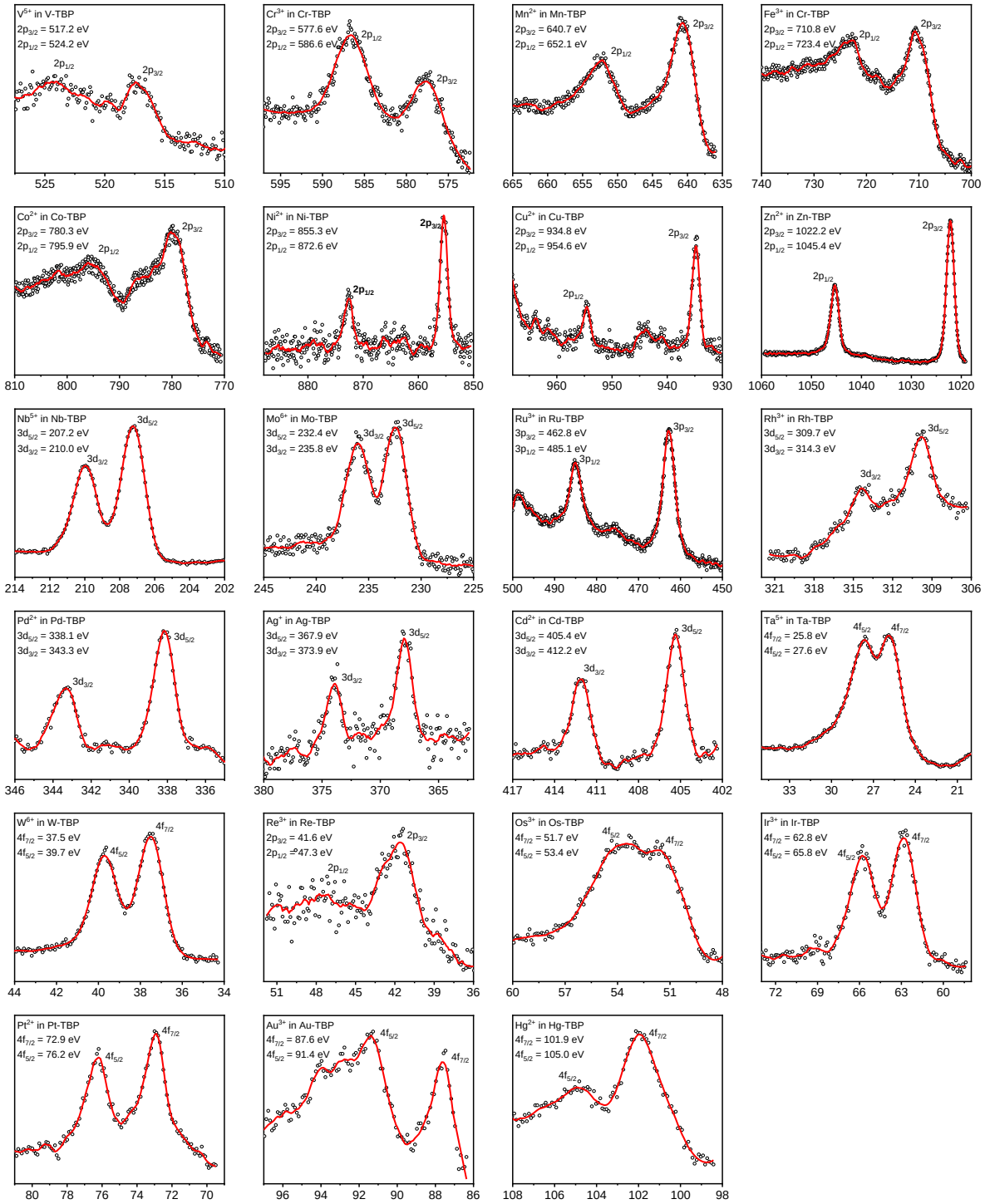

Figure 12-4. XPS analysis of individual M-TBP. The metal ions in M-TBP were determined to be V^{5+}, Cr^{3+}, Mn^{2+}, Fe^{3+}, Co^{2+}, Cu^{2+}, Zn^{2+}, Nb^{5+}, Mo^{6+}, Ru^{3+}, Rh^{3+}, Pd^{2+}, Ag^{+}, Cd^{2+}, Ta^{5+}, W^{6+}, Re^{3+}, Os^{3+}, Pt^{2+}, Au^{3+}, and Hg^{2+}, respectively. These XPS analyses were referenced to the XPS handbook.

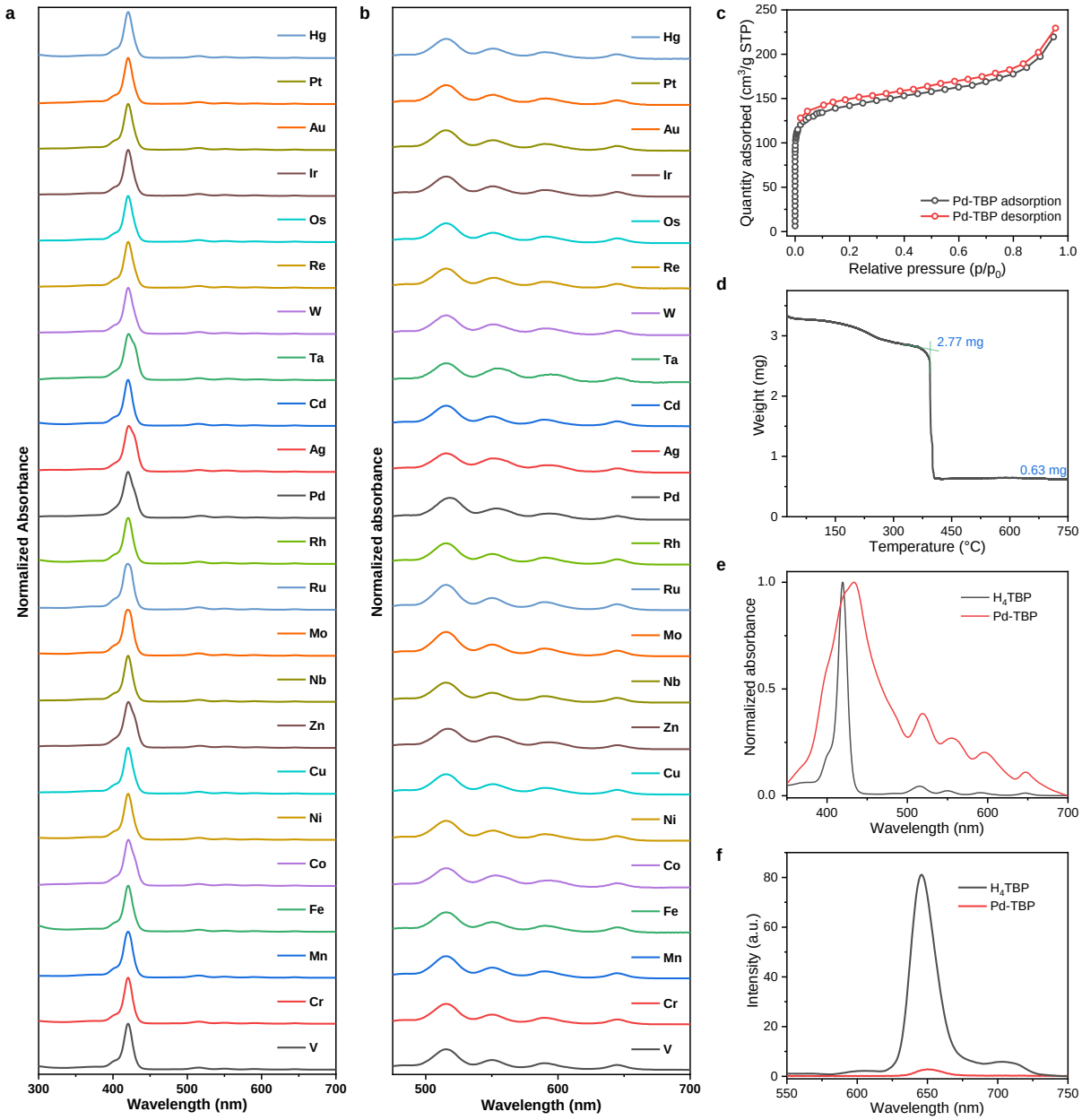

Figure 12-5. General characterization of M-TBP. UV-Vis absorption spectra of digested M-TBP MOFs with (a) normalized Soret bands and (b) magnified Q bands shown. Characterization of Pd-TBP as a representative of M-TBP. (c) Nitrogen sorption isotherm of Pd-TBP at 77 K with BET surface areas of 546.1 m^2/g. (d) TGA of freshly prepared Pd-TBP, with initial weight loss (25-300 °C) corresponding to the removal of adsorbed solvent and subsequent weight loss (300-500 °C) corresponding to the decomposition of Pd_2TBP to 2PdO (2.77 mg to 0.63 mg, 77.3%). (e) UV-Vis spectrum of (red) Pd-TBP and (black) H_4TBP in DMF normalized to Soret band maxima. (f) Fluorescence spectra upon the excitation at 415 nm of 50 μM Pd-TBP (red) and H_4TBP (black) in DMF based on TBP.

Single crystal X-ray diffraction (SXRD) was employed to determine the structures of this library (**Tables 11-3 to 11-10**). Violet square crystals of each M-TBP MOF were obtained

through similar solvothermal reactions at 120 °C (**Table 12-2**). SXRD revealed a conserved **sql** topology within this M-TBP library, with dinuclear metal-oxo chains bridged by TBP ligands to form an approximate 4-fold network with the framework formula of $[M_2(TBP)]^{n+}$ (**Figure 12-6a,b**). These dinuclear metal nodes (M_2) present a unique coordination environment, with one metal atom tetrahedrally coordinated by four carboxylate groups and the other octahedrally coordinated by four carboxylate groups and two solvent molecules (i.e. H_2O, DMF), with average M···O bond lengths of 1.954 ± 0.025 Å and 2.297 ± 0.043 Å, respectively (**Figure 12-6c**). These unusual tetrahedral, octahedral coordination environments and conserved M···O bond lengths were found in each M-TBP structure, regardless of the oxidation state or ionic radius of each metal ion.

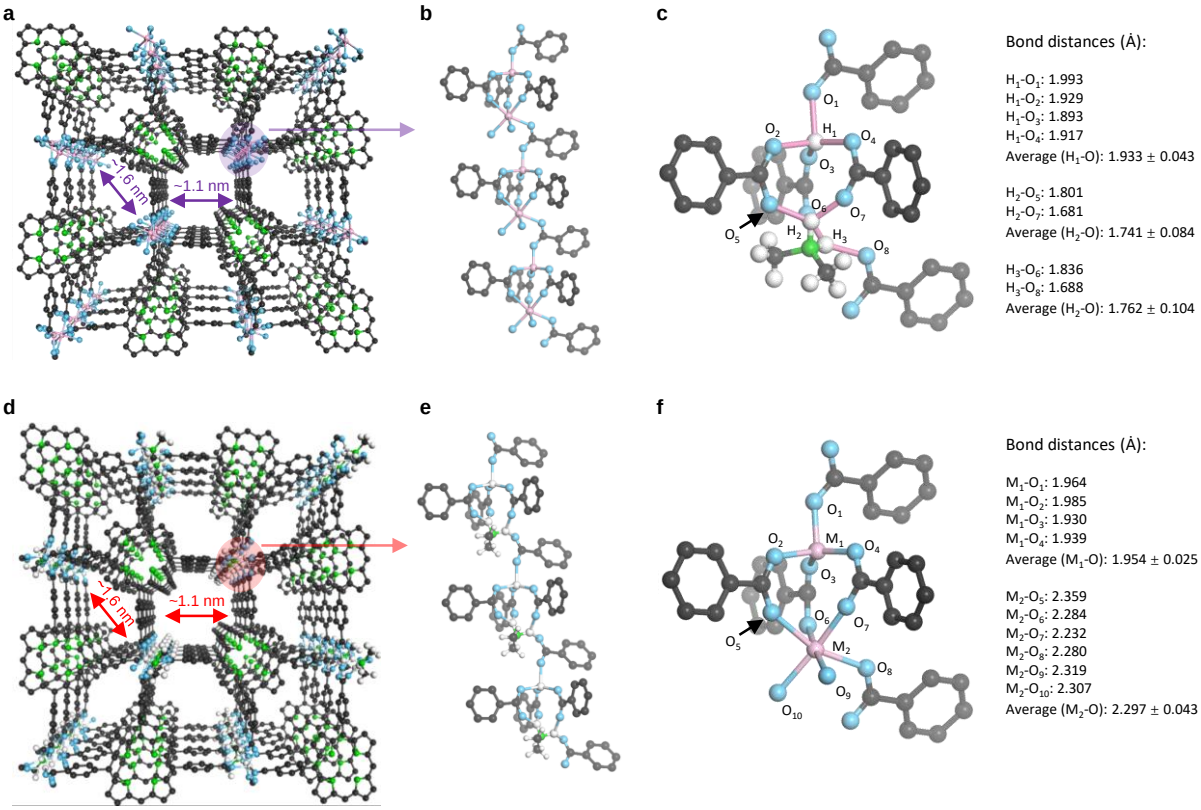

Figure 12-6. Structure of M-TBP and H-TBP. (a) Perspective view of (010) crystal plane of M-TBP structure obtained from single crystal data. (b) Oxo-chain and coordination environment of M_2 SBU within M-TBP. (c) Structure of M_2 nodes with relevant bond distances. (d) Simulated perspective view of the (010) crystal plane of H-TBP structure. (e) Hydrogen-

(Figure 12-6 continued) bonding chain and coordination environment of H_2 (H^+ and $Me_2NH_2^+$) SBU in H-TBP. (f) Structure of H_2 nodes with relevant bond distances. The distance between adjacent porphyrin centers and M_2/H_2 SBUs is ~1.1 nm, while the distance between adjacent M_2 SBUs or H_2 SBUs is ~1.6 nm.

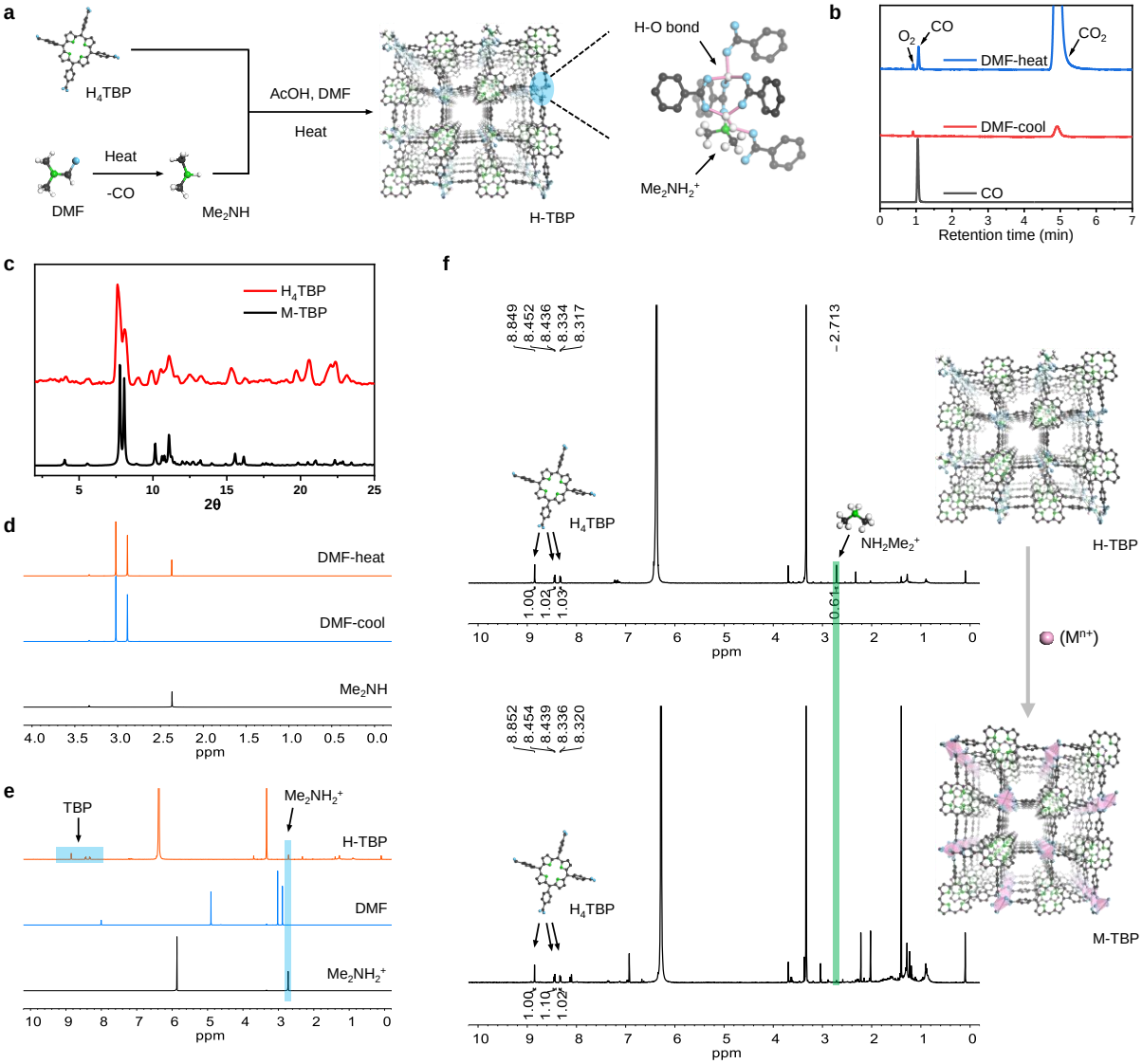

Figure 12-7. Growth mechanisms of H-TBP and M-TBP. (a) Synthetic pathway to H-TBP. (b) CO generation as measured by GC in the headspace of 4.0 mL vials containing (blue) DMF heated to 120 ºC and (red) unheated DMF, with a CO standard shown in black. (c) PXRD patterns of (red) as-synthesized H-TBP powder and (black) simulated M-TBP. (d) Me_2NH generation confirmed by ^1H NMR of DMF heated to 120 ºC (orange) and unheated DMF (blue), with a $Me_2NH_2^+$ standard shown in black. (e) ^1H NMR spectrum of digested H-TBP (orange) with DMF (blue) and $Me_2NH_2^+$ (black) spectra for reference. (f) ^1H NMR spectrum of digested H-TBP, with the H_4TBP: $Me_2NH_2^+$ ratio in quantified to be 1:0.81 based on integration of corresponding signals, and ^1H NMR spectrum of digested Pd-TBP, highlighting the absence of an $Me_2NH_2^+$ signal.

While isostructural MOF libraries have been previously reported, they have been presumed to follow the classical SBU-directed pathway and typically compose a limited number of metal ions with similar physiochemical properties (e.g., some first-row transitional metal ions or lanthanide metal ions).[25, 26] This isostructural M-TBP library, however, incorporates a large range of 23 hard and soft metal ions with different chemical properties, indicating an SBU-independent synthetic pathway.

To elucidate the underlying growth mechanism of these M-TBP MOFs, the shared intermediate was isolated and analyzed (**Figure 12-7a**). This intermediate, determined to be H-TBP (i.e., TBP ligands forming a hydrogen-bonded network), was obtained from synthetic conditions similar to those described above although in the absence of any metal precursor. PXRD of the afforded H-TBP powder revealed the same diffraction pattern as M-TBP derivatives (**Figure 12-7c**). Repeated attempts however failed to obtain-diffraction quality single crystals of H-TBP. ^{1}H NMR of digested H-TBP showed the presence of dimethyl ammonium ($Me_2NH_2^+$) in an approximate 1:1 ratio with TBP, with $Me_2NH_2^+$ being generated from hydrolysis of DMF (**Figure 12-7d,e**). H-TBP was thus proposed to be of the same topological structure as M-TBP, in which TBP ligands are linked by hydrogen-bonded nodes (H_2) with H^+ and $Me_2NH_2^+$ occupying the tetrahedral and octahedral coordination sites, respectively (**Figure 12-6d,e**). The structure of H-TBP was further clarified through VASP calculations, which afforded an average hydrogen-bond distance of 1.7-2.0 Å for the H_2 nodes, within the expected range of strong H-bonds (**Figure 12-6f**). When exposed to a metal precursor (e.g. Pd^{2+}) under similar solvothermal conditions, H^+ and $Me_2NH_2^+$ in H-TBP were displaced by metal ions to form M-TBP, which displayed no apparent $Me_2NH_2^+$ signals in ^{1}H

NMR (**Figure 12-7f**). The synthesis of M-TBP is thus proposed to proceed through a two-step LDCE pathway: first, TBP ligands were self-organized to form H-TBP intermediate with anionic carboxylate groups linked by cationic H^+ and $Me_2NH_2^+$ through H···O bonds; second, metal ions were inserted into H-TBP to generate M-TBP through replacing these H^+ and $Me_2NH_2^+$ and forming M···O bonds.

The energy landscape of the proposed LDCE pathway was analyzed by VASP calculations (**Figure 12-2b**). The formation of representative Pd-TBP was specifically investigated, and was shown to proceed through two distinct processes. The formation of an H-TBP scaffold provides a stabilization of -7.28 kcal·mol^{-1}·TBP^{-1}, while metal intercalation provides an additional stabilization of -2.97 kcal·mol^{-1}·TBP^{-1}. The primary stabilization (i.e., the formation of H-TBP) is the result of π-π stacking of TBP (-4.37 kcal·mol^{-1} per TBP) and hydrogen bonding between TBP and H^+/$Me_2NH_2^+$ (-2.37 kcal·mol^{-1} per bond). H-TBP scaffold formation energetically predominates crystal growth, accounting for 71% of total stabilization, with metal intercalation and SBU-formation accounting for only 29% of total stabilization. To contrast this pathway, Zr-TBP and Hf-TBP were synthesized from synthetic condition similar to those described above, both of which generated PCN-222 structures via a classical SBU-directed pathway (**Figure 12-8a-e**). DFT calculations on Zr-TBP corroborated this proposition, where the formation of Zr_6 SBUs provides a stabilization of -29.88 kcal·mol^{-1}·TBP^{-1} while subsequent ligand exchange provides a stabilization of only -9.38 kcal·mol^{-1}·TBP^{-1}. In Zr-TBP, SBU formation and subsequent ligand exchange account for 76% and 24% of total stabilization, respectively.

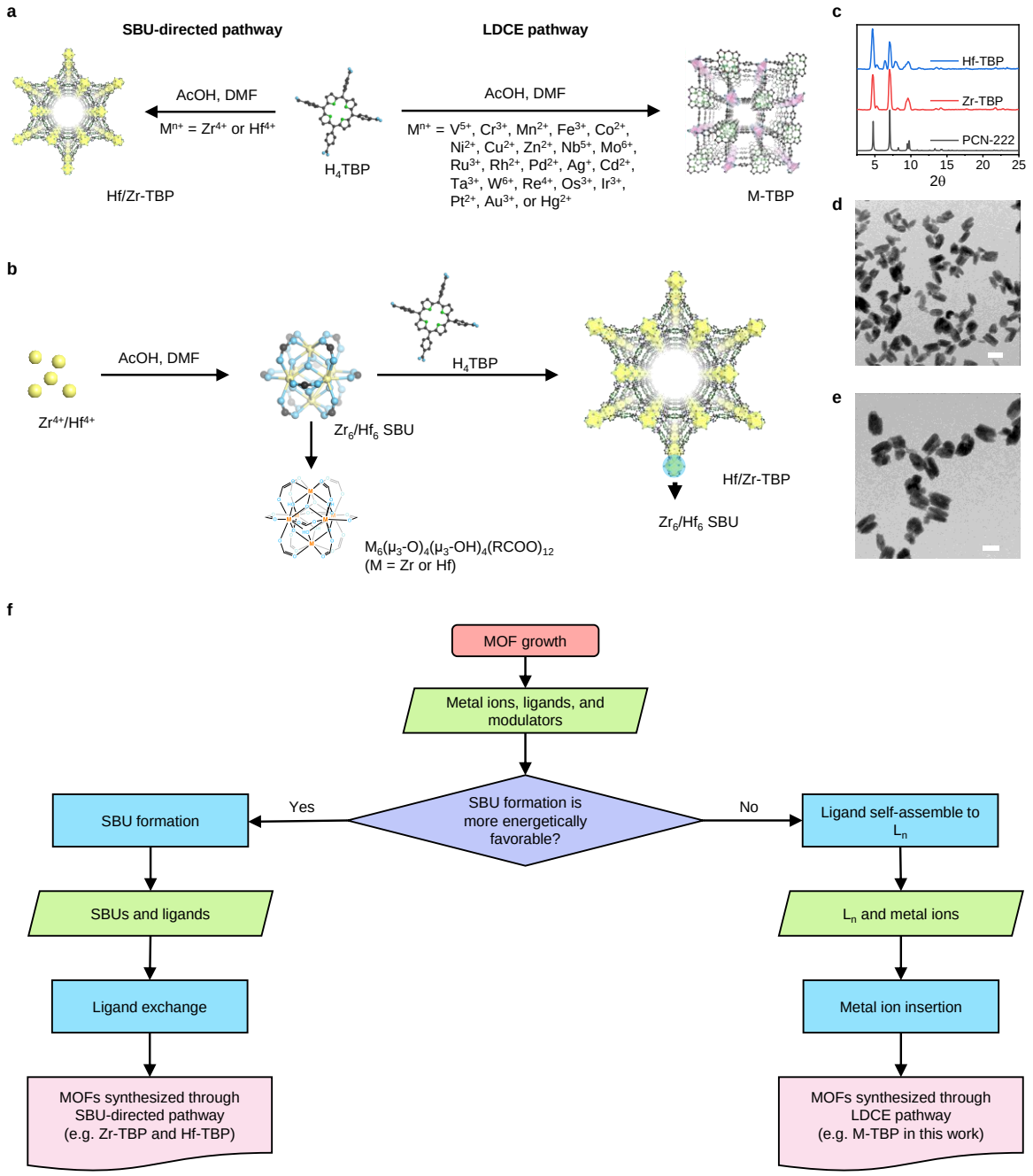

Figure 12-8. Comparison of SBU-directed pathway and LDCE pathway. (a) Summary of each growth mechanism with different metals. (b) Schematic showing the growth mechanism of Hf-TBP/Zr-TBP through the SBU-directed pathway. (c) PXRD patterns of as-synthesized Hf-TBP (blue) and Zr-TBP (red) referenced to the previously reported PCN-222 (black). TEM images of Zr-TBP (d) and Hf-TBP (e). Scale bar: 200nm. (f) Competition between SBU-directed and LDCE pathways towards MOF growth.

MOF growth is proposed to occur as a competition between SBU-directed and LDCE pathways (**Figure 12-8f**). Metals with high affinity to carboxylate or other hard ligands (e.g., Zr) interact strongly with modulators to form SBUs, which is followed by bridging-ligand exchange to form MOFs (e.g., Zr-TBP) via the classical SBU-directed pathway. Ligands that interact strongly through π-π stacking and hydrogen bonding (e.g., TBP), however, can provide this alternative LDCE pathway that remains energetically favorable, such as in the case of Pd-TBP. The LDCE pathway thus provides a mechanism to accommodate a wider variety of metal ions, even those which only weakly coordinate to carboxylate groups (e.g., soft and noble metal ions).

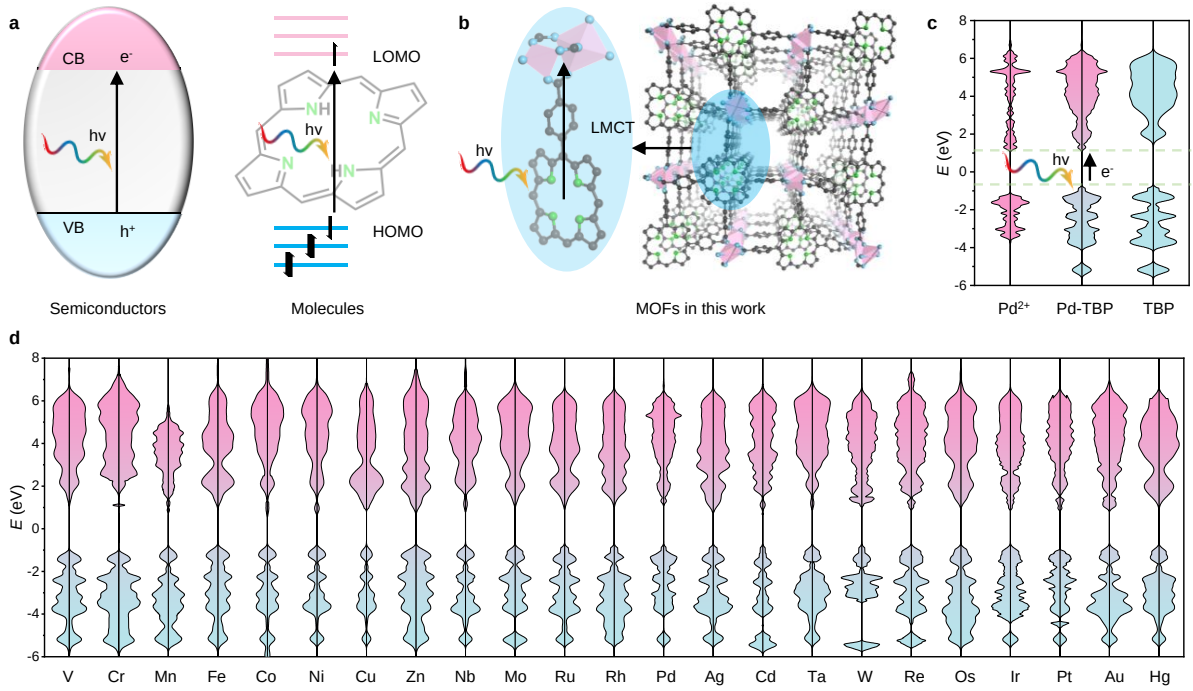

Figure 12-9. Electronic structures of M-TBP. (a) Schematic showing the electronic structures of semiconductors (left) and organic molecules (right) with corresponding electron transfer processes upon photoexcitation. (b) Schematic showing the LMCT process in M-TBP upon photoexcitation. (c) Total (Pd-TBP) and projected (Pd^{2+} and TBP) density of states of Pd-TBP. (d) Total density of states of each M-TBP.

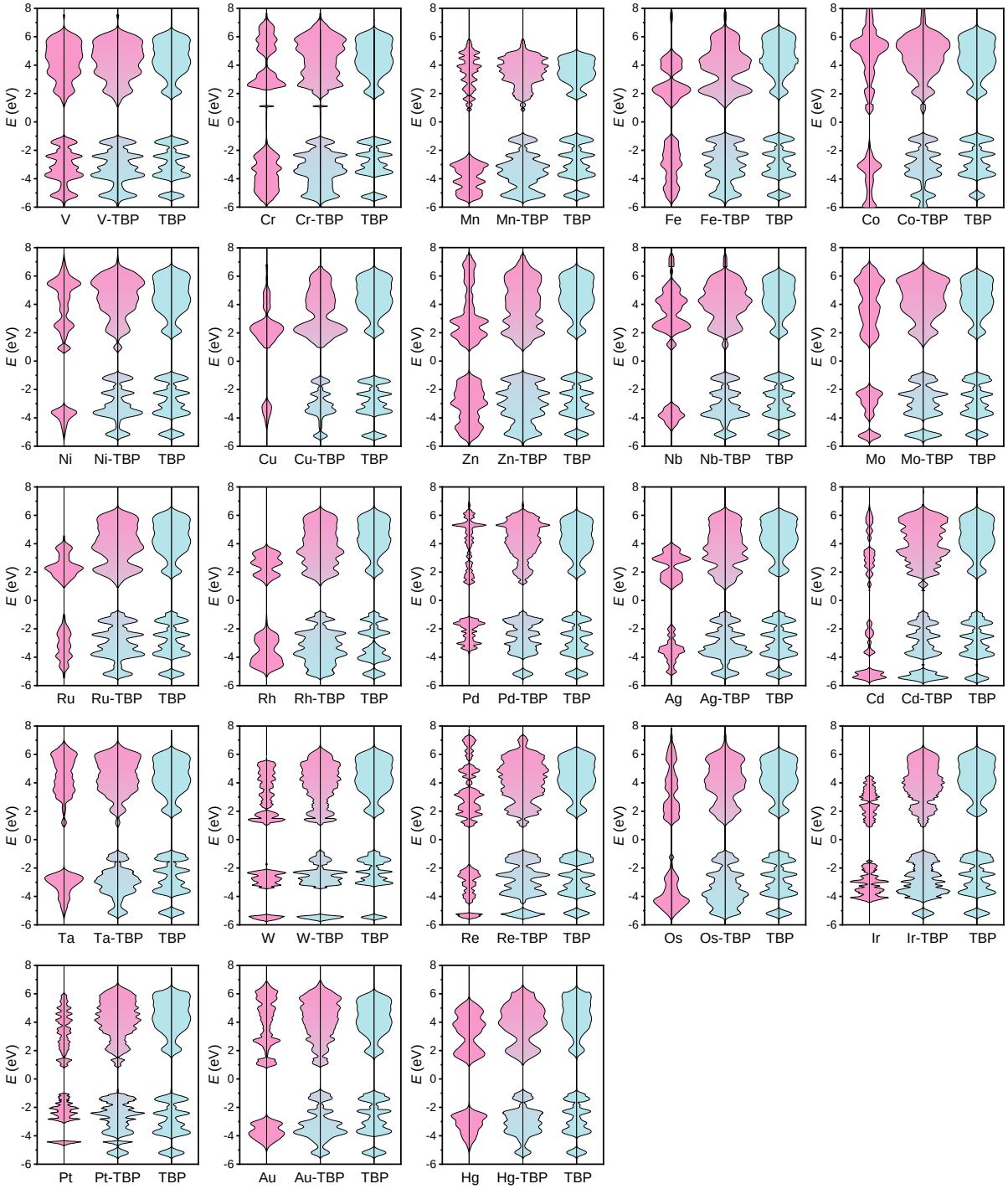

Figure 12-10. Summary of the total (M-TBP) and projected (M ions, TBP) density of states of all the 23 M-TBP. From left to right and top to bottom, M = V, Cr, Mn, Fe, Co, Ni, Cu, Zn, Nb, Mo, Ru, Rh, Pd, Ag, Cd, Ta, W, Re, Os, Ir, Pt, Au, and Hg, respectively.

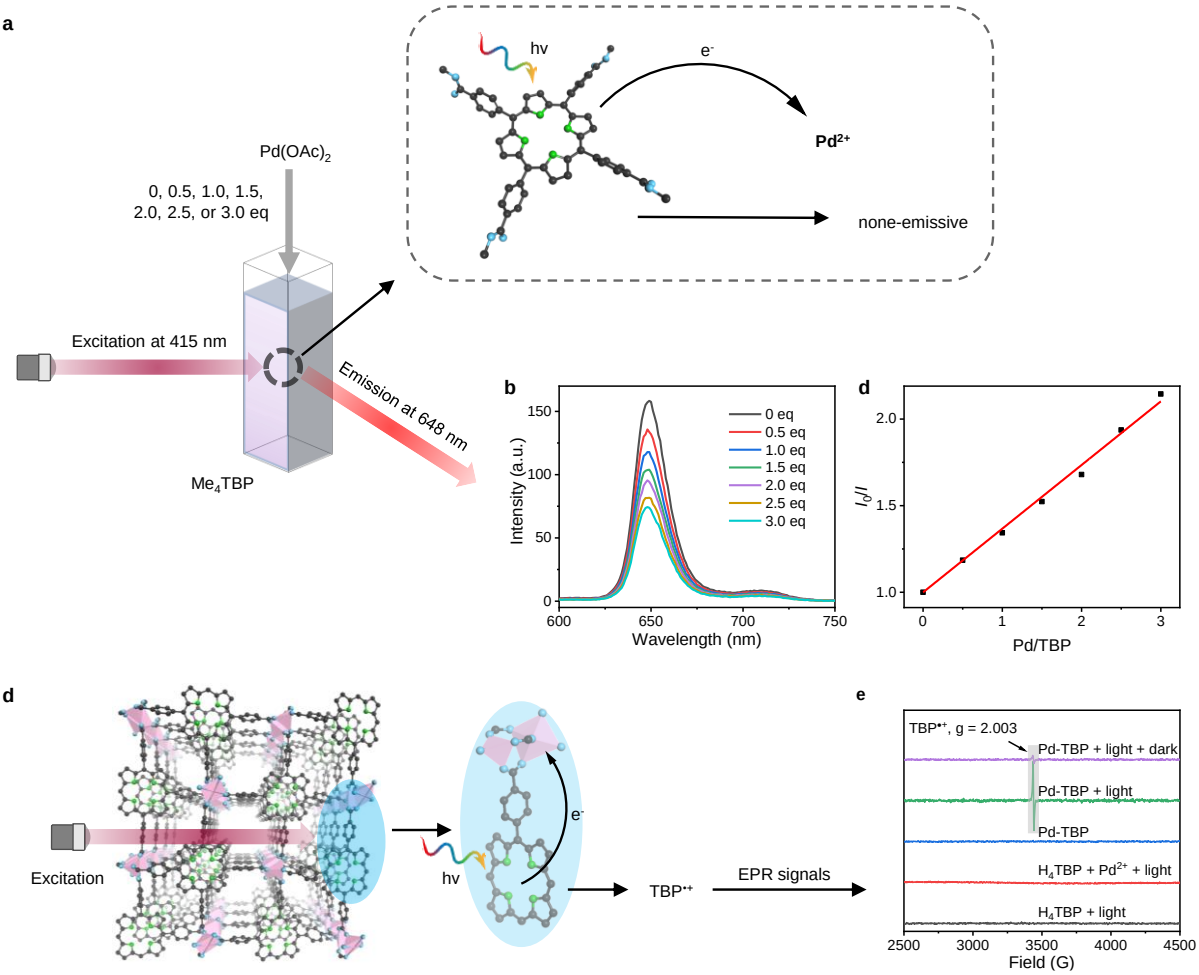

Figure 12-11. LMCT studies. (a) Schematic showing luminescence quenching of Me_4TBP by $Pd(OAc)_2$. (b) Luminescence spectra upon excitation at 415 nm of 50 μM Me_4TBP in DMF with varying concentrations of $Pd(OAc)_2$. (c) Stern-Volmer fitting of I_0/I to the ratio of Pd to TBP. (d) Schematic showing LMCT within M-TBP. (e) EPR spectra of Pd-TBP with and without light irradiation, H_4TBP with light irradiation, and a mixture of H_4TBP and Pd^{2+} with light irradiation, all at 15K.

12.2.2 Electronic structures

Incorporating such a range of metals realizes previously inaccessible frameworks, and as H-TBP could be differentiated into each M-TBP MOF, select functions could be tuned across the library. Photocatalytic properties were specifically investigated herein, as this M-TBP library presented highly tunable electronic structures. The electronic profiles of this library were analyzed by VASP calculations. In contrast to traditional photosensitizing materials, such as semiconductors with band structures or organic molecules with molecular orbitals (**Figure**

12-9a), VASP calculation described the electronic structures of M-TBP as framework orbitals (FOs) (**Figure 12-9c,d and Figure 12-10**). These FOs are hybrids of both the molecular orbitals of TBP and the atomic orbitals of metal ions, where the highest occupied framework orbitals (HOFOs) and lowest unoccupied framework orbitals (LUFOs) are primarily of the character of TBP and metal, respectively. This arrangement of frontier orbitals accommodates LMCT upon photoexcitation to generate $TBP^{\bullet+}$ and reduced metal ions (**Figure 12-9b**). This process was confirmed by both the luminescence quenching of TBP by metal ions (i.e., Pd^{2+}), validating the LMCT process, and $TBP^{\bullet+}$ detection in M-TBP (e.g., Pd-TBP) by EPR upon irradiation (**Figure 12-11**). Similar to the doping of semiconductors, incorporating various metal ions into M-TBP accommodated highly tunable FOs with LUFOs ranging from 0.56 to 1.08 eV and HOFO-LUFO gaps ranging from 1.20 to 1.70 eV (**Table 12-11**).

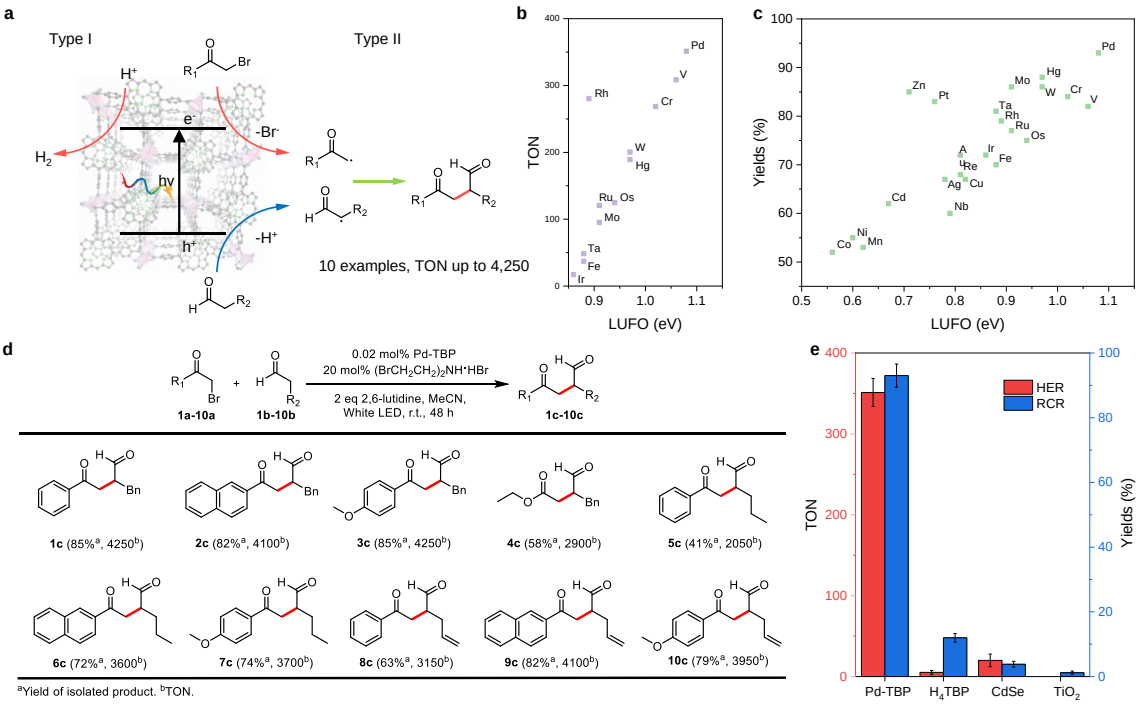

Figure 12-12. Photocatalysis with M-TBP. (a) Schematic of two types of photocatalytic reactions catalyzed by M-TBP. (b) Plot of HER reactivities of M-TBP vs. LUFO energies (LUFO > 0.85 eV). (c) Plots of the RCR reactivities of M-TBP vs. LUFO energies. (d) Substrate scopes of RCR catalyzed by Pd-TBP. (e) Comparison of reactivity between Pd-TBP, H_4TBP, CdSe, and TiO_2.

12.2.3 Photocatalytic reactions

This M-TBP library, with its tunable electronic structures, provided a singular opportunity to systematically optimize photocatalytic activities within a conserved framework, as demonstrated through two types of semiconductor-like photocatalytic reactions (**Figure 12-12a**).[27] In Type I reactions, which were explored through photocatalytic HER, only the reductive element (i.e., LUFO) is involved, specifically in the reduction of protons to dihydrogen. Conversely, in Type II reactions, which were explored through radical coupling reactions (RCR), both reductive (i.e., LUFO) and oxidative (i.e., HOFO) elements are involved, with substrates being either reduced by the LUFO or oxidized by the HOFO to generate two distinct radicals which couple to yield the product. With Type I reactivity, the M-TBP library catalyzed HER with highly tunable TONs ranging from <5 to 351 in a 24-hour period (**Figure 12-13a,b**). With Type II reactivity, the M-TBP library catalyzed RCR with TONs ranging from 2600 to 4650 (**Figure 12-13c,d**). The radical mechanism of these RCRs was confirmed by the capture of reductive (**T1**) and oxidative (**T2**) radicals by TEMPO, revealing a **T1**:**T2** ratio of 9:1 (**Figure 12-14**), indicating that the LUFO has more influence on reactivity. TONs were strongly correlated with the LUFO energy profile of each M-TBP, with Pearson correlation coefficients (*r*) of 0.84 for HER (**Figure 12-12b**) and 0.80 for RCR (**Figure 12-12c**). The highest TONs for both HER and RCR were observed with Pd-TBP, each of which is roughly 10-fold higher than those of homogeneous analogue (i.e., H_4TBP) or semiconductor photocatalysts (i.e., TiO_2 and CdSe), likely due to improved charge separation in comparison to H_4TBP and stronger light absorption than TiO_2 and CdSe, respectively **Figure 12-12e**). To establish the utility of M-TBP MOFs as efficient photocatalysts, the substrate scope for

photocatalytic RCR was expanded using Pd-TBP at 0.2% loading based on TBP (**Figure 12-12d**). Pd-TBP-catalyzed RCR exhibited a board substrate scope with good functional group compatibility to afford coupling products in 41 - 85% isolated yields that correspond to TONs of 2050 - 4250.

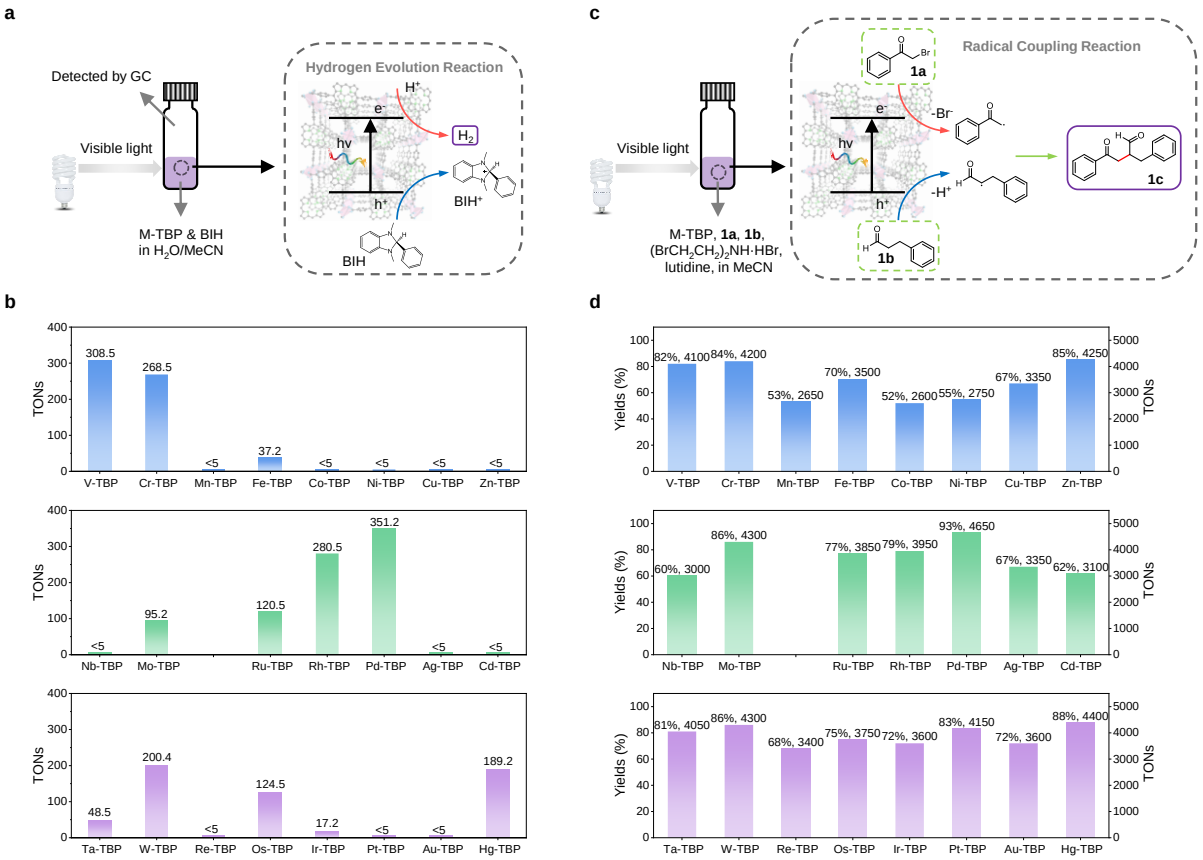

Figure 12-13. M-TBP catalyzed HER and RCR. (a) Schematic of setup and mechanism of M-TBP catalyzed HER. (b) Summary of TONs for HER catalyzed by each M-TBP. (c) Schematic of setup and mechanism of M-TBP catalyzed RCR. (d) Summary of yield and TONs of RCR catalyzed by each M-TBP.

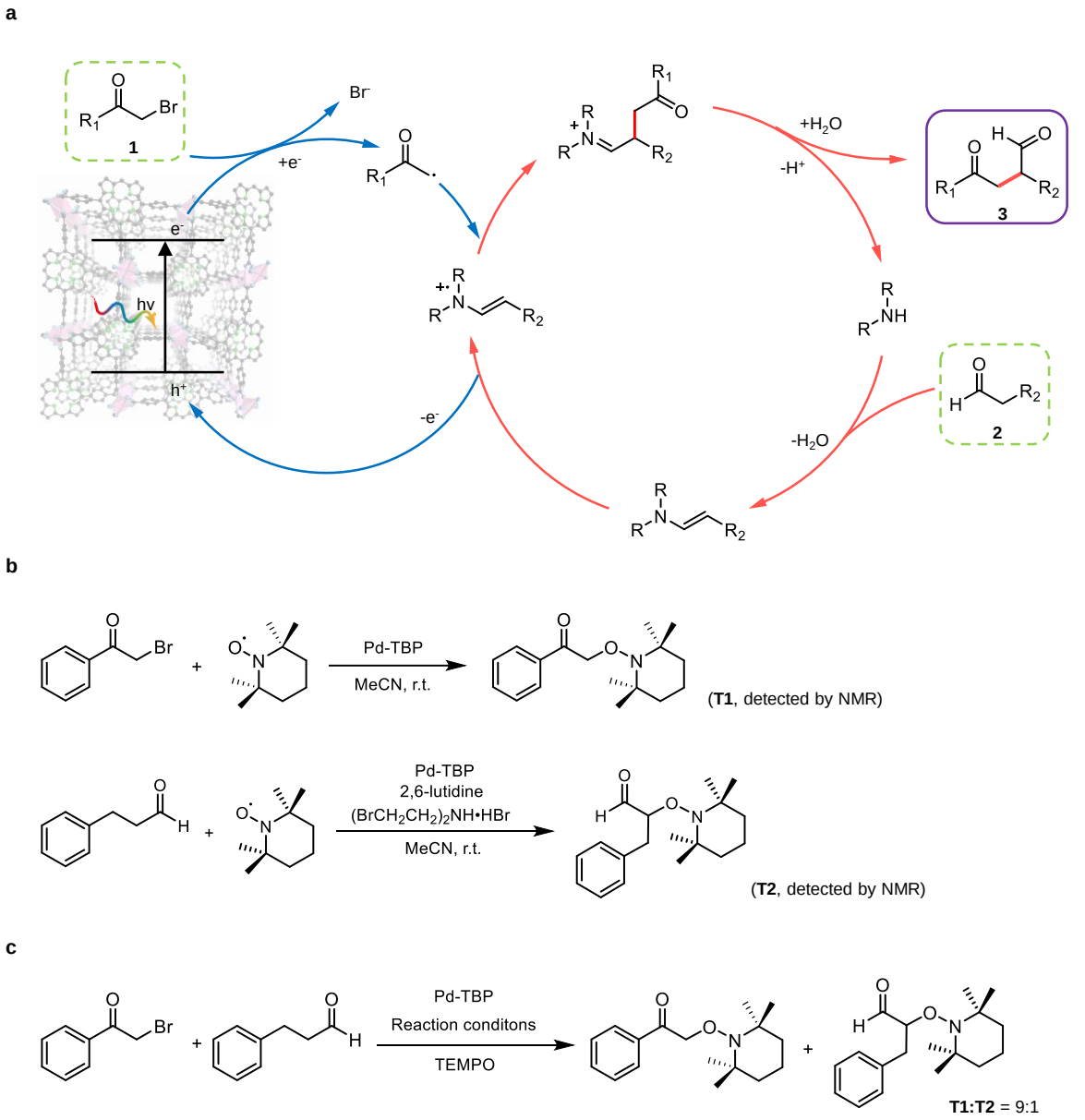

Figure 12-14. Mechanistic studies for M-TBP catalyzed radical coupling reactions. (a) Proposed mechanism for RCR catalyzed by M-TBP. (b) TEMPO trapping experiment for both reductive (**T1** = 1-phenyl-2-((2,2,6,6-tetramethylpiperidin-1-yl)oxy)ethan-1-one) and oxidative (**T2** = 3-phenyl-2-((2,2,6,6-tetramethylpiperidin-1-yl)oxy)propanal) radical intermediates. (c) Radical trapping by TEMPO in reaction conditions.

12.3 Conclusion

In this work, we revealed a novel pathway to MOF synthesis relying upon ligand-directed crystal engineering. Through this new pathway, enduring constraints on metal incorporation are overcome, allowing for unbiased construction of an M-TBP MOF library including each

naturally occurring transition metal in Groups 5 through 12. This pathway realizes the synthesis of MOFs with previously inaccessible metal components, all within a single conserved MOF template, to afford much improved efficiency in photocatalytic HER and RCR reactions. By accommodating metals with diverse physical and chemical properties, this LDCE pathway is poised to expand the scope of MOFs both in structure and function. We envision the same versatility afforded to MOFs by the SBU-directed pathway will be endowed to this LDCE pathway, opening up new possibilities for the field of MOF research.

12.4 Methods and additional tables

General synthetic procedures for M-TBP MOFs. 0.50 mL of metal salt stock solution, 0.50 mL of H_4TBP stock solution, and AcOH were charged to 4.0 mL glass vials. Stock solutions were made in DMF, with molalities and AcOH quantities for individual M-TBP MOFs (M= V, Cr, Mn, Fe, Co, Ni, Cu, Zn, Nb, Mo, Ru, Rh, Pd, Ag, Cd, Ta, W, Re, Os, Ir, Pt, Au, and Hg) tabulated in **Table 12-1**. These vials were sealed and kept in an isothermal oven at 80 ºC to react solvothermally for 24 hours and afford violet precipitate. This precipitate was collected by centrifugation and washed with fresh DMF (3 × 1.0 mL per vial) then fresh ethanol (3 × 1.0 mL per vial). The yield of these M-TBP syntheses based on M were determined by ICP-MS.

General synthetic procedures for M-TBP single crystals. 0.50 mL of metal salt stock solution, 0.50 mL of H_4TBP stock solution, and AcOH were charged to 4.0 mL glass vials. Stock solutions were made in DMF, with molalities and AcOH quantities for individual M-TBP single crystals (M= V, Cr, Mn, Fe, Co, Ni, Cu, Zn, Nb, Mo, Ru, Rh, Pd, Ag, Cd, Ta, W, Re, Os, Ir, Pt, Au, and Hg) tabulated in **Table 12-2**. These vials were sealed and kept in an isothermal oven at 120 ºC to react solvothermally for 7 days and afford violet square-shaped

single crystals. Crystals were collected by centrifugation and washed with fresh DMF (3 × 1.0 mL per vial) then fresh ethanol (3 × 1.0 mL per vial).

M-TBP single crystals. The TBP linkers in M-TBP single crystals were metaled with respective metal ions at various levels. This metalation process was believed to happen after M-TBP single crystals growth, since M-TBP powder could be synthesized under mild conditions with free-base H_4TBP, as proved by the UV-Vis spectra. Therefore, we show the single crystal structure of M-TBP with free-base TBP to represent the structure of M-TBP in this work. Separately, HRTEM images, together with their FFT, revealed a four-fold symmetry, matching the projection of the crystal structure of M-TBP along the (010) axis (**Figure 12-6a**). A distance of ~1.6 nm was measured between each adjacent spot in each HRTEM image, corresponding to the expected distance between adjacent M_2 SBUs.

Synthesis of H-TBP. 1.0 mL of H_4TBP stock solution (1.0 mg per 1.0 mL DMF) and AcOH (50 μL) were charged to a 4.0 mL glass vial. The reaction solution was kept in an isothermal oven at 80 ºC for 4 hours. Violet powders were collected by centrifugation and washed with fresh DMF (3 × 1.0 mL per vial) then fresh methanol (3 × 1.0 mL per vial).

DMF Decomposition. 1.0 mL of DMF was charged to a 4.0 mL vial and sealed with a rubber stopper. Vials were kept in an isothermal oven at 120 ºC for 4 hours, whereupon 200 μL of headspace gas was analyzed by GC to determine the CO generation. Additionally, 10 μL of the heated solution was dissolved into 500 μL of methanol-d_4 and analyzed by ^{1}H NMR to detect the Me_2NH generation.

MOF digestion for ICP-MS analysis. 10 μL of M-TBP ethanol suspension was charged to solution of 980 μL of HNO_3 and 10 μL of HF. The resultant suspension was sonicated for 15

mins and allowed to sit overnight, whereupon 200 μL of the solution was diluted into 7 mL deionized water (H_2O).

MOF digestion for NMR analysis. 1.0 μmol of Pd-TBP or H-TBP based on TBP was collected by centrifugation and dried at room temperature under vacuum (< 0.1 mbar) for 24 hours. The resulting solids were then digested in solutions of 500 μL methanol-d_4 and 50 μL D_3PO_4 and sonicated for 15 min. 50 μL D_2O were subsequently charged to these solutions and each was analyzed by ^{1}H NMR.

MOF digestion for UV-Vis analysis. 10 μL of M-TBP ethanol suspension (1.0 mM based on TBP) was diluted into a solution of DMSO (940 μL) and H_3PO_4 (50 μL). This mixture was sonicated for 15 min. and the resultant solution was analysis by UV-Vis spectroscopy.

VASP calculation. To fully reflect the characteristics of M-TBP, we used periodic systems to study their structures, growth mechanism, and density of states. All calculations were carried out using the VASP [28, 29]. The generalized gradient approximation (GGA) [30, 31] includes the effects of local gradients in the charge density for each point in the materials, which yielded more accurate equilibrium structural parameters than the local density approximation (LDA). Hence, the GGA function was used for cell relaxation and energy calculations. Perdew, Burke, and Ernzerhof (PBE) [31] pseudopotentials were used to describe the ion-electron interactions. Forces on ions were calculated using the Hellmann-Feynman theorem as the partial derivatives of free electronic energies with respect to atomic position, and adjusted using the Harris-Foulkes correction to the forces. In all of periodic calculations, the energy cutoff was set at 500 eV. For the cell and geometric relaxations, the systems were fully relaxed until the forces on each atom presented less than 10^{-3} eV Å^{-1}. Density of states (DOS) calculations used the HSE06

[32] exchange-correlation functional to obtain electronic properties, as HSE06 is powerful in predicting band gaps of materials. A 1×1×1 k-point mesh was used to simplify calculation, as previous studies found that Γ point sampling of the first Brillouin zone is sufficient to obtain accurate electronic properties. Furthermore, the DOS was calculated in a fine energy grid (1801 points) so as to visualize DOS correctly considering narrow band features.

Growth mechanism calculation. To explicate the growth mechanism of the M-TBP MOF, we employed theoretical calculations to model the potential energy profiles of starting materials, intermediates, and products for the two synthetic pathways discussed in this work. These energies were calculated using the VASP. As described in the manuscript, Pd-TBP and Zr-TBP (with PCN-222 topology) were the basis of these calculations for the LDCE and SBU-directed pathways, respectively. The structures of starting material (i.e., $ZrCl_4$, $PdCl_2$ and H_4TBP) and MOF product (i.e., Zr-TBP, Pd-TBP) were obtained from single crystal data. Solvated ionic species (i.e., Cl^-, H^+, H_2O Me_2NH, and $Me_2NH_2^+$) or metal clusters (i.e, $Zr_6O_4(OH)_4$) replaced these starting materials within the unit cell upon optimization for the LDCE and SBU-directed pathways, respectively. For the LDCE pathway, the structures of the H-TBP intermediate was represented with the M-TBP topology with suspected ionic species coordinated within the nodes, all of which was followed by optimization to determine the most energetically preferred coordination modes and structure. Resulting from these optimizations, we propose, as described in the main text, independent pathways for Pd-TBP and Zn-TBP growth, which are described below:

Zr-TBP Growth

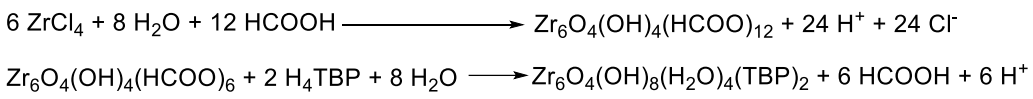

Pd-TBP Growth

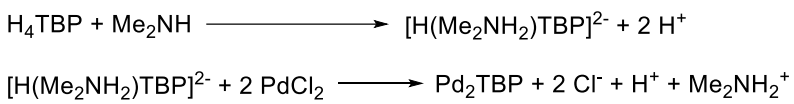

To simplify these calculations, we calculated the energy for each molecular species under solvated conditions. Correspondingly, interactions between starting material and the intermediates in solution were disregarded.

First, geometric relaxation and cell size considerations optimized lattice constants and structures for Pd-TBP and Zr-TBP. Solvated structures of starting materials were also calculated and optimized. The energy profile of these species was next calculated. The obtained energy profile of each species was adjusted according to the reaction coefficient, allowing overall energy change to be obtained.

Second, the energetic contribution of H-TBP formation was calculated. The total energy change of this process derives from four concomitant processes: (1) H_4TBP dissociation, (2) Me_2NH protonation, (3) π - π stacking interaction, and (4) hydrogen-bond formation. These first two steps are the energetically uphill, while the latter two provide stabilization.

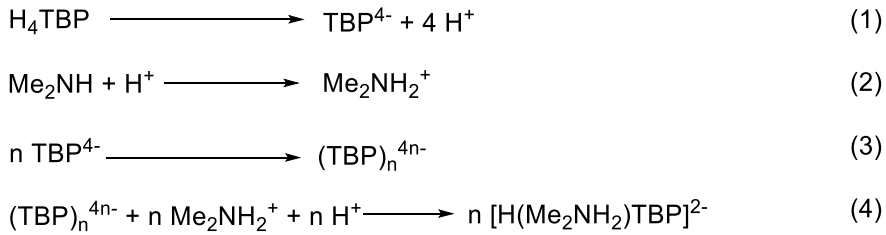

The energy involved in the dissociation of H_4TBP and protonation of Me_2NH were estimated using pK_a and pK_b values of H_4TBP and Me_2NH, respectively, under reaction condition. Contributions from π - π stacking were calculated by removing H^+ and $Me_2NH_2^+$

ions from H-TBP. In the absence of hydrogen bonding any stabilization energy was presumed to come from π - π stacking interactions. These four steps of H-TBP formation, following by (5) metal insertion, together presented the overall growth processes of M-TBP.

Luminescence quenching of Me_4TBP by $Pd(OAc)_2$. $Pd(OAc)_2$ was added incrementally to a Me_4TBP solution in DMF (50 μM) to afford Pd/TBP molar ratios of 0.5, 1.0, 1.5, 2.0, 2.5, and 3.0. A luminescence spectrum was collected for each molar ratio by a fluorimeter with an excitation wavelength at 415 nm. The oxidative quenching of Me_4TBP by Pd^{2+} was supported by fitting obtained intensities at 648 nm to the Pd/TBP ratio ($R_{Pd/TBP}$) using the Stern-Völmer equation:

$$\frac{I_0}{I} = 1 + K_{SV} R_{Pd/TBP}$$

where K_{SV} is the Stern-Völmer constant and I_0/I is the ratio of luminescence intensity of Me_4TBP at 648 nm in the absence and presence of Pd^{2+}. I_0/I revealed a strong linear correlation to the $R_{Pd/TBP}$ with $R^2 = 0.999$ and $K_{SV} = 0.367 \pm 0.006$.

HER. Photocatalytic HER was performed in an external illumination reaction vessel equipped with a magnetic stirrer. Samples were prepared in 4.0 mL glass vials, with each sample containing 2.1 mL of solution (2.0 mL of CH_3CN, 0.1 mL of H_2O). Each sample contained 0.05 μmol of M-TBP based on the incorporated metal (M= V, Cr, Mn, Fe, Co, Ni, Cu, Zn, Nb, Mo, Ru, Rh, Pd, Ag, Cd, Ta, W, Re, Os, Ir Pt, Au, or Hg) and 45 mg BIH. For control experiments, samples were instead prepared with H_4TBP (0.025 μmol), TiO_2 (0.05 μmol based on Ti), and CdSe (0.05 μmol based on Cd). Vials were sealed with rubber septa and degassed by three cycles of freezing in liquid nitrogen for three minutes, degassing under vacuum for five minutes, and refilling with nitrogen while allowing the solution to thaw. Solutions were then irradiated

with a white LED light source for 24 hours while stirring at room temperature. Following reaction, 200 µL of gas in the headspace of each vial were analyzed by GC equipped with a TCD to determine the amount of hydrogen generated.

RCR. All reactions described below were set up in the oxygen-free glove box and performed in an external illumination reaction vessel equipped with a magnetic stirrer. 2-bromoacetophenone (0.5 mmol, **1a**), 3-phenylpropanal (1.0 mmol, **1b),** bis(2-bromoethyl)amine hydrobromide (0.1 mmol) as co-catalyst, and 2,6-lutidine (1.0 mmol) as base were charged to a 4.0 mL glass vial containing MeCN (1 mL). 0.1 µmol of M-TBP based on M (M= V, Cr, Mn, Fe, Co, Ni, Cu, Zn, Nb, Mo, Ru, Rh, Pd, Ag, Cd, Ta, W, Re, Os, Ir, Pt, Au, or Hg) was added as catalyst. For control experiments, samples were prepared with H_4TBP (0.05 µmol), TiO_2 (0.1 µmol based on Ti), and CdSe (0.1 µmol based on Cd) instead of M-TBP. Vials were sealed and irradiated with a white LED light source for 48 hours while stirring at room temperature. Following reaction, the reaction mixture was poured onto H_2O and organics were extracted with Et_2O (3 × 10 mL). The organic solution was combined, washed with H_2O, dried over Na_2SO_4 and concentrated in vacuo. Reaction products and conversion ratios were determined by GC-MS.

Radical capture by TEMPO. T1: The reaction described below was set up in the oxygen-free glove box and performed in an external illumination reaction vessel equipped with a magnetic stirrer. Bromoacetophenone (0.5 mmol, **1a**), Pd-TBP (0.1 µmol based on TBP, 0.02% loading), and TEMPO (1.0 mmol) were charged to a 4 mL vial containing MeCN (1 mL). Vials were sealed and irradiated with a white LED light source for 48 hours while stirring at room temperature. Following reaction, the mixture was poured onto H_2O and extracted with Et_2O (3

× 10 mL). The organic solution was combined, washed with H_2O, dried over Na_2SO_4 and concentrated in vacuo. The crude products were further purified by column chromatography (DCM on silica) to afford TEMPO trapped compound 1-phenyl-2-((2,2,6,6-tetramethylpiperidin-1-yl)oxy)ethan-1-one (**T1)**, as confirmed by ^{1}H NMR.

T2: The reaction described below was set up in the oxygen-free glove box and performed in an external illumination reaction vessel equipped with a magnetic stirrer. 3-Phenylpropanal (1.0 mmol, **1b**), Pd-TBP (0.1 μmol based on TBP, 0.02% loading), and TEMPO (1.0 mmol) were charged to a 4 mL vial containing MeCN (1 mL). Vials were sealed and irradiated with a white LED light source for 48 hours while stirring at room temperature. Following reaction, the mixture was poured onto H_2O and extracted with Et_2O (3 × 10 mL). The organic solution was combined, washed with H_2O, dried over Na_2SO_4 and concentrated in vacuo. The crude products were further purified by column chromatography (DCM on silica) to afford TEMPO trapped compound 3-phenyl-2-((2,2,6,6-tetramethylpiperidin-1-yl)oxy)propanal (**T2)**, as confirmed by ^{1}H NMR.

RCR substrate scope. All reactions described below were set up in the oxygen-free glove box and performed in an external illumination reaction vessel equipped with a magnetic stirrer. Two substrates (0.5 mmol of **1a-10a** and 1.0 mmol of **1b-10b**), Pd-TBP (0.1 μmol based on TBP, 0.02% loading) as catalyst, bis(2-bromoethyl)amine hydrobromide (0.1 mmol) as co-catalyst, and 2,6-lutidine (1.0 mmol) as base were charged to a 4.0 mL glass vial containing MeCN (1 mL). Vials were sealed and then irradiated with a white LED light source for 48 hours while stirring at room temperature. Following reaction, the reaction mixture was poured onto H_2O, and extracted with Et_2O (3 × 10 mL). The organic solution was combined, washed with H_2O,

dried over Na_2SO_4 and concentrated in vacuo. The crude product was further purified by column chromatography (DCM on silica) to afford **1c-10c**, as confirmed by ^{1}H NMR and ^{13}C NMR.

Table 12-1. Details for the synthesis of M-TBP, Zr-TBP, and Hf-TBP MOFs

M-TBP Variant	**Metal Precursor**	**Metal Stock Solution Molality** (μmol/mL DMF)	**H_4TBP Stock Solution Molality** (mg/mL DMF)	**AcOH** (μL)	**Yields determined by ICP-MS**
V-TBP	VOF_3	1.0	2.0	40	32%
Cr-TBP	$CrCl_3•6H_2O$	1.0	2.0	60	35%
Mn-TBP	$MnCl_2•4H_2O$	1.0	2.0	60	26%
Fe-TBP	$FeCl_3•_6H_2O$	1.0	2.0	80	42%
Co-TBP	$CoCl_2•6H_2O$	1.0	2.0	40	29%
Ni-TBP	$NiCl_2•6H_2O$	1.0	2.0	60	36%
Cu-TBP	$CuCl_2•2H_2O$	1.0	2.0	40	33%
Zn-TBP	$Zn(OAc)_2$	1.0	2.0	80	45%
Nb-TBP	$NbCl_5$	1.0	2.0	60	42%
Mo-TBP	$MoOCl_4$	1.0	2.0	80	41%
Ru-TBP	$RuCl_3•xH_2O$	1.0	2.0	40	46%
Rh-TBP	$RhCl_3•xH_2O$	1.0	2.0	60	35%
Pd-TBP	$Pd(OAc)_2$	1.0	2.0	80	32%
Ag-TBP	$AgNO_3$	1.0	2.0	40	33%
Cd-TBP	$CdCl_2•xH_2O$	1.0	2.0	60	33%
Ta-TBP	$TaCl_5$	1.0	2.0	40	42%
W-TBP	WCl_6	1.0	2.0	60	46%
Re-TBP	$ReCl_3$	1.0	2.0	80	48%
Os-TBP	$OsCl_3•3H_2O$	1.0	2.0	40	41%
Ir-TBP	$IrCl_3•xH_2O$	1.0	2.0	60	39%
Pt-TBP	$PtCl_2$	1.0	2.0	80	46%
Au-TBP	$HAuCl_4•3H_2O$	1.0	2.0	40	41%
Hg-TBP	$Hg(OAc)_2$	1.0	2.0	80	38%
Zr-TBP and Hf-TBP with PCN-222 structure					
Zr-TBP	$ZrCl_4$	1.0	2.0	80	56%
Hf-TBP	$HfCl_4$	1.0	2.0	80	64%

Table 12-2. Details for the synthesis of M-TBP single crystals

M-TBP Variant	**Metal Precursor**	**Metal Stock Solution Molality** (mg/mL DMF)	**H_4TBP Stock Solution Molality** (mg/mL DMF)	**AcOH** (µL)
V-TBP	VOF_3	0.30	2.0	200
Cr-TBP	$CrCl_3•6H_2O$	1.20	2.0	200
Mn-TBP	$MnCl_2•4H_2O$	1.20	2.0	180
Fe-TBP	$FeCl_3•_6H_2O$	1.76	2.0	140
Co-TBP	$CoCl_2•6H_2O$	1.20	2.0	120
Ni-TBP	$NiCl_2•6H_2O$	0.32	4.0	200
Cu-TBP	$CuCl_2•2H_2O$	0.42	4.0	200
Zn-TBP	$Zn(OAc)_2$	1.20	2.0	200
Nb-TBP	$NbCl_5$	1.20	2.0	140
Mo-TBP	$MoOCl_4$	1.20	2.0	200
Ru-TBP	$RuCl_3•xH_2O$	1.20	2.0	160
Rh-TBP	$RhCl_3•xH_2O$	1.20	2.0	200
Pd-TBP	$Pd(OAc)_2$	0.88	2.0	180
Ag-TBP	$AgNO_3$	1.20	2.0	200
Cd-TBP	$CdCl_2•xH_2O$	1.20	2.0	200
Ta-TBP	$TaCl_5$	1.20	2.0	200
W-TBP	WCl_6	1.98	2.0	200
Re-TBP	$ReCl_3$	1.80	4.0	180
Os-TBP	$OsCl_3•3H_2O$	1.20	2.0	200
Ir-TBP	$IrCl_3•xH_2O$	0.74	4.0	140
Pt-TBP	$PtCl_2$	1.20	2.0	140
Au-TBP	$HAuCl_4•3H_2O$	1.70	2.0	200
Hg-TBP	$Hg(OAc)_2$	1.56	2.0	160

Table 12-3. Crystallographic information of V-TBP, Cr-TBP and Mn-TBP

Name	V-TBP	Cr-TBP	Mn-TBP
Empirical formula	$C_{48}H_{24}V_3N_4O_{11}$	$C_{48}H_{24}Cr_3N_4O_{10}$	$C_{48}H_{24}Mn_3N_4O_{11}$
Formula weight	985.53	972.71	997.53
Temperature/K	100(2)	100(2)	100(2)
Crystal system	monoclinic	monoclinic	monoclinic
Space group	$P2_1/m$	$P2_1/m$	$P2_1/m$
a/Å	8.3661(7)	8.558(2)	8.4747(4)
b/Å	23.0197(17)	23.052(6)	22.9811(10)
c/Å	21.6707(17)	21.786(5)	21.6619(10)
α/°	90	90	90
β/°	98.210(2)	96.432(4)	97.9360(10)
γ/°	90	90	90
Volume/Å^3	4130.7(6)	4270.8(19)	4178.4(3)
Z	2	2	2
ρ_{calc}g/cm^3	0.792	0.756	0.793
μ/mm^{-1}	0.087	0.096	0.112
F(000)	994.0	984.0	1006.0
2Θ range for data collection/°	2.208 to 37.726	2.188 to 19.26	2.208 to 31.564
Index ranges	$-13 \le h \le 12$ $-35 \le k \le 35$ $-33 \le l \le 33$	$-6 \le h \le 6$ $-18 \le k \le 18$ $-17 \le l \le 17$	$-11 \le h \le 11$ $-29 \le k \le 29$ $-28 \le l \le 28$
Reflections collected	152694	27447	112044
Independent reflections	16716 [R_{int} = 0.0526, R_{sigma} = 0.0272]	2351 [R_{int} = 0.0626, R_{sigma} = 0.0317]	10091 [R_{int} = 0.0443, R_{sigma} = 0.0210]
Data/restraints/parameters	16716/143/328	2351/739/326	10091/73/334
Goodness-of-fit on F^2	1.039	1.032	1.039
Final R indexes [I>=2σ (I)]	R_1 = 0.1380 wR_2 = 0.2649	R_1 = 0.1200 wR_2 = 0.2703	R_1 = 0.1112 wR_2 = 0.2216
Final R indexes [all data]	R_1 = 0.1636 wR_2 = 0.2759	R_1 = 0.1415 wR_2 = 0.2885	R_1 = 0.1282 wR_2 = 0.2307
Largest diff. peak/hole / e Å^{-3}	1.81/-1.46	1.39/-0.76	1.17/-1.37
CCDC	1979759	1979749	1979756

Table 12-4. Crystallographic information of Fe-TBP, Co-TBP and Ni-TBP

Name	Fe-TBP	Co-TBP	Ni-TBP
Empirical formula	$C_{48}H_{24}Fe_3N_4O_{11}$	$C_{48}H_{24}Co_3N_4O_{10}$	$C_{48}H_{24}N_4Ni_3O_{11}$
Formula weight	1000.26	993.50	1008.84
Temperature/K	100.15	100(2)	100.15
Crystal system	monoclinic	monoclinic	monoclinic
Space group	$P2_1/m$	$P2_1/m$	$P2_1/m$
a/Å	7.9287(13)	8.2860(14)	8.1793(11)
b/Å	22.890(3)	22.844(4)	22.855(3)
c/Å	21.964(3)	21.912(4)	21.779(3)
α/°	90	90	90
β/°	96.048(4)	94.680(3)	97.780(3)
γ/°	90	90	90
Volume/Å^3	3963.9(10)	4133.7(12)	4033.8(9)
Z	2	2	2
ρ_{calc}g/cm^3	0.838	0.798	0.831
μ/mm^{-1}	0.134	0.145	0.169
F(000)	1012.0	1002.0	1024.0
2Θ range for data collection/°	2.336 to 27.74	2.34 to 25.102	2.194 to 22.882
Index ranges	$-9 \le h \le 9$ $-26 \le k \le 26$ $-25 \le l \le 25$	$-8 \le h \le 8$ $-23 \le k \le 24$ $-22 \le l \le 22$	$-7 \le h \le 7$ $-21 \le k \le 21$ $-20 \le l \le 20$
Reflections collected	78471	60217	43780
Independent reflections	6582 [R_{int} = 0.0567, R_{sigma} = 0.0309]	5133 [R_{int} = 0.0586, R_{sigma} = 0.0266]	3740 [R_{int} = 0.0751, R_{sigma} = 0.0357]
Data/restraints/parameters	6582/245/334	5133/638/328	3740/582/346
Goodness-of-fit on F^2	1.010	1.034	1.046
Final R indexes [I>=2σ (I)]	R_1 = 0.1327 wR_2 = 0.2591	R_1 = 0.1167 wR_2 = 0.2287	R_1 = 0.1135 wR_2 = 0.2363
Final R indexes [all data]	R_1 = 0.1502 wR_2 = 0.2678	R_1 = 0.1537 wR_2 = 0.2553	R_1 = 0.1393 wR_2 = 0.2540
Largest diff. peak/hole / e Å^{-3}	1.40/-1.10	1.01/-0.68	0.66/-0.97
CCDC	1979738	1979739	1979737

Table 12-5. Crystallographic information of Cu-TBP, Zn-TBP and Nb-TBP

Name	Cu-TBP	Zn-TBP	Nb-TBP
Empirical formula	$C_{48}H_{24}Cu_3N_4O_{10}$	$C_{48}H_{24}Zn_3N_4O_{11}$	$C_{48}H_{24}N_4Nb_3O_{11}$
Formula weight	1007.33	1028.82	1111.44
Temperature/K	100(2)	100(2)	100(2)
Crystal system	monoclinic	monoclinic	monoclinic
Space group	$P2_1/m$	$P2_1/m$	$P2_1/m$
a/Å	8.593(2)	8.7315(6)	8.4764(5)
b/Å	22.987(5)	23.0440(16)	22.9819(10)
c/Å	21.875(5)	21.9688(14)	21.6636(10)
α/°	90	90	90
β/°	95.106(4)	93.1800(10)	97.9310(10)
γ/°	90	90	90
Volume/Å^3	4303.5(17)	4413.5(5)	4179.8(4)
Z	2	2	2
ρ_{calc}g/cm^3	0.777	0.774	0.883
μ/mm^{-1}	0.178	0.196	0.609
F(000)	1014.0	1036.0	1102.0
2Θ range for data collection/°	2.06 to 23.01	2.056 to 28.558	2.208 to 31.662
Index ranges	$-8 \le h \le 8$ $-22 \le k \le 21$ $-20 \le l \le 20$	$-10 \le h \le 10$ $-27 \le k \le 26$ $-25 \le l \le 25$	$-11 \le h \le 11$ $-29 \le k \le 29$ $-28 \le l \le 28$
Reflections collected	45678	78450	112188
Independent reflections	4128 [R_{int} = 0.0867, R_{sigma} = 0.0416]	7857 [R_{int} = 0.0476, R_{sigma} = 0.0268]	10168 [R_{int} = 0.0424, R_{sigma} = 0.0207]
Data/restraints/parameters	4128/275/324	7857/70/334	10168/499/324
Goodness-of-fit on F^2	1.025	1.012	1.060
Final R indexes [I>=2σ (I)]	R_1 = 0.0964 wR_2 = 0.2136	R_1 = 0.0963 wR_2 = 0.2418	R_1 = 0.1277 wR_2 = 0.2600
Final R indexes [all data]	R_1 = 0.1274 wR_2 = 0.2424	R_1 = 0.1140 wR_2 = 0.2547	R_1 = 0.1460 wR_2 = 0.2690
Largest diff. peak/hole / e Å^{-3}	0.90/-1.10	1.50/-2.10	1.48/-2.19
CCDC	1979742	1979740	1979741

Table 12-6. Crystallographic information of Mo-TBP, Ru-TBP and Rh-TBP

Name	Mo-TBP	Ru-TBP	Rh-TBP
Empirical formula	$C_{48}H_{24}Mo_3N_4O_{11}$	$C_{51}H_{31}Ru_3N_5O_{11}$	$C_{48}H_{24}Rh_3N_4O_{11}$
Formula weight	1120.53	1193.02	1141.44
Temperature/K	100(2)	100(2)	100(2)
Crystal system	monoclinic	triclinic	monoclinic
Space group	$P2_1/m$	P-1	$P2_1/m$
a/Å	8.3568(4)	8.7460(19)	8.3852(16)
b/Å	22.9875(10)	21.977(5)	22.973(4)
c/Å	21.6665(10)	22.851(5)	21.720(4)
α/°	90	90.764(3)	90
β/°	97.9820(10)	93.926(4)	97.436(4)
γ/°	90	92.215(3)	90
Volume/Å^3	4121.9(3)	4377.9(17)	4148.8(13)
Z	2	2	2
ρ_{calc}g/cm^3	0.903	0.905	0.914
μ/mm^{-1}	0.670	0.739	0.840
F(000)	1108.0	1184.0	1126.0
2Θ range for data collection/°	2.208 to 33.28	2.078 to 19.788	2.2 to 24.622
Index ranges	$-11 \le h \le 11$ $-31 \le k \le 31$ $-29 \le l \le 29$	$-7 \le h \le 7$ $-18 \le k \le 18$ $-18 \le l \le 18$	$-8 \le h \le 8$ $-23 \le k \le 23$ $-22 \le l \le 22$
Reflections collected	101620	30994	53023
Independent reflections	11729 [R_{int} = 0.0402, R_{sigma} = 0.0211]	4982 [R_{int} = 0.0534, R_{sigma} = 0.0357]	4893 [R_{int} = 0.0465, R_{sigma} = 0.0234]
Data/restraints/parameters	11729/226/327	4982/1059/621	4893/704/333
Goodness-of-fit on F^2	1.124	1.099	1.084
Final R indexes [I>=2σ (I)]	R_1 = 0.1296 wR_2 = 0.30093	R_1 = 0.1607 wR_2 = 0.3370	R_1 = 0.1433 wR_2 = 0.2955
Final R indexes [all data]	R_1 = 0.1451 wR_2 = 0.3193	R_1 = 0.1607 wR_2 = 0.3370	R_1 = 0.1763 wR_2 = 0.3111
Largest diff. peak/hole / e Å^{-3}	1.93/-3.26	1.40/-1.65	1.64/-2.25
CCDC	1979744	1979743	1979754

Table 12-7. Crystallographic information of Pd-TBP, Ag-TBP and Cd-TBP

Name	Pd-TBP	Ag-TBP	Cd-TBP
Empirical formula	$C_{48}H_{24}Pd_3N_4O_{10}$	$C_{48}H_{24}Ag_3N_4O_{11}$	$C_{48}H_{24}Cd_3N_4O_{11}$
Formula weight	1135.91	1156.32	1169.91
Temperature/K	100(2)	100(2)	100(2)
Crystal system	orthorhombic	monoclinic	monoclinic
Space group	Pnma	$P2_1/m$	$P2_1/m$
a/Å	14.932(3)	8.8830(19)	8.1715(6)
b/Å	23.197(4)	23.015(5)	23.0200(14)
c/Å	24.506(4)	21.896(4)	21.7463(14)
α/°	90	90	90
β/°	90	93.568(6)	97.788(2)
γ/°	90	90	90
Volume/Å^3	8488(2)	4467.8(16)	4052.9(5)
Z	4	2	2
ρ_{calc}g/cm^3	0.889	0.860	0.959
μ/mm^{-1}	0.884	0.910	1.060
F(000)	2232.0	1138.0	1144.0
2Θ range for data collection/°	2.7 to 24.546	1.494 to 34.346	2.198 to 31.644
Index ranges	$-15 \le h \le 15$ $-23 \le k \le 23$ $-24 \le l \le 25$	$-12 \le h \le 12$ $-29 \le k \le 26$ $-31 \le l \le 30$	$-10 \le h \le 10$ $-29 \le k \le 30$ $-28 \le l \le 28$
Reflections collected	107738	82969	91340
Independent reflections	4899 [R_{int} = 0.1910, R_{sigma} = 0.0646]	12664 [R_{int} = 0.1395, R_{sigma} = 0.1085]	9929 [R_{int} = 0.0451, R_{sigma} = 0.0219]
Data/restraints/parameters	4899/678/328	12664/678/328	9929/651/334
Goodness-of-fit on F^2	1.045	1.049	1.035
Final R indexes [I>=2σ (I)]	R_1 = 0.1473 wR_2 = 0.3478	R_1 = 0.1645 wR_2 = 0.3410	R_1 = 0.1725 wR_2 = 0.3714
Final R indexes [all data]	R_1 = 0.1854 wR_2 = 0.3829	R_1 = 0.2179 wR_2 = 0.3764	R_1 = 0.1855 wR_2 = 0.3763
Largest diff. peak/hole / e Å^{-3}	2.22/-2.71	2.61/-3.95	2.76/-4.80
CCDC	1979745	1979751	1979746

Table 12-8. Crystallographic information of Ta-TBP, W-TBP and Re-TBP

Name	Ta-TBP	W-TBP	Re-TBP
Empirical formula	$C_{48}H_{20}Ta_{2.03}N_4O_{11}$	$C_{48}H_{24}W_2N_4O_{11}$	$C_{48}H_{24}Re_{2.03}N_4O_{11}$
Formula weight	1200.04	1201.33	1210.70
Temperature/K	100(2)	100(2)	100(2)
Crystal system	monoclinic	monoclinic	triclinic
Space group	$P2_1/m$	$P2_1/m$	P-1
a/Å	8.8116(14)	8.7168(6)	8.549(2)
b/Å	22.950(3)	23.0161(14)	21.765(5)
c/Å	21.853(3)	21.9506(13)	23.031(6)
α/°	90	90	90.000(3)
β/°	93.611(4)	93.1780(10)	90.102(4)
γ/°	90	90	96.440(4)
Volume/Å^3	4410.5(11)	4397.1(5)	4258.6(18)
Z	2	2	2
ρ_{calc}g/cm^3	0.904	0.907	0.944
μ/mm^{-1}	0.619	0.645	0.710
F(000)	1153.0	1153.0	1160.0
2Θ range for data collection/°	1.086 to 27.726	2.058 to 26.596	2.19 to 17.766
Index ranges	$-10 \le h \le 10$ $-26 \le k \le 26$ $-25 \le l \le 25$	$-9 \le h \le 9$ $-25 \le k \le 25$ $-24 \le l \le 24$	$-6 \le h \le 6$ $-16 \le k \le 16$ $-17 \le l \le 17$
Reflections collected	68060	71642	21067
Independent reflections	7369 [R_{int} = 0.1151, R_{sigma} = 0.0733]	6526 [R_{int} = 0.0392, R_{sigma} = 0.0189]	3502 [R_{int} = 0.0550, R_{sigma} = 0.0398]
Data/restraints/parameters	7369/858/329	6526/676/330	3502/1322/548
Goodness-of-fit on F^2	1.048	1.006	0.996
Final R indexes [I>=2σ (I)]	R_1 = 0.1698 wR_2 = 0.3869	R_1 = 0.1719 wR_2 = 0.3812	R_1 = 0.1636 wR_2 = 0.3627
Final R indexes [all data]	R_1 = 0.1873 wR_2 = 0.3975	R_1 = 0.1894 wR_2 = 0.3896	R_1 = 0.1856 wR_2 = 0.3766
Largest diff. peak/hole / e Å^{-3}	2.79/-4.11	2.87/-3.52	1.47/-1.58
CCDC	1979748	1979755	1979747

Table 12-9. Crystallographic information of Os-TBP, Ir-TBP and Pt-TBP

Name	Os-TBP	Ir-TBP	Pt-TBP
Empirical formula	$C_{48}H_{24}Os_{1.98}N_4O_{10}$	$C_{48}H_{24}Ir_2N_4O_{10.6}$	$C_{48}H_{24}Pt_{2.02}N_4O_{10.64}$
Formula weight	1194.26	1210.71	1220.06
Temperature/K	100(2)	100(2)	100(2)
Crystal system	monoclinic	Triclinic	triclinic
Space group	$P2_1/m$	P-1	P-1
a/Å	8.7945(16)	8.3654(4)	8.3604(7)
b/Å	22.947(4)	21.6852(10)	21.6631(17)
c/Å	21.836(4)	23.0057(10)	23.0083(18)
α/°	90	90.0300(10)	89.9920(10)
β/°	93.404(4)	90.0530(10)	89.913(2)
γ/°	90	97.9720(10)	81.785(2)
Volume/Å^3	4398.8(13)	4133.0(3)	4124.3(6)
Z	2	2	2
ρ_{calc}g/cm^3	0.902	0.973	0.982
μ/mm^{-1}	0.708	0.798	0.847
F(000)	1142.0	1158.0	1165.0
2Θ range for data collection/°	1.498 to 19.096	2.206 to 28.778	2.058 to 32.452
Index ranges	$-7 \le h \le 7$ $-17 \le k \le 17$ $-17 \le l \le 17$	$-10 \le h \le 9$ $-25 \le k \le 25$ $-27 \le l \le 27$	$-11 \le h \le 11$ $-28 \le k \le 29$ $-30 \le l \le 30$
Reflections collected	26066	75771	114735
Independent reflections	2335 [R_{int} = 0.0957, R_{sigma} = 0.0463]	14276 [R_{int} = 0.0360, R_{sigma} = 0.0252]	20406 [R_{int} = 0.0451, R_{sigma} = 0.0307]
Data/restraints/parameters	2335/772/335	14276/934/542	20406/888/542
Goodness-of-fit on F^2	1.021	1.024	0.996
Final R indexes [I>=2σ (I)]	R_1 = 0.1542 wR_2 = 0.3406	R_1 = 0.1900 wR_2 = 0.4066	R_1 = 0.1897 wR_2 = 0.3793
Final R indexes [all data]	R_1 = 0.1803 wR_2 = 0.3630	R_1 = 0.2068 wR_2 = 0.4133	R_1 = 0.2009 wR_2 = 0.3853
Largest diff. peak/hole / e Å^{-3}	2.05/-1.79	4.30/-3.41	4.24/-4.58
CCDC	1979752	1979750	1979757

Table 12-10. Crystallographic information of Au-TBP and Hg-TBP

Name	Au-TBP	Hg-TBP
Empirical formula	$C_{48}H_{24}Au_{2.02}N_4O_{10.62}$	$C_{48}H_{24}Hg_2N_4O_{10.62}$
Formula weight	1223.52	1226.81
Temperature/K	100(2)	100(2)
Crystal system	Triclinic	Triclinic
Space group	P-1	P-1
a/Å	8.1728(6)	8.4798(4)
b/Å	21.7491(14)	21.6649(10)
c/Å	23.0198(13)	22.9828(10)
α/°	89.9790(10)	89.9800(10)
β/°	89.9540(10)	89.9590(10)
γ/°	82.212(2)	97.9230(10)
Volume/Å^3	4054.1(5)	4182.0(3)
Z	2	2
ρ_{calc}g/cm^3	1.002	0.974
μ/mm^{-1}	0.905	0.913
F(000)	1168.0	1169.0
2Θ range for data collection/°	2.198 to 30.5	2.208 to 31.258
Index ranges	$-10 \le h \le 10$ $-27 \le k \le 27$ $-28 \le l \le 29$	$-10 \le h \le 10$ $-28 \le k \le 28$ $-29 \le l \le 29$
Reflections collected	84273	108923
Independent reflections	16697 [R_{int} = 0.0417, R_{sigma} = 0.0293]	18583 [R_{int} = 0.0367, R_{sigma} = 0.0252]
Data/restraints/parameters	16697/931/542	18583/941/542
Goodness-of-fit on F^2	1.076	1.041
Final R indexes [I>=2σ (I)]	R_1 = 0.1997 wR_2 = 0.3962	R_1 = 0.1965 wR_2 = 0.3883
Final R indexes [all data]	R_1 = 0.2155 wR_2 = 0.4005	R_1 = 0.2237 wR_2 = 0.3986
Largest diff. peak/hole / e Å^{-3}	4.39/-4.78	4.66/-3.50
CCDC	1979758	1979753

Table 12-11. Frontier orbitals energy of M-TBP.

M-TBP Variant	LUFO (eV)	HOFO (eV)	Band gap (eV)
V-TBP	1.06	-0.64	1.7
Cr-TBP	1.02	-0.49	1.51
Mn-TBP	0.62	-0.65	1.27
Fe-TBP	0.88	-0.56	1.44
Co-TBP	0.56	-0.61	1.17
Ni-TBP	0.6	-0.60	1.2
Cu-TBP	0.92	-0.61	1.53
Zn-TBP	0.71	-0.55	1.26
Nb-TBP	0.79	-0.61	1.4
Mo-TBP	0.91	-0.61	1.52
Ru-TBP	0.91	-0.54	1.45
Rh-TBP	0.89	-0.69	1.58
Pd-TBP	1.08	-0.60	1.68
Ag-TBP	0.79	-0.56	1.35
Cd-TBP	0.67	-0.58	1.25
Ta-TBP	0.88	-0.63	1.51
W-TBP	0.97	-0.61	1.58
Re-TBP	0.81	-0.60	1.41
Os-TBP	0.91	-0.63	1.54
Ir-TBP	0.86	-0.51	1.37
Pt-TBP	0.76	-0.62	1.38
Au-TBP	0.81	-0.67	1.48
Hg-TBP	0.97	-0.68	1.65

12.5 References

1. Furukawa, H.; Cordova, K. E.; O'Keeffe, M.; Yaghi, O. M., The Chemistry and Applications of Metal-Organic Frameworks. *Science* **2013,** *341* (6149), 1230444.
2. Li, H.; Eddaoudi, M.; O'Keeffe, M.; Yaghi, O. M., Design and synthesis of an exceptionally stable and highly porous metal-organic framework. *Nature* **1999,** *402* (6759), 276-279.
3. Yaghi, O. M.; O'Keeffe, M.; Ockwig, N. W.; Chae, H. K.; Eddaoudi, M.; Kim, J., Reticular synthesis and the design of new materials. *Nature* **2003,** *423* (6941), 705-714.
4. Férey, G.; Mellot-Draznieks, C.; Serre, C.; Millange, F.; Dutour, J.; Surblé, S.; Margiolaki, I., A Chromium Terephthalate-Based Solid with Unusually Large Pore Volumes and Surface Area. *Science* **2005,** *309* (5743), 2040.
5. Slater, A. G.; Cooper, A. I., Function-led design of new porous materials. *Science* **2015,** *348* (6238), aaa8075.
6. Banerjee, R.; Phan, A.; Wang, B.; Knobler, C.; Furukawa, H.; Keeffe, M.; Yaghi, O. M., High-Throughput Synthesis of Zeolitic Imidazolate Frameworks and Application to CO_2 Capture. *Science* **2008,** *319* (5865), 939.
7. Mason, J. A.; Oktawiec, J.; Taylor, M. K.; Hudson, M. R.; Rodriguez, J.; Bachman, J. E.; Gonzalez, M. I.; Cervellino, A.; Guagliardi, A.; Brown, C. M.; Llewellyn, P. L.; Masciocchi, N.; Long, J. R., Methane storage in flexible metal–organic frameworks with intrinsic thermal management. *Nature* **2015,** *527* (7578), 357-361.
8. Boyd, P. G.; Chidambaram, A.; García-Díez, E.; Ireland, C. P.; Daff, T. D.; Bounds, R.; Gładysiak, A.; Schouwink, P.; Moosavi, S. M.; Maroto-Valer, M. M.; Reimer, J. A.; Navarro, J. A. R.; Woo, T. K.; Garcia, S.; Stylianou, K. C.; Smit, B., Data-driven design of metal–organic frameworks for wet flue gas CO2 capture. *Nature* **2019,** *576* (7786), 253-256.
9. Nugent, P.; Belmabkhout, Y.; Burd, S. D.; Cairns, A. J.; Luebke, R.; Forrest, K.; Pham, T.; Ma, S.; Space, B.; Wojtas, L.; Eddaoudi, M.; Zaworotko, M. J., Porous materials with optimal adsorption thermodynamics and kinetics for CO2 separation. *Nature* **2013,** *495* (7439), 80-84.
10. Reed, D. A.; Keitz, B. K.; Oktawiec, J.; Mason, J. A.; Runčevski, T.; Xiao, D. J.; Darago, L. E.; Crocellà, V.; Bordiga, S.; Long, J. R., A spin transition mechanism for cooperative adsorption in metal–organic frameworks. *Nature* **2017,** *550* (7674), 96-100.
11. Li, L.; Lin, R.-B.; Krishna, R.; Li, H.; Xiang, S.; Wu, H.; Li, J.; Zhou, W.; Chen, B., Ethane/ethylene separation in a metal-organic framework with iron-peroxo sites. *Science* **2018,** *362* (6413), 443.
12. Gu, C.; Hosono, N.; Zheng, J.-J.; Sato, Y.; Kusaka, S.; Sakaki, S.; Kitagawa, S., Design and control of gas diffusion process in a nanoporous soft crystal. *Science* **2019,** *363* (6425), 387.
13. Ma, L.; Falkowski, J. M.; Abney, C.; Lin, W., A series of isoreticular chiral metal–organic frameworks as a tunable platform for asymmetric catalysis. *Nature Chem.* **2010,** *2* (10), 838-846.
14. Lee, J.; Farha, O. K.; Roberts, J.; Scheidt, K. A.; Nguyen, S. T.; Hupp, J. T., Metal–organic framework materials as catalysts. *Chem. Soc. Rev.* **2009,** *38* (5), 1450-1459.

15. Lu, K.; He, C.; Guo, N.; Chan, C.; Ni, K.; Lan, G.; Tang, H.; Pelizzari, C.; Fu, Y.-X.; Spiotto, M. T.; Weichselbaum, R. R.; Lin, W., Low-dose X-ray radiotherapy–radiodynamic therapy via nanoscale metal–organic frameworks enhances checkpoint blockade immunotherapy. *Nature Biomedical Engineering* **2018,** *2* (8), 600-610.
16. Horcajada, P.; Chalati, T.; Serre, C.; Gillet, B.; Sebrie, C.; Baati, T.; Eubank, J. F.; Heurtaux, D.; Clayette, P.; Kreuz, C.; Chang, J.-S.; Hwang, Y. K.; Marsaud, V.; Bories, P.-N.; Cynober, L.; Gil, S.; Férey, G.; Couvreur, P.; Gref, R., Porous metal–organic-framework nanoscale carriers as a potential platform for drug delivery and imaging. *Nat. Mater.* **2010,** *9* (2), 172-178.
17. Kawamichi, T.; Haneda, T.; Kawano, M.; Fujita, M., X-ray observation of a transient hemiaminal trapped in a porous network. *Nature* **2009,** *461* (7264), 633-635.
18. Rabone, J.; Yue, Y. F.; Chong, S. Y.; Stylianou, K. C.; Bacsa, J.; Bradshaw, D.; Darling, G. R.; Berry, N. G.; Khimyak, Y. Z.; Ganin, A. Y.; Wiper, P.; Claridge, J. B.; Rosseinsky, M. J., An Adaptable Peptide-Based Porous Material. *Science* **2010,** *329* (5995), 1053.
19. Sheberla, D.; Bachman, J. C.; Elias, J. S.; Sun, C.-J.; Shao-Horn, Y.; Dincă, M., Conductive MOF electrodes for stable supercapacitors with high areal capacitance. *Nat. Mater.* **2017,** *16* (2), 220-224.
20. Wang, S.; Lee, J. S.; Wahiduzzaman, M.; Park, J.; Muschi, M.; Martineau-Corcos, C.; Tissot, A.; Cho, K. H.; Marrot, J.; Shepard, W.; Maurin, G.; Chang, J.-S.; Serre, C., A robust large-pore zirconium carboxylate metal–organic framework for energy-efficient water-sorption-driven refrigeration. *Nature Energy* **2018,** *3* (11), 985-993.
21. Lo, S.-H.; Feng, L.; Tan, K.; Huang, Z.; Yuan, S.; Wang, K.-Y.; Li, B.-H.; Liu, W.-L.; Day, G. S.; Tao, S.; Yang, C.-C.; Luo, T.-T.; Lin, C.-H.; Wang, S.-L.; Billinge, S. J. L.; Lu, K.-L.; Chabal, Y. J.; Zou, X.; Zhou, H.-C., Rapid desolvation-triggered domino lattice rearrangement in a metal–organic framework. *Nature Chem.* **2020,** *12* (1), 90-97.
22. Eddaoudi, M.; Moler, D. B.; Li, H.; Chen, B.; Reineke, T. M.; O'Keeffe, M.; Yaghi, O. M., Modular Chemistry: Secondary Building Units as a Basis for the Design of Highly Porous and Robust Metal−Organic Carboxylate Frameworks. *Acc. Chem. Res.* **2001,** *34* (4), 319-330.
23. Rood, J. A.; Boggess, W. C.; Noll, B. C.; Henderson, K. W., Assembly of a Homochiral, Body-Centered Cubic Network Composed of Vertex-Shared Mg12 Cages: Use of Electrospray Ionization Mass Spectrometry to Monitor Metal Carboxylate Nucleation. *J. Am. Chem. Soc.* **2007,** *129* (44), 13675-13682.
24. Deng, H.; Doonan, C. J.; Furukawa, H.; Ferreira, R. B.; Towne, J.; Knobler, C. B.; Wang, B.; Yaghi, O. M., Multiple Functional Groups of Varying Ratios in Metal-Organic Frameworks. *Science* **2010,** *327* (5967), 846.
25. Liu, Q.; Cong, H.; Deng, H., Deciphering the Spatial Arrangement of Metals and Correlation to Reactivity in Multivariate Metal–Organic Frameworks. *J. Am. Chem. Soc.* **2016,** *138* (42), 13822-13825.
26. Skorupskii, G.; Trump, B. A.; Kasel, T. W.; Brown, C. M.; Hendon, C. H.; Dincă, M., Efficient and tunable one-dimensional charge transport in layered lanthanide metal–organic frameworks. *Nature Chem.* **2020,** *12* (2), 131-136.

27. Kisch, H., Semiconductor Photocatalysis for Chemoselective Radical Coupling Reactions. *Acc. Chem. Res.* **2017,** *50* (4), 1002-1010.
28. Kresse, G.; Furthmüller, J., Efficiency of ab-initio total energy calculations for metals and semiconductors using a plane-wave basis set. *Computational Materials Science* **1996,** *6* (1), 15-50.
29. Kresse, G.; Furthmüller, J., Efficient iterative schemes for ab initio total-energy calculations using a plane-wave basis set. *Physical Review B* **1996,** *54* (16), 11169-11186.
30. Perdew, J. P.; Burke, K.; Wang, Y., Generalized gradient approximation for the exchange-correlation hole of a many-electron system. *Physical Review B* **1996,** *54* (23), 16533-16539.
31. Perdew, J. P.; Burke, K.; Ernzerhof, M., Generalized Gradient Approximation Made Simple. *Phys. Rev. Lett.* **1996,** *77* (18), 3865-3868.
32. Krukau, A. V.; Vydrov, O. A.; Izmaylov, A. F.; Scuseria, G. E., Influence of the exchange screening parameter on the performance of screened hybrid functionals. *The Journal of Chemical Physics* **2006,** *125* (22), 224106.